BEHAVIOR AND DESIGN OF SPREAD PRESTRESSED CONCRETE SLAB BEAM BRIDGES

A Dissertation

by

TEVFIK TERZIOGLU

Submitted to the Office of Graduate and Professional Studies of
Texas A&M University
in partial fulfillment of the requirements for the degree of

DOCTOR OF PHILOSOPHY

Chair of Committee,	Mary Beth Hueste
Co-Chair of Committee,	John Mander
Committee Members,	Gary Fry
	Mohammed Haque
Head of Department,	Robin Autenrieth

December 2015

Major Subject: Civil Engineering

ABSTRACT

The Texas Department of Transportation (TxDOT) uses precast prestressed concrete slab beam bridges in a side-by-side configuration for short span bridges in low clearance areas. A new bridge type called a spread slab beam bridge was recently developed using the same concept as spread box beam bridges in which the beams are spaced apart with precast panel stay-in-place forms between beams and a cast-in-place concrete deck. This research presents an evaluation of spread slab beam bridges in terms of design, constructability and performance. The main objective of this project is to develop appropriate design guidelines for this alternative spread slab beam bridge system. Forty-four bridge geometries are designed using standard TxDOT slab beam types to determine the feasible design space. One of the most aggressive geometries with widely spaced slab beams is constructed as a full-scale test bridge and tested under static and dynamic vehicular loads to evaluate constructability and structural performance. Load distribution behavior is investigated during field testing and the measured data is utilized to validate modeling techniques including orthotropic plate analysis, grillage analysis and finite element method based on research findings.

It is concluded that spread slab beam bridges that utilize precast concrete panels with a cast-in-place concrete deck provide a viable construction method for short-span bridges. For the tested bridge, the desired performance is achieved for in-service loading. Field testing shows that beam live load deflections are within the design limits, with no significant cracking or reduction in the overall stiffness of the bridge observed. Experimental load distribution factors (LDFs) are evaluated using alignments that provided the most adverse loading cases. Bridge responses under dynamic loads are larger compared to the static counterparts. The American Association of State Highway Transportation Officials (AASHTO) Load and Resistance Factor Design (2012) LDF equations for spread box beams are reviewed for applicability to spread slab beams and shown to range from being unconservative to very conservative when applied to spread slab beam bridges. Unique LDF expressions are developed for spread slab beam bridges to provide an appropriate estimate of load sharing for beam design.

DEDICATION

This Dissertation is dedicated to my brilliant and loving wife

Fatma Terzioglu

who always believed in me and has been a constant source of support and encouragement during the challenges of graduate school and life

ACKNOWLEDGEMENTS

I would like to express my deepest gratitude to my advisor, Dr. Mary Beth Hueste, and co-advisor, Dr. John Mander, for providing invaluable insight, expertise and guidance throughout the course of this research. I am grateful to Dr. Gary Fry for his support during field testing of the bridge and valuable advice and comments as a committee member. I am also thankful to Dr. Mohammed E. Haque for serving as my committee member.

I would like to thank Dongqi Jiang and Joel Petersen-Gauthier for their contribution and partnership and for being great friends.

I am grateful to the TTI Construction Group at Riverside, led by Gary Gerke and Eddie Haug, who provided advice and assistance during the Riverside Bridge construction. I also wish to thank the many graduate and undergraduate students who assisted in the construction of the Riverside Bridge.

Most importantly, I would like to express my heartfelt gratitude to my parents, Nihat and Ruveyda Terzioglu. None of this would have been possible without their love and continuous support.

This research was conducted at Texas A&M University and supported by TxDOT and FHWA through the Texas A&M Transportation Institute (TTI) as part of Project 0-6722, Spread Precast Concrete Slab Beams. I am also thankful to individuals from the TxDOT project monitoring comittee who were involved with this project and provided invaluable assistance.

TABLE OF CONTENTS

Page

LIST OF FIGURES

Page

LIST OF TABLES

Page

1. INTRODUCTION

1.1 BACKGROUND

Precast prestressed concrete girders have been used effectively in Texas and other states for over 60 years. The majority of these prestressed concrete bridges are simply supported spans where the cast-in-place (CIP) deck slab is made composite with precast pretensioned girders. Currently, the use of precast prestressed concrete girders provides economical bridges for short to medium spans.

Slab-on-girder bridges with medium spans ranging from 50 to 150 ft are typically constructed by seating the precast prestressed girders on bearing pads on the piers or abutments and then casting a concrete deck on top of the girders. Although different types of decks have been constructed over the years, decks in Texas are typically currently constructed to be 8 in. thick and consist of 4 in. thick stay-in-place precast prestressed concrete panels (PCPs) that are placed to span between girders with an additional 4 in. thick CIP two-way reinforced concrete topping slab.

For shorter span lengths, up to 50 ft in length, a variety of alternatives exist to the standard I-girder design. The Texas Department of Transportation (TxDOT) often uses prestressed concrete slab beam bridges as a common alternative, as shown in Figure 1.1. The conventional approach consists of placing the slab beams side-by-side and casting a 5 in. CIP reinforced concrete deck on top of the slab beams. This shallow bridge superstructure system is attractive in locations where there is a low clearance below the bridge. However, conventional slab beam bridges are more expensive compared to standard I-girder bridges that are constructed using PCPs as stay-in-place formwork between girders.

To address this issue TxDOT has shown interest in exploring new bridge systems that may provide more economical solutions for short-span bridges. One such idea that has been developed by TxDOT is to modify the current short span bridge design that uses immediately adjacent prestressed concrete slab beams shown in Figure 1.1(a). The proposed solution is to spread out the slab beams and to use a conventional topped panelized deck as shown in Figure 1.2. It is anticipated that spread slab beam bridges will result in a possible reduction in the overall bridge cost while providing another design alternative for short span bridges. Figure 1.2(b) shows a typical cross-section of a spread slab beam bridge superstructure.

For spread slab-beam construction, the moments and shears imposed by eccentrically located truck loads will differ in the individual slab-beams across the overall bridge deck cross-section. Appropriate girder load distribution factor (LDF) formulas for this case are not available in the *American Association of State Highway and Transportation Officials (AASHTO) LRFD Bridge Design Specifications* (AASHTO 2012) and need to be investigated. While this study aims to improve the overall economy of the proposed spread-slab beam deck configuration, the principal research focus is directed toward developing recommendations for this bridge type, with a particular emphasis on establishing appropriate LDFs for this class of spread slab beam bridges.

1.2 SIGNIFICANCE

Bridges built using prestressed concrete girders topped with PCPs as stay-in-place formwork and a CIP reinforced concrete deck provide an economical approach for bridge construction. Designers and contractors are still investigating the possibilities of building prestressed concrete bridges with greater economy. There are several ways of reducing the overall cost of a bridge. This research focuses on reducing the number of girder lines for slab beam bridges.

TxDOT already utilizes slab beam bridges for short span bridges up to 50 ft in length. While conventional slab beam bridges are used extensively, experience shows they are more expensive than traditional slab-on-I-girder structures on a per square foot basis. Spread slab beam bridges use the same idea as I-girder bridges by spreading the slab beams to reduce the overall cost of that type of bridge. This research investigates the potential of the spread slab beam bridge systems, evaluates the constructability and in-service performance, and develops design recommendations with a focus on appropriate relationships for load distribution factors.

1.3 OBJECTIVES AND SCOPE

The objective of this project is to explore the use of slab beams that are used in a spread configuration for short span bridges and to provide appropriate design recommendations. Finally, Field investigations are undertaken to experimentally observe load distribution factors (LDFs) under static and dynamic truck loading. A spread slab beam bridge with widely spaced slab beams constructed at the Texas A&M University (TAMU) Riverside Campus as part of this research, The purpose of the experimental study is to evaluate the in-service performance

and to measure the shear and moment LDFs during controlled load tests. The development of LDFs for slab beam bridges is achieved using appropriate models that are calibrated with field measurements and exploring the design space to determine appropriate load sharing relationships for this class of bridges.

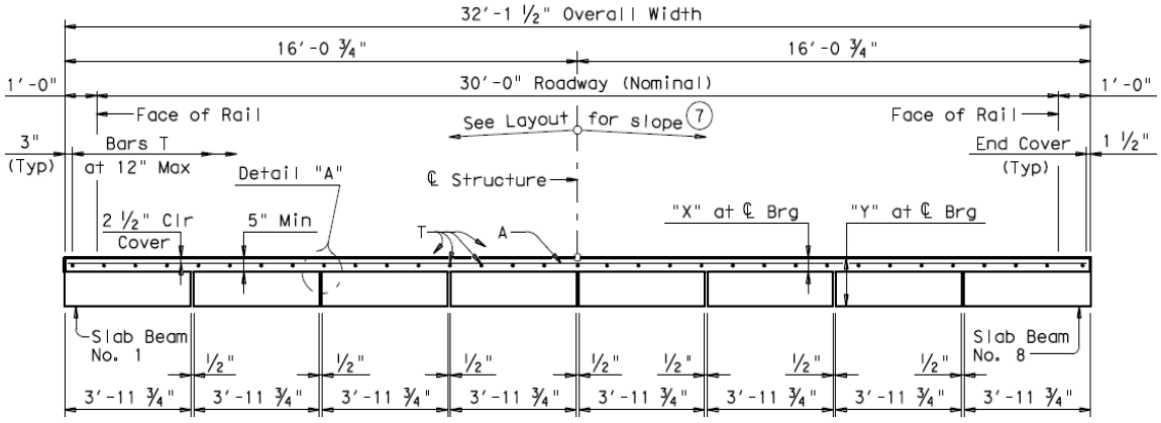

(a) Conventional Prestressed Concrete Slab Beam Bridge Design

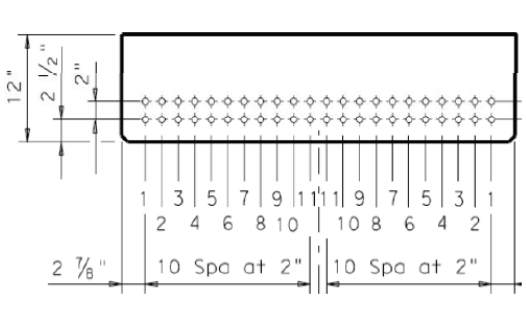

(b) 4SB12 Slab-Beam Prestressing Locations

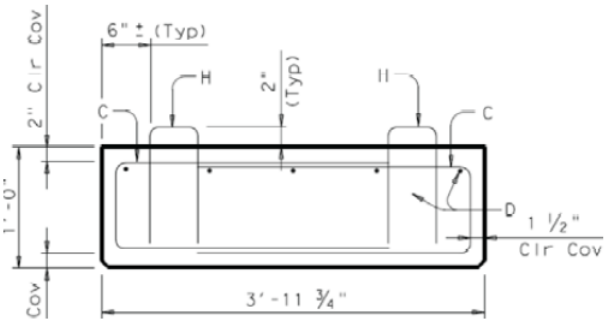

(c) 4SB12 Slab-Beam Mild Steel Reinforcing

Figure 1.1. Typical Details of Prestressed Concrete Slab Beams and Bridge Deck (TxDOT 2013b).

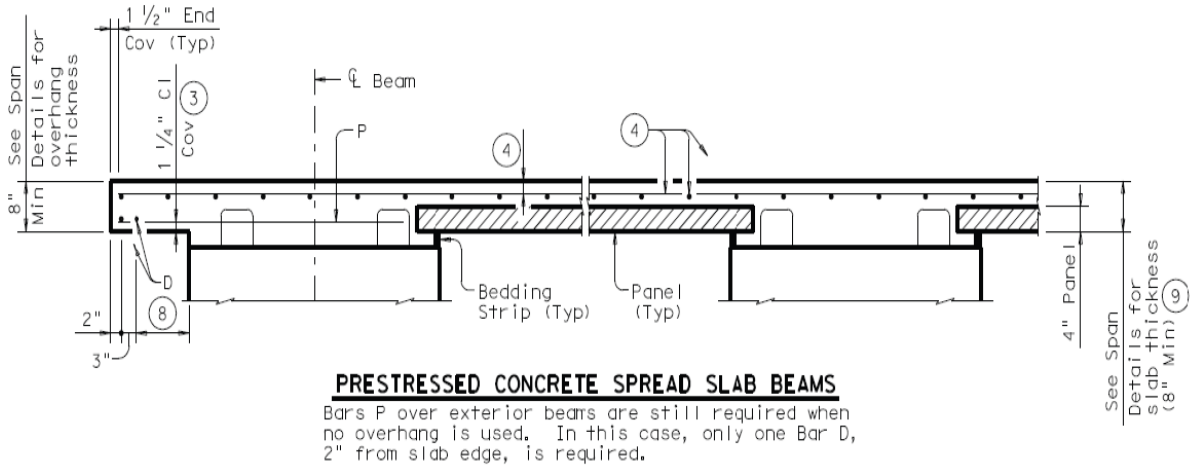

(a) Bridge Deck with PCPs

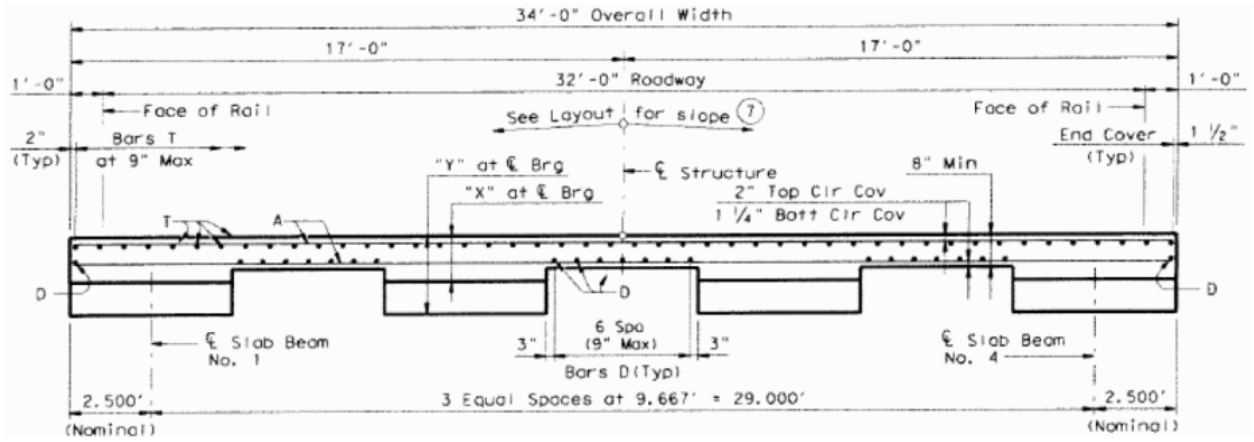

(b) Transverse Section with Fully Cast-in-Place Deck

Figure 1.2. Recent TxDOT Bridge Design Details for Spread Slab Beam Bridges (TxDOT 2013b).

As part of this research, constructability and performance of spread slab beam bridges were evaluated. It was found that the camber of slab beams increase up to 4.5 in. prior to CIP deck placement. The camber increase rate due to creep and the effect of high camber in terms of constructability and long term issues were studied.

Another concern was the development of a longitudinal crack at the transverse center along the length of the bridge. It was anticipated that the crack occurred due to temperature effects. Theoretical aspects of these temperature loads and shrinkage were studied and reasons for this type of cracking was investigated.

The scope of this project also covers modeling the experimental bridge using several theoretical and numerical methods including, grillage method and finite element method (FEM). Accuracy and assumptions of these approaches was discussed in detail.

As part of the LDF study, effect of other parameters that are not included in derivation of proposed LDF equations was also investigated. The effect of vehicle type, vehicle edge distance, skew, overhang and haunch thickness to lateral load distribution was studied.

One of the important parameters that influence the response of a bridge is the skew angle. A parametric study was conducted to evaluate the effect of skew angle to moment and shear response of spread slab beam bridges.

1.4 RESEARCH PLAN

The major objective of this research is to explore the possibility of using slab beams in a spread configuration in order to provide an alternative bridge type for TxDOT for short span bridges that are potentially more economical than conventional slab beam bridges. For that purpose the constructability and issues encountered during construction was discussed. The research includes experimental assessment of spread slab beam system by testing a full-scale field bridge. The bridge data was used to confirm the modeling approach for this bridge configuration. Alternative modeling approaches including finite element and grillage analysis were evaluated. Appropriate live load distribution factors for spread slab beams were developed based on analytical models representing the design space for this bridge type. Three key parameters including beam spacing, span length and beam depth were used for deriving new LDF equations. The proposed LDFs were compared with the AASHTO (2012) spread box beam LDF formulas to investigate their applicability to spread slab beam bridges.

Other important parameters that were neglected in the LDF study were investigated to assess their importance and verify the assumptions. Parametric studies were conducted using FEM analysis. Those parameters can be listed as follows.

- Load Type,
- Vehicle edge distance,
- Haunch thickness,
- Skew angle,
- Overhang.

The following work plan was carried out in order to achieve the objectives of the project. The work plan consists of eight tasks and the details of each task are described herein.

1.4.1 Synthesize Literature and State-of-the-Practice

A comprehensive literature review was compiled related to development of live load distribution factors and available methods of analysis. The comprehensive review includes papers published in journals and conferences, along with agency reports. Very limited information is available in the literature specifically for spread slab beam bridges; however, some information was found for spread box beam bridges. Key findings of the literature review were documented. These findings were used in this study to guide the development of the experimental program along with determination of appropriate live load distribution factors.

1.4.2 Preliminary Designs

Preliminary designs were carried out using the AASHTO LRFD Specifications (2012) and the design guidelines provided in *TxDOT Bridge Design Manual* (TxDOT 2013a) to ensure that the findings can be compared with typical slab beam bridge geometries and standard designs. This comparison provided initial assessment of the potential benefits of a spread slab beam configuration. Material properties, standard slab beam types, and common Texas bridge widths were selected based on input from TxDOT.

Viable spread slab beam bridge geometries were chosen according to practical beam spacing and bridge width criteria. A total of 44 spread slab beams were designed using the maximum permissible concrete design strength. One of the preliminary designs with a large eccentricity due to a wide beam spacing and a relatively longer span length was chosen for the full-scale bridge construction and field testing. The detailed design of that bridge (34 ft wide, 46 ft 7 in. long, using four 5SB15 slab beams) is documented in Appendix A.

1.4.3 Riverside Bridge Design and Construction

A full-scale spread slab beam bridge was constructed and field tested at the Texas A&M University Riverside Campus. The final bridge geometry was determined based on the preliminary designs and the input from TxDOT Project Monitoring Committee (PMC). The spread slab beam bridge has a 46 ft 7 in. (center-to-center of bearing pads) span, 34 ft width, 9 ft 8 in. center-to-center beam spacing, and utilizes four 5SB15 slab beams.

The slab beam girders were produced by Bexar Concrete Works in San Antonio, Texas. Numerous samples were taken from the concrete mixes used to construct the precast girders to test various mechanical properties of the girder concrete. The girders were transported to Riverside Campus and erected on the bridge supports that were constructed in advance such that top of the bridge would be even with the existing runway. Then PCPs were placed between slab beam girders as stay-in-place formwork. After placing the precast components a reinforced concrete cast-in-place (CIP) deck was placed on top of the slab beams. The concrete mixture for the deck concrete was also sampled in order to measure and document the fresh and hardened properties.

This research aims to evaluate the constructability of this type of bridge and provide guidelines and assessments for these difficulties. Issues encountered during the construction are the high camber of slab beams and the development of a longitudinal crack along the length of the bridge. Although these issues were addressed and did not pose a risk for constructability, further investigation for evaluating long term creep effects to camber and the temperature effects to cracking was discussed.

1.4.4 Full Scale Bridge Field Test

The full-scale Riverside Bridge was fully instrumented to evaluate the bridge response under service loads. Load cells that were placed at the abutment seats at both ends of slab beams were used to monitor the load sharing between girders. Measured reactions were used for validating the analytical model and determining experimental live load distribution factors for shear. Deflection measurements along the length of each beam at frequent intervals were recorded using string potentiometers. Moments at the mid-pan of each beam were then inferred using the deflection profiles of the slab beams. In addition, accelerometers were installed to determine the modal characteristics of the bridge. Measured deflection profiles and frequency response were used for verification of the finite element model developed for the bridge.

Secondary instrumentation was also installed for verification of alternative instrumentation methods. Strain gages were installed at the midspan to infer moment LDFs through variation of strains between girders. Calculated moment LDFs were then compared with those calculated from deflection profiles measured using string potentiometers. Linear variable displacement transducers (LVDTs) were used at the supports to measure bearing pad

deformation to infer variation of the reactions between girders. The calculated shear distribution factors were compared with those based on the direct load cell measurements.

The static and dynamic loading of the bridge was achieved using a TTI dump truck and TTI water tanker with known axle weights. Vehicles were placed statically at critical moment and shear locations for investigating the LDFs and evaluating the bridge response. The same vehicles were also driven along the predefined lanes at speeds from 30 to 40 mph. The measured response was used to evaluate the appropriateness of different analytical models and for the validation of the chosen finite element modeling technique.

1.4.5 Analysis of Field Testing Results

All instrumentation readings from the Riverside Bridge were digitally recorded using a PC based data acquisition system. The measured experimental results were processed and reviewed to better understand the in-service response of the spread slab beam system. The measured data was processed to obtain moment and shear distribution factors. The load sharing between slab beam girders for flexural and shear responses were obtained. In addition, deflection profiles in the longitudinal directions of each girder and the frequency response of the bridge were also obtained. The measured response was then used to validate the FEM and grillage analysis modeling techniques to evaluate the accuracy of alternative methods for modeling spread slab beam bridges.

1.4.6 Live Load Distribution Factors

Designing a bridge girder requires computing the moment and shear demands for an individual girder. Calculating the response of an individual bridge girder to a vehicular live load is complex task due to coupled transverse and longitudinal effects. This complexity stems from the variation of girder spacing, span length, vehicle positions, etc. Designers and bridge design specifications simplify the problem by uncoupling the transverse and longitudinal effects using live load distribution factors. The AASHTO LRFD Specifications (2012) lists LDFs for several standard bridge types and their applicable ranges. AASHTO LRFD Specifications (2012) does not have approximate LDFs for spread slab beam bridges. However, spread box beam LDF formulas are provided and was used for preliminary designs. As part of this research, the AASHTO LRFD Specifications (2012) spread box beam formulas were reviewed for their applicability to spread slab beam bridges. Total bridge spans between 31–52 ft and girder

spacings from 6.5 to 11 ft (center-to-center) were investigated for evaluating the LDFs. Load distribution factors were obtained for 31 spread slab beam bridges having different geometries using FEM modeling techniques that were validated using experimental results. Recommendations are provided for LDFs that may be used for design of spread slab beam bridges.

1.4.7 Effect of Additional Parameters

The effect of many geometric and loading parameters were neglected while deriving the LDF equations. Only key parameters; span Length, *L*, beam spacing, *S* and beam depth, *d* were considered for the derivation. A parametric study were conducted to investigate the effect of additional parameters such as, skew, overhang, haunch, vehicle edge distance and load type. Total of 28 different FEM analysis conducted with different geometries or load configurations. Correction factors were developed for the parameters which have prominent effect on LDFs.

1.4.8 Organization of this Dissertation

The above listed tasks and related findings are reported in this dissertation include: (1) an introduction covering the significance, objectives and scope of the research project, (2) a comprehensive synthesis of literature and the current state-of-the-practice, (3) designs of spread slab beam bridges, (4) Riverside Bridge construction and issues, (5) experimental program, results of the full-scale bridge field test, (6) modeling of experimental bridge and verification of modeling approach , (7) results of analytical studies to evaluate the AASHTO (2012) live load distribution factors and development of proposed LDF equations, (8) parametric study to investigate the effect of additional parameters to LDFs, and (8) summary of findings, design recommendations and conclusions.

1.5 OUTLINE

Following this introductory section, Section 2 provides a comprehensive literature review related to slab beam bridges, current analysis methods, and live load distribution factors. Papers and reports published in journals were summarized within this section. Section 3 describes all designs that were investigated in order to bound spread slab beam bridges in terms of ranges of applicability of critical parameters, including beam spacing, span length, and girder depth. Also, the field bridge geometry was selected using these designs. Section 4 summarizes the construction of Riverside Bridge and discuss the constructability issues. High camber of slab beams due to time dependent effects was discussed. Deck cracking due to temperature induced stresses was studied and reported in this section. Section 5 documents the experimental program for the Riverside Bridge. Analyses of the experimental results are provided in this section. Section 6 outlines the current analytical methods for modeling bridges and evaluates the results for the Riverside Bridge by comparing them to experimental results. Section 7 discusses the methods for deriving the current AASHTO LRFD Specifications (2012) LDFs and derivation of new LDFs for spread slab beam bridges following a similar methodology as AASHTO LRFD Specifications (2012). Section 8 provides details of the parametric studies that were conducted to investigate the effect of other parameters such as skew, overhang, haunch, vehicle edge distance and load type. Section 9 presents the summary, conclusions, design recommendations, and recommendations for future research. Appendix A documents a detailed design example for a typical interior prestressed slab beam in a spread slab beam bridge based on the AASHTO LRFD Specifications (AASHTO 2012) and the *TxDOT Bridge Design Manual* (TxDOT 2013a), and using the approximate spread box beam LDFs. The designed bridge geometry is the same as the Riverside Bridge. Appendix B presents the Riverside Bridge construction process with construction photos and drawings. Appendix C provides tabular summaries of the load distribution factor results used for derivation of the proposed load distribution factor formulas. A complete set of drawings for the Riverside Bridge, along with as built information, is provided in the Supplement to the dissertation.

2. LITERATURE REVIEW

2.1 BACKGROUND

Several early studies have focused on developing more economical precast concrete bridge types for short span bridges. The Texas Department of Transportation (TxDOT) sponsored a research study conducted by Panak (1982). This study indicates that prestressed I-beams with cast-in-place slabs and pan girder slabs were the most economical and common bridge types in Texas in the 1960s and 1970s. In 1969 Texas was the first state to use side-by-side precast box beam bridges. In those days the cost of box beam bridges was significantly higher than the other two bridge types. Panak proposed five alternative precast superstructure types including precast concrete box beams, PCI box beams, precast concrete double tee beams, precast concrete voided slabs, and precast concrete solid slabs. Unfortunately none of these alternatives provided more economical solutions in 1980s due to lack of economical manufacturing and construction techniques and lack of competition within the precast industry.

The Louisiana Department of Transportation (DOT) sponsored a research investigation focused on reducing the cost of short span bridges with spans up to 50 ft (McKee and Turner 1975). The study investigated superstructure options that can be erected rapidly while using the erected portions as working platforms. The designs were limited to a 100 ton crane capacity. Several popular precast girder types including voided slabs, channels, and box sections were designed. However, designers indicated that these new designs did not appear to provide more economical solutions. It was concluded that substantial progress in both manufacturing and construction procedures, along with increased competition in the industry, were needed to reduce costs.

Substantial progress has been made in both the construction and precast manufacturing industry during the last thirty years. Also, there have been some changes to the design criteria that impact the design of prestressed concrete bridge structures. Currently, slab beam bridges are used extensively due to their ease of fabrication and transport, along with constructability. However, they are more expensive than traditional prestressed I-Beam and I-Girder bridges because the slab beams are placed immediately adjacent to one another. As such, the proposed spread prestressed slab beam bridge system presents a timely opportunity to revisit this

important class of bridge structures with the goal of increasing the economy of short span bridges.

One key issue for developing a new bridge superstructure system is identifying appropriate live load distribution factors (LDFs). Although there are other viable methods of analysis for calculating moment and shear demands, such as the grillage and the finite element method (FEM), bridge design engineers prefer using approximate LDFs that are provided in the *American Association of State Highway and Transportation Officials* (*AASHTO) Load and Resistance Factor Design (LRFD) Bridge Design Specifications* (AASHTO 2012) for several bridge superstructure types. There are no approximate formulas provided for spread slab beams; part of this study is to determine whether the spread box beam formulas might also be applicable to spread slab beams.

The main topics covered by this literature review include the history of the *S*/*D* LDFs used from 1931 until 2002 in the *AASHTO Bridge Standard Design Specifications* (AASHTO 1996; AASHTO 2002; Newmark 1938). The development, use, and assessment of modern bridge LDFs (AASHTO 1994; AASHTO 2012) are also summarized herein. Analytical models are also discussed, including the FEM and grillage methods of analysis that were used in conjuncture with LDFs to accurately determine and confirm load distribution.

2.2 LIVE LOAD DISTRIBUTION FACTORS (LDF)

Load distribution factors, which refers to wheel load distribution in *AASHTO Standard Specifications for Highway Bridges* and lane load distribution in *AASHTO LRFD Bridge Design Specifications*, are important parameters for calculating the live load response and consequently determining member dimensions. It provides a simplified method of calculating moment and shear demand of an individual girder by treating longitudinal and transverse effects of the vehicle loading as uncoupled. Resulting moments and shears of a girder due to truck loading can simply be calculated by multiplying the moment and shear reactions of an isolated simple beam with live-load distribution factor.

2.2.1 History of Simple S/D Formulas (1931 to 2002)

Early live load distribution factors were developed based on the work by Westergaard (1930) and Newmark (1938) and slightly updated over time as new research became available to

increase accuracy. The concept of LDFs was first introduced by empirical *S/D* formulas in 1931 by *American Association and State Highway Officials* (*AASHO) Standard Specification for Highway Bridges* (AASHO 1931)These formulas, which also known as "S-over" equations, were used by AASHTO in all Standard Specifications for Highway Bridges until the 17th edition (AASHTO 2002). These equations were used to estimate the shear and moment forces that occurs due to vehicle loading in an individual girder within the bridge superstructure. The LDF values were calculated by *S/D* equation, where *S* is the center-to-center spacing of girders and *D* is a constant that depends on the bridge type and geometry.

Figure 2.1 presents the first *S/D* LDF equations for several bridge types provided in first edition of AASHO (1931). And Figure 2.2 shows the *S/D* LDF equations for selected bridge types provided in the last edition (17th edition) of *AASHTO Standard Specification for Highway Bridges* (AASHTO 2002). These figures shows the change in '*D'* coefficients over time. Although these equations were used successfully for many years, researchers noted several shortcomings of empirical '*S*-Over' equations due to changes over many years. (Zokaie et al. 1991). They listed these shortcomings in NCHRP 12-26 report as;

- Inconsistent reduction factors for multi-lane loaded bridges.
- Inconsistent changes of LDF factors for changing lane widths.
- Lack of an approach for verification of LDFs for different bridge types and geometries.

In addition to inconsistencies, *S/D* equations does not take into account many important key parameters such as longitudinal stiffness, span length, skew and continuity. On the other hand there were no other guidelines in AASHTO Standard Specifications for the range of applicability of these simplified equations. Because of these facts, in order to increase the range of applicability of LDF equations for longer spans, skewed and continuous bridges, it was decided to develop new more consistent way of calculating LDFs.

Kind of floor	Floor designed for one traffic lane		Floor designed for two or more traffic lanes	
	Fraction of a wheel load to each stringer	Limiting stringer spacing in feet	Fraction of a wheel load to each stringer	Limiting stringer spacing in feet
	S		S	
Plank	4.0	4.0	3.5	5.0
Strip 4 inches in thickness or wood block on 4 inches plank subfloor	S / 4.5	4.5	S / 3.75	5.5
Strip 6 inches or more in thickness	S / 5.0	5.0	S / 4.0	6.0
Concrete	S / 6.0	6.0	S / 4.5	10.0

S=spacing of stringers in feet.

Figure 2.1. Distribution of Bending Moments in Stringers (AASHO 1931).

Kind of Floor	Bridge Designed for One Traffic Lane	Bridge Designed for Two or more Traffic Lanes
Timber:[a]		
Plank[b]	S/4.0	S/3.75
Nail laminated[c] 4" thick or multiple layer[d] floors over 5" thick	S/4.5	S/4.0
Nail laminated[c] 6" or more thick	S/5.0 If S exceeds 5′ use footnote f.	S/4.25 If S exceeds 6.5′ use footnote f.
Glued laminated[e] Panels on glued laminated stringers		
4" thick	S/4.5	S/4.0
6" or more thick	S/6.0 If S exceeds 6′ use footnote f.	S/5.0 If S exceeds 7.5′ use footnote f.
On steel stringers		
4" thick	S/4.5	S/4.0
6" or more thick	S/5.25 If S exceeds 5.5′ use footnote f.	S/4.5 If S exceeds 7′ use footnote f.
Concrete:		
On steel I-Beam stringers[g] and prestressed concrete girders	S/7.0 If S exceeds 10′ use footnote f.	S/5.5 If S exceeds 14′ use footnote f.
On concrete T-Beams	S/6.5 If S exceeds 6′ use footnote f.	S/6.0 If S exceeds 10′ use footnote f.
On timber stringers	S/6.0 If S exceeds 6′ use footnote f.	S/5.0 If S exceeds 10′ use footnote f.
Concrete box girders[h]	S/8.0 If S exceeds 12′ use footnote f.	S/7.0 If S exceeds 16′ use footnote f.
On steel box girders	See Article 10.39.2.	
On prestressed concrete spread box Beams	See Article 3.28.	
Steel grid:		
(Less than 4" thick)	S/4.5	S/4.0
(4" or more)	S/6.0 If S exceeds 6′ use footnote f.	S/5.0 If S exceeds 10.5′ use footnote f.
Steel bridge Corrugated plank[i] (2" min. depth)	S/5.5	S/4.5

Figure 2.2. Distribution of Wheel Loads in Longitudinal Beams (AASHTO 2002).

2.2.2 Research Studies Evaluating S-Over Equations (1964 - 1991)

Although simple *S/D* equations were over-conservative for many bridge geometries, they were generating reasonably accurate results for girder spacings around 6 ft and bridge spans around 60 ft. These equations were valid for normal bridges (girders perpendicular to abutments) and for simply supported spans. After 1950s most of the modern highway bridges started to have longer spans, skewed supports, curved alignments and continuous interior piers. As the demand for new and challenging bridge superstructure increases, researchers raised the question about accuracy of *S/D* equations and have studied their applicability and suggested new equations for many cases.

2.2.2.1 LDF Studies Conducted on Spread Box Beam Bridges

In 1964 Fritz laboratory at Lehigh University initiated a research for investigating the load distribution behavior of spread box beam bridges. This study was focused on testing five spread box beam bridges to develop design guidelines for bridge engineers. As part of this research Douglas and Vanhorn (1966) conducted an experimental study for Drehersville Bridge with the objective of investigating static load distribution between girders. They found that the experimental load distribution factors were significantly different than the code specified values. At the time of this research AASHTO specified a distribution factor of *S*/5.5 for interior girders of spread box beams.

Guilford and Vanhorn (1967a) conducted a second set of tests on the same bridge to investigate the effect of moving vehicles on load distribution by running the trucks up to 34 mph. The results were compared with the one with crawling speed (2 mph). It was found that the amplification is smaller than the code specified factor and distribution factors was not affected by the increasing vehicle speed.

Schafer and Vanhorn (1967) studied the effect of skew on load distribution by conducting an experimental program on Brookville Bridge in Pennsylvania. The results were compared with a right bridge (Drehersville Bridge) having similar characteristics. They found that deflections and moments as well as load distribution factors were lower that right bridge. The findings does not include any results about the distribution of shear forces.

Lin and Vanhorn (1968) investigated the effect of midspan diaphragms by testing the Philadelphia Bridge. It was found that the deflections and distribution of load is slightly

reduced due to diaphragm when the bridge loaded by one truck. But when the bridge is loaded by two truck the distribution factors were not affected considerably. It was also found that LDFs were significantly lower for interior girders and higher for exterior girders than AASHO specified values. The effect of girder spacing was also studied by comparing the results with those from Drehersville Bridge tests. Distribution factors was found to be higher for larger girder spacing. Experimentally determined moment and deflection distribution coefficients were compared with theoretical values calculated using Guyon-Massonett method, which was developed by M. Y. Guyon based on orthotropic plate theory. Theoretical distribution coefficients were in reasonable agreement with experimental results within 4 to 15 percent range.

2.2.2.2 Development of More Accurate LDF Equations

Sanders and Elleby (1970) conducted a research study to develop more realistic and accurate wheel load distribution factors than S-Over equations. They developed equations for three major bridge types including, beam and slab, multi-beam and cast-in-place concrete box girder bridges. The study was limited for short and medium span bridges up to 120 ft span length. The proposed equations take into account several different key parameters such as aspect ratio (width/span) relative beam to deck stiffness, diaphragm stiffness and material properties. They developed the equations using general plate theory and adopted several modification of plate theory depending on the bridge type. They concluded that the LDF equations provided in AASHO does not provide realistic results for many bridge types because of the neglected parameters. They also stated that the major parameters effecting LDFs are relative flexural and torsional stiffness in longitudinal and transverse directions, bridge width and bridge span.

Brockenbrough (1986) studied LDFs for curved I-Girder bridges in order to investigate the applicability of AASHTO design values and develop more rational factors. The study was conducted using FEM. Models were studied to investigate the effect of central angle, span length, girder stiffness, girder spacing and cross-frame spacing. The parametric study showed that girder stiffness and cross-frame spacing has relatively small effect on the LDFs. The central angle and girder spacing have significant effect on LDFs. The comparative results showed that reasonable design values can be obtained for exterior girders from V-load

modification provided in AASHTO, but they give overly conservative results for interior girders.

Hays et al. (1986) studied lateral distribution factors for simply supported bridges for flexural response using a computer program, SALOD, which was developed for Florida Department of Transportation. The study was focused on prestressed concrete girder, steel girder, T-Beam and flat slab bridges. It was found that the span length considerably effects the flexural LDFs. But AASHTO neglects the effect of span length resulting in unconservative values for short span bridges and very conservative values for long span bridges. On the other hand AASHTO gives a good estimate for the flexural response of exterior girders by using simple beam criterion.

Marx et al. (1986) developed a more detailed formula by considering the effect of girder spacing, girder stiffness, span length, slab thickness and skew for calculating distribution of wheel loads for moment. This new formula considers the multi-lane reduction factor and applicable to all slab-and-beam bridges. Based on the analyzed bridge geometries in this study, it was found that AASHTO S-over equation results in 12 percent unconservative to 32 percent conservative design moments in interior girders compared to FEM values. The proposed equation always give more accurate results being within 7 percent of FEM. On the other hand AASHTO criterion for calculating the bending moments in exterior girders, which treats the slab as if it is simply supported between girders, gives up to 23 percent unconservative results.

The effect of skew on bending moment was also investigated as part of this study. It was found that the moment response reduces as the skew angle increases. The skew reduction factors is below 5 percent up to 30 degree skew. But the effect of skew is more prominent as skew angle gets bigger than 45 degrees. The skew reduction factors can go up to 38 percent for skew angles about 60 degrees.

Bakht and Moses (1988) conducted as study for evaluating the AASHTO load distribution factors and developing more comprehensive formulas for slab-on-girder bridges. It was noted that the overly simplistic S-over formulas do not consider many important bridge parameters such as span length, longitudinal stiffness, edge stiffening, and vehicle edge distance (VED). Whereas the new proposed formula takes into account all these parameters in addition to girder spacing. It was found that edge stiffening and VED can significantly affect the LDFs. The proposed approach is developed similar to AASHOT *S/D* formulas, but

calculating the *D* value by taking into account all bridge parameters. This criteria provides flexibility for the design engineers and gives accurate results when compared with rigorous computer based analysis. *D* value is calculated based on the longitudinal and torsional stiffness, number of lanes, lane width, vehicle edge distance and edge stiffening. The formula inherently includes multi-lane reduction factor.

Khaleel and Itani (1990) conducted a research study to investigate lateral moment LDFs for slab-on-girder bridges for continuous and skewed bridges. FEM models for 112 pretensioned I-girder bridges having girder spacing between 6 to 9 ft, span between 80 to 120 ft and skew angle between 0 to 60 degrees were analyzed. In this study, new procedure for calculating the LDFs were developed. This procedure suggest multiplying *S/D* equation with a skew reduction factor and impact factor and suggests calculating the *D* value as a function of *H*, *b* and *a*, where *H* is the ratio of longitudinal flexural stiffness of composite section to the transverse flexural stiffness of the slab and first introduced by Marx et al. (1986), *b* is the girder spacing and *a* is the half span length. These parameters were introduced based on the idea that the bridge response is a function of relative stiffness of deck to girder and the aspect ratio of *b*/*a*. The proposed equation estimates the moment values within 8 percent of the FEM. For some cases (AASHTO 1989) underestimates the interior girder moments up to 6 percent, but for most cases AASHTO value is up to 40 percent conservative. On the other hand AASHTO simply supported criteria for exterior girders give 28 percent unconservative moment results compared to FEM values. For large spans, large skew, small girder to slab stiffness and small girder spacings, exterior girders control the design. Large skew angle always result in a smaller moment. For interior girders skew reduction factor goes up to 6 percent for angles smaller than 30 degrees and up to 29 percent for 60 degree skew. On the other hand skew reduction is less than 10 percent for exterior girders when the angle is less than 45 degree. It goes up to 20 percent for 60 degree skew.

Bishara et al. (1993) studied the effect of different bridge parameters on the load distribution factor for simply supported I-Beam bridges. New LDF expressions were derived by analyzing 36 different bridge geometries using FEM. These expressions consider the sensitivity of LDF to bridge span, skew angle, bridge width, girder spacing and number of loaded lanes. Proposed formulas were expressed in a similar format to (AASHTO 1989) equations (*S/D*). But *D* values were formulized more accurately by taking into account the

effect of other bridge parameters. It was found that the reduction of moment distribution factor is less than 5 percent for skew angles smaller than 30 degrees and can go up to 28 percent for 60 degree skew. The skew reduction for exterior beams are always smaller than interior beams. Therefore for high skew and long span bridges exterior girders may control the flexural design. In order to find more accurate factors for high skew angles a correction factor was introduced for skew angles larger than 30 degrees.

2.2.3 Development of Current AASHTO LDF Formulas (1985 to 1991)

Current LDF formulas provided in AASHTO (2012) were first introduced in the first edition of *AASTO LRFD Bridge Design Specifications* (AASHTO 1994) and have not been changed since then. These LDF formulas derived by Zokaie et al. (1991) as part of the NCHRP 12-26 research project and covers wide range of bridge types and geometries. While these updated LDF equations are also simplified, they consistently provided conservative results for the bridges within the specified range of bridge geometries. Table 2.1 shows several common bridge types and Table 2.2 lists the new LDF formulas and their range of applicability for these common bridge types introduced in (AASHTO 1994).

Table 2.1. Several Common Bridge Types (AASHTO 1994).

Supporting Components	Type Of Deck	Typical Cross-Section
Steel Beam	Cast-in-place concrete slab, precast concrete slab, steel grid, glued/spiked panels, stressed wood	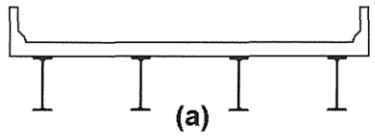 (a)
Closed Steel or Precast Concrete Boxes	Cast-in-place concrete slab	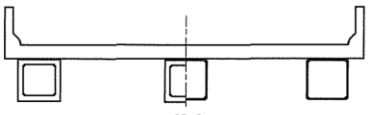 (b)
Open Steel or Precast Concrete Boxes	Cast-in-place concrete slab, precast concrete deck slab	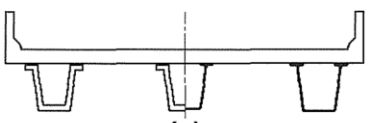 (c)

Table 2.2. LDFs for Moment in Interior Beams (AASHTO 1994).

Type of Superstructure	Applicable Cross-Section from Table 4.6.2.2.1-1	Distribution Factors	Range of Applicability
Wood Deck on Wood or Steel Beams	a, l	See Table 4.6.2.2.2a-1	
Concrete Deck on Wood Beams	l	One Design Lane Loaded: $S/12.0$ Two or More Design Lanes Loaded: $S/10.0$	$S \le 6.0$
Concrete Deck, Filled Grid, Partially Filled Grid, or Unfilled Grid Deck Composite with Reinforced Concrete Slab on Steel or Concrete Beams; Concrete T-Beams, T- and Double T-Sections	a, e, k and also i, j if sufficiently connected to act as a unit	One Design Lane Loaded: $0.06+\left(\frac{S}{14}\right)^{0.4}\left(\frac{S}{L}\right)^{0.3}\left(\frac{K_g}{12.0Lt_s^3}\right)^{0.1}$ Two or More Design Lanes Loaded: $0.075+\left(\frac{S}{9.5}\right)^{0.6}\left(\frac{S}{L}\right)^{0.2}\left(\frac{K_g}{12.0\,Lt_s^3}\right)^{0.1}$	$3.5 \le S \le 16.0$ $4.5 \le t_s \le 12.0$ $20 \le L \le 240$ $N_b \ge 4$ $10{,}000 \le K_g \le 7{,}000{,}000$
		use lesser of the values obtained from the equation above with $N_b = 3$ or the lever rule	$N_b = 3$
Cast-in-Place Concrete Multicell Box	d	One Design Lane Loaded: $\left(1.75+\frac{S}{3.6}\right)\left(\frac{1}{L}\right)^{0.35}\left(\frac{1}{N_c}\right)^{0.45}$ Two or More Design Lanes Loaded: $\left(\frac{13}{N_c}\right)^{0.3}\left(\frac{S}{5.8}\right)\left(\frac{1}{L}\right)^{0.25}$	$7.0 \le S \le 13.0$ $60 \le L \le 240$ $N_c \ge 3$ If $N_c > 8$ use $N_c = 8$
Concrete Deck on Concrete Spread Box Beams	b, c	One Design Lane Loaded: $\left(\frac{S}{3.0}\right)^{0.35}\left(\frac{Sd}{12.0L^2}\right)^{0.25}$ Two or More Design Lanes Loaded: $\left(\frac{S}{6.3}\right)^{0.6}\left(\frac{Sd}{12.0L^2}\right)^{0.125}$	$6.0 \le S \le 18.0$ $20 \le L \le 140$ $18 \le d \le 65$ $N_b \ge 3$
		Use Lever Rule	$S > 18.0$

2.2.3.1 General

NCHRP 12-26 research project (Zokaie et al. 1991) started in 1985 with the objective of developing comprehensive guidelines for wheel load distribution in highway bridges. The study focused on beam-and-slab, box girder, slab, multi-box beam and spread box beam bridges. In order to cover most common bridge types and their geometric properties, several hundred bridges were selected from National Bridge Inventory File (NBIF) and stored in a database. This database was investigated in order to define average values for various parameters such as span length, beam spacing, slab thickness, skew angle etc. For each bridge type, a hypothetical bridge with the mean values of the parameters were defined and called as the "Average Bridge".

In order to provide more comprehensive analysis guidelines, this research classified three levels of analysis. Level 3 is defined as the most accurate analysis method including detailed modeling of the bridge deck utilizing finite element method (FEM). Level 2 analysis uses graphical methods, nomographs and influence surfaces, or simplified computer programs. And Level 1 is the simplified method using wheel load distribution factors for estimating the longitudinal response of a girder. NCHRP 12-26 research mostly focused on level 1 analysis because of its practical use and surprising accuracy compared to higher level of analysis. New LDF formulas were developed for interior and exterior girder moment and shear distribution for single and multiple lane loading.

Live load distribution factor varies depending on the magnitude and position of the wheel line and the response of the bridge superstructure to these loads. NCHRP 12-26 study focused on the response of the bridge for HS family of trucks. Therefore, the formulas provided in AASHTO LRFD are based on AASHTO HS trucks only. A limited parametric study was conducted as part of this research to investigate the variation of LDFs with truck axle spacing. It was found that smaller axle spacing result in higher LDFs and larger gauge widths give smaller LDFs. Figure 2.3 shows several truck types that has different gauge widths and used for the limited parametric study conducted as part of NCHRP 12-26 project. Table 2.3 list the LDFs for these different truck types. The variation of LDF for different truck types was found to be smaller than 1 percent for most of the cases. Therefore they concluded that the new LDF formulas can be used for different truck types with some caution.

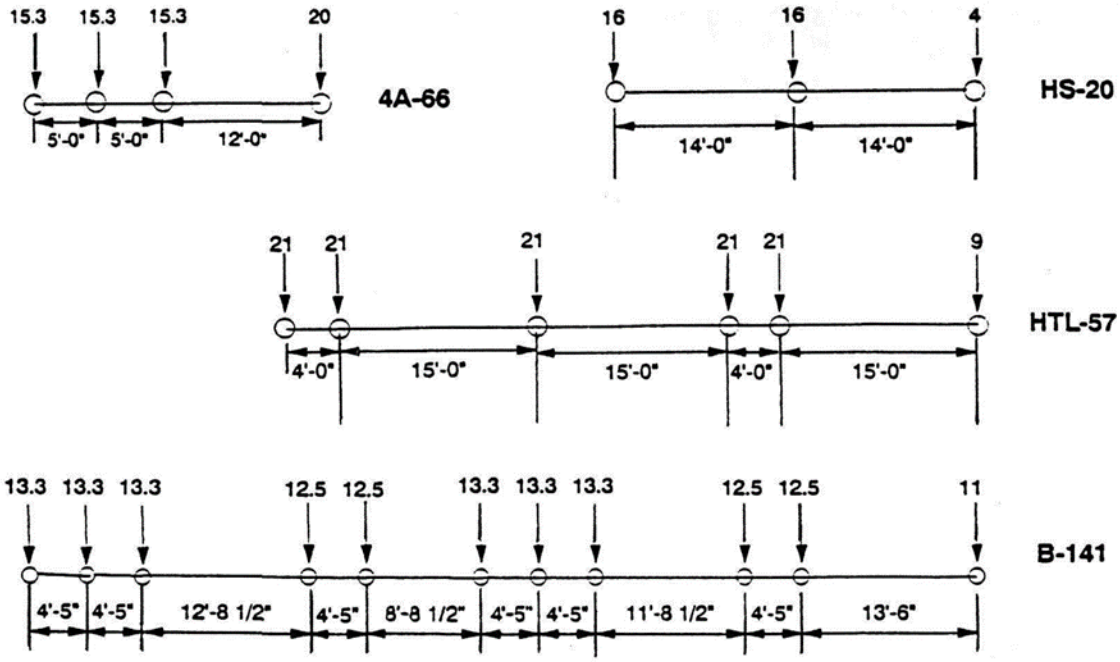

Figure 2.3. Axle Configuration for Truck Types Considered for the Parametric Study (Zokaie et al. 1991).

Table 2.3. LDFs for Various Truck Types for Two Lane Loading (Zokaie et al. 1991).

	DISTRIBUTION FACTOR (g)					PERCENT DIFFERENCE WITH HS-20			
	HS-20	HTL-57	4A-66	B-141	NCHRP 12-26	HTL-57	4A-66	B-141	NCHRP 12-26
Average*	1.293	1.261	1.285	1.268	1.304	-2.4	-0.6	-1.9	+0.9
Max. S (16')	2.220	2.162	2.205	2.178	2.308	-2.6	-0.7	-1.9	+4.0
Min. S (3.5')	0.713	0.717	0.713	0.715	0.755	+0.6	0.0	+0.3	+5.9
Max. L (200')	0.982	0.958	0.983	0.952	1.033	-2.4	+0.1	-3.1	+5.2
Min. L (20')	1.630	1.625	1.624	1.623	1.807	-0.3	-0.3	-0.4	+10.9

*S = 7.5'; L = 64'; t_s = 7.25"; K_g = 560,000 in^4

2.2.3.2 Identifying Key Parameters

The bridge database was studied to identify the range of applicability and variation of each parameter. A sensitivity study was conducted to identify the importance of each parameter for the live load distribution factors. Key parameters that affect the LDFs were determined for different bridge types based on the sensitivity studies. Several bridge finite element models having the same properties except the parameter being investigated were loaded with HS20 trucks and load distribution factors were obtained for moments and shears. Then the variations of LDFs were investigated to evaluate the importance of that parameter. This procedure was used for each parameter being considered for the approximate LDF equations.

The bridge database was also investigated to identify the relationship between different parameters. Several bridge parameters were plotted versus one other to identify any possible relationship between different parameters. The correlation between key parameters such as girder spacing versus slab thickness and span length versus moment of inertia was investigated. This study showed that mostly these parameters are not correlated to each other. Figure 2.4 shows the relationship of slab thickness and girder spacing as an example.

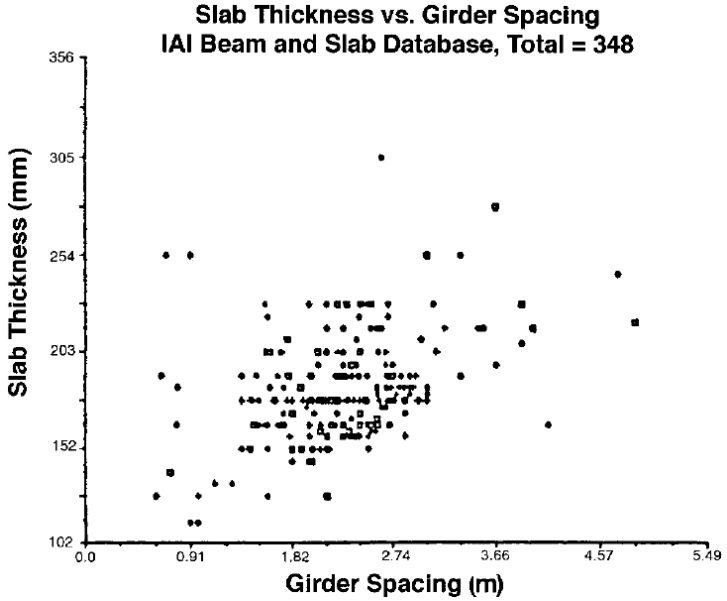

Figure 2.4. Relationship of Slab Thickness and Girder Spacing in Beam-and-Slab Bridges.

2.2.3.3 Loading of Bridge Deck

Live load distribution factors were calculated by loading the bridge with trucks placed at the longitudinal position that produces the maximum moment or shear reaction. Then vehicles were moved transversely across the bridge width. The maximum moment or shear reaction for each position was obtained using accurate computational methods (FEM or Grillage). The maximum of these results was chosen as the critical moment or shear demand. This procedure was repeated for different numbers of trucks that fit on the bridge transversely. The maximum moment and shear reactions were multiplied by the multiple presence factor. The LDF equations in the AASHTO LRFD Specifications implicitly include multiple presence factors. Therefore, the multiple presence factors must only be used when the lever rule is used. Also the vehicle loading was achieved using truck loads only. AASHTO uniform lane loading was not included for the derivation of the AASHTO LRFD LDF equations (Zokaie et al. 1991).

The controlling moment force or shear reaction was selected for one-lane-loaded and multiple-lane-loaded cases. Then a ratio is computed to compare this controlling moment or shear to the moment or shear that is found by analyzing a simply supported isolated beam having the same span length. This ratio represents the live load distribution factor for that particular case. Because different critical positions were analyzed and the maximum was chosen, the LDF formulas provided an envelope of all possible load configurations.

2.2.3.4 LDF Formulation

In order to study current AASTO LRFD live load distribution factors in a systematic manner certain assumptions were made (Zokaie 2000). The effects of each parameter to LDFs were assumed to be independent. Then it was assumed that the effect of each parameter can be modeled using an exponential curve in the form of ax^b. Where x is the value of a parameter in consideration, a and b are the coefficients that were determined based on the variation of LDFs. After defining the effect of each parameter with a power curve, the combined effect can be modeled as multiplication of those power terms with a combined coefficient as:

$$g = a\left(L^{b1}\right)\left(S^{b2}\right)\left(d^{b3}\right)(\ldots) \tag{2.1}$$

The coefficient 'a' can be determined at last after defining the powers of each parameter. The powers were calculated by studying the effect of each parameter to the LDF when only that parameter was changed while keeping the others same. The ratios of successive equations were

used in order to calculate the power of the parameter in consideration. This procedure was repeated for all successive pairs. If the value of the power term is close for all calculation this means that the exponential curve can be used for modeling this parameter. An example calculation for the effect of span length parameter (L) is shown in Equations (2.2) - (2.5).

$$g_1 = a\left(L_1^{b_1}\right)\left(S^{b_2}\right)\left(d^{b_3}\right)(\ldots) \tag{2.2}$$

$$g_2 = a\left(L_2^{b_1}\right)\left(S^{b_2}\right)\left(d^{b_3}\right)(\ldots) \tag{2.3}$$

$$\frac{g_1}{g_2} = \left(\frac{L_1}{L_2}\right)^{b_1} \tag{2.4}$$

$$b_1 = \frac{\ln\left(\frac{g_1}{g_2}\right)}{\ln\left(\frac{L_1}{L_2}\right)} \tag{2.5}$$

For n equations that can be identified through n different FEM that was developed for investigating the effect of L to the LDF, n-1 b_1 values can be calculated. If these values are close to each other, exponential curve can be used to model the effect of L. The same procedure is applied to the other key parameters that are defined in the equation, and all the powers of the parameters can be identified. Then the common coefficient of the final equation (a) can be calculated using the expression provided below.

$$a = \frac{g_0}{\left(L_0\right)^{b_1}\left(S_0\right)^{b_2}\left(d_0\right)^{b_3}(\ldots)} \tag{2.6}$$

2.2.4 Studies Evaluating AASHTO LRFD LDF Equations (1993-2013)

2.2.4.1 Statistical and Analytical Studies

Nowak (1993) conducted a comprehensive statistical research for determining variation of different bridge parameters and developing live load models based on these. Load distribution and multiple presence factor were also considered as part of the model. The response of a bridge to live load modeled as a function of vehicle position, axle configuration, axle weights, girder spacing, span length, multiple presence and stiffness. This study is the first study evaluating the accuracy of the new proposed LDF equations by (Zokaie et al. 1991) Bridges modeled using FEM and assuming linear behavior of girders and slab. Obtained LDFs were compared with *AASHTO Standard Specifications for Highway Bridges* (AASHTO 1989) and the ones proposed by Zokaie et al. (1991). The results were in good agreement with the LDFs calculated from the new proposed formulas for *AASHTO LRFD Bridge Design Specifications* (AASHTO 1994). Whereas, (AASHTO 1989) estimates too conservative values for LDFs in most cases.

A dynamic load model was also developed as a function of road surface condition, dynamic characteristic of the bridge and the vehicle. It was found that dynamic response does not depend on the truck weight. The dynamic load factor (DLF) does not exceed 15 percent of live load for 75 year maximum values. Actual contribution of these parameters to DLF highly dependent on the site conditions.

Chen and Aswad (1996) evaluated the AASHTO LRFD (AASHTO 1994) load distribution factor formulas for simply supported I-girder and spread box beam bridges with large span to depth ratios. It was found that for moderately large span to depth ratios AASHTO LRFD simplified LDFs gives up to 18 percent conservative results for interior beam moments and up to 12 percent conservative results for exterior I-girder and 30 percent conservative for exterior box girder moments. It was suggested that the use of FEM or grillage analysis may reduce the cost of the bridge and increase he span capability.

Zokaie (2000) discussed the details and procedures applied for deriving the AASHTO LRFD load distribution factor equations and compared their accuracy with S-over equations. This study paper was published to explain the necessity of the new introduced relatively complex formulas and answer the questions raised in the bridge engineering community. It was noted that *S/D* equations only considers spacing as a key parameter. Whereas the new

formulas developed as part of NCHRP 12-26 project considers many other important bridge parameters such as span length, flexural stiffness and slab thickness. New proposed formulas were calibrated against a large bridge database and generally gives results within 5 percent of more accurate finite element analysis. The author emphasizes the importance of range of applicability of these equations. These formulas were derived for bridges that have constant spacing, constant skew and constant girder inertia. The vehicles used has constant 6 ft axle width and HS20 axle configuration. For non-standard axle widths and irregular bridge geometries, the designer should use more accurate method such as grillage or FEM, for calculating response of the bridge.

2.2.4.2 Experimental Studies

Kim and Nowak (1997) conducted an experimental study on two simply supported I-girder bridges to study distribution and impact factors. Strain data were obtained using strain gages attached at the bottom of the flanges at the midspan of the bridge. It was suggested that the bridge response under controlled truck load may not reflect the actual bridge behavior under normal traffic. Because the bridge response depend on the vehicle type, speed, transverse position and vehicle edge distance. Therefore the tests conducted under normal traffic for two days. It was found that load distribution factors are consistently lower than the AASHTO values Figure 2.5 shows the mean and maximum values of obtained girder distribution factors and compared to AASHTO Standard Specification and AASHTO LRFD Specification.

Analysis of the processed data also revealed that the influence of closely spaced diaphragm is not considerable. On the other hand the bridge with sparsely spaced diaphragms has more uniform girder distribution factors. In terms of impact factors, the results indicated the increasing strain values reduces the impact factor. Obtained impact factors for large strains were well below the AASHTO specified values.

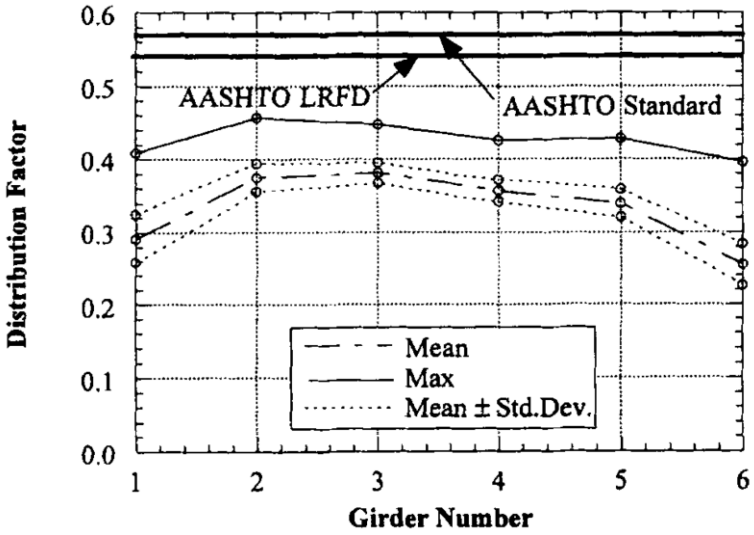

Figure 2.5. Girder Distribution Factors for Two Lane Loading (Kim and Nowak 1997).

Eom and Nowak (2001) conducted an experimental study on 20 steel girder bridges under heavy trucks and recorded girder strains at the midspan of each girder. Load distribution factors were calculated from the experimental strain values as well as from FEM results and compared with AASHTO LRFD (AASHTO 1998) and AASHTO Standard (AASHTO 1996). It was found that code specified values are always conservative. Based on the test results AASHTO standard specification was conservative even for bridges with short span and small girder spacing, and very conservative for long spans having large girder spacing. AASHTO LRFD specified LDFs were more accurate compared to AASHTO standard specification, particularly for long span bridges having large girder spacing. It was noted that for ideal simple support conditions AASTO LRFD load distribution factors are more realistic. But code specified values can be too conservative for evaluating the condition of existing bridges. Existing bridge structures experiences more favorable load sharing due to non-structural components, such as parapets, railing and sidewalks, and partial fixity of bearings. These factors should be taken into account for developing rating equations for existing structures.

Schwarz and Laman (2001) conducted an experimental study on three prestressed concrete I-girder bridges to evaluate their load distribution characteristics and dynamic impact factors. It was found that both AASHTO standard and AASHTO LRFD gives conservative results compared to experimental values. As part of this research these three bridges were also

tested under dynamic loads by passing trucks at different speeds. The results indicate that dynamic load allowance (DLA) decreases with increasing stress. Based on limited number of tests it was observed that DLA increases with increasing vehicle speed. No significant relationship observed between DLA and number of axles and bridge span length.

Barr et al. (2001) studied live load distribution factors for prestressed concrete girder bridges. A 137 ft long span of a three span continuous bridge having 40 degree skew was tested and FEM model was verified by experimental results. After verifying the modeling approach, 24 variation of prestressed concrete girder bridge was modeled for studying moment LDFs. In addition, the effect of lifts, diaphragms, continuity, skew and load type (lane or truck) was also investigated. FEM results was within 6 percent of the experimental values. It was found that AASHTO LRFD (AASHTO 1998) results are up to 28 percent conservative compared to FEM results which were verified with experiment. This difference was due to the effect of end diaphragms, lifts and continuity that were modeled with FEM. Comparison of experimental results, FEM results and code specified moment LDFs for an interior girder is shown in Figure 2.6 The results indicated that increasing skew angle always reduces flexural distribution factors. Load distribution factor was found to be around 10 percent lower for lane loading compared to the truck loading. This may be due to better distribution of loads when applied over some area rather than applying as point loads in the case of truck loading.

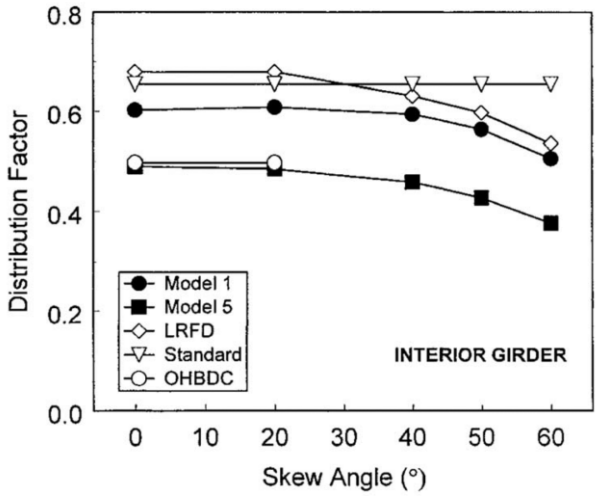

Figure 2.6. Comparison of LDFs for Interior Girder Moments (Barr et al. 2001).

2.3 METHODS FOR ANALYZING BRIDGE SUPERSTRUCTURES

2.3.1 Overview

Analysis of a bridge superstructure under vehicular load is a complex problem and requires lengthy calculation to get analytical solutions. Many theories including plate theories, stiffness methods, grillage method, finite element method and moment distribution procedures were developed over years to analyze the response of different bridge types. All these theories have particular assumptions that makes them applicable to certain bridge superstructures. For slab-on-girder bridge analysis method can be classified following Zokaie`s general classification.

- Level 3 Analysis (Accurate Method)
    - Plate Analysis (Analytical or Numerical Methods)
    - Grid Analysis or Grillage Method (Analytical or Numerical Methods)
    - Finite Element Analysis (FEA) (Numerical Method)
- Level 2 Analysis
    - Graphical Methods,
    - Nomographs,
    - Influence Surfaces,
    - Simple Computer Programs
- Level 1 Analysis (Simplified Method)
    - Approximate LDF Formulas

Simplified load distribution factors have been long used by bridge engineering community and different procedure are available in bridge standards. An extensive literature review is provided for development and assessment of LDFs specified in AASHTO in section 2.2. This section presents the state-of-the art and current practices for accurate methods and methodologies developed for applying these techniques to slab-on-girder bridges.

2.3.2 Plate Analysis

Plate analysis are based on assuming the bridge superstructure as a thin plate having uniform thickness. Depending on the bridge type different assumptions are required to be able to get analytical solution for the bridge response. Therefore, many different plate theories including folded plate theory, articulated plate theory and orthotropic plate theory were developed for analyzing bridges. Detailed literature study was conducted by Sanders and Elleby (1970) about

the development of these theories. It was noted that due to required assumptions, for slab-on-girder bridges, orthotropic plate analysis; for multi-beam bridges, articulated plate analysis and for box girder bridges, folded plate analysis is can be used.

Orthotropic plate analysis of bridge deck was first solved by Guyon (1949). He found analytical solutions for orthotropic deck by assuming a released torsional degree of freedom or fixed torsional degree of freedom and zero Poisson's ratio. His closed form solution was extended by Massonnet (1950) who included other intermediate torsional degrees of freedom. Another extension of the same solution was suggested by Rowe (1955) by inclusion of Poisson's ratio. Other researchers have also worked on finding numerical solution to the orthotropic plate equation. Heins and Looney (1968) employed finite difference method to find an approximate numeric solution and results compared very well with the analytical one.

Although the analytical, closed form, solution of orthotropic plate is readily available, it involves some assumptions. The mathematical model is derived from approximate physical model. The assumptions for creating the mathematical model includes thin plate theory and small deflection assumptions. In addition, bridge superstructure is idealized as equivalent orthotropic plate with uniform thickness in both orthogonal directions, the spacing of beams and diaphragms are assumed to be constant and all connections assumed to fully transfer moment shear and torque.

2.3.3 Grillage Analysis

Grillage analysis is a method in which a bridge superstructure is modeled as an equivalent grillage of rigidly connected beams members at discrete nodes. The geometry and properties of the network of grillage beams, support conditions, and application of loads should represent real bridge. Early studies for analytical solution of a grid work problem was conducted in 1950s. Lazarides (1952) found one of the first analytic solution by solving the deflection compatibility equations at each node.

Lightfoot and Sawko (1959) generalized the solution by solving the grid framework problem using slope deflection analysis. Grillage method become more popular computer-aided analysis methods for bridge decks because of how accurately it can predict the bridge behavior while still being relatively easy to understand and easy to use.

The strategy behind the method is to simply split the bridge up into several equivalent longitudinal and transverse grillages, or beams. These grillages have the same bending and torsional stiffness parameters as the section of the bridge that they are representing. This works best if, in the longitudinal direction, the grillages line up with the centerlines of the beams, therefore keeping these parameters concentrated where they have the largest influence in the physical bridge. Placing grillages at locations known to have high force and stress magnitudes, such as supports and prestressing strands, is also good practice. If the grillage method is set up properly, the model as well as the real bridge should deflect in the same magnitude and shape under the same loads, and the moments, shears, and torsions in the grillages should be the same as those in the section of the actual bridge that they represent. Guidelines for developing grillage models are available in the literature (Hambly 1975; Zokaie et al. 1991). Figure 2.7 shows grillage applications for different bridge superstructures.

Hambly (1976) in his book discusses guidelines for developing accurate grillage configuration. He notes that grillage method has limitations for modeling bridges which obviously behaves in 3D mode. But the response can be adequately captured by some additional care. Equilibrium of all elements in the slab states that torques and twists at any location must be equal in both the longitudinal and transverse directions. However, the grillage model does not contain any principle to meet this criterion. It can be shown though, that if the grillage mesh is fine, meaning that if the grillages are spaced more closely, this orthogonal twisting behavior is modeled approximately as it actually is. This will then ensure that the bridge will deflect in a smooth shape, rather than a wavy shape found in coarse grillage meshes. Another concern with the grillage method is that the moment in a grillage is proportional only to the curvature in that grillage, while in the real bridge the curvature in both directions affects the moment. Again, this difference has again been shown to be negligible for a fine mesh.

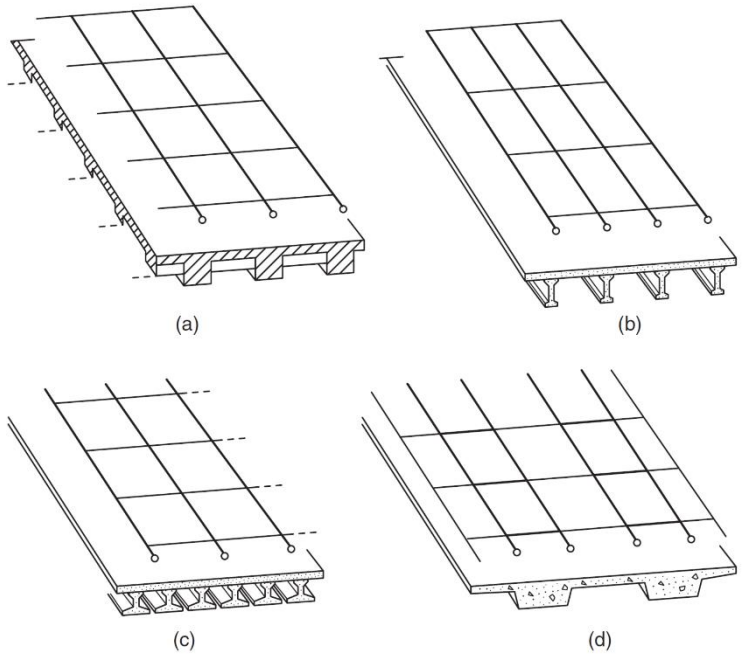

Figure 2.7. Grillage Idealization of Different Bridge Types (Hambly 1991).

Surana and Agrawal (1998) discuss different aspects of the grillage method, and different bridge types that the grillage method can be used. The grillage method can be used accurately for numerous types of bridges, even complicated bridge designs with edge stiffening, large skew, and unusual support conditions may be modeled and understood fairly easily with the grillage method. The method is based on a stiffness matrix approach and essentially converts the bridge structure into a network of longitudinal and transverse line grillages that connect rigidly at the nodes of intersection, much like a space frame matrix analysis approach. These grillages maintain the same stiffness properties as the bridge sections they are replacing, therefore meeting equilibrium conditions at the nodes. The accuracy of the grillage method are also compared with more comprehensive methods such as finite elements.

2.3.4 Finite Element Analysis

Finite element method is a numerical method that is applied by dividing the physical domain into finite elements. FEM provides a powerful tool to develop approximate solution of engineering problems by solving the problem over each element and assembling them for the global domain. Early studies show that many key features of the finite element method was

studied by Hrenikoff (1941) and Courant (1943). But the formal introduction of the complete method is first presented by Turner et al. (1956). The term ‘finite element’ was first used by Clough (1960). Studies on FEM has grown rapidly after then and today there are journal dedicated to finite element methods and its applications. FEM first applied to plane stress problems then its application was extended to plate bending and shell problems.

The FEM can be characterized in three main steps. (1) The given body (domain) is subdivided into simple subdomains which are called finite elements. The collection of these elements are called mesh. (2) Then the physical problem is approximated by a function, generally by a polynomial (called interpolation or base function), and physical variables are related at each node of the element. In this step finite element model of is created. (3) The element equations (finite element model) are assembled to get the global set of equation. The global set of equations can be solved to get displacement at each node. Element stresses and strains can be calculated from these displacements.

FEM has more comprehensive capabilities and higher level of accuracy compared to grillage analysis and plate theories. It allows realistic representation of complex geometries and inclusion of dissimilar material. Whereas grillage and plate theories approximate the geometry and cannot model the eccentricity of bridge girders. The assumptions made for the grillage and plate theories include simplification of 3D bridge superstructure as line elements or uniform thickness plate which reduces the accuracy of the models. With grillage model it is impossible to represent some important physical properties such as interaction between deck and girder, shear lag and support eccentricity. FEM also is an approximate method, but its inherent approximation comes from representing the solution of each element with interpolation functions. The effect of this approximation reduces as small mesh sizes are used. On the other hand, FEM often requires higher level of computational power and skilled specialists which increases the cost of analysis. But the advance of computational power and user friendly software interfaces makes it more accessible.

2.4 FINITE ELEMENT MODELING OF SLAB-ON-GIRDER BRIDGES

2.4.1 General

There are numerous ways for idealizing a bridge superstructure for creating an accurate model that uses finite element method (FEM) models. . FEM modeling of bridge superstructures can be classified as 2D and 3D modeling. Three dimensional FEM modeling allows engineers to accurately represent real physical geometry of the bridge with correct position of support. Sotelino et al. (2004) classified the 3D FEM modeling of bridges into three main categories as; eccentric beam model, detailed beam model and solid deck model. This classification is based on the modeling of primary members; deck slab and girders. Although there are limited studies that models the secondary elements, such as intermediate and/or end diaphragms, majority of the FEM modeling techniques uses primary elements only. In all the studies focusing on LDFs, researchers used linear elastic finite elements as suggested by Zokaie et al. (1991).

2.4.2 2D FEM Modeling of Bridge Superstructures

This type of idealization is one of the early methods that simplifies the bridge superstructure but still keeps a reasonable level of accuracy. In this approach the bridge is modeled as a stiffened plate by defining center of gravity of girders coincident with the center of gravity of slab.

Hays et al. (1986) used the software called SALOD to investigate lateral load distribution characteristic of simple span bridges. Plate elements having five degrees freedom at each node were used for modeling bridge deck and two node frame elements used for modeling girders. Girders are connected along the centerlines of the plate elements neglecting the eccentricity of real structure. All elements were assumed to be linear elastic and all girders assumed to have same moment of inertia. Deck elements over the girders thickened to increasing transverse bending stiffness of prestressed and T-beam bridges. Figure 2.8 shows an example drawing of 2D FEM modeling of slab-on-girder bridge structures. The modeling approach was validated by series of field tests.

2.4.3 3D FEM Modeling of Bridge Superstructures

2.4.3.1 Eccentric Beam Model

Majority of the FEM modeling in the literature falls in to eccentric beam model category. (Barr et al. 2001; Chen and Aswad 1996; Imbsen and Nutt 1978; Marx et al. 1986; Wegmuller and Kostem 1973). In this type of approach, bridge is simplified to reduce the cost of analysis while still maintaining the slab girder interaction. One of the earliest applications of eccentric beam modeling used in 1970s (Imbsen and Nutt 1978; Wegmuller and Kostem 1973). The bridge superstructure is idealized as quadrilateral shell elements which can model both plate bending and membrane actions. The girders are modeled as two node beam elements and eccentrically connected to shell elements via the use of rigid links. Therefore, the actual physical location (eccentricity of girders) can be modeled. Figure 2.9 shows the FE idealization of simplified model.

Wegmuller and Kostem (1973) discussed the discretization of beam-slab structures using plate and beam elements and compared the results with the experiments conducted as part of series of bridge testing at Lehigh University. The bridge superstructure was idealized as a plate element and stiffened by beams running eccentric to the plate elements. Two types of finite elements utilized, plate element which are quadrilateral element having five degrees of freedom at each node and two node stiffener elements. All elements assume small deformation theory and linear elastic behavior. This method provided a tool for analyzing longitudinally and transversely stiffened plates. By separating the forces in the beam and slab, slab stresses could be analyzed more accurately. The accuracy of the method was verified by the field test results.

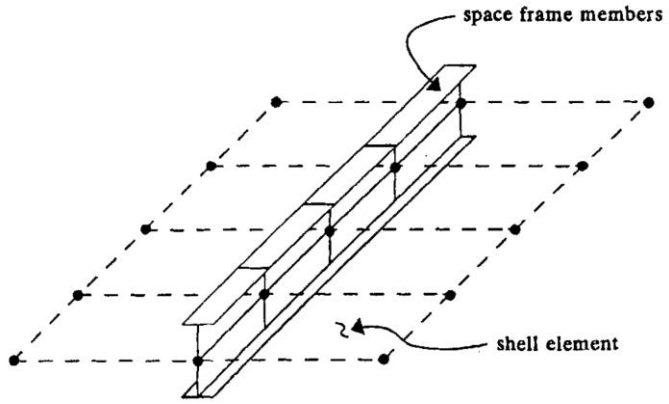

Figure 2.8. 2D FEM Idealization of Slab-on-Girder Bridges (Mabsout et al. 1997).

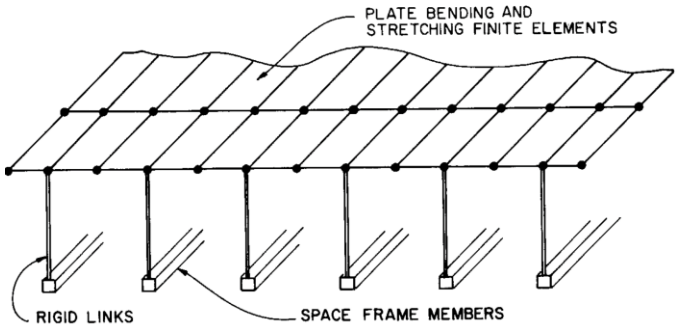

Figure 2.9. Eccentric Beam Model (Imbsen and Nutt 1978).

2.4.3.2 Detailed Beam Model

Brockenbrough (1986) studied lateral LDFs for I-girder bridges using FEM. A commercial software, NASTRAN was used and a detailed beam model were utilized for idealizing the bridge superstructure. Concrete deck were modeled using quadrilateral shell elements, girder flanges were modeled as two node frame elements and girder web was modeled using shell elements. Deck shell elements connected to top flange elements using rigid links. It was discussed that the use of shell elements for the web of the girder provides more realistic results by modeling the lateral bending stiffness of the flange more realistically. The use of bar elements for the entire girder underestimates the lateral bending moments developing in the flange. However moment distribution factors did not change significantly by the improved girder model. Figure 2.10 shows the detailed beam idealization of a bridge deck.

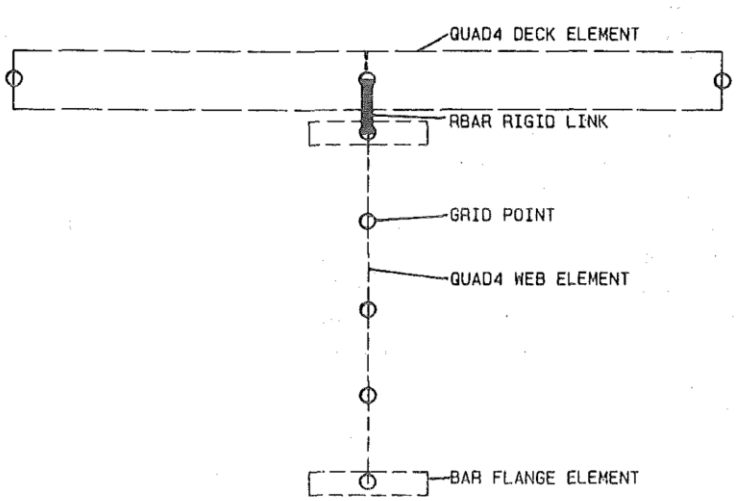

Figure 2.10. Detailed Beam Model (Brockenbrough 1986).

Bishara et al. (1993) also used same modeling technique for discretizing the steel I-girder bridges. FE model utilizing detailed beam model better represent the real physical bridge geometry and eccentricities of primary members as well as the bearing pads. The only difference was that the slab elements were chosen to be three node triangular elements having six degree of freedom at each node. The composite behavior could be achieved by defining rigid elements between the centroid of the deck elements and the top flange beam elements.

2.4.3.3 Solid Deck Model

Tarhini and Frederick (1992) employed isotropic, eight-node three dimensional brick finite elements having three degrees of freedom at each node for modeling the concrete deck. Two flanges and the web was modeled using quadrilateral shell elements having five degrees of freedom at each node. Figure 2.11 shows idealization of bridge members for solid deck modeling approach. For composite action no slip behavior modeled between deck and beam elements. For non-composite action linear springs modeled between solid brick elements and top flange shell elements. It was stated that this idealization provided realistic modeling of the real bridge structure and estimated the moments accurately.

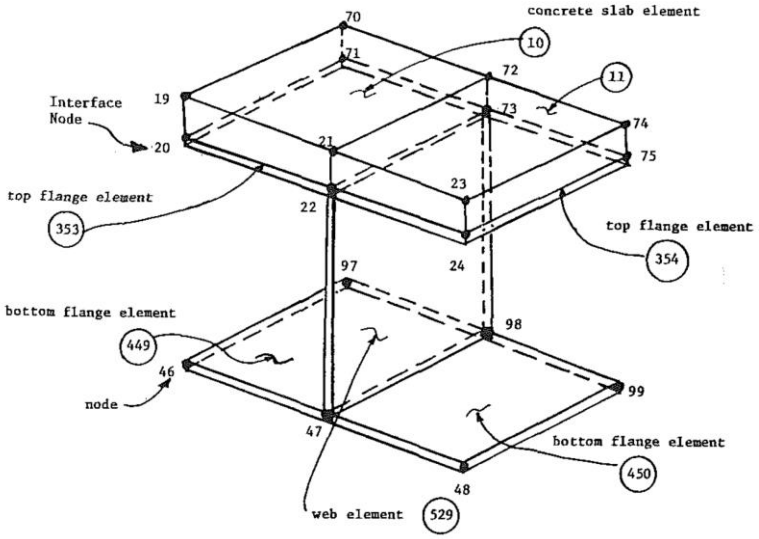

Figure 2.11. Solid Deck Model (Tarhini and Frederick 1992).

Mabsout et al. (1997) studied the accuracy of all four FEM modeling techniques for steel girder bridges and concluded that all these techniques give sufficiently accurate results and eccentric beam model can be used for steel girder bridges to save time form preparing the input file and reduce the computational costs.

3. PRELIMINARY DESIGNS FOR SPREAD SLAB BEAM BRIDGES*

3.1 GENERAL

The research team conducted a detailed parametric study to investigate the potential benefits of using spread slab beam bridges. The main focus of the parametric study was to develop preliminary designs for alternative design parameters and geometries. The design parameters were chosen based on the common TxDOT slab beam types, bridge widths, and girder spacings. The specified material properties chosen are consistent with TxDOT practice. The preliminary designs were carried out following the *AASHTO LRFD Bridge Design Specifications* (AASHTO 2012) and TxDOT *Bridge Design Manual* (TxDOT 2013a). TxDOT standard practices were followed to ensure that the results could be compared to typical TxDOT slab beam bridges.

The example provided in Appendix A describes a detailed design methodology for spread slab beam bridges. The procedure includes service load design based on allowable stresses in flexure, and ultimate flexural strength and shear strength design. The allowable deflection limit and the stress limits at release were also investigated. The details and findings of the parametric study are documented in this section.

3.2 DESIGN PARAMETERS

3.2.1 Geometric Properties of Bridge Alternatives

3.2.1.1 Slab Beam Types

The main geometric bridge design parameters were based on the four different slab beam types and typical TxDOT bridge widths. The four standard slab beam types are differentiated by the width and depth of the beam section, which has a 12 in. or 15 in. depth with a 4 ft or 5 ft width. These standard beam types are named by their width and depth dimensions. For example, the slab beam section with a 4 ft width and 12 in. depth is called 4SB12.

* Previously published work is available to the public through National Technical Information Service. Mary Beth D. Hueste, John B. Mander, Tevfik Terzioglu, Dongqi Jiang, and Joel Petersen-Gauthier (2014). "Spread Prestressed Concrete Slab Beam Bridges: Technical Report." Report No. FHWA/TX-14/0-6722-1, Texas A&M Transportation Institute, College Station, Texas, USA.

The four alternatives are 4SB12, 4SB15, 5SB12, and 5SB15. Figure 3.1 shows the section geometry and strand details of the standard slab beam sections. The 4 ft wide slab beams can hold a maximum of 44 strands, and the 5 ft wide slab beams can hold a maximum of 56 strands. The bottom concrete cover must be 2.5 in., and the spacing between two rows of strand layers is 2 in. center to center.

3.2.1.2 Bridge Widths and Number of Slab Beams

The total bridge widths were based on standard TxDOT bridge practice and the suggestions from the TxDOT Project Monitoring Committee (PMC). A total of six different bridge widths were investigated including 26 ft, 30 ft, 34 ft, 40 ft, and 46 ft wide bridges.

Another initial design parameter is the number of slab beams. Based on the use of stay-in-place precast concrete panels between the slab beams, the clear spacing between beams should not exceed 6 ft. There is no practical limit for the minimum spacing of the slab beams; they have already been used side by side for conventional slab beam bridges. However, for implementing a spread configuration, and in order to investigate all possible cases, the feasible minimum clear spacing between slab beams was chosen to be 2 ft. Based on the total bridge widths and clear spacing requirements, four options are available: three, four, five, or six slab beam girders can be utilized within the bridge width to satisfy the practical limitations discussed above.

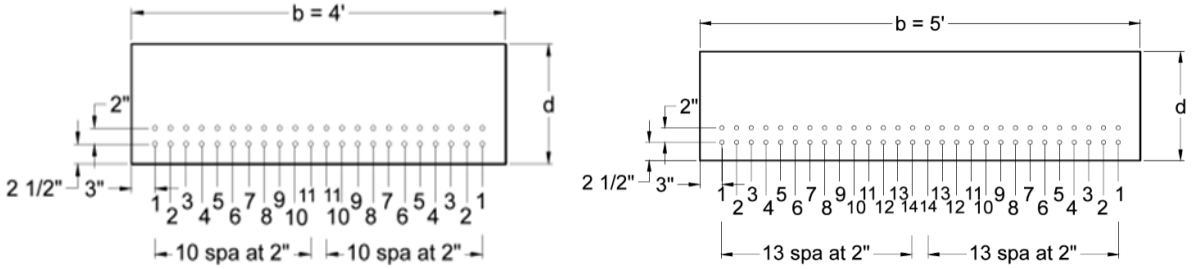

(a) 4 ft Wide Slab Beam (b) 5 ft Wide Slab Beam

Figure 3.1. Section Geometry and Strand Details of Slab Beam Girders.

3.2.1.3 Final Bridge Geometries

Given that there are four possible girder quantities, four different slab beam types, and six different bridge widths, a total of 96 different bridge configurations are possible. The minimum and maximum spacing constraints reduce the number of possibilities to 44 bridges that have clear beam spacings between 2 ft to 6 ft. These 44 bridge geometries are summarized in Table 3.1.

3.2.1.4 Deck Geometry

The cast-in-place deck uses unshored construction with 4 in. thick stay-in-place precast concrete panels (PCPs). A minimum of 4 in. of CIP concrete on top of the PCPs is required by the *TxDOT Bridge Design Manual (TxDOT 2013a)*. The PCPs are placed on bedding strips that are attached along the top longitudinal edges of the slab beams. The details of the PCP section are shown in Figure 1.2. The average bedding strip thickness is assumed to be 2 in. However, the contribution of the haunch to the stiffness of the composite section is neglected because the haunch thickness can vary and may decrease down to 0.5 in. due to the initial camber of the slab beams. The weight of a 2 in. haunch was included in the design loads to be conservative. Therefore, for the calculation of the composite section properties, the total deck thickness was taken as 8 in.

3.2.2 Material Properties and Superimposed Dead Loads

3.2.2.1 Concrete Compressive Strength

The concrete compressive strengths at release and at service (28 days) are key parameters for the design of a prestressed component using allowable stress criteria. To maximize the span lengths, spread slab beam bridge design requires that every available strand position be used. The high prestressing force causes tensile stress exceedance at the ends of the slab beam for almost all configurations. Therefore, the maximum allowable initial concrete compressive strength value was used in the parametric study. The *TxDOT Bridge Design Manual (TxDOT 2013a)* suggests that the maximum initial concrete compressive strength at transfer be limited to 6 ksi with a maximum 28-day concrete compressive strength of 8.5 ksi.

Table 3.1. Alternative Geometries for Parametric Study.

No.	Bridge Width (ft)	Number of Beams	Type of Beam	Clear Beam Spacing (ft)	No.	Bridge Width (ft)	Number of Beams	Type of Beam	Clear Beam Spacing (ft)
1	26	3	5SB12	5.50	23	40	5	5SB12	3.75
2		3	5SB15	5.50	24		5	5SB15	3.75
3		4	5SB12	2.00	25		5	4SB12	5.00
4		4	5SB15	2.00	26		5	4SB15	5.00
5		4	4SB12	3.33	27		6	5SB12	2.00
6		4	4SB15	3.33	28		6	5SB15	2.00
7	30	4	5SB12	3.33	29		6	4SB12	3.20
8		4	5SB15	3.33	30		6	4SB15	3.20
9		4	4SB12	4.67	31	42	5	5SB12	4.25
10		4	4SB15	4.67	32		5	5SB15	4.25
11		5	4SB12	2.50	33		5	4SB12	5.50
12		5	4SB15	2.50	34		5	4SB15	5.50
13	34	4	5SB12	4.67	35		6	5SB12	2.40
14		4	5SB15	4.67	36		6	5SB15	2.40
15		4	4SB12	6.00	37		6	4SB12	3.60
16		4	4SB15	6.00	38		6	4SB15	3.60
17		5	5SB12	2.25	39	46	5	5SB12	5.25
18		5	5SB15	2.25	40		5	5SB15	5.25
19		5	4SB12	3.50	41		6	5SB12	3.20
20		5	4SB15	3.50	42		6	5SB15	3.20
21		6	4SB12	2.00	43		6	4SB12	4.40
22		6	4SB15	2.00	44		6	4SB15	4.40

As noted above, the CIP deck uses unshored construction with 4 in. thick PCPs as stay-in-place forms. The concrete compressive strength at service f_c' of the PCPs is specified to be 5 ksi, and the CIP deck concrete f_c' is specified to be 4 ksi. For the parametric study, the deck compressive strength was conservatively assumed to be 4 ksi throughout, with the PCPs assumed to be part of CIP deck.

3.2.2.2 Prestressing Strands

Two prestressing strand diameters are available. The *TxDOT Bridge Design Manual* (TxDOT 2013a) recommends using 0.5 in. diameter strands but allows for 0.6 in. diameter strands when necessary. The spread slab beam bridge design requires high prestressing forces, but the concrete tensile stress limits at service and at release nearly always control the spread slab beam designs. When all strand locations are used, 0.5 in. diameter strands provide the required prestressing force to stay within the allowable concrete stress limit. Therefore, 0.5 in. diameter seven-wire low-relaxation strands were used with a specified ultimate tensile strength f_{pu} of 270 ksi.

3.2.2.3 Superimposed Dead Loads

The superimposed dead loads include the guardrail and wearing surface. The weight of the guardrail was considered for the superimposed dead load calculations, but the stiffness contribution was neglected. A T551 rail was assumed since it is one of the heaviest guardrail types. The wearing surface was taken to be 2 in. of asphalt having a 0.14 k/ft^3 unit weight.

3.2.3 Summary of Parameters and Design Assumptions

The design parameters used in the parametric study are summarized in Table 3.2. The designs were carried out with the same procedure used for the detailed example provided in Section 3. Like the detailed example, a refined method of analysis was used for the estimation of prestress losses. AASHTO (2012) does not provide approximate LDFs for spread slab beam bridges. Therefore, for these preliminary designs, the AASHTO (2012) spread box beam LDF formulas were used. For service load analysis, the AASHTO HL-93 live load model was adopted. The allowable compressive stress limit at release is given as 0.6 f'_{ci} in the *AASHTO LRFD Bridge Design Specifications* (AASHTO 2012). However, the *TxDOT Bridge Design Manual* (TxDOT 2013a) permits an allowable compressive stress at release of 0.65 f'_{ci}. Therefore, the increased compressive stress limit was adopted for the preliminary designs. The other stress limits were used as defined in AASHTO (2012) and summarized in Appendix A.

All geometric combinations listed in Table 3.1 were investigated to determine the maximum span length versus number of strands provided. Although TxDOT indicated a preference for 5 ft slab beams, the 4 ft sections were included for completeness. The design

procedures outlined in Section 3 were followed for the parametric study. However, for the parametric study, each slab beam was not designed based on a given span length; rather, it was designed based on a given number of strands. Initially, all strand locations were considered to be filled (44 strands for 4 ft wide slab beams and 56 strands for 5 ft wide slab beams) and then two strands were subtracted at each step until the section reached the cracking limit. The maximum achievable span lengths for eight different limit states were calculated at each step. These limit states are as follows:

- Allowable tension stress limit at release.
- Allowable compression stress limit at release.
- Allowable tension stress at time of deck placement.
- Allowable compression stress at time of deck placement.
- Allowable tension stress at service.
- Allowable compression stress at service.
- Ultimate flexural strength.
- Deflection limit at service.

Deflection limit criteria were applied based on AASHTO (2012) Articles 2.5.2.6.2 and 3.6.1.3.2, which indicate that the maximum live load deflection limit may be considered as $L/800$ for general vehicle loading, where L is the span in inches.

The dead load due to self-weight of the slab beam and deck slab is carried by the non-composite slab beam section. The superimposed dead loads (guardrails and wearing surface) and live load are considered to act on the composite section. The results and findings of the parametric study for all viable geometries are presented in the following section. Section 3.4 presents an assessment of the transverse shear and interface shear limit states.

Table 3.2. Alternative Geometries and Design Parameters.

Parameter	Description/Value
Number of Beams	3, 4, 5, or 6
Bridge Width, w (ft)	26, 30, 34, 40, 42, 46
Slab Beam Type	4SB12, 4SB15, 5SB12, 5SB15
Clear Beam Spacing	Varies from 2 ft to 6 ft
Deck Thickness, t_s	8 in.
Haunch Thickness, t_h	Assumed constant 2 in. for weight calculation. Not included for stiffness
Precast Concrete Strength at Release, f'_{ci}	6 ksi
Precast Concrete Strength at Service, f'_c	8.5 ksi
Deck Concrete Strength, f'_{cd}	4.0 ksi
Prestressing Strand Diameter, d_p	0.5 in.
Rail	T551 (0.326 k/ft, distributed to 3 beams from the edge)
Wearing Surface	2 in. thick asphalt assumed
Unit Weight of Concrete, w_c	0.15 kcf
Unit Weight of Asphalt Overlay, w_s	0.14 kcf
Prestressing Strands	0.5 in. diameter 7-wire low-relaxation strands
Ultimate Strength of Prestressing Stands, f_{pu}	270 ksi
Modulus of Elasticity of Strands, E_p	28,500 ksi

3.3 RESULTS OF THE PARAMETRIC STUDY

The achievable span length for a given number of strands was plotted for all eight limit states. All 44 viable geometric configurations listed in Table 3.1 are presented below. Figure 3.2 shows an example chart, where the five curves shown with symbols indicate an upper bound span length solution for the limit state considered. These limit states include the allowable tension and compression stress limits for flexure at service and at the time of deck casting, the ultimate flexural strength limit, and the maximum live load deflection limit. The allowable stress limits at release are upper bounds that limit the number of strands that can be used. The release limit corresponds to the upper bound for the allowable compression or tension limit (whichever governs) at release when no strands are debonded. The debonded release limit corresponds to the upper bound for the allowable compression or tension limit (whichever governs) when some strands are debonded up to 6 ft for 15 in. deep slab beams or up to 9 ft (or 0.2*L* for beams shorter than 45 ft) for 12 in. deep slab beams. For all the analyzed cases, the service tension stress limit and tension stress limit at release (with debonding) control the solution domain. The solution domain between these two curves is shown with yellow shading. The maximum achievable span length is indicated with a red check mark.

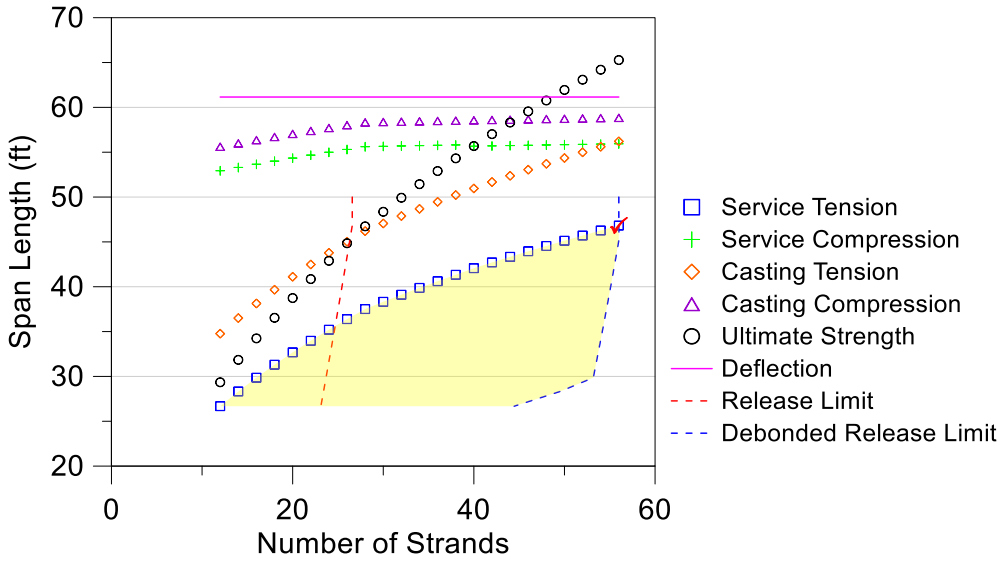

Figure 3.2. Solution Domain for 34 ft Wide Bridge with Four 5SB15 Beams.

The maximum span lengths for all 44 cases considered are listed in Table 3.3. The results are presented for six different bridge widths. The theoretical span length is shown as the maximum span length. The practical span length is the center to center of the bearing pad span length considering that the practical span length is 17 in. shorter than the total bridge span. The total bridge span has been kept to an integer number of feet and is defined as the back-wall-to-back-wall span length in TxDOT practice.

3.3.1 Achievable Span Lengths for 26 ft Wide Slab Beam Bridges

The 26 ft bridge width is the smallest within the bridge alternatives investigated. This is a common slab beam bridge width for a two-lane roadway. Therefore, it is important to note the limits and boundaries of this bridge width using a spread slab beam system. The solution domain charts for 26 ft wide spread slab beam bridge systems are shown in Figure 3.3. The maximum achievable total span was 52 ft when four 5SB15 slab beams were used. This resulted in small clear spacing between slab beams of only 2 ft with the four 5 ft wide slab beams. This span length was the maximum achievable span out of all 44 viable bridge geometries that were considered in this preliminary study. It is possible to achieve a 47 ft span length using just three 5SB15 slab beams, which would result in a 5 ft 6 in. clear spacing between slab beams. Although the beam spacing is relatively large, it is within the allowable limits of the stay-in-place PCPs.

3.3.2 Achievable Span Lengths for 30 ft Wide Slab Beam Bridges

There are six alternative geometries that can be achieved within the spacing limitations for a 30 ft total bridge width. All six design cases are shown graphically in Figure 3.4. The maximum achievable total span is 50 ft, which is 2 ft less compared to the 26 ft wide bridge. Again the maximum span length was achieved when four 5SB15 slab beams were used, resulting in a 3 ft 4 in. clear spacing between slab beams.

The investigation of the six alternatives showed no direct correlation between the achievable span length and the beam spacing. When five 4SB15 slab beams were used, the clear beam spacing was smaller (2 ft 6 in.) and the maximum achievable span was 49 ft, which was 1 ft less than the four 5SB15 case. This shows that the slab beam width has a more prominent effect on the maximum span length as compared to the number of beams. The same observation is valid for all bridge widths.

Table 3.3. Maximum Span Lengths for Spread Slab Beam Bridges.

No.	Bridge Width (ft)	Number of Beams	Type of Beam	Clear Beam Spacing (ft)	Maximum Span (ft)	Practical Span (ft)	Total Bridge Span (ft)
1	26	3	5SB12	5.50	38.57	38.58	40
2		3	5SB15	5.50	45.99	45.58	47
3		4	5SB12	2.00	43.99	43.58	45
4		4	5SB15	2.00	50.78	50.58	52
5		4	4SB12	3.33	40.06	39.58	41
6		4	4SB15	3.33	46.53	45.58	47
7	30	4	5SB12	3.33	42.07	41.58	43
8		4	5SB15	3.33	48.68	48.58	50
9		4	4SB12	4.67	36.96	36.58	38
10		4	4SB15	4.67	44.46	43.58	45
11		5	4SB12	2.50	41.27	40.58	42
12		5	4SB15	2.50	47.77	47.58	49
13	34	4	5SB12	4.67	39.82	39.58	41
14		4	5SB15	4.67	46.82	46.58	48
15		4	4SB12	6.00	34.72	34.58	36
16		4	4SB15	6.00	42.66	42.58	44
17		5	5SB12	2.25	43.43	42.58	44
18		5	5SB15	2.25	50.14	49.58	51
19		5	4SB12	3.50	39.61	39.58	41
20		5	4SB15	3.50	46.04	45.58	47
21		6	4SB12	2.00	42.04	41.58	43
22		6	4SB15	2.00	48.50	47.58	49
23	40	5	5SB12	3.75	41.27	40.58	42
24		5	5SB15	3.75	47.85	47.58	49
25		5	4SB12	5.00	35.76	35.58	37
26		5	4SB15	5.00	43.78	43.58	45
27		6	5SB12	2.00	43.64	43.58	45
28		6	5SB15	2.00	50.34	49.58	51
29		6	4SB12	3.20	39.92	39.58	41
30		6	4SB15	3.20	46.33	45.58	47
31	42	5	5SB12	4.25	40.60	40.58	42
32		5	5SB15	4.25	47.15	46.58	48
33		5	4SB12	5.50	35.62	35.58	37
34		5	4SB15	5.50	43.10	42.58	44
35		6	5SB12	2.40	43.03	42.58	44
36		6	5SB15	2.40	49.68	49.58	51
37		6	4SB12	3.60	38.72	38.58	40
38		6	4SB15	3.60	45.67	45.58	47
39	46	5	5SB12	5.25	38.92	38.58	40
40		5	5SB15	5.25	45.85	45.58	47
41		6	5SB12	3.20	41.89	41.58	43
42		6	5SB15	3.20	48.43	47.58	49
43		6	4SB12	4.40	37.00	36.58	38
44		6	4SB15	4.40	44.43	43.58	45

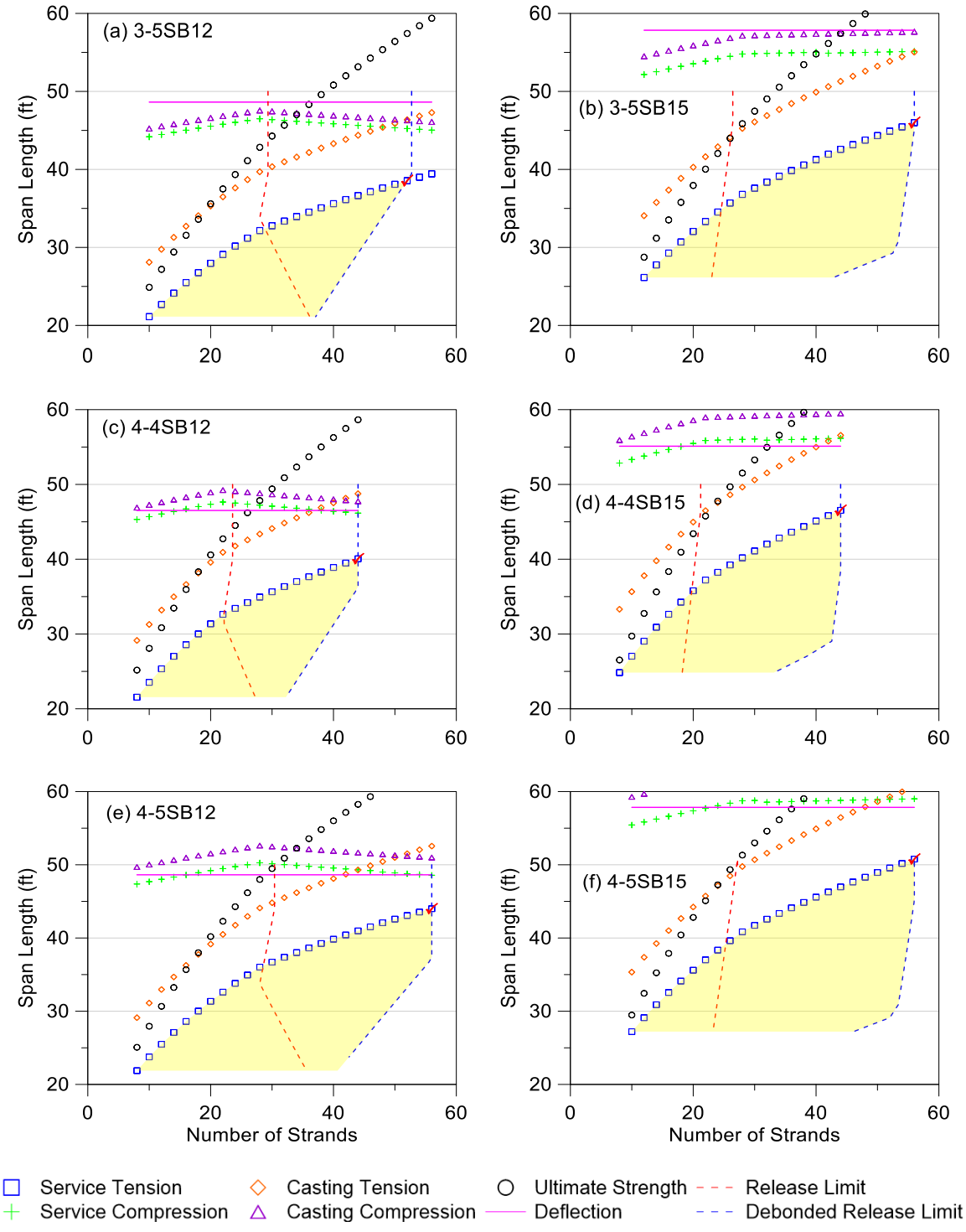

Figure 3.3. Span Length Solution Domain for 26 ft Wide Spread Slab Beam Bridges.

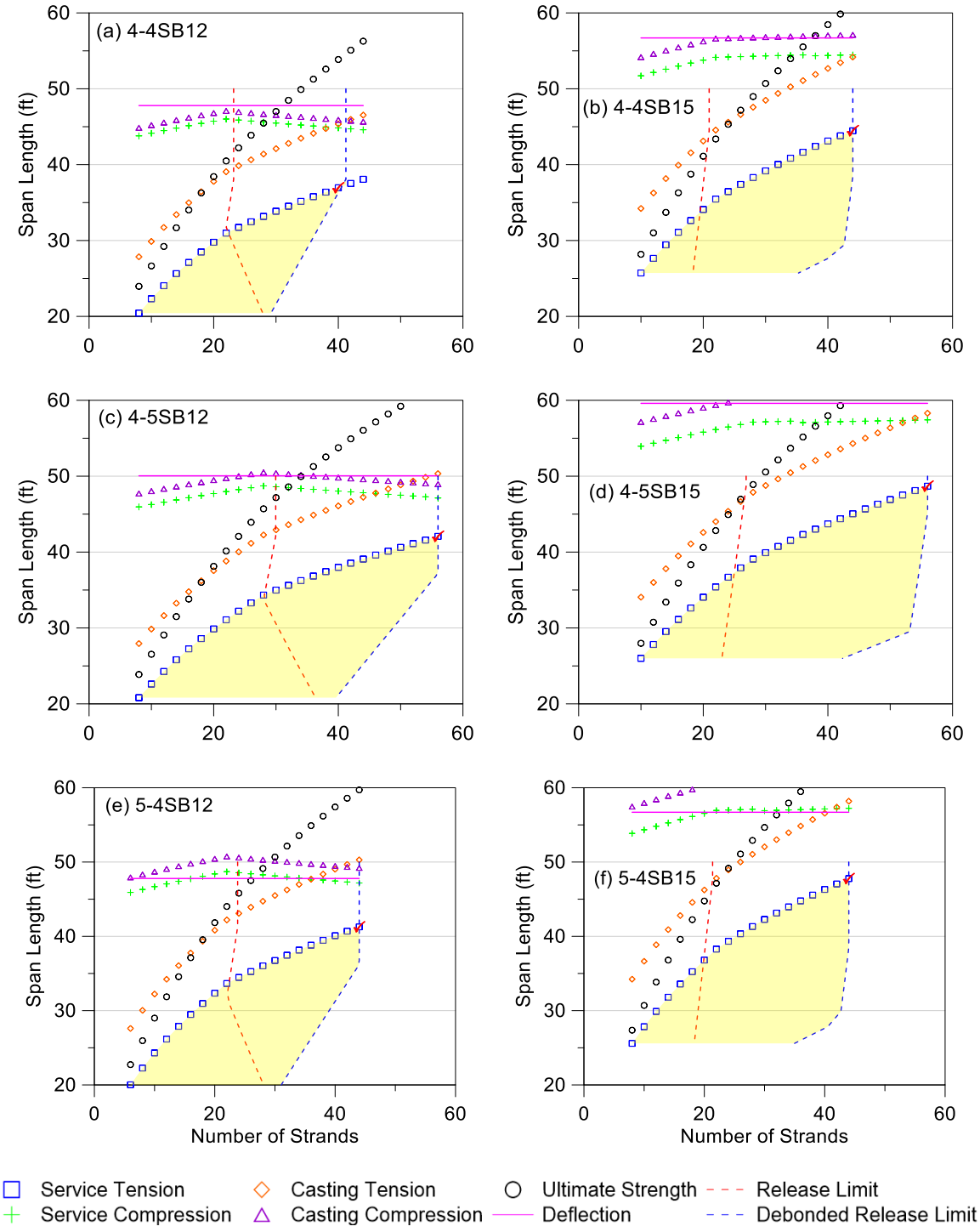

Figure 3.4. Span Length Solution Domain for 30 ft Wide Spread Slab Beam Bridges.

3.3.3 Achievable Span Lengths for 34 ft Wide Slab Beam Bridges

Another common slab beam bridge width is 34 ft, which has 10 different possible spread slab beam bridge geometries. Figure 3.5 presents span length solution domains for all 10 cases. The maximum achievable span is 51 ft when five 5SB15 slab beams are used.

The smallest maximum achievable span length out of all 44 bridge alternatives is for a 34 ft wide bridge with only four 4SB12 slab beams. The clear beam spacing is 6 ft and the maximum achievable span is 37 ft. The 12 in. slab beam depth results in relatively smaller span lengths as expected due to its smaller moment of inertia coupled with the limited strand positions in the 4 ft width.

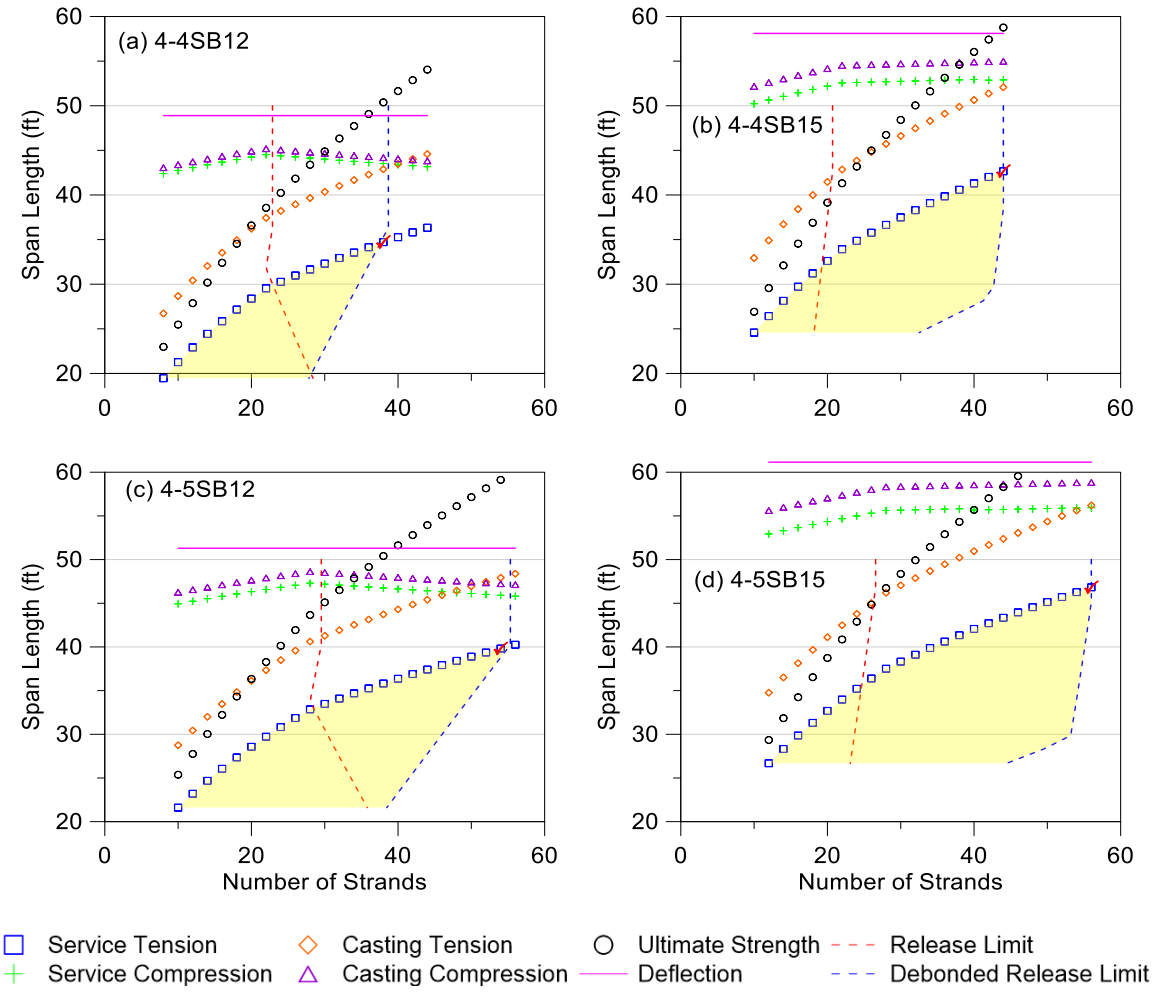

Figure 3.5. Span Length Solution Domain for 34 ft Wide Spread Slab Beam Bridges.

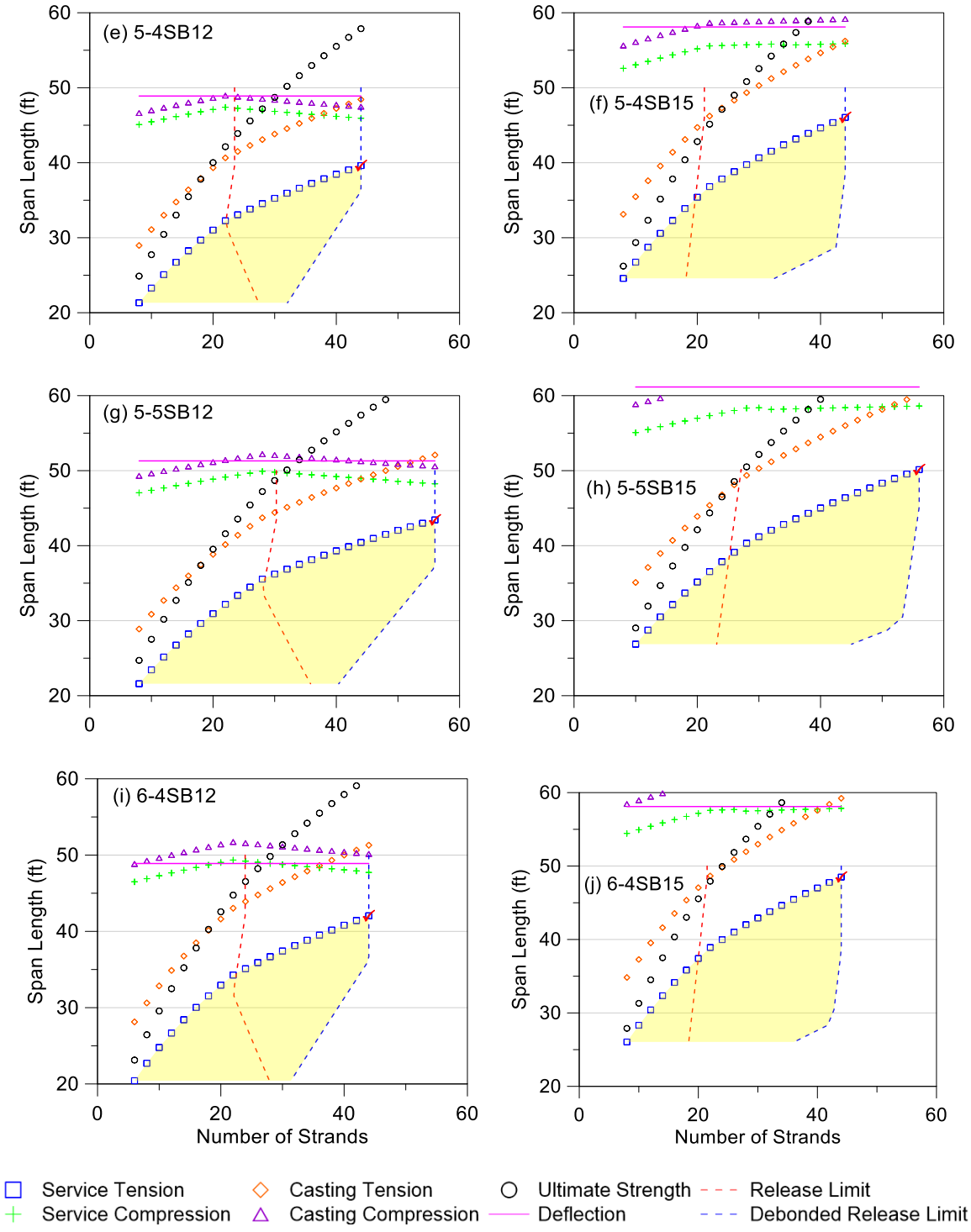

Figure 3.5. Continued.

3.3.4 Achievable Span Lengths for 40 ft Wide Slab Beam Bridges

Although wider bridge widths are not very common for slab beam bridge types, several wider bridge widths for three lanes (40 ft, 42 ft, and 46 ft) were included in the parametric study based on the PMC's suggestions. The solution domains for a 40 ft bridge width are shown in Figure 3.6. Due to the increased bridge width, the number of girders cannot be less than five in order to satisfy practical slab beam spacing criteria. A total of eight different practical spread slab beam geometries can be achieved for 40 ft wide bridges.

A 40 ft bridge width is the smallest common TxDOT bridge width for a three-lane bridge. The preliminary designs that were included in the parametric study showed that the spread slab beam configuration could be utilized for three-lane bridges up to 51 ft span length. This maximum achievable span was obtained for six 5SB15 slab beams and resulted in the smallest beam clear spacing of 2 ft.

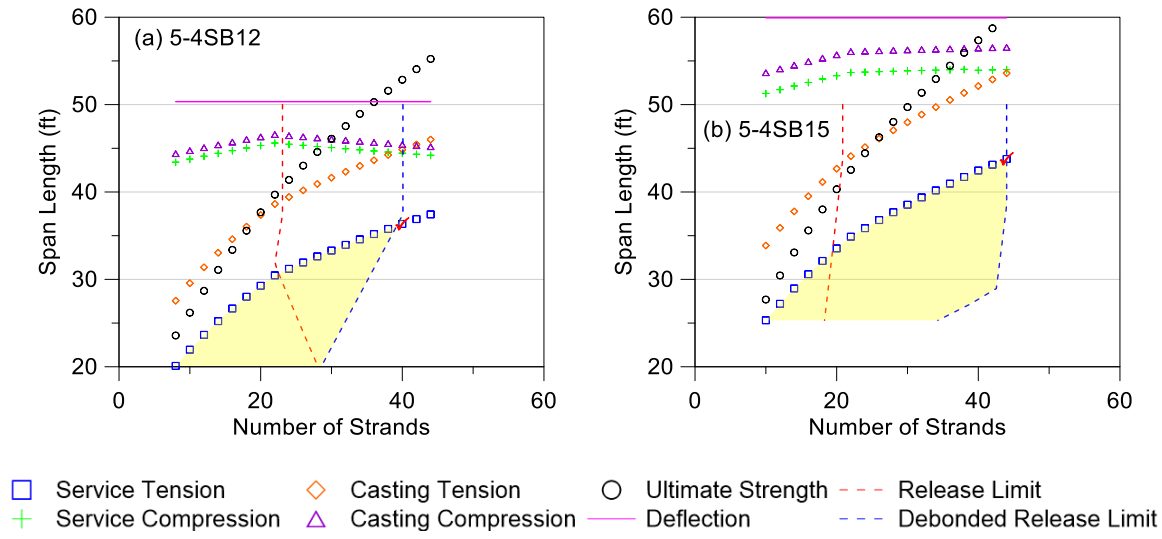

Figure 3.6. Span Length Solution Domain for 40 ft Wide Spread Slab Beam Bridges.

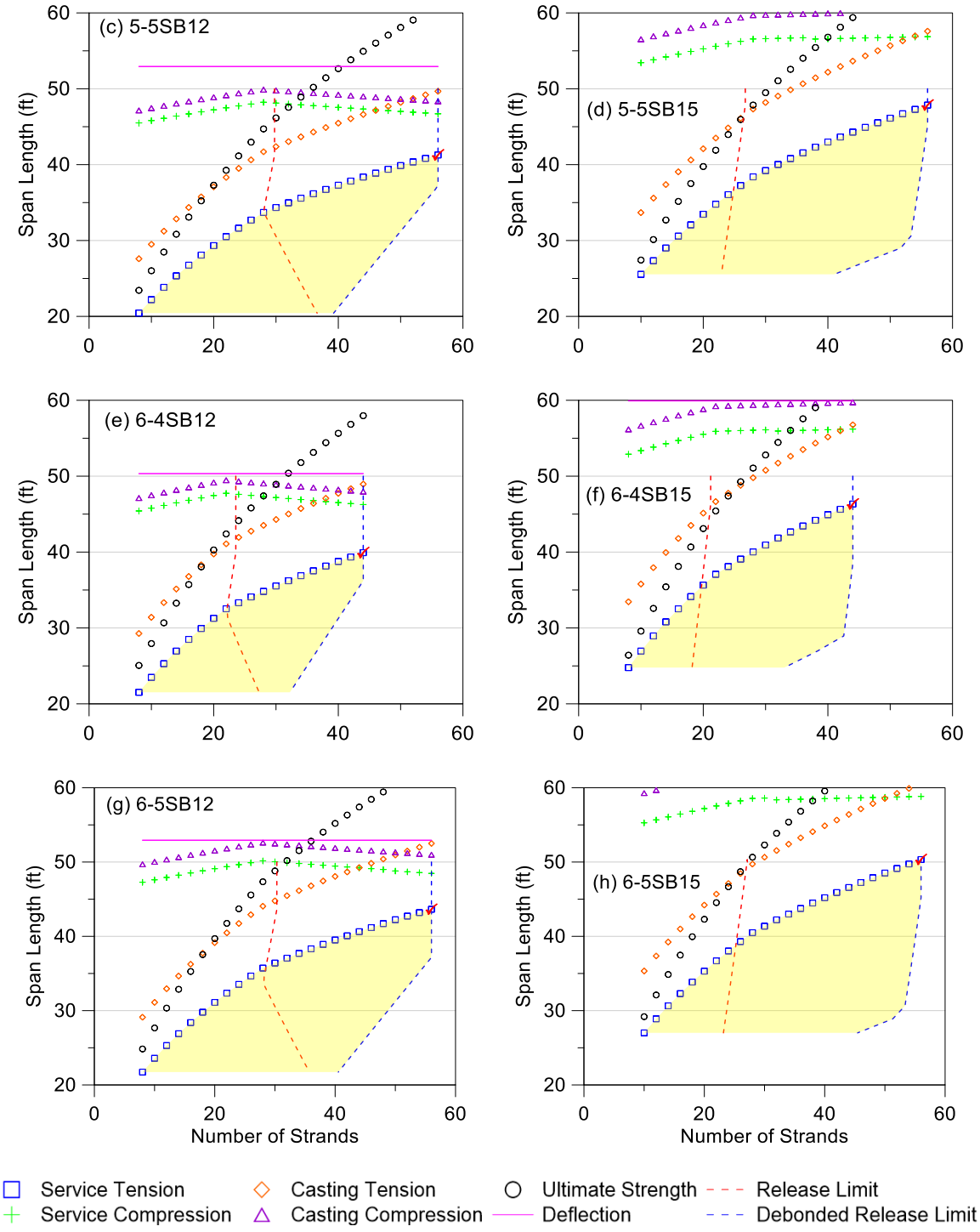

Figure 3.6. Continued.

3.3.5 Achievable Span Lengths for 42 ft Wide Slab Beam Bridges

Another common bridge width is 42 ft. Although it is very close to the 40 ft bridge width and will give similar results, the research team included it in the parametric study for completeness. The results for 42 ft wide spread slab beam bridges are shown in Figure 3.7.

Similar to 40 ft wide bridges, there are eight possible geometries that satisfy the spacing requirements. Either five or six slab beams can be used to maintain the practical spacing limits. The maximum achievable span length is 51 ft and corresponds to the use of six 5SB15 slab beams.

One of the smallest maximum span lengths is observed within the 42 ft bridge width group. Only a 38 ft span length is achievable when five 4SB12 slab beams are used. This also creates one of the highest eccentricities, with a 5 ft 6 in. clear spacing between slab beams.

3.3.6 Achievable Span Lengths for 46 ft Wide Slab Beam Bridges

The widest common TxDOT bridge width is 46 ft. There are six possible spread slab beam bridge geometries for a 46 ft wide bridge. All six cases were investigated, and the results are shown in Figure 3.8. The maximum achievable span length is 49 ft, which corresponds to the use of six 5SB15 slab beams with a 3.2 ft clear spacing between slab beams.

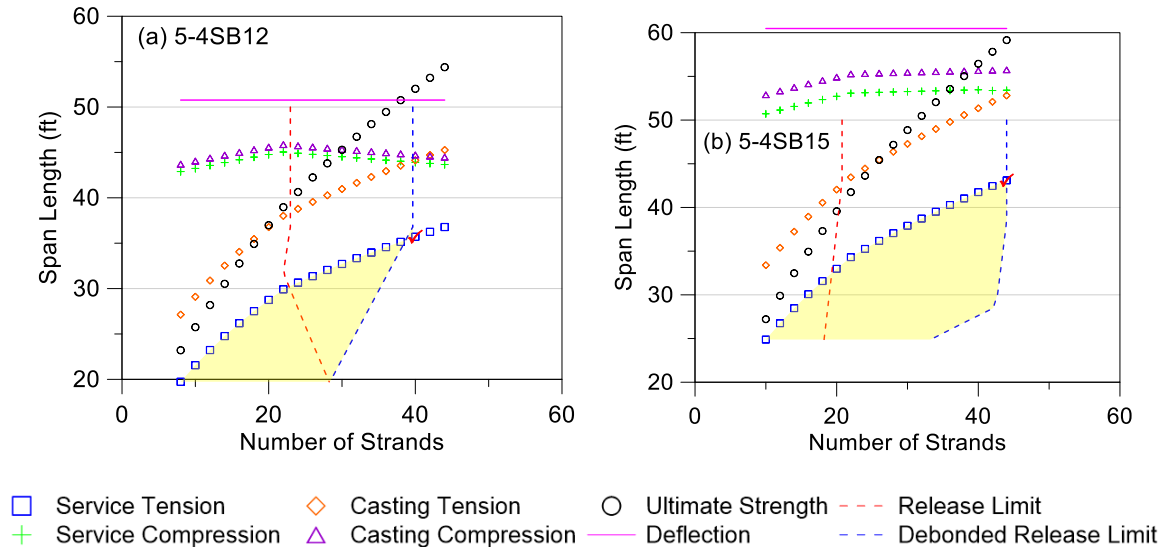

Figure 3.7. Span Length Solution Domain for 42 ft Wide Spread Slab Beam Bridges.

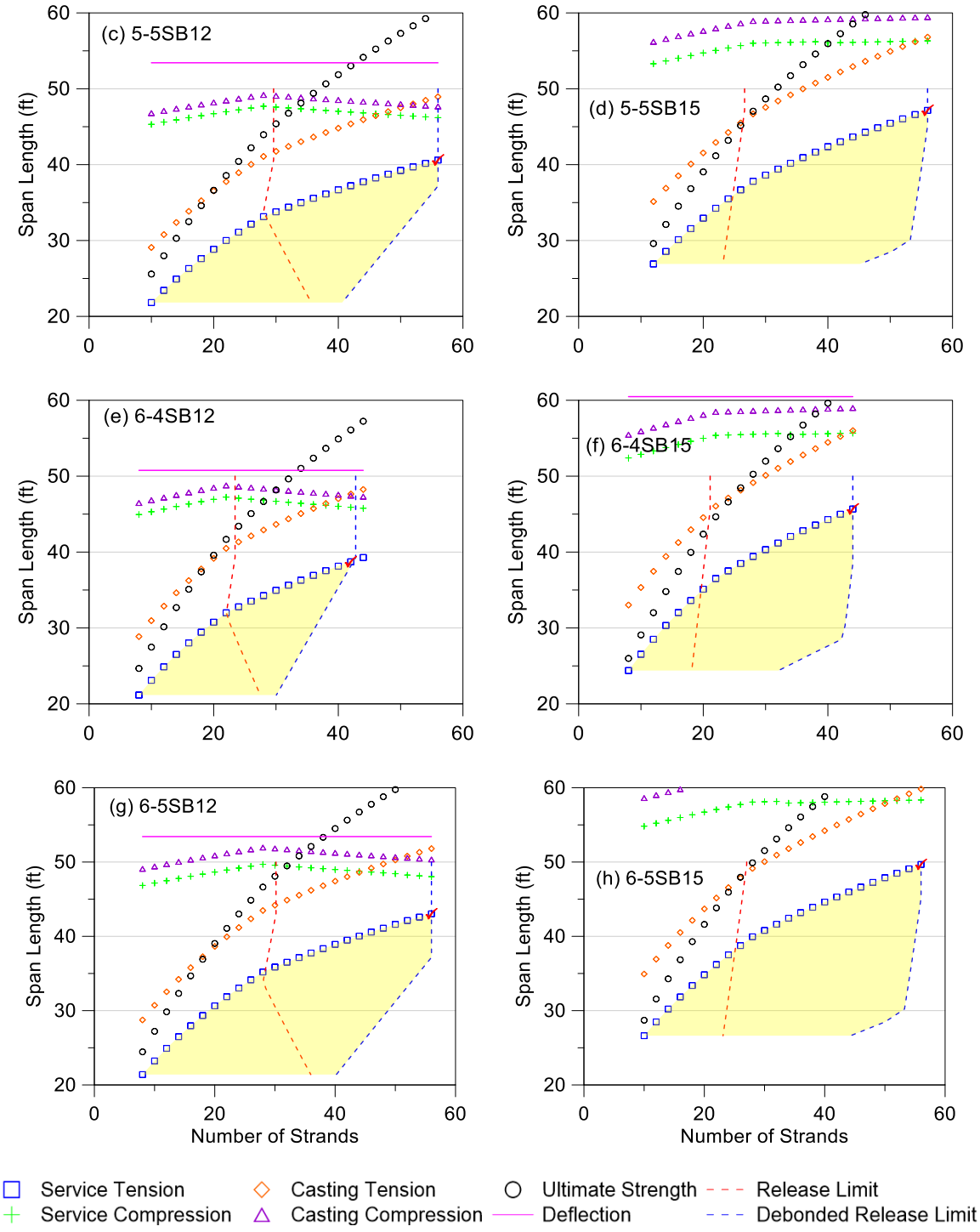

Figure 3.7. Continued.

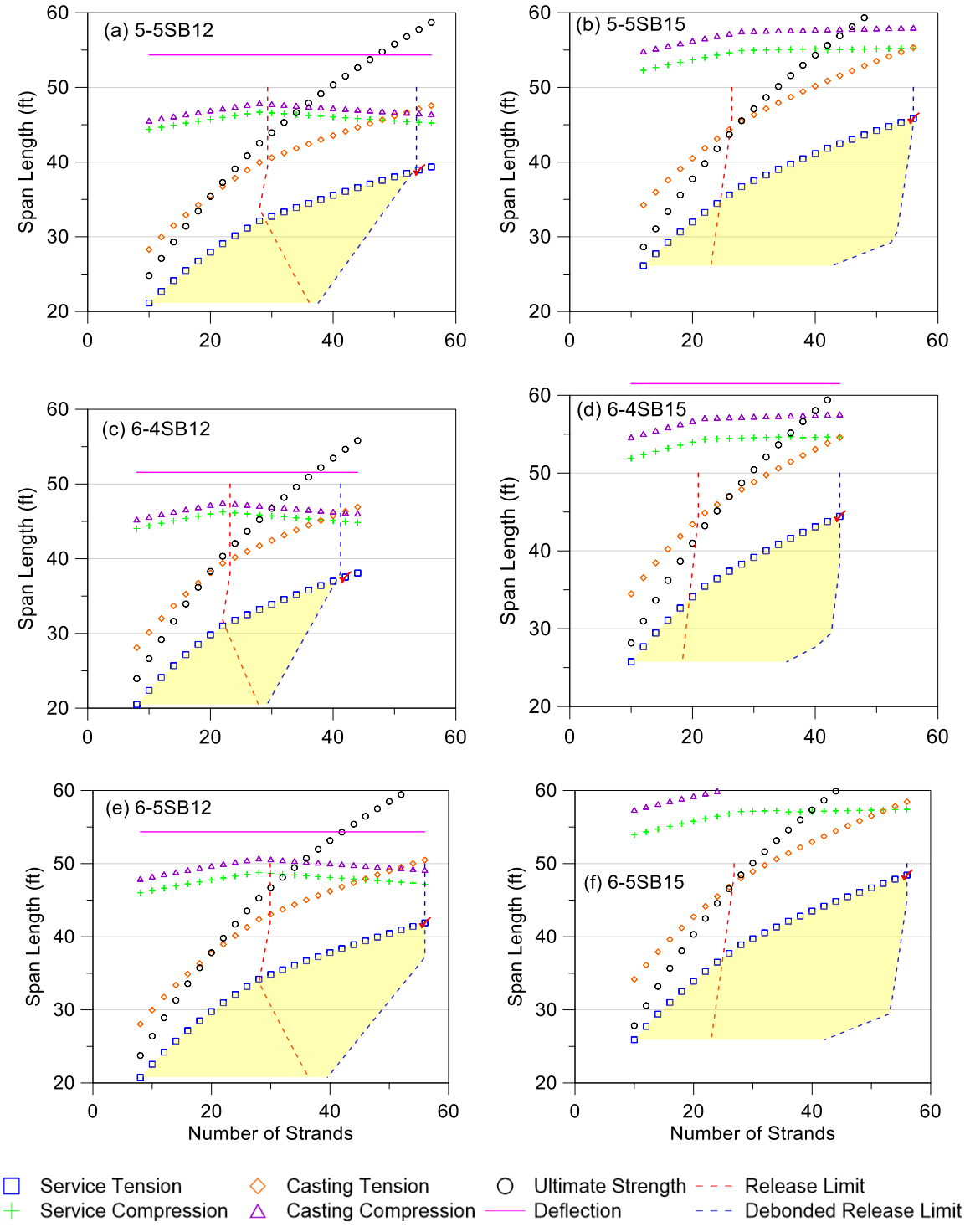

Figure 3.8. Span Length Solution Domain for 46 ft Wide Spread Slab Beam Bridges.

3.4 SHEAR LIMIT STATES

The parametric study described in the first part of this section considered the flexural limit states to determine span length limits for various bridge geometries. As an additional check, the shear limit states were checked based on the requirements of AASHTO (2012). The transverse shear capacity of the standard slab beam types were evaluated under service loads in accordance with AASHTO (2012) Article 5.8.3.4. The interface shear resistance was also checked using the requirements provided in AASHTO (2012) Article 5.8.4. Appendix A provides detailed procedures for transverse and interface shear limit state checks for the Riverside Bridge. Shear checks of four critical bridge superstructure geometries utilizing the 4SB12, 4SB15, 5SB12, and 5SB15 standard slab beam types are summarized in this section. Details of transverse and interface shear reinforcement are shown in Figure 3.9 and Figure 3.10.

3.4.1 Transverse Shear Design Check of Critical Bridges

A total of four bridges having the largest beam spacing for the parametric study were chosen and analyzed under service loads. Design shear forces and corresponding moments are listed in Table 3.4. The shear capacity of these slab beam sections was checked at three critical locations where different transverse shear reinforcement spacing was provided (C-bars in Figure 3.9). The locations of these critical sections are as follows:

- Section A: Face of support (maximum shear demand for 4 in. C-bar spacing).
- Section B: Shear critical section (maximum shear demand for 6 in. C-bar spacing).
- Section C: End of reinforced zone containing 6 in. C-bar spacing (maximum shear demand for 9 in. or 12 in. C-bar spacing, depending on slab beam width).

The *AASHTO LRFD Bridge Design Specifications* (Article 5.8.2.4; (AASHTO 2012) requires that the following equation must be satisfied at each section.

$$V_r = \phi V_n \geq V_u \tag{3.1}$$

Where:

V_r = Design shear resistance, kip.

V_n = Nominal shear resistance, kip.

V_u = Factored shear force, kip.

ϕ = Strength reduction factor for shear = 0.9 for normal weight concrete.

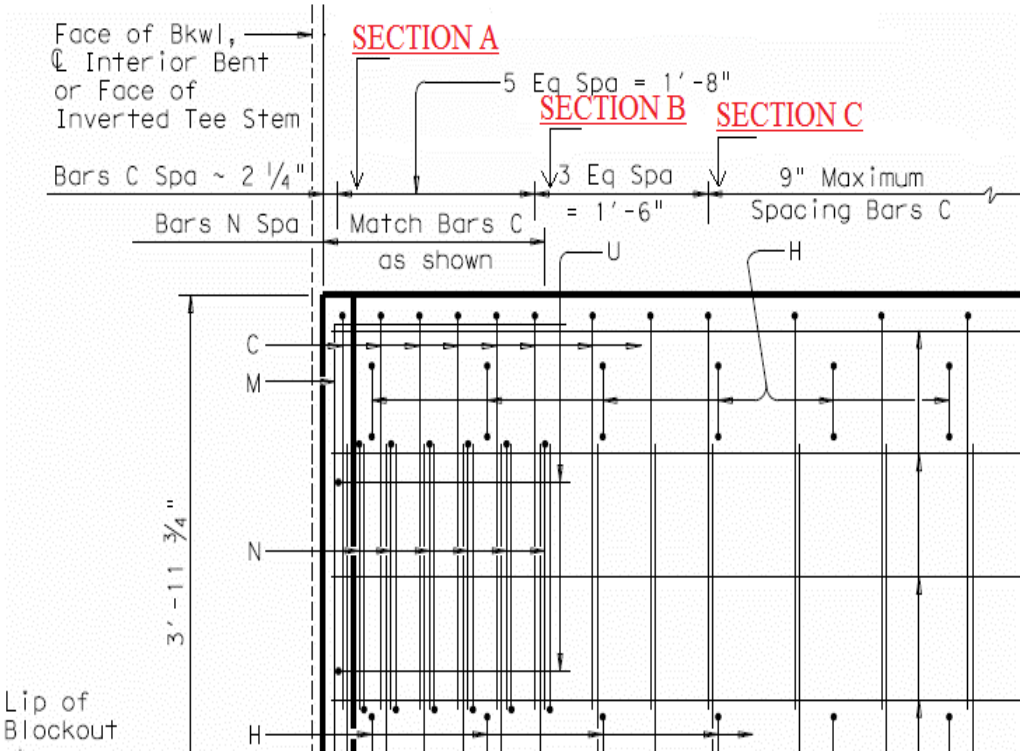

Figure 3.9. Sections Checked for Shear (TxDOT 2013b).

The shear resistance at three critical sections for all four bridges was calculated using the sectional design model provided in AASHTO (2012). The nominal shear resistance at a given section is the sum of the concrete contribution to shear strength, the transverse reinforcement shear strength, and the component of the prestressing force in the direction of the applied shear.

$$V_n = V_c + V_s + V_p \tag{3.2}$$

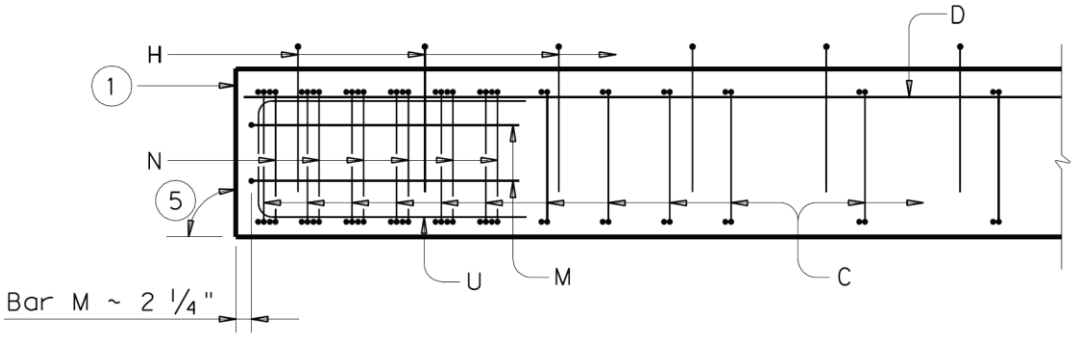

(a) Elevation View

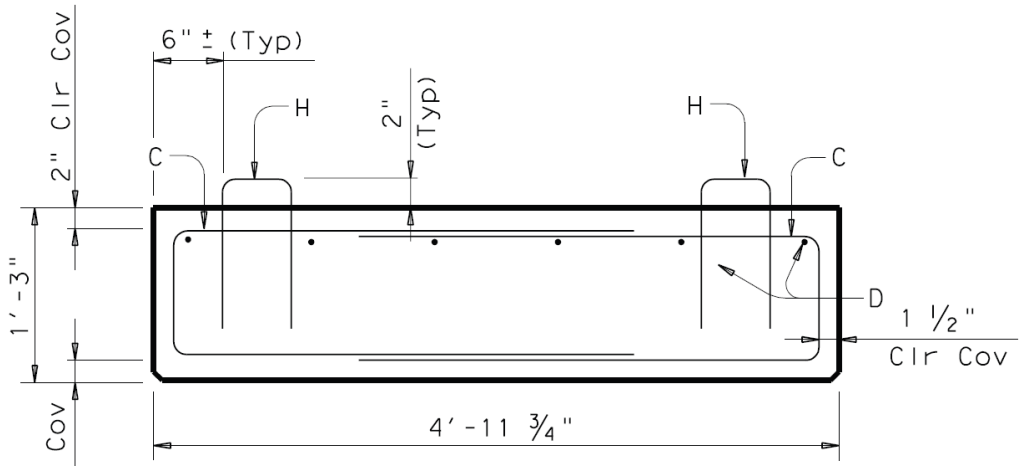

(b) Section View

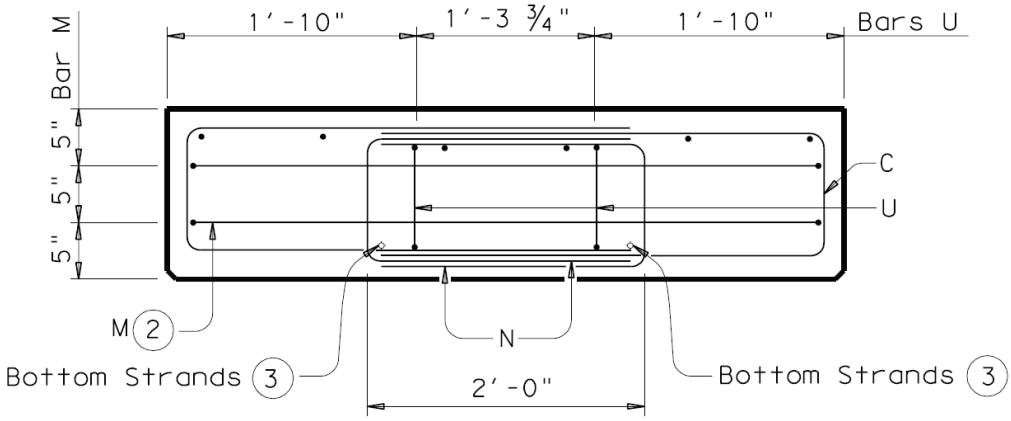

(c) End Zone Reinforcing

Figure 3.10. Shear Reinforcement Detail for 5SB15 Slab Beams (TxDOT 2013b).

Where:

V_c = Nominal shear resistance provided by tensile stresses in the concrete, kip.

V_s = Shear resistance provided by shear reinforcement, kip.

V_p = Component of the effective prestressing force in the direction of the applied shear, kip (V_p = 0 because all strands are straight).

The shear resistance provided by the concrete is calculated using the following AASHTO expression.

$$V_c = 0.0316\beta\sqrt{f_c'}\,b_v d_v \qquad (3.3)$$

Where:

f_c' = Design concrete compressive strength at 28 days (f_c' = 8.5 ksi).

b_v = Effective web width, in.

d_v = Effective shear depth, in.

d_e = Effective depth for bending, in.

d_v = Larger of $0.9d_e$ or $0.72h$, in.

The shear resistance provided by the shear reinforcement is calculated using the following AASHTO expression.

$$V_s = A_v f_y \frac{d_v}{s}\cot\theta \qquad (3.4)$$

Where:

β = Factor indicating the ability of diagonally cracked concrete to transmit tension between cracks.

A_v = Area of transverse reinforcing steel (in^2) within a distance *s* (in.).

f_y = Yield strength of transverse steel reinforcement, ksi (f_y = 60 ksi).

θ = Angle of inclination of diagonal compressive struts, degrees.

To determine the nominal shear resistance provided by the concrete and shear reinforcement (V_c , V_s) the β and θ parameters must be calculated. For prestressed members, β and θ are computed using Equations (3.5) and (3.6).

$$\beta = \frac{4.8}{(1+750\varepsilon_s)} \frac{51}{(39+s_{xe})} \tag{3.5}$$

$$\theta = 29 + 3500\varepsilon_s \tag{3.6}$$

Where:

ε_s = Longitudinal strain in the web (assumed positive for tension) found using Equation (3.6).

s_{xe} = Crack spacing parameter.

$$\varepsilon_s = \frac{|M_u / d_v| + 0.5N_u + |V_u - V_p| - A_{ps} f_{po}}{E_s A_s + E_p A_{ps}} \tag{3.7}$$

The *AASHTO LRFD Bridge Design Specifications* (Article 5.8.3.4; (AASHTO 2012) state that the parameter f_{po} is appropriate for both pretensioned and post-tensioned members when taken as follows.

$$f_{po} = 0.7 f_{pu} = 189 \text{ ksi} \tag{3.8}$$

The net longitudinal strain (ε_s) values for all four beams are negative even if half the strands are debonded. In this case, AASHTO states that ε_s may be taken as zero or the denominator of Equation (3.7) is changed to $(E_s A_s + E_p A_{ps} + E_c A_{ct})$. The value for ε_s was conservatively taken as zero for the transverse shear strength check.

Shear capacities for all four slab beams at the three critical sections are summarized in Table 3.7. Half of the reduced nominal shear strength contribution of the concrete ($0.5\phi V_c$) is slightly lower than the ultimate factored shear V_u within the end zone region. Therefore, transverse shear reinforcement is required. The values for V_s based on the standard transverse reinforcing steel provided for each slab beam type were calculated. It was found that the values for the reduced nominal shear capacity (ϕV_n) for all selected critical bridge superstructures were higher than the corresponding values of V_u. Therefore, the transverse steel currently provided in the TxDOT standard slab beam details was adequate based on the design calculations.

Table 3.4. Selected Bridge Geometries.

No.	Beam Type	Bridge Width (ft)	Center-to-Center Span (ft)	No. Strands per Beam
1	5SB12	26	38.58	52
2	5SB15	26	45.58	56
3	4SB12	34	34.58	38
4	4SB15	34	42.58	44

Table 3.5. Positions of Shear Check Sections.

No.	Beam Type	Section A (in.)	Section B (in.)	Section C (in.)
1	5SB12	13	20	42
2	5SB15	13	24	42
3	4SB12	13	20	38
4	4SB15	13	24	38

Note: Distances are from end of beam.

Table 3.6. Design Forces for Selected Bridges.

No.	V_u (kip)			M_u (kip/ft)		
	Section A	Section B	Section C	Section A	Section B	Section C
1	183	180	105	171	262	438
2	208	204	128	192	356	569
3	163	161	88	153	236	357
4	190	186	113	176	325	479

Table 3.7. Nominal Shear Capacity of Selected Bridges.

No.	Beam Type	Section	A_v (in^2)	s (in.)	b_v (in.)	d_v (in.)	β	θ (deg.)	V_c (kip)	V_s (kip)	V_n (kip)
1	5SB12	A	0.8	4.0	60	16.65	3.96	29	364	360	725
		B	0.4	5.5	60	16.65	3.96	29	364	131	495
		C	0.4	9.0	60	16.65	3.96	29	364	80.1	444
2	5SB15	A	0.8	4.0	60	19.35	3.73	29	399	419	818
		B	0.4	5.5	60	19.35	3.73	29	399	152	552
		C	0.4	12	60	19.35	3.73	29	399	69.8	469
3	4SB12	A	0.8	4.0	48	16.65	3.96	29	291	360	652
		B	0.4	6.0	48	16.65	3.96	29	291	120	412
		C	0.4	9.0	48	16.65	3.96	29	291	80.1	371
4	4SB15	A	0.8	4.0	48	19.35	3.73	29	319	419	738
		B	0.4	6.0	48	19.35	3.73	29	319	140	459
		C	0.4	12	48	19.35	3.73	29	319	69.8	389

3.4.2 Interface Shear Design Check for Standard Slab Beam Types

3.4.2.1 General

An example of a detailed interface shear design check is shown in Appendix A for the Riverside Bridge. Interface shear designs for the selected critical bridge geometries were conducted using the same procedure. Researchers took cohesion (c) and friction (μ) factors from AASHTO (2012). These parameters were selected for a CIP concrete slab on a clean girder surface not intentionally roughened (c = 0.075 and μ = 0.6) based on observed surface conditions for precast slab beams during fabrication.

AASHTO (2012) Article 5.8.4 indicates that the reduced nominal interface shear resistance V_{ri} should be greater than the factored interface shear force due to the total load at service.

$$V_{ri} = \phi V_{ni} \tag{3.9}$$

In addition, the design should satisfy:

$$V_{ri} \geq V_{ui} \tag{3.10}$$

Where:

V_{ni} = Nominal interface shear resistance, kip/ft.

ϕ = Strength reduction factor for shear = 0.9 for normal weight concrete.

V_{ui} = Factored interface shear force due to the total load, kip/ft.

According to AASHTO (2012) Article 5.8.4, the minimum reinforcement area crossing the interface area shall satisfy:

$$A_{vf} \geq \frac{0.05 A_{cv}}{f_y} \tag{3.11}$$

Where:

A_{vf} = Area of shear friction reinforcement, in^2.

A_{cv} = Area of concrete section resisting shear transfer, in^2.

f_y = Specified minimum yield strength of reinforcing bars, ksi.

Equation (3.11) suggests that 5 ft wide slab beams shall have minimum 0.56 in^2/ft interface shear reinforcement and 4 ft slab beams shall have minimum 0.44 in^2/ft interface

shear reinforcement. The TxDOT standard slab beam details satisfy this requirement by having a 0.8 in^2/ft reinforcing bar area crossing the interface plane.

Kovach and Naito (2008) suggested that the ACI 318-08 (2008) and AASHTO (2007) requirements for the interface shear design are highly conservative and a greater reliance can be placed on the cohesion of the concrete interface. ACI 318-08 allows a maximum of 80 psi horizontal shear stress for an unreinforced interface if the contact surface is clean, free of laitance, and intentionally roughened to 0.25 in. AASHTO (2007) allows a maximum of 240 psi horizontal shear stress for similar conditions if the minimum reinforcement requirement is disregarded. Kovach and Naito (2008) reported that previous research has shown that the same amount of roughened interface can achieve an average of 450 psi horizontal shear stress capacity (Evans and Chung 1969; Hanson 1960; Nosseir and Murtha 1971). Kovach and Naito (2008) concluded that the shear strength values obtained from the experiments are about six to 10 times greater than the values presented by ACI 318-08 for unreinforced composite sections. In addition, composite beams with a broom finish can achieve a horizontal shear capacity of 435 psi.

Waveru (2015) conducted an experimental research study as part of TxDOT project 0-6718 to investigate the horizontal shear strength provided by the short embedment length of the interface shear reinforcement provided in side-by-side slab beam and box beam bridges that have only a 5 in. thick CIP concrete deck. The tested slab beams were cast using both conventional concrete and self-consolidating concrete (SCC), both with a wood float finish, which results in a smoother interface for SCC as compared to conventional concrete. Although the 2 in. embedment length of the interface shear reinforcement did not provide sufficient development length, the full-scale tests showed that the actual boundary conditions could provide confinement to develop the reinforcement. The compressive force due to loading in positive bending prevented the reinforcement from pulling out. At ultimate horizontal shear capacity the reinforcement provided a minor contribution, with horizontal shear mainly resisted by friction, cohesion, and aggregate interlock of the concrete interface. The interface shear reinforcement engaged following slip at the interface. Waveru noted that the AASHTO equation overestimates the contribution of the interface shear reinforcement at ultimate conditions because the bars cannot yield. The strength of the interface shear steel was found to be 30 percent of the expected contribution at horizontal shear failure.

TxDOT standard drawings do not specify an intentionally roughened surface for precast slab beams. The interface shear design was conducted using two alternative methods permitted in the AASHTO LRFD specifications, including a sectional method and global force equilibrium. Each method is discussed below.

3.4.2.2 Sectional Method

The sectional method uses simplified elastic beam behavior, where for a unit length (1 ft) segment, the factored shear force may be calculated as:

$$V_{ui} = \frac{12V_u}{d_v} \tag{3.12}$$

Where:

V_{ui} = Factored interface shear force per length, kip/ft.

V_u = Factored shear force at section, kip.

AASHTO (2012) Article 5.8.4 states that the nominal shear resistance (V_{ni}) of the interface shear plane at the shear critical section shall be taken as:

$$V_{ni} = cA_{cv} + \mu\left(A_{vf}\, f_y + P_c\right) \tag{3.13}$$

Where:

A_{cv} = $b_v L_v$ = Area of concrete engaged in interface shear transfer, in^2.

b_v = Width of the interface, in.

L_v = Length of the interface, in.

A_{vf} = Area of interface shear reinforcement, in^2.

P_c = Permanent net compressive force acting normal to the shear plane, kip (assumed to be zero).

c = Cohesion factor = 0.075 ksi for not intentionally roughened surface.

μ = Friction factor = 0.6 for not intentionally roughened surface.

f_y = Yield stress of reinforcement, ksi.

The interface shear resistance for each selected bridge was determined for the TxDOT standard slab beam interface shear reinforcement. The computed values are listed in Table 3.8. As the table shows, the reduced total nominal interface shear resistance (ϕV_{ni}) is not sufficient

for these critical spread slab beam bridges at the locations of maximum shear demand when the beam surface is not intentionally roughened, which was the case for the standard slab beams used for the Riverside Bridge. Therefore, the standard interface shear reinforcement must be increased for spread slab beam bridges with relatively large spacings and spans. Or the beam surface can be roughened to 0.25 in. in order to have a higher cohesion factor and shear friction coefficient. Nominal interface shear resistances for an intentionally roughened surface and the same amount of interface shear reinforcement are also provided in Table 3.8. Note that the bridges selected for investigation had the largest shear forces in the parametric study for each slab beam type.

For all four selected critical bridge geometries, the typical slab beam interface shear reinforcement does not satisfy the design requirements provided in AASHTO (2012) Article 5.8.4 when the beam surface is not intentionally roughened, as observed for the Riverside Bridge slab beams. However, if the surface is roughened to a 0.25 in. amplitude, the standard interface shear reinforcement area is adequate. The required amount of interface shear reinforcement was then investigated for these selected bridges using the global force equilibrium approach.

3.4.2.3 Global Force Equilibrium

AASHTO (2012) Commentary C5.8.4.1 notes that a global force equilibrium method may be used to determine the distribution of interface shear reinforcement. The beam horizontal shear over a segment is calculated from the change in compression forces between two points, as shown in Figure 3.11.

Table 3.8. Interface Shear Check for Selected Bridges Using Sectional Method.

Interface Shear Parameters at Critical Section					Intentionally Roughened to 0.25 in.			Not Intentionally Roughened		
No.	Beam Type	A_{cv} (in^2)	A_{vf} (in^2)	V_{ui} (kip/ft)	c (ksi)	μ	ϕV_{ni} (kip/ft)	c (ksi)	μ	ϕV_{ni} (kip/ft)
1	5SB12	672	0.8	162	0.28	1.0	213	0.075	0.6	71.3
2	5SB15	672	0.8	151	0.28	1.0	213	0.075	0.6	71.3
3	4SB12	528	0.8	145	0.28	1.0	177	0.075	0.6	61.6
4	4SB15	528	0.8	138	0.28	1.0	177	0.075	0.6	61.6

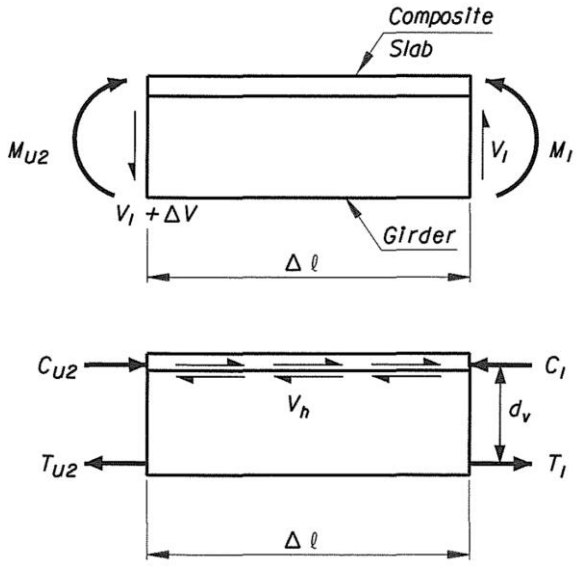

Figure 3.11. Horizontal Shear Demand—Global Force Equilibrium (AASHTO 2012).

In Figure 3.11, the following equations and parameters are employed.

$$C_1 = M_1 / d_v \tag{3.14}$$

$$V_h = C_1 - C_2 \tag{3.15}$$

$$v_h = \frac{C_1 - C_2}{l \cdot b_v} \tag{3.16}$$

Where:

C_1 = Compression force above the shear plane associated with M_1, kip.

C_{U2} = Compression force above the shear plane associated with M_{U2}, kip.

M_1 = Factored moment at Section 1.

M_{U2} = Factored moment at Section 2.

d_v = Distance between the centroid of the tension steel and the mid-thickness of the slab, in.

b_v = Width of the interface, in.

l = Length of the considered interface plane, in.

V_h = Horizontal shear force demand within the horizontal shear plane considered, kip.

v_h = Horizontal shear stress demand within the horizontal shear plane considered, ksi.

Horizontal shear demands were calculated between the support and quarter point of the span length and between the quarter point and midspan locations, along with the corresponding interface shear reinforcement requirements.

For the selected critical bridge geometries, the standard interface shear reinforcement between the support and quarter span length must be doubled, while the minimum interface shear reinforcement may be used for the region between the quarter span and midspan for these standard slab beam types.

Table 3.9. Interface Shear Design Using Global Force Equilibrium.

Parameter					Support to Quarter Span			Quarter Span to Midspan		
No.	**Beam Type**	***c*** **(ksi)**	**μ**	A_{cv} **(in²)**	A_{vf} **(in²/ft)**	ϕV_{ni} **(kip)**	V_h **(kip)**	A_{vf} **(in²/ft)**	ϕV_{ni} **(kip)**	V_h **(kip)**
1	5SB12	0.075	0.6	6480	1.8	1000	992	0.56	455	258
2	5SB15	0.075	0.6	7660	1.6	1110	1110	0.56	535	310
3	4SB12	0.075	0.6	4570	1.7	784	777	0.44	322	206
4	4SB15	0.075	0.6	5620	1.7	965	941	0.44	393	253

3.4.2.4 Development Length of Interface Shear Reinforcement

The interface shear resistance of the composite section is calculated based on the full yield strength of the reinforcement. Therefore, the interface shear reinforcement (denoted as H-bars in standard TxDOT drawings) should have sufficient development length into the slab beam and into the CIP deck concrete.

The required development length for the H-bars was calculated using AASHTO (2012) Article 5.11.2.4. The basic development length for a hooked bar l_{hb} with yield strength not exceeding 60 ksi can be calculated as:

$$l_{hb} = \frac{38 d_b}{\sqrt{f_c'}} \tag{3.17}$$

The parameter d_b is the diameter of the interface shear reinforcement (0.5 in. for the #4 H-bars in TxDOT (2013b) standard drawings). A modification factor of 0.7 can be applied because the cover normal to the plane of hook is not less than 2.5 in.

$$l_{hb} = 0.7 \times \frac{38 \times 0.5}{\sqrt{4}} = 6.65 \text{ in.}$$

Note that near midspan, the total CIP concrete thickness may be as low as 8.5 in., which includes a minimum 8 in. thick deck plus a 0.5 in. thick bedding strip. To maintain 2.5 in. clear cover, the hook height should be limited to 6 in. within the midspan region. To avoid using different extensions of the H-bars above the slab beams, a 6 in. dimension is suggested for all H-bars. The required development length can be further reduced to 6 in. using the excess reinforcement factor as long as the ratio of steel area required to steel area provided is 0.90 or less. For the critical bridge geometries considered, this would require the use of slightly more interface steel area than noted in Table 3.9 for the region between the support and quarter span.

3.5 SUMMARY

The research team conducted a parametric study to investigate preliminary designs for spread slab beam bridges. The effects of different parameters such as beam depth, beam width, number of beams, and beam spacing on the resulting maximum span length are summarized in Table 3.3. The following observations were made based on the results of the parametric study.

3.5.1 Parametric Study Observations

1. For all bridge widths considered (26 ft, 30 ft, 34 ft, 40 ft, and 46 ft), it is possible to span approximately 50 ft.
2. For 26 ft and 30 ft wide bridges, maximum span lengths of 50 ft 7 in. and 48 ft 7 in., respectively, are achieved when four 5SB15 slab beams are used.
3. For 34 ft wide bridges, the use of five 5SB15 slab beams results in a 49 ft 7 in. span length.
4. In order to achieve the maximum possible span length for 40 ft, 42 ft, or 46 ft wide bridges, six 5SB15 slab beams must be used.
5. The slab beam depth is the most prominent parameter for achieving longer span lengths.
6. Beam depth and beam width have a more prominent effect on the maximum span length as compared to the number of beams.
7. In general, smaller beam spacing results in a greater span length.
8. For the same number of slab beams, 4SB15 beams allow greater span lengths compared to 5SB12 beams despite a larger beam spacing. This shows that the beam depth effect is more pronounced than the beam spacing and beam width effects.

3.5.2 Shear Reinforcement

1. The current transverse and interface shear reinforcement provided in the standard TxDOT slab beam sections should be maintained as a minimum for spread slab beam designs.
2. The standard transverse shear reinforcement currently provided by TxDOT for standard slab beam types satisfies the required transverse shear strength criteria for the critical spread slab beam bridge geometries investigated in the parametric study.
3. Because the shear per beam increases in a spread configuration, the shear requirements should be carefully reviewed during design to ensure that the standard transverse and interface shear reinforcement is adequate. In particular, the interface shear reinforcement (H-bars) may need to be increased in the end regions for more shear critical cases when the beam surface is not intentionally roughened to a 0.25 in. amplitude.

4. Based on observed typical precast fabrication practices, standard slab beams do not have an intentionally roughened surface. The manufacturing process currently includes the use of self-consolidating concrete, and curing is achieved by submerging the beams in water and leaving the surface untouched. Therefore, the slab beam surface ends up being relatively smooth.
5. The design checks indicate that interface shear reinforcement (H-bars) area per foot length can potentially be reduced for the midspan regions. However, the interface shear reinforcement area per foot length may need to be increased for the end regions of standard slab beams, particularly for the more shear critical cases with longer spans and wider beam spacings.
6. Until further research is conducted to evaluate the interface shear strength of slab beam bridges, the research team recommends maintaining the use of the interface shear reinforcement based on current practice and performance of conventional slab beam bridges. Interface shear reinforcement requirements should be checked as part of spread slab beam bridge designs.
7. The H-bars provided for interface shear should be properly developed into both the precast slab beams and the CIP deck. Therefore, the standard H-bar detail should be modified to extend 6 in. into the CIP deck to provide the required development length. Note that sufficient steel area should be provided to justify this dimension, which is slightly smaller than the calculated hook length. This reduction is justified based on maintaining the ratio of area of steel required to area of steel provided at or below 0.90.

4. DESIGN AND CONSTRUCTION OF RIVERSIDE BRIDGE*

4.1 DESIGN OF AN INTERIOR SLAB BEAM

This section illustrates a summary of structural design procedure for an interior precast prestressed slab beam used in a spread configuration for the simply supported Riverside Bridge. The design is based on the American Association of State Highway and Transportation Officials (AASHTO) *Load and Resistance Factor Design (LRFD) Specifications* (2012). Also the recommendations provided in the *Texas Department of Transportation* (*TxDOT) Bridge Design Manual—LRFD* (TxDOT 2013a) are considered in the design. The detailed design procedure is discussed further in Appendix A.

4.1.1 Geometric and Material Properties

Figure 4.1 shows the bridge cross-section and Table 4.1 summarizes the geometric and material properties for the Riverside Bridge. The spread slab beam bridge considered has a 46 ft 7 in. center-to-center of bearing pad span length, with a roadway width of 32 ft and total width of 34 ft. The minimum deck thickness is 8 in. between slab beams.

This design follows TxDOT standard procedures, which is to include a constant 2 in. haunch thickness in the girder weight but neglect the contribution of the haunch to the girder stiffness. Therefore, the total thickness of the bridge deck is taken as 8 in. constant throughout. Vehicular live load is considered as the AASHTO LRFD Specifications (2012) HL-93 loading, consisting of a combination of HS20 design truck or design tandem, whichever is more critical, and a design lane load of 0.64 kips/ft.

According to the AASHTO LRFD Specifications (2012) Article 3.6.1.1.1, the number of design lanes is the integer part of the ratio of (w/12), where w is the clear roadway width between curbs or barriers. The value of w is 32 ft for this example, so the bridge that is being described herein is a two-lane bridge. The AASHTO LRFD Specifications (2012) define the effective flange width as being the tributary width, which is the center-to-center spacing of girders (9 ft 8 in. for the interior girders).

* Previously published work is available to the public through National Technical Information Service. Mary Beth D. Hueste, John B. Mander, Tevfik Terzioglu, Dongqi Jiang, and Joel Petersen-Gauthier (2014). "Spread Prestressed Concrete Slab Beam Bridges: Technical Report." Report No. FHWA/TX-14/0-6722-1, Texas A&M Transportation Institute, College Station, Texas, USA.

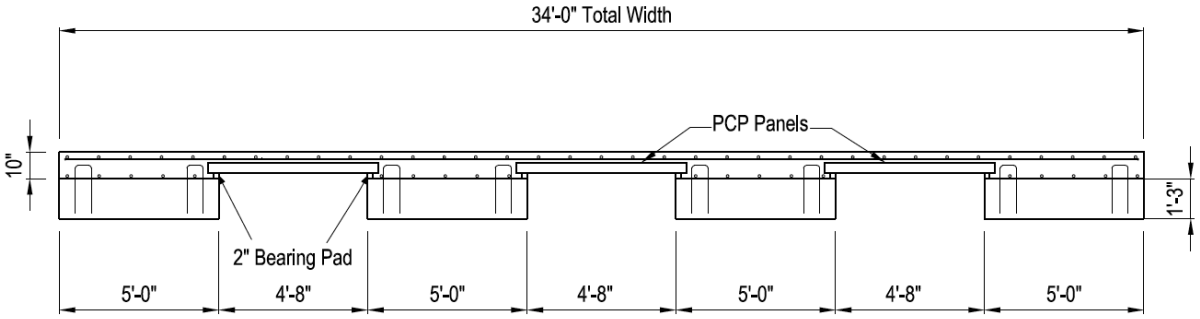

Figure 4.1. Bridge Cross-Section.

Table 4.1. Geometric and Material Properties of the Riverside Bridge.

Parameter	Description/Value
Span Length (Center-to-Center of Bearing Pad), L	46 ft 7 in.
Total Bridge Width, w	34 ft
Slab Beam Type	5SB15 (5 ft width, 15 in. depth)
Center-to-Center Beam Spacing, S	9 ft 8 in.
Deck Thickness, t_s	8 in.
Haunch Thickness, t_h	Assumed constant 2 in.
Rail	T551 (0.326 kips/ft)
Wearing Surface	2 in. thick asphalt assumed
28-Day Concrete Compressive Strength of Deck, $f_{cd}^{'}$	4.0 ksi
Initial Concrete Compressive Strength of Precast Slab Beam, $f_{ci}^{'}$	6.0 ksi
28-Day Concrete Compressive Strength of Precast Slab Beam, $f_{c}^{'}$	7.0 ksi
Unit Weight of Concrete, w_c	0.15 kcf
Unit Weight of Asphalt Overlay, w_s	0.14 kcf
Prestressing Strands	7-wire low-relaxation strands
Ultimate Strength of Prestressing Stands, f_{pu}	270 ksi
Modulus of Elasticity of Strands, E_p	28,500 ksi

The *TxDOT Bridge Design Manual* (TxDOT 2013a) provides limits for the compressive strength of the concrete. The compressive strength of the concrete at release $f_{ci}^{'}$ is specified to be between 4–6 ksi, and the compressive strength of the concrete at service $f_{c}^{'}$ is specified to be between 5–8.5 ksi.

4.1.1.1 Cross-Sectional Properties

The geometric dimensions and strand positions for a 5SB15 slab beam girder are provided in Figure 4.2. The number and arrangement of prestressing strands follow the standard strand configuration that is set for TxDOT slab beam types.

Table 4.2 shows the moment of inertia and section modulus of the slab beam itself and for the composite section. Detailed calculation of these parameters is provided in Appendix A.

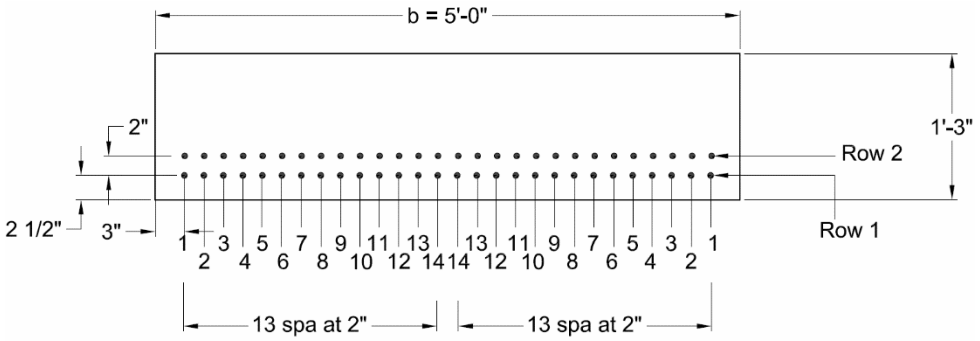

(a) Typical 5SB15 Slab Beam Section and Strand Configuration.

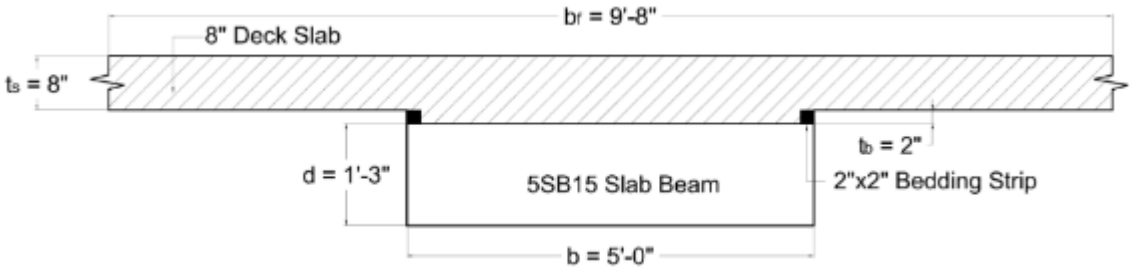

(b) Dimensions of Composite Cross-Section.

Figure 4.2. Precast Slab Beam and Composite Beam Sections.

Table 4.2. Sectional Properties.

Parameter	Slab Beam	Composite Section
Moment of Inertia (in^4)	16,875	72,753
Section Modulus Referenced to Bottom Fiber (in^3)	2,250	5,803
Section Modulus Referenced to Top Fiber (in^3)	2,250	6,954
Section Modulus Referenced to Top of Precast Slab Beam (in^3)	2,250	29,542

The haunch thickness is neglected, as suggested by the *TxDOT Bridge Design Manual* (TxDOT 2013a). The haunch thickness depends on the precast beam camber and may be smaller than 2 in. In some locations it may be as small as 0.5 in. Therefore, it is conservative to assume zero haunch thickness when determining cross-sectional properties. On the other hand, an average 2 in. haunch thickness is included in the self-weight calculation to avoid being unconservative in the load calculations.

4.1.2 Shear Force and Bending Moment Response

Structural analysis of the superstructure was conducted using the AASHTO LRFD Specifications (2012) approximate analysis approach, which utilizes live load distribution factors for truck and uniform lane loading.

Structural response of an interior girder was calculated when the vehicle is at the critical moment and shear position for combined loading. Combined loading includes the dead load of all structural components, superimposed dead loads, and the design live load.

4.1.2.1 Dead Load

Dead load is assumed to act on the non-composite slab beam section because the section is not composite when the deck concrete is fresh. Superimposed dead loads are assumed to act after the composite action between the slab beam girders and deck slab takes place. According to the *TxDOT Bridge Design Manual* (TxDOT 2013a), the wearing surface load can be equally distributed among four girders, and the rail load can be distributed to no more than three girders

from the edge of the deck. Table 4.3 summarizes the dead loads for different components of the composite section.

4.1.2.2 Live Load

AASHTO LRFD Specifications (2012) Article 3.6.1.2 specifies the design live load as HL-93, which consists of a combination of the design truck with dynamic allowance or the design tandem with dynamic allowance, whichever produces greater moments and shears, and design lane load without dynamic allowance.

AASHTO LRFD Specifications (2012) Table 3.6.2.1-1 specifies the dynamic load effects as a percentage of the static live load effects and to be taken as 33 percent of the static load effects for all limit states except the fatigue limit state and 15 percent for the fatigue limit state.

Figure 4.3 shows the HS20 design truck and design tandem. For the Riverside Bridge, which is a simply supported span, the design truck gives more critical moment and shear responses when the axle spacing between the front and middle axles and the axle spacing between the middle and rear axles are equal and 14 ft.

The lane load consists of a load of 0.64 kips/ft uniformly distributed in the longitudinal direction (AASHTO LRFD Specifications (2012) Article 4.6.2.2). The bending moments due to vehicular live load can be distributed to individual girders using the simplified approximate load distribution factor formulas specified by the AASHTO LRFD Specifications (2012).

There is no spread slab beam configuration defined in AASHTO LRFD Specifications (2012), therefore, formulas for spread box beam bridges were used for preliminary design. Live load distribution factor (LDF) formulas for moment and shear for interior girders are provided in AASHTO LRFD Specifications (2012) Tables 4.6.2.2.2b-1 and 4.6.2.2.3a-1. Table 4.4 summarizes the moment and shear LDFs for the one-lane loaded (g_{M1}, g_{V1}) and two-lane loaded (g_{M2}, g_{V2}) cases. The maximum values control the design for moment and shear actions.

Table 4.3. Dead Load of Different Components.

Description	Self-Weight	Wearing Surface	Rail
Weight, (kips/ft)	2.029	0.198	0.217

Table 4.4. Load Distribution Factors.

	g_{M1}	g_{M2}	g_{V1}	g_{V2}
LDF	0.41	0.68	0.68	0.86

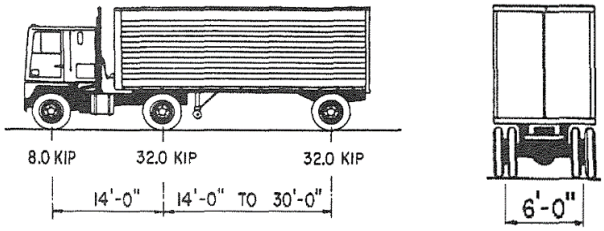

(a) HS20 Design Truck (AASHTO 2012)

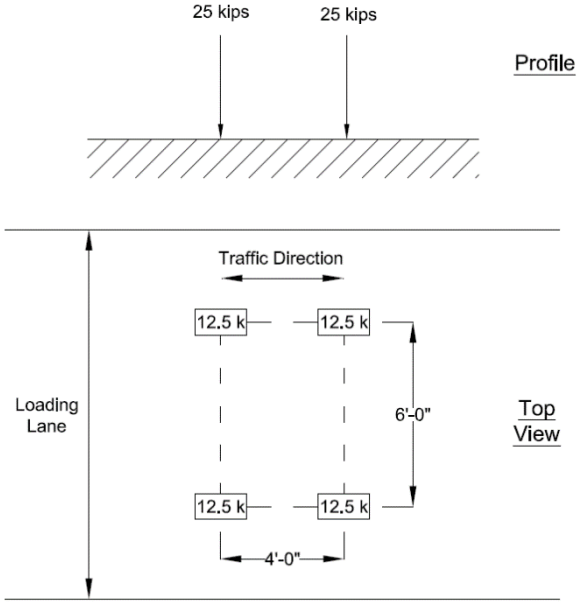

(b) Design Tandem

Figure 4.3. AASHTO HL-93 Design Vehicles.

4.1.2.3 Maximum Shear and Moment

The critical shear force is obtained when the rear axle of the HS20 truck is located at the critical shear section. The critical shear section was calculated based on the empirical formulas provided in the AASHTO LRFD Specifications and it is about 2 ft from the center of the bearing pad. Detailed calculations are presented in Appendix A. The shear forces calculated for dead and live loads when the vehicle is at this critical shear position are presented in Figure 4.4.

The moment critical longitudinal position of the HS20 truck was calculated based on the maximum design moment that occurs due to the combined effect of dead and live loads. Then the corresponding design moment was calculated for the combined loading. The maximum moment occurs at 2 ft 4 in. from the midspan for the HS20 truck, whereas the maximum moment for the uniform lane load and dead loads occurs at the midspan. This means the maximum moment for combined loading occurs somewhere between these two points. This point and the corresponding vehicle position were calculated using the influence line method.

Figure 4.5(b) shows unfactored moments for dead load of structural components (DC), dead load of wearing surface and utilities (DW), design truck live load (HS20), and uniform design lane live load (Lane). Figure 4.5(c) shows the total moments when all the live loads are multiplied by the moment distribution factor and dynamic allowance applied to the HS20 load. Table 4.5 shows the critical shear and moment values.

Another calculation was done when the vehicle is located at a critical moment position for the HS20 truck only (HS20 critical). For a series of point loads over a simply supported span, the maximum moment occurs under the load closest to the resultant when the load and resultant are placed equidistant from midspan. This approach is more commonly used due to its simplicity. For an HS20 truck that has the second and rear axles 14 ft apart, the critical moment position occurs when the second axle is 2 ft 4 in. away from the midspan. The results for this case are presented in Appendix A. Although the maximum moment results are close, the combined load critical position gives a slightly higher maximum moment, and it was used for further calculations.

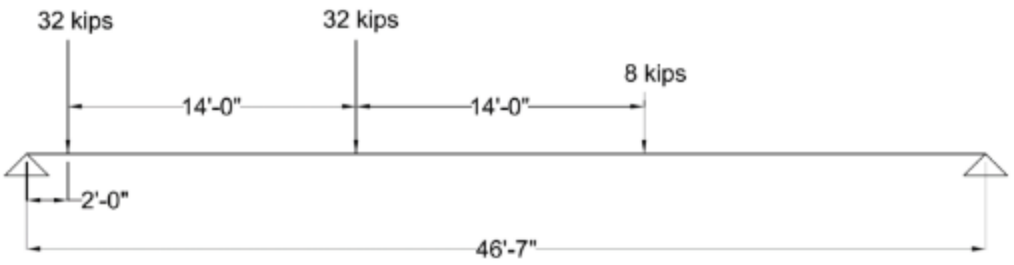

(a) Shear Critical Position for HS20 Truck

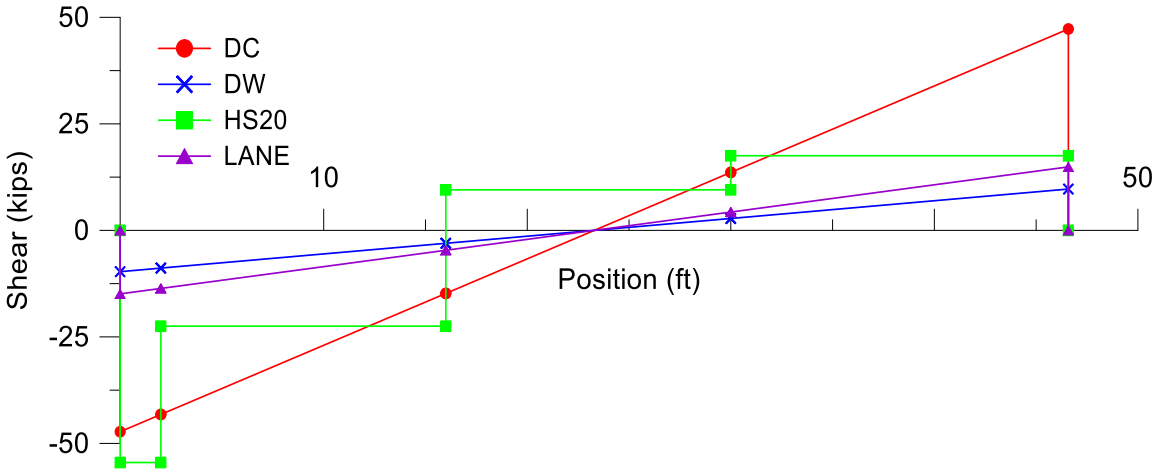

(b) Shear Forces for Shear Critical Position

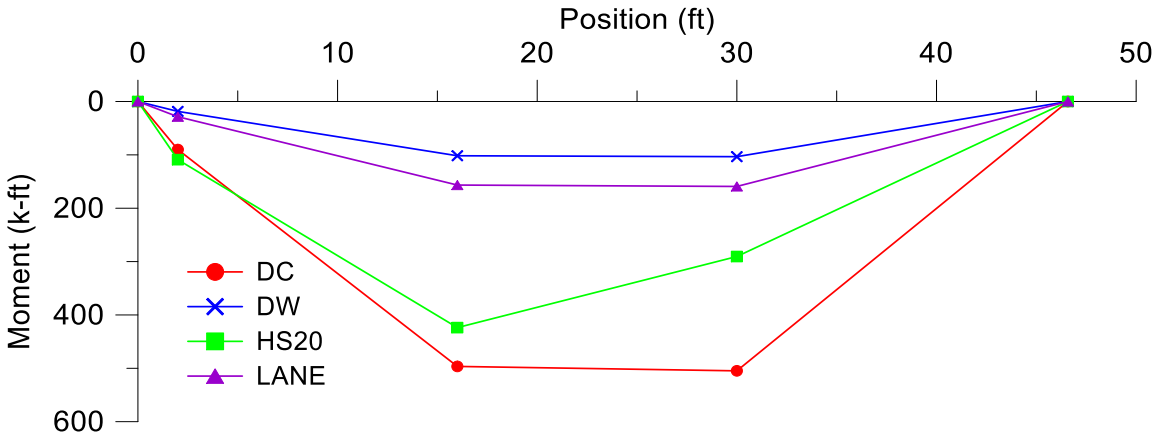

(c) Moments for Shear Critical Position

Figure 4.4. Shear Forces and Moments for Shear Critical Position of HS20.

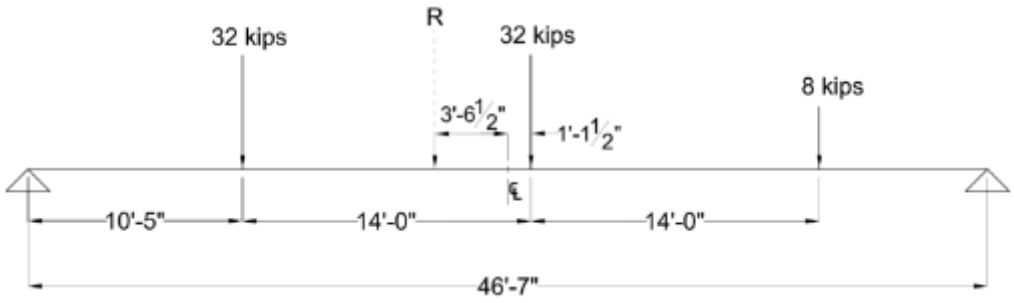

(a) Moment Critical Position of HS20 Truck

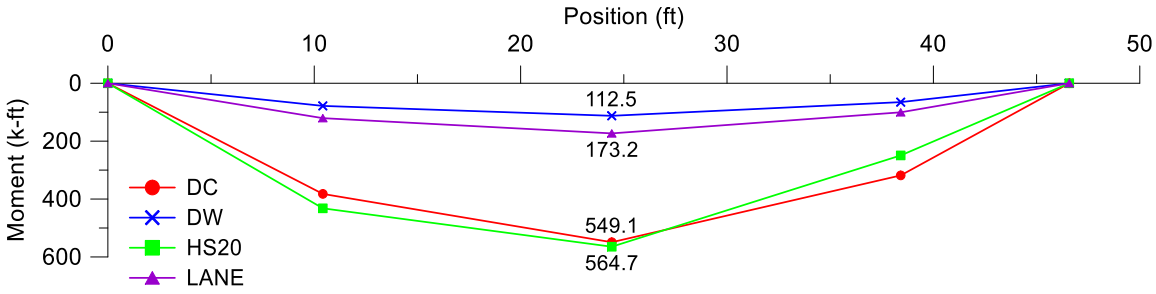

(b) Unfactored Bending Moments

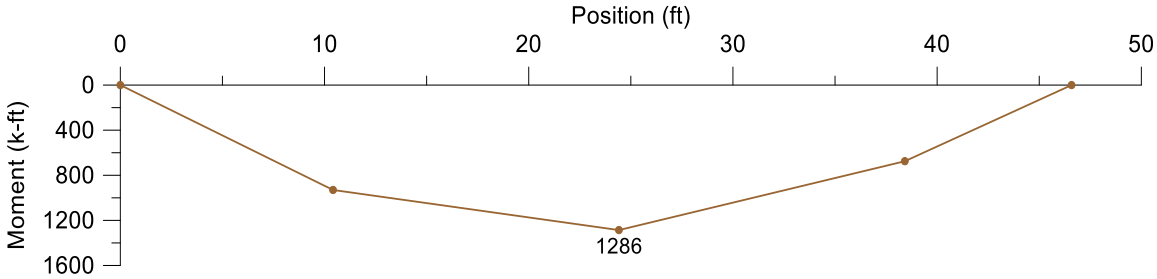

(c) Total Unfactored Bending Moment

Figure 4.5. Bending Moment Response for Combined Loading Critical Position.

Table 4.5. Maximum Shear and Moment Results at Critical Sections.

Response	Dead Load (DC)	Superimposed Dead Load (DW)	HS20	Uniform Lane
Shear Force (kips)	43.20	8.85	54.48	13.63
Moment (kip-ft)	549.1	112.5	564.7	173.2

4.1.3 Flexural Design for Prestressing Force

The required prestressing force under service loads was calculated at the critical moment section for the composite beam. Other critical section stresses were checked under the calculated prestressing force for the non-composite beam section only at transfer and at the time of deck casting prior to composite action.

4.1.3.1 Mid-Span Stresses due to Service Loads

AASHTO LRFD Specifications (2012) Table 3.4.1-1 specifies load combinations for various limit states. The load combinations that are critical for the designed bridge are as follows.

Service I—Check compressive stresses in prestressed concrete components:

$Q = 1.00(DC + DW) + 1.00(LL + IM)$

Service III—Check tensile stresses in prestressed concrete components:

$Q = 1.00(DC + DW) + 0.80(LL + IM)$

Strength I—Check ultimate strength [LRFD Table 3.4.1-1 & 2]:

Maximum $Q = 1.25(DC) + 1.50(DW) + 1.75(LL + IM)$

Minimum $Q = 0.90(DC) + 0.65(DW) + 1.75(LL + IM)$

Where:

DC = Dead load of structural components and nonstructural attachments.

DW = Dead load of wearing surface and utilities.

LL = Vehicular live load.

IM = Vehicular dynamic load allowance.

The maximum tensile stress at the bottom fiber of the slab beam girder f_b was calculated using the Service-III load combination as shown in Equation (4.1). The live load moment at service can be calculated as $M_{LL} = g_M(1.33M_{TR} + M_L)$, where M_{TR} is the maximum moment due to the truck loading and M_L is the moment due to the uniformly distributed lane load.

$$f_b = \frac{M_b + M_s}{S_b} + \frac{M_{ws} + M_r + 0.8M_{LL}}{S_{bc}} = 4.20 \text{ ksi} \qquad (4.1)$$

The maximum compressive stress at the top fiber of the slab beam girder at service is calculated using the Service-I load combination as shown in Equation (4.2).

$$f_t = \frac{M_b + M_s}{S_t} + \frac{M_{ws} + M_r + M_{LL}}{S_{tg}} = 3.23 \text{ ksi} \quad (4.2)$$

Where:

M_b = Bending moment due to self-weight of the slab beam at the moment critical section, kip-ft.

M_s = Bending moment due to CIP deck slab at the moment critical section, kip-ft.

M_{ws} = Bending moment due to wearing surface at the moment critical section, kip-ft.

M_r = Bending moment due to rail at the moment critical section, kip-ft.

M_{LL} = Bending moment due to truck load including impact plus the distributed lane load at the moment critical section, kip-ft.

4.1.3.2 Allowable Stress Limits

The tensile stress limit at transfer, F_{ti}, was calculated using Equation (4.3) as specified in the AASHTO LRFD Specifications (2012) Table 5.9.4.1.2-1. This limit allows the use of an increased tensile stress limit in areas with minimum bonded reinforcement.

$$F_{ti} = 0.24\sqrt{f_{ci}^{'}} = 0.59 \text{ ksi} \quad (4.3)$$

TxDOT Bridge Design Manual—LRFD (TxDOT 2013a) specifies a higher compressive stress limit at transfer than the one provided in AASHTO LRFD Specifications (2012), as shown in Equation (4.4).

$$F_{ci} = 0.65 f_{ci}^{'} = 3.90 \text{ ksi} \quad (4.4)$$

The tensile and compressive stress limits for prestressed concrete at the service limit state after losses for fully stressed components, F_t and F_c, is given in AASHTO LRFD Specifications (2012) Table 5.9.4.2.2-1 and was calculated using Equation (4.5) and (4.6).

$$F_t = 0.19\sqrt{f_c^{'}} = 0.50 \text{ ksi} \quad (4.5)$$

$$F_c = 0.45 f_c^{'} = 3.15 \text{ ksi} \tag{4.6}$$

4.1.3.3 Required Prestressing Force after Losses

The required prestressing force at service based on the tensile stress limit can be calculated using Equation (4.7).

$$-\frac{F_{req}}{A_b} - \frac{F_{req} e}{S_b} + f_b \le F_t \tag{4.7}$$

Where:

F_{req} = Total required prestressing force after all losses to satisfy allowable stress limits, kips.

e = Eccentricity of prestressing force (4 in. for 5SB15 section when all 56 strand slots are used), in.

f_b = Bottom fiber tensile stress at service, ksi.

F_t = Tensile stress limit at service after all losses occur, ksi.

Using the above calculated tensile stress limit and the stresses due to imposed loads at service, Equation (4.7) yields that $F_{req} > 1280$ kips.

The required prestressing force at service based on the compressive stress limit can be calculated using Equation (4.8). This relationship requires that $F_{req} > 120$ kips

$$-\frac{F_{req}}{A_b} + \frac{F_{req} e}{S_t} - f_t \ge F_c \tag{4.8}$$

The tensile stress limit controls the design and the total prestressing force should be at least 1280 kips in order to satisfy stress limits under service load conditions. The required number of strands can be calculated from Equation (4.9).

$$F = N\left(A_{ps}\right)\left(f_{pe}\right) \tag{4.9}$$

Where:

N = Number of prestressing strands.

f_{pe} = Effective prestressing stress of one strand after all losses, ksi.

A_{ps} = Nominal cross-sectional area of a prestressing strand (0.153 in^2 for 0.5 in. diameter strand), in^2.

4.1.3.4 Total Prestress Loss

Total prestress losses were calculated according to the empirical formulas provided in AASHTO LRFD Specifications (2012) Article 5.9.5 as shown in Equation (4.10).

$$\Delta f_{pT} = \Delta f_{pES} + \Delta f_{pLT} \tag{4.10}$$

Where:

Δf_{pT} = Total prestress loss, ksi.

Δf_{pES} = Sum of losses due to elastic shortening at the time of application of prestress, ksi.

Δf_{pLT} = Losses due to long-term shrinkage and creep of concrete and relaxation of the prestressing steel, ksi.

4.1.3.4.1 Losses Due to Elastic Shortening

The prestress loss due to elastic shortening in pretensioned members was calculated using Equation (4.11).

$$\Delta f_{pES} = \frac{E_p}{E_{ct}} f_{cgp} \tag{4.11}$$

Where:

E_p = Modulus of elasticity of prestressing steel, ksi.

E_{ct} = Modulus of elasticity of concrete at transfer, ksi.

f_{cgp} = Concrete stress at the center of gravity of prestressing tendons due to the prestressing force immediately after transfer and the self-weight of the member at the section of maximum moment, ksi.

For prestress loss calculations, the number of strands must be known. On the other hand, the required number of strands depends on the magnitude of the prestressing loss. This requires an iterative process. This calculation was carried out using an iterative calculation starting with 25 percent assumed total loss.

The above equation yielded that $\Delta f_{pES} = 15.62$ ksi and initial prestress after elastic shortening losses was calculated as $f_{pt} = 202.5 - 15.62 = 186.9$ ksi.

4.1.3.4.2 Refined Method for Estimating Time-Dependent Losses

AASHTO LRFD Specifications (2012) Article 5.9.5.4 provides a refined method for estimating the amount of prestress loss. The loss in the prestressing strands due to time-dependent effects, Δf_{pLT}, is calculated using Equation (4.12).

$$\Delta f_{pLT} = \left(\Delta f_{pSR} + \Delta f_{pCR} + \Delta f_{pR1}\right)_{id} + \left(\Delta f_{pSD} + \Delta f_{pCD} + \Delta f_{pR2} - \Delta f_{pSS}\right)_{df} \qquad (4.12)$$

Where:

$\left(\Delta f_{pSR} + \Delta f_{pCR} + \Delta f_{pR1}\right)_{id}$ = Sum of time-dependent losses between transfer and deck placement, ksi.

$\left(\Delta f_{pSD} + \Delta f_{pCD} + \Delta f_{pR2} - \Delta f_{pSS}\right)_{df}$ = Sum of time-dependent prestress losses after deck placement, ksi.

Δf_{pSR} = Prestress loss due to shrinkage between transfer and deck placement, ksi.

Δf_{pCR} = Prestress loss due to creep between transfer and deck placement, ksi.

Δf_{pR1} = Prestress loss due to relaxation of strands between transfer and deck placement, ksi.

Δf_{pSD} = Prestress loss due to shrinkage between deck placement and final time, ksi.

Δf_{pCD} = Prestress loss due to creep between deck placement and final time, ksi.

Δf_{pR2} = Prestress loss due to relaxation of strands between deck placement and final time, ksi.

Δf_{pSS} = Prestressing gain due to shrinkage of deck in composite section, ksi.

Details for calculating the prestress losses are provided in Appendix A. Equation (4.12) yielded that $\Delta f_{pLT} = 37.2$ ksi from Equation (4.10) total prestress loss was calculated as:

$$\Delta f_{pT} = 15.62 + 37.21 = 52.83 \text{ ksi}$$

Effective prestress after all losses, $f_{pe} = f_{pi} - \Delta f_{pT} = 202.5 - 52.83 = 149.7$ ksi.

Then Equation (4.9) gives $N = \dfrac{F_{req}}{A_{ps} f_{pe}} = 55.9 \approx 56$ strands.

4.1.3.5 Stress Check at Transfer

The initial prestressing stress before losses was $f_{pt} = 202.5$ ksi, and the initial prestressing force per strand was $F_{pt} = f_{pt} A_{ps} = 202.5 \times 0.153 = 30.98$ kips. The initial stress for checking the beam end stresses should take the elastic shortening losses into account.

The initial stresses due to prestress immediately after transfer is a function of the initial prestressing force (due to the f_{cgp} parameter in the Δf_{pES} calculation). Therefore, the initial prestressing force immediately after transfer, F_{pi}, is assumed to be 90 percent of F_{pt}, and the calculation was iterated until the desired accuracy was obtained for the F_{pi} value.

According to the *TxDOT Bridge Design Manual* (TxDOT 2013a), the prestress force may be assumed to vary linearly from zero at the end of the tendon to a full stress state at a distance of $60 d_b = 60 \times 0.5 = 30$ in. This distance is the transfer length over which the prestressing force is transferred to the concrete by bonding in pretensioned members.

Another component for designing the debonding of strands is the total span length of slab beams. The support locations are not strictly defined during the storage of precast beams, Therefore, the span length conservatively considered as the total length of slab beams, which is 48 ft.

The tensile stress in the precast concrete beam at the section located at the end of the transfer length was higher than the allowable stress. Therefore some of the strands were debonded. The stress state at the top and bottom surface was calculated at 1 ft increments until no stress exceedance occurred. Detailed calculations to determine debonding length requirements are provided in Appendix A.

Table 4.6 and Table 4.7 summarize the tensile and compressive stress states at the critical section immediately after transfer including elastic shortening losses. Based on the allowable stress limit at transfer, six strands should be debonded up to 3 ft from each end of the beam and four strands should be debonded up to 6 ft from each end of the beam.

Table 4.6. Stress Check at Critical Sections after Transfer.

x (ft)	T_i (kips)	Bottom Row	Top Row	N	$N_{debonded}$	F_{pi} (kips)	e (in.)	M_g (kip-ft)	$f_{b\ release}$ (ksi)	$f_{t\ release}$ (ksi)
0.0	0.0	22	28	50	6	0.0	3.88	0.0	0.000	0.000
1.0	11.4	22	28	50	6	568.0	3.88	22.0	-1.493	0.231
2.0	22.8	22	28	50	6	1137.9	3.88	43.1	-2.997	0.468
2.5	28.5	22	28	50	6	1423.6	3.88	53.3	-3.752	0.588
3.0	28.5	22	28	50	6	1424.7	3.88	63.3	-3.702	0.536
4.0	28.4	24	28	52	4	1477.8	3.92	82.5	-3.779	0.495
5.0	28.5	24	28	52	4	1480.1	3.92	100.8	-3.688	0.399
6.0	28.5	24	28	52	4	1482.2	3.92	118.1	-3.601	0.307
7.0	28.3	28	28	56	0	1585.2	4.00	134.5	-3.862	0.339

Table 4.7. Elastic Shortening Loss at Critical Sections.

x (ft)	**$(F_{pi})_{assumed}$ (kips)**	**f_{cgp} (ksi)**	**Δf_{pES} (ksi)**	**f_{pi} (ksi)**	**F_{pi} (kips)**
0.0	1417	2.84	17.23	185.3	1417
1.0	1420	2.78	16.89	185.6	1420
2.0	1422	2.73	16.57	185.9	1422
2.5	1424	2.70	16.41	186.1	1424
3.0	1425	2.68	16.26	186.2	1425
4.0	1478	2.76	16.75	185.8	1478
5.0	1480	2.71	16.47	186.0	1480
6.0	1482	2.67	16.20	186.3	1482
7.0	1585	2.88	17.49	185.0	1585

4.1.4 Ultimate Strength Check

Prestressed concrete members are assumed to remain uncracked under service loads, and the allowable stress design philosophy is adopted from the AASHTO LRFD Specifications (2012). The specifications also require an ultimate strength check of prestressed members that are designed based on allowable stresses. Design requirements for flexural members are summarized in AASHTO LRFD Specifications (2012) Article 5.7.3. The neutral axis depth at ultimate conditions was calculated using Equation (4.13).

$$c = \frac{A_{ps} f_{pu} + A_s f_s - A_s' f_s'}{0.85 f_c' \beta_1 b + k A_{ps} \left(\frac{f_{pu}}{d_p} \right)} = 6.29 \text{ in.} \quad (4.13)$$

Where:

k = 0.28 for low-relaxation strands.

f_c' = Specified compressive strength of concrete, 5 ksi.

β_1 = Ratio of the depth of the equivalent uniformly stressed compression block assumed in the strength limit state to the actual depth of the compression zone, 0.85 for 4 ksi specified concrete compressive strength.

d_p = Distance from extreme compression fiber to the centroid of the prestressing strands, in.

Then the average stress in prestressing steel, f_{ps} can be calculated using.

$$f_{ps} = f_{pu} \left(1 - k \frac{c}{d_p} \right) = 246.2 \text{ ksi} \quad (4.14)$$

Where:

f_{ps} = Average stress in prestressing steel, ksi.

c = Neutral axis depth, in.

The nominal flexural resistance of the slab beam can be calculated using Equation (4.15).

$$M_n = A_{ps} f_{ps} \left(d_p - \frac{a}{2} \right) = 3046 \text{ kip-ft} \quad (4.15)$$

The maximum moment under service loads was calculated using the Strength I load combination provided above.

$$M_u = 1.25(549.1) + 1.5(112.5) + 1.75(625) = 1949 \text{ kip-ft}$$

The factored nominal ultimate strength capacity of the section is greater than the factored ultimate moment under service loads. The ultimate strength requirement is satisfied.

$$\phi M_n = 0.9(3046) = 2741 \text{ kip-ft} > M_u = 1949 \text{ kip-ft}$$

4.1.5 Shear Design of an Interior Slab Beam

The shear resistance of the slab beam girder is checked using the guidelines provided by AASHTO LRFD Specifications (2012) Article 5.8.2. The shear resistance at the shear critical location is checked, and the required reinforcement is calculated. Due to the large cross-sectional area of the slab beam girders, the shear resistance of the concrete itself satisfies the required shear strength for most of the bridge geometries considered. For challenging geometries with wide beam spacing, the minimum shear reinforcement is adequate.

4.1.5.1 Transverse Shear Design

The nominal shear resistance at a given section is the sum of the concrete contribution, transverse reinforcement, and transverse component of the prestressing force.

$$V_n = V_c + V_s + V_p \tag{4.16}$$

Where:

V_c = Contribution of concrete to the shear strength, kips.

V_s = Contribution of steel to the transverse shear resistance, kips.

V_p = Component of prestressing force in the direction of applied shear, kips.

The shear critical section was calculated using the empirical formulas provided in the AASHTO LRFD Specifications (2012) and is located at $d_v = 0.9d_e = 22$ in. where d_e is the effective depth for bending.

The ultimate factored design shear at 22 in. from the support was calculated using the Strength I load combination.

$$V_u = 1.25V_{DC} + 1.5V_{DW} + 1.75V_{LL} = 196.8 \text{ kips}$$

The shear resistance provided by the component of the prestressing force in the direction of the applied shear was 0, because the strands are horizontal.

The shear resistance provided by the concrete was calculated using Equation (4.17).

$$V_c = 0.0316\beta\sqrt{f_c'}\,b_v d_v \tag{4.17}$$

The shear resistance provided by the shear reinforcement was calculated using Equation (4.18).

$$V_s = A_v f_y \frac{d_v}{s} \cot\theta \tag{4.18}$$

Where:

β = Factor indicating the ability of diagonally cracked concrete to transmit tension between cracks.

A_v = Area of transverse reinforcing steel (in^2) within a distance *s*, in.

f_y = Yield strength of the transverse steel reinforcement, ksi.

θ = Angle of inclination of diagonal compressive struts.

The parameters, β and θ are calculated using Equations (4.19) and (4.20)

$$\beta = \frac{4.8}{(1+750\varepsilon_s)} \frac{51}{(39+s_{xe})} = 3.88 \tag{4.19}$$

$$\theta = 29 + 3500\varepsilon_s = 29^o \tag{4.20}$$

Where:

ε_s = Longitudinal strain in the web (assumed positive for tension), in./in. ε_s =0, since the calculated value strain is negative.

s_{xe} = Crack spacing parameter, in. The parameter s_{xe} is a function of shear depth and maximum aggregate size and was calculated as 24.1 in.

Transverse steel currently provided in the *TxDOT Bridge Division Standard Drawings* (TxDOT 2013b) standard slab beam details is shown in Figure 3.10 as C bars using #4 bars and having 0.40 in^2/ft reinforcing bar area. Using the calculated β and θ values, the shear strength of the section can be determined as:

$$V_c = 0.0316(3.88)\sqrt{7}(60)(17.55) = 341.6 \text{ kips}$$

$$V_s = 0.4(60)\frac{17.55}{12}\cot(29) = 63.3 \text{ kips}$$

$$\phi V_n = 0.9(404.9) = 364.4 \text{ kips} > V_u = 196.8 \text{ kips}$$

Therefore, the transverse steel currently provided in the TxDOT standard slab beam details is adequate.

4.1.5.2 Interface Shear Design

The factored interface shear resistance must be greater than the factored interface shear force due to total load at service.

$$\phi V_{ni} \geq V_{ui} \tag{4.21}$$

Where:

ϕ = Resistance factor for shear, ϕ=0.9.

V_{ni} = Nominal interface shear resistance, kips.

V_{ui} = Factored interface shear force due to total load, kips.

AASHTO LRFD allows the use of sectional methods or global force equilibrium for interface shear design as described in Section 3. The sectional method is used here for checking the interface shear reinforcement that is provided in the standard slab beam details. For a unit length segment, the factored shear force may be calculated using Equation (4.22).

$$V_{ui} = \frac{12V_u}{d_v} = 152.4 \text{ kip/ft} \tag{4.22}$$

Where:

d_v = Distance between the centroid of the tension steel and the mid-thickness of the slab, in.

The nominal shear resistance at the interface plane can be calculated as

$$V_{ni} = cA_{cv} + \mu\left(A_{vf}\, f_y + P_c\right) = 79.2 \text{ kip/ft} \tag{4.23}$$

Where:

A_{cv} = $b_{vi}L_{vi}$ = Area of concrete that is engaged in interface shear transfer, in^2.

A_{vf} = Area of interface shear reinforcement, in^2.

P_c = Permanent net compressive force acting normal to the shear plane, kips.

c = Cohesion factor, ksi.

μ = Friction factor.

f_y = Yield stress of reinforcement, ksi.

Then the factored total interface shear force can be calculated as:

$$\phi V_{ni} = 0.9(79.2) = 71.3 \text{ kips/ ft} < V_{ui}$$

The amount of interface shear reinforcement provided for the standard slab beam type cannot achieve the required interface shear strength. The interface shear reinforcement must be increased from 0.8 in^2/ft to 3.2 in^2/ft if the entire beam is designed using the sectional method and the surface is not intentionally roughened. However, this value is reduced to 1.8 in^2/ft for the first quarter of the span if global force equilibrium is used. A detailed methodology for determining interface shear demand of segments using global force equilibrium is shown in Section 3. If #4 (H bars in TxDOT standard drawings) bars are used, the first quarter of the span can have six legs at an 8 in. spacing and the middle section can remain as four legs at a 12 in. spacing.

4.2 RIVERSIDE BRIDGE CONSTRUCTION

The experimental part of this research includes building a full-scale spread slab beam bridge and testing it under service loads to evaluate the performance. The obtained experimental measurements were then used to verify computational models. The Riverside Bridge was built as an on-grade bridge. The elevation of the finished deck is the same as the adjoining runway. In order to create a bridge span, the runway pavement in the immediate area was removed and the soil below was excavated to a certain depth, which allowed a minimum clearance for installation of instrumentation. Details of the construction process are provided in Appendix B.

4.2.1 Design and Construction of Substructure Components

4.2.1.1 Reinforced Concrete Retaining Wall

Figure 4.6 shows the cross-section of the retaining wall in relation with the existing runway. Several options for stabilizing the soil below the runway adjacent to the bridge were evaluated including steel sheet pile, cantilever retaining wall, and trenched retaining wall. Sheet pile and cantilever retaining wall options were relatively expensive. Instead, a trenched retaining wall was built and tied into the existing runway slab at the top and embedded into the soil at the base.

The retaining wall was designed based on the soil pressure and a possible surcharge that may result due to a vehicle driving near the wall. One layer of #4 rebar mesh was provided at the mid-thickness of the 8 ft high and 8 in. thick retaining wall.

Figure 4.7 shows the installed rebar mesh and concrete pour. The reinforcing bars for the wall were tied on the existing runway and lowered into the excavated trench with a forklift. The retaining wall concrete was specified as TxDOT Class C concrete having 3600 psi compressive strength and a 5.0–5.5 in. slump.

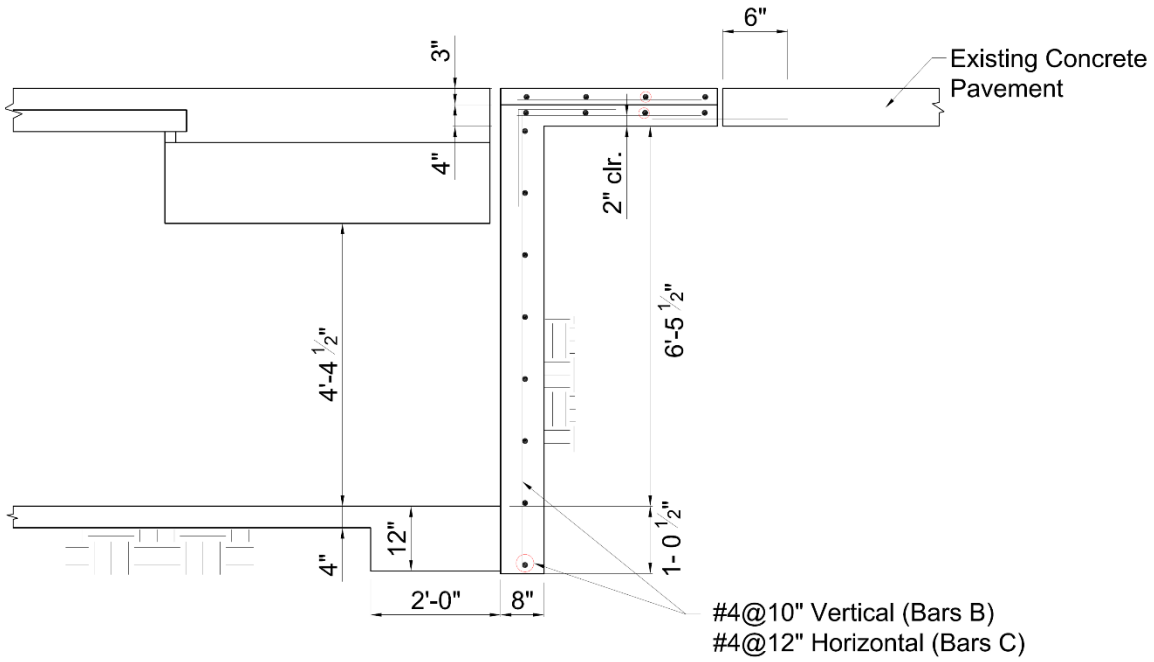

Figure 4.6. Retaining Wall Cross-Section Detail.

(a) Retaining wall Reinforcing Mesh

(b) Retaining Wall Concrete Pour

Figure 4.7. Retaining Wall Construction.

4.2.1.2 Reinforced Concrete Slab on Grade

Figure 4.8 presents the elevations of the slab-on-grade below the transverse centerline of the bridge. The slab was sloped toward the center of the bridge in the north-south direction and toward the west edge where the future drainage pit would be located.

Figure 4.9 shows construction of the reinforced concrete slab-on-grade. The on-grade slabs were poured in two steps. First, the 12 ft wide, 12 in. deep slabs below the north and south footings were poured and then the 4 in. deep middle slab was poured.

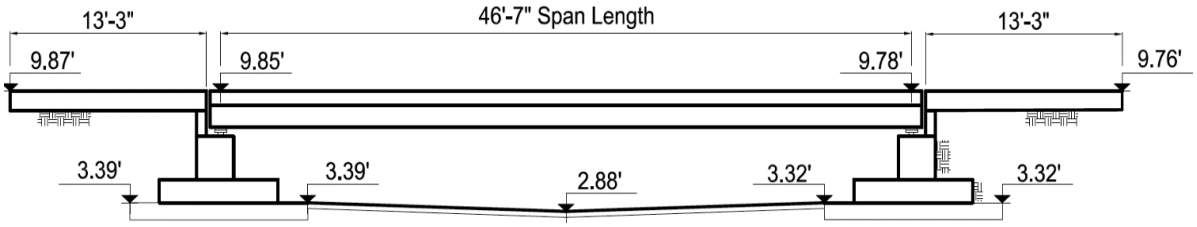

Figure 4.8. Target Elevations.

(a) Formwork and Reinforcement

(b) Slab-on-Grade Pour

Figure 4.9. Slab-on-Grade Construction.

4.2.1.3 Footing and Abutment Construction

The use of spread footings was determined to be the most economical foundation for this short-span bridge. The spread footing was designed by taking into account the highly plastic soil conditions of the site, which has high shrink-swell potential. The footing was designed according to the *TxDOT Geotechnical Manual* (2012) and the AASHTO LRFD Specifications (2012).

Because of the shallow depth of the abutment, overturning moment was not an issue. In addition, the large contact area of the 34 ft long footing provided adequate resistance against sliding. The geometry of the footing was controlled by the bearing pressure. Based on the bearing capacity of the soil (2246 psf), an 8 ft wide spread footing was found to be satisfactory according to allowable stress design.

Figure 4.10 shows the reinforcement details and geometry of the footings and abutments. The reinforcement for the footing was designed based on ultimate strength design and the AASHTO LRFD Specifications (2012). Although it was possible to achieve adequate strength with a 12 in. depth, the depth of the footing was increased to 16 in., and 20 percent more flexural reinforcement was provided for additional rigidity.

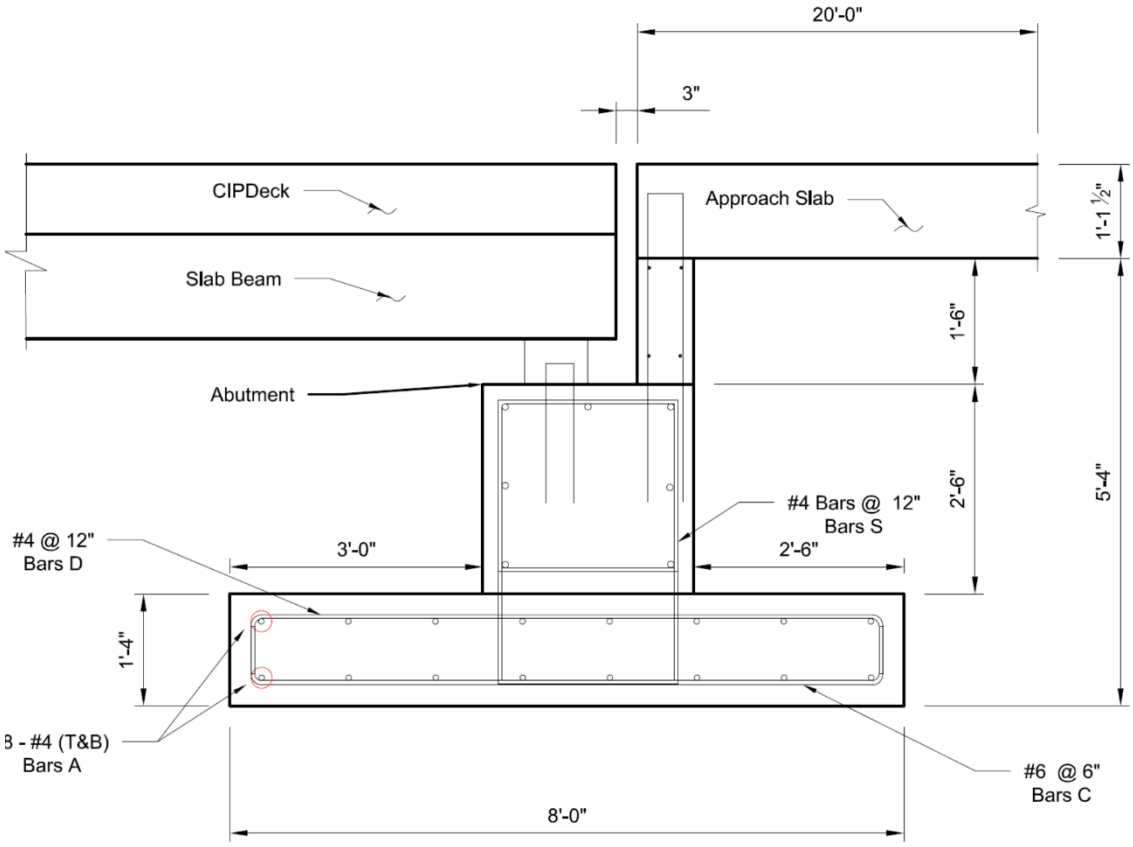

Figure 4.10. Reinforcement Detail of Footings and Abutments.

Figure 4.11 shows the reinforcement and concrete pour of the footings and abutments. After placement of the rebar, previously prepared formwork pieces were assembled for the footing construction. Concrete for all substructure components was specified as TxDOT Class C having 3600 psi compressive strength. The footing and abutment were cast in two different pours due to the geometry of the members.

Figure 4.12 shows all substructure components after removal of formwork, ready to support the precast members. The formwork for all the substructure components was removed before the start of the backfilling operation. A total of 350 tons of Type A Grade 1 backfill material was used to backfill the abutments.

(a) Footing Reinforcement

(b) Footing Concrete Pour

(c) Abutment Reinforcement

(d) Abutment Concrete Pour

Figure 4.11. Footing and Abutment Construction.

Figure 4.12. Substructure after Removal of the Forms.

4.2.2 Production and Placement of Precast Components

Figure 4.13 shows the detailed dimensions and the geometry of the superstructure components. The bridge superstructure is composed of four slab beam girders spaced at 4 ft 8 in. apart, PCPs that span between girders as stay-in-place forms, and a CIP reinforced concrete deck that combines all the pieces and creates the monolithic bridge superstructure.

The slab beam girders are standard TxDOT 5SB15 slab beams, and the PCPs are 4 in. thick, 8 ft long, and 5 ft 4 in. wide. The CIP deck thickness varies along the length due to the camber of the girders. The minimum deck thickness at the center of the bridge is 8 in. including the PCP thickness.

4.2.2.1 Fabrication of Precast Slab Beams and PCPs

The prestressed slab beam girders were designed based on the AASHTO LRFD Specifications (2012) and TxDOT Bridge Design Manual (TxDOT 2013a). The mild steel reinforcing bars were placed based on the standard TxDOT drawing PSB 5SB15. The only detail that was changed was the length of the H-bars. The height of the H bars was increased to 6 in. above the slab beam surface because the increased deck thickness allowed the H bar height to be increased to provide proper development length into the CIP deck slab. Detailed drawings and tendon layout are provided in Appendix B.

The prestressed slab beam and PCP construction was performed by Bexar Concrete Works in San Antonio, Texas. Figure 4.14 shows the slab beam construction process, with the reinforcing cage fabrication. Each of the 56 strands were stressed up to 31 kips of prestressing force, and specified strands were debonded up to 6 ft from both ends of the girders. The concrete was specified as self-consolidating concrete (SCC), having a compressive strength at release of 6 ksi and a compressive strength at service (28 days) of 7 ksi.

Eighteen 8 ft long PCPs were cast to span the three openings between the 48 ft long slab beams. The width of the panels is 5 ft 4 in. As transverse reinforcement, 0.5 in. diameter prestressing strands, stressed at 16.1 kips per strand, were placed at 6 in. spacing. The concrete for the PCPs was specified as TxDOT Class H with a release strength of 4 ksi and 28-day compressive strength of 5 ksi.

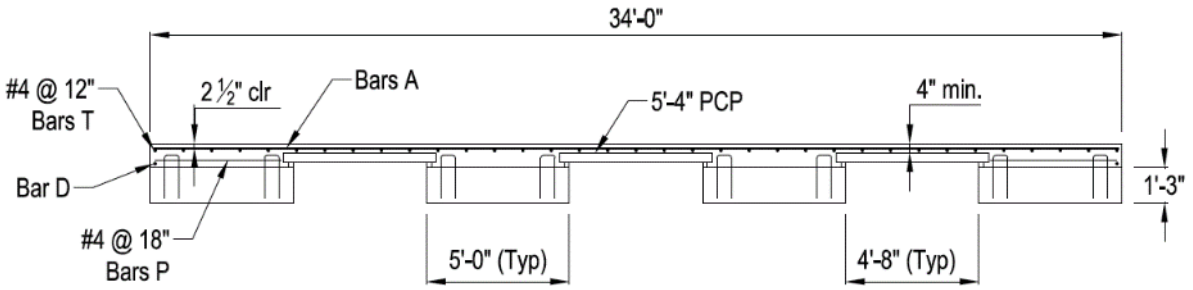

Figure 4.13. Riverside Bridge Superstructure.

(a) Slab Beam Reinforcement (b) Slab Beam Concrete Pour

Figure 4.14. Production of Precast Prestressed Slab Beams.

4.2.2.2 Placement of Precast Members

Figure 4.15 shows the load cell assembly placed at both ends before the slab beam erection. There are two different load cell assemblies due to the two-bearing-pad and one-bearing-pad configurations. At the south end of the bridge, there are two bearing pads (9 in. x 9 in.) at the corners of the slab beams. At the north end of the bridge, the bearing pads (9 in. x 18 in.) are at the center of the bridge. The load cells were placed between a 1 in. thick bottom steel plate and a 1.5 in. thick top steel plate.

Figure 4.16 (a) shows the precast members during erection. Four slab beams were positioned at their locations. The spacing between the slab beams was 4 ft 8 in. per design.

(a) North End Load Cell Assembly

(b) South End Load Cell Assembly

(c) Bridge Span Ready for Girder Placement

Figure 4.15. Load Cell Layout.

The total camber of the slab beams was measured to be 4.5 in. before the erection of the PCPs. This value was about 50 percent higher than the estimated camber. This higher than expected camber may cause construction delays and impact tight construction schedules. Excessive camber is one of the difficulties encountered during construction. The design camber, which is the total upward deflection after deck placement, was calculated based on the deflection estimates and the observed actual camber before PCP erection. The beams were expected to deform about 0.4 in. after the erection of PCPs and about 1.2 in. more after the CIP deck pour. Therefore, the bedding strip profile was adjusted accordingly to compensate for the approximately 3 in. camber difference between midspan and ends of slab beams. Based on these dimensions, the bedding strip depth was taken to be 0.5 in. at the midspan and 3.5 in. at the end of the slab beams, changing linearly in between.

(a) Slab Beam Placement

(b) Precast Panel Erection

Figure 4.16. Placement of Precast Members.

4.2.3 Deck and Approach Slab Construction

Figure 4.17(a) shows the reinforcing bar details and orientation for the CIP deck slab. The bridge deck reinforcing bars, consisting of #5 transverse reinforcing bars at 6 in. spacing and #4 longitudinal bars at 12 in. spacing, were placed over the PCPs based on the *TxDOT Bridge Division Standard Design Drawings* (TxDOT 2013b).

Figure 4.17(b) shows the deck concrete pour. The deck concrete was specified to be TxDOT Class S with a 4000 psi specified compressive strength. The concrete was cured by covering it with wet blankets and a plastic sheet for four days. However, a longitudinal temperature crack developed along the transverse centerline of the deck within the several days after pour.

Figure 4.18 shows the reinforcement layout of the approach slab. The first 20 ft of the approach slab from the end of the bridge was designed as a 13 in. deep approach slab having two layers of reinforcing mesh, and the remaining 9 ft was designed as a 7 in. deep reinforced concrete slab having one layer of reinforcing mesh. A 1 in. thick bituminous expansion joint material was glued at both ends of the bridge as a separation between the bridge deck and approach slab. A 1 in. thick Styrofoam board was glued along the east edge of the bridge as an expansion joint between the bridge and joining runway.

Figure 4.18(b) shows the concrete pour of the approach slabs. The concrete for the approach slabs was specified as TxDOT Class S having 4000 psi specified compressive strength. The top of the deck elevation was about 1.5 in. higher than the existing runway because of the high beam camber as compared to the predicted camber. This difference required the use of a gradual slope away from the bridge at both bridge ends over a 29 ft length.

(a) Deck Reinforcement

(b) Deck Concrete Pour

Figure 4.17. Deck Construction.

(a) Approach Slab Reinforcement

(b) Approach Slab Concrete Pour

Figure 4.18. Approach Slab Construction.

4.3 CONSTRUCTION CHALLENGES

One of the objectives of this research was to evaluate the constructability of the spread slab beam superstructure geometry and identify the challenges that may come up due to the new proposed configuration. The issues encountered during the construction were identified and discussed as part of this section. One challenge was the higher camber of the prestressed slab beams due to the relatively higher prestressing force required for the spread slab beam system. Another issue was the early-age longitudinal temperature crack that developed along the centerline of the deck.

4.3.1 Larger Camber

The longitudinal prestressing was applied eccentrically to the centroid of the slab beam section in order to counteract the downward deflection due to gravity loads and service loads. The upward deflection of a flexural member due to this eccentricity is called camber. The amount of camber depends on several factors, such as the amount of prestressing force, prestress losses, span length, section properties, modulus of elasticity of concrete, time, humidity, and concrete strength.

Predicting the camber accurately is important for design and construction of bridges. The amount of camber is a critical parameter in order to be able to adjust the haunch thickness throughout the span length at the time of PCP erection. However, prediction of deflections to a high degree of accuracy is not possible even in controlled conditions, due to prestress losses and strength gain of concrete at early ages. The camber prediction for the Riverside Bridge was 30 percent lower than the observed value. The bedding strip profile was adjusted accordingly, but the top of deck elevation at the abutments was 1 in. higher than the target value.

Because of the uncertainty in camber predictions, a simplified method was developed by Martin (1977) for elastic deformations. This simplified method is also known as the "multiplier method" and has been widely used by various design codes and design manuals. The multiplier method suggests multiplying the elastic camber and deflections at the time of load application for estimating the deflections at a later time. This method is still being used by the PCI Design Handbook (2010) and has been adopted by the AASHTO LRFD Specifications. It should be noted that the AASHTO LRFD Specifications do not provide methods for camber estimation, but provides relationships to predict prestress losses and the creep coefficient.

4.3.1.1 PCI Method

The PCI method uses the multiplier method to estimate the camber and deflections at prestress transfer, at the time of erection or CIP slab placement, and at some final time in the future.

The total deflection at transfer was calculated as the sum of elastic deflections due to self-weight and camber due to eccentricity of prestressing force as given in Equation (4.24)

$$\delta(t_i) = \delta_c(t_i) - \delta_b(t_i) \tag{4.24}$$

Where:

t = Time, days

$\delta(t_i)$ = Total upward deflection at time t_i, in.

t_i = Time of prestress transfer, 1 day.

$\delta_c(t_i)$ = Upward camber deflection due to prestressing force only at time t_i, in.

$\delta_b(t_i)$ = Downward deflection due to self-weight of the beam at time t_i, in.

The camber deflection at midspan for straight strands placed eccentrically to the concrete section centroid can be calculated using Equation (4.25). Derivation of this equation is provided in Appendix A.

$$\delta_c(\mathrm{t}) = y\left(\frac{L}{2}\right) = \frac{F(\mathrm{t})e}{E(\mathrm{t})I}\left(\frac{L^2}{8}\right) \tag{4.25}$$

Where:

F = Prestressing force, kips.

e = Eccentricity of the strands, in.

E = Modulus of elasticity of concrete, ksi.

I = Moment of inertia of the slab beam section, in^4.

L = Span length, in.

The total deflection at the time of bridge erection was calculated by multiplying the initial camber and self-weight deflections with factors that account for short term creep, provided in the PCI Design Manual Section 4.8.4 (PCI 2010) as given in Equation (4.26)

$$\delta(\mathrm{t_e}) = 1.8\delta_c(\mathrm{t}_i) - 1.85\delta_{\mathrm{b}}(\mathrm{t_i}) - \delta_{\mathrm{sd}} \tag{4.26}$$

Where:

δ_{sd} = Deflection due to superimposed dead loads, such as rails and wearing surface, in.

t_e = Time of precast member erection, 14 days.

The value of $\delta_{sd} = 0$ for the Riverside Bridge, because there is no rail or additional superimposed dead loads. The term t_e is considered to be the time of PCP erection for the Riverside Bridge, because this is the critical time for determining bedding strip thickness.

The total deflection at a final time in the distant future can be calculated similarly but using different multipliers to account for long-term creep effects. The PCI multipliers for long-term creep are given as

$$\delta(t_f) = 2.45\delta_c(t_i) - 2.7\delta_b(t_i) - 2.3\delta_d - 3\delta_{sd} \quad (4.27)$$

Where:

δ_d = Deflection due to composite deck slab, in.

t_f = Final time in the distant future, days.

4.3.1.2 AASHTO Method

The AASHTO LRFD Specifications (2012) provide camber predictions using the multiplier method with the creep coefficients given in Article 5.4.2.3.

The total deflection at transfer is calculated similar to the PCI method. The total deflection at erection can be calculated using Equation (4.28).

$$\delta(t_e) = \left(\delta_c(t_i) - \delta_b(t_i)\right)\left(1 + \psi(t_e - t_i)\right) \quad (4.28)$$

Where:

ψ = Creep coefficient provided in AASHTO LRFD Specifications (2012).

The calculation details for the creep coefficient are given in Appendix A. The creep coefficient between time t_2 and t_3 due to applied load at time t_1 is calculated as

$$\psi(t_3, t_2) = \psi(t_3, t_1) - \psi(t_2, t_1) \quad (4.29)$$

The total camber prediction at a final time can then be calculated as follows.

$$\delta(t_f) = \left(\delta_c(t_i) - \delta_b(t_i)\right)\left(1 + \psi(t_f - t_i)\right) - (\delta_p + \delta_d)\left(1 + \psi(t_f - t_i) - \psi(t_d - t_i)\right) \quad (4.30)$$

4.3.1.3 Time-Step Method

The AASHTO LRFD Specifications (2012) provide refined prediction equations for prestress losses and creep coefficients. However, the specifications do not specify a procedure for camber or deflection predictions. The time-step method provides camber estimation utilizing time specific losses at each step. The detailed procedure for camber calculation using the time step method is provided in Appendix A.

The method in Appendix A can be used to estimate total camber deflections at any time using Equation (4.31).

$$\delta_c(\mathrm{t}) = \delta_c(\mathrm{t_i}) - \sum_0^t \left(\delta_c(\mathrm{t}_{n-1}) - \delta_c(\mathrm{t}_n)\right) + \sum_0^t \left(\psi(\mathrm{t}_n - \mathrm{t_i}) - \psi(\mathrm{t}_{n-1} - \mathrm{t_i})\right)\left(\delta_c(\mathrm{t}_{n-1})\right) \quad (4.31)$$

Where *n*-1 and *n* defines the beginning and end of each time step. The first term in the equation is the camber deflection at the time of transfer; the second term is the decrease in the camber deflection due to prestress loss resulting from creep, shrinkage, and relaxation; and the third term is the increase in the camber due to creep. Then the total deflection at any time step can be estimated using the following relationship.

$$\delta(\mathrm{t}) = \delta_c(\mathrm{t}) - \delta_\mathrm{b}(\mathrm{t_i})\left(1 + \psi(\mathrm{t} - \mathrm{t_i})\right) \quad (4.32)$$

4.3.1.4 Comparison of Different Methods

The upward deflection of an interior slab beam was estimated using three different methods: PCI, AASHTO, and time-step. The camber prediction at transfer is identical for all methods given that the initial prestressing force is calculated after elastic shortening losses for all methods.

Figure 4.19 shows camber predictions for the AASHTO and time-step methods over time. The PCI method is not included because it only provides a camber estimate at two stages, at an early stage (erection of the deck) and at a distant final time. It can be observed that the camber predictions of both the time-step method and AASHTO method are very close for the early ages of concrete up to two weeks. At the time of deck placement this difference increases up to 15 percent.

Table 4.8 summarizes total upward deflection (camber) at several critical construction stages and the estimated values at corresponding times. The actual average camber of the slab beams was measured just before the erection of the PCPs as 4.5 in. The total upward deflection value after PCP erection and deck placement were calculated by subtracting the calculated deflection due to the tributary self-weight of the PCPs and CIP deck from the initial measured camber.

Figure 4.20 shows a bar chart comparison for the different camber prediction methods and actual camber values at two critical stages. The camber after deck placement is important because the haunch thickness and the final top of deck elevation depend on the accuracy of this final design camber value

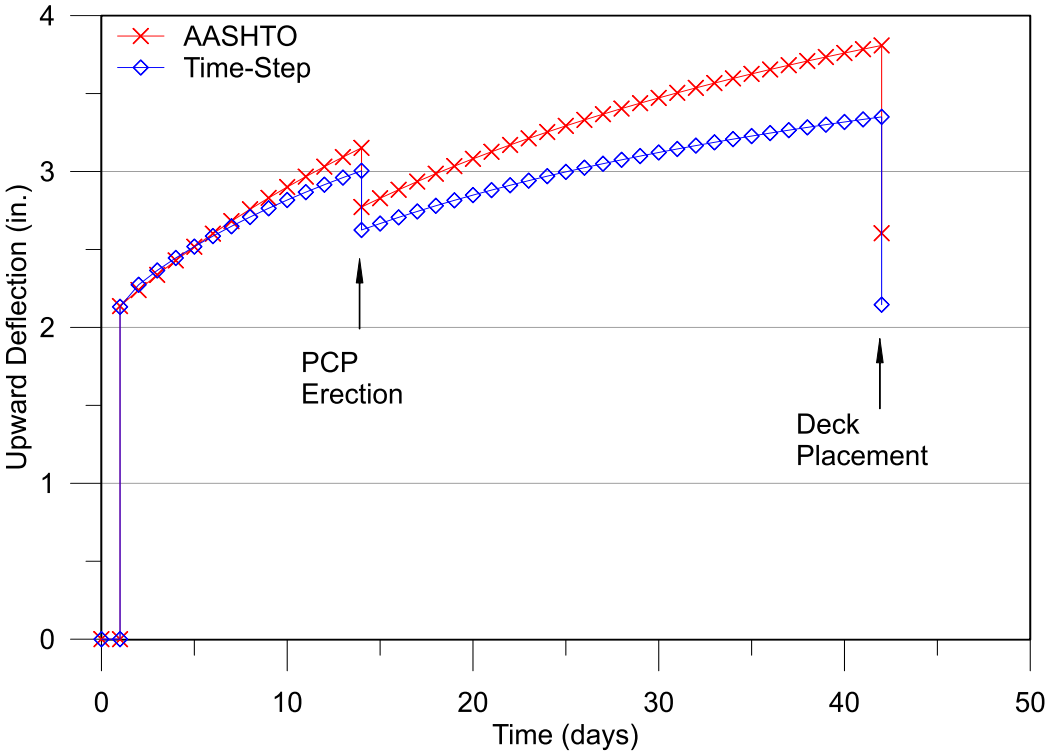

Figure 4.19. Camber Prediction at Different Construction Stages.

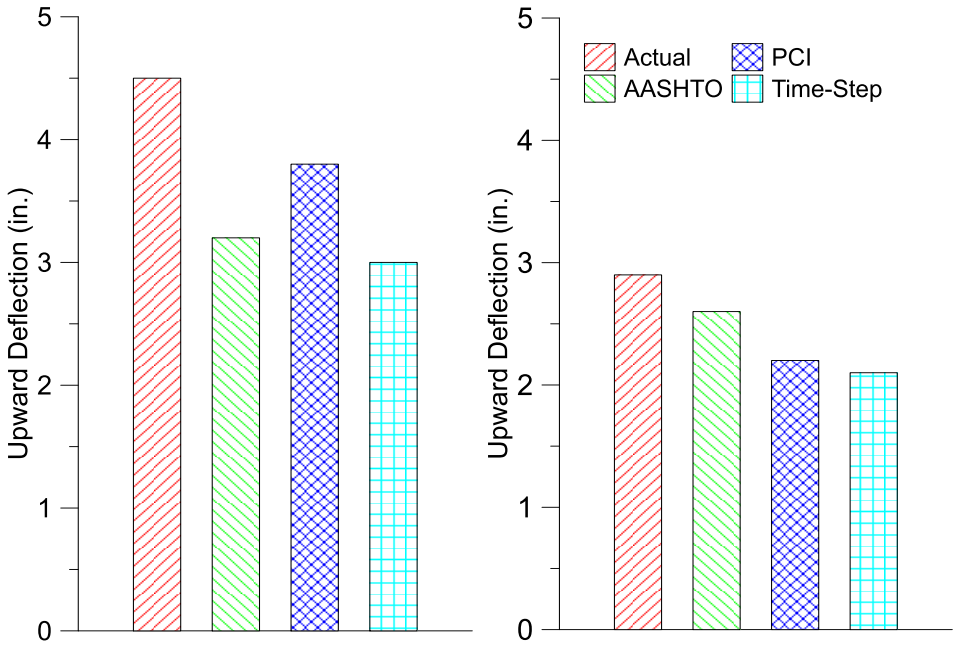

(a) Before PCP Erection (b) After Deck Placement

Figure 4.20. Camber Comparison at Critical Construction Stages.

Table 4.8. Total Upward Deflection at Different Stages.

Time	δ_{Actual} (in.)*	δ_{AASHTO} (in.)	δ_{PCI} (in.)	$\delta_{Time\text{-}Step}$ (in.)
At Transfer, 1 day	-	2.2	2.2	2.2
Before PCP Erection, 14 days	4.5	3.2	3.8	3.0
After PCP Erection, 14 days	4.1	2.8	3.4	2.6
Before Deck Placement, 42 days	-	3.8	3.4	3.3
After Deck Placement, 42 days	2.9	2.6	2.2	2.1

*Note: camber measured before PCP erection. Additional values are computed based on calculated deflections due to PCP and deck weight.

All three methods estimate cambers that are lower than the actual camber at the early ages of concrete up to two weeks. At two weeks, the PCI method gave a 20 percent lower camber estimate and the AASHTO method gave a 40 percent lower camber estimate. The camber predictions were closer at 42 days (after deck placement). The AASHTO method was only 10 percent lower than the value determined based on the measured value and additional elastic deflections.

4.3.2 Early Age Deck Cracking

A longitudinal deck crack developed along the centerline of the Riverside Bridge. It was first seen five days after the CIP deck concrete placement. It is believed that the crack developed because of thermal stresses within the first couple of days. The cooling of the deck creates tensile stresses at the top of the deck, and the friction between the composite deck and slab beams creates a large amount of restraint.

Early-age deck cracking develops due to heat of hydration and ambient conditions. Many researchers have long identified these thermal stresses as the primary reason for the bridge deck cracking together with drying shrinkage. However, the effect of drying shrinkage can be minimized when the concrete is wet cured with blankets and plastic sheets during the first several days after casting. Thermal stresses develop because of differential temperature distribution through the depth of bridge superstructure given that the superstructure is restrained for some degrees of freedom. The degree of restraint determines the amount of stress development.

4.3.2.1 Ambient Conditions and Restraints

The deck concrete was cast on October 1, 2013 at 8:00 a.m. Curing blankets were placed in the afternoon; then they were watered and covered with black plastic sheet. The maximum temperature was 98 °F and the humidity was 70 percent that afternoon. On October 2, 2013 the weather was cloudy most of the day. The average temperature was 80 °F and the humidity was 78 percent. There was a thunderstorm around 12:00 p.m., which resulted in a 3.8 in./h precipitation rate within 5 minutes.

The entire deck concrete warmed up because of the heat of hydration and the high ambient temperature during the first day, and the concrete temperature became even higher because of the black plastic sheet covering the deck. During the second day, under ambient weather conditions the top surface cooled down faster relative to the bottom of the deck concrete, where the CIP deck becomes composite with the precast members. With the heavy rain the top surface cooled down even faster, creating a more adverse differential temperature profile.

The transverse axial and rotational movements were resisted by the friction between CIP deck and precast components. Figure 4.1 shows the cross-section of the superstructure where the CIP deck was made composite with precast slab beams and PCPs. The CIP deck concrete casted over precast PCPs. The water in the fresh deck concrete was free to evaporate at the top whereas the bottom was protected by precast members which leads to differential shrinkage strains. The effect of differential shrinkage strain can be considered as an equivalent temperature drop at the top.

The composite connection prevents the deck concrete from contracting and rotating freely which results in tensile stresses due to primary thermal stress. In addition the continuity over the two interior slab beams also provides restraint against hogging curvature, which also results in tensile stresses at the top. This secondary effect is called secondary thermal stress.

4.3.2.2 Thermal Stress Analysis

Figure 4.21 shows the temperature gradient across the depth of the deck section. Top surface of the CIP deck cools down faster at the top of the deck compared to more protected bottom which creates differential temperature profile across the depth. Primary stresses induced by

this bilinear thermal gradient can be calculated using simple statics. If there is no restraint the free strain profile can be calculated as

$$\varepsilon_{free} = \alpha T(\mathrm{y}) \tag{4.33}$$

Where:

$T(y)$ = Differential temperature distribution, °F.

α = Linear coefficient of thermal expansion, 1/°F.

Plain section remain plain assumption holds true and final strain profile of the composite section must be linear. Because of bilinear nature of the differential temperature profile the difference between final strain, $\varepsilon(y)$ and free strain $\alpha T(y)$, results in a primary thermal stress. Then the total restrained stress can be calculated from as

$$f(\mathrm{y}) = \mathrm{E}\left(\varepsilon(\mathrm{y}) - \alpha\,\mathrm{T}(\mathrm{y})\right) \tag{4.34}$$

Applied temperature distribution can be converted into stress as $E\alpha T$. Where T is the temperature difference between top and bottom of CIP deck. There is an equivalent axial force and bending moment associated with temperature distribution. Equivalent axial force F corresponding to a temperature drop of magnitude T at the top of the deck can be calculated as

$$F = \frac{1}{2} E\alpha(-T)\mathrm{d} \tag{4.35}$$

This force corresponds to uniform axial stress of $0.5E\alpha(-T)d/2d = -0.25E\alpha T$. Then the equivalent bending moment can be expressed as

$$M = \frac{1}{2} E\alpha(-T)d\left(\frac{2d}{3}\right) \tag{4.36}$$

The corresponding bending stress then can be calculated as $My/I = -0.5E\alpha T$. The difference between free thermal stress and the stress resulting from axial and bending strains gives the residual stress trapped in the section. This residual stress is called the primary thermal stress. The maximum tensile stress due to primary stresses ,f_{t1}, at the top of the deck can be calculated as

$$f_{t1} = \mathrm{E}\left(\varepsilon_{final} - \varepsilon_{free}\right) = \mathrm{E}\left[(-0.25\alpha T - 0.5\alpha T) - \alpha(-T)\right] = 0.25E\alpha T \tag{4.37}$$

The deck can be considered as a continuous beam over the two interior slab beams. The deck is first allowed to hog downward due to the differential temperature profile by removing the interior support provided by the beams. Then a restraining moment is applied at the beam

locations to satisfy compatibility at interior supports. Figure 4.21 illustrates the procedure for calculating the restraining moments provided by interior supports where the deck is continuous (Priestley 1978).

The final moment M' was calculated by moment distribution. Then the tensile stress at the top of the deck due to secondary thermal stresses f_{t2} can be calculated as

$$f_{t2} = \frac{M'}{S} = \frac{1.2EI\phi}{I/d} = \frac{1.2E\alpha \mathrm{T}}{2} \tag{4.38}$$

Where:

ϕ = $\frac{\alpha \mathrm{T}}{2d}$ = final curvature.

4.3.2.3 Total Transverse Tensile Stress at the Transverse Mid-Section

The total thermal stress at the critical section, where the temperature crack was observed, can be calculated by summing the primary and secondary thermal stresses at that section.

$$f_t = \frac{E\alpha \mathrm{T}}{4} + \frac{1.2E\alpha \mathrm{T}}{2} = 0.85E\alpha \mathrm{T} \tag{4.39}$$

Because the early age deck cracking occurred within the first day, the modulus of elasticity of concrete and the tensile strength of concrete at one day must be estimated. Both of these parameters can be written as a function of time using the 28-day properties and time dependent coefficient suggested by Naaman (2004). Some of the mechanical properties of concrete, which are necessary for thermal stress calculations, are provided in Table 4.9. Modulus of elasticity (MOE) and modulus of rupture (MOR) values at 28 days were obtained from material tests, while 1-day MOE and MOR values were estimated using Equations (4.40) and (4.41).

Table 4.9. Deck Concrete Material Properties.

MOE 28d (ksi)	MOR 28d (ksi)	MOE 1d (ksi)	MOR 1d (ksi)	α ($1/^{\circ}F$)
6460	0.85	3560	0.47	6.0×10^{-6}

$$E(\mathrm{t}) = \mathrm{E}(28)\sqrt{\frac{t}{b+ct}} \tag{4.40}$$

$$F_t(\mathrm{t}) = F_t(28)\sqrt{\frac{t}{b+ct}} \tag{4.41}$$

Where:

F_t = Tensile strength based on modulus of rupture, ksi.

b = 2.33, Constant for rate of increase.

c = 0.99, Constant for the ultimate value.

Once the MOE and tensile strength value is estimated at one day, the minimum temperature drop that can develop a tensile crack can be calculated by rearranging Equation (4.39) and using the nominal tensile strength capacity.

$$\mathrm{T} = \frac{F_t}{0.85E\alpha} = 26\ ^{\circ}\mathrm{F} \tag{4.42}$$

This shows that if the temperature drop causes a differential temperature difference more than 26 $^{\circ}$F, thermal stresses exceeds the tensile strength capacity, which leads to a longitudinal crack. As discussed earlier drying shrinkage takes place even if the concrete is cured properly. Previous research studies showed that early age shrinkage strains within the first day for properly cured slabs may be around 50 microstrain which corresponds to 8 $^{\circ}$F equivalent temperature difference. Which means that 8 $^{\circ}$F of the required differential temperature difference for cracking (26 $^{\circ}$F) might have been consumed by early age drying shrinkage.

Although there is no temperature data for the Riverside Bridge deck, it can be anticipated that under the above explained ambient conditions and non-ideal curing practices, the temperature difference between top and bottom of the CIP concrete might have reached the 26 $^{\circ}$F thermal stress limit for cracking.

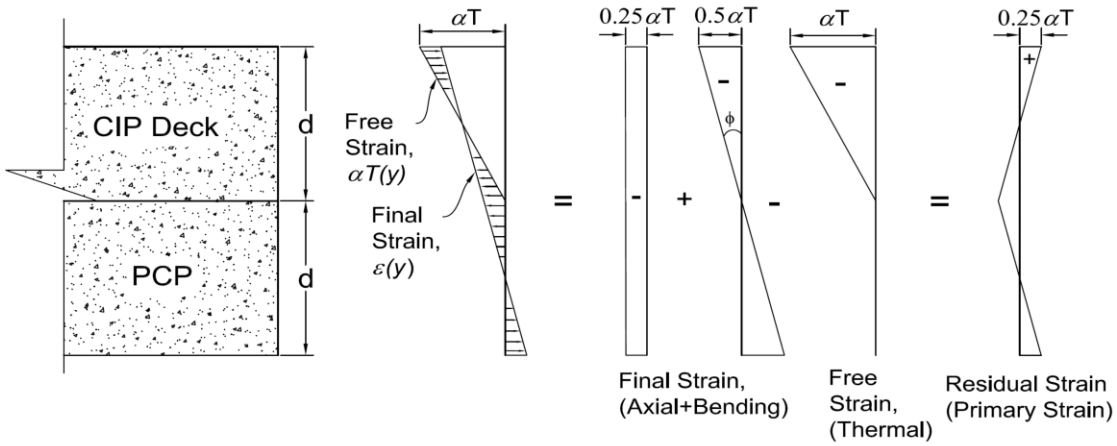

(a) Primary thermal strains in the deck cross-section

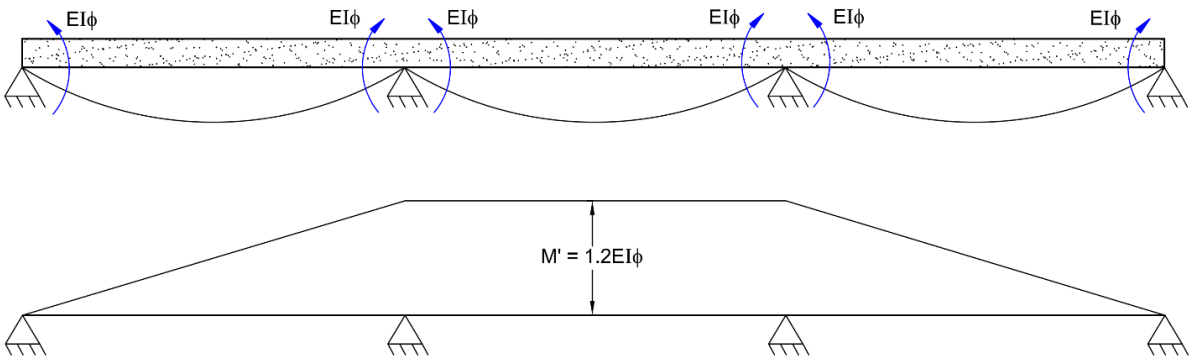

(b) Continuity moments that induce secondary thermal stresses

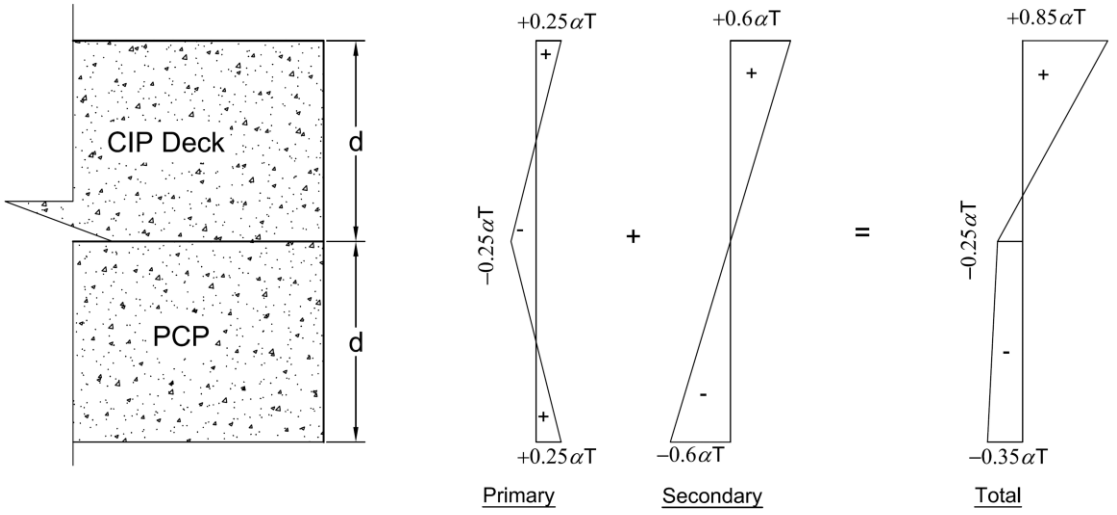

(c) Total thermal strains

Figure 4.21. Primary Thermal Stresses in the Deck Cross-Section.

4.4 SUMMARY AND FINDINGS

This section summarizes the design of an interior slab beam for the Riverside Bridge. The construction process for the Riverside Bridge, including all substructure components, is also summarized. In the final section construction challenges were discussed. The following conclusions were drawn.

1. A challenging spread slab beam bridge geometry with a relatively large beam spacing and the longest possible span length for this spacing was designed and constructed a the TAMU Riverside Campus. All 56 strand locations within the 5SB15 slab beam section were used to meet the tension stress limit at service. This aggressive design for this bridge system introduced several design and construction challenges including requirements for interface shear reinforcement and higher than predicted camber.
2. Design of the interior beam was controlled by the allowable tensile stress limit at service and the allowable tensile stress limit at transfer. Six strands were debonded up to 6 ft from both ends of the beam to prevent tensile stress exceedance at transfer.
3. A relatively high average camber was observed due to the large prestressing force required for the selected beam spacing and span. The actual camber was 15 to 30 percent higher than the estimated camber values based on different methods. Methods using the multiplier method (PCI and AASHTO) provided more accurate camber estimates as compared to the Time-Step method. Inaccurate camber estimation might cause construction delay for tight construction schedules. It may also affect the final top of deck elevation due to higher haunch thicknesses at the abutments or piers.
4. The interface shear reinforcement provided in TxDOT standard drawings can be reduced near the midspan; however, the standard reinforcement needed to be increased for the end regions of the beam if the beam surface is not intentionally roughened.
5. Thermal stresses may cause early-age deck cracking if the differential temperature drop over the deck thickness exceeds certain limits. Concrete warms up due to heat of hydration within the first day, then cools down due to ambient temperature. Practices such as covering with a black plastic sheet, which increases the temperature further, should be avoided. A sudden temperature drop at the deck surface creates a differential temperature profile, which can lead to cracking at the top of the deck as observed at the Riverside Bridge.

5. EXPERIMENTAL STUDY OF RIVERSIDE BRIDGE*

5.1 GENERAL

One of the main objectives of this research project was to identify moment and shear load distribution factors (LDFs) for spread slab beam bridges. The experimental part of the research project consisted of building a full-scale spread slab beam bridge and testing it under service loads in order to assess the constructability and serviceability of the bridge, and to study live load distribution factors. For that purpose, a simply supported bridge was designed and built at the edge of a runway located at the Texas A&M University Riverside Campus. Figure 5.1 shows the bridge site location and plan view.

5.2 GENERAL DESCRIPTION OF RIVERSIDE BRIDGE

As depicted in Figure 5.2, the bridge has a 46 ft 7 in. span length (from center to center of the bearing pads) and an overall width of 34 ft. The bridge superstructure has four slab beam girders spaced at 4 ft 8 in. clear spacing with prestressed concrete panels (PCPs) between the slab beams as stay-in-place (SIP) forms. The slab beam girders are standard TxDOT 5SB15 slab beams. The 4 in. thick PCPs are 8 ft long and have an overall width of 5 ft 4 in. The CIP deck thickness varies slightly along the length to accommodate the camber of the prestressed slab beams. The minimum deck overall topping plus PCP thickness at the center of the bridge is 8 in. Figure 5.2 and Figure 5.3 show detailed drawings of the bridge superstructure and substructure components, which were designed based on the AASHTO LRFD Bridge Design Specifications (AASHTO 2012) and TxDOT Bridge Design Manual (TxDOT 2013a).

All the substructure components are reinforced concrete and were designed based on ultimate strength design requirements. Reinforced concrete spread footings were used to support the abutments. A reinforced concrete slab on grade was poured in order to create a working surface. The thickness of the slab on grade increased to 12 in. under the spread footing locations.

* Previously published work is available to the public through National Technical Information Service. Mary Beth D. Hueste, John B. Mander, Tevfik Terzioglu, Dongqi Jiang, and Joel Petersen-Gauthier (2014). "Spread Prestressed Concrete Slab Beam Bridges: Technical Report." Report No. FHWA/TX-14/0-6722-1, Texas A&M Transportation Institute, College Station, Texas, USA.

(a) Location of Bridge Site (Google Maps 2005)

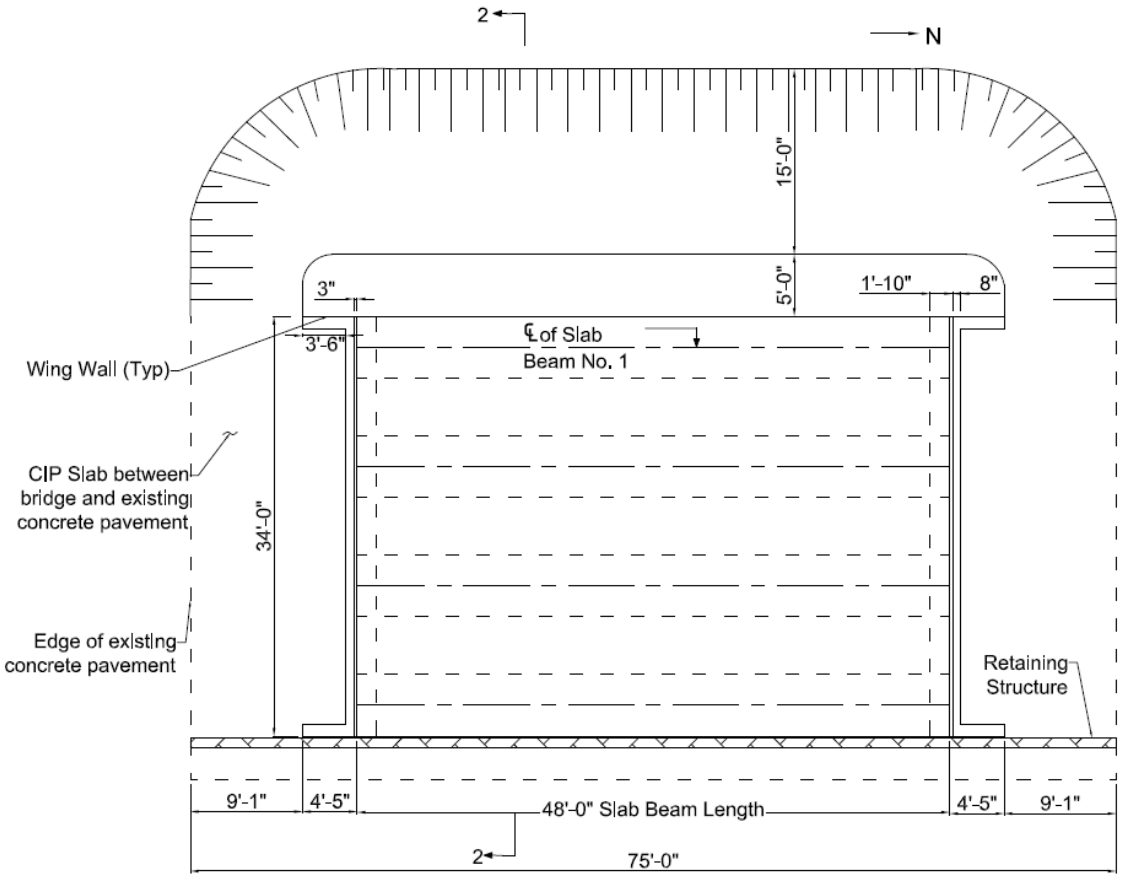

(b) Plan View

Figure 5.1. Bridge Location and Plan View.

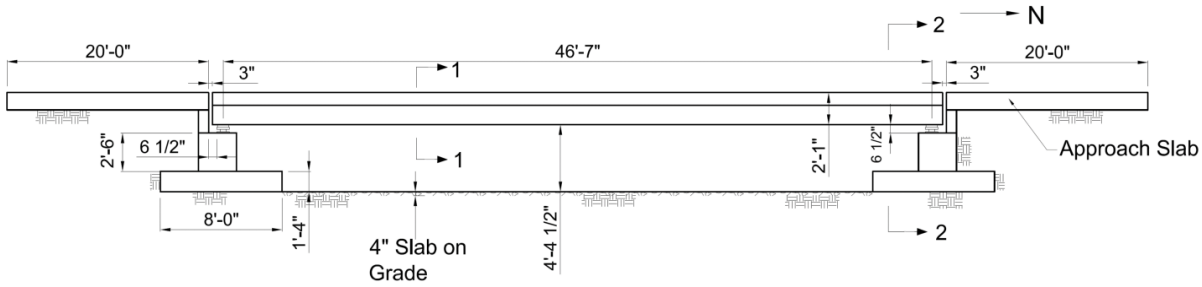

(a) Side Elevation View

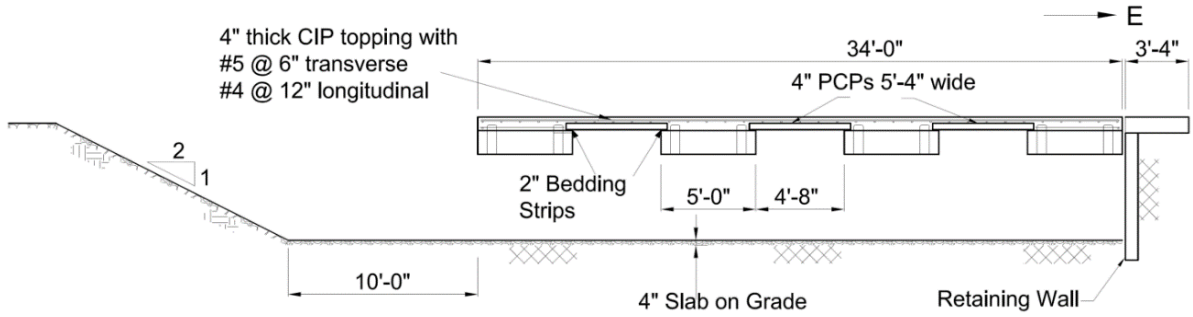

(b) Section 1-1: Cross-Section of Spread Slab Beam Deck

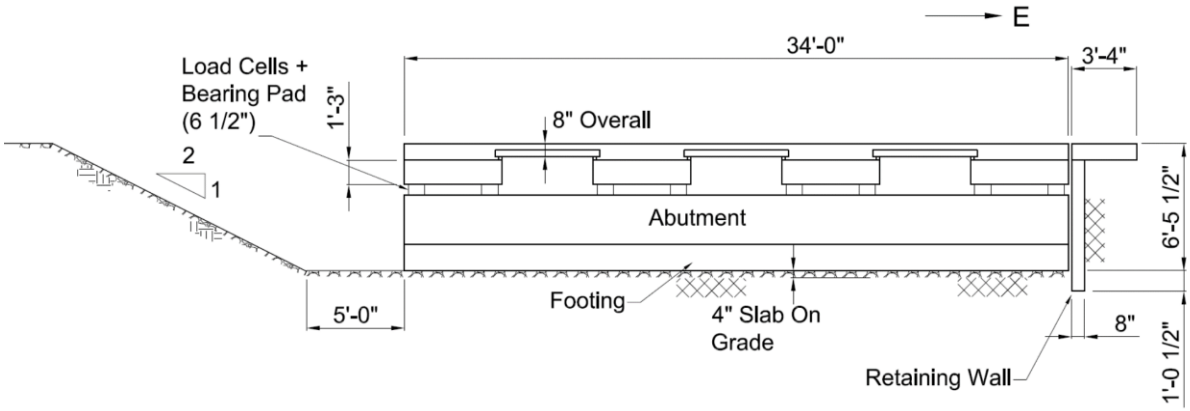

(c) Section 2-2: Cross-Section at Abutment

Figure 5.2. The Riverside Bridge Superstructure.

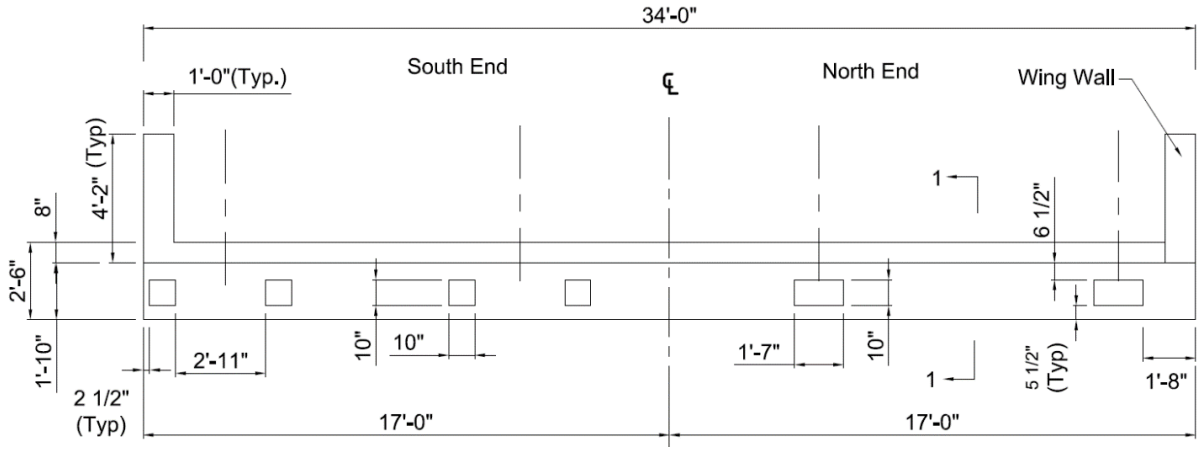

(a) Plan View at Abutment

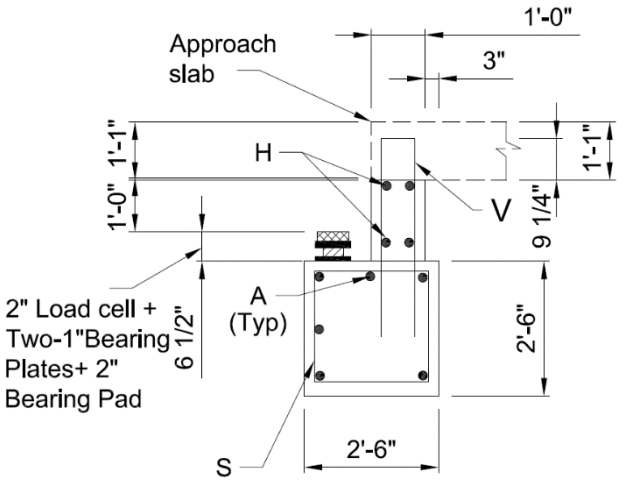

(b) Cross-Section 1-1 at Abutment

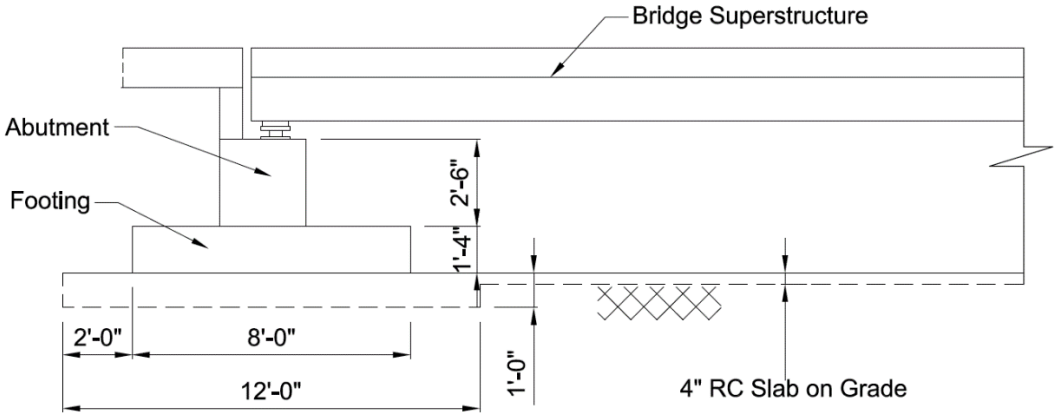

(c) Side Elevation of Abutment

Figure 5.3. The Riverside Bridge Substructure.

5.2.1 Load Cell Assembly and Bridge Superstructure

Figure 5.4 presents several photographs that show the load cell assembly and placement at each abutment. One of the difficulties when investigating live load distribution factors is the identification of shear reactions for individual girders. For the test bridge, load cell assemblies were placed beneath each girder before the erection of the slab beams. The load cell assembly consists of a 1 in. thick bottom steel plate and a 1.5 in. thick top plate sandwiching a 100-kip rated load cell (Figure 5.4(b). There are two different load cell assemblies as a result of a two-bearing-pad and a one-bearing-pad configuration, as shown in Figure 5.4(a) and (b). Figure 5.4(a) shows the south end of the bridge where there are two bearing pads (9x9 in.) at the slab beam ends, one at each corner, with 10x10 in. steel plates. Figure 5.4(b) shows the north end of the bridge where there is one bearing pad (9x18 in.) at the centerline of each slab beam; the steel plates are 10x20 in. The bottom plates were placed and attached to their exact locations using a high early strength grout. Load cells were placed inside small circular indentations machined on the steel plates. Then the top steel plates were also machined and placed on the button of the load cells.

After the erection of the slab beams, bedding strips were cut to the required depth. The bedding strip depth was calculated according to the camber of the slab beams. Bedding strip depth can be a minimum of 0.5 in. and a maximum of 4 in. according to the TxDOT Bridge Design Manual (TxDOT 2013a). Based on these calculations, the bedding strip depth was decided to be 0.5 in. at the midspan and 3.5 in. at the end of the slab beams, changing linearly in between. The width of the bedding strips was 2 in., as specified by TxDOT Bridge Design Manual (TxDOT 2013a). Figure 5.5 shows a view of precast beams and panels during erection. A total of 18 PCPs were placed along the span between slab beams (six for each clear space). According to the TxDOT Bridge Design Manual (TxDOT 2013a), the length of the PCP projecting past the bedding strip should be at least 1.5 in. For the Riverside Bridge, this length was designed to be 2 in. During the erection of the PCPs, the construction crew ensured a minimum projection of at least 1.5 in. was provided along each edge for all panels.

(a) South End Load Cell Assembly and Layout

(b) North End Load Cell Layout

(c) Bridge Span Ready to Receive Slab Beams

Figure 5.4. Load Cell Assembly and Layout.

(a) Slab Beam Placement

(b) Bedding Strip Application

(c) Placement of Precast Concrete Panels

Figure 5.5. Placement of Precast Slab Beams and Panels.

5.3 INSTRUMENTATION OF BRIDGE

Figure 5.6 shows the detailed naming and position of each sensor that was used during preliminary testing. The instrumentation of the Riverside Bridge was designed based on the objectives of the research program. A total of 16 load cells were placed at both ends of each slab beam during the construction process. The load cells are used to determine the load sharing between slab beams under vehicle loading and the corresponding shear distribution factors.

The moments for each girder can be calculated from the deflection profiles of the slab beams. In order to obtain the moments, at least three deflection values along the length must be known, but more points are advantageous for numerical differentiation using recorded deflection values. Based on the available channels on the data acquisition system it was decided that a total of 10 string potentiometers per girder would be used.

A total of four tests were conducted to investigate load sharing between girders for the spread slab beam bridge at Riverside. The first three tests included preliminary testing to explore the appropriate instrumentation layout and methods to determine shear and moment LDFs.

The preliminary instrumentation layout suggested using the string potentiometers at seven stations. For three of those seven stations, string potentiometers were provided at both edges of the slab beams to capture torsional deformations of the slab beam girders.

In order to be able to capture natural frequency and mode shapes of the girders during dynamic testing, a total of eight accelerometers were attached on the bottom of the slab beams. Five accelerometers were attached along one of the interior beams, and the remaining three accelerometers were attached at the midspan locations of each of the other slab beams.

The data acquisition system used for testing is capable of supporting 64 channels with one main box. There were 16 load cells (eight at each end of the bridge), 40 string potentiometers, and eight accelerometers attached to the bridge, for a total of 64 channels of data. In order to have one fixed instrumentation setup, an initial configuration for the location of each device was determined.

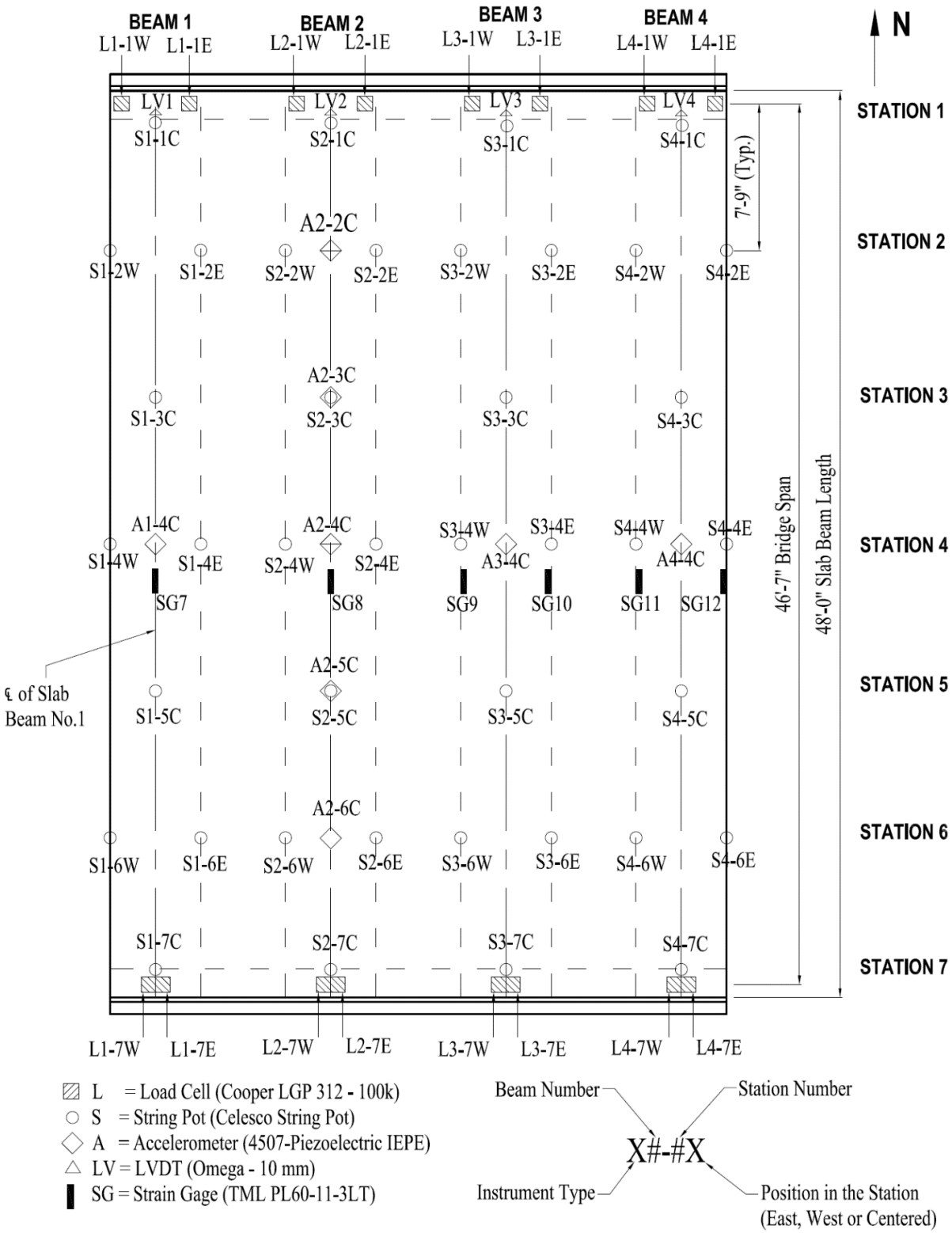

Figure 5.6. Initial Instrumentation Layout and Labeling.

The instrumentation layout shown in Figure 5.6 includes the labeling of all sensors, based on this layout. The locations of the sensors were labeled according to the station numbers and the beam number. The location of the sensors, except the string potentiometers, remained the same throughout the experimental program. The sensors shown were attached at the bottom surface of the slab beams. The only sensors on the top surface (deck surface) were six strain gages (SG1–SG6) that were attached at the same position in the plan as the bottom strain gages.

5.4 TESTING OF INDIVIDUAL SLAB BEAMS

Figure 5.7 shows a photograph of a typical layout for the accelerometers on a slab beam. Accelerometers were attached along one of the slab beams to identify frequency characteristics of an individual non-composite slab beam. Accelerometers were attached at the top surface of the slab beam at 6 ft 8 in. spacing starting at the center of the bearing pad. Before casting the deck concrete, the data acquisition system was connected to the load cells to obtain the individual weights of the slab beam girders and test the performance of the load cells. Data were processed, and individual beam reactions at the north and south ends of each beam were obtained.

Individual slab beam support reactions are also listed in Table 5.1. An approximate weight calculation based on the unit weight of concrete shows that the weight of the 48 ft long 5SB15 slab beam is 44 kips. The load cell readings showed the average weight of the four slab beams as 44.7 kips, which is reasonably close when the reinforcing bars, non-uniformity of the beams, and sensitivity of load cells are considered. The signal from the load cells during the 30-second time interval is very quiet and stable. Figure 5.8 shows the results from preliminary testing of the individual slab beam.

Figure 5.7. Accelerometer Positions for Individual Beam Test.

Figure 5.9(a) shows the amplitude-frequency plot for the tested slab beam based on the accelerometer close to midspan. The accelerometer data were processed in the frequency domain, and the first two natural frequencies of the slab beam were obtained. Because there were eight accelerometers on the beam, the mode shapes for these two modes were also captured.

Figure 5.9(b) shows the amplitude spectrum along the length, which is an indicator of the mode shapes. The natural frequency of the beam is 3.9 Hz and the natural frequency of the second mode is 28.9 Hz. A relatively low natural vibration period is a result of high stiffness due to a high amount of prestressing and high modulus of elasticity. The mode shapes can be clearly identified from the amplitude spectrum. The first mode corresponds to the flexural bending mode, and the second mode is the second bending mode of the beam.

Table 5.1. Individual Slab Beam Weights.

	North Reaction (kips)	South Reaction (kips)	Beam Weight (kips)
Beam 1	22.3	22.0	44.3
Beam 2	22.1	22.7	44.8
Beam 3	22.4	22.2	44.6
Beam 4	22.2	22.9	45.1

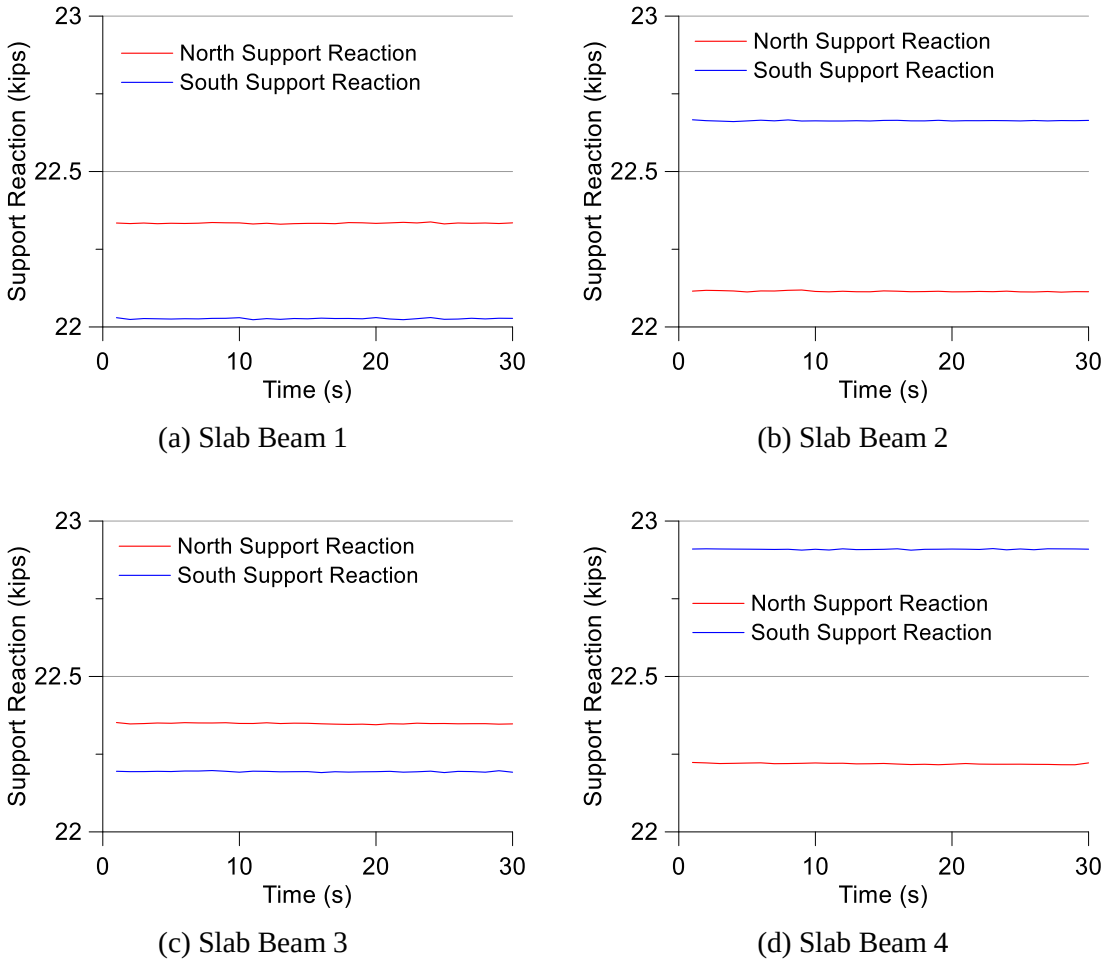

(a) Slab Beam 1

(b) Slab Beam 2

(c) Slab Beam 3

(d) Slab Beam 4

Figure 5.8. Slab Beam Support Reactions before Deck Pour.

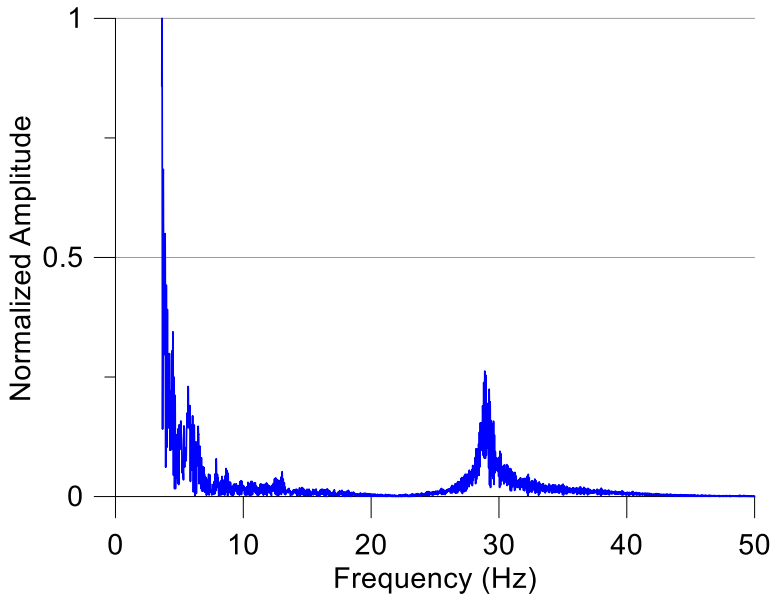

(a) Modal Frequencies for Slab Beam 4

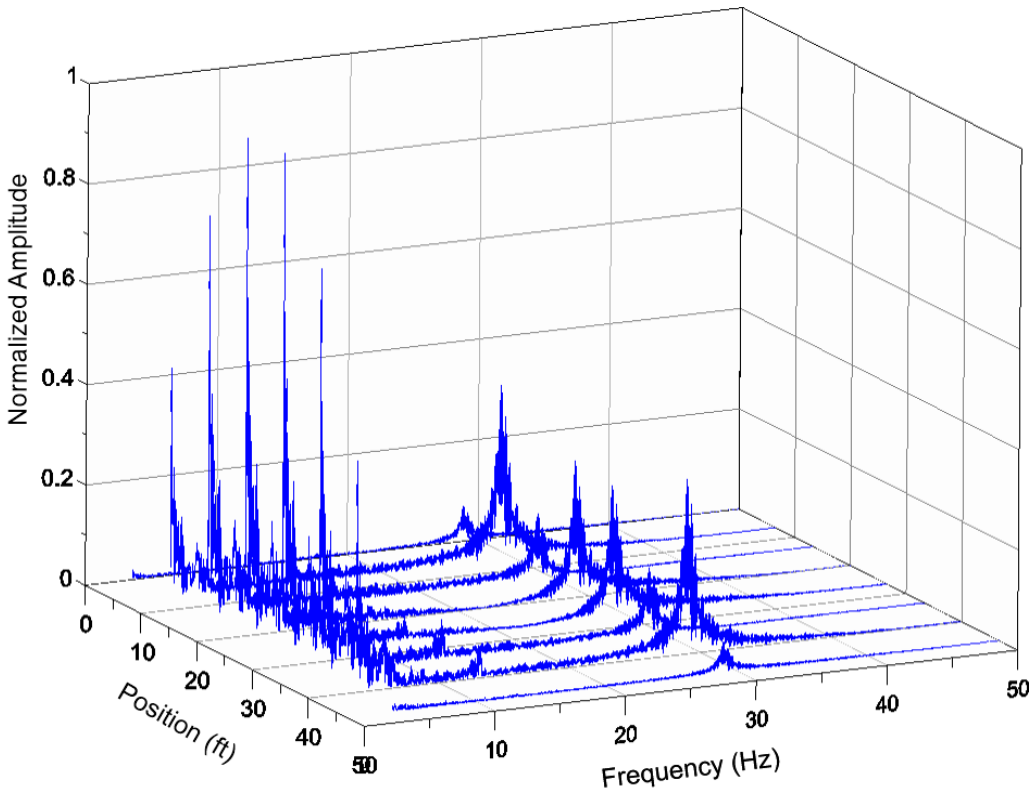

(b) Amplitude Spectrum along the Length of Slab Beam 4

Figure 5.9. Dynamic Characteristics of a Slab Beam.

5.5 TESTING OF RIVERSIDE BRIDGE

5.5.1 Test Vehicles

Figure 5.10 shows the photographs of both test trucks used during the Riverside Bridge testing. Two different TTI vehicles were used for static and dynamic testing of the Riverside Bridge. The TTI dump truck was loaded with a steel frame to increase its weight to approximately 32 kips. The TTI water tanker was filled and weighed approximately 88 kips total; however, only two axles weighing about 75 kips could be positioned on the bridge span. For each test case, all three axles of the TTI dump truck were on the bridge. However, only the rear axle of the TTI water tanker, which weighed about 38 kips, was used for the moment critical and north support shear cases. The rear axle and middle axle of the water tanker (weighing approximately 75 kips) was on the bridge for the south support shear critical case.

5.5.2 Preliminary Testing

Three trial tests were conducted prior to the final comprehensive testing of the Riverside Bridge. The trial testing allowed determination of the appropriate instrumentation types and configurations for use in final testing to obtain the experimental shear and moment live load distribution factors. Table 5.2 provides a summary of the tests performed on the Riverside Bridge.

5.5.2.1 Load Cells and Data Acquisition System (Trial 1)

The first preliminary static test (Trial 1) was conducted in November 14, 2013, in order to test the load cells and data acquisition system. Only the load cells were in place during preliminary testing. The rear axles of a TTI trailer were used as a static load placed to maximize the beam shear. All 16 load cells performed well, and the shear distribution factors could be identified. However, the use of this particular trailer was abandoned because the total weight of the rear axles was around 20 kips, which is relatively small compared to design tandem loading, and increasing the load was not possible. A TTI water tanker and a TTI dump truck were used for the remaining tests.

(a) TTI Dump Truck

(b) TTI Water Tanker

Figure 5.10. Test Vehicles Used for Riverside Bridge Tests.

Table 5.2. Riverside Bridge Tests.

Description	Test Date	TTI Vehicles	Deployed Instruments	String Potentiometer Layout for Moment
Trial 1	Nov. 14, 2013	Trailer	Load Cells	Distributed along span with 7' 9" spacing
Trial 2	Feb. 21, 2014	Dump Truck Water Tanker	Load Cells, String Potentiometers, LVDTs, Strain Gages	Distributed along span with 7' 9" spacing
Trial 3	April 2, 2014	Dump Truck Water Tanker	Load Cells, String Potentiometers, LVDTs, Strain Gages, Accelerometers	Clustered at midspan with 1' 3" spacing
Final Test	May 7, 2014	Dump Truck Water Tanker	Load Cells, String Potentiometers, LVDTs, Strain Gages, Accelerometers	Clustered at midspan with 3' 11" spacing

5.5.2.2 Support Reactions, Midspan Moments, and Distribution Factors (Trial 2)

A second preliminary static test (Trial 2) was conducted on February 21, 2014. Load cells were in place to measure support reactions and determine corresponding shear distribution factors. Linear variable displacement transducers (LVDTs) were also installed at each beam end in order to infer shear distribution factors by measuring bearing pad deformations. The reliability of the LVDTs was evaluated by comparing the corresponding shear LDFs to the ones obtained by direct measurement of reactions by load cells. All 40 string potentiometers were installed at equal spacing along the entire span, as shown in Figure 5.6, to infer moment LDFs by measuring the deflection profile for each slab beam. Strain gages were also installed at midspan of each beam as a secondary way of inferring moment LDFs by measuring the midspan curvature. Dynamic load testing was not planned at the time of Trial 2; therefore, the accelerometers were not installed.

5.5.2.3 Support Reactions, Midspan Moments, and Distribution Factors (Trial 3)

Figure 5.11 shows the instrument layout of the preliminary static test (Trial 3) that was conducted on April 2, 2014, with modified string potentiometer spacing. The string potentiometers were clustered at the center of the slab beams with 15 in. spacing. The accelerometers were also attached for the dynamic test. The rest of the instrumentation was kept the same as the previous test.

The analysis of the data indicated that the string potentiometer spacing was too close to determine meaningful moment LDFs. The sensitivity of the string potentiometers was not sufficient to differentiate the displacement differences at very close intervals. The string potentiometers used for the test are capable of detecting up to 0.005 in. deflection. Smaller deflection measurements than that are not reliable. The April test showed that the deflection change between stations that were 15 in. apart was smaller than 0.003 in. Based on the investigation of deflection profiles from the preliminary tests and analytical predictions it was determined that a spacing of 4 ft between successive stations, as compared to 8 ft spacing, was preferable for determining the midspan moment while still giving displacement differences that could be reliably measured by the string potentiometers.

5.5.2.4 Static and Dynamic Load Tests

Figure 5.12 shows the detailed layout of the instruments for the May tests, and the results are reported in Section 4.6. The final comprehensive static and dynamic tests of the Riverside Bridge were conducted on May 7, 2014. The instrumentation layout was kept the same as Trial 3, except the spacing of the string potentiometers was modified.

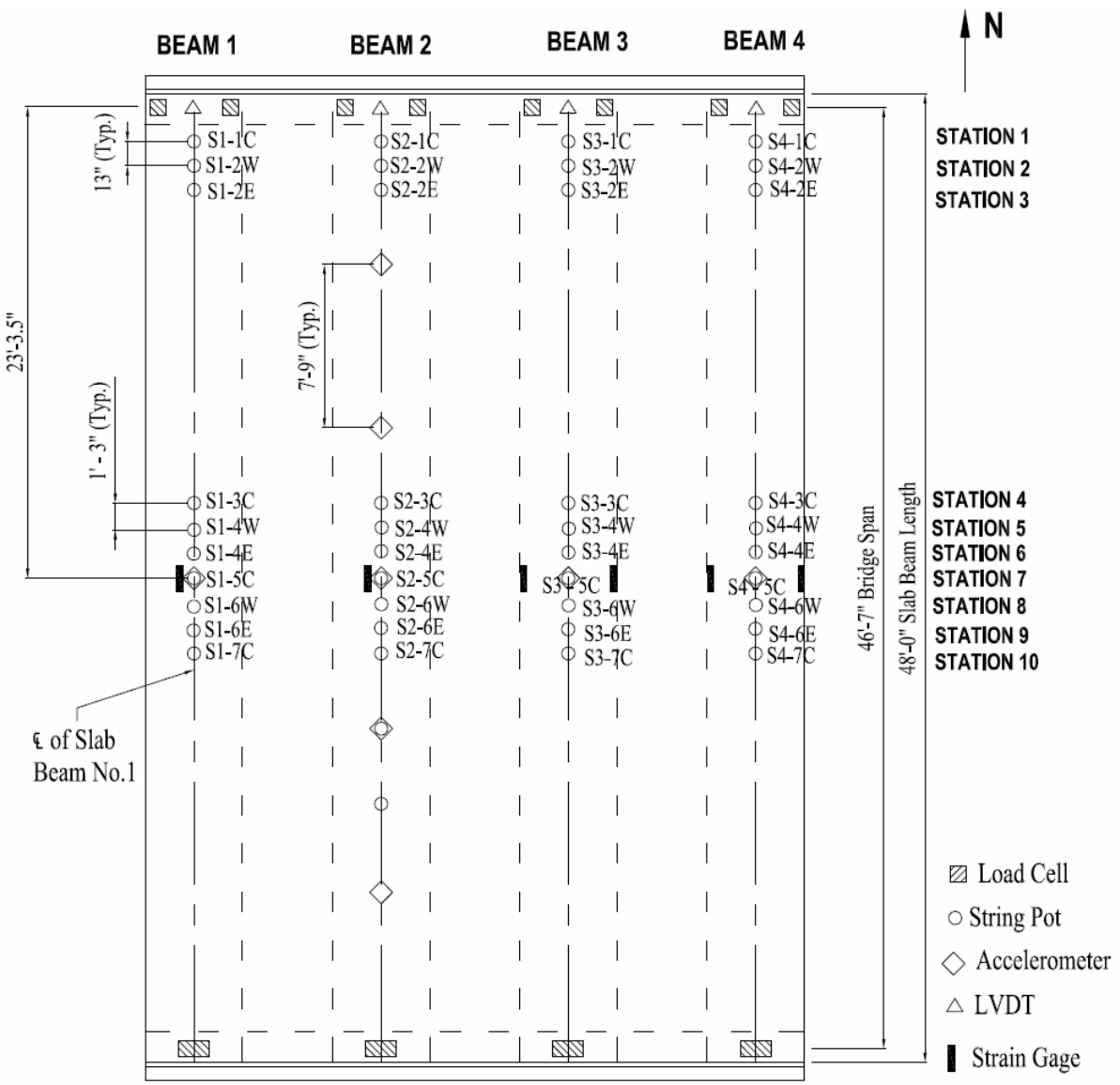

Figure 5.11. Instrumentation Layout for Trial 3.

5.5.2.5 Longitudinal Vehicle Positions

Individual axle weights of the test vehicles were determined using portable scales. Axle spacing was measured and the location of the resultant force was determined. The maximum bending moment in a beam occurs when the resultant of the three axles and the second axle are located at an equal distance from the midspan location. This is called the critical moment position in the longitudinal direction.

The maximum shear in a beam member occurs when the load is located a member depth away from the support (St. Venant's shear principle; (Ugural and Fenster 2012). According to St. Venant's principle, for the Riverside Bridge, the centroid of the rear axle should be located 25 in. from the centerline of the bearing pads. This loading case creates maximum shear stresses at one member depth away. Two different shear critical longitudinal positions, one at the south support and one at the north support, were defined.

The longitudinal positions of the dump truck and water tanker are shown in Figure 5.13 and Figure 5.14, respectively. A total of three longitudinal positions were defined for each vehicle: south support, center (near midspan), and north support. All axles of the dump truck were on the bridge for each of the three longitudinal positions. For the north support case, the dump truck was turned around in order to achieve the highest shear force and create similar loading to the south support case. In the case of the water tanker, only the rear axles (similar to a design tandem loading) were placed on the bridge for the center and north support cases. For the south support position of the water tanker, the middle set of axles was also on the bridge, which created the highest total load. Therefore, the south and north support positions of the water tanker did not induce the same shear force.

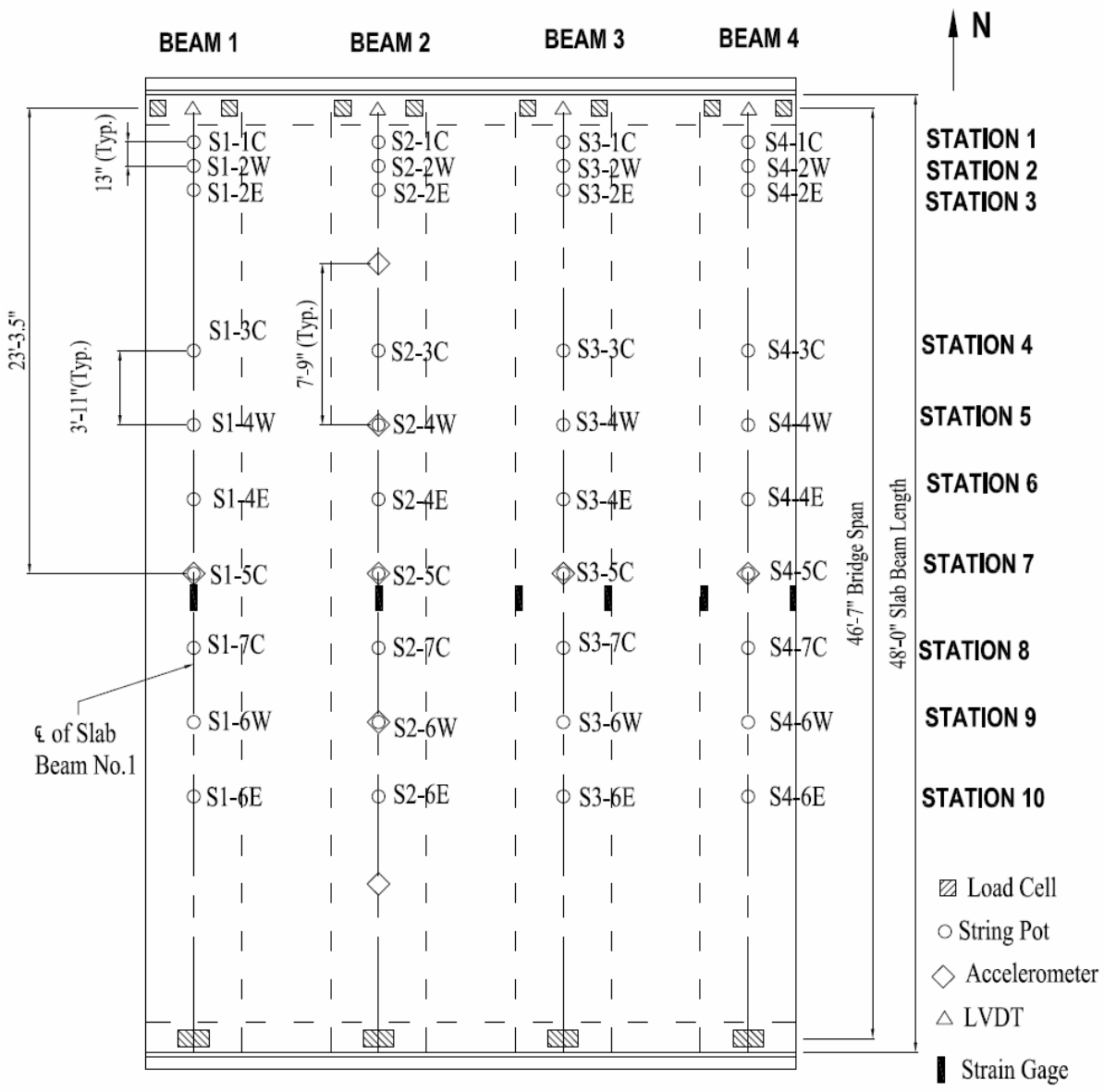

Figure 5.12. Instrumentation Layout for May Tests.

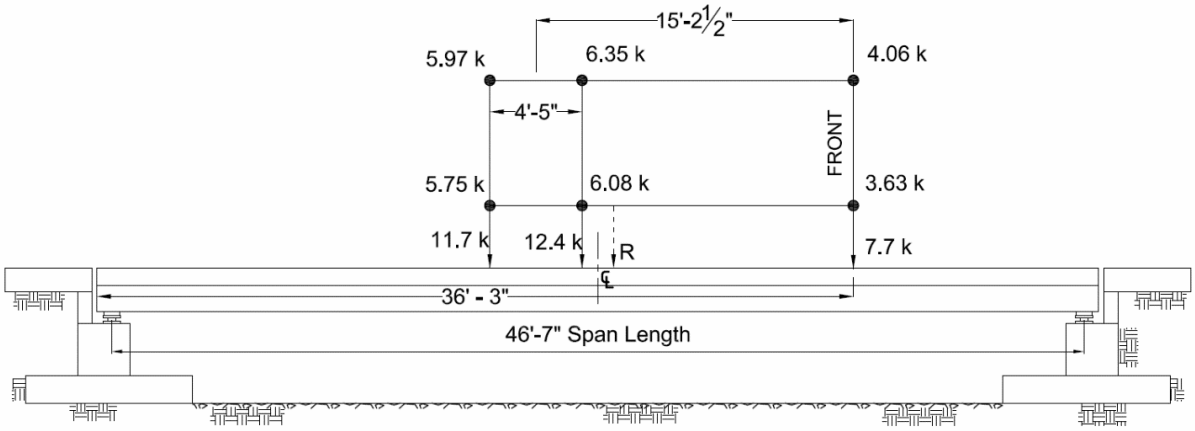

(a) Moment Critical Position near Midspan

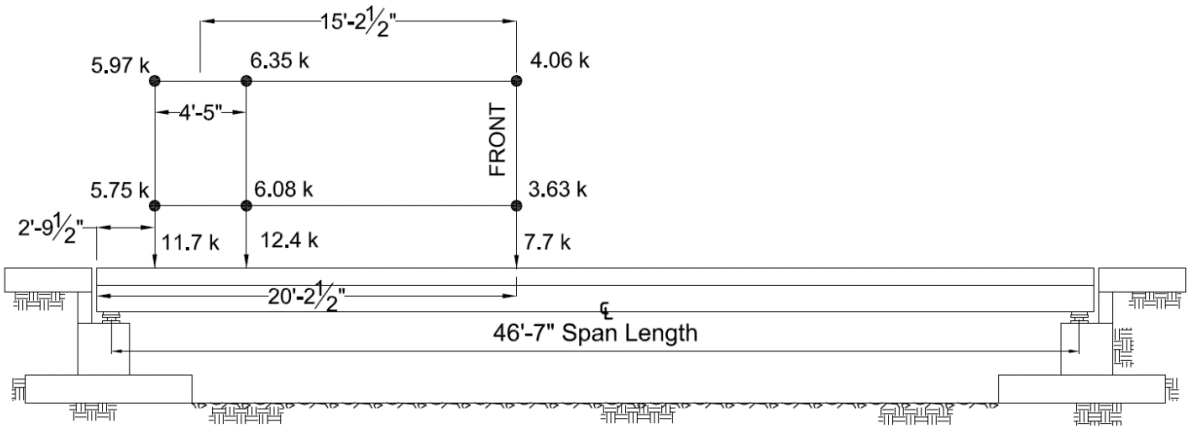

(b) South Support Shear Critical Position

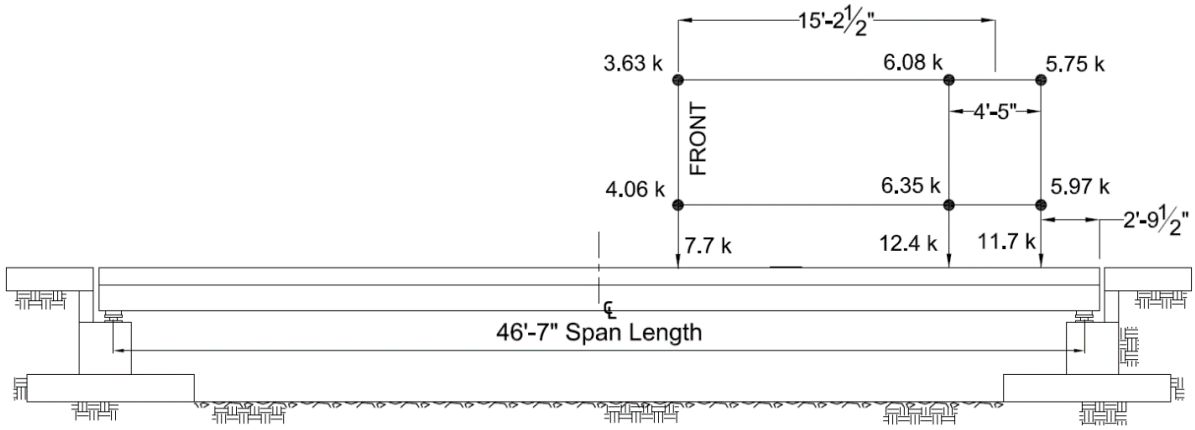

(c) North Support Shear Critical Position

Figure 5.13. Longitudinal Positions of Dump Truck.

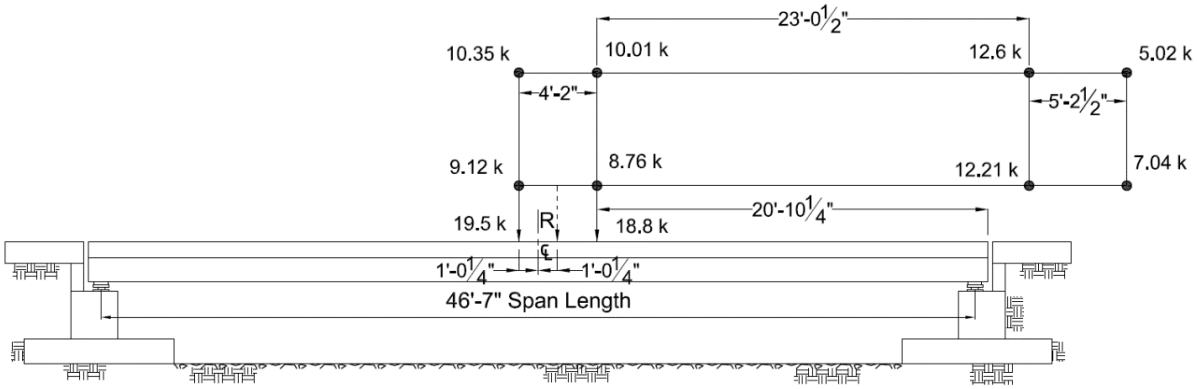

(a) Moment Critical Position near Midspan

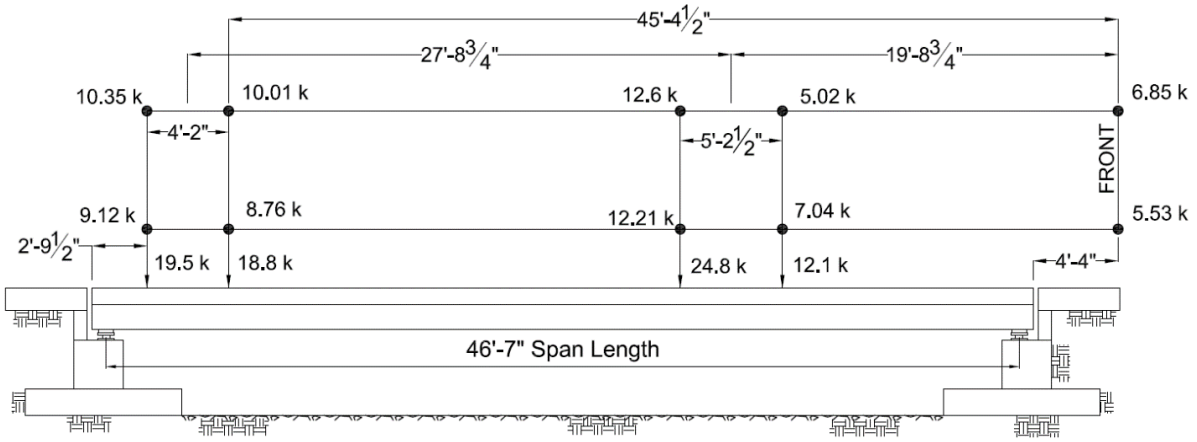

(b) South Support Shear Critical Position

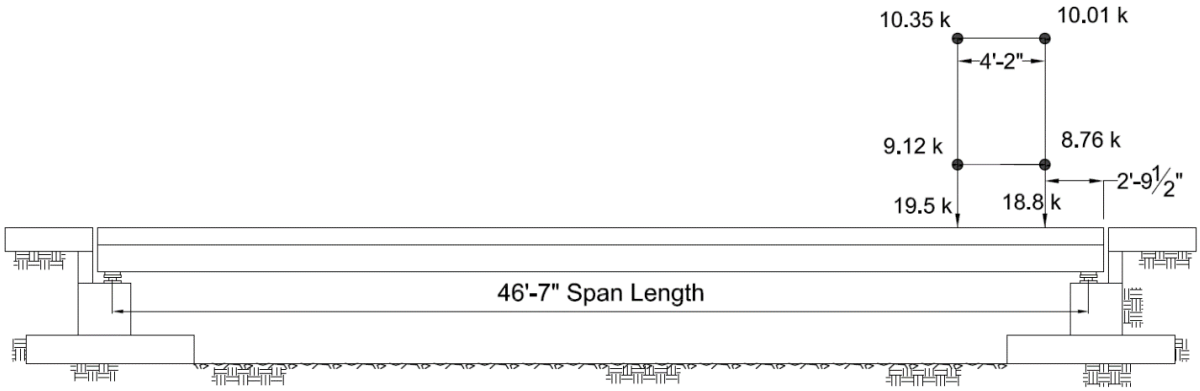

(c) North Support Shear Critical Position

Figure 5.14. Longitudinal Positions for Water Tanker.

5.5.2.6 Transverse Alignments

The transverse alignments are shown in Figure 5.15. For dynamic tests, the vehicles were driven along the same four alignments. The Riverside Bridge is a two-lane bridge, and the critical moment and shear force occur when both lanes are loaded. According to the AASHTO LRFD Specifications (2012) Article 3.6.1.3.1, the minimum vehicle distance from the edge of a design lane is 2 ft. Therefore, the minimum lateral distance between two trucks traveling in adjacent lanes is 4 ft. The edge of a lane can be at the edge of the bridge, such as when two bridges are built side by side. When the tire thickness is taken into account, the center of the exterior tire can be 1 ft away from the edge. In light of the above-mentioned criteria, a total of four transverse alignments were defined.

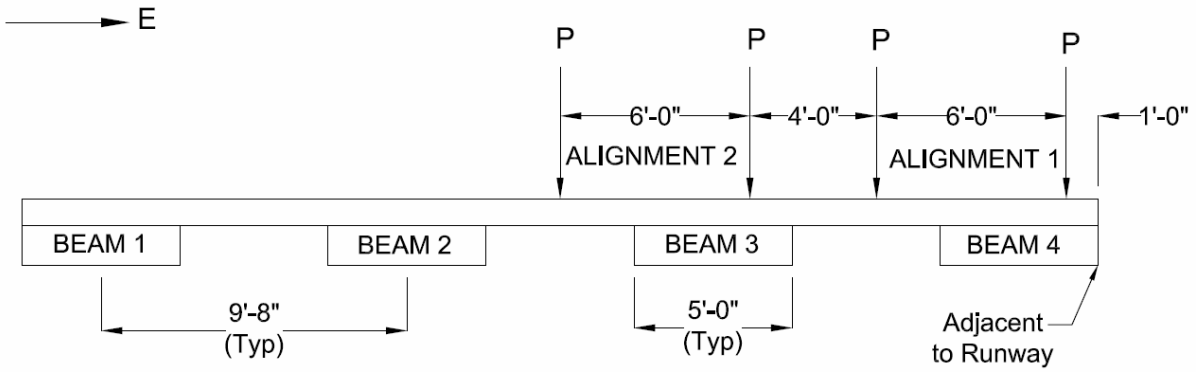

(a) Exterior Girder Critical Case

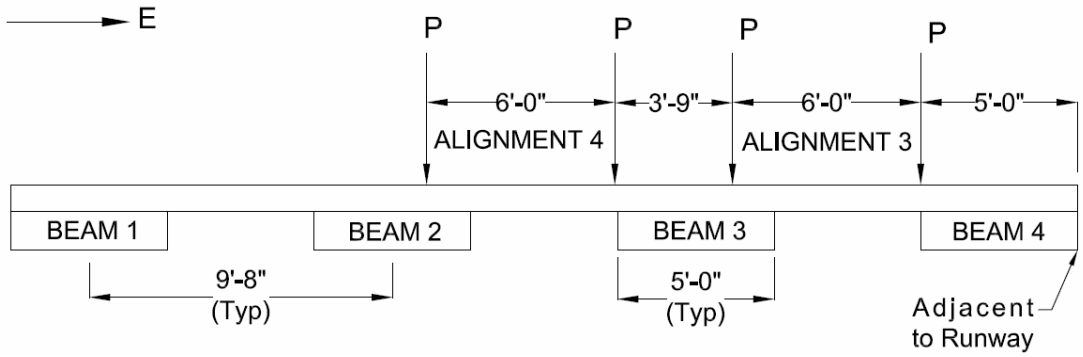

(b) Interior Girder Critical Case

Figure 5.15. Transverse Alignments for Static and Dynamic Tests.

Live load distribution factors are different for exterior and interior girders. The transverse alignments were selected based on the load configuration that gives the critical moment or shear reaction for exterior and interior slab beams. The case where Alignment 1 and Alignment 2 are loaded gives the highest moment LDFs for both the exterior and interior slab beams. The same load case gives shear critical loading for the exterior beam. The case where Alignment 3 and Alignment 4 are loaded gives the highest shear LDF for an interior slab beam. These alignments were set during the preliminary tests and confirmed with the FE model of the bridge.

5.5.2.7 Instrumentation

The Riverside Bridge was instrumented using string potentiometers, LVDTs, load cells, accelerometers, and strain gages during the tests conducted on May 7, 2014. The detailed instrumentation layout is shown in Figure 5.12 above. Instrumentation readings and physical observations were carefully documented during field testing of the Riverside Bridge. These experimental results were processed and reviewed to better understand the in-service response of the spread slab beam bridge system. The load sharing observed in the field tests provided input to the development of load distribution factors for this bridge system.

The experimental results presented in the next section are from the tests conducted on May 7, 2014. Ten string potentiometers were attached to each beam. Seven potentiometers were clustered at the center of each beam with 3 ft 11 in. spacing to obtain sufficient measurements of the deflection profile in the midspan region. An additional three string potentiometers were attached at each beam end with a 13 in. spacing to investigate the possibility of determining the shear force distribution from deflection data. Theoretically, only four data points are necessary for determining the shear reaction. Including the deflection data obtained from the LVDT at the bearing pad level gave a total of four deflection measurements per beam near the north support. The rest of the sensors were attached at their fixed locations, as defined in Figure 5.6 above. The deflection profiles were obtained when the dump truck was at the longitudinal center of the bridge (moment critical position).

5.6 ANALYSIS OF TEST RESULTS

5.6.1 Load Distribution Factor Calculation Method

The load distribution factor, g, is defined as the ratio of maximum load effect created on the bridge girder due to HL-93 loading to the maximum load effect created on an isolated beam element due to same loading.

A similar approach as that in the AASHTO LRFD Specifications (2012) was followed for live load distribution factor calculation. For calculating the load distribution factors, a one-dimensional isolated beam having the same span length as the bridge is analyzed under uniform lane load and HS20 truck or tandem load. The maximum beam force (moment and shear), F1D-Girder, and the longitudinal position of the vehicle for maximum moment and shear are recorded. The bridge is loaded by the same vehicle at the same longitudinal position for different transverse positions. The maximum force, F2D-Girder, that occurs for interior girders and exterior girders are measured and recorded. Then the load distribution factor g is determined as:

$$g = \frac{F_{2D-Girder}}{F_{1D-Girder}} \tag{5.1}$$

The forces are moments or shears depending on the analysis. The force that is obtained from the single isolated beam analysis is always obtained by loading it with one vehicle only. However, the actual experimental bridge or the FEM model of the bridge should be analyzed for the one-lane-loaded and two-or-more-lanes-loaded cases. This means F1D-Girder is always a moment or shear of an exterior or interior girder calculated using one vehicle and a uniform lane load, whereas F2D-Girder includes multiple vehicles and multiple lanes.

The number of design lanes is computed according to AASHTO LRFD Specifications (2012) Article 3.6.1.1.1. The number of design lanes is equal to the integer part of the ratio of the clear roadway width in feet divided by 12 ft, which resulted in two lanes for the Riverside Bridge.

Although the maximum load distribution factor occurs due to the two-lane-loaded case, the one-lane-loaded case was also investigated.

$$g_{M-INT} = \frac{M_{INT,2D}}{M_{1D}} \tag{5.2}$$

$$g_{V-INT} = \frac{V_{INT,2D}}{V_{1D}} \tag{5.3}$$

Where:

$g_{M\text{-}INT}$ = Moment distribution factor of interior girders for one-lane-loaded case if $M_{INT,2D}$ is due to one-lane loading. Moment distribution factor of interior girders for two-lane-loaded case if $M_{INT,2D}$ is due to two-lane loading.

M_{INT-2D} = Maximum moment for all interior girders, kip-ft.

M_{1D} = Moment due to one-lane loading, kip-ft.

$g_{V\text{-}INT}$ = Shear distribution factor of interior girders for one-lane-loaded case if $V_{INT,2D}$ is due to one-lane loading. Shear distribution factor of interior girders for two-lane-loaded case if $V_{INT,2D}$ is due to two-lane loading.

$V_{INT,2D}$ = Maximum shear for all interior girders, kips.

V_{1D} = Shear due to one-lane loading, kips.

The exterior girder load distribution factors are calculated similar to interior girders.

$$g_{M-EXT} = \frac{M_{EXT,2D}}{M_{1D}} \tag{5.4}$$

$$g_{V-EXT} = \frac{V_{EXT,2D}}{V_{1D}} \tag{5.5}$$

Where:

$g_{M\text{-}EXT}$ = Moment distribution factor of exterior girders for one-lane-loaded case if $M_{INT,2D}$ is due to one-lane loading. Moment distribution factor of exterior girders for two-lane-loaded case if $M_{INT,2D}$ is due to two-lane loading.

$M_{EXT,2D}$ = Maximum moment for all exterior girders, kip-ft.

$g_{V\text{-}EXT}$ = Shear distribution factor of exterior girders for one-lane-loaded case if $V_{INT,2D}$ is due to one-lane loading. Shear distribution factor of exterior girders for two-lane-loaded case if $V_{INT,2D}$ is due to two-lane loading.

$V_{EXT,2D}$ = Maximum shear for all exterior girders, kips.

For both the interior and exterior distribution factors, the longitudinal position of the vehicle is calculated based on the single isolated beam loading with one vehicle only. This position is used as the critical position for moment for both the one-dimensional and 2D analyses.

5.6.2 Experimental Results for Dump Truck Loading

5.6.2.1 Deflection Profiles Due to Dump Truck Static Loading

The static loading was achieved using a dump truck at four different alignments and three different longitudinal positions along each alignment, as described in Figure 5.13 and Figure 5.15. Figure 5.16 shows an example static loading case with the dump truck at one of the positions. The total gross weight of the dump truck was approximately 31 kips with the measured wheel loads provided in Figure 5.13. The deflection profiles obtained from all string potentiometers are shown in Figure 5.17.

The maximum deflection (0.12 in.) was observed at Beam 4 when the vehicle was located at the center of Alignment 1. The deflection profiles changed as the vehicle moved transversely. Maximum deflections were observed for Beam 4 when the vehicle was at Alignment 1 and Alignment 3. Beam 3 had the highest deflection when the vehicle was at Alignment 2. Beam 2 had the highest deflection when the vehicle was moved to Alignment 4.

Mechanical properties of the superstructure concrete, closest to the day of bridge testing, are summarized in Table 5.3. For experimental moment calculations, the modulus of elasticity of the concrete was assumed to be 10 percent higher at the day of testing than the material test results. Complete data for tested mechanical properties of the concrete are provided in Appendix B.

Table 5.3. Mechanical Properties of Riverside Bridge Concrete.

Superstructure Component	Age of Concrete (days)	Compressive Strength (ksi)	Modulus of Elasticity (ksi)
Slab Beams	56	11.25	5349
Precast Concrete Panels	28	9.93	5489
CIP Deck	28	6.45	6467

Figure 5.16. Static Loading with Dump Truck.

5.6.2.2 Moment Results for Dump Truck Static Loading

5.6.2.2.1 Measured Data

One of the main objectives of this research was to identify moment LDFs. The moments at the midspan were obtained using the deflection profile from seven string potentiometers that were clustered at the center of the beams. A third-order polynomial having the form shown in Equation (5.6) was fit through the deflection curve. The curvature of the fitted curve was calculated by twice differentiating the fitted third-order polynomial using Equation (5.6). The moment at midspan was then calculated using the curvature at midspan and multiplying it by EI. The moment at midspan was calculated for each one of the four beams for the moment critical position of the vehicles.

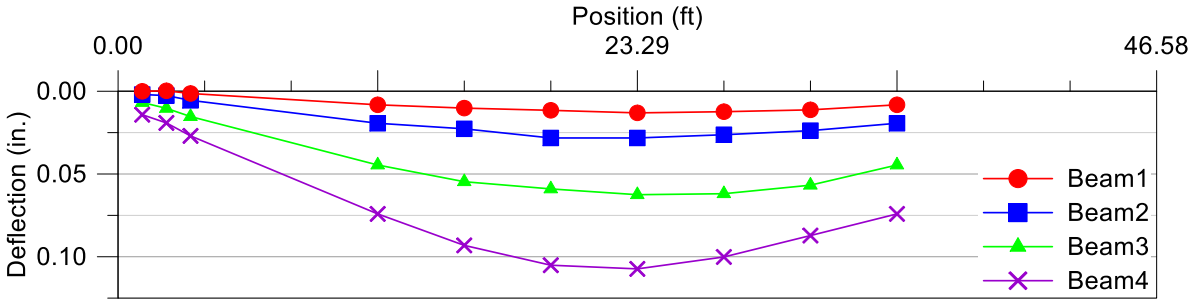

(a) Beam Deflections for Alignment 1

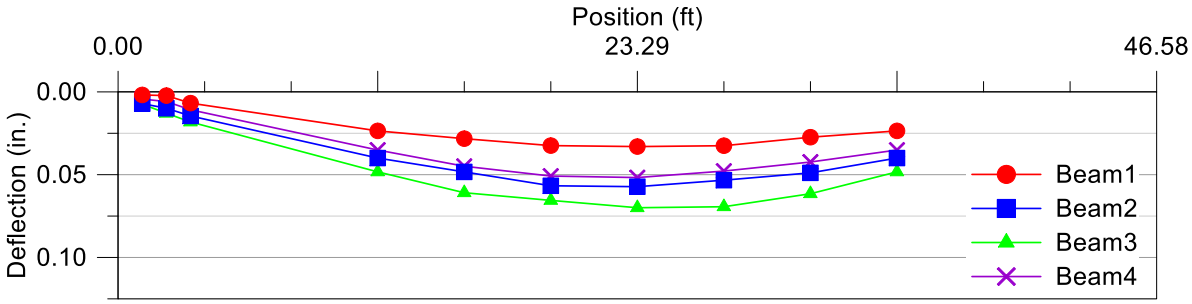

(b) Beam Deflections for Alignment 2

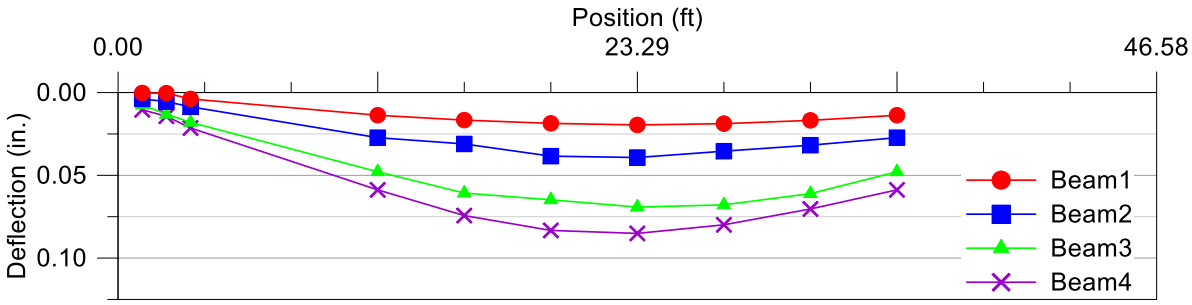

(c) Beam Deflections for Alignment 3

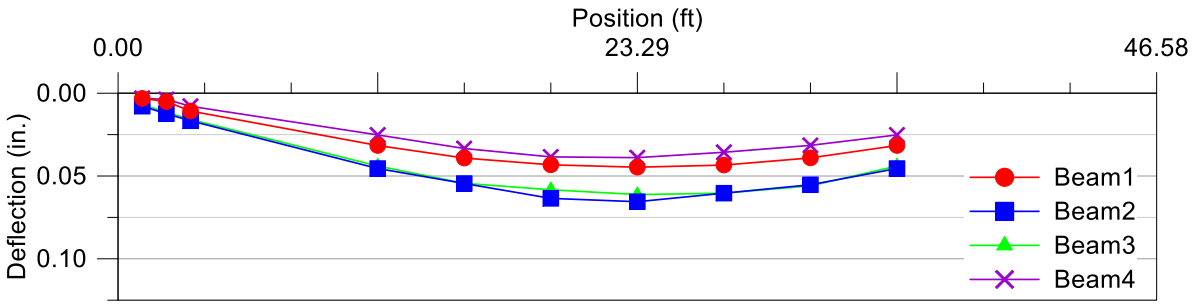

(d) Beam Deflections for Alignment 4

Figure 5.17. Deflection Profiles for Dump Truck Load.

$$y = ax^3 + bx^2 + cx + d \tag{5.6}$$

$$y'' = 6ax + 2b \tag{5.7}$$

$$M(x) = EI\,y'' \tag{5.8}$$

Moments at midspan were also calculated using strain values obtained from strain gages. Only the strain gages attached at the bottom surface of the slab beams were used together with the theoretical center of gravity. Strain gages at the top deck surface were attached to determine the experimental center of gravity of the composite sections for interior and exterior beams. However, the top strain gages did not provide the intended data. They captured strains were not only due to longitudinal stresses but also due to the longitudinal components of surface stresses in multiple directions because of local stresses applied by the wheel loads. Therefore, the moments were calculated using the theoretical center of gravity and bottom strain gages. The theoretical centroid could be calculated accurately because the modulus of elasticity (Ec) of the beams and deck concrete was determined for different ages of the concrete.

5.6.2.2.2 Experimental Moment Distribution Factors

The moment reactions and moment distribution factors calculated using two different methods (string potentiometers and strain gages) were plotted and are compared in Figure 5.18. The maximum moment values and experimental moment LDFs for the interior and exterior girders based on string potentiometer measurements are listed in Table 5.4. The critical moment distribution factors are obtained when both lanes are loaded for a two-lane bridge. Therefore, the results of two different alignments were superimposed to obtain two-lane-loaded results. Alignment 1+2 and Alignment 3+4 were already defined as alignment couples that allow two trucks traveling as close as possible to each other.

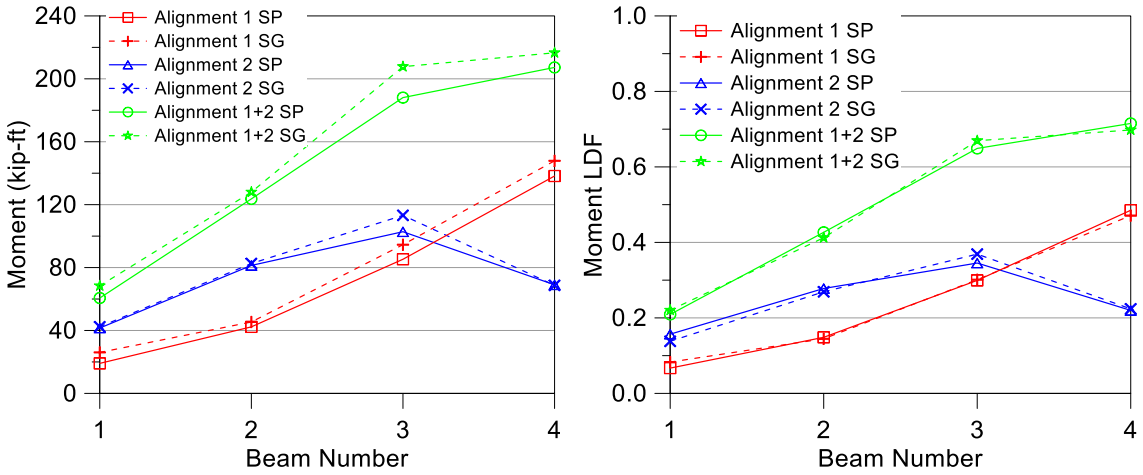

(a) Moments for Alignment 1+2

(b) Moment LDFs for Alignment 1+2

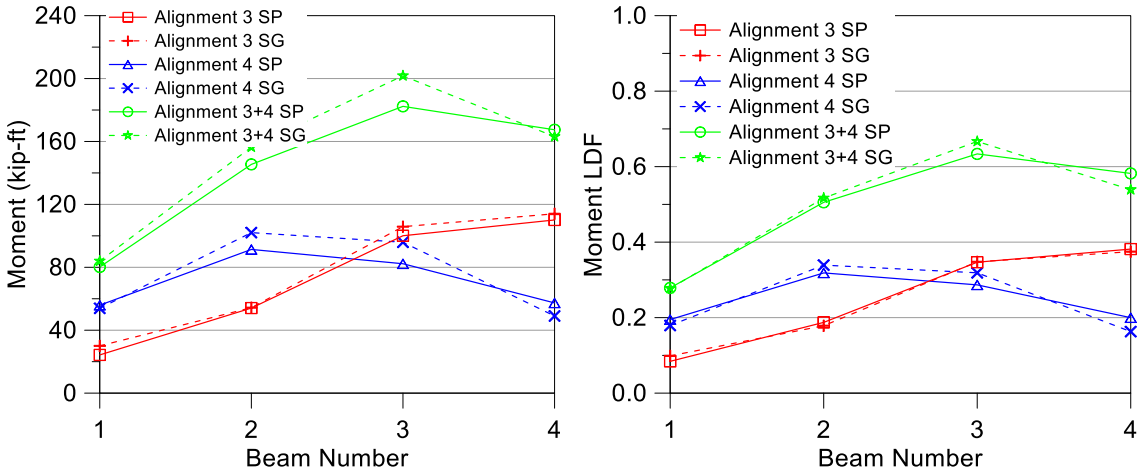

(c) Moments for Alignment 3+4

(d) Moment LDFs for Alignment 3+4

Note: SP = String Potentiometer, SG = Strain Gage

Figure 5.18. Midspan Moments and Moment LDFs for Dump Truck Loading.

Table 5.4. Maximum Moment Results for Dump Truck Loading.

No. Lanes Loaded	Slab Beam ID	Max. Moment (kip-ft)	Exp. Moment LDF	Transverse Load Position
One Lane	Beam 3 (Interior)	103	0.35	Alignment 2
	Beam 4 (Exterior)	138	0.49	Alignment 1
Two Lanes	Beam 3 (Interior)	188	0.65	Alignment 1+2
	Beam 4 (Exterior)	207	0.72	Alignment 1+2

The results indicate that the moments obtained using bottom strain gage data are slightly higher than those calculated using string potentiometer data. However, the moment LDF values are similar with the two different measurement methods providing consistent results. The moments calculated using string potentiometer data are used as the experimental values for further comparison in the following sections. The maximum moment LDFs recorded due to the dump truck loading are 0.65 for an interior beam and 0.72 for an exterior beam when Alignment 1+2 is loaded.

Midspan moments were calculated based on strain gage measurements, and experimental moment LDFs were obtained using the relative moment sharing between slab beams. The measured midspan moment values are listed in Table 5.5, and the corresponding moment LDFs are provided in Table 5.6.

Table 5.5. Moments Based on Strain Gage Data for Dump Truck Loading (kip-ft).

Load Case	Beam 1	Beam 2	Beam 3	Beam 4
Alignment 1	26	45	95	148
Alignment 2	42	83	113	69
Alignment 3	30	54	106	114
Alignment 4	54	102	96	49

Table 5.6. Moment LDFs Based on Strain Gage Data for Dump Truck Loading.

Load Case	Beam 1	Beam 2	Beam 3	Beam 4
Alignment 1	0.08	0.14	0.30	0.47
Alignment 2	0.14	0.27	0.37	0.22
Alignment 3	0.10	0.18	0.35	0.37
Alignment 4	0.18	0.34	0.32	0.16

5.6.2.3 North Support Shear Results for Dump Truck Loading

5.6.2.3.1 Static Results

North support reactions and experimental shear load distribution factors for all alignments are shown in Figure 5.19. Maximum reactions and experimental shear LDFs for interior and exterior girders are presented in Table 5.7. The support reactions at both the north and south ends of each beam were recorded using load cells. To create the maximum reactions, the rear axle of the dump truck was located close to the supports. For the north support critical case, the vehicle was facing toward the north, and for the south support critical case, the vehicle was facing toward the south. The maximum exterior beam shear LDF = 0.78 was recorded when Alignment 1+2 was loaded. The maximum interior beam shear LDF = 1.02 was obtained when Alignment 3+4 was loaded.

5.6.2.3.2 Dynamic Results

Figure 5.19 shows amplified north support reactions due to dynamic impact. Reaction data recorded during the dynamic tests were analyzed and compared to the static data. For the dynamic tests, the dump truck was driven at a speed of 40 mph along the same four transverse alignments used for the static tests. The total north support reaction was calculated for each time step. Individual north support beam reactions were recorded at the time step when the total north support reaction attained its maximum value.

For all the dynamic tests, vehicles were driven from south to north. The dynamic amplification at the north support was prominent when the dump truck was driven along Alignment 2. The amplification was about 37 percent for Beam 3. This is larger than the standard 33 percent increase for impact specified by the AASHTO LRFD Specifications (2012). One of the reasons for this high value may be the asphalt patch that was in line with Alignment 2 at the south end of the bridge. The maximum dynamic impact for Beam 4 was about 17 percent when the dump truck was driven along Alignment 3. Beam 2 had 19 percent dynamic amplification for the Alignment 4 dynamic load test.

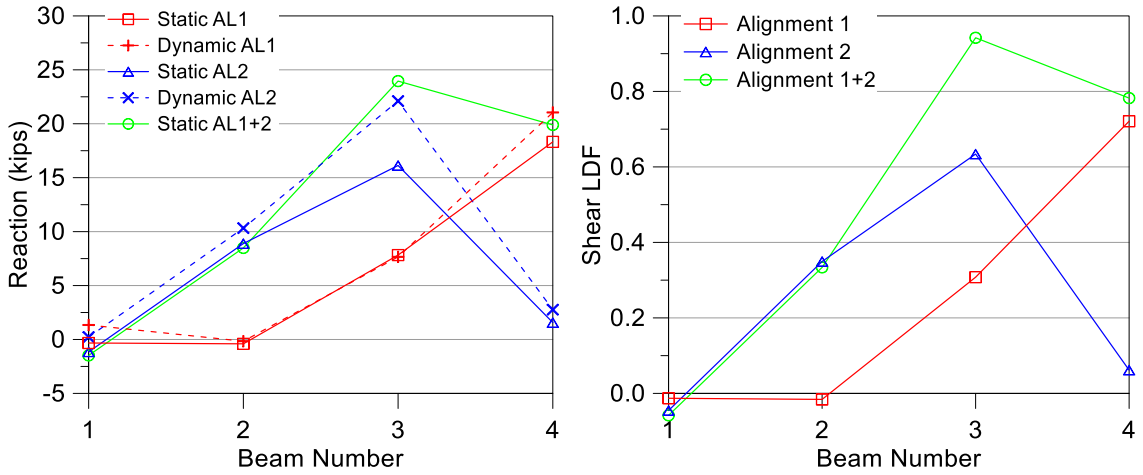

(a) Reactions for Alignment 1+2

(b) Shear LDFs for Alignment 1+2

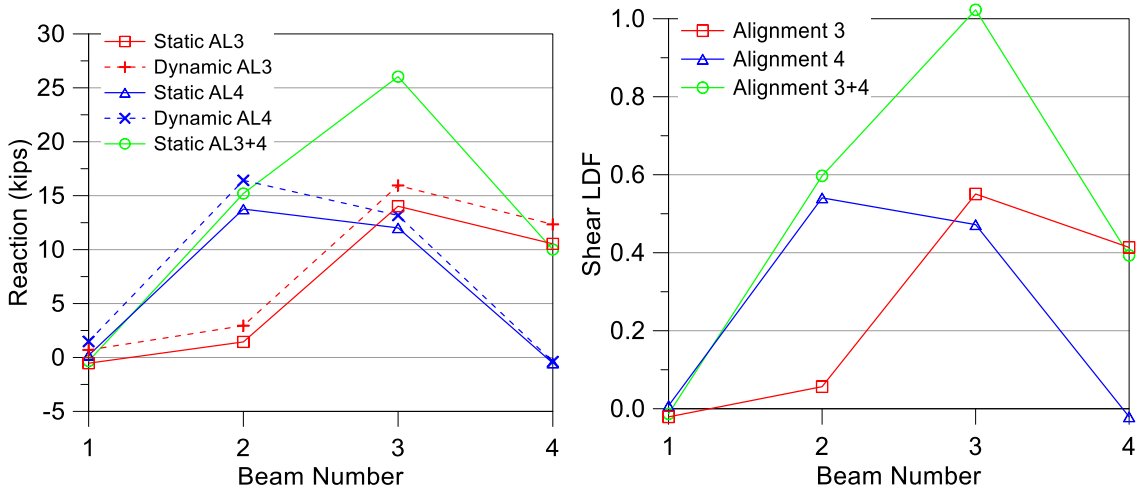

(c) Reactions for Alignment 3+4

(d) Shear LDFs for Alignment 3+4

Figure 5.19. North Reactions and Experimental Shear LDFs for Dump Truck Loading.

Table 5.7. Maximum North Support Shear Results for Dump Truck Loading.

No. Lanes Loaded	Slab Beam ID	Max. Reaction (kips)	Exp. Shear LDF	Transverse Load Position
One Lane	Beam 3 (Interior)	16.1	0.63	Alignment 2
	Beam 4 (Exterior)	18.3	0.72	Alignment 1
Two Lanes	Beam 3 (Interior)	26.0	1.02	Alignment 3+4
	Beam 4 (Exterior)	19.8	0.78	Alignment 1+2

5.6.2.4 South Support Shear Results for Dump Truck Loading

5.6.2.4.1 Static Results

Maximum reaction values and shear LDFs for interior and exterior girders are summarized in Table 5.8. Figure 5.20 shows shear forces and experimental shear LDFs for both static and dynamic loading. A similar analysis approach was followed to calculate shear LDFs for the south support reactions. The maximum shear LDF for an exterior beam was 0.80 and was obtained when Alignment 1+2 was loaded. A maximum shear LDF of 0.92 was measured for an interior girder for Alignment 3+4. The experimental shear LDF for the interior girder was lower compared to the north support loading case. This difference may be due to differential tire reactions between wheel lines. The driver side of the vehicle is slightly heavier than the passenger side.

5.6.2.4.2 Dynamic Results

The observed maximum dynamic amplification at the south support was 35 percent. This value was obtained for Beam 2 when the vehicle was driven along Alignment 2. An interesting observation was that there was no dynamic amplification for Beams 3 and 4 when the vehicle was driven along Alignment 1 or 3. The south end reaction for Beam 1 even decreased for the Alignment 1 dynamic load test.

Dynamic amplifications observed for the north support are more prominent than the south support dynamic amplifications. Ratios of the dynamic reaction to static reaction for each alignment, corresponding to the beams that had the maximum reaction, are listed in Table 5.9.

The difference between north support and south support impact factors may be due to the relationship between the dump truck's vibration frequency and structure's natural frequency. The vehicle was traveling from south to north and evidently entered the bridge with an impact when it crossed the south end, and that effect was reduced as it crossed the north end. The time and position of these jumps are related to the vehicle's vibration frequency as well as the location of the bump before the bridge.

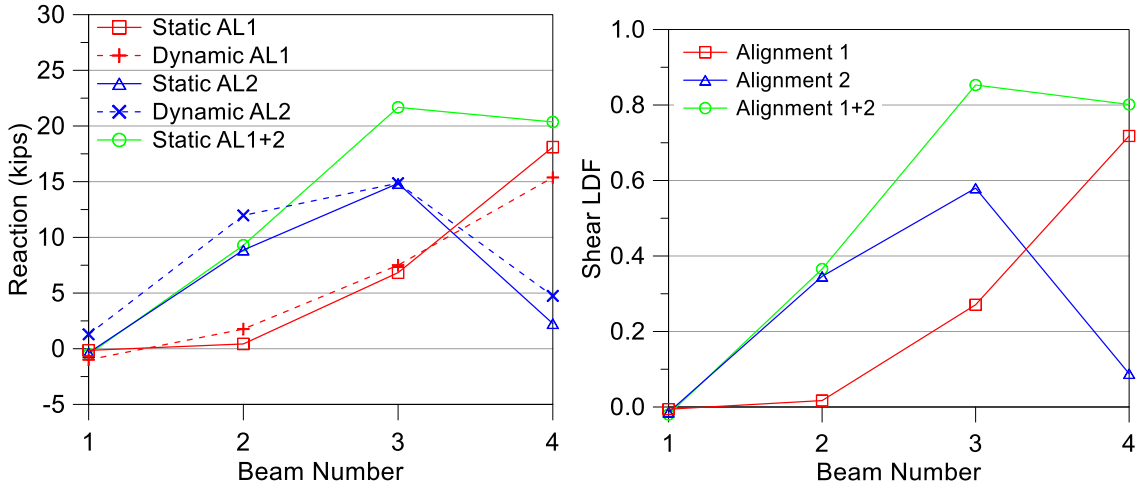

(a) Reactions for Alignment 1+2

(b) Shear LDFs for Alignment 1+2

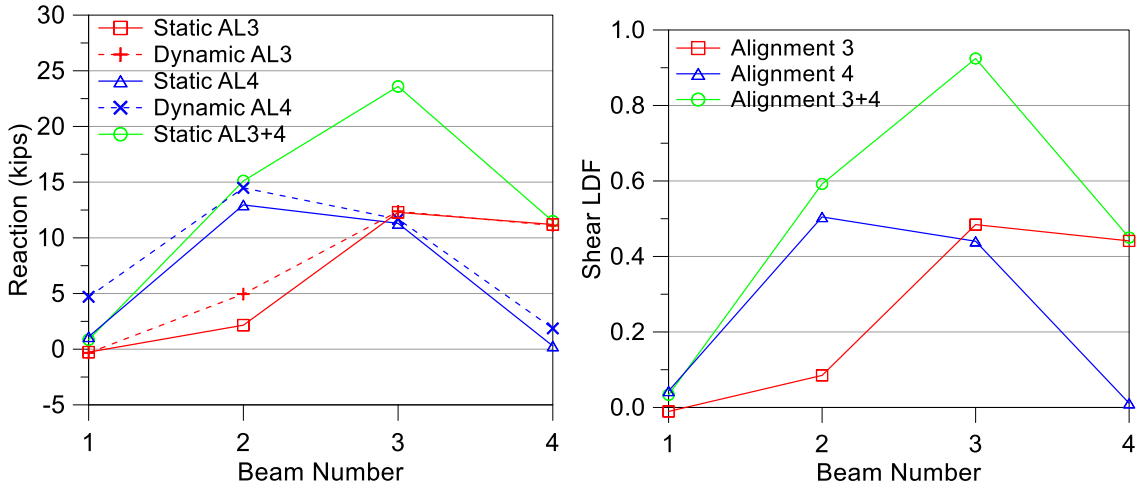

(c) Reactions for Alignment 3+4

(d) Shear LDFs for Alignment 3+4

Figure 5.20. South Support Reactions and Shear LDFs for Dump Truck Loading.

Table 5.8. Maximum South Support Shear Results for Dump Truck Loading.

No. Lanes Loaded	Slab Beam ID	Max. Reaction (kips)	Exp. Shear LDF	Transverse Load Position
One Lane	Beam 3 (Interior)	14.9	0.58	Alignment 2
	Beam 4 (Exterior)	18.1	0.72	Alignment 1
Two Lanes	Beam 3 (Interior)	23.6	0.92	Alignment 3+4
	Beam 4 (Exterior)	20.4	0.80	Alignment 1+2

Table 5.9. Dynamic Amplifications for Dump Truck Tests.

Alignment	Dynamic/Static Reaction		Beam with Maximum Reaction
	North Support	South Support	
Alignment 1	1.15	0.85	Beam 4
Alignment 2	1.37	1.00	Beam 3
Alignment 3	1.14	1.01	Beam 3
Alignment 4	1.19	1.12	Beam 2

5.6.3 Experimental Results for Water Tanker Loading

5.6.3.1 Deflection Profiles Due to Water Tanker Static Loading

Because of the axle spacing of the water tanker, only two axles could be placed on the bridge at the same time. The water tanker's rear axles were used to represent the close axle spacing defined for the design tandem loading in the AASHTO LRFD Specifications (2012) (two 25-kip axles that are 4 ft apart), with a total load for the rear axles of 38.3 kips. For deflection studies and moment analysis, the rear axles were placed at the moment critical position (longitudinal center) of the bridge, as shown in Figure 5.14 above.

Figure 5.21 shows deflection profiles of each slab beam for the four different transverse alignments.

5.6.3.2 Moment Results for Water Tanker Static Loading

The rear axles were placed at the longitudinal moment critical position, which was calculated based on a simply supported single beam analysis. Moment results for the water tanker loading for each alignment and for two-lane-loaded cases are shown in Figure 5.22. The maximum moments and experimental moment LDFs for interior and exterior girders are listed in Table 5.10.

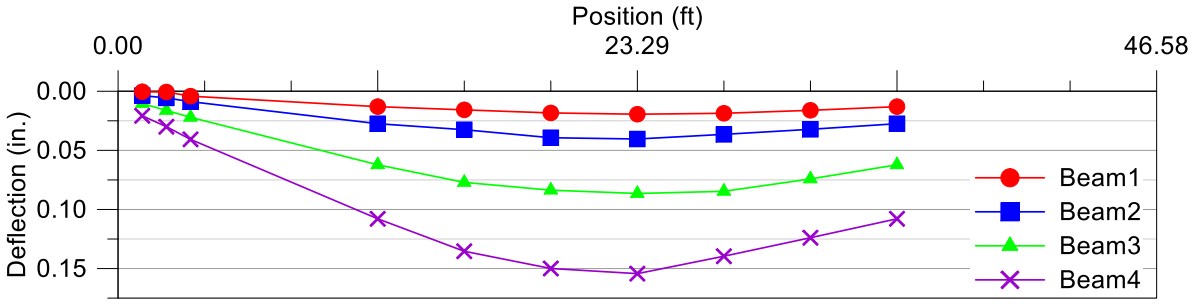

(a) Beam Deflections for Alignment 1

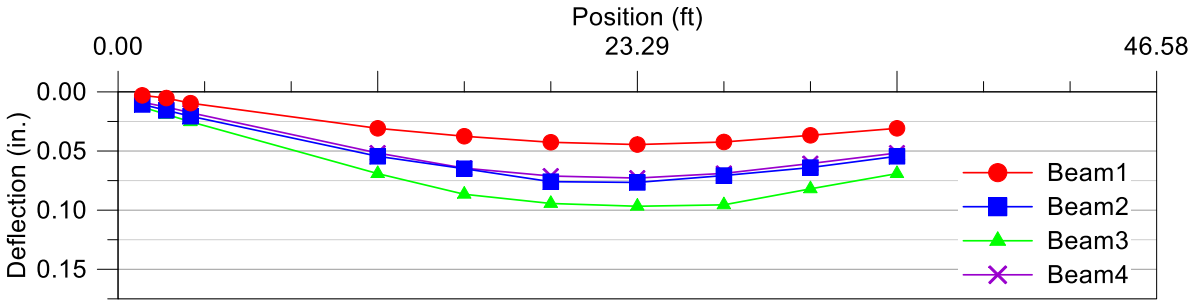

(b) Beam Deflections for Alignment 2

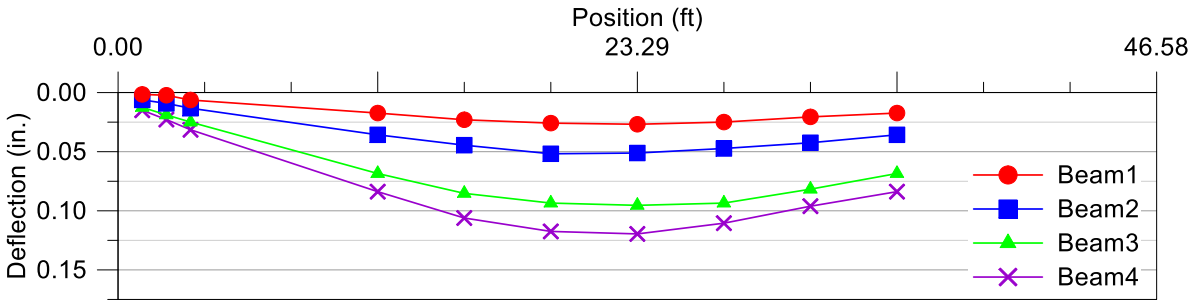

(c) Beam Deflections for Alignment 3

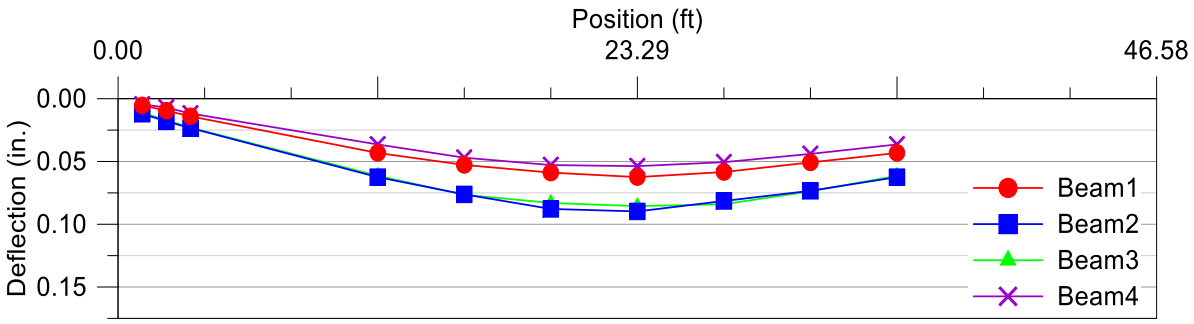

(d) Beam Deflections for Alignment 4

Figure 5.21. Deflection Profiles for Water Tanker Load.

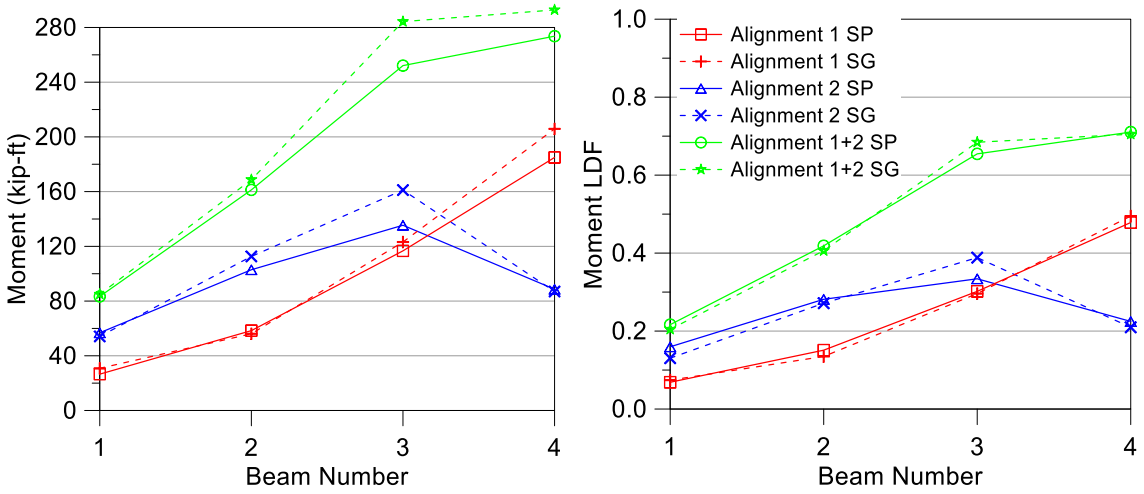

(a) Moments for Alignment 1+2

(b) Moment LDFs for Alignment 1+2

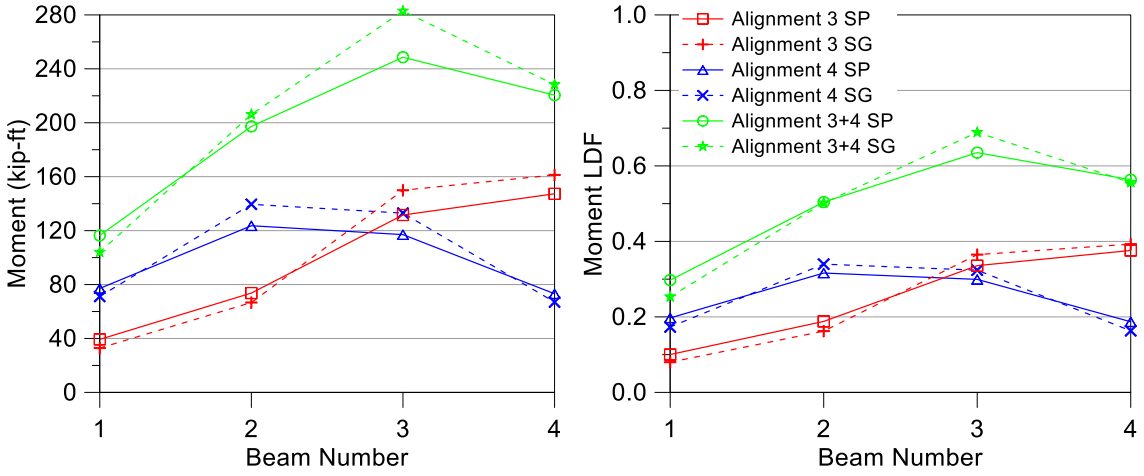

(c) Moments for Alignment 3+4

(d) Moment LDFs for Alignment 3+4

Figure 5.22. Midspan Moments and Moment LDFs for Water Tanker Loading.

Table 5.10. Maximum Moment Results for Water Tanker Tests.

No. Lanes Loaded	Slab Beam ID	Max. Moment (kip-ft)	Exp. Moment LDF	Transverse Load Position
One Lane	Beam 3 (Interior)	135	0.33	Alignment 2
	Beam 4 (Exterior)	185	0.48	Alignment 1
Two Lanes	Beam 3 (Interior)	252	0.65	Alignment 1+2
	Beam 4 (Exterior)	274	0.71	Alignment 1+2

Midspan moment values for water tanker loading for four alignments are provided in Table 5.11, and the corresponding moment LDF values are listed in Table 5.12. The maximum experimental moment LDF for an interior beam is 0.65 and was observed for Beam 3 for Alignment 1+2. Similarly, the maximum exterior beam moment LDF is 0.71 and was obtained due to loading on Alignment 1+2. The moment values that are calculated from bottom strain gage values and theoretical centroids are slightly higher than the values calculated through curve fitting of the deflection data. On the other hand, the computed moment LDFs are very close for the two different measurement techniques. The moment values determined from the string potentiometer measurements were used for further comparison to numerical models. The moment values are higher compared to the dump truck loading due to the heavier load of the water tanker. However, the moment LDFs are very close to those calculated for the dump truck loading.

Table 5.11. Moments Based on Strain Gage Data for Water Tanker Loading (kip-ft).

Load Case	Beam 1	Beam 2	Beam 3	Beam 4
Alignment 1	31	56	123	206
Alignment 2	54	113	161	87
Alignment 3	33	67	150	161
Alignment 4	71	140	133	67

Table 5.12. Moment LDFs Based on Strain Gage Data for Water Tanker Loading.

Load Case	Beam 1	Beam 2	Beam 3	Beam 4
Alignment 1	0.07	0.13	0.30	0.49
Alignment 2	0.13	0.27	0.39	0.21
Alignment 3	0.08	0.16	0.36	0.39
Alignment 4	0.17	0.34	0.32	0.16

5.6.3.3 North Support Shear Results for Water Tanker Static Loading

The north support shear loading was achieved by placing the rear axles of the TTI water tanker on the bridge near the north support. The inner rear axle was placed 25 in. from the centerline of the bearing pads. More details showing the longitudinal positioning of the water tanker are provided in Figure 5.14 above. The maximum north support reactions and experimental shear distribution factors are summarized in Table 5.13. The north support shear results are shown in Figure 5.23.

The vehicle was traveling from south to north for all three longitudinal positions in order to make the testing procedure more convenient and create one more alternative loading. Therefore, unlike the dump truck tests, the north support and south support loadings were not the same. For the south support, the critical case occurred when both the rear axles and the middle axles were on the bridge. For the moment critical and north support critical cases, only the rear axles were on the bridge.

There are no comparable dynamic results for the north support reactions due to the length of the vehicle and the static north support shear critical position of the water tanker. The dynamic maximum north support reaction was due to of the application of both the rear axles and the middle axles, whereas the static north support critical loading was achieved by placing only the rear axles close to the north support. Therefore, there are no dynamic results to directly compare to the static north support reactions.

The maximum shear LDF for the interior girders was 1.07 and was recorded when Alignment 3+4 was loaded. The maximum shear LDF of 0.82 was obtained for an exterior girder when Alignment 1+2 was loaded. The LDF values when the north support was loaded by the water tanker are about 5–10 percent higher compared to the dump truck tests. The weight of the dump truck was approximately 31 kips and was applied by three axles, where the front axle was 15 ft 2.5 in. away from the rear axles; in contrast, the water tanker's rear axles weighed approximately 38 kips, and the load was applied by the two rear axles, which were 4 ft 2 in. apart. The difference between the north support LDFs for the dump truck and water tanker may be due to the longitudinal positions of the axles. The water tanker axles were closely spaced and concentrated close to the north support.

5.6.3.4 South Support Shear Results for Water Tanker Loading

Table 5.14 lists the maximum south support reactions and experimental shear LDFs. Figure 5.24 shows the south support shear results for static and dynamic loading for the water tanker loading. The south support critical loading case was achieved when the rear axles were placed close to the south support and the middle axles were past the midspan of the bridge. This loading case resulted in the maximum bridge live load with the vehicles used for testing. The total weight on the bridge was 75.2 kips and was applied by four axles that were better distributed along the length compared to the north support critical loading.

The maximum experimental shear LDF of 0.92 was obtained for an interior beam when Alignment 3+4 was loaded. The exterior girders attained a maximum shear LDF of 0.80 for the Alignment 1+2 case. The south support shear LDF values for the water tanker are very close to the dump truck results, unlike in the north support case. As noted above, the total load of the water tanker was better distributed along the length for the south support shear critical loading, and the resulting reactions at the south support were lower as compared to the north support test. This finding indicates that the concentrated loads placed close to the support to maximize the reaction create a more adverse case that results in higher shear LDFs.

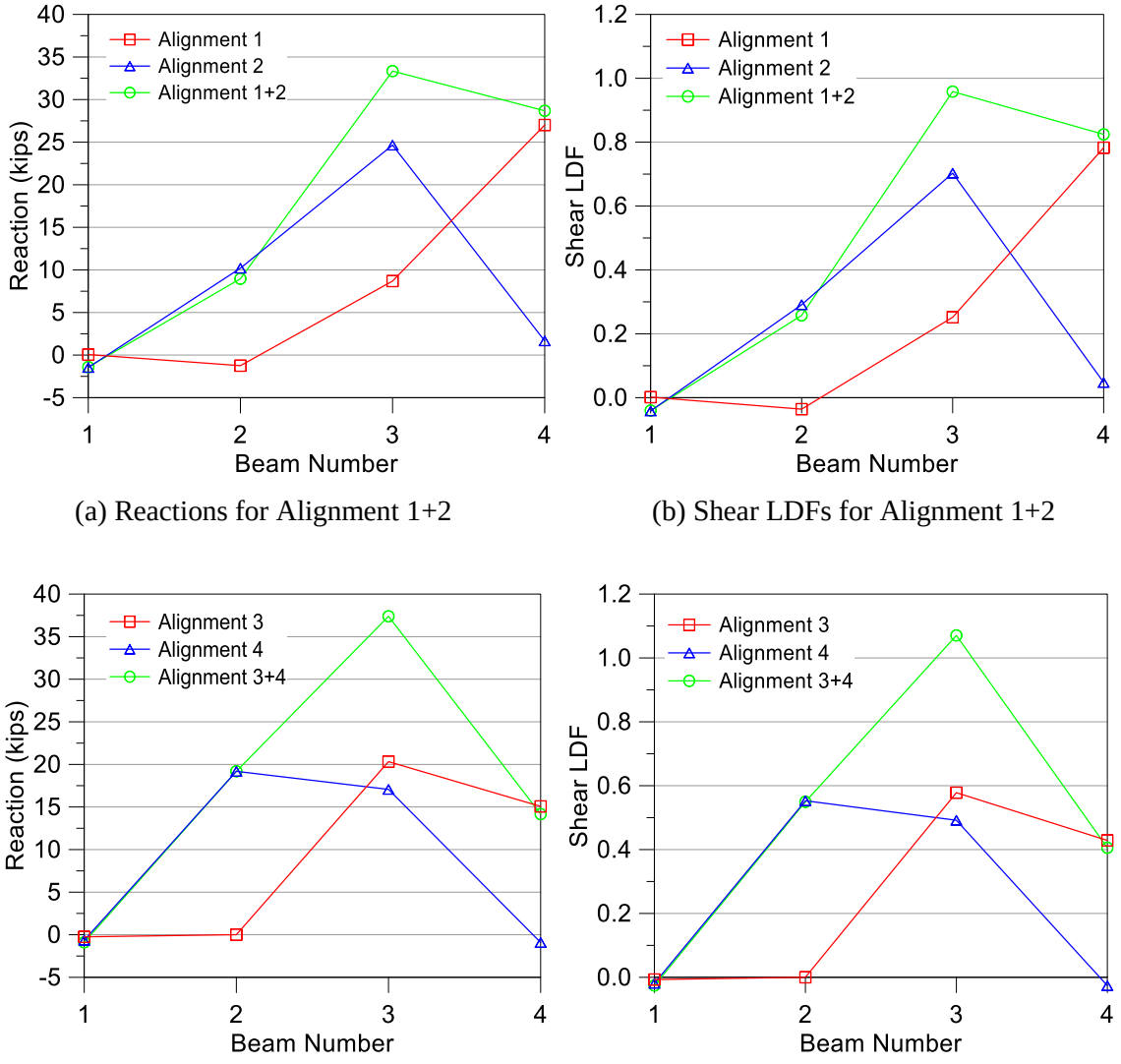

(a) Reactions for Alignment 1+2

(b) Shear LDFs for Alignment 1+2

(c) Reactions for Alignment 3+4

(d) Shear LDFs for Alignment 3+4

Figure 5.23. North Support Reactions and Shear LDFs for Water Tanker Loading.

Table 5.13. Maximum North Support Shear Results for Water Tanker Tests.

No. of Lanes Loaded	Slab Beam No.	Maximum Reaction (kips)	LDF	Load Position
One Lane	Beam 3 (Interior)	24.7	0.70	Alignment 2
	Beam 4 (Exterior)	27.0	0.78	Alignment 1
Two Lanes	Beam 3 (Interior)	37.4	1.07	Alignment 3+4
	Beam 4 (Exterior)	28.7	0.82	Alignment 1+2

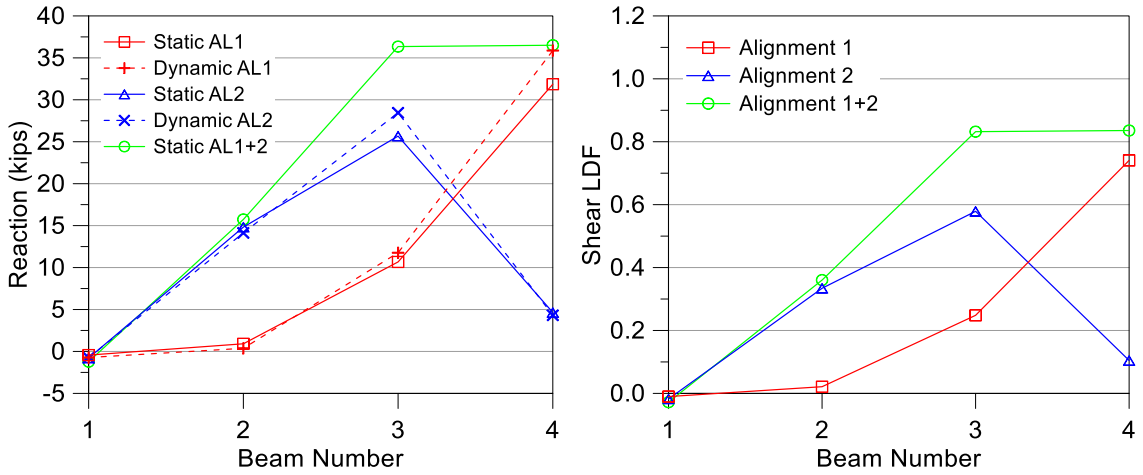

(a) Reactions for Alignment 1+2

(b) Shear LDFs for Alignment 1+2

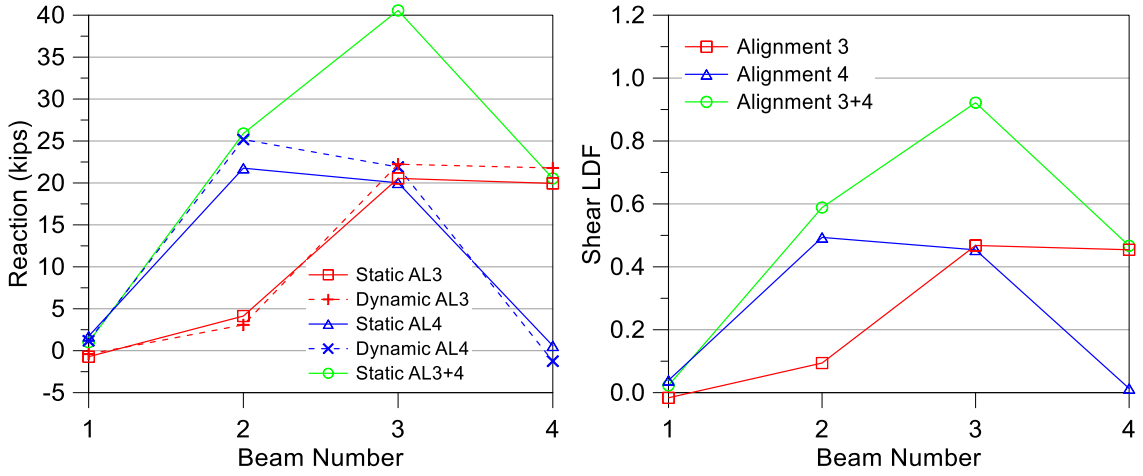

(c) Reactions for Alignment 3+4

(d) Shear LDFs for Alignment 3+4

Figure 5.24. South Support Reactions and Shear LDFs for Water Tanker Loading.

Table 5.14. Maximum South Support Reactions for Water Tanker.

No. Lanes Loaded	Slab Beam ID	Max. Reaction (kips)	Exp. Shear LDF	Tranverse Load Position
One Lane	Beam 3 (Interior)	25.7	0.58	Alignment 2
	Beam 4 (Exterior)	31.9	0.74	Alignment 1
Two Lanes	Beam 3 (Interior)	40.6	0.92	Alignment 3+4
	Beam 4 (Exterior)	36.5	0.84	Alignment 1+2

5.6.4 Dynamic Characteristics of Riverside Bridge

The research team identified the dynamic properties of the bridge by evaluating the acceleration data in the frequency domain. A total of eight accelerometers were attached to the bridge. Five accelerometers were attached to the bottom of Beam 2 and distributed in the longitudinal direction. The other three were attached at the midspan of the remaining three slab beams to capture transverse mode shapes. Figure 5.12 shows the exact layouts of the accelerometers.

Modal analysis of the bridge was conducted by running the dump truck along two different alignments and also by applying an impulse at selected points with a sledge hammer. The impulse loading test was conducted to identify possible vehicle structure interaction. The impulse test was conducted by hitting a sledge hammer on the deck surface at the longitudinal midspan and at three different transverse locations: east edge, west edge, and center. Obtained modal frequencies from impulse testing and vehicle tests are summarized in Table 5.15.

Mode shapes were identified during the dump truck testing along Alignment 1. The normalized amplitudes of each mode plotted along Beam 2 (longitudinal direction) and in the transverse direction are shown in Figure 5.25.

Table 5.15. First Three Modal Frequencies.

Description	Vehicle Speed (mph)	1st Mode (Hz)	2nd Mode (Hz)	3rd Mode (Hz)
Impulse	N.A.	5.22	8.22	13.8
Alignment 1	40	5.37	7.97	13.5
Alignment 2	40	5.37	7.94	13.3

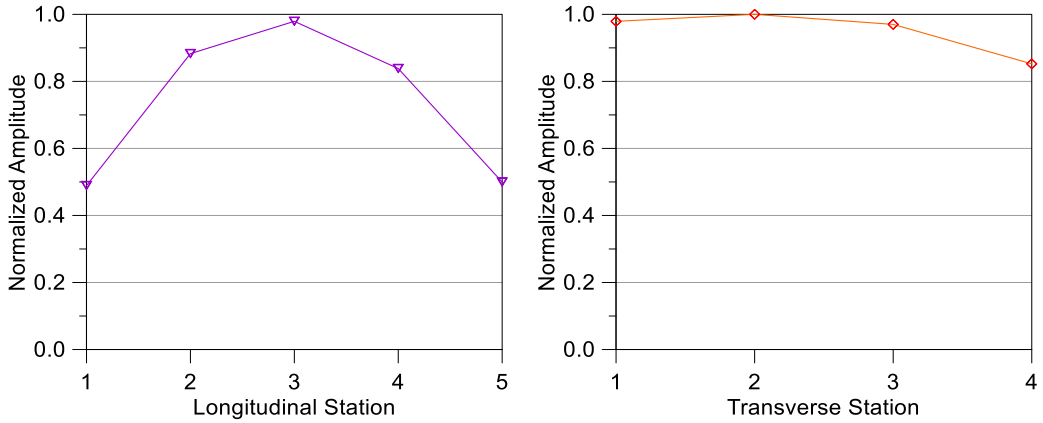

(a) 1st Mode Shape

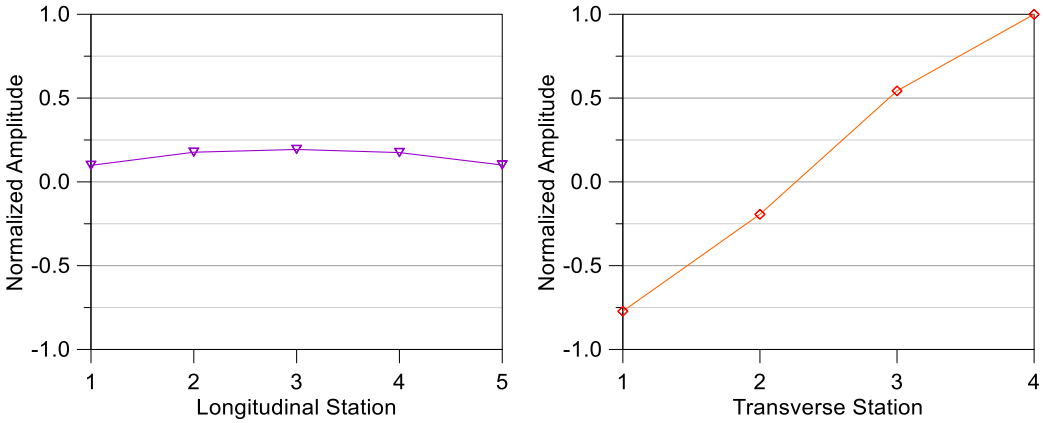

(b) 2nd Mode Shape

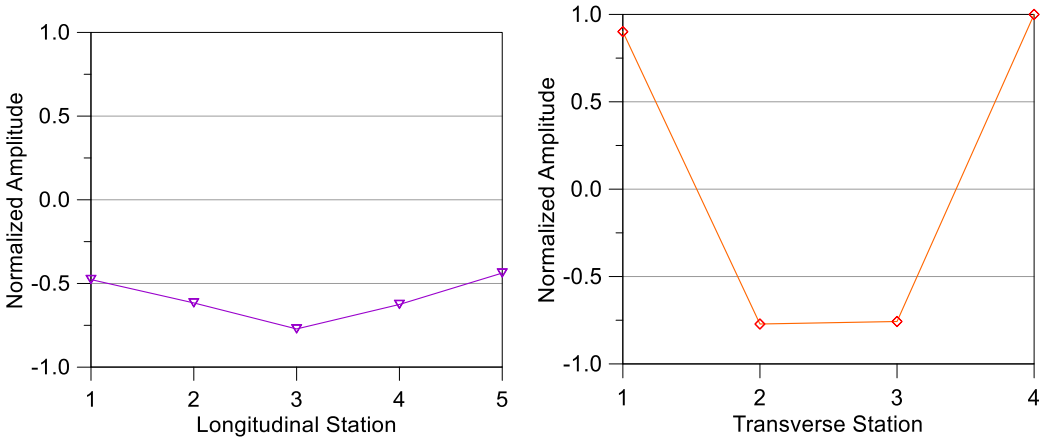

(c) 3rd Mode Shape

Figure 5.25. Identified Mode Shapes in Longitudinal and Transverse Directions.

5.7 SUMMARY AND FINDINGS

5.7.1 Constructability and Related Observations

This research investigated the possibility of using slab beams in a spread configuration for short-span bridges. A full-scale bridge utilizing widely spaced (4 ft 8 in. clear) slab beams was constructed at the Texas A&M University Riverside Campus, and then the research team tested the bridge under static and dynamic service loads. Based on the observations during construction and experimental investigation of the Riverside Bridge, the following conclusions were drawn with respect to constructability and related observations.

1. Spread slab beam bridge systems that utilize PCPs with a CIP concrete deck, similar to I-girder bridges, provide a viable construction method for short-span bridges approximately 30–50 ft long.
2. Spread prestressed slab beam bridge construction was successfully implemented for the Riverside test bridge.
3. Camber of the spread slab beams tends to increase due to higher prestressing forces. Thus, the bedding strip installation can require increased depths (up to 4 in. total) at the beam ends. Camber should be evaluated as part of spread slab beam bridge designs to ensure the value is acceptable with regard to construction and serviceability considerations.
4. Care should be taken during deck curing to avoid any unexpected cracking. For the Riverside Bridge, a single longitudinal crack was observed on the deck surface along the entire length of the bridge at the transverse centerline (centered on a PCP). The crack occurred within the first week after deck placement. The width did not increase after the crack appeared. It appears that the crack developed because of stresses due to combined shrinkage and differential temperature effects. The crack may potentially be due to hot weather and inadequate curing. However, the deck was sprayed with water daily and covered with a curing blanket and plastic sheet during the first four days. It appears that this type of crack is not related to the spread slab beam implementation.

5.7.2 Field Testing

Field testing was conducted for the Riverside Bridge to investigate the effect of beam spacing on the structural behavior of the composite bridge system. Experimental results were processed and reviewed, and are summarized below.

1. The desired performance was achieved for in-service loading. During field testing, the beam live load deflections were within the design limits. No major cracking or reduction in the overall stiffness of the bridge superstructure was observed during static and dynamic testing (up to 40 mph). The Riverside Bridge remained in the linear range of behavior when the water tanker loading of about 75 kips (slightly above HS20 loading) was applied.
2. Experimental LDFs were evaluated using alignments that provided the most adverse loading cases. The following observations were made for the Riverside Bridge, which was tested with a dump truck and a water tanker.
    a) Experimental shear LDFs for both interior and exterior girders were about 5 percent higher when the Riverside Bridge was loaded with the rear axle of the water tanker compared to the dump truck loading. This may be due to more concentrated loading achieved with the water tanker.
    b) Experimental moment LDFs were similar for both the dump truck and the water tanker loadings for the Riverside Bridge.
3. Bridge responses under dynamic loads were larger compared to static values. In spite of the changes in moment magnitude under dynamic loading, the moment LDFs were quite similar to their static counterparts.
4. The observed bridge responses under dynamic loads were larger when compared to the static counterparts. Evidently, for short-span bridges, the dynamic impact may exceed the AASHTO LRFD Specifications (2012) design value of 33 percent. However, the observed impact depended upon the position of the approach bump as well as the dynamic characteristics of the vehicle and the bridge.

6. MODELING OF RIVERSIDE BRIDGE

6.1 GENERAL

One of the main objectives of this research is to derive moment and shear LDFs for spread slab beam bridges. The experimental results obtained from the field testing of the Riverside Bridge were used to investigate different modeling approaches. These modeling techniques include orthotropic plate analysis, grillage analysis and the finite element method (FEM). Moment and shear predictions from computational models were compared with experimentally obtained values. The FEM modeling technique, which gave good agreement with the test results, was then utilized for further investigation in the parametric study for developing moment and shear LDF formulas. The FEM modeling approach providing the best agreement with the experimental values was used to develop additional FEM models having varying geometries to investigate the effect of different parameters, as described in Chapters 7 and 8.

There are many analytical and computational methods for analyzing beam and slab bridges, as summarized in Section 2. Previous studies have shown that when considering many analytical methods, orthotropic plate theory predicts the behavior of beam and slab bridges more accurately than other analytical methods (Sanders and Elleby 1970). Whereas computational methods such as grillage analysis and FEM analysis have provided the best results with the least number of assumptions. These computational methods were used to estimate the moment and shear actions of the Riverside Bridge.

6.2 ORTHOTROPIC PLATE ANALYSIS

An orthotropic plate is the common name for plates that have uniform but different elastic properties in the two orthogonal directions. In this method the bridge superstructure is represented by an equivalent orthotropic plate with uniform thickness. Longitudinal stiffnesses are calculated based on the composite beam and slab section. Transverse stiffnesses are calculated based on the deck stiffness alone. With this approach beam properties are modified to provide an equivalent continuous medium, for consideration in the longitudinal direction. This geometric simplification requires that the beams are equally spaced, which is generally the case in practice. Considering these assumptions the orthotropic plate behavior satisfies the

following fourth order partial differential equation (PDE)(Timoshenko and Woinowsky-Krieger 1959).

$$D_x \frac{\partial^4 w}{\partial x^4} + 2H \frac{\partial^4 w}{\partial x^2 \partial y^2} + D_y \frac{\partial^4 w}{\partial y^4} = p(\mathrm{x}, \mathrm{y}) \qquad (6.1)$$

where,

D_x = $E_x I_x$, flexural rigidity per unit width in x direction.

D_y = $E_y I_y$, flexural rigidity per unit width in y direction.

$2H$ = $D_{xy} + D_{yx}$, sum of orthogonal torsional rigidities.

I_x = Moment of inertia per unit width in x direction.

I_y = Moment of inertia per unit width in y direction.

E_x = Modulus of elasticity of concrete in x direction.

E_y = Modulus of elasticity of concrete in y direction.

D_{xy} = Torsional rigidity per unit width in the x direction.

D_{yx} = Torsional rigidity per unit width in the y direction.

$p(x,y)$ = Load function depending on the live load on the bridge.

A beam and slab bridge can be represented as an equivalent orthotropic plate with uniform thickness having different elastic properties in two orthogonal directions. The governing equation for such a plate is given by the PDE in Equation (6.1). There are two classical methods dealing with the rectangular plates under flexure, which are the methods developed by Navier (1785-1836) and Levy (1838-1910). Navier`s method deals with plates that are simply supported along all four edges and assumes the double sine series for both load and deflections.

Levy`s method was developed for the analysis of plates that have two opposite sides simply supported and other edges can be subjected to any arbitrary boundary conditions. Figure 6.1 illustrates a schematic plan view of the considered orthotropic plate under concentrated load with two opposite edges simply supported and the other two edges free. The Poisson's ratio is assumed to be zero. Then the simply supported edges at x=0 and x=a should have deflections and moments equal to zero. The boundary conditions at the free edges at y=0 and y=b requires that there are neither bending and twisting moments, nor shear force (Timoshenko and Woinowsky-Krieger 1959). These boundary conditions can be summarized as

$$\left.\begin{aligned} &w(0,y) = w(a,y) = 0 \\ &w_{xx}(0,y) = w_{xx}(a,y) = 0 \\ &w_{yy}(x,0) = w_{yy}(x,b) = 0 \\ &w_{yyy}(x,0) + 2w_{xxy}(x,0) = w_{yyy}(x,b) + 2w_{xxy}(x,\mathrm{b}) = 0 \end{aligned}\right\} \tag{6.2}$$

where w is the deflection, w_{xx} represents the second derivative with respect to x and w_{yyy} represents the third derivative with respect to y.

Levy`s approach represents the solution as a single Fourier series that automatically satisfies boundary conditions along $x=0$ and $x=a$ as

$$w(x,y) = \sum_{m=1}^{\infty} F_m(y) \sin\left(\frac{m\pi x}{a}\right) \tag{6.3}$$

It is further assumed that the loading function $p(x,y)$ can be represented with a single Fourier series as well,

$$p(x,y) = \sum_{m=1}^{\infty} p_m(y) \sin\left(\frac{m\pi x}{a}\right) \tag{6.4}$$

where the P_m coefficients can be obtained as

$$P_m(y) = \frac{2}{a}\int_0^a p(x,y) \sin\left(\frac{m\pi x}{a}\right) dx \tag{6.5}$$

Considering the governing PDE in Equation (6.1) and the Fourier representations of deflection and loading function given in Equations (6.3) and (6.4), the following ordinary differential equation (ODE) is obtained.

$$D_y \frac{d^4 F_m}{dy^4} - 2\left(\frac{m\pi}{a}\right)^2 H \frac{d^2 F_m}{dy^2} + D_x \left(\frac{m\pi}{a}\right)^4 F_m = P_m \tag{6.6}$$

In the case of a concentrated load P_0 acting at a location (x_0, y_0), the loading function $p(x,y)$ can be expressed using the characteristic function of the rectangle centered at (x_0, y_0) (see Figure 6.1) as

$$p(x,y) = \lim_{\substack{u\to 0 \\ v\to 0}} \frac{P_0}{uv} \chi_{[x_0-u/2, x_0+u/2]}(x)\, \chi_{[y_0-v/2, y_0+v/2]}(y) \tag{6.7}$$

The Fourier coefficients P_m can then be calculated from Equation (6.5) using the loading function given in Equation (6.7) as

$$P_m(\mathrm{y}) = \lim_{\substack{u\to 0\\ v\to 0}} \frac{2P_0}{auv}\chi_{[y_0-v/2,y_0+v/2]}(y)\int_{x_0-u/2}^{x_0+u/2} sin\left(\frac{m\pi x}{a}\right)dx \tag{6.8}$$

Evaluating the integral yields

$$P_m(\mathrm{y}) = \lim_{\substack{u\to 0\\ v\to 0}} \frac{2P_0}{auv}\frac{2a}{m\pi}\chi_{[y_0-v/2,y_0+v/2]}(y)\sin\left(\frac{m\pi x_0}{a}\right)\sin\left(\frac{m\pi u}{2a}\right) \tag{6.9}$$

Since

$$\lim_{u\to 0}\frac{\sin\left(\frac{m\pi u}{2a}\right)}{\left(\frac{m\pi u}{2a}\right)} = 1 \qquad \text{and} \qquad \lim_{v\to 0}\frac{1}{v}\chi_{[y_0-v/2,y_0+v/2]}(\mathrm{y}) = \delta(\mathrm{y}-\mathrm{y}_0)$$

$$P_m(\mathrm{y}) = \frac{2P_0}{a}\sin\left(\frac{m\pi x_0}{a}\right)\delta(\mathrm{y}-\mathrm{y}_0) \tag{6.10}$$

The Fourier coefficients of the loading function, P_m given in Equation (6.10) can be used together with the Equation (6.6) to obtain the fourth order ordinary differential equation (ODE) for F_m as

$$D_y\frac{d^4F_m}{dy^4} - 2\left(\frac{m\pi}{a}\right)^2 H\frac{d^2F_m}{dy^2} + D_x\left(\frac{m\pi}{a}\right)^4 F_m = \frac{2P_0}{a}\sin\left(\frac{m\pi x_0}{a}\right)\delta(\mathrm{y}-\mathrm{y}_0) \tag{6.11}$$

subject to the following boundary conditions which is calculated from Equation (6.2) and (6.3)

$$\left.\begin{aligned} &\frac{d^2F_m}{dy^2} = 0 && \text{for } y = 0 \text{ and } y = b\\ &\frac{d^3F_m}{dy^3} = 2\left(\frac{m\pi}{a}\right)^2\frac{dF_m}{dy} && \text{for } y = 0 \text{ and } y = b \end{aligned}\right\} \tag{6.12}$$

The ODE given by Equation (6.11) together with boundary conditions given in Equation (6.12) can be solved using the variation of parameters method. For practical purposes this ODE was solved using Mathematica and the obtained F_m values back substituted into Equation (6.3) to obtain the final deflected shape. Elastic flexural and torsional stiffness coefficients were calculated per unit length, using the values given in Table 6.1 and Table 6.2. Figure 6.2 shows the deflection fields for Alignment 1 and Alignment 3.

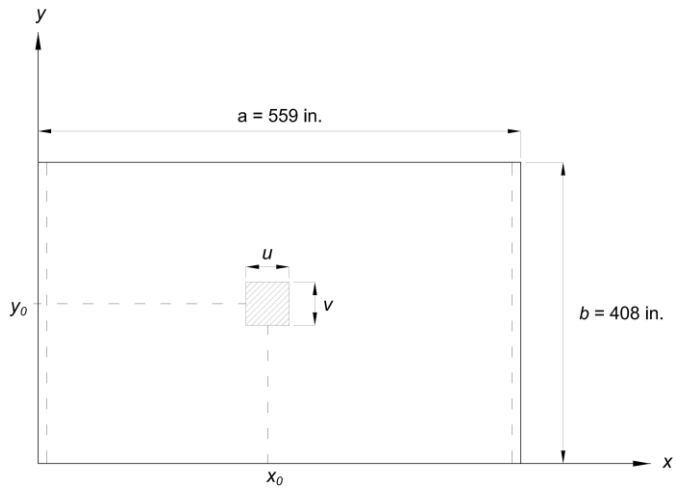

Figure 6.1. Orthotropic Plate Representation of Riverside Bridge with a Point Load.

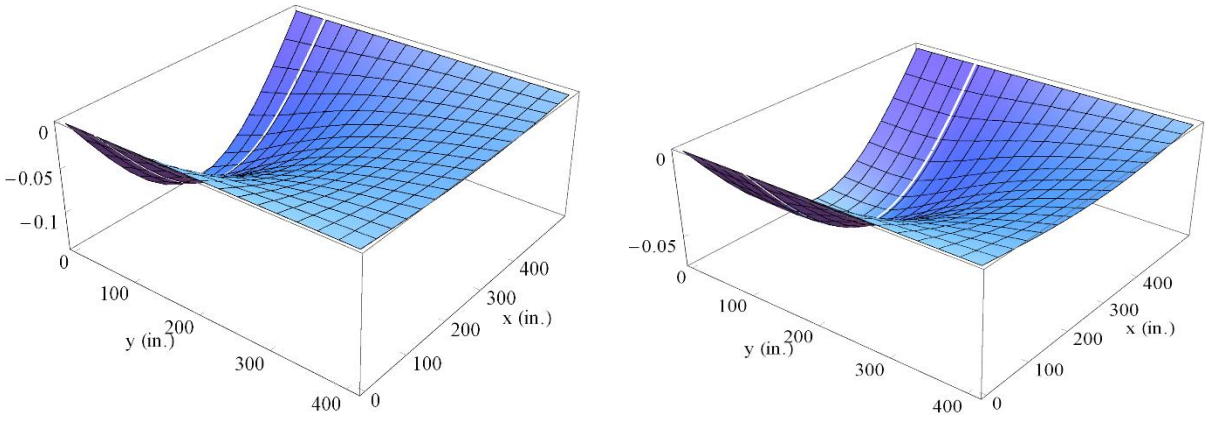

(a) Alignment 1 (b) Alignment 3

Figure 6.2. Displacement Field Obtained from Orthotropic Plate Analysis.

6.3 GRILLAGE MODEL

Grillage analysis is historically the most basic type of computational modeling technique for analyzing slab and beam bridges. This method idealizes the bridge superstructure by assuming that it may be represented by a mesh of frame elements in each of the two orthogonal directions. This assumption reduces the real structure in 2D plane grillage where longitudinal members represent composite T-beam with associated slab and transverse members represent the slab only. Grillage analysis was first introduced by Lightfoot and Sawko (1959) in the early days

of matrix structural analysis and has been widely used since that time. The method provides a simplified approach by reducing the number of degrees of freedom. Although this method provides sufficiently accurate predictions, it requires more time for modeling the elastic parameters and loading arrangement correctly as compared to current available FEM software with modern user-friendly graphical interfaces. The Riverside Bridge grillage model was developed following the guidelines provided by Hambly (1975) and Zokaie et al. (1991).

6.3.1 Grillage Layout and Member Properties

Longitudinal grillage members were placed along the centerline of the beams, which is a typical approach for slab and beam bridge decks. The transverse grillage member spacing was adjusted so that the spacing was less than 10 percent of the span length. Additional transverse grillage members were provided at 25 in. away from the support line for placing the rear axle loads for the shear critical case.

Figure 6.3 shows the grillage layout for the Riverside Bridge. Longitudinal grillage members are modeled as composite T-sections considering the slab beam and tributary width of the deck. Because the modulus of elasticity of the deck and beams is not the same, transformed sections were used for the composite T-sections.

Moment of inertia, *I*, and torsional constant, *J*, are two important parameters for correctly modeling the flexural and torsional stiffness of grillage members. These are automatically calculated by the section designer within the SAP2000 (2014) software, which was used for analyzing the grillage model. SAP2000 permits the user to define a section with one uniform material property, which is an issue when there are three different concrete layers and strengths within the bridge superstructure: the precast slab beam, PCPs, and CIP deck. PCPs were assumed to be part of the deck, which resulted in an average 9 in. constant deck thickness.

Table 6.1 and Table 6.2 list the geometric and material properties of all grillage members used for modeling the bridge. The deck is present in both the longitudinal and transverse directions. Therefore the deck torsional constant is multiplied by 0.5 as suggested by Parke and Hewson (2008). The reduced torsional constant was calculated using the section designer of SAP2000 and then applied as a stiffness modifier for the torsional constant parameter only.

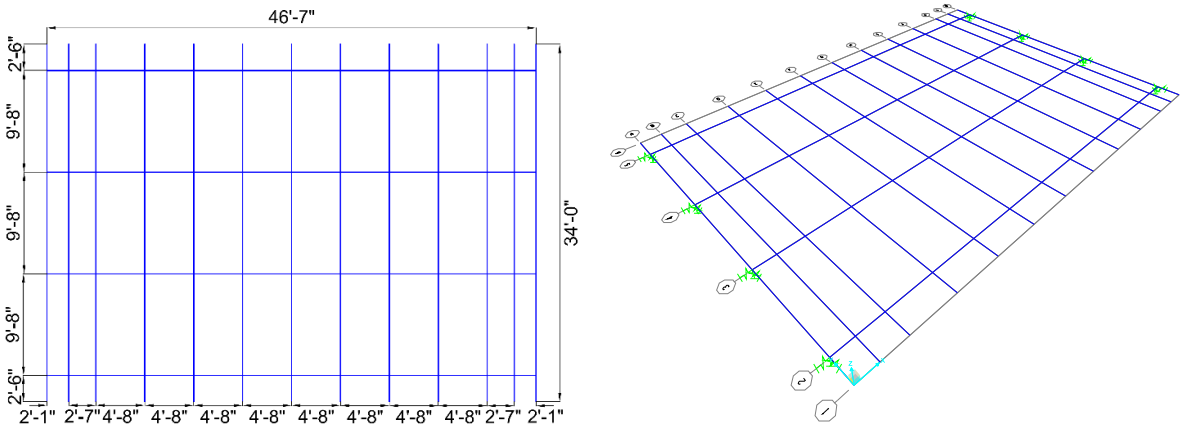

(a) Plan View (b) 3D View

Figure 6.3. Grillage Model Member Layout.

Table 6.1. Longitudinal Grillage Member Properties.

Parameter	Exterior Member	Interior Member
Deck Width (in.)	106	139
Deck Depth (in.)	9	9
Beam Width (in.)	60	60
Beam Depth (in.)	15	15
Modulus of Elasticity (ksi)	5880	5880
Moment of Inertia (in^4)	90,000	101,000
Torsional Constant (in^4)	193,000	214,000

Table 6.2. Transverse Grillage Member Properties.

Parameter	Exterior Member	First Interior Member	Interior Members
Deck Width (in.)	22	6	56
Deck Depth (in)	11	10	9
Modulus of Elasticity (ksi)	7050	7050	7050
Moment of Inertia (in^4)	2440	500	3400
Torsional Constant (in^4)	3350	225	6100

6.3.2 Support Conditions and Loading

The slab beams were seated on bearing pads at the support locations. There is one 9 in. by 18 in. bearing pad at the transverse center at the north end of each slab beam. Whereas, 9 in. by 9 in. bearing pads were placed close to the corners at the south end of each slab beam. One sample from each bearing pad type were tested under cyclic axial load. Their behavior was linear elastic within the service load range. The compressive stiffness is 1270 kip/in and 6100 kip/in for the small and larger bearing pads, respectively. The lateral stiffness of these pads were calculated as 5 kip/in and 10 kip/in, respectively, based on the shear modulus (100.6 psi). The rotational stiffness were taken as zero due to the load cell setup, which is very close to ideal pin support conditions.

Figure 6.4 shows typical load positions for a moment critical and a shear critical case. The longitudinal and transverse vehicle positions for different alignments were provided in Section 5. In this section only vehicle tests using the dump truck are compared with the computational predictions. The wheel positions do not correspond to the grillage locations in most cases. Therefore the loads were distributed to the nearest transverse grillage by linear interpolation to create an equivalent loading effect. The distribution of the loads in such a manner is one of the assumptions that is not ideal, but it gives a sufficiently close load configuration.

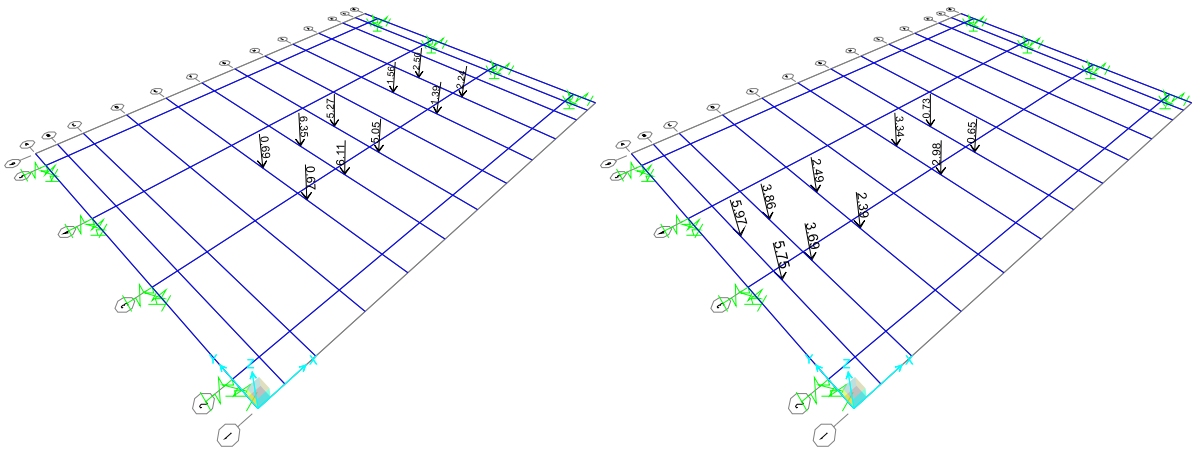

(a) Moment Critical Position (b) Shear Critical Position

Figure 6.4. Dump Truck Loading for a Typical Case.

6.4 FINITE ELEMENT MODEL

FEM provides a powerful and versatile computational approach for modeling the exact geometry of the bridge necessitating very few simplifying assumptions. A 3D finite element model that uses solid brick elements enables representation of the correct bridge geometry including the vertical positions of the boundary conditions. Two different commercial software were utilized to compare analysis accuracy. One of them is Abaqus (2013), which is a general purpose FEM software for solving a broad range of engineering problems. The second one is Computers and Structures (2015), which is more specific to bridge engineering.

6.4.1 Model Description

Detailed geometric and material properties of the Riverside Bridge were introduced in Section 5. The bridge superstructure was modeled using a three dimensional (3D) FEM model with two different commercial programs: Abaqus (Dassault Systemes 2013) and CSiBridge (Computers and Structures 2015). The vertical locations of the beams and deck, as well as the locations of supports, were reflected accurately by the 3D FEM model. Three-dimensional eight-node solid brick elements with three degrees of freedom at each node were utilized for the FEM models. Figure 6.5 shows the FEM models created with the two programs.

Table 6.3 lists some of the major properties of the bridge. The Riverside Bridge has a span length (center-to-center of bearing pads) of 46 ft 7 in and a 34 ft total width. The slab beams are spaced at 9 ft 8 in. The deck has a variable thickness along the length due to camber of slab beams. In addition 4 in. thick PCPs span between beams. These panels are considered as part of the CIP deck. Therefore a 9 in. constant deck thickness was assumed for both FEM models.

Table 6.3. Major Geometric and Material Properties.

Span Length	Total Bridge Width	Beam Type	Beam Spacing	Average Deck Thickness	MOE of Beam Concrete (ksi)	MOE of Deck Concrete (ksi)	Poisson`s Ratio
46' - 7"	34' - 0"	5SB15	9' - 8"	9 in.	5880	7050	0.2

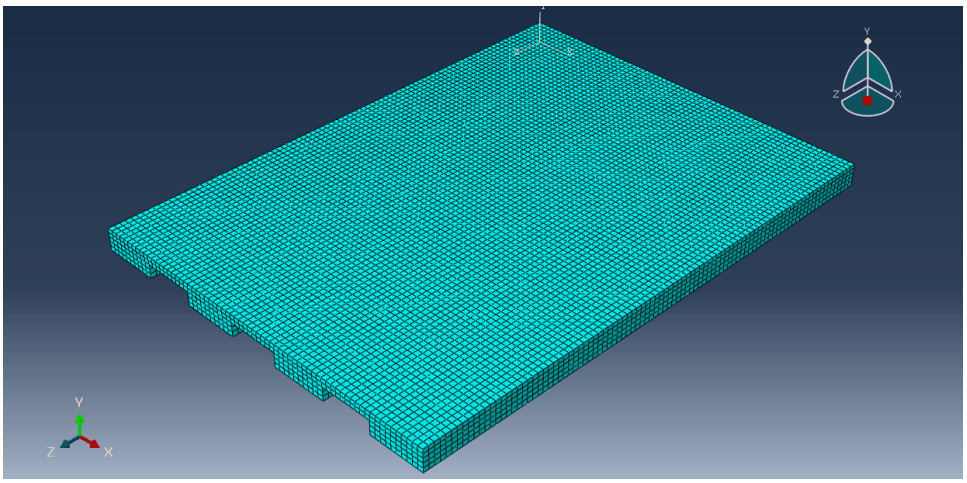

(a) Abaqus Model

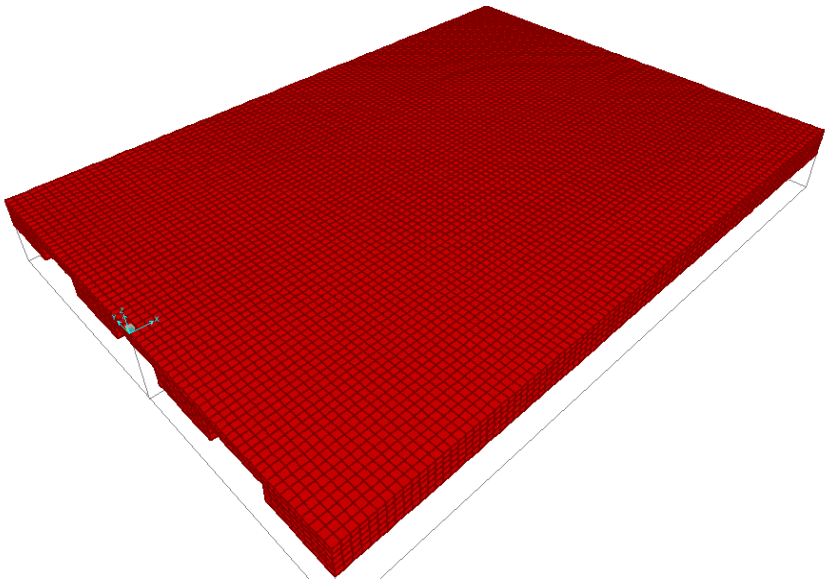

(b) CSiBridge Model

Figure 6.5. Finite Element Model 3D Mesh View.

6.4.2 Loading and Support Conditions

Vehicles were placed on the deck surface at their actual positions during the test. Each wheel load was applied as a concentrated load. The CSiBridge software allows defining concentrated loads with respect to a reference point giving the coordinates of the load. However, the Abaqus software requires that the concentrated load be applied at the nodes. Although a very dense 6 in. mesh size was used, most of the time the wheel load position did not correspond to a defined node. A Matlab routine was created to distribute the concentrated loads to the neighboring nodes based on linear shape functions. This Matlab routine produces an input file for concentrated loads given the layout and loads of each wheel of the vehicle.

Boundary conditions at each end of the beams were modeled as 3D springs having vertical and horizontal stiffness values as defined in Section 6.3.2.

6.4.3 Mesh Sensitivity Study

The FEM models were created using eight node brick elements. These models were divided into equally spaced nodes in all three major directions. Five different models were produced with 6, 12, 18, 24, and 36 in. maximum mesh sizes throughout using the CSiBridge Software.

Table 6.4 summarizes the moment and shear predictions obtained from the FEM models having different mesh sizes. The moment and shear predictions were obtained for one of the critical moment and critical shear cases along Alignment 1.

Figure 6.6 shows the comparison of moment and shear results and the corresponding lateral LDFs for different meshed FEM models.

6.5 RESULTS OF ANALYTICAL STUDY

6.5.1 Deflections and Modal Properties

Figure 6.7 shows the comparison of deflection results to orthotropic plate analysis. The calculated deflection values when the vehicle was located at Alignment 1 overestimated the test results about 10 percent, whereas when the vehicle was at Alignment 3 the estimated maximum deflection was about 20 percent lower than the test result. The reason may be that the orthotropic plate analysis assumes a uniform thickness, and thereby neglects any edge stiffening effects present. Due to lower stiffness of the edges, the orthotropic plate solution gives over estimated deflections for the loads close to the free edges.

Table 6.4. FEM Support Reactions and Moment Results with Different Mesh Sizes.

Mesh Size	Support Reaction (kips)				Moment (kip-ft)			
	Beam 1	Beam 2	Beam 3	Beam 4	Beam 1	Beam 2	Beam 3	Beam 4
36 in.	0.3	0.6	6.1	16.1	24.2	45.1	88.1	120.9
24 in.	0.0	0.3	6.6	19.5	22.7	43.9	88.2	122.7
18 in.	-0.1	0.2	6.6	19.6	22.3	43.6	88.4	123.3
12 in.	-0.1	0.1	6.6	19.8	21.6	43.1	88.6	124.5
6 in.	-0.3	0.0	6.6	20.1	20.9	42.6	88.9	125.6
Test	-0.3	-0.4	6.8	18.1	19.0	42.3	85.3	138.2

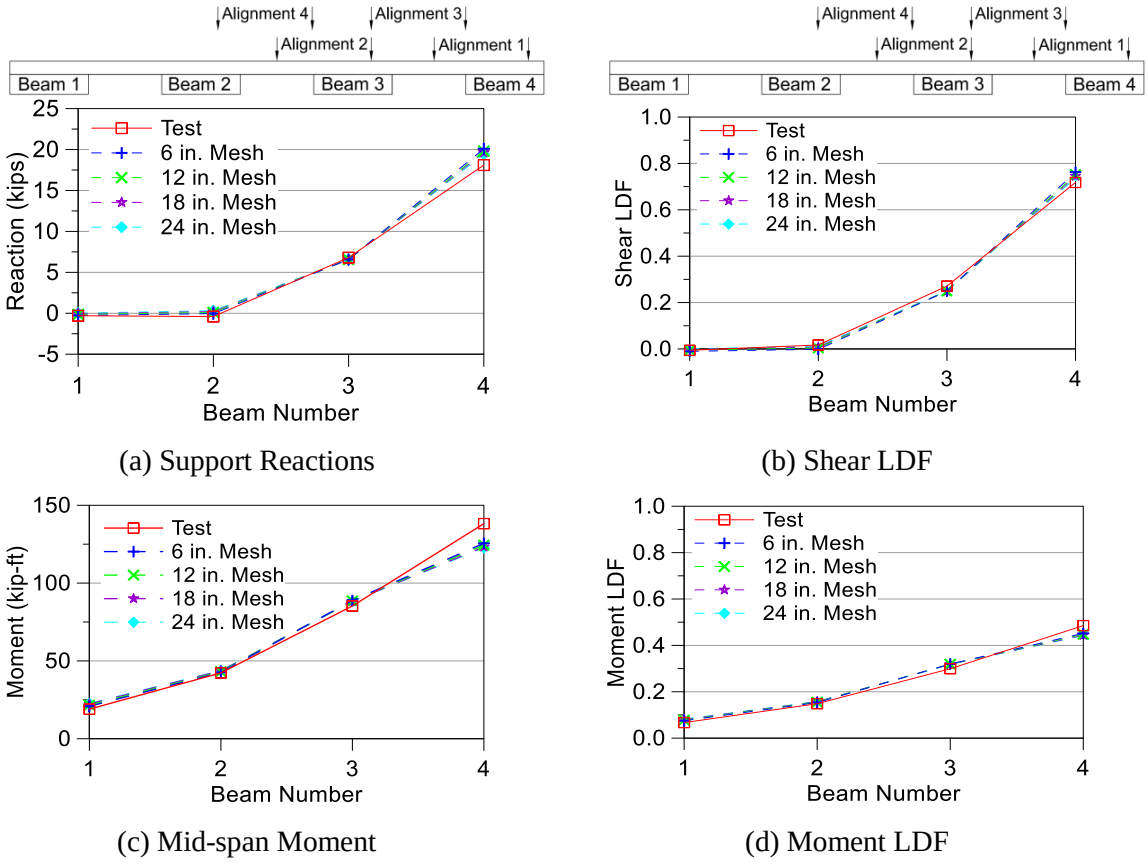

(a) Support Reactions

(b) Shear LDF

(c) Mid-span Moment

(d) Moment LDF

Figure 6.6. Comparison of Shear and Moment Results with Different Mesh Sizes.

Figure 6.8 shows the deflection fields obtained from the Abaqus software when the dump truck was located at four different alignments. The experimentally observed deflections were compared to those predicted by the two commercial FEM programs. Figure 6.9 shows the comparison of deflection values for all four alignments.

Table 6.5 summarizes the maximum beam deflections for different alignments obtained from test measurements and FEM predictions. It shows that both FEM models can predict the deflection profiles reasonably well. The maximum difference between the measured and predicted deflections is 0.010 in. for Abaqus and 0.012 in. for CSiBridge results. It should be noted that string potentiometers work best within a 0.005 in. resolution.

It is important to accurately model the dynamic characteristics of the bridge to ensure it is properly modeled by the FEM software. The experimentally observed modal properties were compared with the FEM predictions of Abaqus and CSiBridge software. Figure 6.10 shows the mode shapes from FEM analysis and Figure 6.11 presents a comparison of all three mode shapes with the experimentally derived mode shapes. Table 6.6 lists the experimental and computational natural frequencies for the first three modes. The predicted natural frequencies and mode shapes from both programs are in good agreement with the test results. Although the amplitudes of the second and third mode shapes seems slightly off from the test values, the patterns follows the same corresponding shape.

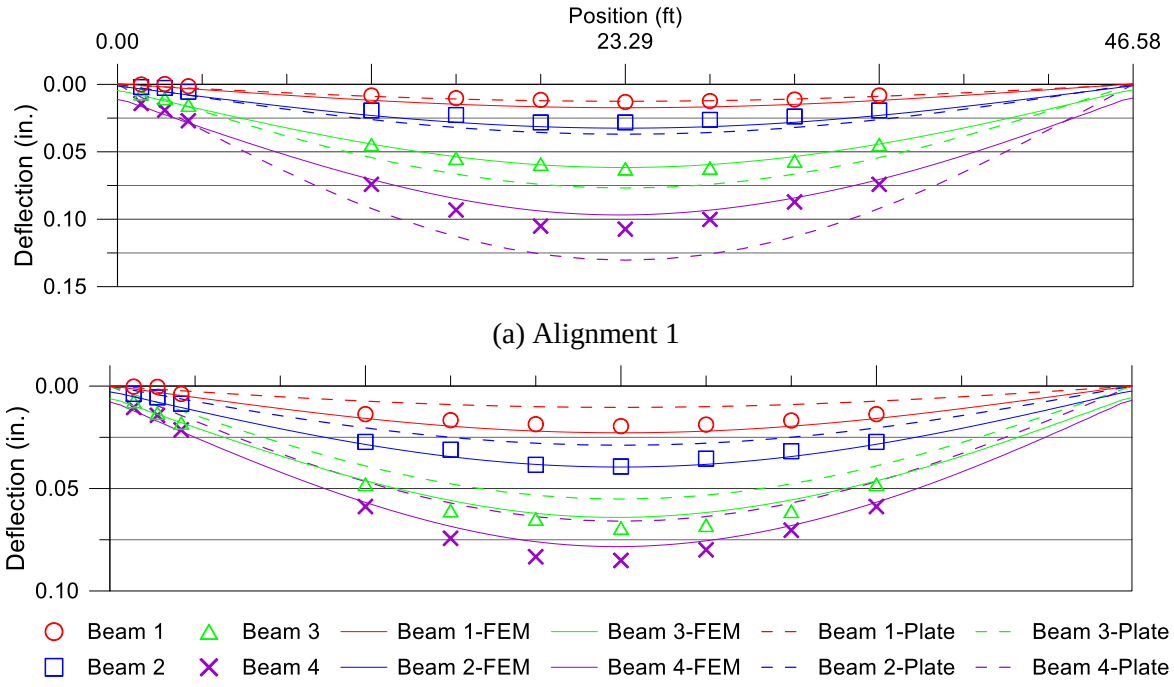

(a) Alignment 1

(b) Alignment 3

Figure 6.7. Comparison of Deflections with Orthotropic Plate Analysis.

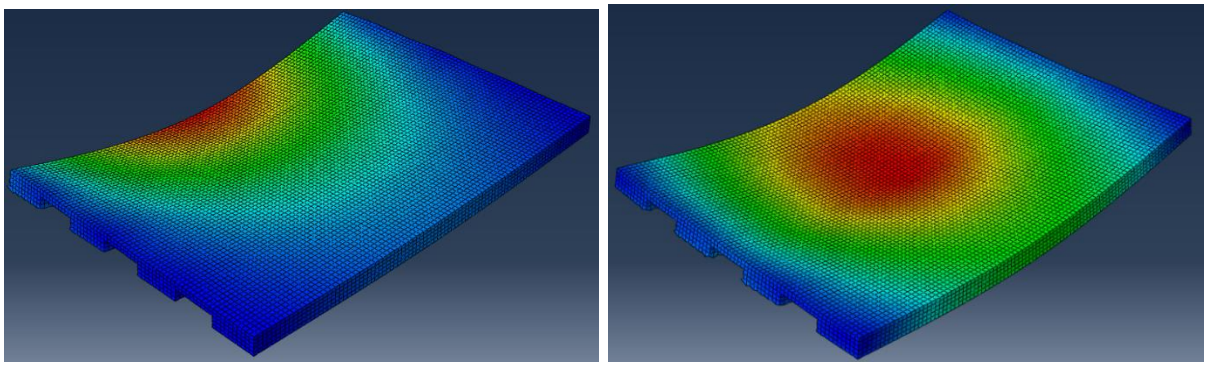

(a) Alignment 1 (b) Alignment 2

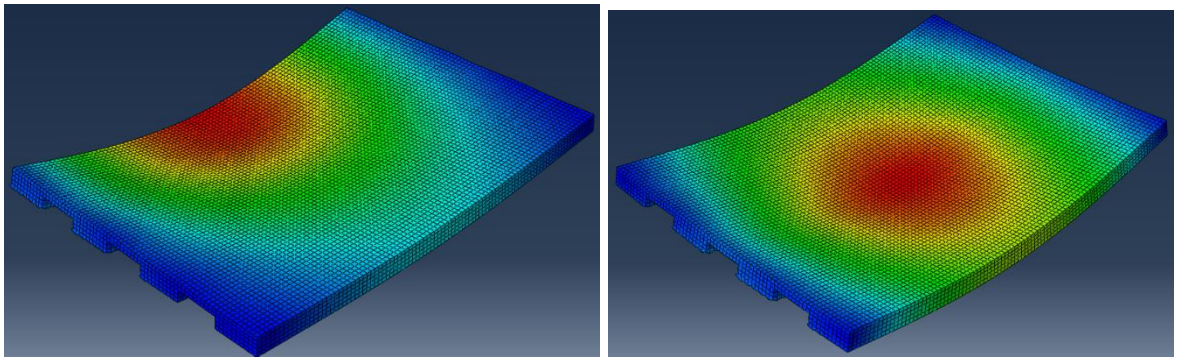

(a) Alignment 3 (b) Alignment 4

Figure 6.8. Deflection Field Obtained from Abaqus Software.

Table 6.5. Maximum Beam Deflections under Vehicle Load.

Description		Beam 1 Deflection (in.)	Beam 2 Deflection (in.)	Beam 3 Deflection (in.)	Beam 4 Deflection (in.)
Alignment 1	Test	0.013	0.028	0.063	0.107
	Abaqus	0.017	0.032	0.062	0.097
	CSiBridge	0.015	0.031	0.059	0.095
Alignment 2	Test	0.033	0.057	0.070	0.052
	Abaqus	0.035	0.053	0.063	0.053
	CSiBridge	0.033	0.051	0.060	0.050
Alignment 3	Test	0.020	0.039	0.069	0.085
	Abaqus	0.022	0.039	0.064	0.078
	CSiBridge	0.021	0.038	0.061	0.075
Alignment 4	Test	0.045	0.066	0.061	0.039
	Abaqus	0.046	0.059	0.057	0.041
	CSiBridge (in.)	0.044	0.057	0.054	0.038

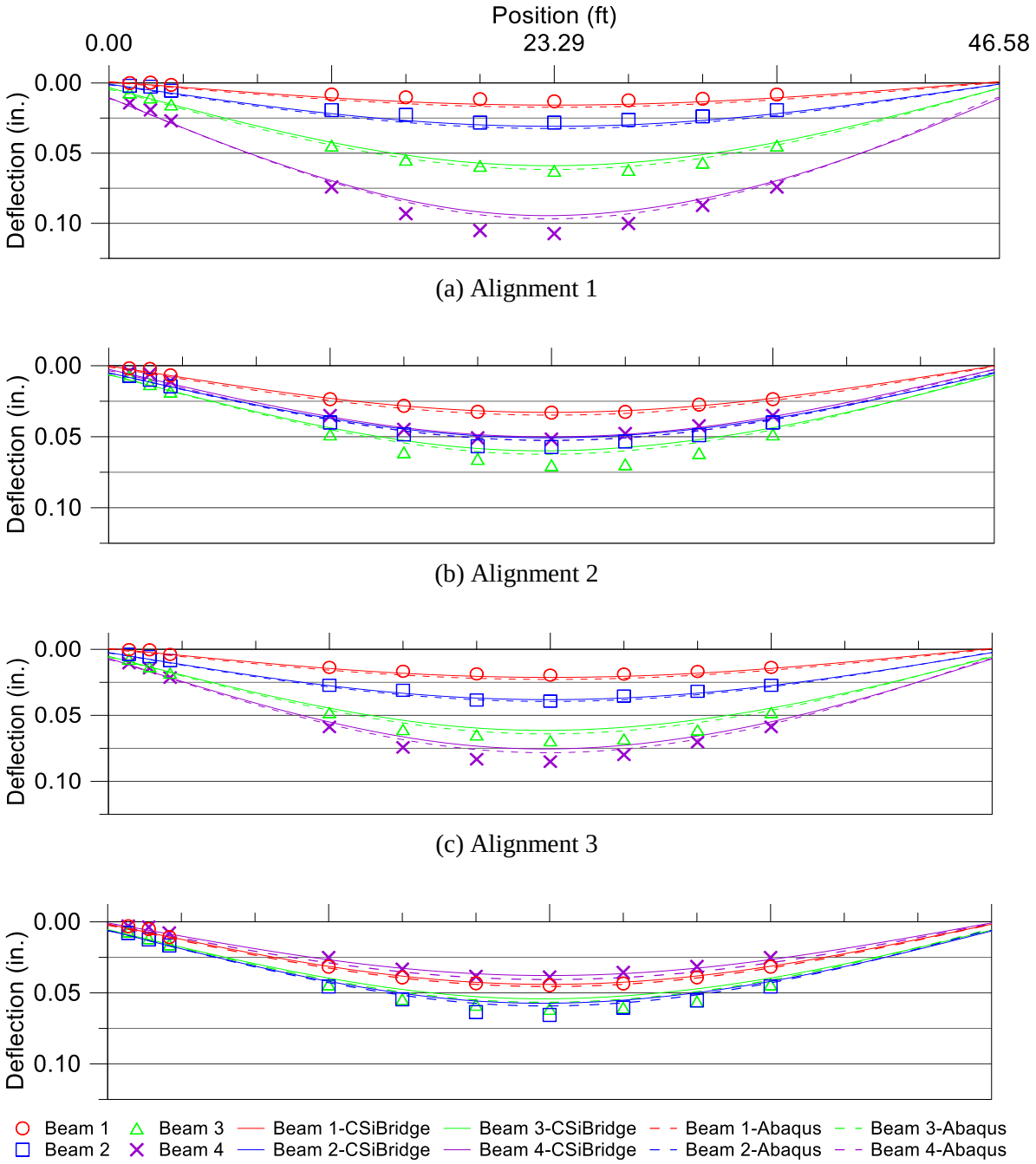

(a) Alignment 1

(b) Alignment 2

(c) Alignment 3

(d) Alignment 4

Figure 6.9. Comparison of Experimental Deflection Profiles with FEM.

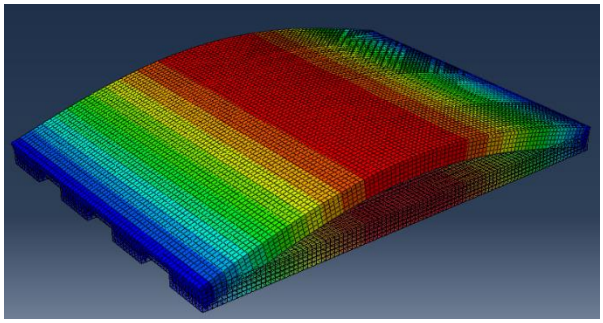

(a) 1st Mode – Abaqus (5.6 Hz)

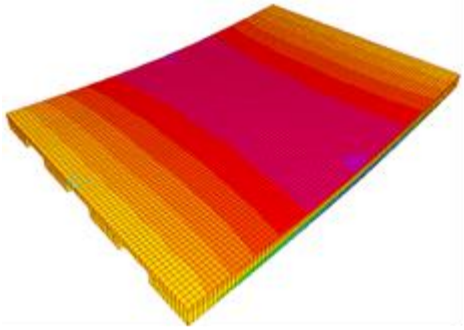

(b) 1st Mode – CSiBridge (5.9 Hz)

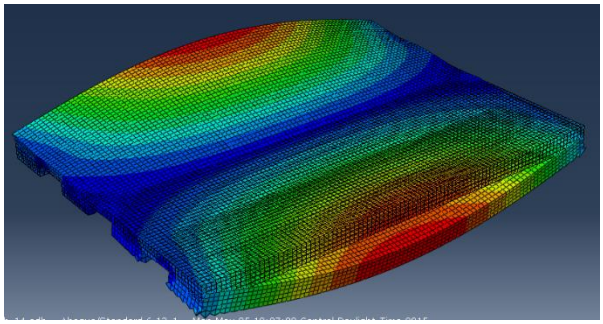

(c) 2nd Mode – Abaqus (8.3 Hz)

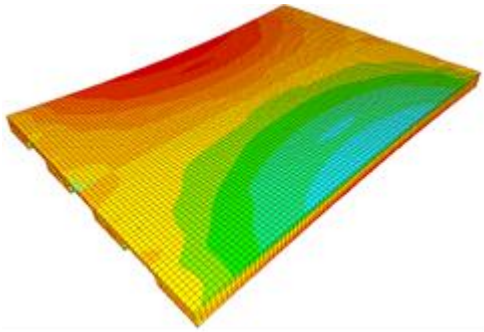

(d) 2nd Mode – CSiBridge (8.6 Hz)

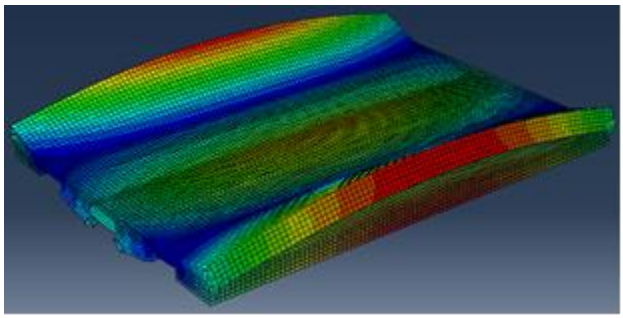

(e) 3rd Mode – Abaqus (14.6 Hz)

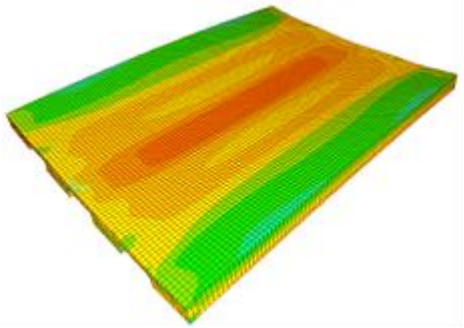

(f) 3rd Mode – CSiBridge (14.8 Hz)

Figure 6.10. Mode Shapes from FEM Analysis.

Table 6.6. Experimental and Computational Frequencies.

Description	1st Mode (Hz)	2nd Mode (Hz)	3rd Mode (Hz)
Test	5.5	8.2	13.8
Abaqus	5.6	8.3	14.6
CSiBridge	5.9	8.6	14.8

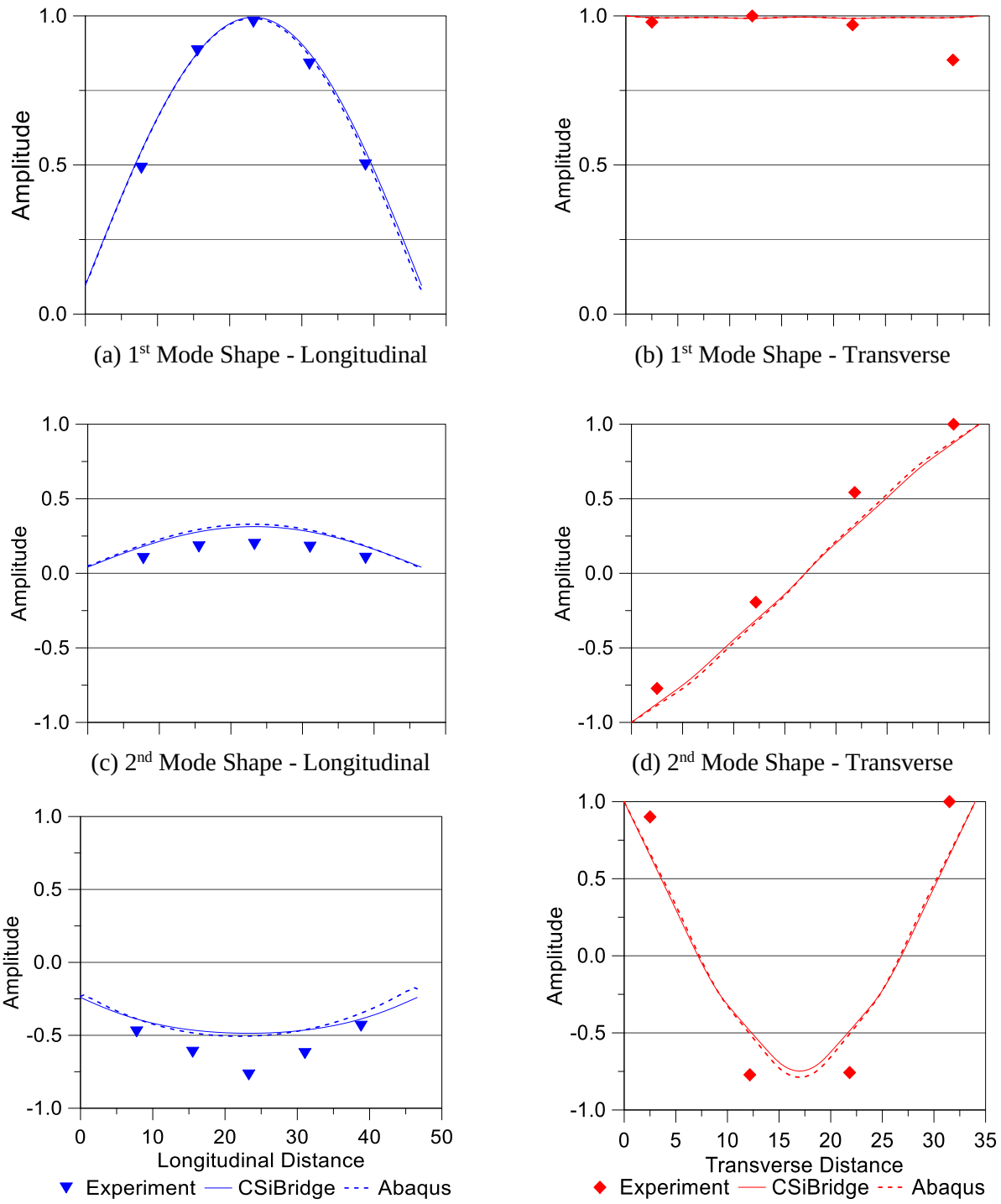

(a) 1st Mode Shape - Longitudinal

(b) 1st Mode Shape - Transverse

(c) 2nd Mode Shape - Longitudinal

(d) 2nd Mode Shape - Transverse

(e) 3rd Mode Shape - Longitudinal

(f) 3rd Mode Shape - Transverse

Figure 6.11. Comparison of Experimental Mode Shapes with FEM.

6.5.2 Computational and Experimental Moment and Shear Results

Figure 6.12 shows the comparison of moment LDFs obtained from the orthotropic plate analysis. The moment LDFs for Alignment 1 and 3 were calculated when the dump truck was located at the critical moment position. Although the deflection profiles calculated from plate analysis did not accurately capture the test results because of the assumptions, the moment LDF values are in good agreement with experimental observations.

Maximum moment and shear responses of each slab beam for moment and shear critical longitudinal positions of the dump truck were estimated using grillage and FEM models. The lateral distribution of live loads between girders were then calculated from these moment and shear estimates.

Figure 6.13 shows the comparison of moment and moment LDF curves for all four alignments across the bridge with the test results. The graphs illustrate that both the grillage and the FEM computational results show good agreement with the test results. Although the Abaqus moment results were slightly closer to the test results when compared with CSiBridge, the CSiBridge values are within 3-5 percent of the Abaqus moment values. On the other hand, the moment LDFs calculated from the two different FEM programs (Abaqus and CSiBridge) were quite similar.

Figure 6.14 presents a comparison of computational and experimental north support reactions and shear LDFs. The variation of shear responses and shear LDFs were plotted across the bridge to visualize the lateral load sharing. Both grillage and FEM results show promise while being slightly on the conservative side compared to the experimental observations.

Figure 6.15 shows a comparison of test results and computational predictions for the south support shear actions. The south support critical position of the dump truck was identical to the north support shear critical case. But the support conditions were slightly different due to bearing pad layout where the north end of the beams has a single pad configuration while the south end of the beams have a two pad configuration with different vertical and lateral stiffness values, as described in Section 6.3.2. Consequently, the south end support reactions were slightly smaller when compared to the north end reactions. The differences were also captured by the computational models.

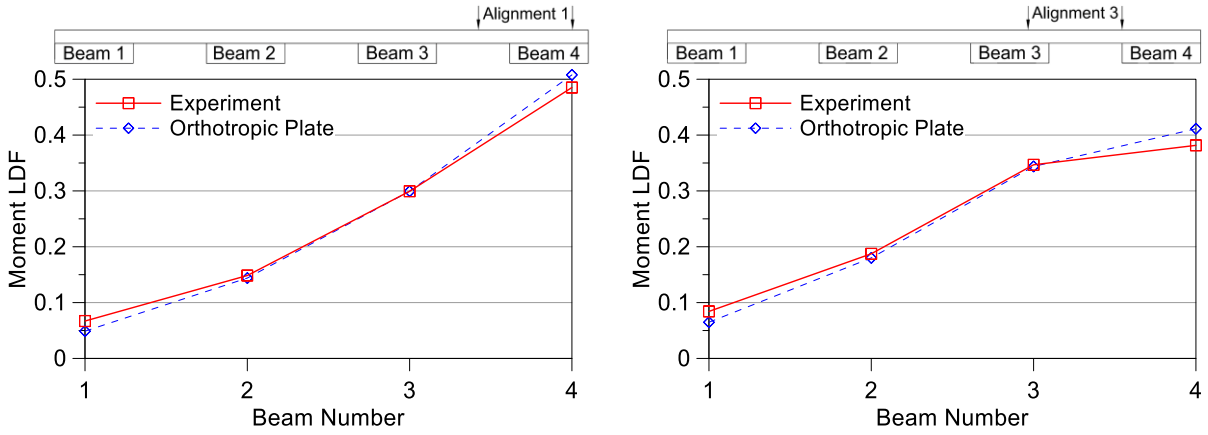

(a) Alignment 1 (b) Alignment 3

Figure 6.12. Comparison of Moment LDFs with Orthotropic Plate Analysis.

The figures present and compare the variation of moment and shear results across the bridge to visualize lateral load sharing between girders. However, the maximum of these responses controls the design of an interior or exterior beam. Table 6.7 to Table 6.9 summarize the critical moment, north support shear, and south support shear results. Maximum values are also plotted as bar charts in Figure 6.16 to Figure 6.18 for visual inspection of the accuracy of the computational methods. It is evident that the grillage model provides slightly conservative estimates for critical moment results, whereas the FEM model estimates for moments are slightly unconservative. Shear predictions obtained from both FEM programs and grillage analysis are in close agreement (within 5 percent) with the test results for most of the maximum shear cases.

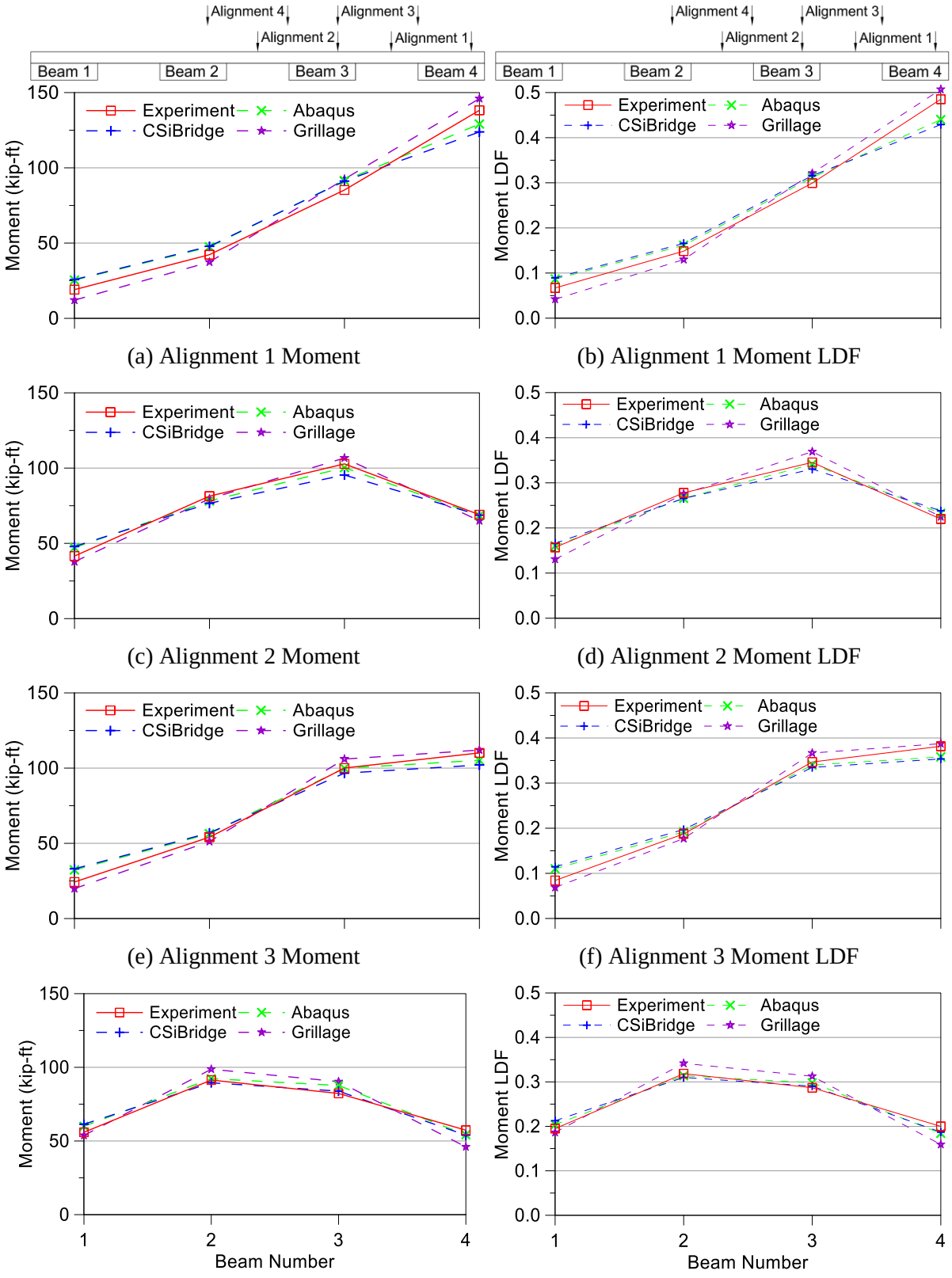

(a) Alignment 1 Moment

(b) Alignment 1 Moment LDF

(c) Alignment 2 Moment

(d) Alignment 2 Moment LDF

(e) Alignment 3 Moment

(f) Alignment 3 Moment LDF

(g) Alignment 4 Moment

(h) Alignment 4 Moment LDF

Figure 6.13. Comparison of Moment and Moment LDFs.

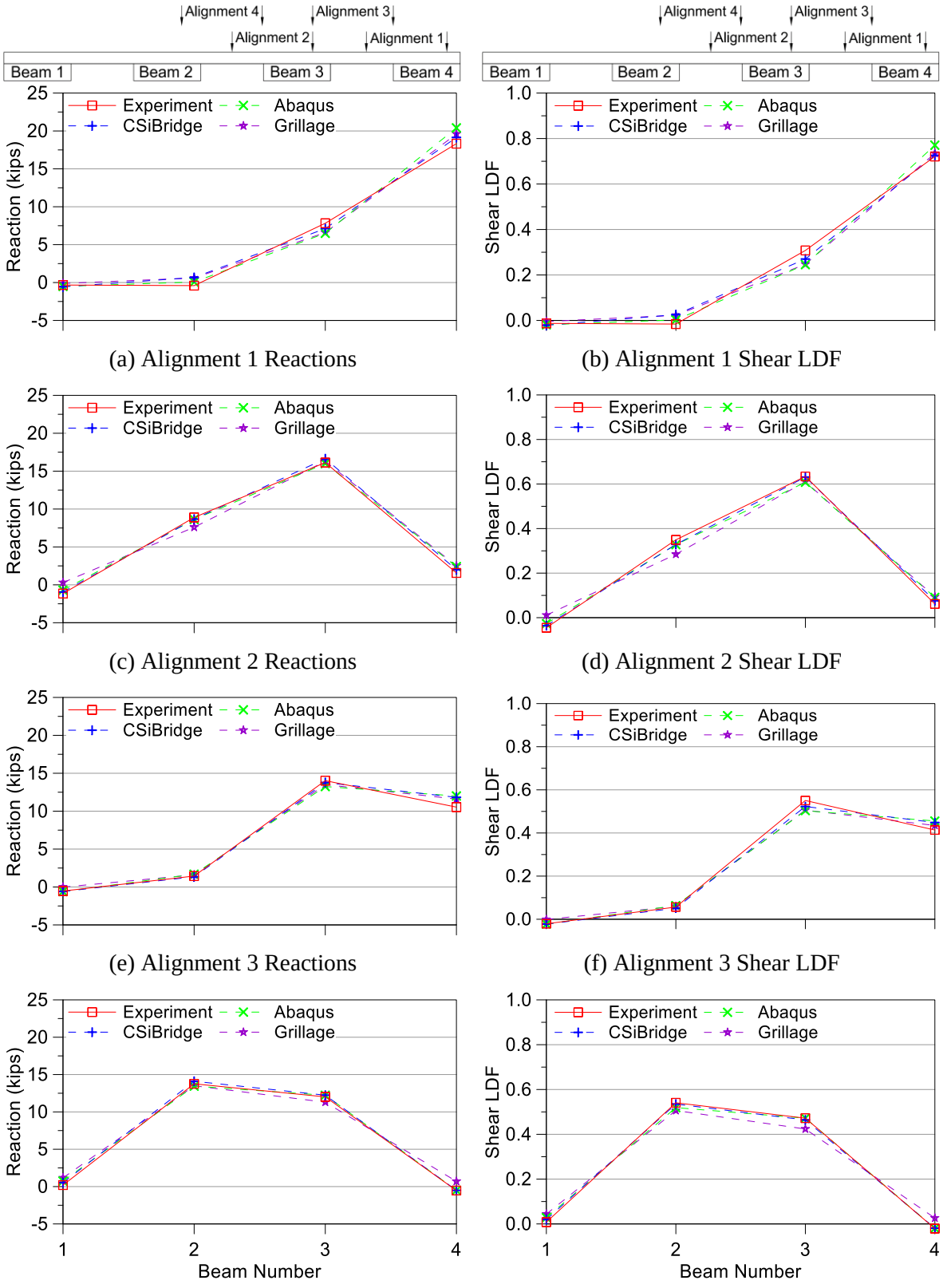

(a) Alignment 1 Reactions

(b) Alignment 1 Shear LDF

(c) Alignment 2 Reactions

(d) Alignment 2 Shear LDF

(e) Alignment 3 Reactions

(f) Alignment 3 Shear LDF

(g) Alignment 4 Reactions

(h) Alignment 4 Shear LDF

Figure 6.14. Comparison of North Support Reactions and Shear LDFs.

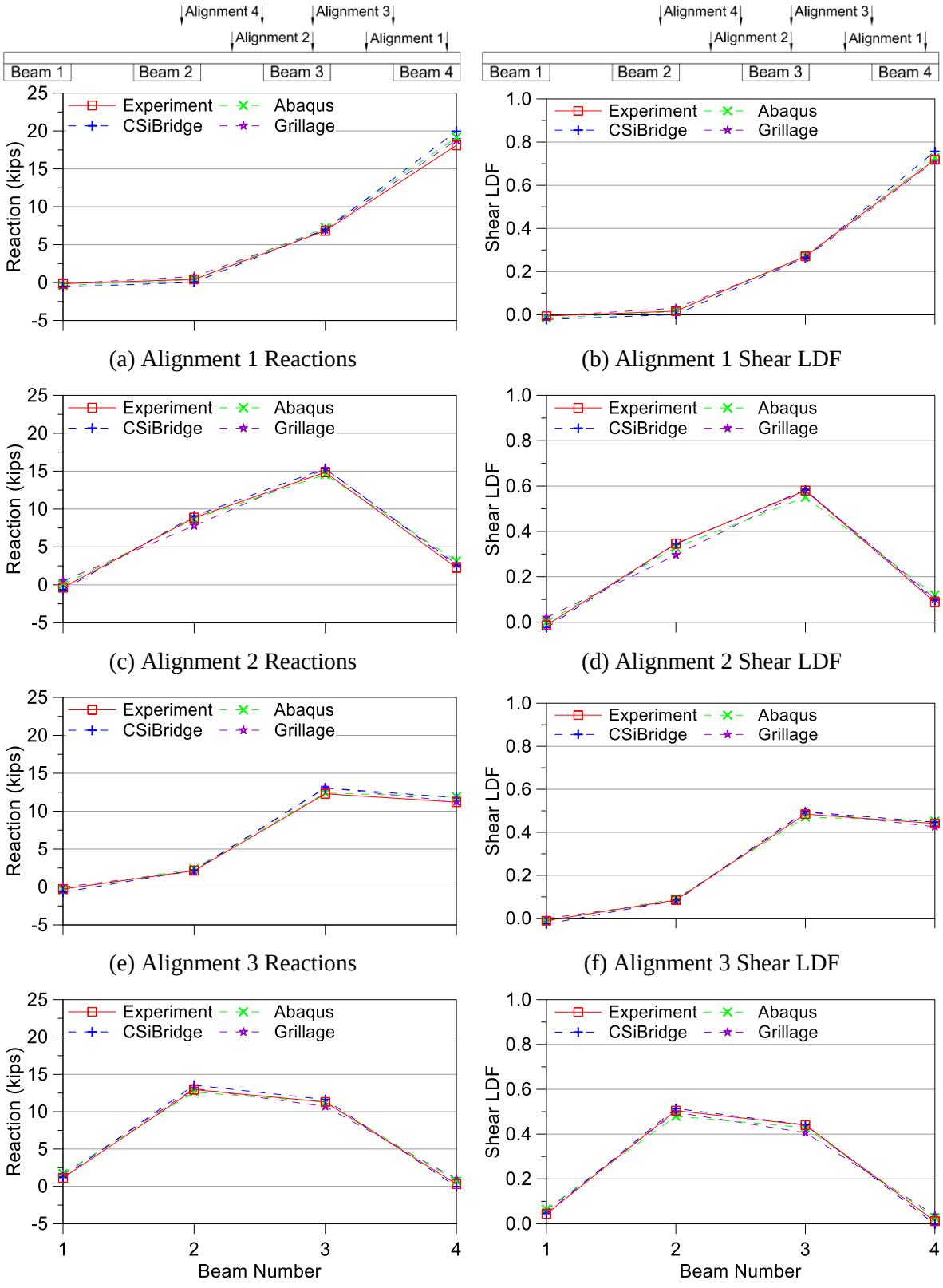

(a) Alignment 1 Reactions

(b) Alignment 1 Shear LDF

(c) Alignment 2 Reactions

(d) Alignment 2 Shear LDF

(e) Alignment 3 Reactions

(f) Alignment 3 Shear LDF

(g) Alignment 4 Reactions

(h) Alignment 4 Shear LDF

Figure 6.15. Comparison of South Support Reactions and Shear LDFs.

Table 6.7. Maximum Moment Results.

Description	Moment (kip-ft)		Moment LDF	
	Interior	Exterior	Interior	Exterior
Test	102.8	138.2	0.35	0.49
Abaqus	100.3	129.1	0.34	0.44
CSiBridge	95.4	123.9	0.33	0.43
Grillage	106.7	146	0.37	0.51

Table 6.8. Maximum North Support Shear Results.

Description	North Support Shear (kips)		Shear LDF	
	Interior	Exterior	Interior	Exterior
Test	16.1	18.3	0.63	0.72
Abaqus	16.0	20.4	0.61	0.77
CSiBridge	16.6	19.1	0.63	0.73
Grillage	16.3	19.6	0.61	0.73

Table 6.9. Maximum South Support Shear Results.

Description	South Support Shear (kips)		Shear LDF	
	Interior	Exterior	Interior	Exterior
Test	14.9	18.1	0.58	0.72
Abaqus	14.6	19.1	0.56	0.73
CSiBridge	15.4	19.9	0.58	0.76
Grillage	15.3	18.8	0.58	0.71

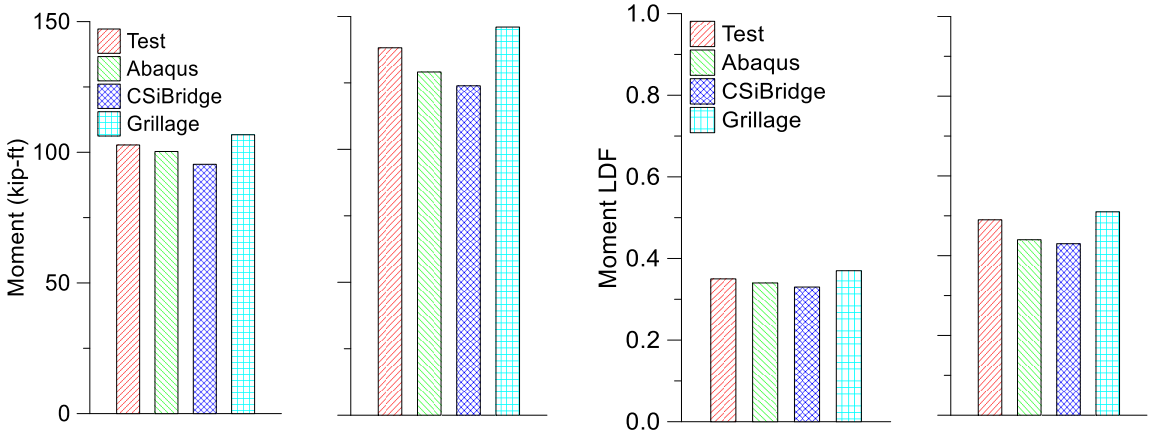

(a)Interior Moment (b) Exterior Moment (c) Interior Moment LDF (d) Ext. Moment LDF

Figure 6.16. Comparison of Critical Moment Results.

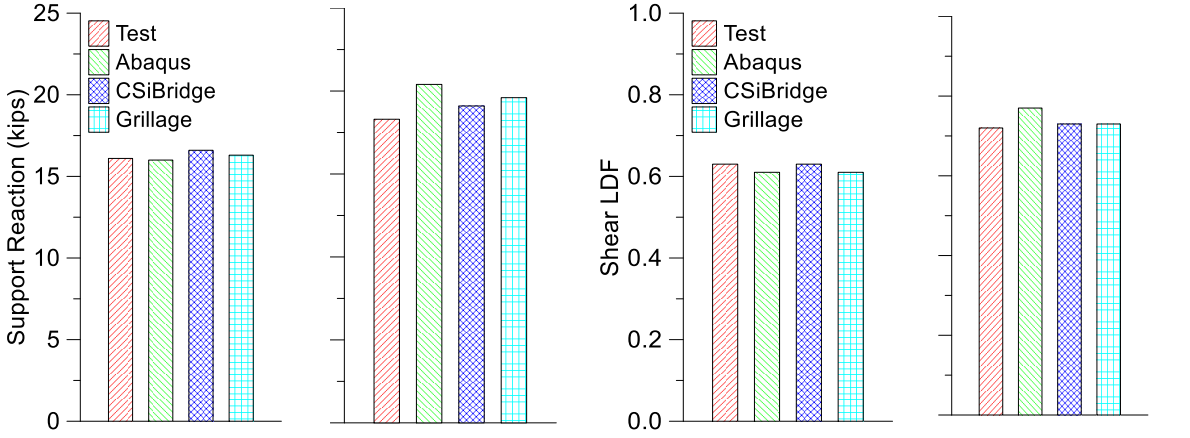

(a) Interior Shear (b) Exterior Shear (c) Interior Shear LDFs (d) Exterior Shear LDFs

Figure 6.17. Comparison of Critical North Support Shear Actions.

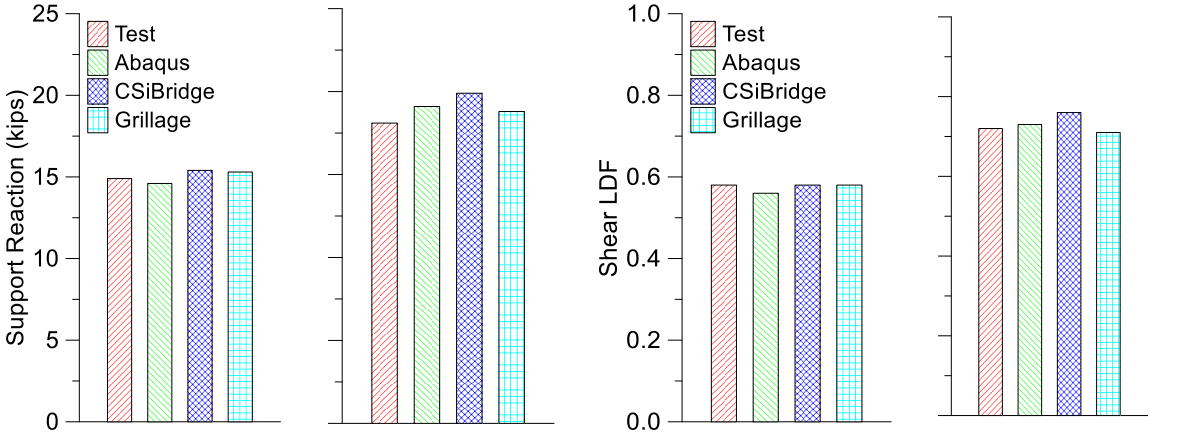

(a) Interior Shear (b) Exterior Shear (c) Interior Shear LDFs (d) Exterior Shear LDFs

Figure 6.18. Comparison of Critical South Support Shear Actions.

6.6 SUMMARY AND FINDINGS

Various solutions were explored to determine LDFs that are used in bridge deck analysis The following conclusions drawn from the comparison of test results based on field measurements at the Riverside Bridge and the computational results.

1. Orthotropic plate analysis cannot estimate deflections particularly accurately due to the assumptions and approximations considered. Maximum deflection values vary 10 to 30 percent from the test results. However the moment LDF values are in a good agreement with experimentally inferred values.
2. Deflection predictions obtained from both FEM analysis programs (Abaqus and CSiBridge) show moderately good agreement with the experimental results. At the location of maximum deflection the difference was 0.01 in. with an associated 0.005 in. accuracy in experimental observations.
3. Estimated natural frequencies from both FEM programs were very close to the experimentally observed results. Mode shapes obtained from the FEM models also compare well with the mode shapes inferred from experimental observations.
4. Moment and shear LDFs calculated from the moment and shear predictions of both FEM programs were in good agreement with the test results. When carefully developed, the grillage model also predicts the moment and shear response accurately.

Although all analysis methods investigated may be considered sufficiently accurate and could be used for further development of LDF formulas, one should use the best available analysis tools. Because the Abaqus and CSiBridge predictions were both quite close to the test results, the CSiBridge software was used for developing additional models (discussed in future chapters) due to the ease of developing and analyzing bridge models with this program. The user-friendly interface of the CSiBridge program minimizes the potential for pre- and post-processing errors.

7. LOAD DISTRIBUTION FACTORS FOR SPREAD SLAB BEAM BRIDGES*

7.1 INTRODUCTION

The complexity of calculating the design moment and shear actions for an individual bridge girder member under imposed live plus impact loads necessitates simplified analysis methods. The design moment and shear demands for an individual beam or bridge girder depend on various parameters such as the position of the load, the girder spacing, the span length, and the relative deck-to-girder stiffness. In order to simplify the design process, a longstanding methodology has evolved whereby a multiple girder bridge deck can be reduced to permit the structure to be a one-girder line or beam element. Thus, load distribution factors are applied to convert a single lane load into the actions necessary to design one girder and its associated deck slab.

The objective of the study described in this section is the empirical derivation of live load distribution factors (LDFs) for the interior and exterior girders of spread slab beam bridges for span lengths within the range of 31 to 51 ft. The proposed load distribution factor expressions were derived by analyzing 31 bridge models using the finite element method (FEM), with each bridge model having different geometries. Proposed equations were obtained using a methodology similar to that adopted for developing the LDF equations found in the AASHTO LRFD Bridge Design Specifications (AASHTO 2012). The parameters for the equations were chosen based on similar formulas used for spread box beam bridges in the current AASHTO LRFD Specifications (2012). FEM analyses were used to determine the effect of the chosen parameters, which are span length, beam spacing and beam depth.

7.2 FORMULATION OF LOAD DISTRIBUTION FACTORS

Equations for LDFs were developed following the same methodology as Zokaie et al. (1991) and Zokaie (2000) for the AASHTO LRFD Specifications (2012). The effects of each parameter on LDFs were assumed to be independent. It was also assumed that the effect of

* Previously published work is available to the public through National Technical Information Service. Mary Beth D. Hueste, John B. Mander, Tevfik Terzioglu, Dongqi Jiang, and Joel Petersen-Gauthier (2014). "Spread Prestressed Concrete Slab Beam Bridges: Technical Report." Report No. FHWA/TX-14/0-6722-1, Texas A&M Transportation Institute, College Station, Texas, USA.

each parameter could be modeled using a power function of the general form ax^b, where x is the parameter under consideration, and a and b are the coefficients that were determined by nonlinear least squares regression. After defining the separate effect of each parameter with a power curve, the combined effect was modeled by multiplying those power terms with a combined coefficient as follows:

$$g = a\left(L^{b1}\right)\left(S^{b2}\right)\left(d^{b3}\right)(\ldots) \tag{7.1}$$

where the coefficient a was determined once all the parameters (b_1, b_2, b_3) were established. The powers were calculated by studying the effect of each parameter with respect to the LDF when only that parameter was changed while keeping the other parameters constant.

The same procedure was applied to all key parameters in the equation. Then the common coefficient of the final equation (a) was calculated using the expression provided below.

$$a_i = \frac{g_i}{\left(L_i\right)^{b_1}\left(S_i\right)^{b_2}\left(d_i\right)^{b_3}} \tag{7.2}$$

Naturally, slightly different values of a_i will result for each specific (i^{th}) bridge design. Therefore, an average or a design value was adopted to form a universally applicable solution for the design space.

7.2.1 Methods for Developing LDFs

The following approach was used for developing LDFs:

1. A number of bridges were designed and modeled using the FEM.
2. Trucks were placed in numerous locations to obtain the most adverse combination for midspan moment and beam shear for interior and exterior slab beams. Cases for one and multiple lanes loaded were considered. Thus, for each bridge a matrix of LDFs was calculated and tabulated by group types.
3. For each bridge within a specific grouping, all parameters (except one) were held constant (the variable), and a log-log graph of LDF versus the key variable was plotted. A nonlinear least square best fit was found for the form $y = ax^b$, where in particular the parameter b, the slope of the log-log plot, was obtained, plotted, and recorded.

4. Once all results for the power indices were found, the value of a_i for the i_{th} bridge was determined such that:

$$a_i = \frac{g_i}{(L)^{b_1}(S)^{b_2}(d)^{b_3}} \tag{7.3}$$

5. Collectively, when all values of a_i were plotted they formed a lognormal distribution for which the median of all a_i values (that is the geometric mean, $\tilde{a}$ or 50th percentile) gives the overall "best fit" for all bridges, and the lognormal standard deviation β_D describes the dispersion in the load demand actions.
6. Formulas were grouped by type, such as moments, shears, one-lane cases, and multiple-lane cases.
7. A reexamination of the resulting empirical formulas from Step 6 was made and then rationally adjusted to provide revised versions that are more compatible with companion formulas in the AASHTO LRFD Specifications (2012). The coefficients were adjusted so that there is approximately a non-exceedance probability of 5 percent (lognormal minus 1.65 lognormal standard deviations), and the final empirical design LDF formulas are mostly conservative (i.e., 95 percent chance of being conservative).

7.3 METHODS FOR THE MOMENT AND SHEAR DESIGN ACTIONS FOR A MATRIX OF SLAB BEAM BRIDGES

Live load distribution factors were evaluated for selected bridge geometries, using the results computed with FEM analysis. The parametric study was conducted to define the boundaries of the problem. The findings of the parametric study are summarized in Section 3. Alternative bridge geometries for derivation of LDF formulas were defined utilizing the results of the parametric study. Moment and shear LDFs for each bridge superstructure alternative were obtained from the FEM results. These LDFs were then compared with the distribution factors obtained from the proposed equations and the AASHTO LRFD Specifications (2012) spread box beam formulas.

7.3.1 Alternative Bridge Superstructure Geometries Considered

It is important to note the applicable range for each parameter under consideration. These are:

- Bridge Span: 31 ft ≤ L ≤ 51 ft
- Beam Spacing: 6.5 ft ≤ S ≤ 11 ft
- Beam Depth: 12 in. ≤ d ≤ 21 in.

Spread beam bridges are one of the new TxDOT bridge superstructure types. TxDOT specifies a standard deck slab thickness of 8 in. for these bridges. Because slab thickness was considered constant for all bridges, the relative slab-to-beam stiffness was not directly considered, and slab beam thickness was considered as a parameter instead. One of the assumptions for the preliminary designs was to initially use spread box beam formulas for the 31 prototype designs. Therefore, it was presumed that the equations will include the same parameters as the spread box beam formulas, which are span length, beam spacing, and beam depth. The parameter selection is consistent with the findings of Zokaie et al. (1991) documented in the NCHRP 12-26 report. According to the sensitivity study Zokaie et al. conducted, the most sensitive parameter for LDF calculation is the girder spacing, S. The second most sensitive parameter is span length, L. The longitudinal stiffness parameter affects the LDF slightly. Figure 7.1 shows a generalized bridge with the key parameters.

Table 7.1 presents the design attributes chosen for the overall general design space. The prototype bridges are grouped by their principal parameters (L, S, and d) for the first 25 bridges. Thereafter, Bridges 26 through 31 are a general assortment of structures not included as part of the parameter identification but rather for general use in validating the identified parameters.

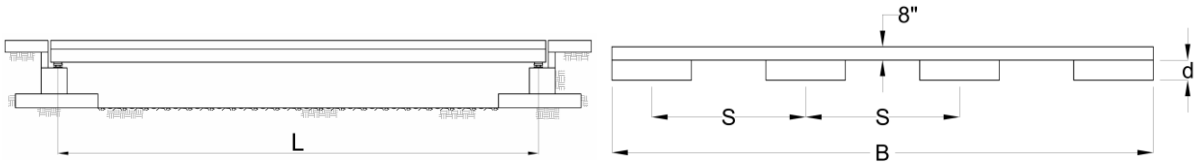

(a) Elevation View (b) Section View

Figure 7.1. Key Geometric Parameters for Spread Slab Beam Bridges.

Table 7.1. Alternative Bridge Geometries for LDF Study.

No.	Number of Beams	Type of Beam	Bridge Width (ft)	Clear Beam Spacing (ft)	Beam Spacing (ft)	Span Length
L = Span Length Effect						
1	4	5SB15	34	4.67	9.67	45′-7″
2	4	5SB15	34	4.67	9.67	44′-7″
3	4	5SB15	34	4.67	9.67	41′-7″
4	4	5SB15	34	4.67	9.67	39′-7″
5	4	5SB15	34	4.67	9.67	37′-7″
6	4	5SB15	34	4.67	9.67	33′-7″
7	4	5SB15	34	4.67	9.67	29′-7″
S = Beam Spacing Effect						
8	4	5SB15	26	2.00	7.00	44′-7″
9	4	5SB15	28	2.67	7.67	44′-7″
10	4	5SB15	30	3.33	8.33	44′-7″
11	4	5SB15	32	4.00	9.00	44′-7″
12	4	5SB15	34	4.67	9.67	44′-7″
13	4	5SB15	36	5.33	10.33	44′-7″
14	4	5SB15	38	6.00	11.00	44′-7″
15	5	5SB15	40	3.75	8.75	44′-7″
16	5	5SB15	42	4.25	9.25	44′-7″
17	5	5SB15	44	4.75	9.75	44′-7″
18	5	5SB15	46	5.25	10.25	44′-7″
d = Beam Depth Effect						
19	4	5SB12.0	34	4.67	9.67	39′-7″
20	4	5SB13.5	34	4.67	9.67	39′-7″
21	4	5SB15.0	34	4.67	9.67	39′-7″
22	4	5SB16.5	34	4.67	9.67	39′-7″
23	4	5SB18.0	34	4.67	9.67	39′-7″
24	4	5SB19.5	34	4.67	9.67	39′-7″
25	4	5SB21.0	34	4.67	9.67	39′-7″
General—Verification and Evaluation (*L*, *S*, and *d*)						
26	4	4SB12	26	3.33	7.33	39′-7″
27	5	4SB12	30	2.50	6.50	40′-7″
28	4	4SB12	34	6.00	10.00	35′-7″
29	5	5SB15	34	2.25	7.25	49′-7″
30	5	4SB12	40	5.00	9.00	36′-7″
31	6	5SB15	40	2.00	7.00	49′-7″

All 31 bridges were modeled using a detailed FEM analysis. LDFs were calculated from the moment and shear forces obtained from these 31 models. The FEM analysis was performed using CSiBridge (Computers and Structures 2015) software. Each of the 31 single-span bridge superstructures was modeled using eight-node isotropic solid elements having three degrees of freedom at each node. A maximum of 12 in. mesh size was utilized throughout based on a mesh sensitivity study (see Section 6).

Table 7.2 lists the parameters adopted for the 31 prototype designs. Values of the design parameters were chosen in accordance with TxDOT standard design and construction practice.

Table 7.2. Bridge Parameters and Material Properties for LDF Study.

Parameter	Description/Value
Center-to-Center of Bearing Pad Span Length, L	29 ft 7 in. $\leq$ L $\leq$ 49 ft 7 in.
Total Bridge Width, B	26 ft $\leq$ B $\leq$ 46 ft
Center-to-Center Beam Spacing, S	6.5 ft $\leq$ S $\leq$ 11 ft
Slab Beam Width	4 ft and 5 ft
Slab Beam Thickness	12 in. $\leq$ d $\leq$ 21 in.
Deck Thickness, t_s	8 in.
Concrete Compressive Strength for Beams	f_c' = 8.5 ksi
Concrete Compressive Strength for Deck	f_c' = 4 ksi
Modulus of Elasticity of Slab Beam Concrete	E_b = 4933 ksi
Modulus of Elasticity of Deck Concrete	E_d = 3834 ksi
FEM Element Size	12 in.
Boundary Conditions	Only Vertical Degree of Freedom Fixed
Haunch Thickness, t_h	Neglected

7.3.2 Lane Loading Analysis

Figure 7.2 presents the various spatial alignments adopted for the bridge deck analysis. These alignments were arranged in such a fashion that the most adverse combination of moments and shears would be captured through rigorous analysis.

Many load cases were investigated using the AASHTO LRFD Specifications (2012) design truck loading and uniform lane loading. The CSiBridge software simulates vehicles moving along the bridge and gives the maximum moment or shear forces for each girder utilizing the influence line method. Thus, there was no need to define critical positions in the longitudinal direction.

The transverse positions were selected based on the allowable travel distances in the AASHTO LRFD Specifications (2012), field observations, and engineering judgment. Transverse positions of the lanes were defined by dividing the bridge into as many 12 ft wide lanes as possible. Vehicles and uniform lane loading were then allowed to move within their own lane for multiple-lane-loaded cases. For the one-lane-loaded case, the vehicle was permitted to pass between lanes. Therefore, a transverse loading position crossing the design lane could be defined for the single-lane-loaded case to achieve the most critical loading for an interior girder. In cases where vehicles moved within their own lanes, they were moved in the transverse direction in 2 ft increments.

Bridges that have a roadway width greater than or equal to 36 ft were considered to be three-lane bridges. A similar procedure was followed when determining the critical transverse positions for truck loading. Because only half of the bridge was analyzed due to symmetry, the third lane load was placed as closely as possible to the interior edge of the design lane. The AASHTO LRFD Specifications (2012) design lane load (0.64 kip/ft) was applied over a 6 ft width in the transverse direction for each loaded design lane.

Table 7.3 lists the computational results of the LDF values for Bridges 1 through 25. The most critical moment and shear LDFs were obtained for the multiple-lane-loaded interior beam case, and these cases are highlighted in Table 7.3.

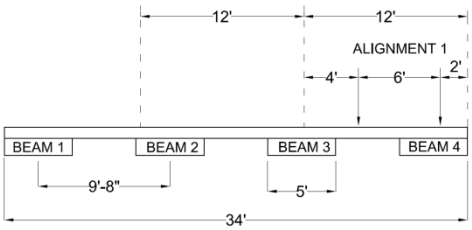

(a) One Lane Loaded—Exterior Beam

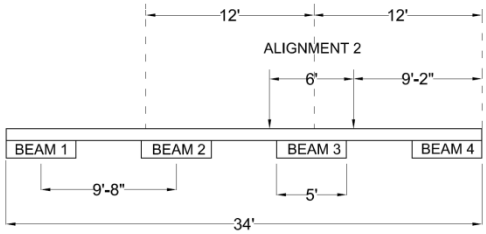

(b) One Lane Loaded—Interior Beam

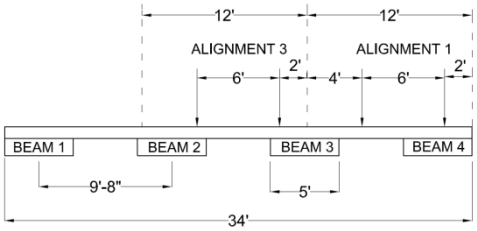

(c) Two Lanes Loaded—Exterior Beam

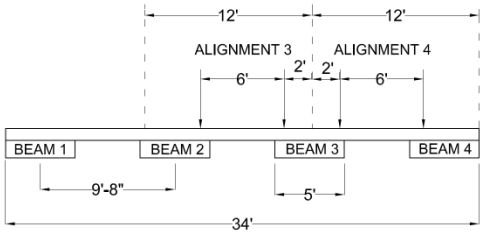

(d) Two Lanes Loaded—Interior Beam

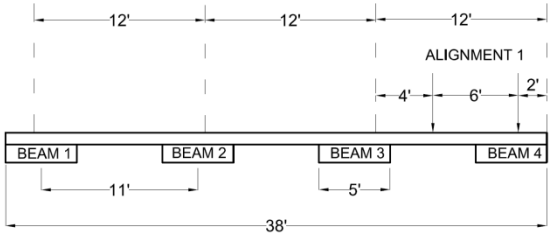

(e) One Lane Loaded—Exterior Beam

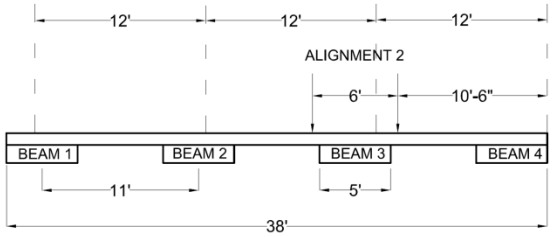

(f) One Lane Loaded—Interior Beam

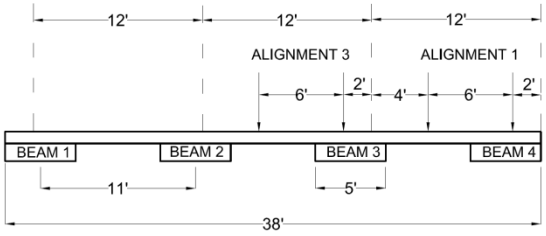

(g) Two Lanes Loaded—Exterior Beam

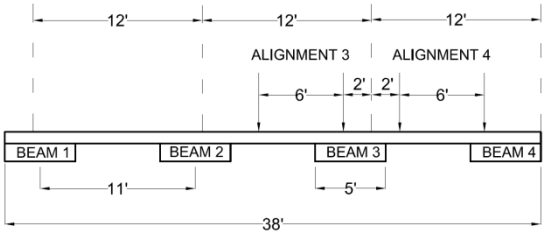

(h) Two Lanes Loaded—Interior Beam

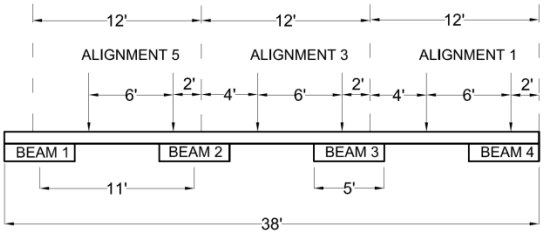

(i) Three Lanes Loaded—Exterior Beam

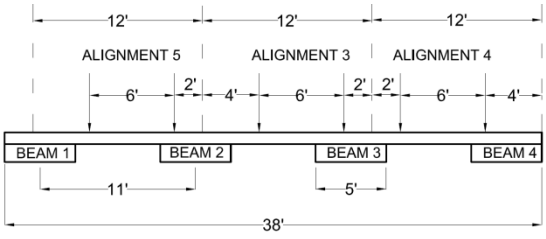

(j) Three Lanes Loaded—Interior Beam

Figure 7.2. Transverse Positions for Two-Lane and Three-Lane Bridges.

Table 7.3. LDFs for Evaluating the Key Parameters.

						One Lane Loaded				Multiple Lanes Loaded			
						Interior Beam		Exterior Beam		Interior Beam		Exterior Beam	
L = Span Length													
No.	Width	No. of Beams	Beam Type	S (ft)	L	g_M	g_V	g_M	g_V	g_M	g_V	g_M	g_V
1	34′ 0″	4	5SB15 d=15″	9′ 8″	29′-7″	0.55	0.85	0.63	0.71	0.76	0.96	0.66	0.63
2					33′-7″	0.51	0.81	0.59	0.69	0.72	0.93	0.65	0.63
3					37′-7″	0.48	0.79	0.56	0.70	0.69	0.91	0.64	0.64
4					39′-7″	0.47	0.77	0.54	0.70	0.68	0.90	0.63	0.64
5					41′-7″	0.45	0.76	0.52	0.70	0.66	0.89	0.62	0.64
6					44′-7″	0.43	0.74	0.50	0.69	0.64	0.87	0.61	0.64
7					45′-7″	0.42	0.73	0.49	0.70	0.64	0.87	0.60	0.65
S = Beam Spacing													
No.	L	No. of Beams	Beam Type	Bridge Width (ft)	S (ft)	g_M	g_V	g_M	g_V	g_M	g_V	g_M	g_V
8	44′ 7″	4	5SB15 d=15	26	7.00	0.36	0.57	0.39	0.56	0.53	0.64	0.51	0.55
9				28	7.67	0.38	0.64	0.41	0.60	0.56	0.67	0.53	0.57
10				30	8.33	0.40	0.68	0.44	0.63	0.59	0.77	0.55	0.59
11				32	9.00	0.41	0.71	0.46	0.66	0.62	0.83	0.58	0.61
12				34	9.67	0.43	0.74	0.50	0.69	0.64	0.87	0.61	0.64
13				36	10.33	0.45	0.76	0.53	0.73	0.67	0.92	0.64	0.68
14				38	11.00	0.47	0.78	0.56	0.77	0.74	0.96	0.67	0.71
15		5		40	8.75	0.39	0.70	0.45	0.65	0.59	0.80	0.55	0.60
16				42	9.25	0.40	0.72	0.47	0.67	0.62	0.84	0.58	0.62
17				44	9.75	0.42	0.73	0.50	0.70	0.64	0.87	0.60	0.64
18				46	10.25	0.43	0.75	0.52	0.73	0.66	0.90	0.63	0.67
d = Beam Depth													
No.	L	Width (ft)	Beam Spacing (ft)	No. Beams	Type of Beam	d (in.)	g_M	g_V	g_M	g_V	g_M	g_V	g_M	g_V
19	39′ 7″	34″ 0″	9′ 8″	4	5SB	12.0	0.45	0.74	0.52	0.69	0.66	0.87	0.62	0.64
20						13.5	0.46	0.75	0.53	0.69	0.67	0.88	0.63	0.64
21						15.0	0.47	0.77	0.54	0.70	0.68	0.90	0.63	0.64
22						16.5	0.48	0.79	0.55	0.70	0.69	0.91	0.63	0.63
23						18.0	0.49	0.80	0.57	0.71	0.70	0.93	0.64	0.63
24						19.5	0.50	0.81	0.58	0.71	0.71	0.94	0.64	0.63
25						21.0	0.51	0.82	0.59	0.71	0.72	0.95	0.65	0.63

7.4 EMPIRICAL MODELING OF THE LDF RESULTS

Table 7.4 presents the results of the powers (b_1, b_2, b_3) fitted in accordance with the least square analysis in log-log space. The results were also plotted in log-log graphs, provided in Figure 7.3 through Figure 7.5.

The effect of each chosen key parameter (span length, beam spacing, and beam depth), on live load distribution factors was investigated. Load distribution factors for all eight formulas, for each girder, and for each of the 31 bridge geometries were obtained from the FEM models and used for developing the empirical LDFs for design applications. The maximum moment and shear values for interior and exterior girders were obtained from the FEM analysis. These moment and shear forces for one-, two-, and three-lane-loaded cases were multiplied with the AASHTO LRFD Specifications (2012) multiple presence factors of 1.2, 1.0, and 0.85, respectively. Then the LDFs for all eight formulas were calculated by dividing the maximum moment (or shear value) with the moment (or shear value) of an isolated simply supported beam having the same span length.

Table 7.4. Powers of the Fitted Curves.

			Formula	Span, L		Spacing, S		Beam Depth, *d*	
				b_1	R_2	b_2	R_2	b_3	R_2
Moment LDF	Interior Beam	One Lane Loaded	1	-0.6125	0.996	0.5208	0.923	0.2166	0.992
		Multiple Lanes Loaded	2	-0.4002	0.994	0.6537	0.946	0.1393	0.993
	Exterior Beam	One Lane Loaded	3	-0.6108	0.985	0.7976	0.984	0.2011	0.997
		Multiple Lanes Loaded	4	-0.2211	0.974	0.5886	0.940	0.0744	0.999
Shear LDF	Interior Beam	One Lane Loaded	5	-0.3296	0.999	0.6626	0.954	0.1967	0.999
		Multiple Lanes Loaded	6	-0.2337	0.999	0.9337	0.977	0.1616	1.000
	Exterior Beam	One Lane Loaded	7	-0.0329	0.206	0.6862	0.993	0.0663	0.999
		Multiple Lanes Loaded	8	0.0662	0.890	0.5758	0.96	0.0324	0.995

7.4.1 Sensitivity of LDF to Span Length *L*

Figure 7.3 presents the effect of span length L on LDFs. One of the most important parameters influencing the LDFs is the span length of the bridge. In order to evaluate the variation of the LDF with changing span length, all other parameters were kept constant and the span length was changed between 29 ft 7 in. to 45 ft 7 in. The complete list of the seven bridge superstructures is provided in Table 7.1 and labeled with bridge numbers 1 to 7. The calculated LDF values for these seven bridge decks are listed in Table 7.3, where g_M is the moment LDF and g_V is the shear LDF. The LDF values listed in Table 7.3 were also plotted on a log-log graph to provide visual examination of the effect of the span length on the LDFs.

7.4.2 Sensitivity of LDF to Beam Spacing *S*

Figure 7.4 depicts in log-log space the sensitivity of beam spacing S on LDFs. LDFs are most sensitive to the changes in beam spacing. A total of 11 superstructure geometries were modeled to evaluate the variation of LDFs with beam spacing. The investigation of the effect of beam spacing on LDFs revealed that the relationship between beam spacing and LDFs was more prominent for all the LDF cases except the one-lane-loaded moment in interior beams. A complete list of maximum LDF values is summarized in Table 7.3.

7.4.3 Sensitivity of LDF to Beam Depth *d*

Figure 7.5 shows how variation in beam depth d affects the LDFs. Although there are only two different standard slab beam depths, 12 in. and 15 in., seven different beam depths were analyzed to develop more data points to fit a power curve and gain a better understanding of the effect of beam depth. A total of seven hypothetical beam depths between 12 in. to 21 in. were introduced, and seven bridge superstructures were modeled for investigating the influence of beam depth on LDFs. As discussed earlier, beam depth somewhat affects the LDF but is not as prominent as beam spacing and span length. An investigation of the graphs for the sensitivity of beam depth shows that the LDF values for shear in an exterior beam are not sensitive to the beam depth. The slopes of these curves are almost zero. All eight LDF values for each bridge analyzed are summarized in Table 7.3.

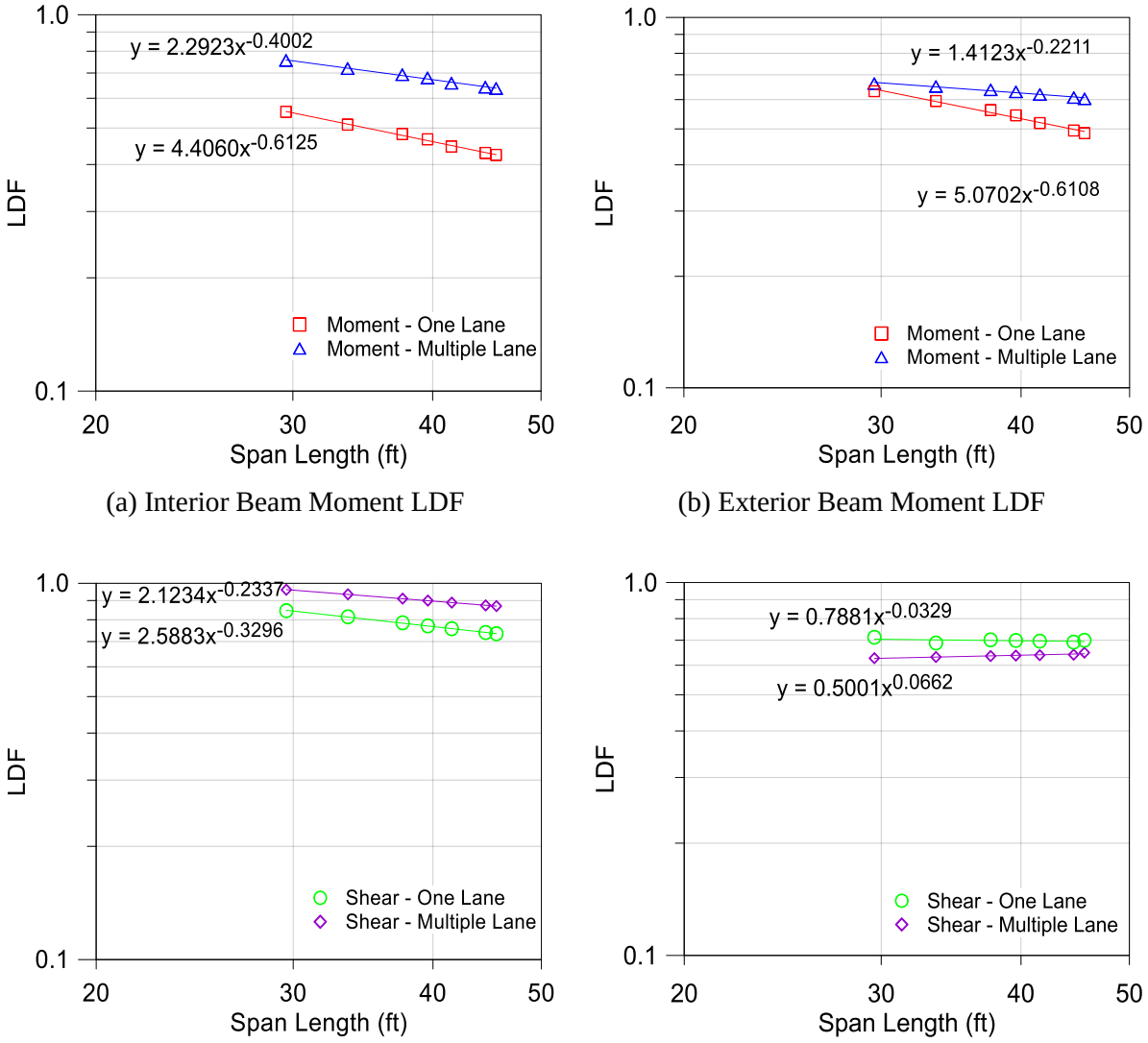

(a) Interior Beam Moment LDF

(b) Exterior Beam Moment LDF

(c) Interior Beam Shear LDF

(d) Exterior Beam Shear LDF

Figure 7.3. Effect of Span Length on Load Distribution Factor.

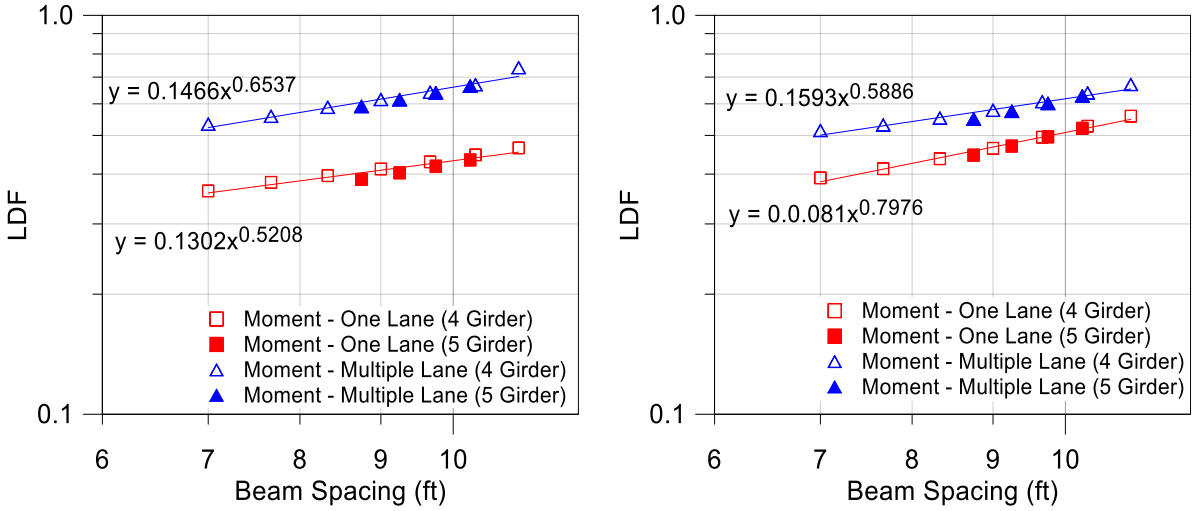

(a) Interior Beam Moment LDF

(b) Exterior Beam Moment LDF

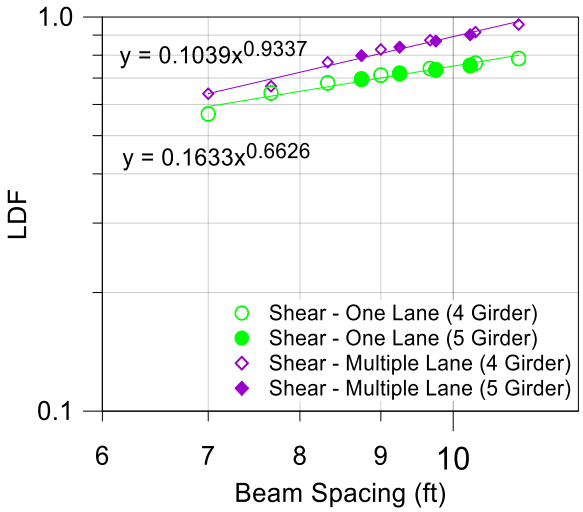

(c) Interior Beam Shear LDF

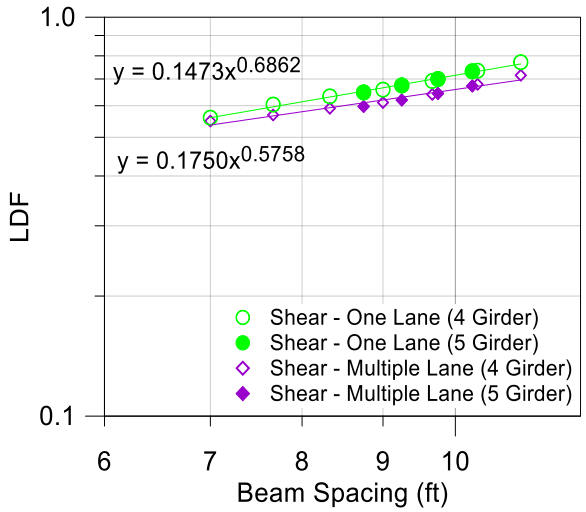

(d) Exterior Beam Shear LDF

Figure 7.4. Effect of Beam Spacing on Load Distribution Factor.

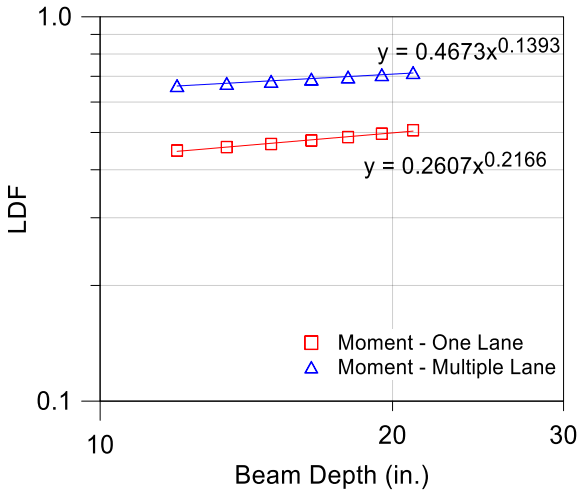

(a) Interior Beam Moment LDF

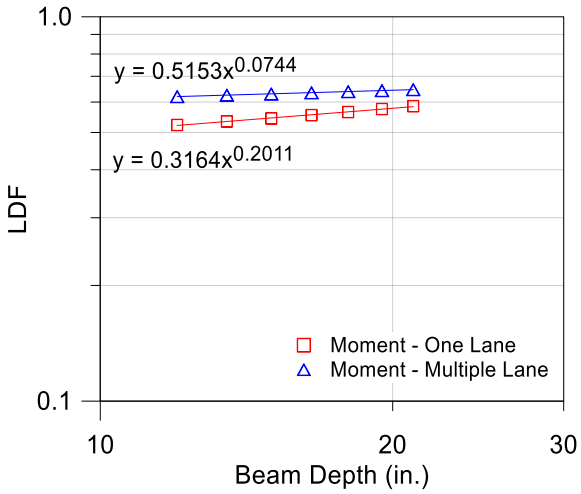

(b) Exterior Beam Moment LDF

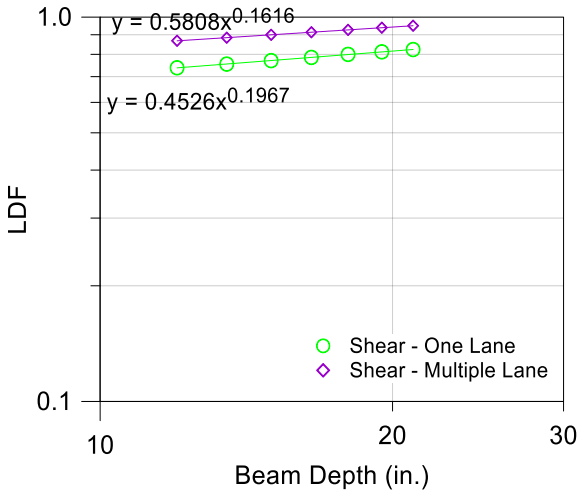

(c) Interior Beam Shear LDF

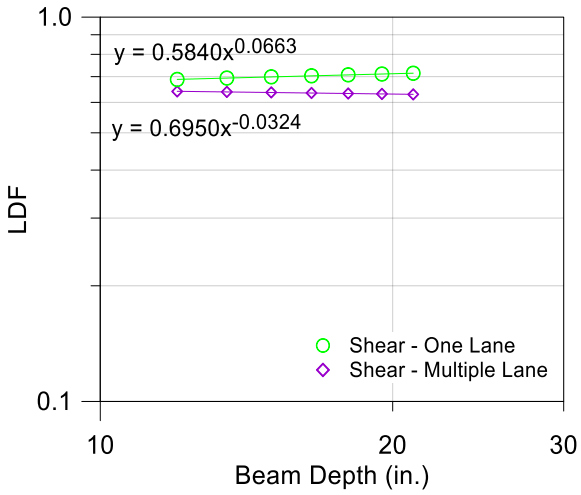

(d) Exterior Beam Shear LDF

Figure 7.5. Effect of Beam Depth on Load Distribution Factor.

7.5 DERIVATION OF LDF FORMULAS

Table 7.5 lists all of the coefficients calculated for the 31 bridges and eight LDF formulas. The columns corresponding to critical moment and shear LDFs are shaded. The previous section documents how the powers of the parameters were determined by fitting a power curve through for each one of the eight LDF cases. A total of 25 bridges were modeled using FEM in order to find the powers of the key parameters. Because some assumptions were made and some parameters were neglected, it was crucial to verify the accuracy of the assumptions and the proposed equations. For that purpose, six more bridge superstructures were defined; four of them utilize 4SB12 slab beams, and the other two have the longest span length achievable using a spread slab beam configuration. The geometries of these additional bridge superstructures are listed in Table 7.1. The LDFs obtained from an accurate FEM analysis for these six bridges were also included in the calculation of coefficients for new equations.

Live load distribution factors for each one of the 31 bridge superstructures for all eight LDF cases, including moment in interior and exterior beams and shear in interior and exterior beams, were obtained and are listed in Appendix C. These FEM values were also compared with those obtained from the AASHTO LRFD Specifications (2012) spread box beam formulas, theoretical LDFs, and new proposed LDF equation values. The equations for these LDF values are provided in Table 7.6.

The calculation of the *a* coefficient for one of the LDF cases is explained herein. For a given bridge superstructure, the coefficient *a* can be calculated using Equation (7.3). This calculation results in 31 different a coefficients that are close but slightly different from each other. The median (average of $\ln a_i$ values) of these coefficients was used as an initial estimate, while the lognormal standard deviation, β, was used as a measure of scatter of the results. Note that when $\beta < 0.2$, the lognormal standard deviation was approximately equal to the coefficient of variation for a normal distribution. Note also that the two distributions have a similar shape and either could be used, but the lognormal distribution is the most appropriate due to their linear nature when plotted on log-log paper. The final *a* coefficient for that specific LDF case was calculated to minimize the lognormal standard deviation, β. This procedure was repeated for all eight LDF cases for calculating the coefficients of the theoretical equations.

Table 7.5. Coefficients of the Formulas for Each Bridge.

Domain	Case No.	L	S	d	a_i Values for Equations							
					1	2	3	4	5	6	7	8
Span Length	1	29.58	9.67	15.0	0.75	0.46	0.48	0.30	0.34	0.16	0.14	0.15
	2	33.58	9.67	15.0	0.75	0.46	0.48	0.30	0.34	0.16	0.14	0.15
	3	37.58	9.67	15.0	0.76	0.46	0.49	0.31	0.34	0.16	0.14	0.15
	4	39.58	9.67	15.0	0.76	0.46	0.49	0.31	0.34	0.16	0.14	0.15
	5	41.58	9.67	15.0	0.75	0.46	0.48	0.30	0.34	0.16	0.14	0.15
	6	44.58	9.67	15.0	0.75	0.46	0.48	0.30	0.34	0.16	0.14	0.15
	7	45.58	9.67	15.0	0.75	0.46	0.48	0.30	0.34	0.16	0.14	0.15
Beam Spacing	8	44.58	7.00	15.0	0.75	0.47	0.49	0.31	0.32	0.16	0.14	0.15
	9	44.58	7.67	15.0	0.75	0.46	0.48	0.30	0.34	0.16	0.14	0.15
	10	44.58	8.33	15.0	0.75	0.46	0.48	0.30	0.34	0.17	0.14	0.15
	11	44.58	9.00	15.0	0.75	0.46	0.47	0.30	0.34	0.17	0.14	0.15
	12	44.58	9.67	15.0	0.75	0.46	0.48	0.30	0.34	0.16	0.14	0.15
	13	44.58	10.33	15.0	0.75	0.46	0.48	0.31	0.33	0.16	0.14	0.15
	14	44.58	11.00	15.0	0.76	0.48	0.49	0.31	0.33	0.16	0.14	0.15
	15	44.58	8.75	15.0	0.71	0.45	0.47	0.29	0.34	0.17	0.14	0.15
	16	44.58	9.25	15.0	0.72	0.45	0.47	0.29	0.34	0.16	0.14	0.15
	17	44.58	9.75	15.0	0.73	0.45	0.48	0.30	0.33	0.16	0.14	0.15
	18	44.58	10.25	15.0	0.74	0.46	0.48	0.30	0.33	0.16	0.14	0.15
Beam Depth	19	39.58	9.67	12.0	0.76	0.46	0.49	0.31	0.34	0.16	0.14	0.15
	20	39.58	9.67	13.5	0.76	0.46	0.49	0.31	0.34	0.16	0.14	0.15
	21	39.58	9.67	15.0	0.76	0.46	0.49	0.31	0.34	0.16	0.14	0.15
	22	39.58	9.67	16.5	0.76	0.46	0.49	0.31	0.34	0.16	0.14	0.15
	23	39.58	9.67	18.0	0.76	0.46	0.49	0.31	0.34	0.16	0.14	0.15
	24	39.58	9.67	19.5	0.76	0.46	0.49	0.31	0.34	0.16	0.14	0.15
	25	39.58	9.67	21.0	0.77	0.46	0.49	0.31	0.34	0.16	0.14	0.15
Others	26	39.58	7.33	12.0	0.78	0.47	0.50	0.30	0.34	0.17	0.14	0.14
	27	40.58	6.50	12.0	0.71	0.43	0.48	0.28	0.32	0.15	0.14	0.14
	28	35.58	10.00	12.0	0.78	0.47	0.48	0.30	0.34	0.17	0.13	0.14
	29	49.58	7.25	15.0	0.71	0.43	0.47	0.28	0.33	0.15	0.14	0.15
	30	36.58	9.00	12.0	0.76	0.44	0.48	0.29	0.34	0.17	0.13	0.14
	31	49.58	7.00	15.0	0.67	0.43	0.46	0.28	0.31	0.14	0.14	0.14
Median (50th Percentile)					0.7469	0.4567	0.4814	0.3001	0.3354	0.1625	0.1385	0.1468
Lognormal standard deviation, β_D					0.0295	0.0271	0.0182	0.0279	0.0226	0.0342	0.0173	0.0222

Table 7.6. LDF Equations.

			No.	AASHTO Spread Box Beam Formulas	Least Square Best Fit Relations	Proposed LDF Design Equations
Moment LDF	Interior Beam	One Lane Loaded	1	$\left(\frac{S}{3.0}\right)^{0.35}\left(\frac{Sd}{12.0L^2}\right)^{0.25}$	$0.747S^{0.521}\frac{d^{0.217}}{L^{0.613}}$	$\left(\frac{S}{2.3}\right)^{0.35}\left(\frac{Sd}{12.0L^2}\right)^{0.25}$
		Multiple Lanes Loaded	2	$\left(\frac{S}{6.3}\right)^{0.6}\left(\frac{Sd}{12.0L^2}\right)^{0.125}$	$0.457S^{0.654}\frac{d^{0.139}}{L^{0.4}}$	$\left(\frac{S}{6.3}\right)^{0.6}\left(\frac{Sd}{12.0L^2}\right)^{0.125}$
	Exterior Beam	One Lane Loaded	3	Lever Rule	$0.482S^{0.798}\frac{d^{0.201}}{L^{0.611}}$	$\left(\frac{S}{1.7}\right)^{0.5}\left(\frac{Sd}{12.0L^2}\right)^{0.3}$
		Multiple Lanes Loaded	4	$g_{ext}=e\cdot g_{\text{int}}$ $e=0.97+\frac{d_e}{28.5}$	$0.301S^{0.589}\frac{d^{0.074}}{L^{0.221}}$	$\left(\frac{S}{9}\right)^{0.5}\left(\frac{Sd}{12.0L^2}\right)^{0.1}$
Shear LDF	Interior Beam	One Lane Loaded	5	$\left(\frac{S}{10}\right)^{0.6}\left(\frac{d}{12.0L}\right)^{0.1}$	$0.336S^{0.663}\frac{d^{0.197}}{L^{0.330}}$	$\left(\frac{S}{3.7}\right)^{0.65}\left(\frac{d}{12.0L}\right)^{0.25}$
		Multiple Lanes Loaded	6	$\left(\frac{S}{7.4}\right)^{0.8}\left(\frac{d}{12.0L}\right)^{0.1}$	$0.163S^{0.934}\frac{d^{0.162}}{L^{0.234}}$	$\left(\frac{S}{5}\right)^{0.9}\left(\frac{d}{12.0L}\right)^{0.2}$
	Exterior Beam	One Lane Loaded	7	Lever Rule	$0.139S^{0.686}\frac{d^{0.066}}{L^{0.033}}$	$\left(\frac{S}{15.7}\right)^{0.7}$
		Multiple Lanes Loaded	8	$g_{ext}=e\cdot g_{\text{int}}$ $e=0.8+\frac{d_e}{10}$	$0.147S^{0.576}\frac{d^{-0.032}}{L^{-0.066}}$	$\left(\frac{S}{19}\right)^{0.6}$

Range of Applicability for Proposed LDF Design Equations:
31 ft $\le L \le$ 51 ft, 6.5 ft $\le S \le$ 11 ft, 12 in. $\le d \le$ 21 in.

For deriving the new proposed design oriented equations, a slightly different approach was adopted to ensure a slight measure of conservatism. One of the objectives while deriving the equations was to keep the format of the LDF formulas similar to the AASHTO LRFD Specifications (2012) spread box formulas as much as possible. The criterion was to keep the lognormal standard deviation β as small as possible; note the smallest β value exists when the theoretical powers are used. Thus, in order to derive formulas that are similar to those in the AASHTO LRFD Specifications (2012) for spread box beams, the powers of the parameters were kept the same or as similar as reasonable to ensure β remained close to the theoretical equation. For the other cases where using the same power gives higher β values, the powers were chosen based on the theoretical power values and the format of the AASHTO LRFD

Specifications (2012) spread box beam formulas. The principal proposed coefficient *a* was increased by accepting 5 percent exceedance criterion, which means that up to 5 percent of the cases analyzed were permitted to be unconservative (smaller) compared to the more accurate FEM-based LDF values. All eight proposed LDF formulas for moment and shear are listed in Table 7.6.

LDFs obtained from the FEM analysis were compared with those calculated from the AASHTO LRFD Specifications (2012) spread box beam equations, the best fit theoretical equations, and the proposed design equations. The comparison of these three LDF equations versus FEM results is shown in the graphs provided in Figure 7.6 through Figure 7.13.

7.5.1 LDF for Moment in Interior Beam

Figure 7.6 provides plots of the moment results for the 31 bridges that were modeled using FEM. In the figure, the FEM solutions are considered exact. Therefore, the LDFs obtained from theoretical equations, new proposed equations, and the AASHTO LRFD Specifications (2012) spread box beam formulas are compared to the FEM-based LDFs. Each data point on the graphs represents an LDF for a specific case. Figure 7.6 shows the comparison of moment LDFs in interior slab beams for the one-lane-loaded case. The cumulative probabilities of the ratios (Theory/FEM, Proposed/FEM, and AASHTO/FEM) are also plotted to better visualize the distribution of each data point and their probability of occurrence.

The solid red line in Figure 7.6(d) represents the lognormal model curve for the proposed equation. The model curve is a lognormal curve that has the same lognormal standard deviation and median as the ratios of the proposed equation. For the one-lane-loaded moment in interior beams, 80 percent of the results from the AASHTO LRFD Specifications (2012) formula are unconservative when compared to the exact FEM LDFs.

Figure 7.7 shows the comparative graphs for the multiple-lane-loaded moment in interior beams. The AASHTO LRFD Specifications (2012) formulas are slightly higher than the FEM values. Therefore, the spread box beam formula for the multiple-lane-loaded moment in interior beams was kept the same. All the LDF values for moment in interior beams are listed in Table C.1 and Table C.2 in Appendix C.

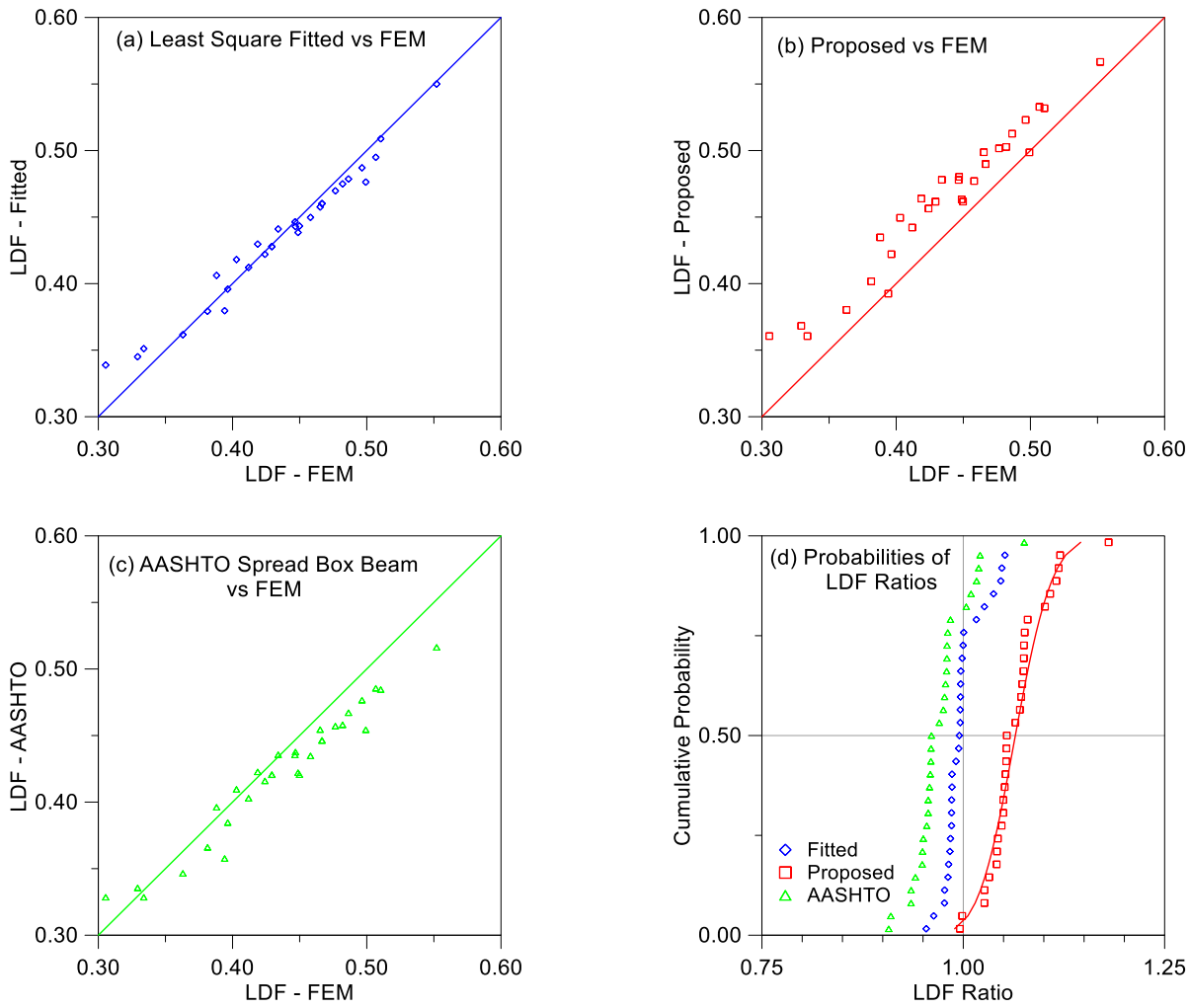

Figure 7.6. Comparison of LDFs for One-Lane-Loaded Moment in Interior Beams.

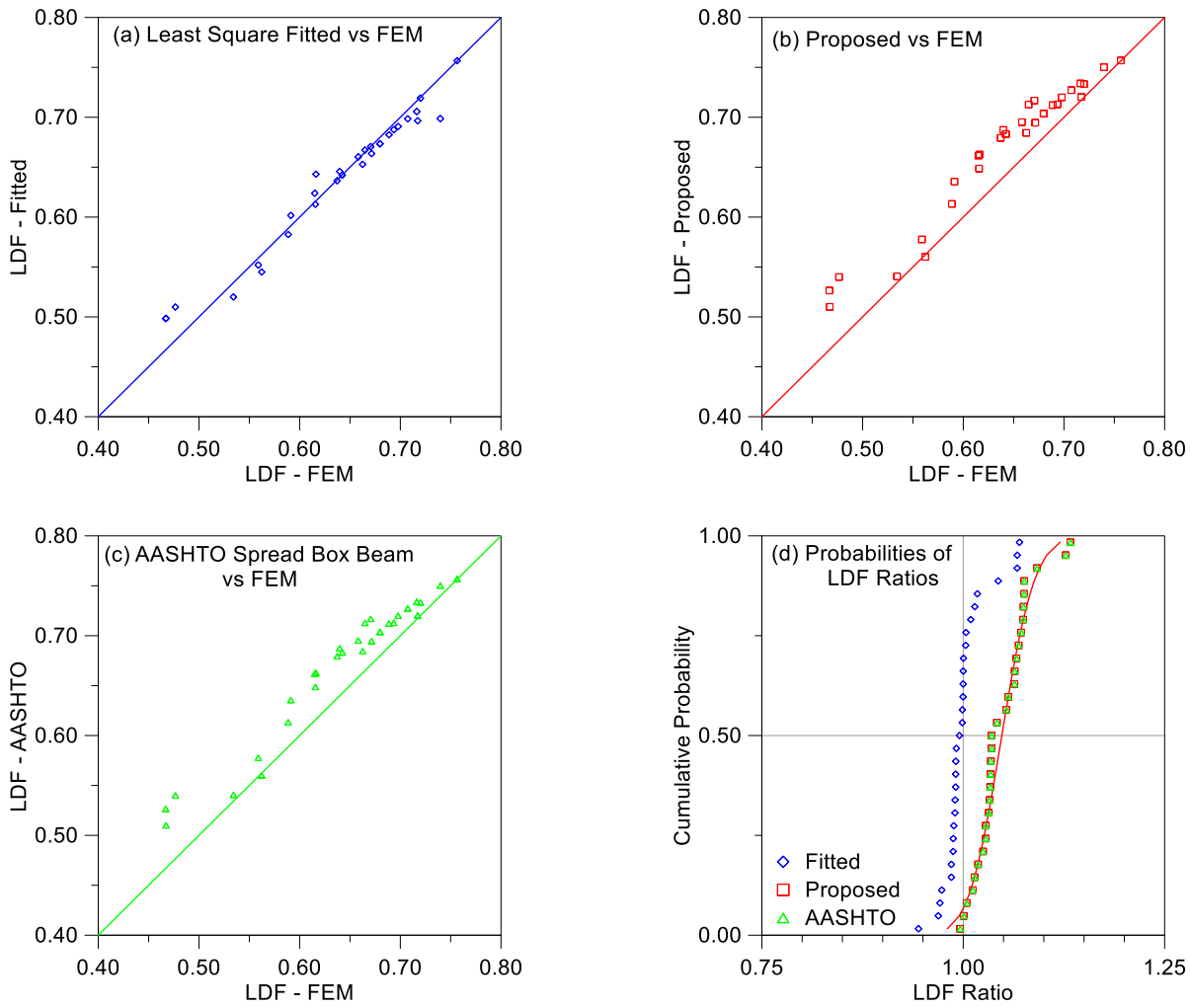

Figure 7.7. Comparison of LDFs for Multiple-Lane-Loaded Moment in Interior Beams.

7.5.2 LDF for Moment in Exterior Beam

The LDF values for all 31 bridges for moment in exterior beams are listed in Table C.3 and Table C.4 in Appendix C. These results were plotted for visual investigation in Figure 7.8 and Figure 7.9. The proposed equations give slightly conservative results for all points. Comparison of the AASHTO LRFD Specifications (2012) values with FEM LDFs revealed that the calculation of moment LDF for the one-lane-loaded case using the lever rule gives excessively conservative results. These AASHTO LRFD Specifications (2012) values are more than 50 percent conservative. A new equation having a similar layout as the interior beam formulas is introduced instead of the lever rule.

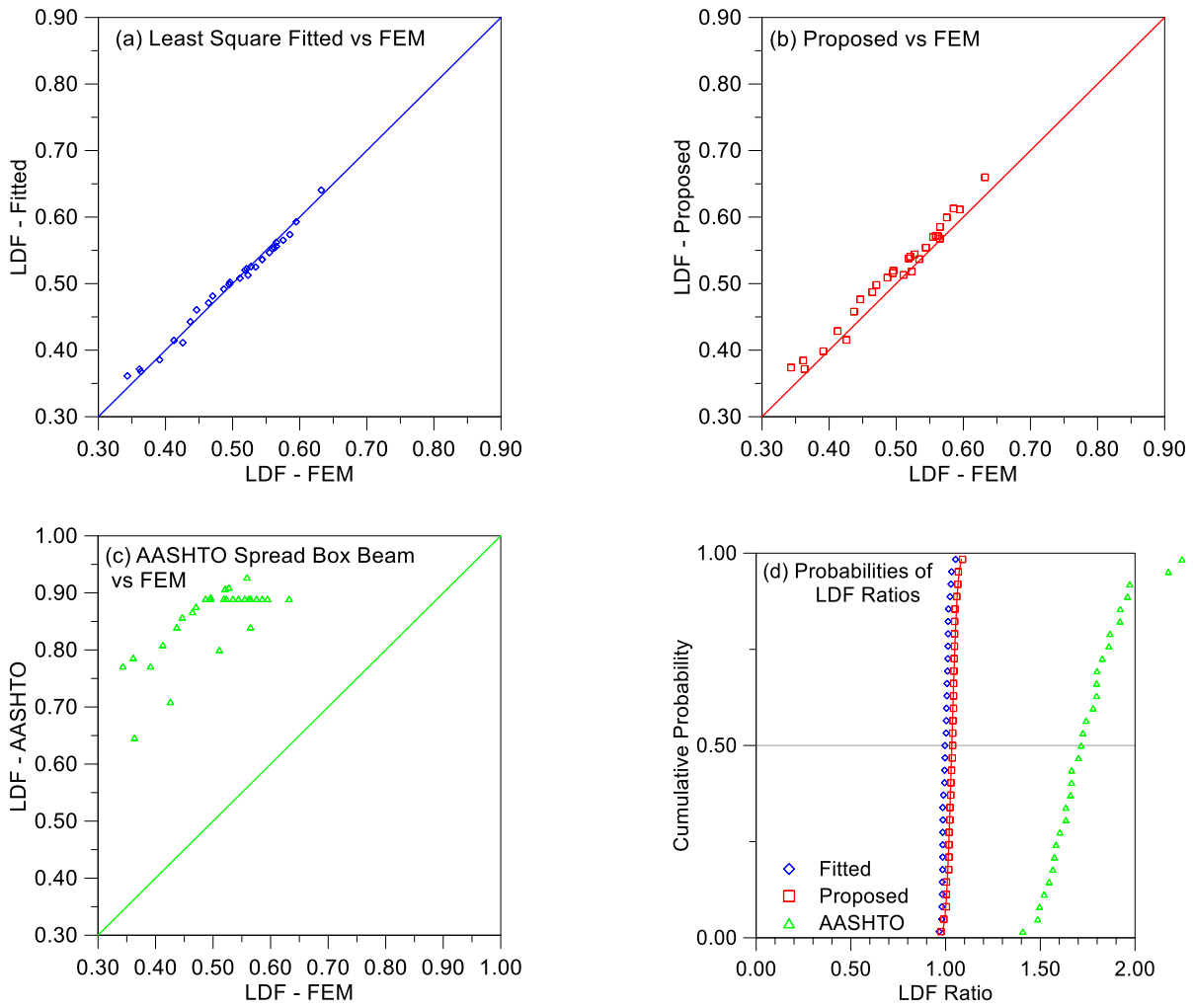

Figure 7.8. Comparison of LDFs for One-Lane-Loaded Moment in Exterior Beams.

The AASHTO LRFD Specifications (2012) spread box beam formula for moment in exterior beams for the multiple-lane-loaded case is obtained by adjusting the interior moment LDF with a certain multiplier. This multiplier is a function of the distance of an exterior beam from the interior face of the rail. For spread slab beam bridges, rails were not considered due to the above discussed reasons. Therefore, the parameter d_e was taken as the distance from the edge of the bridge. LDF values calculated from the AASHTO equation are 10–25 percent higher compared to FEM values. Therefore, a new equation having a similar format with other moment LDF equations was introduced. The new proposed equation gives slightly conservative results.

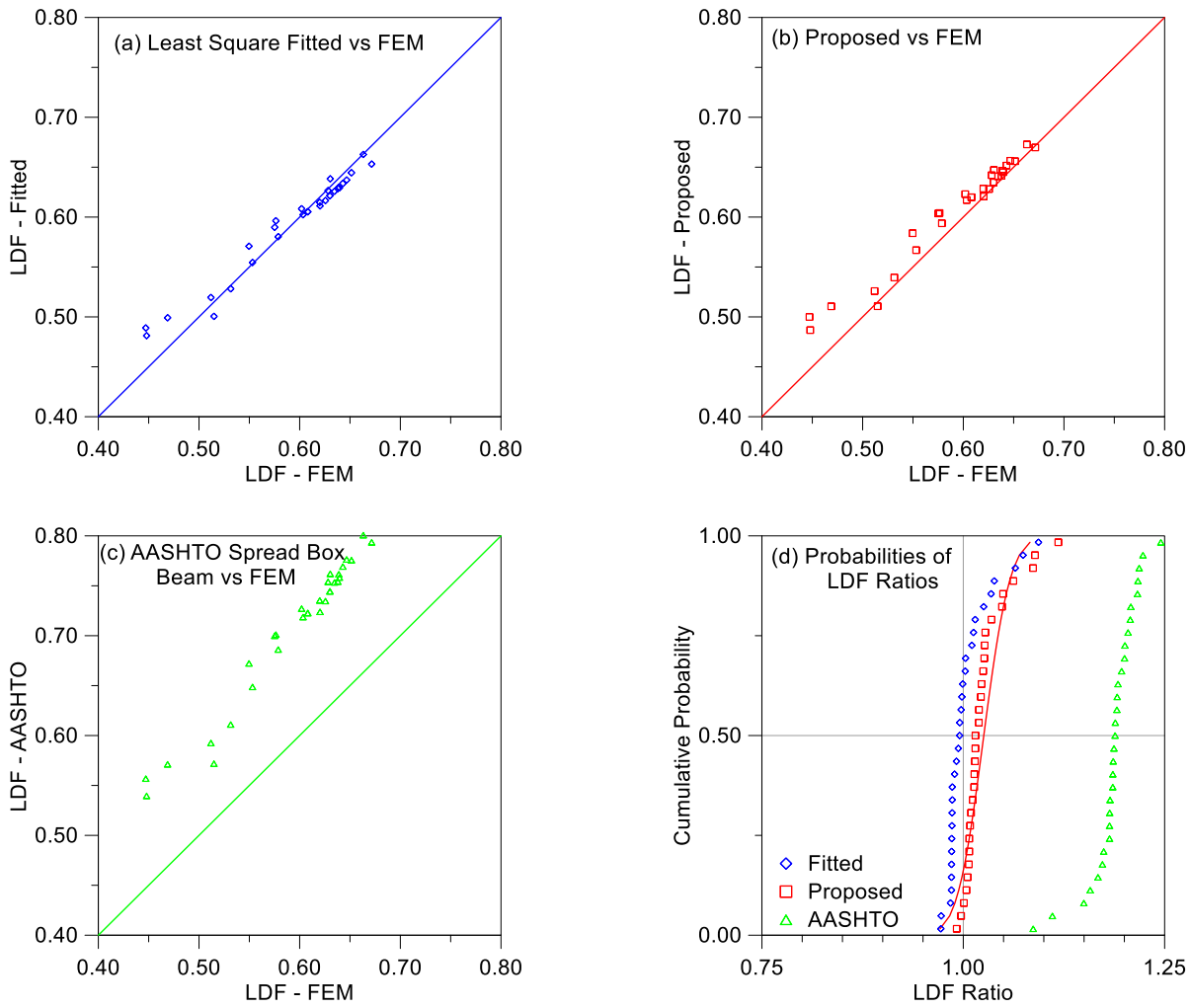

Figure 7.9. Comparison of LDFs for Multiple-Lane-Loaded Moment in Exterior Beams.

7.5.3 LDF for Shear in Interior Beam

Investigation of the LDFs for shear in interior beams revealed that the AASHTO LRFD Specifications (2012) values are unconservative for both one-lane-loaded and multiple-lane-loaded cases. This finding is consistent with the observations made during the experimental program. Therefore, new shear LDF equations are introduced that give higher LDF values. The parameters in the new shear LDF equations were arranged similar to the AASHTO LRFD Specifications (2012) spread box beam formulas. Figure 7.10 and Figure 7.11 show the comparative plots and probability plots for shear in interior beams. All the shear LDF values for shear in interior beams are listed in Table C.5 and Table C.6 in Appendix C.

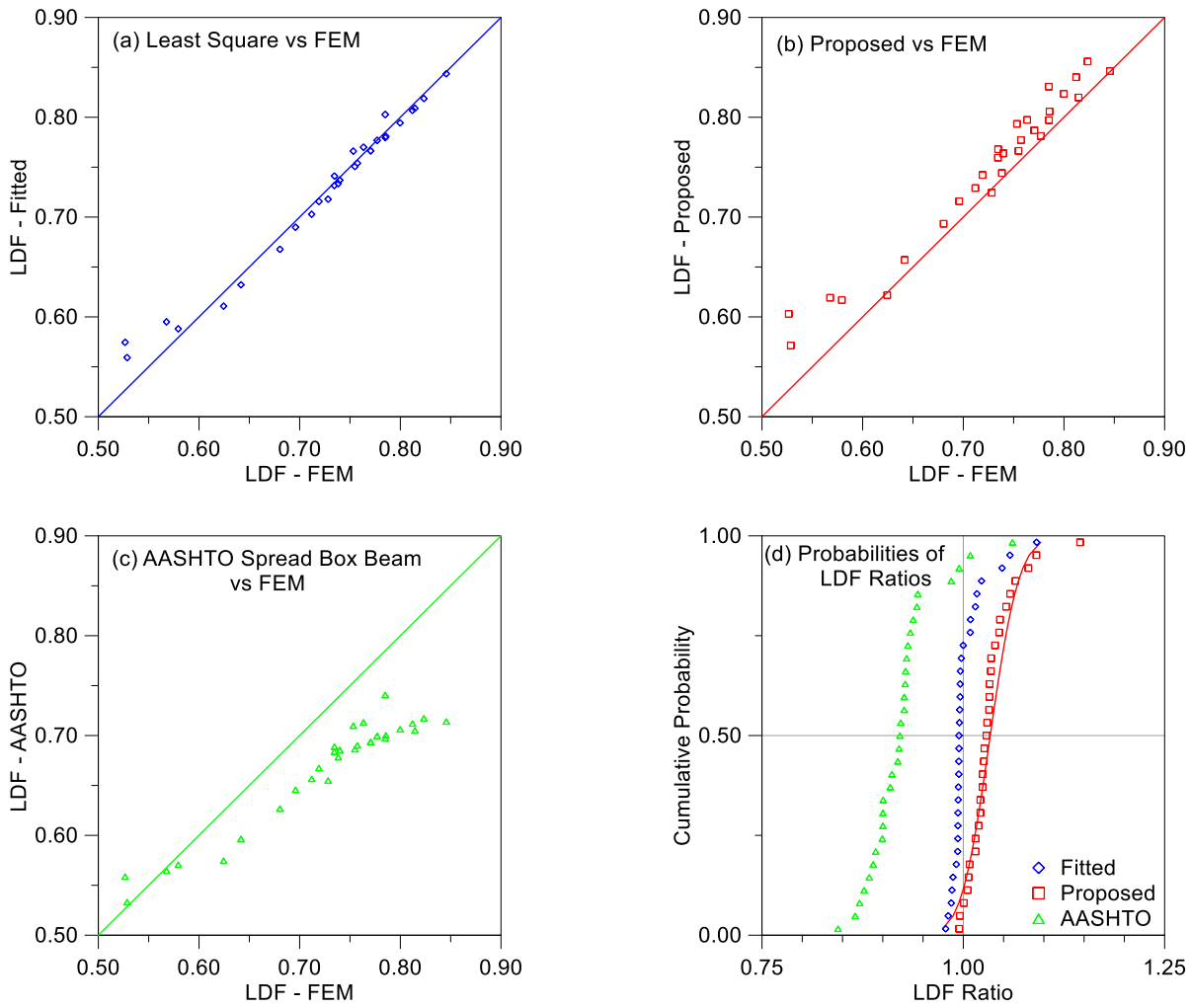

Figure 7.10. Comparison of LDFs for One-Lane-Loaded Shear in Interior Beams.

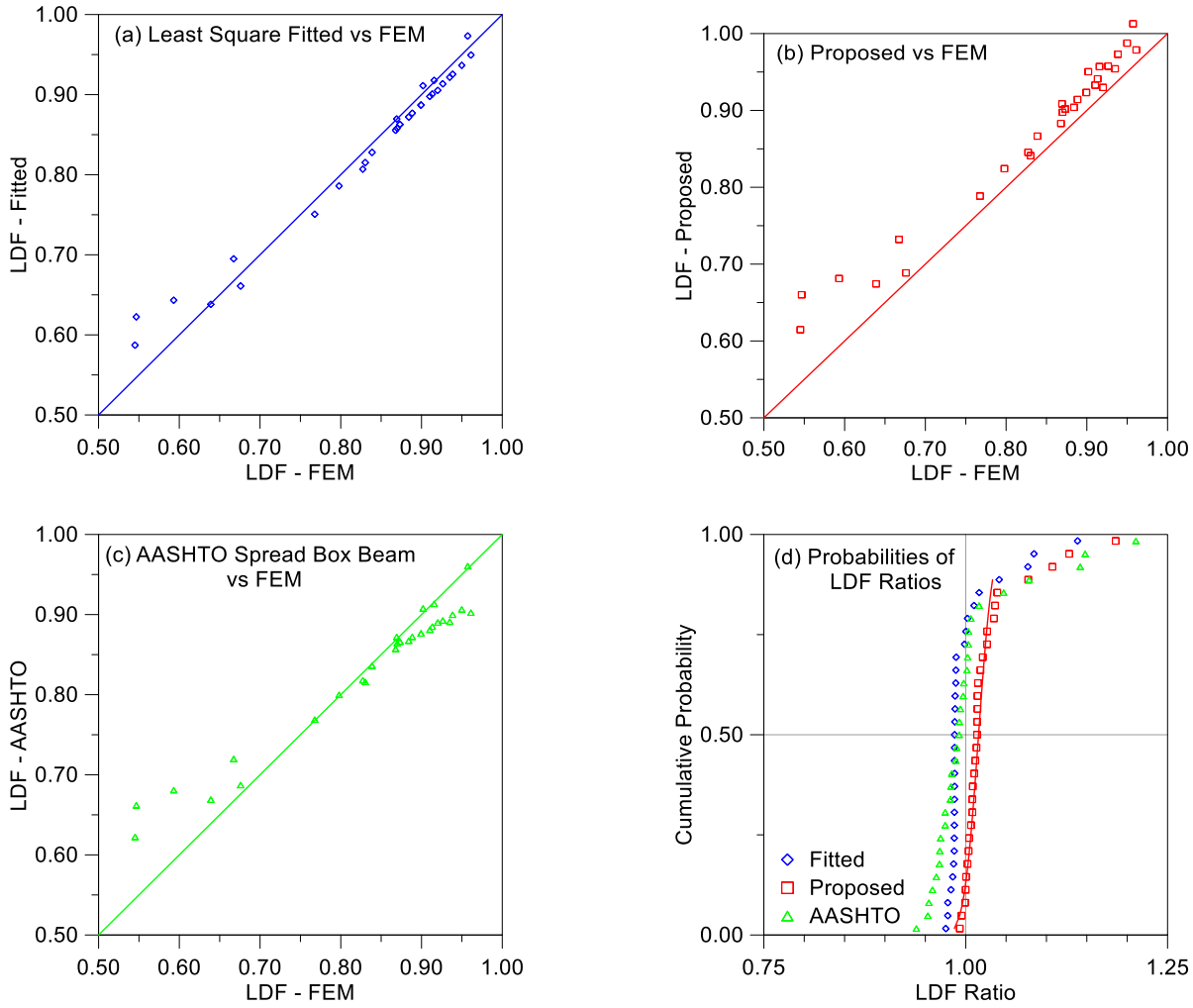

Figure 7.11. Comparison of LDFs for Multiple-Lane-Loaded Shear in Interior Beams.

7.5.4 LDF for Shear in Exterior Beams

Comparative plots showing all three LDF equations for shear in exterior beams versus the FEM results are shown in Figure 7.12 and Figure 7.13. Detailed LDF values are also listed in Table C.7 and Table C.8 in Appendix C. The AASHTO LRFD Specifications (2012) spread box beam formulas give an average 25 percent conservative LDFs for one-lane-loaded and more than 30 percent conservative LDFs for multiple-lane-loaded shear in exterior beams. The AASHTO LRFD Specifications (2012) specify use of the lever rule for determining exterior girder shear for the one-lane-loaded case. The lever rule gives overly conservative shear LDF values for the considered spread slab beam bridges.For the case of multiple-lane-loaded shear in exterior beams, the shear LDF is calculated by multiplying the interior beam shear LDF by a coefficient that is a function of the distance of the exterior beam from the edge of the bridge. This results in a very conservative LDF values.

Current TxDOT practice suggest designing all girders same as an interior girder to account for possible future widening of a bridge. If all slab beams are designed same as an interior slab beam, the AASHTO LRFD Specifications (2012) spread box beam formulas for shear in interior beam give slightly conservative results for the one-lane-loaded shear LDFs in exterior slab beams. On the other hand, the AASHTO LRFD Specifications (2012) formulas for multiple-lanes-loaded shear in interior beams are around 30 percent conservative for the shear LDFs in exterior beams. Therefore, the use of the AASHTO LRFD Specifications (2012) spread box beam equations for shear LDFs based on the interior beam shear demand could provide a reasonable estimate of shear for spread slab beams.

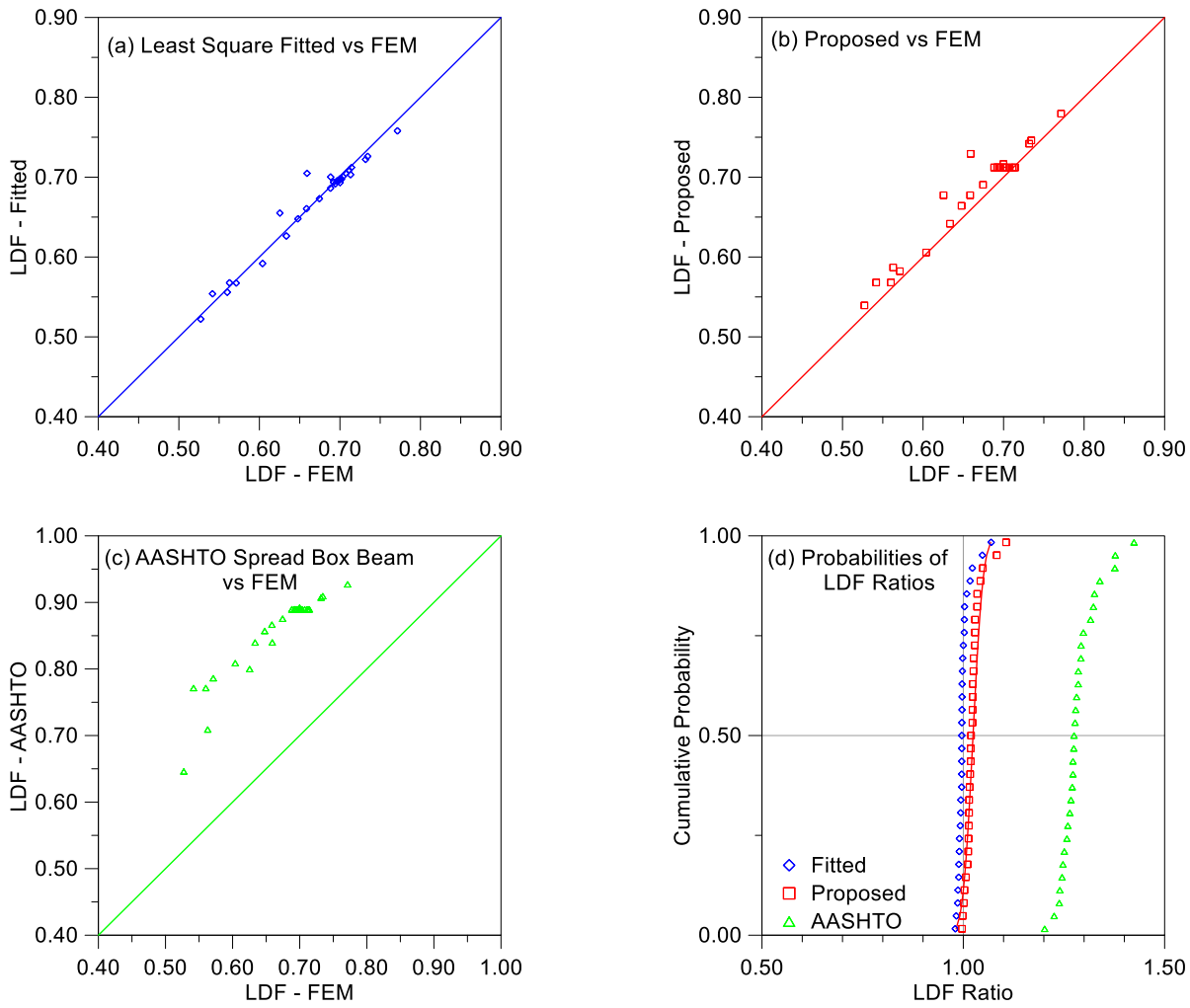

Figure 7.12. Comparison of LDFs for One-Lane-Loaded Shear in Exterior Beams.

Spread slab beam bridges are designed without a cantilever. In addition, rail thickness was not considered for the LDF study because of the possibility of having the interior edge of a bridge within a design lane for two adjacent bridges (similar to the US 69 Bridge). Therefore, the distance of the exterior beam from the edge of the bridge remains the same for all equal width beams. Because there are only two different standard slab beam widths, the variation of the shear LDF for exterior beams due to the exterior beam position is not critical. The new proposed shear LDFs in exterior beams consider the beam spacing as a more important parameter instead of the distance of the exterior beam from the edge. The obtained LDF values are slightly higher than the FEM results as intended.

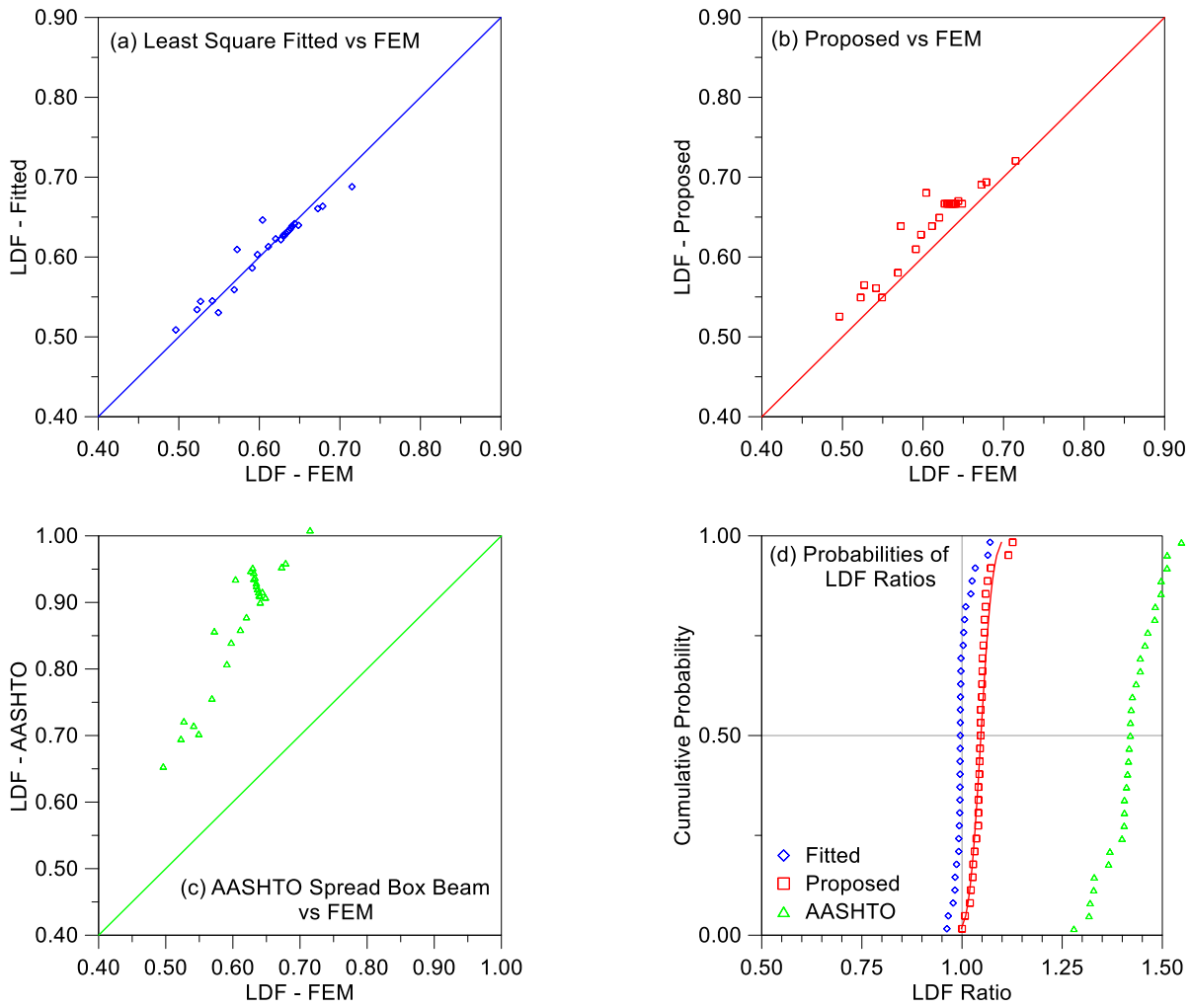

Figure 7.13. Comparison of LDFs for Multiple-Lane-Loaded Shear in Exterior Beams.

7.6 FINDINGS AND DESIGN RECOMMENDATIONS

LDFs were empirically derived for interior and exterior girders of spread slab beam bridges for span lengths within the range of 31 to 51 ft. Proposed equations were derived using a methodology similar to that adopted for developing the LDF equations found in the AASHTO LRFD Specifications (2012). A total of 31 bridge FEM models were developed and analyzed, with each bridge model having a different superstructure geometry selected from the domain investigated during the parametric study. Based on the comparative study conducted for three different sets of equations (AASHTO LRFD Specifications (2012) spread box beam formulas, theoretical best fit equations from FEM analysis, and new proposed LDF equations) the following conclusions were drawn.

1. The AASHTO LRFD Specifications (2012) LDF equations for spread box beams were reviewed for applicability to spread slab beams. The AASHTO LRFD Specifications (2012) LDFs range from being unconservative to very conservative.
    a) For interior beams, the AASHTO LRFD Specifications (2012) spread box beam formulas give slightly unconservative LDFs for the one-lane-loaded moment, whereas they are slightly conservative for the multiple-lane-loaded moment. Therefore, the new proposed equations match the AASHTO LRFD Specifications (2012) spread box beam formulas for the multiple-lane-loaded moment in interior beams.
    b) For exterior beams, the LDF values are always overestimated by the AASHTO LRFD Specifications (2012) spread box beam formulas.
    c) For one-lane-loaded shear and moment in exterior beams, the AASHTO LRFD Specifications (2012) suggest using the lever rule, which produces overly conservative LDFs (an average of 50 percent conservative for moment and 30 percent conservative for shear). Therefore, new LDF equations were proposed for exterior beams that are only slightly conservative compared to the FEM results.
    d) For multiple-lane-loaded moment and shear in exterior beams, the AASHTO LRFD Specifications (2012) suggest multiplying interior beam LDFs with a coefficient that is a function of the distance of the exterior beam from the interior edge of the rail. This parameter is not an effective parameter for the

spread slab beam bridges considered in this study. This approach produces up to 25 percent conservative results for moment and an average of 40 percent conservative results for shear in exterior beams. Thus, new LDF equations are suggested for multiple-lane-loaded moment and shear in exterior beams.

2. Unique LDF expressions were developed for spread slab beam bridges to provide an appropriate level of conservatism. The new proposed equations produce slightly conservative results for all LDF cases when compared with the LDFs calculated from FEM analysis. The proposed moment LDF for interior slab beams (multiple lanes loaded) is identical to the AASHTO LRFD Specifications (2012) spread box beam equation.
3. Examining the analytical results and recommended LDF formulas for spread slab beams reveal that some of the formulas govern the design most of the time.
    a) For all LDF equations, except for shear in exterior beams, multiple-lane-loaded formulas provide higher LDFs that control the design.
    b) For shear in interior beams, the multiple-lane-loaded shear LDF formula always gives higher results.
    c) For shear in exterior beams, the one-lane-loaded LDF formula gives higher results.
    d) For moment in both interior and exterior beams, multiple-lane-loaded formulas result in the highest LDF values.
4. Common TxDOT practice for precast prestressed concrete bridges is to design all the girders the same as an interior girder in order to take into account possible future widening of the bridge. Therefore, all girders are designed based on interior girder shear and moment demands, unless the exterior demands are greater.
5. The two governing proposed LDF design equations for multiple-lane-loaded interior beams are:

    For moments: $\left(\frac{S}{6.3}\right)^{0.6}\left(\frac{Sd}{12.0L^2}\right)^{0.125}$

    For shear: $\left(\frac{S}{5}\right)^{0.9}\left(\frac{d}{12.0L}\right)^{0.2}$

    where, 31 ft $\le L \le$ 51 ft, 6.5 ft $\le S \le$ 11 ft and 12 in. $\le d \le$ 21 in.

Using the above results, the LDFs obtained from these two formulas were plotted against span length for different beam spacings for common 15 in. deep slab beams and are shown in Figure 7.14. The solid lines show the LDF values within the applicable span length range, and the dashed lines show slightly beyond the applicable span range.

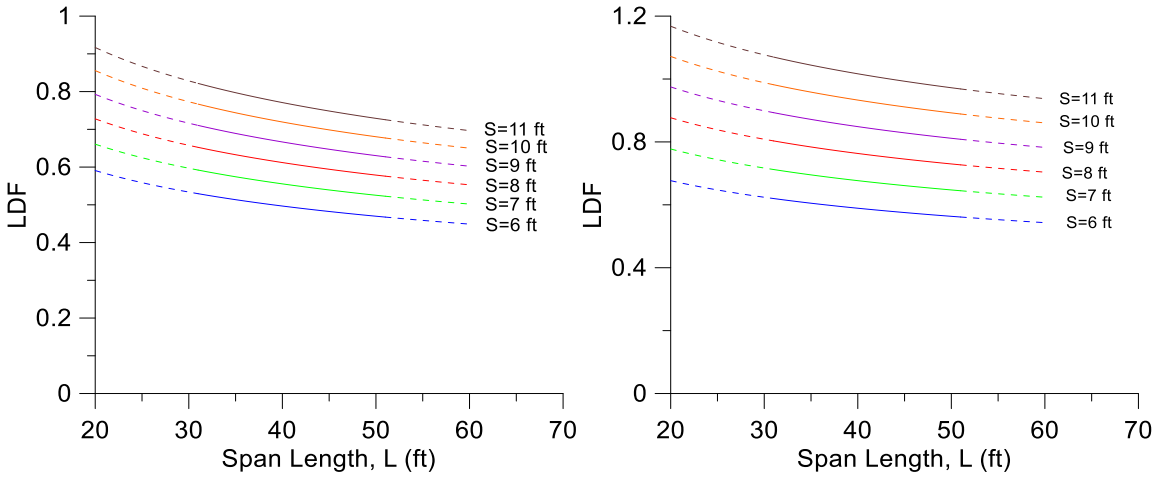

(a) Moment LDF (b) Shear LDF

Figure 7.14. LDF Solution Domain for 15 in. Slab Beams Based on Proposed Multiple-Lane-Loaded Interior Beam Formulas.

8. EFFECT OF ADDITIONAL PARAMETERS ON LOAD DISTRIBUTION FACTORS

8.1 GENERAL

LDF equations were developed using the key parameters, span length (L), beam spacing (S) and beam depth (d). These parameters were chosen based on similar formulas used for spread box beam bridges in the current AASHTO LRFD Specifications (2012). Therefore, the effect of other parameters were completely neglected. However it has been known that certain other parameters such as skew angle, overhang, haunch thicknes and vehicle edge distance may have a significant effect on the lateral distribution of the applied loads.

This section primarily focuses on developing correction factors for the additional parameters that have a prominent effect on the LDFs. Other parameters that may have a minor effect were also investigated. A similar methodology was followed as in the previous section and in the AASHTO LRFD Specifications (2012). It was assumed that the effect of each parameter on LDFs are not correlated. The variation of LDFs due to changes in the parameter under consideration were studied while keeping all the other parameters constant. A total of 28 different analyses were conducted using FEM.

Table 8.1 lists the details of the analyzed bridge geometries and load variations. One of the challenging geometries that uses four 5SB15 slab beams, having a 45 ft 7 in. span length, and a 34 ft total bridge width was chosen as the baseline bridge. Then each parameter under consideration was independently altered to evaluate the variation in LDFs as that parameter changes. The bridges are grouped based on the parameter being studied. A total of 17 bridges were considered with different geometries including skew angle (θ), overhang length (d_e), and haunch thickness (t_h). Another seven prototype bridges have the geometry of the baseline bridge but different load conditions. A final four bridges not part of the empirical equation derivation were independently analyzed to validate the identified correction factors.

Table 8.2 summarizes the geometric and material properties used in the FEM models of the bridges as well as the range of the investigated parameters. All 28 bridges were analyzed using Computers and Structures (2015) FEM software. Bridge superstructures were modeled using eight-node isotropic solid elements having three degrees of freedom at each node. A maximum of a 12 in. mesh size was used throughout based on a mesh sensitivity study.

Table 8.1. Alternative Bridge Geometries for LDF Study of Additional Parameters.

No.	No. of Beams	Beam Type	Bridge Width (ft)	Beam Spacing (ft)	Span Length	Parameter
θ = Skew Angle Effect						Skew Angle (º)
1	4	5SB15	34	9.67	45′-7″	0
2	4	5SB15	34	9.67	45′-7″	15
3	4	5SB15	34	9.67	45′-7″	30
4	4	5SB15	34	9.67	45′-7″	40
5	4	5SB15	34	9.67	45′-7″	45
6	4	5SB15	34	9.67	45′-7″	50
7	4	5SB15	34	9.67	45′-7″	60
d_e = Overhang Effect						Overhang (ft)
8	4	5SB15	34	9.67	45′-7″	0
9	4	5SB15	36	9.67	45′-7″	1
10	4	5SB15	38	9.67	45′-7″	2
11	4	5SB15	40	9.67	45′-7″	3
12	4	5SB15	42	9.67	45′-7″	4
t_h = Haunch Thickness Effect						Haunch (in.)
13	4	5SB15	34	9.67	45′-7″	0
14	4	5SB15	34	9.67	45′-7″	1
15	4	5SB15	34	9.67	45′-7″	2
16	4	5SB15	34	9.67	45′-7″	3
17	4	5SB15	34	9.67	45′-7″	4
d_{ve} = Vehicle Edge Distance (VED) Effect						VED (ft)
18	4	5SB15	34	9.67	45′-7″	0
19	4	5SB15	34	9.67	45′-7″	1
20	4	5SB15	34	9.67	45′-7″	2
21	4	5SB15	34	9.67	45′-7″	3
Load Type						Load
22	4	5SB15	34	9.67	45′-7″	Lane Only
23	4	5SB15	34	9.67	45′-7″	HS20 Only
24	4	5SB15	34	9.67	45′-7″	Lane + HS20
General—Verification and Evaluation						
25	4	4SB12	34	10	35′-7″	$\theta = 45^o$
26	4	4SB12	26	7.33	39′-7″	$\theta = 50^o$
27	4	4SB12	34	10	35′-7″	$d_e = 4$
28	4	4SB12	34	10	35′-7″	$d_{ve} = 0$

Table 8.2. Bridge Properties and Applicable Ranges of Parameters.

Parameter	Description/Value
Center-to-Center of Bearing Pad Span Length, L	35 ft 7 in. $\leq L \leq$ 45 ft 7 in.
Total Bridge Width, W	26 ft $\leq W \leq$ 42 ft
Center-to-Center Beam Spacing, S	7.33 ft $\leq S \leq$ 10 ft
Slab Beam Width	4 ft or 5 ft
Slab Beam Thickness	12 in. or 15 in.
Deck Thickness, t_s	9 in.
Modulus of Elasticity of Slab Beam Concrete	E_b = 5883 ksi
Modulus of Elasticity of Deck Concrete	E_d = 7054 ksi
FEM Element Size	12 in.
Boundary Conditions	1270 kip/in vertical and 5 kip/in horizontal springs
Haunch Thickness, t_h	12 in. $\leq t_h \leq$ 15 in.
Skew Angle, θ	$0^o \leq \theta \leq 60^o$ (same skew at both end)
Overhang, d_e	0 ft $\leq d_e \leq$ 4 ft

8.2 METHODS FOR DEVELOPING CORRECTION FACTORS

8.2.1 Methodology

A systematic procedure was developed for analyzing the relationship between each parameter and the LDFs. Procedure for a specific parameter can be summarized as the following;

1. The bridges within the group for the specified parameter being considered were modeled using FEM method.
2. These models were loaded along several different alignments to produce critical moment and shear actions for interior and exterior beams for one lane or multiple lane loading. These combinations produces a total of eight different critical load cases for each bridge. For each model eight LDFs were calculated and recorded.
3. Then LDFs versus the parameter were plotted for all eight LDF cases using a liner-linear chart. These plots were then used for visual inspection of the sensitivity of the specific LDF to the changes in the parameter considered. Based on this initial

investigation, if a specific LDF is sensitive to this parameter, a correction factor was derived through the following steps.

4. The LDF that is sensitive to the parameter in consideration was divided by the LDF of the base bridge. (For skew angle, the base bridge is the right bridge. For haunch thickness, the base bridge has zero haunch thickness). This ratio gives the correction factor for that specific bridge. In order to get an average value the LDF ratio versus the parameter plot was created and a linear least square (LS) best fit was found for this case. The equation of the LS best fit is the correction factor for this specific LDF case and parameter. The corrected LDF can then be calculated as:

$$g' = rg \tag{8.1}$$

   where r is the correction factor for considered parameter, g is the LDF calculated based on key parameter (L, S and d).
5. The above four steps were repeated for all parameters and for all eight LDF cases.
6. Finally these empirical formulas were rationally adjusted based on a 5 percent non-exceedance probability, and proposed formulas were developed for important parameters and for sensitive LDF cases.

8.2.2 Vehicle Loading of FEM Models

AASHTO LRFD HL93 loading was considered to analyze the bridge decks. The adopted loading approach was slightly different than what was used by Zokaie et al. (1991). Truck plus uniform lane loading was considered rather than just truck load. This approach is more realistic because the AASHO LRFD Specifications (2012) LDFs are also multiplied by the uniform lane loading. Moreover, instead of placing the vehicle at a specific longitudinal position to create critical moment and shear effects, vehicles were run along defined alignments. CSiBridge software caters for moving load analysis by using the influence line method.

Transverse positions were defined to create most adverse loading conditions for exterior and interior girders. Bridge decks were divided into 12 ft wide lanes. AASHTO LRFD trucks were then placed within the defined lanes. Many different transverse alignments were analyzed by moving the vehicles 2 ft at each time within their defined lanes. For one-lane-loaded cases, vehicles were allowed to pass between lanes in order to have more critical loading for interior girders. Several example loadings for critical cases are shown in Figure 7.2.

The above described transverse positioning approach was followed for studying the effect of all parameters except vehicle edge distance (VED). In order to analyze the sensitivity of LDFs to VED, several load cases that are not allowed in the AASHTO LRFD Specifications (2012) must be considered. The above defined transverse alignments consider that the vehicle can travel a minimum 2 ft away from the edge of defined lane or the face of rail. However, to investigate the effect of VED the additional alignments at 0 ft and 1 ft from the edge were defined.

Figure 8.1 shows several transverse alignments for one-lane and two-lanes loaded cases that were defined for investigating the effect of VED. A vehicle was placed exactly at the edge of the bridge and moved 1 ft transversely at each step. For two-lanes-loaded case a second vehicle was placed within the second lane as close as possible to the edge of the design lane to create the most critical loading for the exterior beam.

8.3 EFFECT OF GEOMETRIC VARIATIONS ON LDF

The effect of different geometric parameters to LDF have long been studied for different bridge superstructures. In addition to key parameters several additional parameters such as skew angle, overhang and haunch thickness were found to be somewhat important in terms of transverse load sharing.

Table 8.3 lists the LDFs for the additional geometric parameters, skew angle, overhang, and haunch thickness. The results were grouped based on the parameter in consideration. All three groups use the same base bridge geometry. Seven bridge superstructures, which had skew angles changing from 0 to 60 degrees, were modeled and analyzed for investigating the effect of skew angle. Another five bridges with an overhang between 0 to 4 ft, were modeled for studying the effect of overhang. Although this group used the same baseline bridge, the total bridge width changed due to the additional overhang. Note this did not violate the rule of changing one parameter at a time, because the total bridge width was not considered as a geometric parameter. The last group had four different haunch thicknesses between 0 to 4 in. The haunch thickness was modeled as part of slab beams and assumed that the small difference between modulus of elasticity of the deck concrete and beam concrete was negligible.

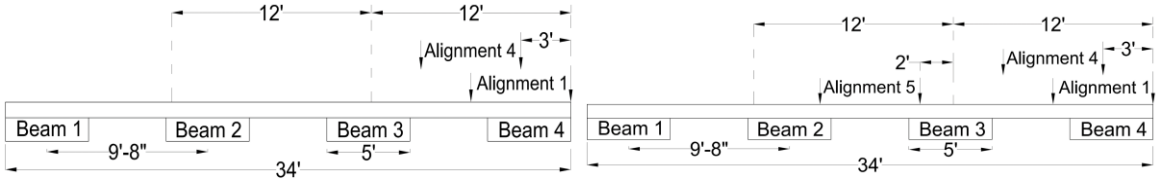

(a) One-Lane-Loaded (b) Two-Lanes-Loaded

Figure 8.1. Typical Transverse Alignments for VED Study.

Table 8.3. LDF for Investigating Effect of Additional Geometric Parameters.

							One Lane Loaded				Multiple Lanes Loaded			
							Interior Beam		Exterior Beam		Interior Beam		Exterior Beam	
							θ = Skew Angle							
No.	L	No. of Beams	Beam Type	S (ft)	Bridge Width	θ (°)	g_M	g_V	g_M	g_V	g_M	g_V	g_M	g_V
1	45′ 7″	4	5SB15 d = 15"	9.67	34	0	0.42	0.73	0.49	0.71	0.64	0.86	0.61	0.67
2						15	0.41	0.65	0.48	0.79	0.61	0.85	0.59	0.78
3						30	0.36	0.63	0.43	0.90	0.55	0.81	0.52	0.90
4						40	0.35	0.62	0.42	0.95	0.49	0.83	0.47	0.97
5						45	0.34	0.63	0.40	0.97	0.46	0.83	0.44	0.98
6						50	0.30	0.61	0.37	0.95	0.42	0.86	0.39	0.97
7						60	0.22	0.67	0.27	0.95	0.34	0.92	0.28	0.95
						d_e (ft)	d_e = Overhang							
8	45′ 7″	4	5SB15 d = 15"	9.67	34	0	0.42	0.73	0.49	0.71	0.64	0.86	0.61	0.67
9					36	1	0.42	0.72	0.53	0.84	0.69	0.85	0.67	0.80
10					38	2	0.41	0.72	0.58	0.94	0.69	0.81	0.72	0.91
11					40	3	0.41	0.72	0.61	1.02	0.69	0.78	0.77	1.00
12					42	4	0.40	0.72	0.64	1.10	0.69	0.77	0.81	1.09
						t_h (in.)	t_h = Haunch Thickness							
13	45′ 7″	4	5SB15 d = 15"	9.67	34	0	0.42	0.73	0.49	0.71	0.64	0.86	0.61	0.67
14						1	0.43	0.73	0.50	0.71	0.64	0.87	0.62	0.67
15						2	0.43	0.74	0.50	0.71	0.64	0.88	0.62	0.67
16						3	0.44	0.74	0.51	0.72	0.65	0.88	0.62	0.67
17						4	0.44	0.74	0.51	0.72	0.65	0.89	0.63	0.67

8.3.1 Effect of Skew Angle

Figure 8.2 shows the effect of the skew angle on the shear and moment LDFs. These four plots were investigated to evaluate the sensitivity of LDFs to the changes in the skew angle. Moment LDFs for both interior and exterior beams are smaller with increasing skew angle. This reduction in the moment LDF can be around 60 percent for skew angles of 60 degrees. Shear LDFs for the obtuse angle end of the exterior beams increased with the increasing skew angle and may result in up to a 50 percent increase in the shear force. On the other hand interior beam shear LDFs do not change significantly, as can be seen from Figure 8.2(c). Therefore a skew correction factor was not derived for shear LDFs in interior beams.

Figure 8.3 shows the ratio of LDFs at any skew angle to the LDFs at zero skew, which is plotted against $cos\theta$ for moment and $sin\theta$ for shear LDFs. The trigonometric identities were chosen based on the best fit regression curve and to simplify the correction factor equations. AASHTO LRFD Specification (2012) provides skew correction factors as a function of $\tan\theta$. For spread box beam bridges, the skew correction factor for moments is $1.05-0.25\tan\theta$. Therefore skew correction factors for moments in spread slab beam bridges were derived using two alternative methods; one using $\tan\theta$ (Figure 8.4) and the other one using $\cos\theta$ (Figure 8.3). It can be seen from the LS best fit curves that both $tan\theta$ and $cos\theta$ provide a sufficiently good fit for moment correction factors. One could use a correction factor that uses $\tan\theta$ similar to AASHTO LRFD format. However the propoposed skew correction factor for spread slab beam bridges for moments is based on $\cos\theta$, because it provides a simpler and more transparent equation.

AASHTO LRFD Specification (2012) provides skew correction factors for shear as a function of $tan\theta$, S, L and d, which did not provide a better fit for the available data for shear LDFs. On the other hand, the regression curve with $sin\theta$ provided a superior model based on the coefficient of determination parameters.

Moment LDFs constantly reduced with increasing skew angle, whereas shear LDFs for exterior girder increases up to 45 degree and start to slightly decrease from a 45 to 60 degree skew. In general multiple-lane-loaded cases were more affected by the changes in skew angle than were the one-lane-loaded cases.

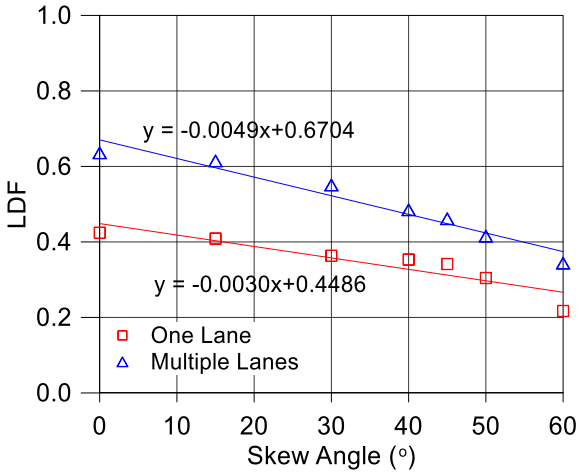

(a) Interior Beam Moment

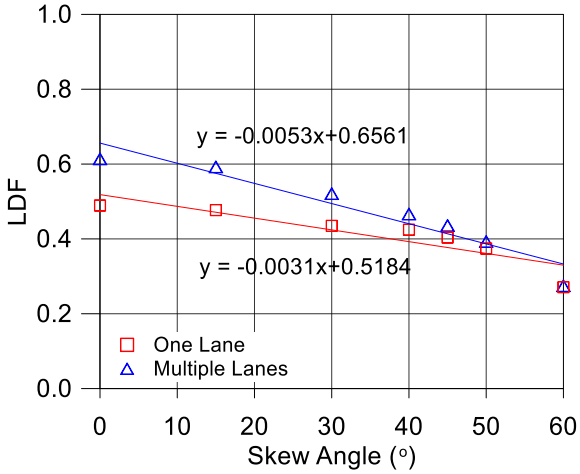

(b) Exterior Beam Moment

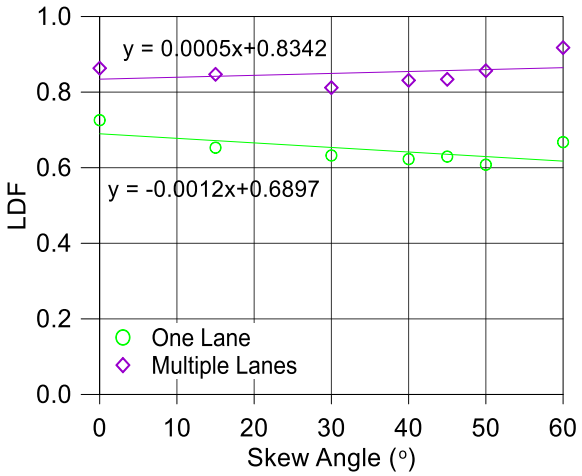

(c) Interior Beam Shear

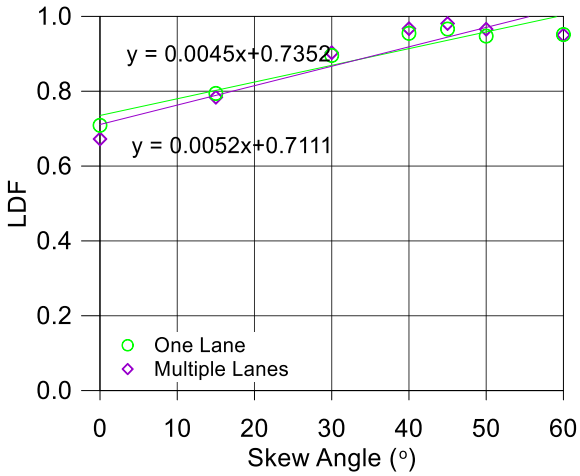

(d) Exterior Beam Shear

Figure 8.2. Effect of Skew Angle on LDFs.

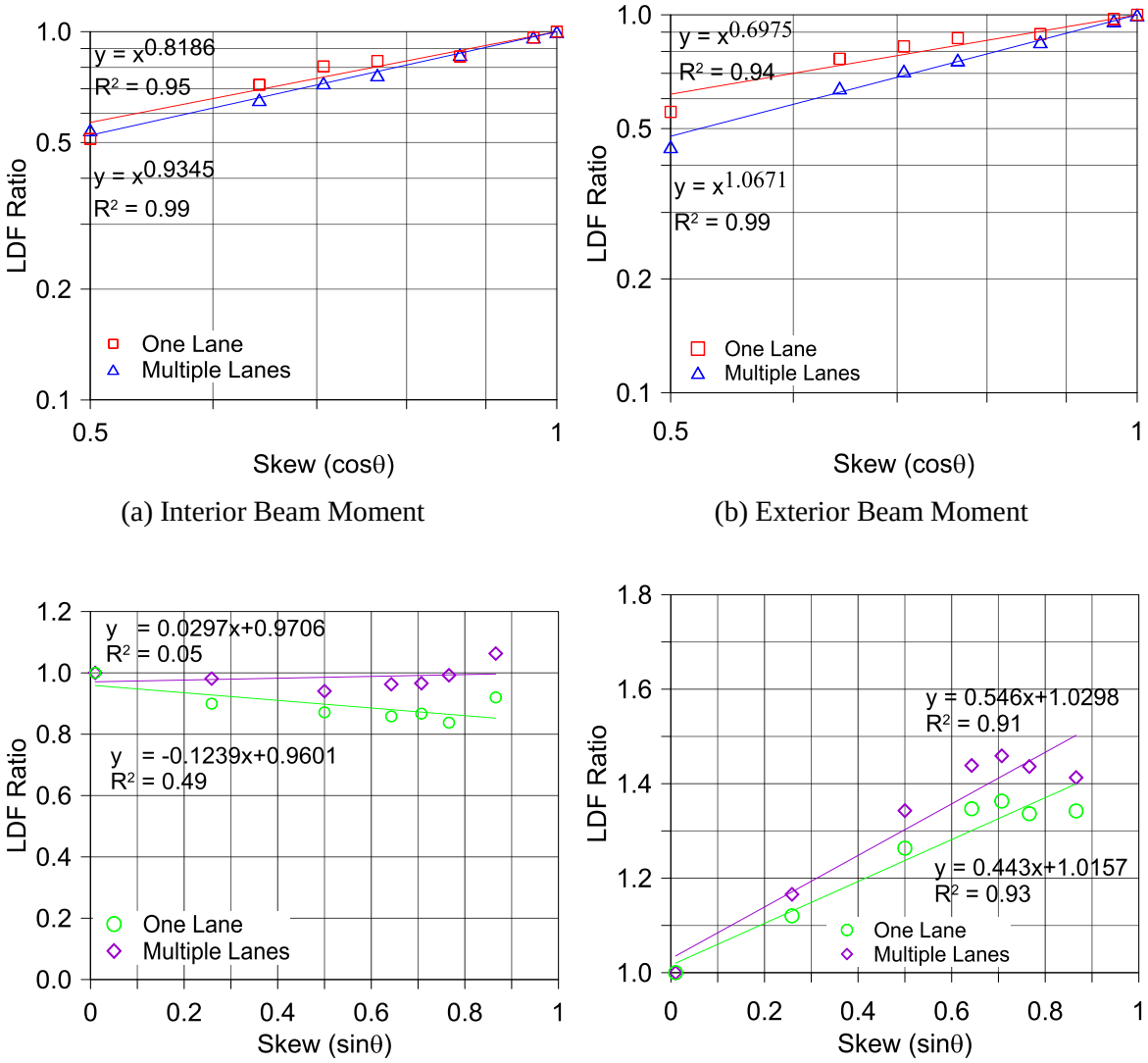

(a) Interior Beam Moment

(b) Exterior Beam Moment

(c) Interior Beam Shear

(d) Exterior Beam Shear

Figure 8.3. Skew Angle Correction Factor.

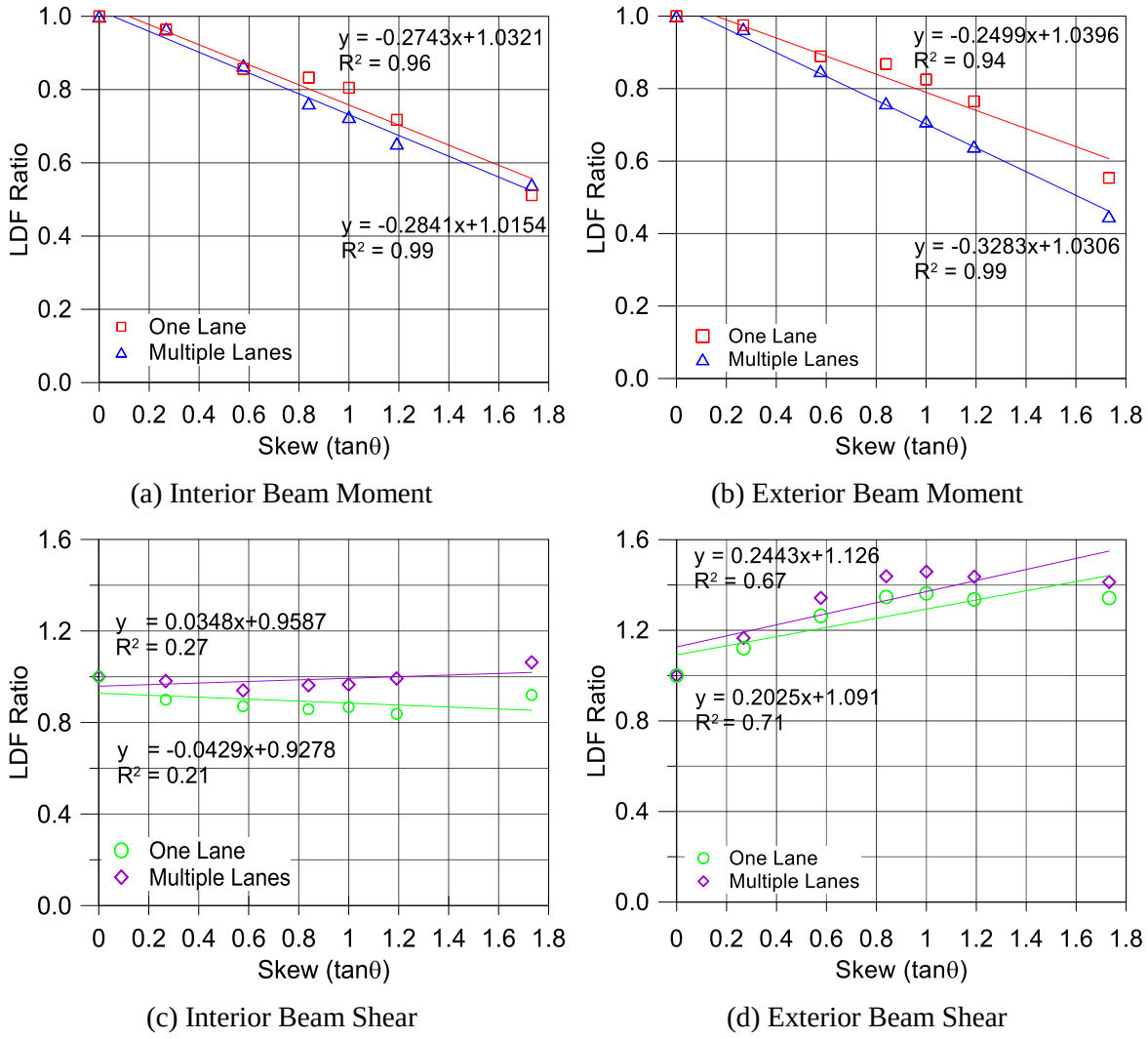

(a) Interior Beam Moment

(b) Exterior Beam Moment

(c) Interior Beam Shear

(d) Exterior Beam Shear

Figure 8.4. Skew Angle Correction with *tanθ*.

8.3.2 Effect of Overhang

In many design and construction operations it is inevitable to have an overhang because of curves or widening of the bridge superstructure. The additional extension changes the moment and shear demands especially for exterior beams. To investigate the effect of this change, a total of five different geometries, which have an overhang length changing from 0 ft to 4 ft were modeled and analyzed using various different loadings. Moment and shear LDFs were calculated from the moments and shear responses for the interior and exterior beams.

Figure 8.5 shows the variation of LDFs as the overhang increases. The composite section stiffness increases as the overhang length increases, which in return attracts more moment and shear to the exterior beam. In addition, due to the extra width, the centerline of the vehicles can move closer or beyond the exterior girder. This results in an increase for the exterior moment and shear LDFs. On the other hand the trend of the interior beam moment and shear LDFs stays almost horizontal, which implies that their effect can be neglected. Therefore overhang correction factors were developed for exterior beams only.

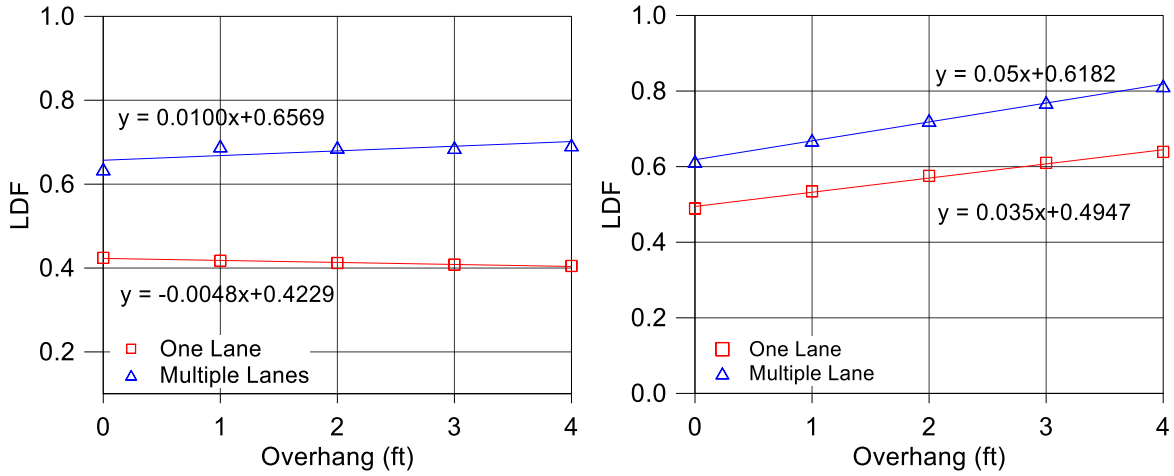

(a) Interior Beam Moment

(b) Exterior Beam Moment

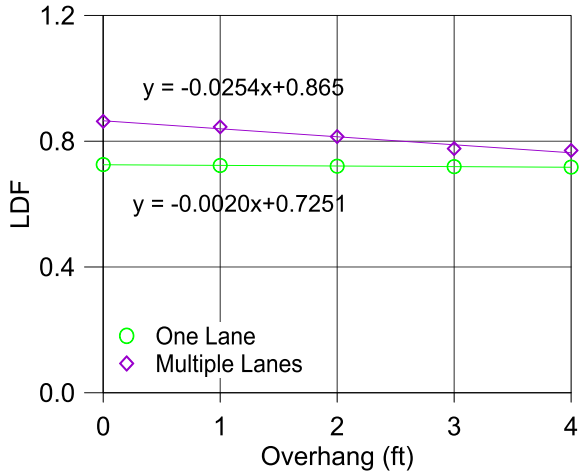

(c) Interior Beam Shear

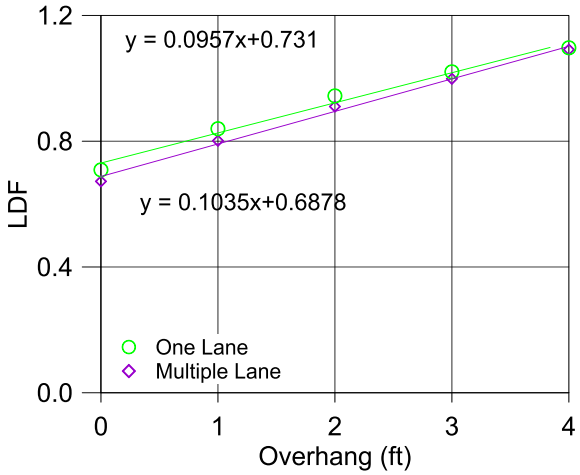

(d) Exterior Beam Shear

Figure 8.5. Effect of Overhang on LDFs.

Figure 8.6 shows the ratio of LDFs at a given overhang length to the zero length overhang case. These ratios were plotted and a linear least square (LS) fit was found. The equation of the LS best fit regression defines the correction factor. Both moment and shear LDFs increases with overhang. Shear LDFs were more sensitive to changes in the overhang compared to moment LDFs.

8.3.3 Effect of Haunch Thickness

The haunch thickness slightly increases the girder stiffness, which would attract more moment and shear, if the girders had differential haunch thicknesses. In most practical applications prestressed slab beam girders are produced under identical conditions which results in the same haunch thickness for all girders. Because there is no relative difference between the haunch thicknesses, an additional haunch thickness does not affect load sharing between girders.

A total of five FEM models having haunch thicknesses from 0 in. to 4 in. were analyzed and the LDFs for moment and shear were calculated. These LDF values were plotted versus the haunch thickness for visual inspection. Figure 8.7 shows the variation of LDFs as the haunch thickness increases. Haunch thickness does not have a significant effect on either moment or shear LDFs as the LS best fit has almost a horizontal trend for all LDF cases.

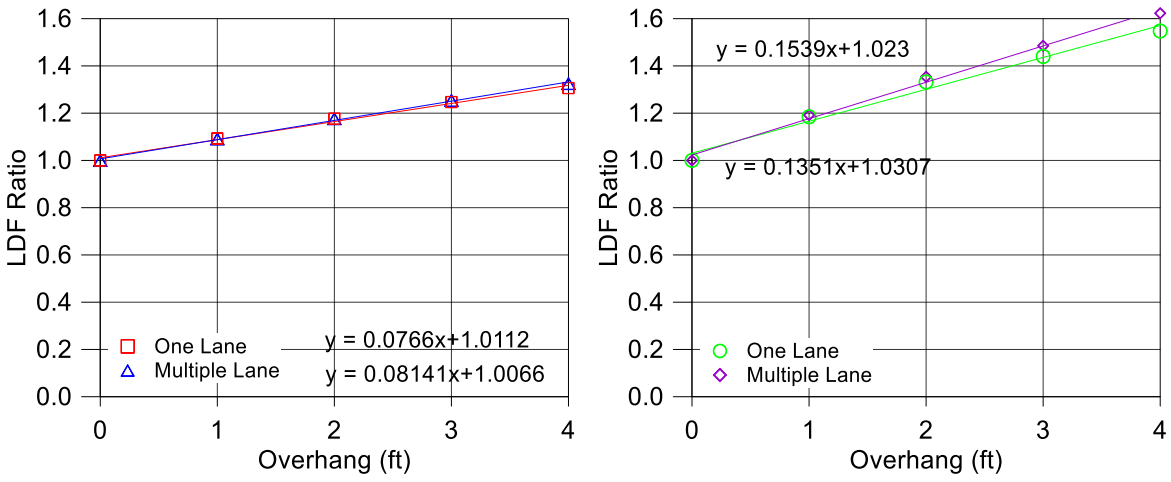

(a) Moment (b) Shear

Figure 8.6. Overhang Correction Factor for Exterior Beams.

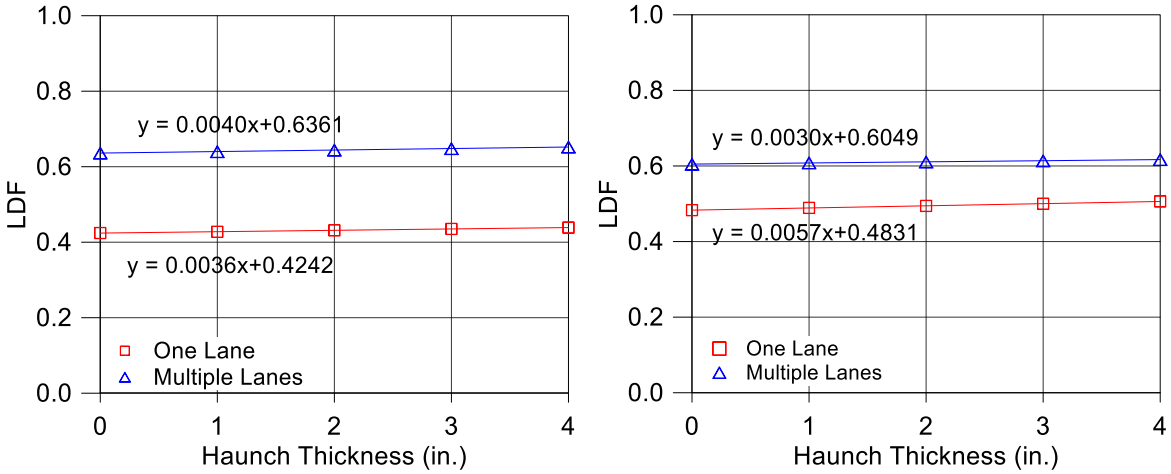

(a) Interior Beam Moment

(b) Exterior Beam Moment

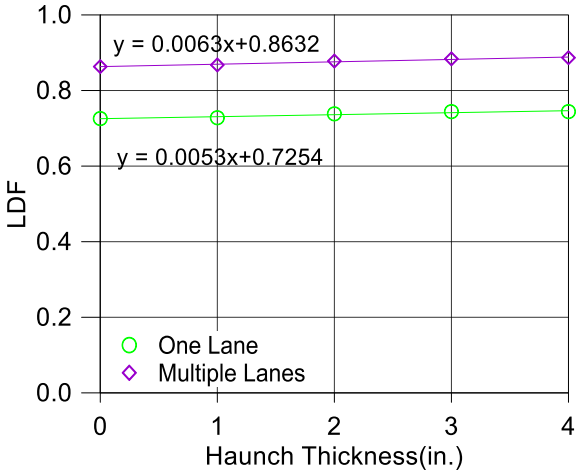

(c) Interior Beam Shear

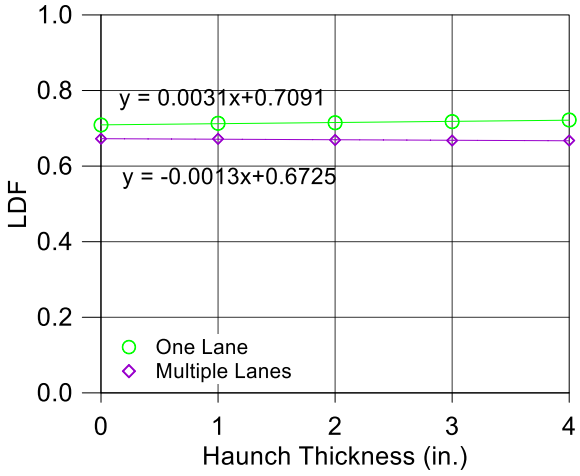

(d) Exterior Beam Shear

Figure 8.7. Effect of Haunch Thickness on LDFs.

8.4 EFFECT OF LOAD VARIATIONS ON LDF

Researchers have long been studied different vehicle loadings that create adverse load cases. These loading conditions include the variation in the axle width, axle spacing, vehicle edge distance, and existence of constant car traffic. The AASHTO LRFD Specifications (2012) utilize the HL93 loading, which has been investigated by several researchers and demonstrated to provide a sufficient representation of actual vehicle loading that exists throughout the United States. HL93 loading requires HS20 or tandem loading, whichever produces higher demand,

together with a 0.64 kips/ft uniform distributed lane load to account for existing car traffic. In this study, the HL93 loading is considered to model the vehicle traffic on the bridge accurately and therefore axle width and axle spacing were not investigated.

An additional parameter VED, which has been neglected in the HL93 load model, was also investigated. AASHTO LRFD Specifications (2012) assume that the vehicle may travel up to 2 ft from the face of the rail or the edge of the design lane and LDFs were derived assuming this criteria. This requirement dictates that the truck cannot be closer than 2 ft from the edge of a bridge. However, field investigations show that in some cases a turning lane may allow vehicles to travel along the edge of a bridge. Although this is not critical for interior girders, it may significantly affect the exterior girder moment and shear demands.

The AASHTO LRFD Specification (2012) HL93 load model is based on truck plus lane loading. Although the LDFs provided in AASHTO LRFD were derived using truck loads alone, lane loading uses the same LDFs. The sensitivity of LDFs to load type was also investigated to evaluate any potential differences. In this study truck plus lane loading were adapted for the derivation of LDF equations and correction factors.

Table 8.4 lists the LDFs obtained for the parametric study conducted for seven different analyses, four of them were for the effect VED and three for effect of load type. The first group of analyses were conducted by changing the vehicle edge distance from 0 ft to 3 ft while keeping all other parameters constant. Only the exterior beam LDFs were investigated, because the assigned positions did not create critical loading for the interior girder. The second group of analyses were conducted to investigate the effect of load type by analyzing the baseline bridge with the HS20 truck alone, lane loading alone, and HS20 plus lane loading combined.

Table 8.4. LDFs for Investigating Effect of Load Type and Vehicle Edge Distance.

							One Lane Loaded				Multiple Lanes Loaded			
							Interior Beam		Exterior Beam		Interior Beam		Exterior Beam	
							Vehicle Edge Distance							
No.	L	No. of Beams	Beam Type	S (ft)	Bridge Width (ft)	d_{ve} (ft)	g_M	g_V	g_M	g_V	g_M	g_V	g_M	g_V
18	45′- 7″	4	5SB15 d = 15"	9.67	34	0	0.37	0.22	0.53	0.89	0.60	0.61	0.65	0.82
19						1	0.37	0.29	0.51	0.81	0.61	0.67	0.63	0.75
20						2	0.38	0.40	0.48	0.69	0.62	0.75	0.60	0.65
21						3	0.39	0.46	0.46	0.62	0.62	0.80	0.58	0.59
						Load	Load Type							
22	45′- 7″	4	5SB15 d = 15"	9.67	34	Lane	0.38	0.60	0.47	0.71	0.62	0.84	0.60	0.67
23						HS20	0.44	0.76	0.49	0.71	0.64	0.88	0.62	0.68
24						Lane + HS20	0.42	0.73	0.49	0.71	0.64	0.86	0.61	0.67

8.4.1 Effect of Vehicle Edge Distance

Figure 8.8 shows the sensitivity of LDFs to VED. This parametric variation was aimed to investigate the effect of VED on exterior girder LDFs. Interior girder shear LDFs are also plotted for completeness. Interior beam shear LDFs increase with the VED as the vehicle gets closer to the interior beam. However the critical LDF value for an interior beam was not obtained with the loading cases investigated herein.

Exterior beam LDFs become larger as the VED approaches zero. Shear LDFs were more sensitive to VED than the moment LDFs. The baseline bridge used a minimum 2 ft VED as the most critical case for deriving the LDF equations. Therefore a correction factor for the exterior beam shear and moment LDFs was necessary. When the vehicle travels along the edge (VED = 0), exterior girder moment LDFs may increase up to 14 percent and shear LDFs may increase up to 30 percent compared to 2 ft edge distance.

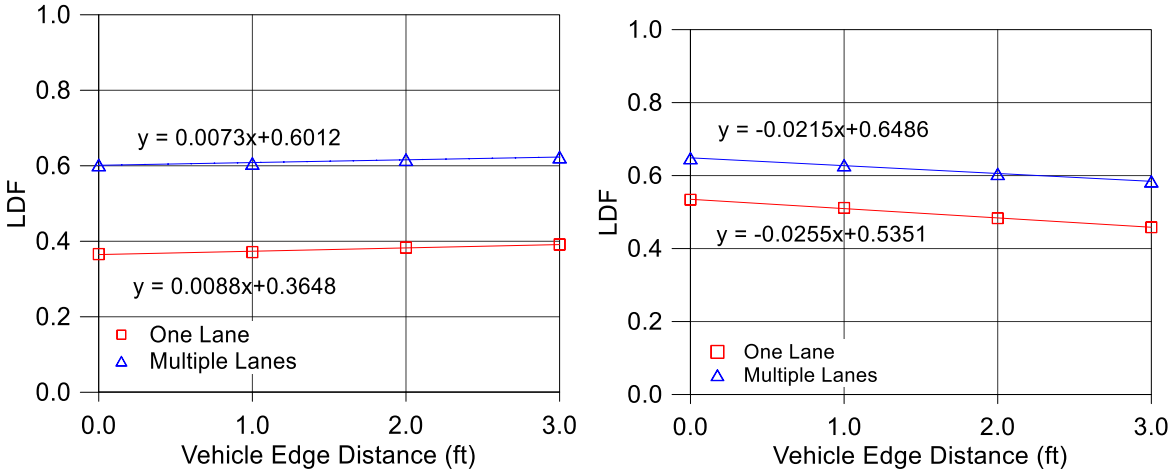

(a) Interior Beam Moment

(b) Exterior Beam Moment

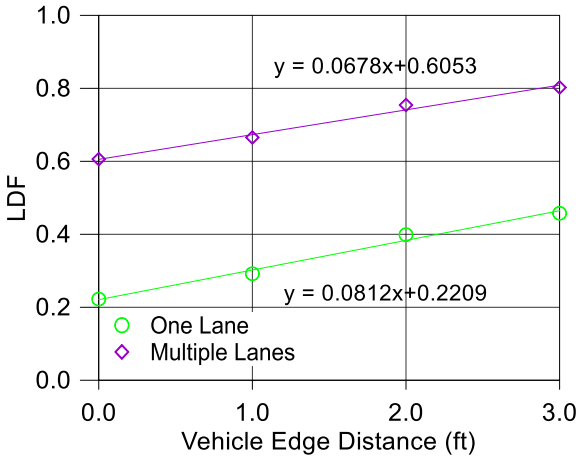

(c) Interior Beam Shear

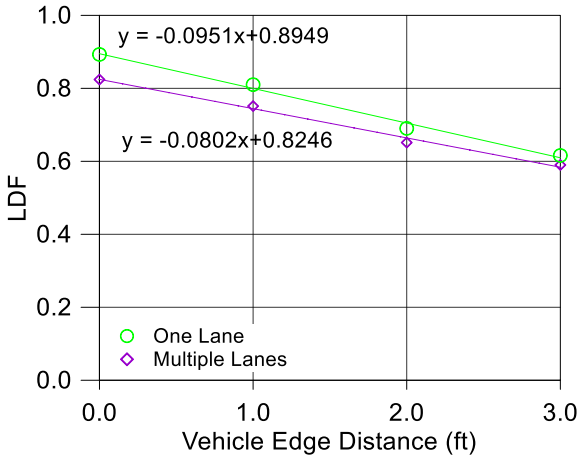

(d) Exterior Beam Shear

Figure 8.8. Effect of VED on LDFs.

Figure 8.9 shows the ratio of LDFs at any VED to the LDFs when VED = 2 ft versus the VED. Linear least-square (LS) best fit relations were determined for all four exterior beam LDF cases. The equations for these functions provide the best fit correction factor through the four data points.

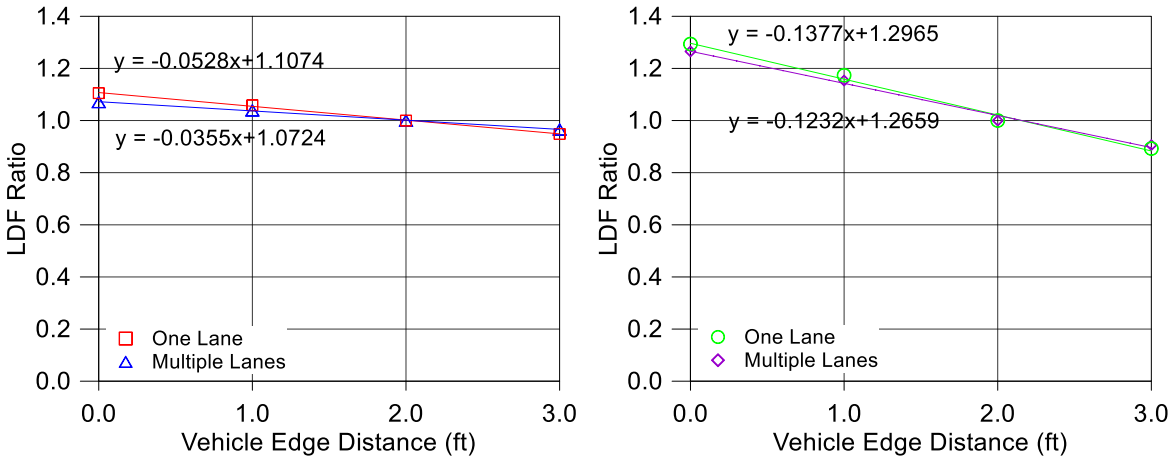

(a) Moment (b) Shear

Figure 8.9. VED Correction Factor for Exterior Beam.

8.4.2 Effect of Load Type

In practice the design moments and shears include lane loading, which provides a significant portion of the design forces. Hence, the lane loading was included in all the FEM analysis for deriving LDF equations and correction factors. The derivation of the LDF equations for the AASHTO LRFD Specifications (2012) did not consider lane loading. The analysis showed that the bridges that were analyzed with only lane loading have smaller moment and shear reactions compared to only truck loading due to better, more uniform distribution of loads.

Three different load cases were investigated by analyzing the base bridge under lane load only, truck load only, and truck plus lane load. The loads were applied along the same transverse alignments as before, which produces the critical moment and shear actions.

Figure 8.10 shows bar charts comparing the LDFs for three load types. When only lane loading was applied the interior beam moment LDF was 14 percent smaller for the one lane loaded case and the shear LDF was 25 percent smaller compared to only truck loading. Whereas the reduction of LDFs for multiple-lane-loaded cases was only about 5 percent.

On the other hand, truck plus lane loading produces LDFs close to truck only cases. HS20 plus lane loading always gives slightly (around 1-3 percent) lower LDFs than the only HS20 loaded case. This observation shows that using only vehicle loading produces slightly conservative results compared to vehicle plus lane loading.

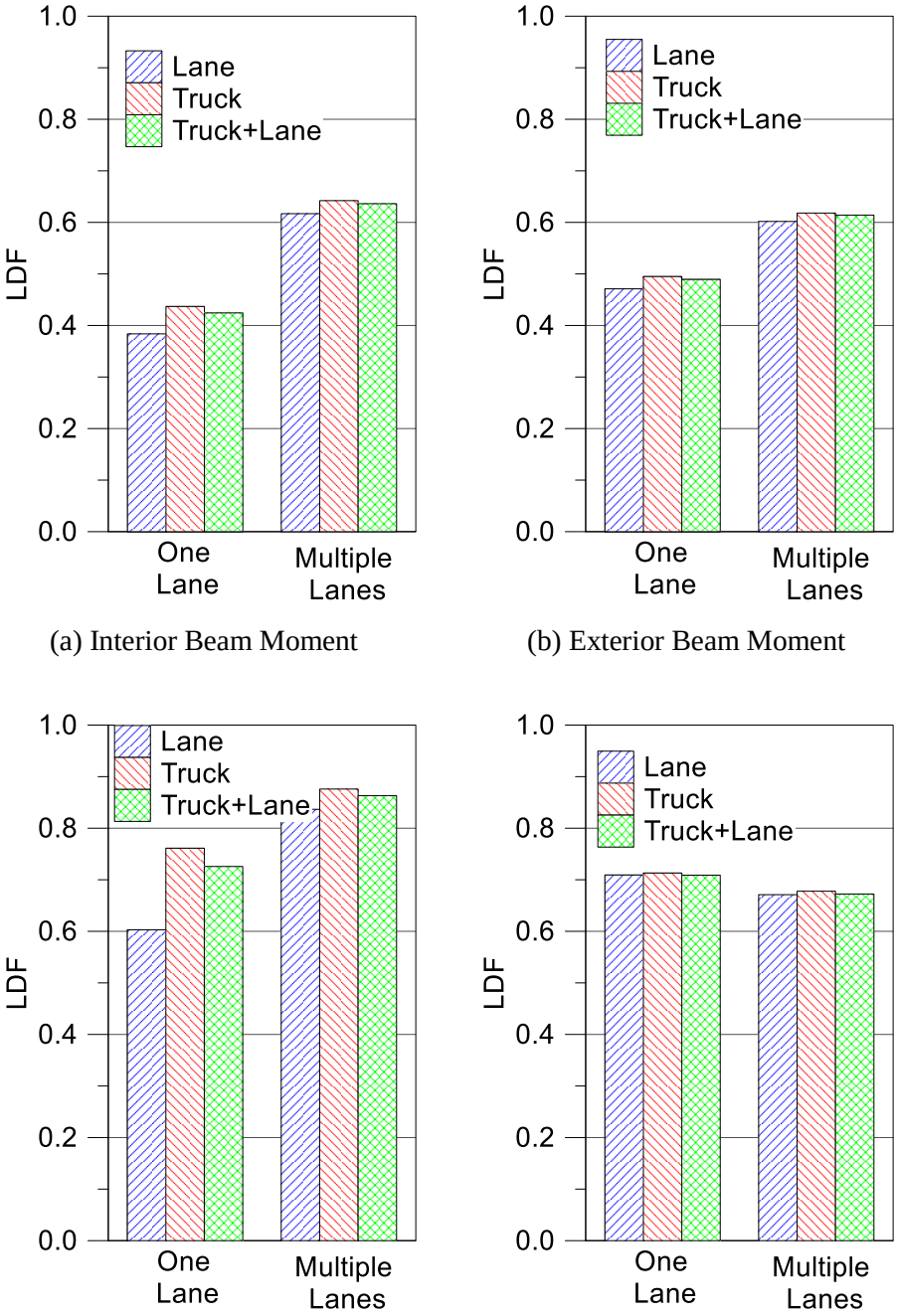

(a) Interior Beam Moment

(b) Exterior Beam Moment

(c) Interior Beam Shear

(d) Exterior Beam Shear

Figure 8.10. Effect of Load Type.

8.5 VALIDATION OF CORRECTION FACTORS FOR KEY PARAMETERS

The sensitivity of LDFs to the studied parameters were investigated and three parameters have found to be significant. These parameters are skew angle, overhang, and vehicle edge distance. The methodology and graphs for theoretical best fit equations were documented in the Section 8.3.

Table 8.5 summarizes the correction factor equations obtained with the linear LS best fit analysis and provides the R-squared values for these best fit regression curves. Overhang and VED correction factors were calculated for exterior girders only because interior girders are not sensitive to these parameters. Skew angle correction factors were derived using $cos\theta$ and $sin\theta$ relations, because they provided a better fit to the available LDF data compared to the $tan\theta$ used in the AASHTO LRFD Specifications (2012) correction factors.

Table 8.5. Formulas of the Fitted Curves.

			θ		d_e		d_{ve}	
			r	R^2	r	R^2	r	R^2
Moment LDF	Interior Beam	One Lane Loaded	$(\cos\theta)^{0.8186}$	0.95	-	-	-	-
		Multiple Lanes Loaded	$(\cos\theta)^{0.9345}$	0.99	-	-	-	-
	Exterior Beam	One Lane Loaded	$(\cos\theta)^{0.6975}$	0.94	$1.012 + 0.077d_e$	0.990	$1.107 - 0.053d_{ve}$	0.99
		Multiple Lanes Loaded	$(\cos\theta)^{1.0671}$	0.99	$1.005 + 0.077d_e$	0.990	$1.072 - 0.036d_{ve}$	0.99
Shear LDF	Exterior Beam	One Lane Loaded	$1.02 + 0.44\sin\theta$	0.93	$1.039 + 0.119d_e$	0.97	$1.297 - 0.138d_{ve}$	0.99
		Multiple Lanes Loaded	$1.03 + 0.55\sin\theta$	0.91	$1.047 + 0.139d_e$	0.97	$1.266 - 0.123d_{ve}$	0.99

8.5.1 Formulating the Proposed Correction Factors

Table 8.6 lists the LDF equations for skew angle correction factors. The AASHTO LRFD Specifications (2012) spread box beam correction factors were evaluated for their applicability. More realistic proposed equations were found through reexamination by adjusting the resulting empirical best fit relations calculated in the previous section. Equations were adjusted such that there is about 5 percent non exceedance probability of occurrence.

Least squares best fit power equations were used for derivation of moment reduction factors rather than the linear relation used in the AASHTO LRFD Specifications (2012). Power relations provide a slightly better fit and simplified formulas. On the other hand linear best fit relations were used for shear LDFs, but unlike AASHTO LRFD Specifications (2012), dependence on key parameters (L,S and d) was eliminated for the simplified formulation.

A total of 16 bridges were modeled and analyzed using FEM in order to find the best fit correction factor equations for the three parameters under consideration. Because some assumptions were made and only one baseline bridge geometry was used for the parametric investigation, it was considered important to verify the accuracy of the correction factors using alternative geometries. Four more bridge superstructures using 4SB12 slab beams were modeled and analyzed. Two of the bridges had 45 and 50 degree skew angles, while the third one had a 4 ft overhang, and the last one was analyzed with zero vehicle edge distance. The detailed geometries of these additional bridges are provided in Table 8.1. The LDFs obtained from FEM analysis for these four additional models were also included in the final adjustment of the proposed correction factors.

Table 8.7 and Table 8.8 provide correction factors for overhang and vehicle edge distance, respectively. The AASHTO LRFD Specifications (2012) does not have any correction factor for overhang and vehicle edge distance. LDFs calculated from accurate FEM analysis were than compared with those calculated from AASHTO LRFD spread box beam equations, the LS best fit equations, and the proposed equations. The comparison of these LDF values are shown in Figure 8.11 through Figure 8.15. Also cumulative distributions of LDF ratios (LS fitted/FEM, Proposed/FEM and AASHTO/FEM) are plotted to better observe the relative dispersion in the computed outcomes. A lognormal distribution is fitted to the final adjusted empirical data as a solid red line in the figures.

Table 8.6. LDF Reduction Factors for Skew Angle.

			AASHTO Spread Box Beam Correction Factor	Least Square Fitted Correction Factor	Proposed Correction Factor	Range of Applicability for Proposed Correction Factors
Moment LDF	Interior Beam	One Lane Loaded	$1.05 - 0.25\tan\theta \le 1.0$	$(\cos\theta)^{0.8186}$	$(\cos\theta)^{0.7}$	$0^\circ \le \theta \le 60^\circ$
		Multiple Lanes Loaded	$1.05 - 0.25\tan\theta \le 1.0$	$(\cos\theta)^{0.9345}$	$(\cos\theta)$	
	Exterior Beam	One Lane Loaded	$1.05 - 0.25\tan\theta \le 1.0$	$(\cos\theta)^{0.6975}$	$(\cos\theta)^{0.7}$	
		Multiple Lanes Loaded	$1.05 - 0.25\tan\theta \le 1.0$	$(\cos\theta)^{1.0671}$	$(\cos\theta)$	
Shear LDF	Exterior Beam	One Lane Loaded	$1.0 + \frac{\sqrt{\frac{Ld}{12}}}{6S}\tan\theta$	$1.02 + 0.44\sin\theta$	$1.0 + 0.75\sin\theta$	
		Multiple Lanes Loaded	$1.0 + \frac{\sqrt{\frac{Ld}{12}}}{6S}\tan\theta$	$1.03 + 0.55\sin\theta$	$1.0 + 0.75\sin\theta$	

Table 8.7. Correction Factors for Overhang.

			Least Square Fitted Correction Factor	Proposed Correction Factor	Range of Applicability for Proposed Correction Factors
Moment LDF	Exterior Beam	One Lane Loaded	$1.012 + 0.077d_e$	$1.0 + 0.08d_e$	$0 \text{ ft} \le d_e \le 4 \text{ ft}$
		Multiple Lanes Loaded	$1.005 + 0.077d_e$	$1.0 + 0.08d_e$	
Shear LDF	Exterior Beam	One Lane Loaded	$1.039 + 0.119d_e$	$1.0 + 0.17d_e$	
		Multiple Lanes Loaded	$1.047 + 0.139d_e$	$1.0 + 0.17d_e$	

Table 8.8. Correction Factor for Vehicle Edge Distance.

			Least Square Fitted Correction Factor	Proposed Correction Factor	Range of Applicability for Proposed Correction Factors
Moment LDF	Exterior Beam	One Lane Loaded	$1.107 - 0.053d_{ve}$ $d_{ve} \le 2$ ft	$1+\left\langle \frac{2-d_{ve}}{20} \right\rangle$	$0 \text{ ft} \le d_{ve} \le 3 \text{ ft}$
		Multiple Lanes Loaded	$1.072 - 0.036d_{ve}$ $d_{ve} \le 2$ ft	$1+\left\langle \frac{2-d_{ve}}{20} \right\rangle$	
Shear LDF	Exterior Beam	One Lane Loaded	$1.297 - 0.138d_{ve}$ $d_{ve} \le 2$ ft	$1+\left\langle \frac{2-d_{ve}}{8} \right\rangle$	
		Multiple Lanes Loaded	$1.266 - 0.123d_{ve}$ $d_{ve} \le 2$ ft	$1+\left\langle \frac{2-d_{ve}}{8} \right\rangle$	

8.5.2 LDFs for Moment in Interior Beams

A total of 20 bridges were modeled and analyzed for developing correction factors for three additional parameters. The LDF values were calculated by multiplying the corresponding LDFs with a correction factor. The correction factor might be a skew correction, overhang correction or VED correction depending on the parameter.

For moment in interior beams only nine bridges were plotted because other bridge geometries do not have correction factors for interior beams and they are irrelevant to the parametric study for moment in interior beams. All LDFs were plotted against those obtained from FEM analyses, where FEM results are considered to be "exact".

Figure 8.11 shows the comparison for one-lane-loaded moment LDFs in interior beams with the corresponding FEM values. Each data point on the graphs represent a LDF value corresponding to one of the bridge models. Figure 8.11(d) presents the cumulative probabilities of each LDF point. The red solid line represents the model curve of proposed corrected LDFs. Proposed LDFs were adjusted with an approximately 5 percent exceedance limit, and therefore provide slight conservatism for most analyzed cases. On the other hand the AASHTO LRFD equations, which were calculated by multiplying the corresponding LDF with skew reduction factors, gives unconservative values for almost half of the analyzed geometries.

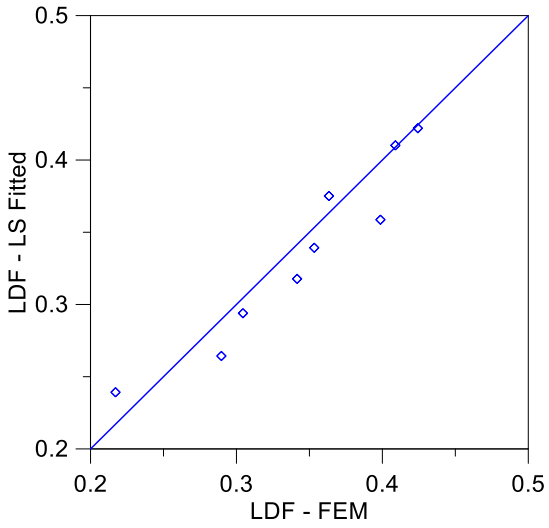

(a) LS Fitted vs FEM

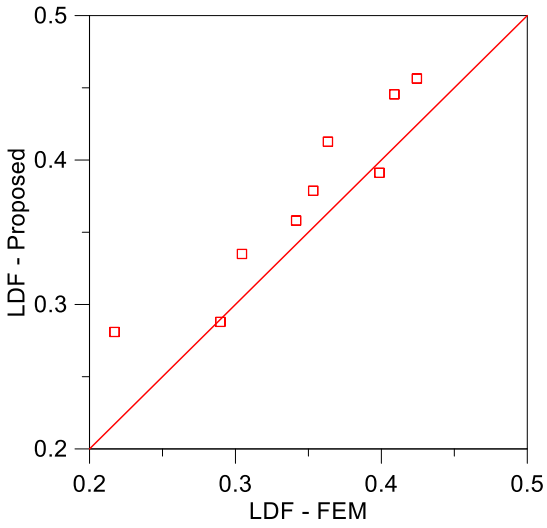

(b) Proposed vs FEM

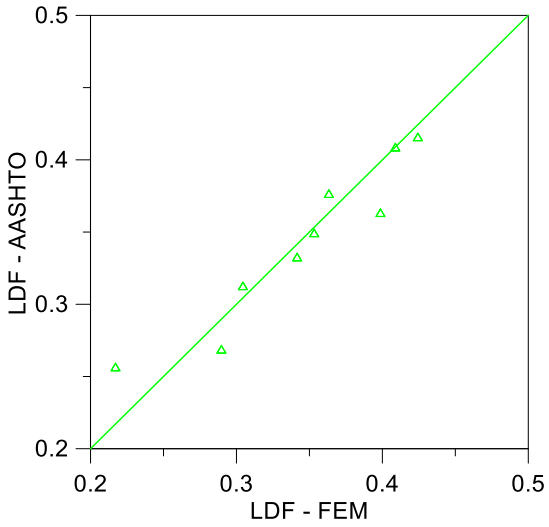

(c) AASHTO Spread Box vs FEM

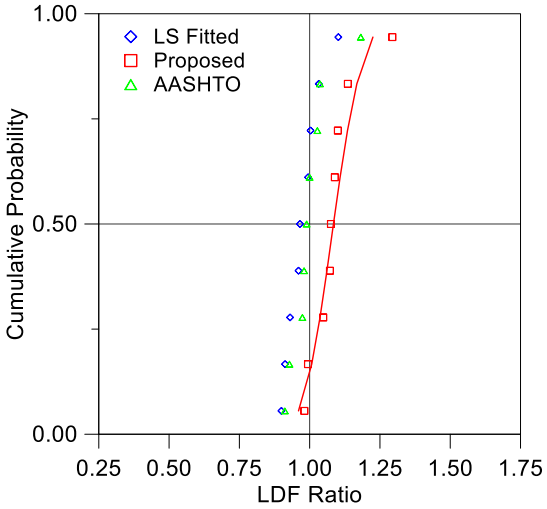

(d) Cumulative Probabilities of LDF Ratios

Figure 8.11. LDF Comparison for One-Lane-Loaded Moment in Interior Beams.

Figure 8.12 shows the comparison of moment LDFs in interior beams for multiple lane loaded bridges. LDF values calculated using the proposed equations are slightly conservative as intended. On the other hand AASHTO LRFD Specifications (2012) spread box beam reduction factors result in up to 20 percent conservative values. The AASHTO reduction factor uses a linear best fit relation with $tan\theta$ for modeling the effect of skew. A proposed equation having a similar format as AASHTO LRFD Specification (2012) could be used, but a more straight forward formula that uses a cosine function is proposed instead.

8.5.3 LDFs for Moment in Exterior Beams

Figure 8.13 shows the comparison of moment LDFs in exterior beams for the one-lane-loaded case. The proposed equations are intentionally derived with a 5 percent non-exceedance limit. This intentional result can be seen from the comparative plot or cumulative probability plot. The AASHTO LRFD Specifications (2012) values are overly conservative despite the applied reduction factor. The AASHTO LRFD suggests using the lever rule for one-lane-loaded moment LDFs in exterior beams; this results in values that are typically 50 percent conservative when no reduction factor is applied as in the case of overhangs.

Figure 8.14 shows the comparison of moment LDFs in exterior beams for multiple-lane-loaded case. The comparison reveals that the AASHTO LRFD Specification (2012) moment reduction factors result in overly conservative results for skew angles larger than 30 degrees. Although the AASHTO LRFD Specifications (2012) LDF equations do not provide correction factors for overhang and vehicle edge distance, they result in slightly conservative results most of the time, because of the inherent conservatism in the original LDF equation. This inherent conservatism was observed in the previous section for the LDF equation when no overhang or VED was considered.

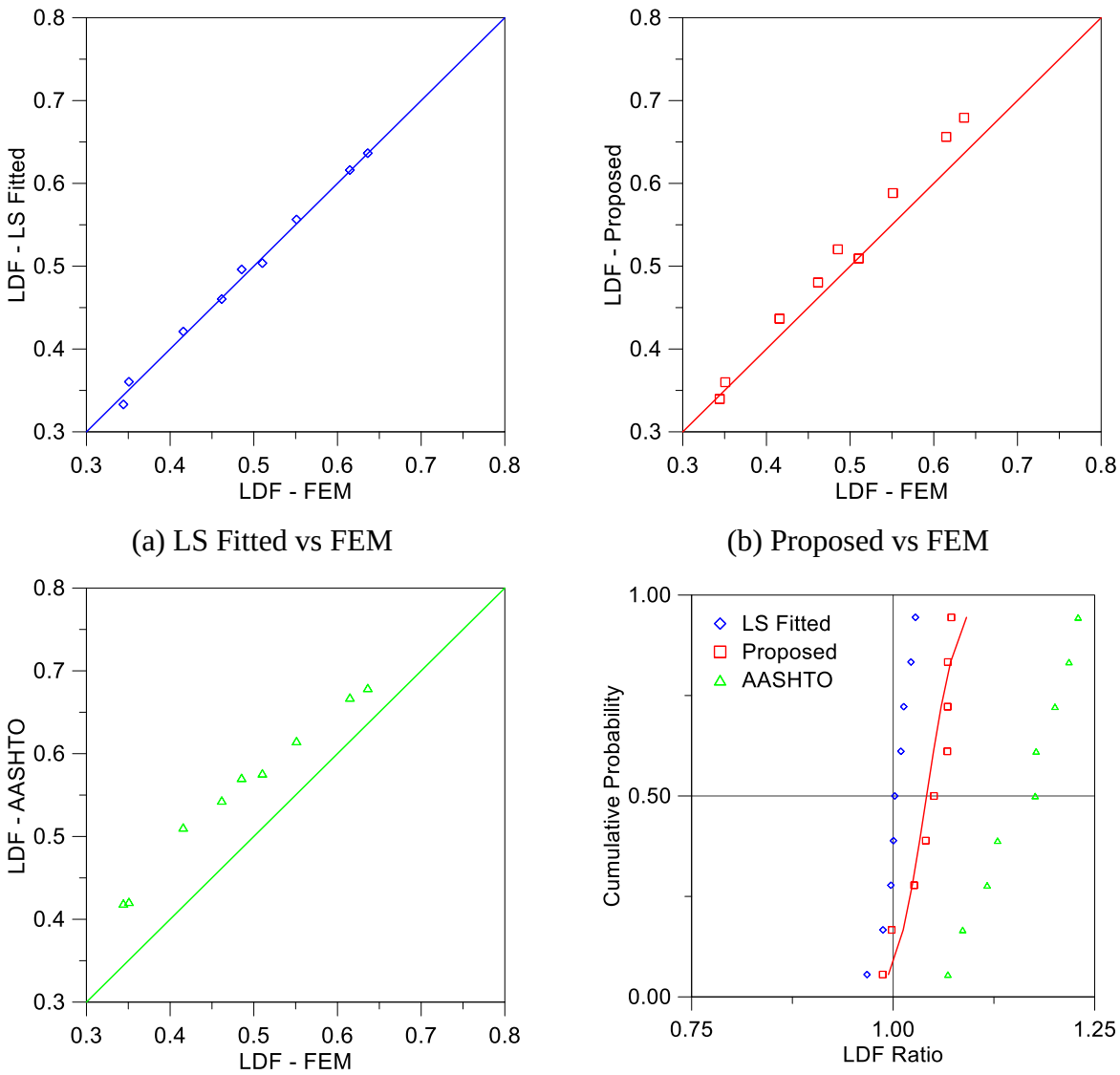

(a) LS Fitted vs FEM

(b) Proposed vs FEM

(c) AASHTO Spread Box vs FEM

(d) Cumulative Probabilities of LDF Ratios

Figure 8.12. LDF Comparison for Multiple-Lanes-Loaded Moment in Interior Beams.

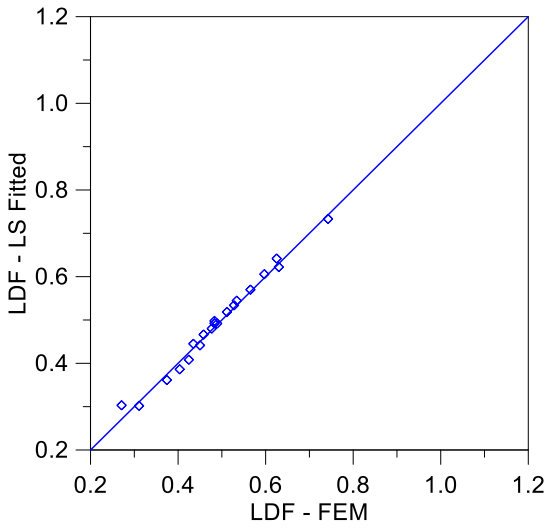

(a) LS Fitted vs FEM

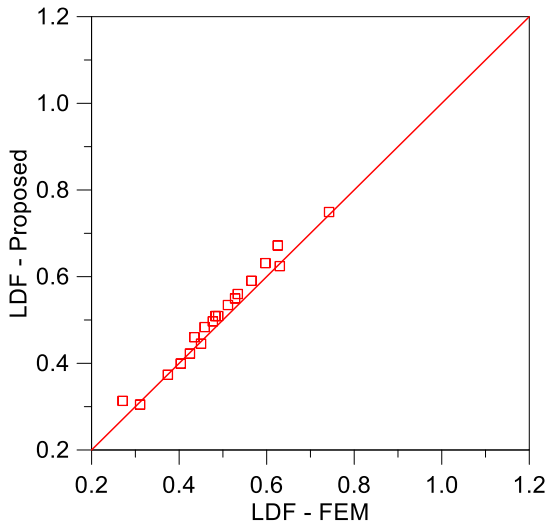

(b) Proposed vs FEM

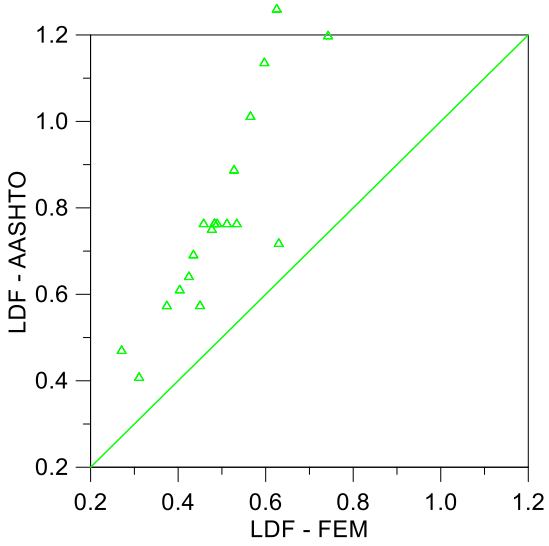

(c) AASHTO Spread Box vs FEM

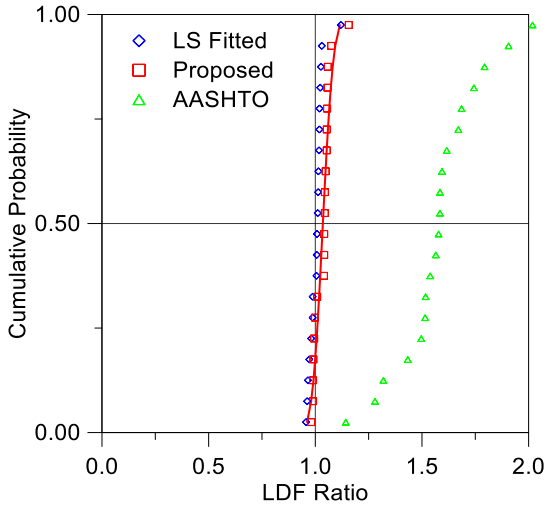

(d) Cumulative Probabilities of LDF Ratios

Figure 8.13. LDF Comparison for One-Lane-Loaded Moment in Exterior Beams.

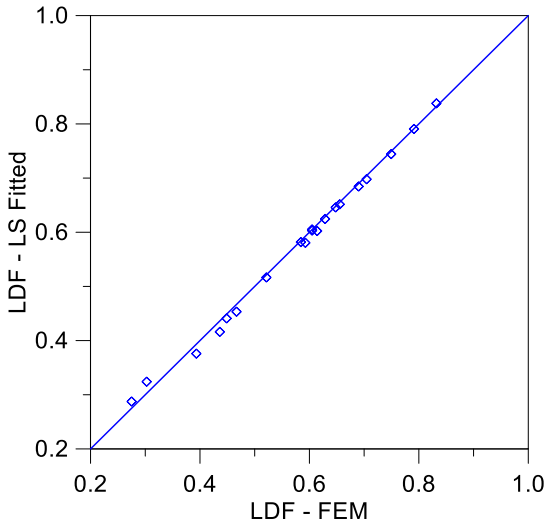

(a) LS Fitted vs FEM

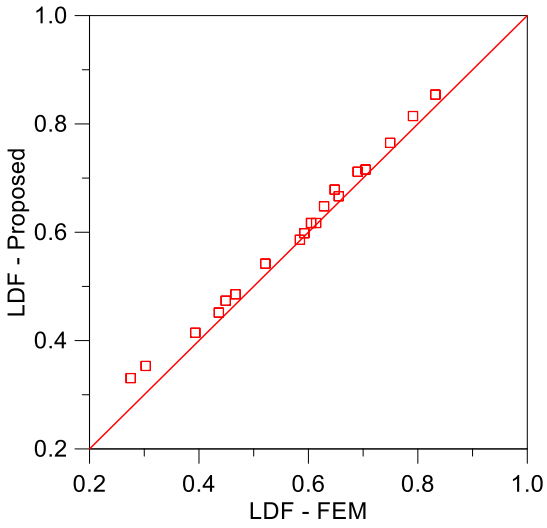

(b) Proposed vs FEM

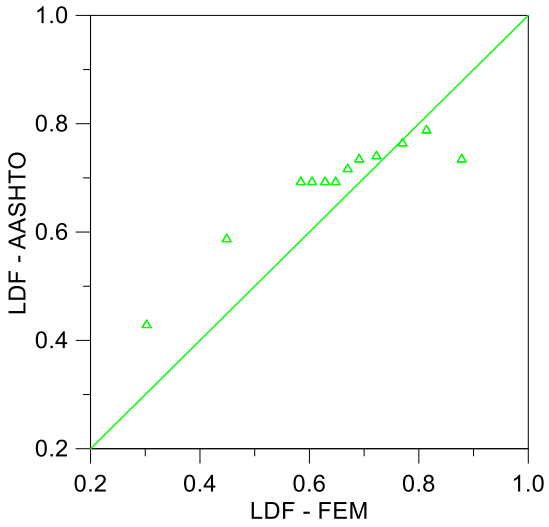

(c) AASHTO Spread Box vs FEM

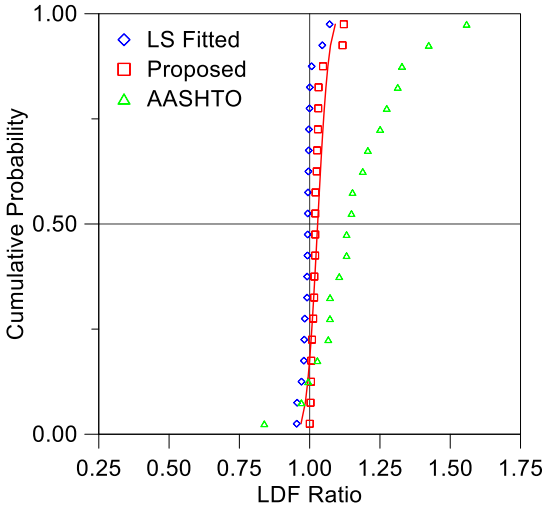

(d) Cumulative Probabilities of LDF Ratios

Figure 8.14. LDF Comparison for Multiple-Lanes-Loaded Moment in Exterior Beams.

8.5.4 LDFs for Shear in Exterior Beams

Skew reduction factors for shear LDFs in exterior beams were derived using a LS best fit linear equation in the previous section. It can be observed that the LDF values increase for up to a 40 degree skew then there is slight decrease for skews up to 60 degrees. Although this type of data can best be modeled with a polynomial curve, a linear best fit relation with sine functions were used because this provides a simple equation and give sufficiently close results. Figure 8.15 shows the comparison of shear LDFs in interior beams for the one-lane-loaded case. The proposed correction factors are about 20 percent conservative for skew angles larger than 50 degrees.

On the other hand the AASHTO LRFD Specifications (2012) LDF correction factors are unconservative for skew angles larger than 30 degrees despite the overly conservative nature of the original LDF equations. Although there is no correction factors for overhang, the AASHTO LRFD equation results in slight conservative values because of the overly conservative LDF equations for shear in exterior beams.

Figure 8.16 presents the LDF comparison for shear in exterior beams for the multiple-lanes-loaded case. The AASHTO LRFD values change from being unconservative to very conservative. On the other hand the proposed equations results in slight conservative values for most cases.

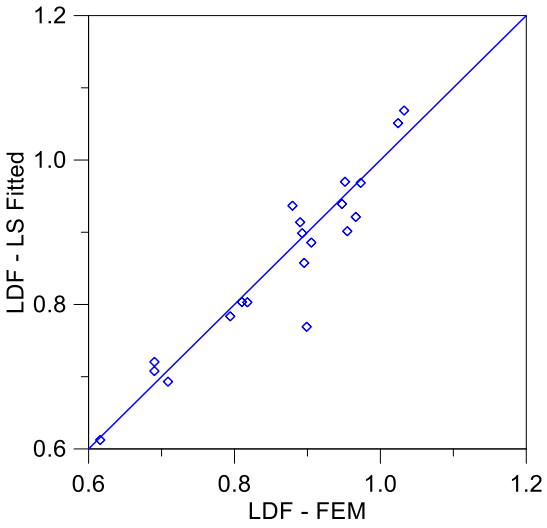

(a) LS Fitted vs FEM

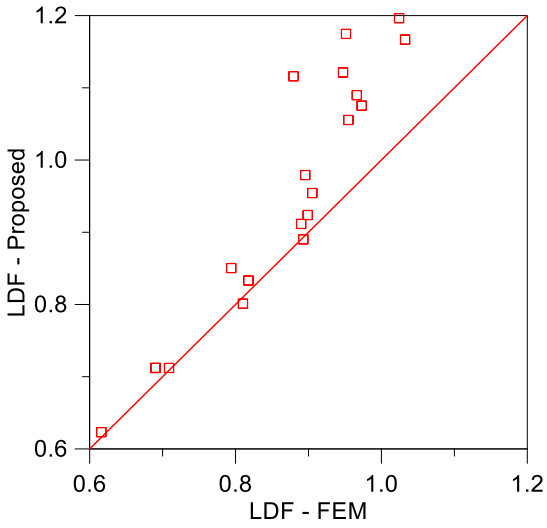

(b) Proposed vs FEM

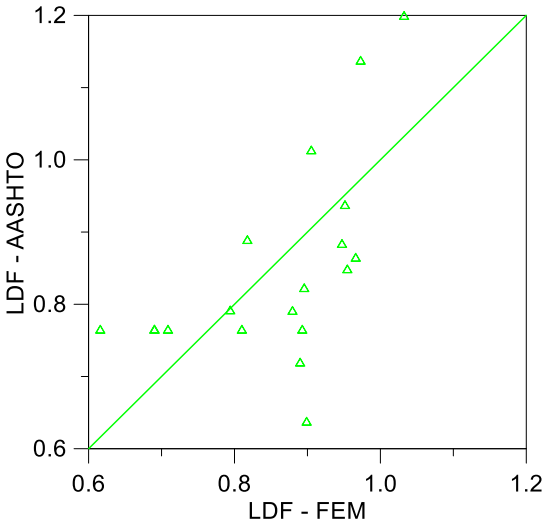

(c) AASHTO Spread Box vs FEM

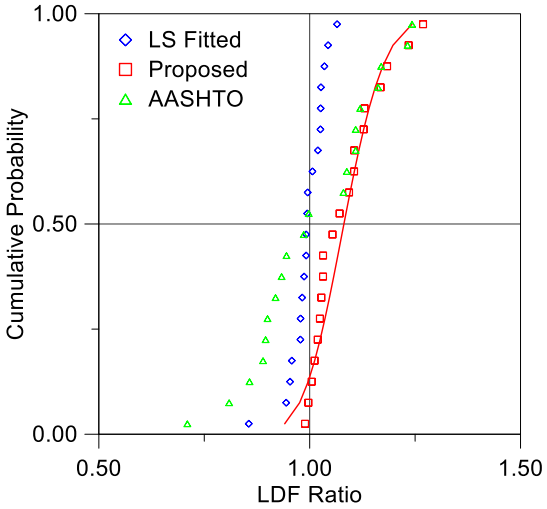

(d) Cumulative Probabilities of LDF Ratios

Figure 8.15. LDF Comparison for One-Lane-Loaded Shear in Exterior Beams.

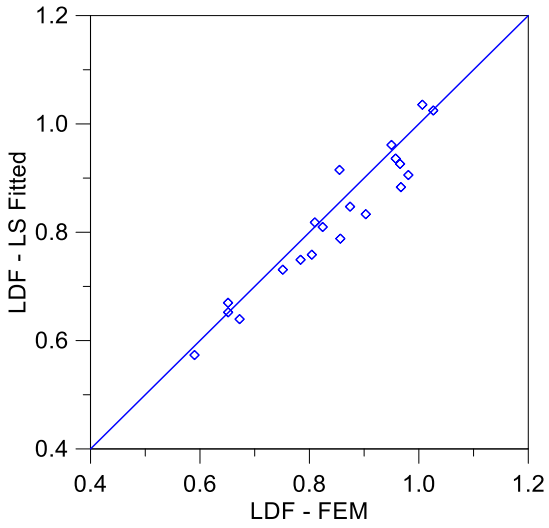

(a) LS Fitted vs FEM

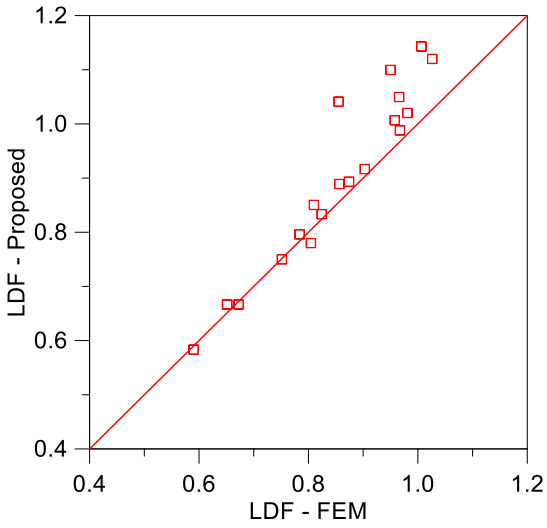

(b) Proposed vs FEM

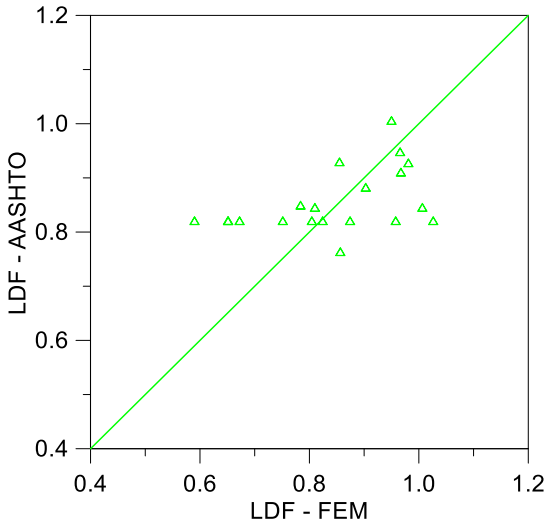

(c) AASHTO Spread Box vs FEM

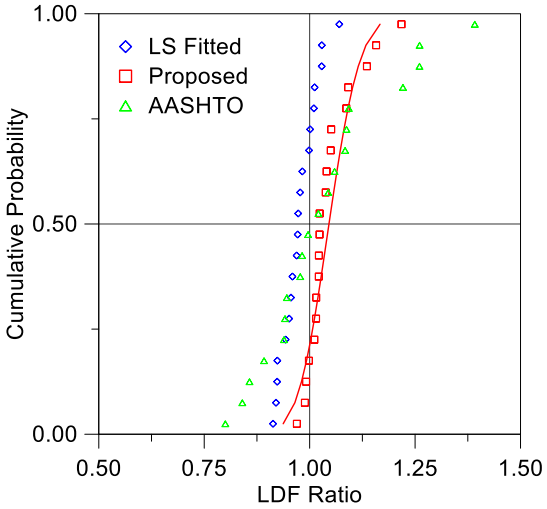

(d) Cumulative Probabilities of LDF Ratios

Figure 8.16. LDF Comparison for Multiple-Lanes-Loaded Shear in Exterior Beams.

8.6 DISCUSSION

Correction factors were developed for skew angle, overhang, and vehicle edge distance. Based on the comparative study conducted for these three sets of parameters, simplified correction factors were developed for spread slab beam bridges to provide a sufficient level of conservatism.

The AASHTO LRFD spread box beam equations together with skew correction factors range from being overly conservative to unconservative. The AASHTO LRFD skew reduction factors result in slightly conservative LDF values for moment in interior beams for multiple-lanes-loaded case. However, they are slightly unconservative for one-lane-loaded case. They give very conservative results for moment in exterior beams. On the other hand they are unconservative when the overhang is larger than 3 ft because AASHTO LRFD does not provide correction for overhang.

In practice exterior girders are designed the same as an interior girder to take into account the possible future widening of a bridge, as long as the design is conservative. Considering this common practice the applicability of proposed interior LDFs to exterior beams was evaluated to observe if the correction factors for VED and overhang are necessary when all beams are designed as interior beams.

Figure 8.17 shows the comparison of the proposed interior beam LDFs to the exterior beam LDF values obtained from FEM. Solid symbols are for VED parameter (d_{ve} = 0 ft, 1 ft, 2 ft, 3 ft right to left) and empty symbols represent overhang length (d_e = 0 ft, 1 ft, 2 ft, 3 ft, 4 ft left to right). If the symbol is above the diagonal line, this indicates that the interior beam LDF gives a conservative value for the considered exterior beam. If the exterior beam is designed using the corresponding proposed interior beam LDF equations the following observations can be made.

- In the case of one-lane-loaded analysis, moment LDFs would be unconservative. Shear LDFs would be unconservative for VED $d_{ve} \leq 1$ ft and overhang $d_e \geq 1$ ft.
- In the case of multiple-lanes-loaded analysis, both moment and shear LDFs would be unconservative for overhang $d_e \geq 2$ ft, but they would be conservative for any VED.
- Examining the LDF results reveals that multiple-lanes-loaded cases govern the design at all times for interior beams. Therefore if the exterior girder is designed the same as the interior girder, a correction factor is needed only when the overhang $d_e \geq 2$ ft.

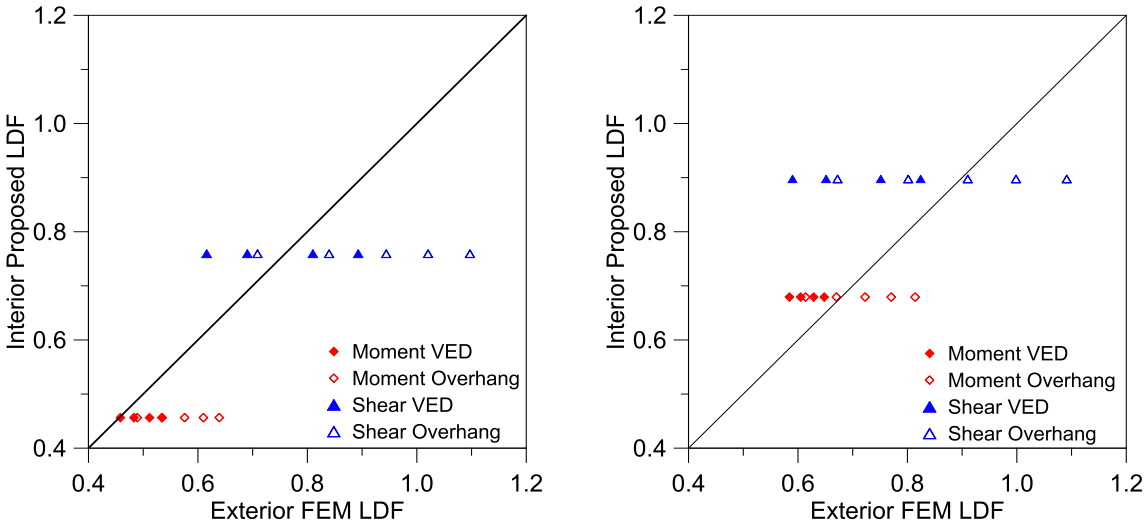

(a) One-Lane-Loaded (b) Multiple-Lanes Loaded

Figure 8.17. Comparison of Interior Proposed to Exterior FEM LDFs

8.7 CONCLUSIONS

The sensitivity of moment and shear LDFs in interior and exterior beams for one-lane- or multiple-lanes-loaded cases to several geometric and loading parameters was evaluated. These parameters were skew angle, overhang, haunch thickness, vehicle edge distance, and load type. A total of 28 FEM models were analyzed and LDFs obtained to evaluate these parameters. The range of applicability for proposed LDF design equations and correction factors in the following equations are: 31 ft $\leq L \leq$ 51 ft, 6.5 ft $\leq S \leq$ 11 ft, 12 in. $\leq d \leq$ 21 in., $0^\circ \leq \theta \leq 60^\circ$, 0 ft $\leq d_e \leq$ 4 ft and 0 ft $\leq d_{ve} \leq$ 3 ft The following conclusions were drawn:

1. Variation in the skew angle significantly affects the LDFs for moment in interior and exterior beams. Cosine based correction factors are proposed. In addition, the shear LDFs of the obtuse angle end of the exterior beams increases considerably and sine based correction factor are proposed accordingly. When all girders are designed based on interior girder demands, the two governing proposed correction factors for skew for multiple-lanes-loaded interior beams are:

   For moments: $\cos\theta$

   For shear: $1.0 + 0.75\sin\theta$

2. Variation in overhang and vehicle edge distance increases moment and shear LDFs in exterior beams. On the other hand, interior beam LDFs are not affected considerably by these parameters. Hence proposed correction factors were derived for shear and moment LDFs in exterior beams. The proposed corrections factors are:

   For moments: $VED = 1 + \left\langle \frac{2 - d_{ve}}{20} \right\rangle$, Overhang $= 1 + 0.08 d_e$

   For shear: $VED = 1 + \left\langle \frac{2 - d_{ve}}{8} \right\rangle$, Overhang $= 1 + 0.17 d_e$

3. LDFs are not sensitive to changes in haunch thickness. Although haunch thickness increases the stiffness of the composite section, it does not change the LDFs because the haunch thickness was considered to increases the same amount for all girders.
4. When the analysis were done with only uniform lane loading, LDF values are about 15 to 25 percent lower compared to the only truck loaded analysis. On the other hand, truck plus lane loading gives only 1-3 percent lower LDFs compared to the only truck loaded case.
5. If all beams are designed the same as an interior beam, two governing proposed LDF design equations for multiple-lane-loaded interior beams when the overhang is smaller than 2 ft become:

   For moments: $\left(\frac{S}{6.3}\right)^{0.6} \left(\frac{Sd}{12.0L^2}\right)^{0.125} (\cos\theta)$

   For shear: $\left(\frac{S}{5}\right)^{0.9} \left(\frac{d}{12.0L}\right)^{0.2} (1.0 + 0.75\sin\theta)$

6. An overhang correction factor must be included when the overhang is greater than or equal to 2 ft. Then the combined universal proposed LDF design equation can be expressed as:

   For moments: $\left(\frac{S}{6.3}\right)^{0.6} \left(\frac{Sd}{12.0L^2}\right)^{0.125} (\cos\theta)(1 + 0.08 d_e)$

   For shear: $\left(\frac{S}{5}\right)^{0.9} \left(\frac{d}{12.0L}\right)^{0.2} (1.0 + 0.75\sin\theta)(1 + 0.17 d_e)$

9. SUMMARY, CONCLUSIONS AND RECOMMENDATIONS

9.1 SUMMARY

The Texas Department of Transportation (TxDOT) uses precast prestressed concrete slab beams in a side-by-side configuration especially in low clearance areas for short span bridges ranging from 30−50 ft. While conventional slab beam bridges are used extensively, experience shows they are more expensive than traditional slab-on-I-girder structures on a per square foot basis. Spread slab beam bridges use the same concept as I-girder bridges by spreading the slab beams to reduce the overall cost. The objective of this project is to investigate the use of slab beams that are spread apart with 4 in. thick precast concrete panel (PCP) stay-in-place (SIP) forms between beams and 8 in. thick CIP reinforced concrete topping deck. This research investigated the potential of the spread slab beam bridge systems, evaluated constructability and in-service performance, and developed design recommendations with a focus on appropriate relationships for load distribution factors.

Forty-four variations of spread slab beam bridge geometries were designed using standard TxDOT slab beam types to determine the feasible design space. One of the most aggressive designs with widely spaced slab beams was constructed at full-scale at the Texas A&M University Riverside campus. The bridge was tested under static and dynamic vehicular loads to evaluate constructability, structural performance, and to provide experimental data for verification of computational models.

Alternative modeling approaches including finite element analysis, grillage analysis, and orthotropic plate solutions directly from the governing PDEs were evaluated. Appropriate live load distribution factors for spread slab beams were developed based on analytical models representing the design space for this class of spread slab beam bridge. The LDF equations were developed for key parameters including beam spacing (S), span length (L), and beam depth (d), and the effect of skew and overhang were included as correction factors. Results can be reduced down to two simple formulas for design based LDFs, one for moments and another for shear.

9.2 ALTERNATIVE DESIGNS

9.2.1 Parametric Study

A detailed parametric study was conducted to investigate the design space for spread slab beam bridges. A total of 44 spread slab beams were designed using the maximum permissible concrete design strength. One of the preliminary designs with a large eccentricity due to a wide beam spacing and a relatively longer span length was chosen for the full-scale bridge construction and field testing. Based on the results of the parametric study, the following observations were made.

1. An approximately 50 ft span length is possible for any standard bridge width.
2. Minimum beam spacing was considered as 2 ft. Hence for all bridge widths the maximum achievable span resulted when the beam spacing is close to 2 ft.
    a. For 26 and 30 ft wide bridges, an approximately 50 ft span is achievable, when four 5SB15 slab beams are used.
    b. In order to achieve around 50 ft span length for 40, 42, and 46 ft wide bridges six 5SB15 slab beams must be utilized.
    c. The results of code-based preliminary designs indicate that it is a safe approach to provide two beams per design lane as a rule of thumb.
3. The effect of several critical parameters including beam width, beam depth, number of beams, and beam spacing on the maximum achievable span was investigated.
    a. A smaller beam spacing always results in a longer span length.
    b. For the same number of slab beams, 4SB15 beams allow greater span lengths compared to 5SB12 beams despite a larger beam spacing. This shows that the beam depth effect is more pronounced than the beam spacing and beam width effects.
    c. Beam depth and beam width have a more prominent effect on the maximum span length as compared to the number of beams.

9.2.2 Shear Design

1. The standard transverse shear reinforcement currently provided for TxDOT standard slab beam types satisfies the required transverse shear strength criteria for the critical spread slab beam bridge geometries investigated in the parametric study.
2. The standard interface shear reinforcement currently provided for TxDOT standard slab beam types does not satisfy the required interface shear strength for critical bridge geometries when the beam surface is not intentionally roughened to a 0.25 in. amplitude.
    a. The typical precast manufacturing process currently includes the use of self-consolidating concrete and curing, which is achieved by submerging the beams in water and leaving the surface untouched. Therefore, the slab beam surface finish is relatively smooth. This process also leaves a white residue on the concrete surface that further reduces the concrete-to-concrete bonding strength of the interface concrete. Therefore slab beams surface should be considered as smooth.
    b. The design checks indicate that interface shear reinforcement (H-bars) area per foot length can potentially be reduced for the midspan regions. However, the interface shear reinforcement area per foot length may need to be increased for the end regions of standard slab beams, particularly for the more shear critical cases with longer spans and wider beam spacings.
    c. The standard H-bar detail for interface shear reinforcement should be modified to extend 6 in. into the CIP deck to provide the required development length.

9.3 CONSTRUCTIBILITY

In order to reduce costs, a new bridge type called a spread slab beam bridge was recently developed by TxDOT using a similar concept as spread box beam bridges in which the beams are spaced apart. A full-scale spread slab beam bridge utilizing widely spaced slab beams was constructed and tested under static and dynamic vehicular loads to evaluate constructability and structural performance. The following conclusions are drawn with respect to constructability and related observations.

1. One of the challenging geometries with large beam spacing having the longest possible span length was designed and constructed as the Riverside Bridge. All 56 strand locations of the 5SB15 slab beam were used to provide sufficient flexural capacity at service. This challenging design introduced several design and construction difficulties including interface shear strength and excessive camber.
2. Design of the interior beam was controlled by the allowable tensile strength limit at service and the allowable tensile strength limit at transfer. A total of six strands were debonded up to 6 ft from both ends of the beam to prevent tensile stress exceedance at transfer.
3. Relatively high average camber was observed due to the large prestressing force relative to the member depth. The actual camber was 15 to 30 percent higher than the estimated camber values with different methods. Methods using the multiplier method (AASHTO and PGSuper) provided more accurate camber estimation compared to the time-step method. Inaccurate camber estimation may cause construction delays for tight construction schedules. It may also affect the final elevation due to higher haunch thicknesses at the abutments or piers.
4. Thermal stresses may cause early-age deck cracking if the differential temperature drop exceeds a certain limit of about 18 ºF (10 ºC) as concrete warms up due to heat of hydration within the first day, then cools down due to ambient temperature. Practices such as covering with black polythene sheet, which increases the temperature further, should be avoided. A sudden temperature drop at the deck surface creates a differential temperature profile, which may lead to cracking at the top of the deck.
5. Spread slab beam bridge systems that utilize PCPs with a CIP concrete deck, similar to I-girder bridges, provide a viable construction method for short-span bridges, approximately 30–50 ft long.

9.4 FIELD TESTING

Field testing of the full-scale Riverside Bridge was undertaken to experimentally observe the structural response and measure LDFs under static and dynamic truck loading. The purpose of these field studies was to evaluate the in-service performance and to measure the shear and

moment LDFs during controlled load tests. Experimental results were processed and reviewed, leading to the following conclusions.

1. The bridge was tested using total vehicle loads up to 75 kips and vehicle speeds up to 40 mph. The deflections were within the design limits and no major cracking or reduction in the overall stiffness of the bridge was observed.
2. It was observed that more closely spaced axle loads create higher load distribution factors. Shear LDFs were about 5 percent higher for a water tanker truck loading compared to dump truck loading where the load is better distributed along the length.
3. The observed bridge responses under dynamic loads were larger when compared to the static counterparts. Evidently, for short-span bridges, the dynamic impact may exceed the AASHTO LRFD Specifications (2012) design value of 33 percent.

9.5 MODELING

The experimental results obtained from the field testing of the Riverside Bridge were used to validate different modeling approaches. These techniques include orthotropic plate analysis, grillage analysis, and the finite element method (FEM). Two different commercial software were utilized to compare FEM analysis accuracy: (1) Abaqus (2013), (2) CSiBridge (2015), which is more specific to bridge engineering. Moment and shear predictions from computational models were compared with experimentally obtained ones. The following conclusions were obtained.

1. Orthotropic plate analysis did not provide a very accurate deflection predictions due to inherent assumptions and approximations. Maximum deflection values are 10 to 30 percent away from test results. However the moment LDF values are in good agreement with experimental values.
2. Deflection predictions obtained from both FEM software shows moderately good agreement with the experimental results.
3. Estimated natural frequencies from both software were very close to the test results. Mode shapes obtained from FEM models also compare well with the experimental ones.
4. Moment and shear LDFs calculated from the moment and shear predictions of both FEM software were in a good agreement with test results. When carefully developed,

the grillage model also predicts moment and shear response quite accurately.

5. Although both grillage analysis and FEM models can be considered sufficiently accurate and could be used for further development of LDFs, one should use the best available analysis tools. Because Abaqus and CSiBridge predictions were both quite close to test results, CSiBridge software was used for additional models, due to the relative ease of developing and analyzing bridge models.

9.6 LIVE LOAD DISTRIBUTION FACTORS

9.6.1 Derivation of LDF Equations

New live load distribution factor equations were developed for spread slab beam bridge systems. Empirical LDF equations for moment and shear in interior and exterior beams for one-lane- and multiple-lanes-loaded cases were derived for span lengths within the range of 31 to 51 ft. A total of 31 different bridges were modeled and analyzed using FEM. Proposed equations were obtained using a methodology similar to that adopted for developing the LDF equations found in the AASHTO LRFD Specifications (AASHTO 2012). The key parameters (span length *L*, beam spacing *S*, and beam depth *d*) for the LDF equations were chosen based on similar formulas used for spread box beam bridges in the current AASHTO LRFD Specifications (2012). Based on the comparative study conducted for three different sets of equations (AASHTO LRFD Specifications (2012) spread box beam formulas, theoretical best fit equations from FEM, and new proposed LDF equations), the following conclusions were drawn.

1. Unique LDF equations were developed for spread slab beam bridges to provide an appropriate level of conservatism. The new proposed equations produce slightly conservative results for all LDF cases when compared with the LDFs calculated from FEM analysis. The proposed LDF equation for moment in interior beams for the multiple-lanes-loaded case is identical to the AASHTO LRFD Specifications (2012) spread box beam equation.
2. Examining LDF values obtained from FEM analysis and proposed LDF formulas revealed that for all LDF equations, except for shear in exterior beams, multiple-lane-loaded formulas provide higher LDFs that control the design.

3. Common TxDOT practice for precast prestressed concrete bridges is to design all the girders the same as an interior girder in order to take into account possible future widening of the bridge. Therefore, all girders are designed based on interior girder shear and moment demands, unless the exterior demands are greater. The two governing proposed LDF equations for an interior girder for the multiple-lanes-loaded case are:

   For moments: $\left(\frac{S}{6.3}\right)^{0.6}\left(\frac{Sd}{12.0L^2}\right)^{0.125}$

   For shear: $\left(\frac{S}{5}\right)^{0.9}\left(\frac{d}{12.0L}\right)^{0.2}$

   where 31 ft $\leq L \leq$ 51 ft, 6.5 ft $\leq S \leq$ 11 ft, 12 in. $\leq d \leq$ 21 in.

4. The AASHTO LRFD Specifications (2012) spread box beam LDFs were reviewed for applicability to spread slab beams.
   a. For moment in interior beams, spread box beam formulas result in slightly unconservative LDFs for the one-lane-loaded case, whereas they are slightly conservative for the multiple-lanes-loaded case. Therefore, the new proposed equations match the AASHTO LRFD Specifications (2012) spread box beam formulas for the multiple-lane-loaded moment in interior beams.
   b. For shear in interior beams, spread box beam formulas are unconservative for most of the bridge geometries for both one-lane- and multiple-lanes-loaded cases.
   c. For moment and shear in exterior beams for one-lane-loaded, the AASHTO LRFD Specifications (2012) suggest using the lever rule, which produces overly conservative LDFs (an average of 50 percent conservative for moment and 30 percent conservative for shear).
   d. For moment and shear in exterior beams with multiple-lanes-loaded, the AASHTO LRFD Specifications (2012) suggest multiplying interior beam LDFs with a coefficient that is a function of the distance of the exterior beam from the interior edge of the rail. This parameter is not an effective parameter for the spread slab beam bridges considered in this study. This approach produces up to 25 percent conservative results for moment and an average of 40 percent conservative results for shear in exterior beams.

9.6.2 Effect of Additional Parameters

The above mentioned LDF equations were developed using the key parameters, span length (L), beam spacing (S), and beam depth (d) only. The effect of other parameters such as skew angle, overhang, haunch thickness, and vehicle edge distance were not considered and may have a significant effect on the lateral distribution of the loads in certain special circumstances. Therefore the effect of these additional parameters on LDFs were evaluated and correction factors were derived for those cases that have a prominent effect. A total of 28 different analysis were conducted and the following conclusions were drawn:

1. Variation in the skew angle significantly affects the LDFs for moment in interior and exterior beams. Cosine based correction factors are proposed. In addition, the shear LDFs of the obtuse angle end of the exterior beams increases considerably and sine based correction factors are proposed accordingly. When all girders are designed based on interior girder demands, the two governing proposed correction factors for skew for multiple-lanes-loaded interior beams are:

   For moments: $\cos\theta$

   For shear: $1.0 + 0.75\sin\theta$

   where, $0^\circ \leq \theta \leq 60^\circ$.

2. Variation in overhang and vehicle edge distance increases moment and shear LDFs in exterior beams. On the other hand, interior beam LDFs are not affected considerably by these parameters. Hence proposed correction factors were derived for shear and moment LDFs in exterior beams. These correction factors are:

   For moments: $< 1 + \frac{2 - d_{ve}}{20} >$

   For shear: $< 1 + \frac{2 - d_{ve}}{8} >$

   where, 0 ft $\leq d_{ve} \leq$ 3 ft.

3. LDFs are not sensitive to changes in haunch thickness. Although haunch thickness increases the stiffness of the composite section, it does not change the LDFs because haunch thickness was considered to increase the same amount for all girders.

4. When the analysis were done with only uniform lane loading, LDF values are about 15 to 25 percent lower compared to only truck loaded analysis. On the other hand, truck plus lane loading gives only 1-3 percent lower LDFs compared to only truck loaded case.

9.7 DESIGN IMPLICATIONS

For the design of a spread slab beam bridge, the following practices are recommended:

1. The interface shear reinforcement area per foot length can potentially be reduced for the midspan regions, but may need to be increased for the end regions of standard slab beams.
2. The new proposed LDF formulas for spread slab beam bridges are valid within the specified applicable range. For spread slab beam bridges outside of this range, more accurate analysis should be performed on a case-by-case basis.
3. If all the slab beams within a bridge are designed based on interior girder moment and shear demands, the two governing proposed LDF design equations when the overhang is smaller than 2 ft are given as

   For moments: $$\left(\frac{S}{6.3}\right)^{0.6}\left(\frac{Sd}{12.0L^2}\right)^{0.125}\left(\cos\theta\right)$$

   For shear: $$\left(\frac{S}{5}\right)^{0.9}\left(\frac{d}{12.0L}\right)^{0.2}\left(1.0+0.75\sin\theta\right)$$

   where, 31 ft $\le L \le$ 51 ft, 6.5 ft $\le S \le$ 11 ft, 12 in. $\le d \le$ 21 in. and $0^\circ \le \theta \le 60^\circ$.
4. Standard TxDOT slab beams are utilized to their design limits as the spacing between girders and the span length increase. Therefore, it is a good practice to use at least two slab beams per design lane to reduce the high demand on the slab beams. Generally, bridge geometries utilizing less than two slab beams per lane experience excessive shear demand, which in turn may lead to interface shear problems and excessive camber that results in impractical haunch thicknesses. Interface shear and camber must be carefully checked if the designer chooses to use less than two beams per design lane.

9.8 RESEARCH RECOMMENDATIONS

Recommendations to extend the results of this research include the following.

1. Similar to other bridges using conventional topped panelized decks, the spread slab beam system may be prone to longitudinal cracking along the beam panel keyways due to differential movements of beams that may occur due to vehicle loads or imperfections during the construction. A new panel system that has a longer transverse prestressing strand length into the CIP deck concrete, which can force the bridge deck to act as a unified slab by providing enough development length may be suggested. These new panels can be designed up to 50 ft length to facilitate accelerated bridge construction (ABC). The PCPs can have all the transverse and longitudinal reinforcement pre-fabricated which may provide potential saving from on-site labor costs. The design and constructability of the proposed panel system should be investigated through experimental research.
2. The code based live load models considers the dynamic response as a percentage of static response. A limited full speed vehicle test conducted during this research and several early studies showed that dynamic amplification may be bigger than the code-based impact factors depending on the surface conditions and vehicle dynamics. A more comprehensive analysis method for determining the coupled bridge-vehicle vibrations by considering parameters such as vehicle speed, road surface conditions, dynamic properties of the bridge and vehicle, can be developed. A live load model that considers vehicle structure interaction can provide better understanding of dynamic forces on the bridge. Such a methodology can also provide reliable dynamic information for assessment and performance evaluation of bridges.
3. In order to draw general conclusions about dynamic amplification, further testing that investigates different vehicle types, different speeds, and different approach bump sizes and conditions should be conducted.
4. In this research study, the skew correction factors were investigated for bridges having same skew angle at both end of the bridge and without any horizontal curve. The proposed skew correction factors must be evaluated in terms of applicability to bridges having different skew angles at two ends. The proposed correction factors for overhang and skew must be evaluated for bridges that have both horizontal curve and skew.

REFERENCES

AASHO (1931). "Standard Specifications for Highway Bridges, 1st Edition." American Association of State Highway Officials, Washington, DC.

AASHTO (1989). "Standard Specifications for Highway Bridges, 14th Edition." American Association of State Highway and Transportation Officials, Washington, DC.

AASHTO (1994). "AASHTO LRFD Bridge Design Specifications, 1st Edition." American Association of State Highway and Transportation Officials, Customary US Units, Washington, DC.

AASHTO (1996). "Standard Specifications for Highway Bridges, 16th Edition." American Association of State Highway and Transportation Officials, Washington, DC.

AASHTO (1998). "AASHTO LRFD Bridge Design Specifications, 2nd Edition." American Association of State Highway and Transportation Officials, Washington, DC.

AASHTO (2002). "Standard Specifications for Highway Bridges, 17th Edition." American Association of State Highway and Transportation Officials, Washington, DC.

AASHTO (2007). "AASHTO LRFD Bridge Design Specifications, 4th Edition." American Association of State Highway and Transportation Officials, Washington, DC.

AASHTO (2012). "AASHTO LRFD Bridge Design Specifications, 6th Edition." American Association of State Highway and Transportation Officials, Washington, DC.

ACI 318-08 (2008). "Building Code Requirements for Structural Concrete and Commentary."American Concrete Institute, Farmington Hills, MI.

ASTM (2009). "American Society for Testing and Materials (ASTM) " *C1611, Test Method for Slump Flow of Self-Consolidating Concrete,* West Conshohocken, Philadelphia.

ASTM (2010a). "American Society for Testing and Materials (ASTM)." *C39/C39M , Standard Test Method for Compressive Strength of Cylindrical Concrete Specimens,* West Conshohocken, Philadelphia.

ASTM (2010b). "American Society for Testing and Materials (ASTM)." *C78/C78M, Standard Test Method for Flexural Strength of Concrete (Using Simple Beam with Third-Point Loading),* West Conshohocken, Philadelphia.

ASTM (2010c). "American Society for Testing and Materials (ASTM)." *C470/C470M, Specification for Molds for Forming Concrete Test Cylinders Vertically,* West Conshohocken, Philadelphia.

ASTM (2011). "American Society for Testing and Materials (ASTM)." *C496/C496M, Standard Test Method for Splitting Tensile Strength of Cylindrical Concrete Specimens,* West Conshohocken, Philadelphia.

ASTM (2012a). "American Society for Testing and Materials." *C31/31M, Standard Practice for Making and Curing Concrete Test Specimens in the Field*, West Conshohocken, Philadelphia.

ASTM (2012b). "American Society for Testing and Materials (ASTM)." *C143, Standard Test Method for Slump of Hydraulic Cement Concrete*, West Conshohocken, Philadelphia.

ASTM (2013). "American Society for Testing and Materials." *C138, Standard Test Method for Density (Unit Weight), Yield, and Air Content (Gravimetric) of Concrete*, West Conshohocken, Philadelphia.

Bakht, B., and Moses, F. (1988). "Lateral Distribution Factors for Highway Bridges." *Journal of Structural Engineering*, 114(8), 1785-1803.

Barr, P. J., Oberhard, M. O., and Stanton, J. F. (2001). "Live Load Distribution Factors in Prestressed Concrete Girder Bridges." *J Bridge Eng*, 6(5), 298-306.

Bishara, A. G., Liu, M. C., and El-Ali, N. D. (1993). "Wheel Load Distribution on Simply Supported Skew I-Beam Composite Bridges." *Journal of Structural Engineering*, 119(2), 399-419.

Brockenbrough, R. L. (1986). "Distribution Factors for Curved I-Girder Bridges." *Journal of Structural Engineering*, 112(10), 2200-2215.

Chen, Y., and Aswad, A. (1996). "Stretching Span Capability of Prestressed Concrete Bridges under AASHTO LRFD." *J Bridge Eng*, 1(3), 112-120.

Clough, R. W. (1960). "The Finite Element Method in Plane Stress Analysis." *Journal of Structural Division, ASCE, Proceedings of 2nd Conference on Electronic Computation*, 345-378.

Computers and Structures, I. 2014. SAP2000 Version 17, Berkeley, California, USA.

Computers and Structures, I. 2015. CSiBridge, Integrated 3-D Bridge Analysis, Design and RatingComputers and Structures, Inc., Berkeley, California, USA.

Courant, R. (1943). "Variational Methods for the Solution of Problems of Equilibrium and Vibrations." *Bulletin of the Maerican Mathematical Society*, 49, 1-23.

Dassault Systemes, S. A. 2013. Abaqus, version 6. Abaqus, Inc, Providence, RI, USA.

Douglas, W. J., and Vanhorn, D. A. (1966). "Lateral Distribution of Static Loads in a Prestressed Concrete Box-Beam Bridge - Drehersville Bridge." *Project 315*, Fritz Engineering Laboratory, Department of Civil Engineering, Lehigh University, Bethlehem, Pennsylvania.

Eom, J., and Nowak, A. S. (2001). "Live Load Distribution for Steel Girder Bridges." *J Bridge Eng*, 6(6), 489-497.

Evans, R. H., and Chung, H. W. (1969). "Horizontal Shear Failure of Prestresses Composite T-Beams with Cast-in-Situ Lightweight Concrete Deck." *Concrete*, 3(4), 124-126.

Gessner (2012). "Geotechnical Engineering Study, Bridge Abutments."

Google Maps (2005). <https://www.google.com/maps>. (July 15, 2014).

Guilford, A. A., and Vanhorn, D. A. (1967a). "Lateral Distribution of Dynamic Loads in a Prestressed Concrete Box-Beam Bridge - Drehersville Bridge." *Project 315*, Fritz Engineering Laboratory, Department of Civil Engineering, Lehigh University, Bethlehem, Pennsylvania.

Guyon, Y. (1949). "Calcul des Ponts Dalles." *Ann. des Ponts et Chaussees*, 119(29), 555-589.

Hambly, E. C. (1975). "Grillage Analysis Applied to Cellular Bridge Decks." *The structural engineer*, 53(7), 267-276.

Hambly, E. C. (1976). *Bridge Deck Behaviour*, Halsted Press, New York, NY.

Hambly, E. C. (1991). *Bridge Deck Behaviour*, Taylor & Francis, New York, NY.

Hanson, N. W. (1960). "Precast-Prestressed Concrete Bridges; 2. Horizontal Shear Connections." *Journal of the Research and Development Laboratories, Portland Cement Association*, 2(2), 38-58.

Hays, C. O., Sessions, L. M., and Berry, A. (1986). "Further Studies on Lateral Load Distribution Using Finite Element Method." Transportation Research Board, Transportation Research Record, Washington, D.C.

Heins, C. P., and Looney, C. T. G. (1968). "Bridge Analysis Using Orthotropic Plate Theory." *Proceedings ASCE*, 94(ST2), 565-569.

Hrenikoff, A. (1941). "Solution of Problems in Elasticity by the Framework Method." *Journal of Applied Mechanics, Transactions of the ASME*, 8, 169-175.

Imbsen, R. A., and Nutt, R. V. (1978). "Load Distribution Study on Highway Bridges Using STRUDL Finite Element Analysis Capabilities." *Computing in Civil Engineering*, 639-654.

Khaleel, M. A., and Itani, R. Y. (1990). "Live-Load Moments for Continuous Skew Bridges." *Journal of Structural Engineering*, 116(9), 2361-2373.

Kim, S., and Nowak, A. S. (1997). "Load Distribution and Impact for I-Girder Bridges." *J Bridge Eng*, 2(3), 97-104.

Kovach, J. D., and Naito, C. (2008). "Horizontal Shear Capacity of Composite Concrete Beams without Interface Ties." *ATLSS*, Lehigh University, Bethlehem, PA.

Lazarides, T. O. (1952). "The Design and Analysis of Open-Work Prestressed Concrete Beam Grillages." *Civil Engineering and Public Works Rev.*, 47(552), 471-473.

Lightfoot, E., and Sawko, F. (1959). "Structural Frame Analysis by Electronic Computer: Grid Frameworks by Generalised Slope Deflection." *Engineering*(187), 18-20.

Lin, C. S., and Vanhorn, D. A. (1968). "The Effect of Midspan Diaphragms on Load Distribution in a Prestressed Concrete Box-Beam Bridge - Philedelphia Bridge." *Project 315*, Fritz Engineering Laboratory, Department of Civil Engineering, Lehigh University, Bethlehem, Pennsylvania.

Mabsout, M. E., Tarhini, K. M., Frederick, G. R., and Tayar, C. (1997). "Finite Element Analysis of Steel Girder Highway Bridges." *J Bridge Eng*, 2(3), 83-87.

Martin, L. D. (1977). "A Rational Method for Estimating Camber and Deflection of Precast Prestressed Members." *Pci J*, 100-108.

Marx, H. J., Khachaturian, N., and Gamble, W. L. (1986). "Development of Design Criteria for Simply Supporter Skew Slab-and-Girder Bridges." University of Illinois at Urbana-Champaign.

Massonnet, C. (1950). "Methods of Calculation of Bridges with Several Longitudinal Beams, Taking into Account their Torsional Resistance." *International Association of Bridge and Structural Engineering Publication*, 10, 147-182.

McKee, D. C., and Turner, H. T. (1975). "Design and Review of Precast Concrete Bridge Elements." FHWA and Luisiana Department of Highways, FHWA-LDH-LSU(75-1ST).

Naaman, A. E. (2004). *Prestressed Concrete Analysis and Design : Fundamentals*, Techno Press, Ann Arbor, MI.

Newmark, N. M. (1938). "A Distribution Procedure for Analysis of Slabs Continuous over Flexibale Beams."University of Illinois, Urbana , IL.

Nosseir, S. B., and Murtha, R. N. (1971). "Ultimate Horizontal Shear Strength of Prestresses Split Beams."Naval Civil Engineering Laboratory Technical Report NCEL TR.

Nowak, A. S. (1993). "Live Load Model for Highway Bridges." *Struct Saf*, 13, 53-66.

Panak, J. J. (1982). "Economical Precast Concrete Bridges." *FHWA-TX-83-08+226-1F Final Rpt.*, FHWA and Texas Department of Highway & Public Transportation, Austin, TX.

Parke, G., and Hewson, N. (2008). *ICE Manual of Bridge Engineering*, Thomas Telford, London, UK.

PCI (2010). "PCI Design Handbook." Precast/Prestressed Concrete Institute, Chicago, IL.

PGSuper (2013). "PGSuper Design Guide." Texas Department of Transportation, https://ftp.dot.state.tx.us/pub/txdot-info/library/pubs/bus/bridge/pgsuper_design_guide.pdf.

Priestley, M. J. N. (1978). "Design of Concrete Bridges for Temperature Gradients." *American Concrete Institute (ACI)*, 75(23), 209-217.

Rowe, R. E. (1955). "A Load Distribution Theory for Bridge Slabs Allowing for the Effect of Poisson`s Ratio." *Concrete Resources*, 7(20), 69-78.

Sanders, W. W., and Elleby, H. A. (1970). "Distribution of Wheel Loads on Highway Bridges." National Cooperative Highway Research Program, Highway Research Board.

Schafer, T., and Vanhorn, D. A. (1967). "Structural Response of a 45° Skew Prestressed Concrete Box-Girder Highway Bridge Subjected to Vehicular Loading - Brookville Bridge." *Project 315*, Fritz Engineering Laboratory, Department of Civil Engineering, Lehigh University, Bethlehem, Pennsylvania.

Schwarz, M., and Laman, J. A. (2001). "Response of Prestressed Concrete I-Girder Bridges to Live Load." *J Bridge Eng*, 6(1), 1-8.

Sotelino, E., Liu, J., Chung, W., and Phuvoravan, K. (2004). "Simplified Load Distribution Factor for Use in LRFD Design." *Joint Transportation Research Program*, 1-148.

Surana, C. S., and Agrawal, R. (1998). *Grillage Analogy in Bridge Deck Analysis*, Narosa Publishing House, London, UK.

Tarhini, K. M., and Frederick, G. R. (1992). "Wheel Load Distribution in I-Girder Highway Bridges." *Journal of Structural Engineering*, 118(5), 1285-1294.

Timoshenko, S. P., and Woinowsky-Krieger, S. (1959). *Theory of Plates and Shells*, McGrawHill, New York.

Trejo, D., Hueste, M. B. D., and Kim, Y. G. (2008). "Characterization of Self-Consolidating Concrete for Design of Precast, Prestressed Bridge Girders ", Texas Transportation Institute Texas Department of Transportation.

Turner, M. J., Clough, R. W., Martin, H. C., and Topp, L. J. (1956). "Stiffness and Deflection Analysis of Complex Structures." *Journal of the Aeronautical Sciences*, 23(9), 805-823.

TxDOT (2012). "TxDOT Geotechnical Manual." Texas Department of Transportation, http://onlinemanuals.txdot.gov/txdotmanuals/geo/geo.pdf.

TxDOT (2013a). "TxDOT Bridge Design Manual - LRFD." Texas Department of Transportation, http://onlinemanuals.txdot.gov/txdotmanuals/lrf/lrf.pdf.

TxDOT (2013b). "TxDOT Bridge Division Standard Drawings." Texas Department of Transportation, http://www.txdot.gov/insdtdot/orgchart/cmd/cserve/standard/bridge-e.htm.

Ugural, A. C., and Fenster, S. K. (2012). *Advanced Mechanics of Materials and Aplied Elasticity*, Prentice Hall.

Waveru, R. N. (2015). "Strength of Horizontal Shear Reinforcement with Limited Development." Doctor of Philosophy, The University of Texas at Arlington.

Wegmuller, A. W., and Kostem, C. N. (1973). "Finite Element Analysis of Plates and Eccentrically Stiffened Plates." *Fritz Engineering Laboratory Report*, Lehigh University.

Westergaard, H. M. (1930). "Computation of Stresses in Bridge Slabs due to Wheel Loads." *Public Roads*, 11(1), 1-23.

Zokaie, T. (2000). "AASHTO-LRFD Live Load Distribution Specifications." *ASCE Journal of Bridge Engineering*, 5(2), 131-138.

Zokaie, T., Imbsen, R. A., and Osterkamp, T. A. (1991). "Distribution of Wheel Loads on Highway Bridges." *NCHRP Project Report 12-26*, Transportation Research Board, Washington, DC.

APPENDIX A

DESIGN EXAMPLE FOR INTERIOR 5SB15 SPREAD SLAB BEAM

A.1 GENERAL

The following design illustrates a typical structural design procedure for an interior precast prestressed slab beam used in a spread configuration for a simply supported bridge. The design is based on the American Association of State Highway and Transportation Officials (AASHTO) Load and Resistance Factor Design (LRFD) Specifications (2012). Also the recommendations provided in the Texas Department of Transportation (TxDOT) Bridge Design Manual—LRFD (TxDOT 2013a) are considered in the design. The parameters used in this example are for the Riverside Bridge, which was constructed for this project and is discussed further in Section 4.

A.2 GEOMETRIC AND MATERIAL PROPERTIES OF THE BRIDGE

A.2.1 Bridge Geometry

Figure A.1 shows the bridge cross-section and Table A.1 summarizes the geometric parameters for the considered bridge. The spread slab beam bridge considered has a 46 ft 7 in. center-to-center of bearing pad span length, with a roadway width of 32 ft and total width of 34 ft. The bridge superstructure consists of four 5SB15 slab beams with 9 ft 8 in. center-to-center spacing. Precast prestressed concrete panels (PCP) that are 4 in. thick are used as stay-in-place forms between slab beams. The thickness of the cast-in-place (CIP) deck on top of the PCP is 4 in. Therefore, the total deck thickness is 8 in. between slab beams. However, due to camber, the deck thickness may be 0.5–4.0 in. thicker on top of the slab beams. This example follows TxDOT standard design procedure, which is to include a constant 2 in. haunch thickness in the girder weight but neglect the contribution of the haunch to the girder stiffness. Therefore, the total thickness of the bridge deck is taken as 8 in. constant everywhere. The CIP concrete bridge deck is designed to act compositely with the slab beam girders. The wearing surface is considered as 2 in. thick asphalt. Vehicular live loading is considered as the AASHTO LRFD Specifications (2012) HL-93 loading, consisting of a combination of HS20 design truck or design tandem, whichever is more critical, and a design lane load of 0.64 kips/ft. The precast prestressed beams are standard 5SB15 type slab beams. The width of the slab beams is b = 5 ft, and the depth of the slab beam is d = 15 in.

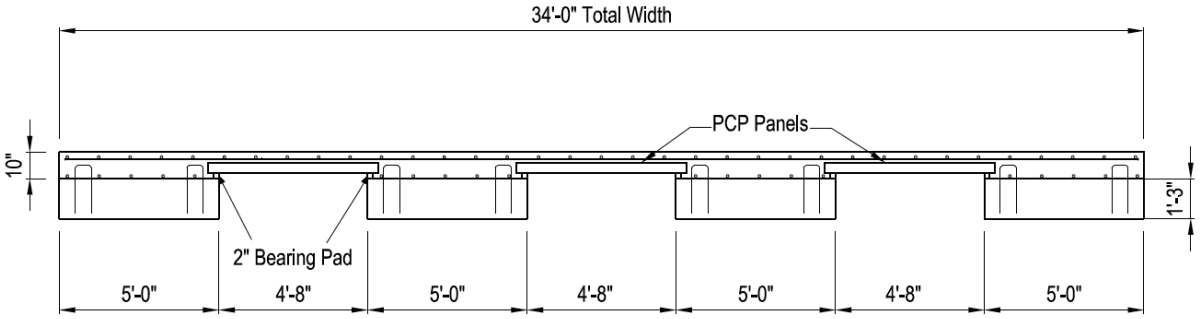

Figure A.1. Bridge Cross-Section.

Table A.1. Geometric Properties.

Parameter	Description/Value
Span Length (Center-to-Center of Bearing Pad), L	46 ft 7 in.
Total Bridge Width, w	34 ft
Slab Beam Type	5SB15 (5 ft width, 15 in. depth)
Center-to-Center Beam Spacing, S	9 ft 8 in.
Deck Thickness, t_s	8 in.
Haunch Thickness, t_h	Assumed constant 2 in. for weight calculation. Not included for stiffness calculation.
Rail	T551 (0.326 kips/ft, distributed to three beams from the edge)
Wearing Surface	2 in. thick asphalt assumed

The construction process of the superstructure consists of two phases. The first phase is the erection of the precast prestressed components, which includes precast prestressed slab beams and PCPs. The second phase is the casting of the CIP concrete deck on top of the PCPs. This type of construction process reduces the construction time and saves the contractor from constructing and shoring the formwork.

The number of design lanes is computed according to the AASHTO LRFD Specifications (2012) Article 3.6.1.1.1 as the number of design lanes is the integer part of the ratio of (w/12), where w is the clear roadway width between curbs or barriers. The value of w is 32 ft for this example, so the bridge that is being described herein is a two-lane bridge.

The bridge is constructed using the precast slab beams in a spread configuration. In order to maximize the load variation between slab beams, the spacing between the slab beams is maximized. Only four slab beams are used, resulting in a clear spacing of 4 ft 8 in. between slab beam girders.

In order to calculate section properties, the effective flange width needs to be calculated. The AASHTO LRFD Specifications (2012) define the effective flange width as being the tributary width, which is the center-to-center spacing of girders (9 ft 8 in. for the interior girders).

A.2.2 Material Properties

The material properties for the bridge are summarized in Table A.2. The specified 28-day compressive strength for the CIP deck is 4 ksi. Normal weight concrete is assumed throughout the construction with a 0.15 kcf unit weight.

Precast prestressed concrete slab beams are considered as self-consolidating concrete (SCC). Because the initial compressive stress limit is one of the controlling parameters for spread slab beam bridge design, the maximum permissible compressive strength at release is used. The TxDOT Bridge Design Manual (TxDOT 2013a) provides limits for the compressive strength of the concrete. The compressive strength of the concrete at release ($f_{ci}^{'}$) is specified to be between 4–6 ksi, and the compressive strength of the concrete at service ($f_{c}^{'}$) is specified to be between 5–8.5 ksi.

The standard prestressing for the slab beam girders is 0.5 in. diameter (nominal cross-sectional area of A_{ps} = 0.153 in2), seven-wire, low-relaxation strands having an ultimate strength, f_{pu}, of 270 ksi. The yield strength for this type of strand is defined by manufacturers as $f_{py} = 0.9 f_{pu} = 243$ ksi and the modulus of elasticity is considered as $E_p = 28{,}500$ ksi.

Mild steel reinforcement used for foundation elements, abutments, slab beams, and deck is specified to be American Society for Testing and Materials (ASTM) A615 Grade 60 steel with a modulus of elasticity of $E_s = 29{,}000$ ksi.

A.2.3 Cross-Sectional Properties

The geometric dimensions and strand positions for a 5SB15 slab beam girder are provided in Figure A.2. The number and arrangement of prestressing strands follow the standard strand configuration that is set for TxDOT slab beam types. Based on geometric constraints and cover requirements, 56 strands (28 strands per row) can be placed in two rows with a 2 in. center-to-center spacing.

A.2.3.1 Precast Slab Beam

The moment of inertia about the centroid of the slab beam, I_b, is determined as:

$$I_b = \frac{1}{12} b d^3 = \frac{(60)(15)^3}{12} = 16{,}875 \text{ in}^4 \quad \text{(A.1)}$$

The section modulus referenced to extreme bottom fiber of the girder is:

$$S_b = \frac{I_b}{y_b} = \frac{16{,}875}{7.5} = 2250 \text{ in}^3 \quad \text{(A.2)}$$

The section modulus of the slab beam referenced to extreme top fiber of the girder is:

$$S_t = \frac{I_b}{y_t} = \frac{16{,}875}{7.5} = 2250 \text{ in}^3 \quad \text{(A.3)}$$

A.2.3.2 Composite Slab Beam and Deck Section

The tributary area for one girder is calculated based on the geometric properties of the bridge and number of girders used. The composite section has a 9 ft 8 in. flange width and an 8 in. slab thickness. The geometric dimensions of the composite section are shown in Figure A.2.

Table A.2. Specified Nominal Material Properties.

Parameter	Description/Value
28-Day Concrete Compressive Strength of Deck, $f_{cd}^{'}$	4.0 ksi
Initial Concrete Compressive Strength of Precast Slab Beam, $f_{ci}^{'}$	4.0–6.0 ksi
28-Day Concrete Compressive Strength of Precast Slab Beam, $f_{c}^{'}$	5.0–8.5 ksi
Unit Weight of Concrete, w_c	0.15 kcf
Unit Weight of Asphalt Overlay, w_s	0.14 kcf
Prestressing Strands	7-wire low-relaxation strands
Ultimate Strength of Prestressing Stands, f_{pu}	270 ksi
Modulus of Elasticity of Strands, E_p	28,500 ksi

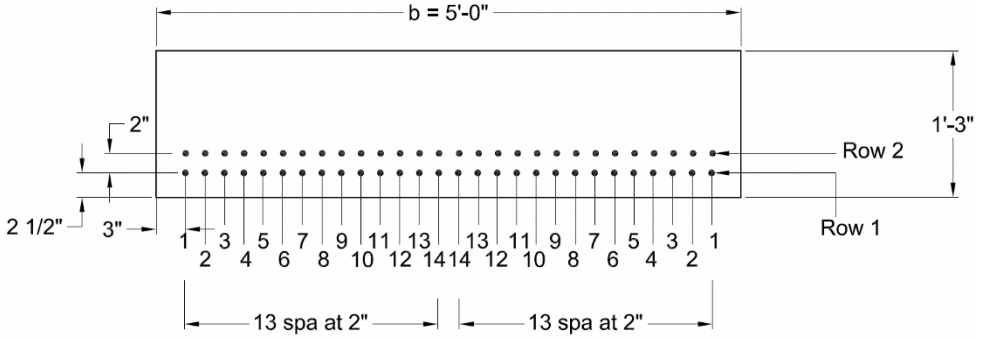

(a) Typical 5SB15 Slab Beam Section and Strand Configuration.

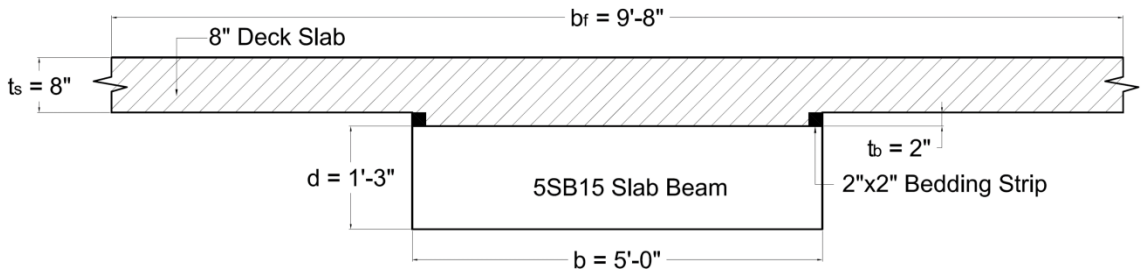

(b) Dimensions of Composite Cross-Section.

Figure A.2. Precast Slab Beam and Composite Beam Sections.

The values for the modulus of elasticity for the CIP deck and the precast concrete slab beam are different. Therefore, transformed section properties are calculated using the modular ratio between the CIP deck slab and precast prestressed slab beam girder. For the preliminary design example, a concrete compressive strength of f_c' =7 ksi was used for slab beams.

The modular ratio is determined as:

$$\eta = \frac{E_{cd}}{E_c} = \sqrt{\frac{f_{cd}'}{f_c'}} = \sqrt{\frac{4}{7}} = 0.756 \quad \text{(A.4)}$$

Where:

E_{cd} = Modulus of elasticity of deck concrete, ksi.

E_b = Modulus of elasticity of slab beam concrete, ksi.

The transformed effective flange width is 87.69 in.

The haunch thickness is neglected, as suggested by the TxDOT Bridge Design Manual (TxDOT 2013a). The haunch thickness depends on the precast beam camber and may be smaller than 2 in. In some locations it may be as small as 0.5 in. Therefore, it is conservative to assume zero haunch thickness when determining cross-sectional properties. This assumption is used in the following calculation. On the other hand, an average 2 in. haunch thickness is included in the self-weight calculation to avoid being unconservative in the load calculations.

The transformed section properties are found as follows. The gross area of the transformed section is calculated using the expression below.

$$A_{gt} = b_e t_s + bd = 1601.5 \text{ in}^2 \quad \text{(A.5)}$$

The distance from the centroid of the composite section to the extreme top fiber of the slab (y_{tc}) is determined using the following expression.

$$y_{tc} = \frac{\left[(b_e t_s)\frac{t_s}{2} + (bd)\left(t_s + \frac{d}{2}\right)\right]}{A_{gt}} = \frac{\left[(87.688)(8)(4) + (60)(15)(15.5)\right]}{1{,}601.5} = 10.5 \text{ in.} \quad \text{(A.6)}$$

The distance from the centroid of the composite section to the extreme bottom fiber of the girder, y_{bc}, is determined as:

$$y_{bc} = H - y_{tc} = 23 - 10.46 = 12.54 \text{ in.} \quad \text{(A.7)}$$

Where:

H = Total depth of the composite section, in.

The moment of inertia about the centroid of the composite section is found using Equation (A.8).

$$I_c = \frac{1}{12} b_e t_s^3 + t_s b_e \left(y_{tc} - \frac{t_s}{2} \right)^2 + \frac{1}{12} bd^3 + bd \left(y_{bc} - \frac{d}{2} \right)^2 \quad \text{(A.8)}$$

$$I_c = \frac{1}{12} 87.69(8)^3 + 87.69(8)(6.46)^2 + \frac{1}{12}(60)(15)^3 + (60)(15)(5.04)^2$$
$$= 72,753 \text{ in}^4$$

The composite section modulus referenced to the extreme bottom fiber of the girder, S_{bc}, is found using Equation (A.9).

$$S_{bc} = \frac{I_c}{y_{bc}} = \frac{72,753}{12.54} = 5803 \text{ in}^3 \quad \text{(A.9)}$$

The composite section modulus referenced to the extreme top fiber of the slab, S_{tc}, is found using Equation (A.10).

$$S_{tc} = \frac{I_c}{y_{tc}} = \frac{72,753}{10.46} = 6954 \text{ in}^3 \quad \text{(A.10)}$$

The composite section modulus referenced to the top fiber of the precast girder, S_{tg}, is found using Equation (A.11).

$$S_{tg} = \frac{I_c}{y_{tg}} = \frac{72,753}{2.46} = 29,542 \text{ in}^3 \quad \text{(A.11)}$$

Where y_{tg} is the distance of the top fiber of the precast beam to the centroid of the composite section and is calculated as:

$$y_{tg} = y_{tc} - t_s = 10.46 - 8 = 2.46 \text{ in.} \quad \text{(A.12)}$$

A.3 STRESS LIMITS

All structural components must be designed to satisfy all appropriate service limit states. For prestressed or partially prestressed concrete structural components, these limit states are stress limit states. All concrete sections must be investigated at transfer and at service stress limits.

A.3.1 Allowable Stress Limits for Concrete

Allowable stress limits are specified in the AASHTO LRFD Specifications (2012). Slab beams are structural concrete members with bonded prestressing tendons. For the tensile stress limit check at service, the longitudinal members should be analyzed under load combination Service III, as specified in AASHTO LRFD Specifications (2012) Table 3.4.1-1.

A.3.1.1 Allowable Stress Limits at Transfer

The tensile stress limit at transfer, F_{ti} , is used as specified in the AASHTO LRFD Specifications (2012) Table 5.9.4.1.2-1. This limit allows the use of an increased tensile stress limit in areas with bonded reinforcement. The amount of bonded reinforcement is determined based on the tensile force at the critical section. The tensile stress limit in the sections with bonded reinforcement assuming an uncracked section, where reinforcement is proportioned using $0.5 f_y$, before losses is given as:

$$F_{ti} = 0.24\sqrt{f_{ci}^{'}} = (0.24)\sqrt{6} = 0.588 \text{ ksi} \quad \text{(A.13)}$$

AASHTO LRFD Specifications (2012) specifies a compressive stress limit before losses, F_{ci} , for pretensioned and post-tensioned concrete members in Article 5.9.4.1.1 as $0.6 f_{ci}^{'}$ However, TxDOT Bridge Design Manual—LRFD (TxDOT 2013a) specifies an increased compressive stress limit at transfer. The compressive stress limit at transfer before losses is given as:

$$F_{ci} = 0.65 f_{ci}^{'} = (0.65)(6) = 3.9 \text{ ksi} \quad \text{(A.14)}$$

A.3.1.2 Allowable Stress Limits at Service

The tensile stress limit for prestressed concrete at the service limit state after losses for fully stressed components, F_t , is given in AASHTO LRFD Specifications (2012) Table 5.9.4.2.2-1 as:

$$F_t = 0.19\sqrt{f_c^{'}} = 0.19\sqrt{7} = 0.503 \text{ ksi} \quad \text{(A.15)}$$

For the compressive stress limit state, service limit state load combination Service I, specified in AASHTO (2012) Table 3.4.1-1, is used. The compressive stress limit for

prestressed concrete at the service limit state after losses, F_c, is given in AASHTO LRFD Specifications (2012) Table 5.9.4.2.1-1 as:

$$F_c = 0.45 f_c^{'} = (0.45)(7) = 3.15 \text{ ksi} \quad \text{(A.16)}$$

A.3.2 Stress Limits for Prestressing Strands

AASHTO LRFD Specifications (2012) Table 5.9.3-1 specifies tensile stress limits for tendons due to prestress or at the service limit state. For a low-relaxation strand, the stress limit prior to transfer, f_{pbt}, and at the service limit state after all losses, f_{pe}, is provided as:

Before transfer: $f_{pbt} \leq 0.75 f_{pu} = 202.5 \text{ ksi}$

At service: $f_{pe} \leq 0.8 f_{py} = 194.4 \text{ ksi}$

A.4 STRUCTURAL ANALYSIS RESULTS

Structural analysis of the superstructure is conducted using the AASHTO LRFD Specifications (2012) approximate analysis approach, which utilizes live load distribution factors for truck and uniform lane loading. Based on the approximate analysis approach, an interior slab beam composite section is analyzed statically. The effective width of the concrete deck slab is taken as the tributary width perpendicular to the axis of the member, which is the center-to-center spacing between slab beams.

A.4.1 Shear Forces and Bending Moments for a Typical Interior Girder

Bending moments of an interior girder are calculated when the vehicle is at the critical bending moment location for combined loading. Combined loading includes the dead load of all structural components, superimposed dead loads, and the design live load.

A.4.1.1 Dead Load

Dead load is assumed to act on the non-composite slab beam section because it will be in place when the deck concrete is fresh. Although the haunch thickness is neglected when calculating the composite section modulus, the weight of the haunch concrete is included in the dead load calculation considering an average 2 in. thick haunch.

The dead load of all structural components and nonstructural attachments is determined as:

$$DC = \gamma_c(A_b + A_h + A_s) = 0.15 \times (5 \times 1.25 + 5 \times 0.17 + 9.67 \times 0.67) = 2.03 \text{ kips/ft} \quad \text{(A.17)}$$

Where:

γ_c = Density of the concrete, kips/ft^3.

A_b = Cross-sectional area of the slab beam, ft^2.

A_s = Cross-sectional area of the deck slab, ft^2.

A_h = Cross-sectional area of the haunch section, ft^2.

A.4.1.2 Superimposed Dead Load

Superimposed dead loads are assumed to act after the composite action between the slab beam girders and deck slab takes place. According to TxDOT Bridge Design Manual (TxDOT 2013a), the wearing surface load can be equally distributed among four girders, and the rail load can be distributed to no more than three girders from the edge of the deck.

The weight of the 2 in. asphalt wearing surface, W_{ws}, is calculated using the following expression.

$$W_{ws} = \frac{0.14 \times \left(\frac{2}{12} \times 34 \right)}{4} = 0.198 \text{ kips/ft}$$

The weight of T501 rails or barriers, W_r, on each interior girder is calculated as:

$$W_r = \frac{2 \times 0.326}{3} = 0.217 \text{ kips/ft}$$

The dead load of wearing surfaces and utilities (including the rails), DW, is calculated using Equation (A.18).

$$DW = W_{ws} + W_r = 0.415 \text{ k/ft} \quad \text{(A.18)}$$

A.4.1.3 Live Load

AASHTO LRFD Specifications (2012) Article 3.6.1.2 specifies the design live load as HL-93, which consists of a combination of the design truck with dynamic allowance or the design tandem with dynamic allowance, whichever produces greater moments and shears, and design lane load without dynamic allowance.

A.4.1.3.1 Design Truck and Lane Loads

Figure A.3(a) shows the HS20 design truck and tire load positions. For a simply supported span, the design truck gives more critical moment when the distance between the second and rear axles is constantly equal and 14 ft.

Figure A.3(b) shows the load positions for a design tandem, which consists of a pair of 25-kip axles spaced 4.0 ft apart. For simply supported spans, the tandem loading governs for spans shorter than 40 ft.

The lane load consists of a load of 0.64 kips/ft uniformly distributed in the longitudinal direction (AASHTO LRFD Specifications (2012) Article 4.6.2.2). The bending moments due to vehicular live load can be distributed to individual girders using the simplified approximate distribution factor formulas specified by AASHTO LRFD Specifications (2012) if the following conditions are met.

- Width of the slab is constant.
- Number of girders is not less than four.
- Girders are parallel and of the same stiffness.
- Roadway part of the overhang is $de \leq 3.0$ ft.
- Curvature in plan is less than 4 degrees.
- Cross-section of the bridge girder is consistent with one of the cross-sections given in AASHTO LRFD Specifications (2012) Table 4.6.2.2.1-1.

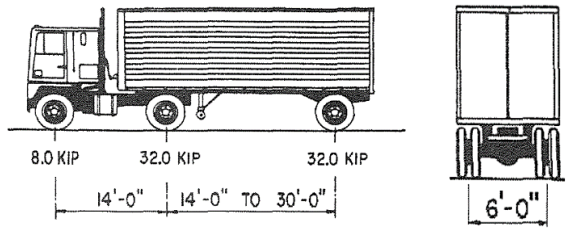

HS20 Design Truck (AASHTO 2012)

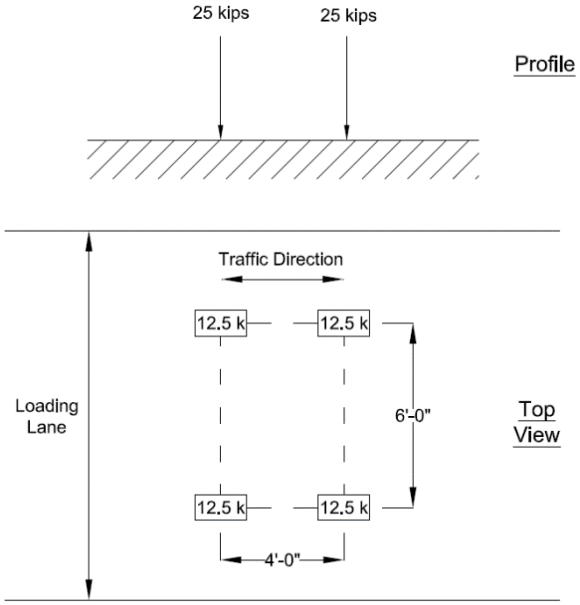

Design Tandem

Figure A.3. AASHTO HL-93 Design Vehicles.

A.4.1.3.2 Live Load Distribution Factors

Although there is no spread slab beam configuration defined in AASHTO LRFD Specifications (2012), spread box beam formulas are used per TxDOT`s suggestion as a preliminary design guide. Live load moment and shear distribution factors for interior girders are provided in AASHTO LRFD Specifications (2012) Tables 4.6.2.2.2b-1 and 4.6.2.2.3a-1.

Moment distribution factor for one design lane loaded case, g_{M1}, is calculated as:

$$g_{M1} = \left(\frac{S}{3.0}\right)^{0.35} \times \left(\frac{Sd}{12.0L^2}\right)^{0.25} = \left(\frac{9.67}{3.0}\right)^{0.35}\left(\frac{9.67\times 15}{12\times 46.58^2}\right)^{0.25} = 0.41 \qquad \text{(A.19)}$$

Moment distribution factor for two design lane loaded case, g_{M2}, is calculated as:

$$g_{M2} = \left(\frac{S}{6.3}\right)^{0.6} \times \left(\frac{Sd}{12.0L^2}\right)^{0.125} = \left(\frac{9.67}{6.3}\right)^{0.6} \times \left(\frac{9.67 \times 15}{12 \times 46.58^2}\right)^{0.125} = 0.68 \qquad \text{(A.20)}$$

Shear distribution factor for one design lane loaded case, g_{V1}, is calculated as:

$$g_{V1} = \left(\frac{S}{10}\right)^{0.6} \times \left(\frac{d}{12.0L}\right)^{0.1} = \left(\frac{9.67}{10}\right)^{0.6} \times \left(\frac{15}{12 \times 46.58}\right)^{0.1} = 0.68 \qquad \text{(A.21)}$$

Shear distribution factor for two design lane loaded case, g_{V2}, is calculated as:

$$g_{V2} = \left(\frac{S}{7.4}\right)^{0.8} \times \left(\frac{d}{12.0L}\right)^{0.1} = \left(\frac{9.67}{7.4}\right)^{0.8} \times \left(\frac{15}{12 \times 46.58}\right)^{0.1} = 0.86 \qquad \text{(A.22)}$$

Where:

g_M = $Max(g_{M1,}g_{M2}) = 0.676$ lanes/girder.

g_V = $Max(g_{V1,}g_{V2}) = 0.86$ lanes/girder.

g_M = Live load moment distribution factor.

g_v = Live load shear distribution factor.

S = Girder spacing, ft.

L = Girder span, ft.

d = Depth of the girder, in.

A.4.1.3.3 Dynamic Load Allowance

AASHTO LRFD Specifications (2012) Table 3.6.2.1-1 specifies the dynamic load effects as a percentage of the static live load effects and to be taken as 33 percent of the static load effects for all limit states except the fatigue limit state and 15 percent for the fatigue limit state.

A.4.2 Influence Line Analysis

Figure A.4 presents the load cases for the influence line analysis used herein. Bending moment and shear force due to truckload at any section at a distance x and for a truck position z are calculated as the truck passes over the span.

$$R_{TR} = 8 \times \left(1 - \frac{z}{L}\right) + 32 \times \left(1 - \frac{z+14}{L}\right) + 32 \times \left(1 - \frac{z+28}{L}\right) \qquad \text{(A.23)}$$

$$V_{TR} = \begin{cases} g_V \times 1.33 \times R_{TR} & x \le z \\ g_V \times 1.33 \times (R_{TR} - 8) & z < x \le z + 14 \\ g_V \times 1.33 \times (R_{TR} - 40) & z + 14 < x \le z + 28 \\ g_V \times 1.33 \times (R_{TR} - 72) & x > z + 28 \end{cases} \quad \text{(A.24)}$$

$$M_{TR} = \begin{cases} g_M \times 1.33 \times R_{TR} x & x \le z \\ g_M \times 1.33 \times (R_{TR} x - 8(\mathrm{x} - \mathrm{z})) & z < x \le z + 14 \\ g_M \times 1.33 \times (R_{TR} x - 8(\mathrm{x} - \mathrm{z}) - 32(\mathrm{x} - \mathrm{z} - 14)) & z + 14 < x \le z + 28 \\ g_M \times 1.33 \times (R_{TR} x - 8(\mathrm{x} - \mathrm{z}) - 32(2\,\mathrm{x} - 2\,\mathrm{z} - 42)) & x > z + 28 \end{cases} \quad \text{(A.25)}$$

Where:

R_{TR} = Reaction force at the left end support, kips.

V_{TR} = Shear force as a function of truck position and location, kips.

M_{TR} = Bending moment as a function of truck position and location, kip-ft.

It is shown that the design tandem loading does not give the critical moment for a simply supported span that is longer than 40 ft. The maximum bending moment and shear forces are calculated using the influence line method. The shear force and bending moment at each section x (ft) are formulated based on the position of the tandem, z (ft), as it passes over the span.

$$R_{TN} = 25 \times \left(1 - \frac{z}{L}\right) + 25 \times \left(1 - \frac{z+4}{L}\right) \quad \text{(A.26)}$$

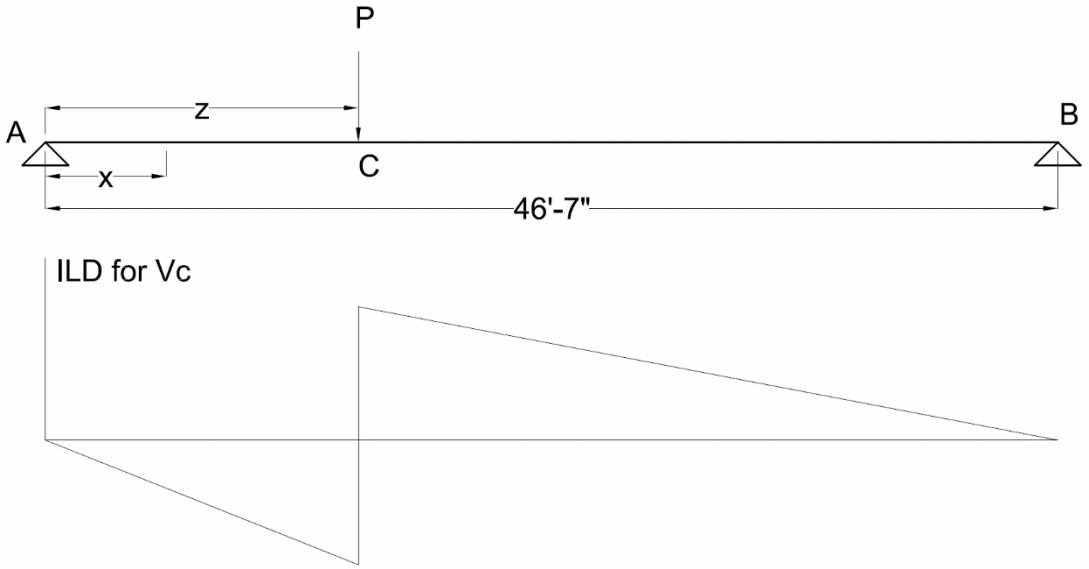

(a) Influence Line Diagram (ILD) for Shear for a Representative Point Load

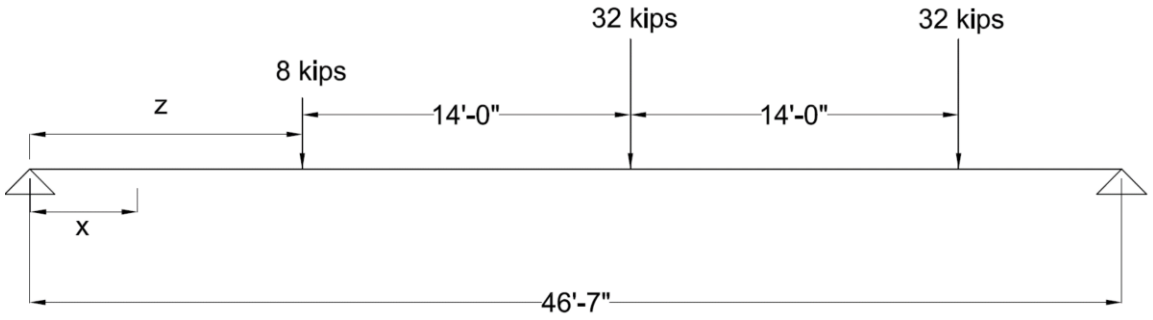

(b) HS20 Truck

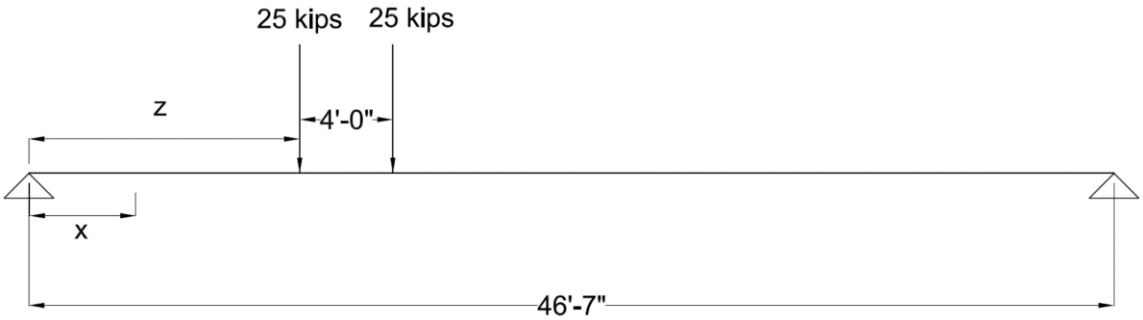

(c) Design Tandem

Figure A.4. Load Cases for Influence Line Analysis.

A.4.3 Maximum Moment and Shear

Design moment for an interior girder is calculated for two different vehicle positions in order to show the difference. The first calculation is done when the vehicle is located at a critical moment position for the HS20 truck only (HS20 critical). For a series of point loads over a simply supported span, the maximum moment occurs under the load closest to the resultant when the load and resultant are placed equidistant from midspan. For an HS20 truck that has second and rear axles 14 ft apart, the critical moment position is when the second axle is 2 ft 4 in. away from the midspan. The vehicle position and all the moment results for that vehicle position are shown in Figure A.5.

The second calculation is done when the vehicle is located at a critical moment position for the combined loading (combined loading critical). The maximum moment occurs at 2 ft 4 in. away from the midspan for the HS20 truck, whereas the maximum moment for the uniform lane load and dead loads occurs at the midspan. This means the maximum moment for combined loading occurs somewhere in between these two points. This point is calculated using more refined analysis by the influence line method. The results of this loading case are shown in Figure A.6. Although the maximum moment results are close, the second calculation gives a little higher maximum moment, and this is the one that should be used.

The shear forces and bending moments due to uniform dead loads and uniform superimposed dead loads, V_D and M_D, at any section at a distance x are calculated using the following expressions, where the uniform load is denoted as w.

$$M_D = \frac{wL}{2}x - \frac{wx^2}{2} \tag{A.27}$$

$$V_D = \frac{wL}{2} - wx \tag{A.28}$$

Superimposed dead loads are calculated separately since they will be acting on the composite section, whereas the self-weight of the beam and the deck slab will act on the girders only.

$$V_{TN} = \begin{cases} g_V \times 1.33 \times R_{TN} & x \le z \\ g_V \times 1.33 \times (R_{TN} - 25) & z < x \le z + 4 \\ g_V \times 1.33 \times (R_{TN} - 50) & x > z + 4 \end{cases} \tag{A.29}$$

$$M_{TN} = \begin{cases} g_M \times 1.33 \times R_{TN} x & x \le z \\ g_M \times 1.33 \times (R_{TN} x - 25(\mathrm{x} - \mathrm{z})) & z < x \le z + 4 \\ g_M \times 1.33 \times (R_{TN} x - 25(2\,\mathrm{x} - 2\,\mathrm{z} - 4)) & x > z + 4 \end{cases} \quad \text{(A.30)}$$

Where:

R_{TN} = Reaction force at the left end support, kips.

V_{TN} = Shear force as a function of tandem position and location, kips.

M_{TN} = Bending moment as a function of tandem position and location, kip-ft.

Shear forces and bending moments due to uniformly distributed lane load of 0.64 kips/ft are calculated using the following expressions.

$$V_{LL} = \frac{wL}{2} - wx \quad \text{(A.31)}$$

$$M_{LL} = \frac{wL}{2} x - \frac{wx^2}{2} \quad \text{(A.32)}$$

Where:

V_{LL} = Shear force due to uniformly distributed design lane load, kips.

M_{LL} = Moment due to uniformly distributed design lane load, kip-ft.

The bending moment results when the vehicle is at the HS20 critical position are shown in Figure A.5. Plot (b) shows unfactored moments for dead load of structural components (DC), dead load of wearing surface and utilities (DW), design truck live load (HS20), and uniform design lane live load (Lane). Plot (c) shows the total moments when all the live loads are multiplied by the moment distribution factor and dynamic allowance applied to the HS20 load.

The bending moment results when the HS20 truck is at the combined critical position are shown in Figure A.6. The bending moments are calculated using Equations (A.32) to (A.35), similar to the other case, but this time, all the loads are combined together to figure out the critical moment position of the vehicle. The combined moment results are shown in Figure A.6(b).

$$R_{TR} = 8 \times \left(1 - \frac{z}{L}\right) + 32 \times \left(1 - \frac{z+14}{L}\right) + 32 \times \left(1 - \frac{z+28}{L}\right) \quad \text{(A.33)}$$

$$V_{TR} = \begin{cases} g_V \times (1.33 \times R_{TR} + 0.64\frac{L}{2} - 0.64x) + W\frac{L}{2} - Wx & x \le z \\ g_V \times (1.33 \times (R_{TR} - 8) + 0.64\frac{L}{2} - 0.64x) + W\frac{L}{2} - Wx & z < x \le z + 14 \\ g_V \times (1.33 \times (R_{TR} - 40) + 0.64\frac{L}{2} - 0.64x) + W\frac{L}{2} - Wx & z + 14 < x \le z + 28 \\ g_V \times (1.33 \times (R_{TR} - 72) + 0.64\frac{L}{2} - 0.64x) + W\frac{L}{2} - Wx & z + 28 < x \end{cases} \quad \text{(A.34)}$$

$$M_{TR} = \begin{cases} g_M\left(1.33R_{TR}x + 0.64\frac{L}{2}x - 0.64\frac{x^2}{2}\right) + W\frac{L}{2}x - W\frac{x^2}{2} & x \le z \\ g_M\left(1.33\left(R_{TR} - 8(\mathrm{x} - \mathrm{z})\right) + 0.64\frac{L}{2}x - 0.64\frac{x^2}{2}\right) + W\frac{L}{2}x - W\frac{x^2}{2} & z < x \le z + 14 \\ g_M\left(1.33\left(R_{TR} - 8(\mathrm{x} - \mathrm{z}) - 32(\mathrm{x} - \mathrm{z} - 14)\right) + 0.64\frac{L}{2}x - 0.64\frac{x^2}{2}\right) + W\frac{L}{2}x - W\frac{x^2}{2} & z + 14 < x \le z + 28 \\ g_M\left(1.33\left(R_{TR} - 8(\mathrm{x} - \mathrm{z}) - 32(2\,\mathrm{x} - 2\,\mathrm{z} - 42)\right) + 0.64\frac{L}{2}x - 0.64\frac{x^2}{2}\right) + W\frac{L}{2}x - W\frac{x^2}{2} & z + 28 < x \end{cases}$$

(A.35)

Where:

W = Sum of all dead loads (DC+DW), kips.

L = Span length, ft.

The maximum bending moment is obtained when the second axle of the design truck is 1 ft 1.5 in. away (combined loading critical position) from the midspan and the distance between the second axle and rear axle is 14 ft.

The bending moment values that are shown in the total bending moments plot (c) include the dynamic allowance and live load distribution factors, but they are not multiplied by any load factors. The design values should be multiplied by the load combination factors.

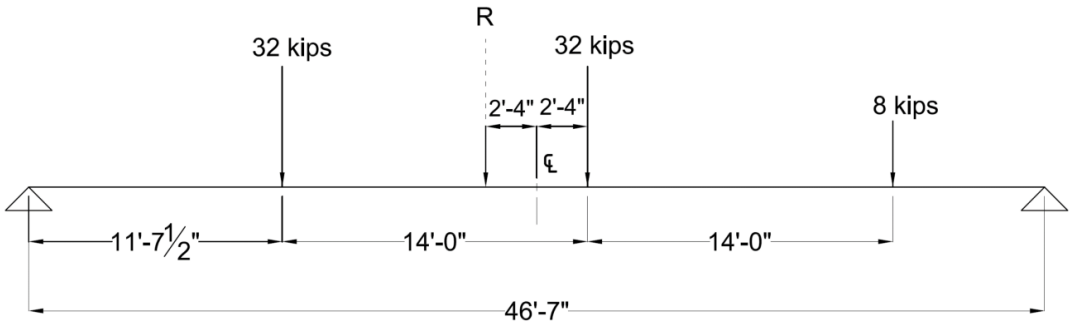

(a) HS20 Truck Position

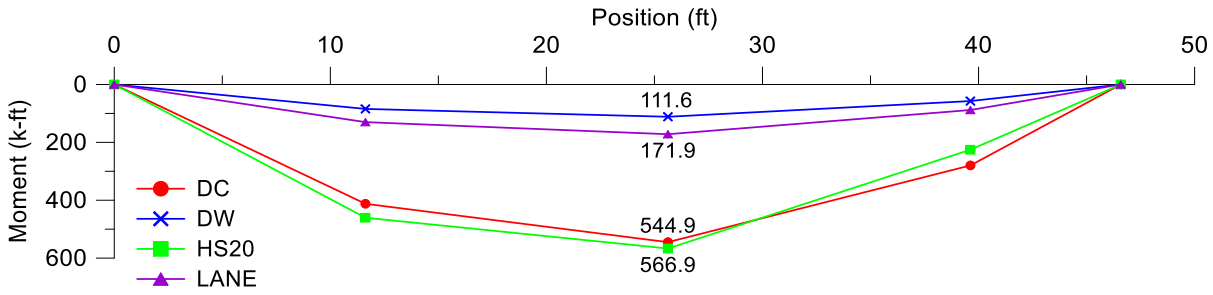

(b) Unfactored Bending Moments

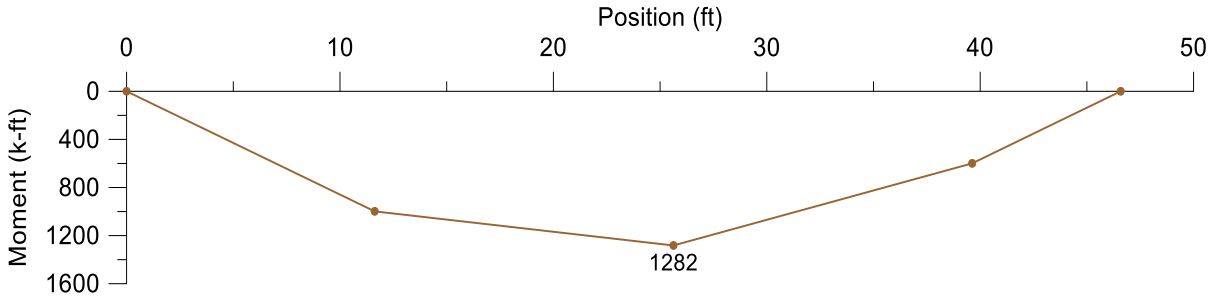

(c) Total Bending Moments

Figure A.5. Bending Moments When the Vehicle is at Critical Position for HS20 Loading.

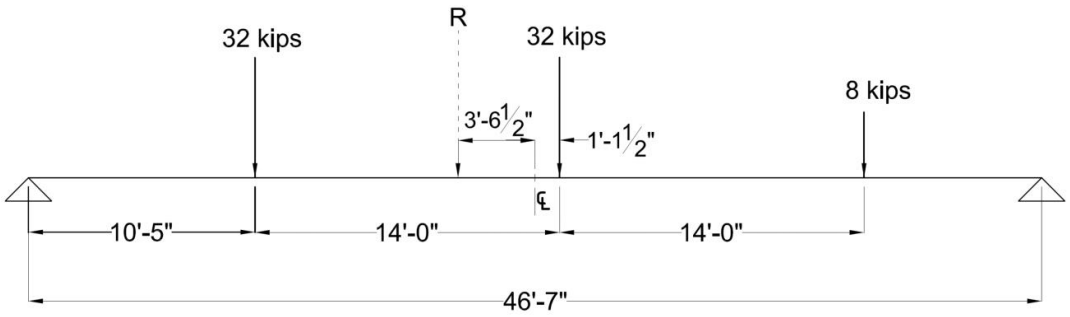

(a) HS20 Truck Position

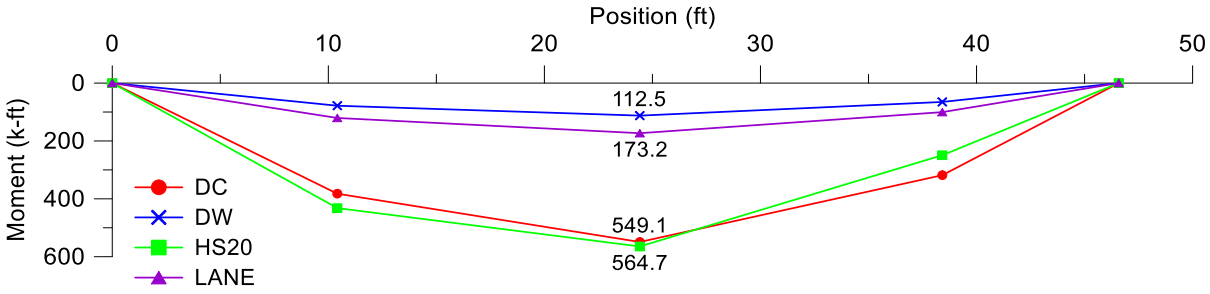

(b) Unfactored Bending Moments

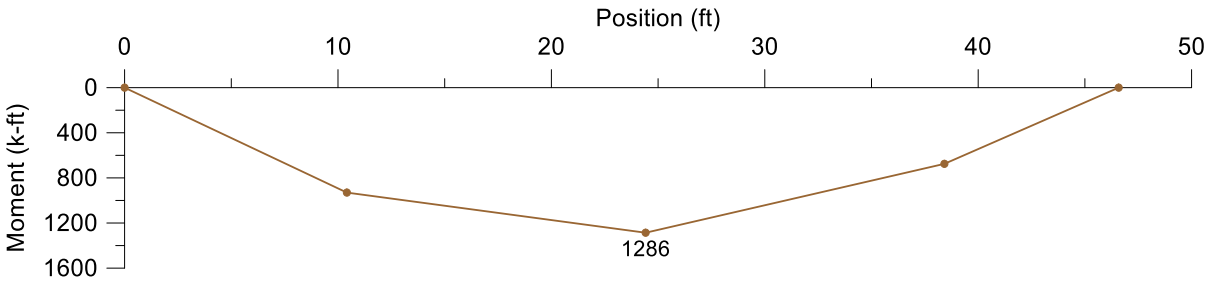

(c) Total Bending Moments

Figure A.6. Bending Moments When Vehicle is at Critical Position for Combined Loading.

A.4.4 Load Combinations

AASHTO LRFD Specifications (2012) Article 3.4.1 states that the total load effect can be calculated using certain service state load combinations. Service I and Service III load combinations are used for the design of a prestressed bridge superstructure as an uncracked section.

Service I load combination relates to the normal operational use of the bridge with a 55 mph wind and all loads taken at their nominal values. Service III load combination for longitudinal analysis relates to tension in prestressed concrete superstructures with the objective of crack control and to principal tension in the webs of segmental concrete girders.

AASHTO LRFD Specifications (2012) Table 3.4.1-1 specifies load combinations for various limit states. The load combinations that are critical for the designed bridge are as follows.

Service I—Check compressive stresses in prestressed concrete components:

$$Q = 1.00(DC + DW) + 1.00(LL + IM)$$

Service III—Check tensile stresses in prestressed concrete components:

$$Q = 1.00(DC + DW) + 0.80(LL + IM)$$

Strength I—Check ultimate strength [LRFD Table 3.4.1-1 & 2]:

$$\text{Maximum } Q = 1.25(DC) + 1.50(DW) + 1.75(LL + IM)$$

$$\text{Minimum } Q = 0.90(DC) + 0.65(DW) + 1.75(LL + IM)$$

Where:

- DC = Dead load of structural components and nonstructural attachments.
- DW = Dead load of wearing surface and utilities.
- LL = Vehicular live load.
- IM = Vehicular dynamic load allowance.

A.5 DESIGN FOR PRESTRESSING FORCE

A.5.1 Stresses at Midspan Due to Service Loads

Design of prestressed slab beams is based on the service limit stresses at the critical moment section of the bridge, assuming that the section is uncracked. The required prestressing force under service loads is calculated at the critical moment section. Other critical section stresses

are checked under the calculated prestressing force at transfer and at service after all prestressing losses.

A.5.1.1 Tensile Stress at Extreme Bottom Fiber of Interior Girder Due to Imposed Loads, f_b (Service III)

The maximum tensile stress at the bottom fiber of the slab beam girder is calculated using Equation (A.36). Live load moment at service (M_L) is calculated by multiplying the combined live load due to vehicle loading, which includes 33 percent dynamic impact, and AASHTO LRFD Specifications (2012) uniform distributed live load (0.64 kips/ft) with moment LDF.

$$f_b = \frac{M_b + M_s}{S_b} + \frac{M_{ws} + M_r + 0.8M_{LL}}{S_{bc}} \tag{A.36}$$

$$M_{LL} = g_M(1.33M_{TR} + M_L) = 0.676 \times (1.33 \times 564.7 + 173.2) = 624.8 \text{ kip-ft}$$

$$f_b = \frac{549.1 \times 12}{2{,}250} + \frac{(112.5 + 0.8 \times 624.8) \times 12}{5802.88} = 4.20 \text{ ksi}$$

A.5.1.2 Compressive Stress at Top Fiber of Interior Girder Due to Imposed Loads, f_t (Service I)

Maximum compressive stress at the top fiber of the slab beam girder at service is calculated using Equation (A.37).

$$f_t = \frac{M_b + M_s}{S_t} + \frac{M_{ws} + M_r + M_{LL}}{S_{tg}} \tag{A.37}$$

$$f_t = \frac{549.1 \times 12}{2250} + \frac{(112.5 + 624.8) \times 12}{29{,}542} = 3.23 \text{ ksi}$$

Where:

M_b = Bending moment due to self-weight of the slab beam at the moment critical section, kip-ft.

M_s = Bending moment due to CIP deck slab at the moment critical section, kip-ft.

M_{ws} = Bending moment due to wearing surface at the moment critical section, kip-ft.

M_r = Bending moment due to rail at the moment critical section, kip-ft.

M_L = Bending moment due to truck load plus the distributed lane load at the moment critical section, kip-ft.

The stress due to service loads and prestressing stresses should be within the allowable stress limits that are defined above.

A.5.1.3 Tensile Stress Limit

Tensile stress due to imposed loads at service shall satisfy the allowable tensile stress limit as defined in AASHTO LRFD Specifications (2012). Required prestressing force at service based on tensile stress limit can be calculated using Equation (A.38).

$$-\frac{F_{req}}{A_b}-\frac{F_{req}e}{S_b}+f_b<F_t \tag{A.38}$$

Where:

F_{req} = Total required pretension force after all losses to satisfy allowable stress limits, kips.

e = Eccentricity of prestressing force (4 in. when all 56 strand slots are used), in.

f_b = Bottom fiber tensile stress at service, ksi.

F_t = Tensile stress limit at service after all losses occur, ksi.

$$-\frac{F_{req}}{900}-\frac{F_{req}\times 4}{2250}+4.2<0.503 \text{ ksi}$$

$$\Rightarrow F_{req}=1280 \text{ kips}$$

A.5.1.4 Compressive Stress Limit

Required prestressing force at service based on compressive stress limit can be calculated using Equation (A.39).

$$-\frac{F_{req}}{A_b}+\frac{F_{req}e}{S_t}-f_t>F_c \tag{A.39}$$

Where:

F_c = Compressive stress limit at service after losses, ksi.

$$-\frac{F_{req}}{900}+\frac{F_{req}\times 4}{2250}-3.23>-3.15 \text{ ksi}$$

$$\Rightarrow F_{req}=120 \text{ kips}$$

The total prestressing force should be at least 1280 kips in order to satisfy stress limits under service load conditions.

The number of strands can be calculated as:

$$F=N\left(A_{ps}\right)\left(f_{pe}\right) \quad \text{(A.40)}$$

Where:

N = Number of prestressing strands.

f_{pe} = Effective prestressing stress of one strand after all losses, ksi.

A_{ps} = Nominal cross-sectional area of a prestressing strand (0.153 in^2 for 0.5 in. diameter strand), in^2.

In order to be able to calculate number of strands, prestress losses should be calculated.

A.5.2 Total Loss of Prestress

In pretensioned members, prestressing losses result from elastic shortening at the time of prestressing and long-term losses. Long-term losses for prestressed members include shrinkage, creep, and strand relaxation. Total prestress losses are calculated according to the empirical formulas provided in AASHTO LRFD Specifications (2012) Article 5.9.5. The formulas provided are for normal weight concrete only and valid for specified concrete strength up to 15 ksi.

$$\Delta f_{pT}=\Delta f_{pES}+\Delta f_{pLT} \quad \text{(A.41)}$$

Where:

Δf_{pT} = Total prestress loss, ksi.

Δf_{pES} = Sum of losses due to elastic shortening at the time of application of prestress, ksi.

Δf_{pLT} = Losses due to long-term shrinkage and creep of concrete and relaxation of the steel, ksi.

A.5.2.1 Losses Due to Elastic Shortening

The loss due to elastic shortening in pretensioned members is calculated as:

$$\Delta f_{pES} = \frac{E_p}{E_{ct}} f_{cgp} \tag{A.42}$$

Where:

E_p = Modulus of elasticity of prestressing steel, ksi.

E_{ct} = Modulus of elasticity of concrete at transfer, ksi.

f_{cgp} = Concrete stress at the center of gravity of prestressing tendons due to prestressing force immediately after transfer and the self-weight of the member at the section of maximum moment, ksi.

F_i = Total prestressing force immediately after transfer.

$$f_{cgp} = \frac{F_i}{A} + \left(\frac{e}{d/2}\right)\left(\frac{F_i e}{S} - \frac{M_b}{S}\right) \tag{A.43}$$

For loss calculations, the number of strands used must be known. On the other hand, the required number of strands depends on the prestressing loss. This requires an iterative process. This calculation is carried out using an iterative calculation starting with 25 percent assumed total loss. The results show that all the prestressing strand locations must be used in order to achieve allowable stress limits under service loads.

$$F_i = N f_{pt} A_{ps} \tag{A.44}$$

$$f_{pi} = 0.75 \times 270 = 202.5 \text{ ksi}$$

Where:

f_{pi} = Prestressing stress immediately prior to transfer, ksi.

f_{pt} = Initial prestressing stress immediately after transfer, ksi.

$$f_{pt} = f_{pi} - \Delta f_{pES} \tag{A.45}$$

For calculating total prestressing force just after transfer, initial prestress after transfer, which depends on the elastic shortening loss, must be known. The initial prestress after transfer is assumed to be 90 percent of the prestress before transfer and analysis iterated until acceptable

accuracy is achieved. The iterative calculation shows that the initial prestress after transfer is $f_{pt} = 186.9$ ksi.

$$F_i = 56 \times 186.88 \times 0.153 = 1601.2 \text{ kips}$$

$$f_{cgp} = \frac{1601.2}{900} + \left(\frac{4}{7.5}\right) \times \left(\frac{1601.2 \times 4}{2250} - \frac{254.3 \times 12}{2250}\right) = 2.574 \text{ ksi}$$

$$E_p = 28{,}500 \text{ ksi and } E_c = 33{,}000 w_c^{1.5} \sqrt{f'_{ci}} \,(\text{ksi}) = 4696 \text{ ksi}$$

$$\Delta f_{pES} = \frac{28500}{4696}(2.574) = 15.62 \text{ ksi}$$

Initial prestress after elastic losses is calculated as, $f_{pt} = 202.5 - 15.62 = 186.9$ ksi, which is the same as the initial prestressing stress estimate.

A.5.2.2 Approximate Calculation of Time-Dependent Losses

Long term prestress losses are calculated using the approximate equation provided in AASHTO LRFD Specifications (AASHTO 2012) Article 5.9.5.3.

$$\Delta f_{pLT} = 10 \frac{\left(f_{pi} A_{ps}\right)}{A_g} \gamma_h \gamma_{st} + 12 \gamma_h \gamma_{st} + \Delta f_{pR} \tag{A.46}$$

Where:

γ_h = Correction factor for relative humidity of the ambient air.

$$\gamma_h = 1.7 - 0.01H = 1.7 - 0.01(70) = 1 \tag{A.47}$$

H = Average annual ambient relative humidity (%), which is obtained from AASHTO LRFD Specifications (2012) Figure 5.4.2.3.3-1.

γ_{st} = Correction factor for specified concrete strength at the time of prestress transfer to the concrete member.

$$\gamma_{st} = \frac{5}{1 + f'_{ci}} \tag{A.48}$$

Δf_{pR} = Estimate of relaxation loss taken as 2.4 ksi for low-relaxation strands.

f_{pt} = Prestressing steel stress immediately prior to transfer, ksi.

$$\Delta f_{pLT} = 10 \times \frac{202.5 \times 56 \times 0.153}{900} \times 1 \times \frac{5}{7} + 12 \times 1 \times \frac{5}{7} + 2.4 = 24.74 \text{ ksi}$$

A.5.2.3 Refined Method for Estimating Time-Dependent Losses

Prestressing stress reduces over time due to elastic shortening and time-dependent effects. The total loss is calculated as cumulative of these losses. The prediction of prestress loss is important to accurately estimate the camber. AASHTO LRFD Specifications (2012) Article 5.9.5.4 provides a refined method for estimating the amount of prestress loss.

The prestressing loss in prestressing strands due to time-dependent effects, Δf_{pLT}, is determined as:

$$\Delta f_{pLT} = \left(\Delta f_{pSR} + \Delta f_{pCR} + \Delta f_{pR1}\right)_{id} + \left(\Delta f_{pSD} + \Delta f_{pCD} + \Delta f_{pR2} - \Delta f_{pSS}\right)_{df} \quad \text{(A.49)}$$

Where:

$\left(\Delta f_{pSR} + \Delta f_{pCR} + \Delta f_{pR1}\right)_{id}$ = Sum of time-dependent losses between transfer and deck placement, ksi.

$\left(\Delta f_{pSD} + \Delta f_{pCD} + \Delta f_{pR2} - \Delta f_{pSS}\right)_{df}$ = Sum of time-dependent prestress losses after deck placement, ksi.

Δf_{pSR} = Prestress loss due to shrinkage between transfer and deck placement, ksi.

Δf_{pCR} = Prestress loss due to creep between transfer and deck placement, ksi.

Δf_{pR1} = Prestress loss due to relaxation of strands between transfer and deck placement, ksi.

Δf_{pSD} = Prestress loss due to shrinkage between deck placement and final time, ksi.

Δf_{pCD} = Prestress loss due to creep between deck placement and final time, ksi.

Δf_{pR2} = Prestress loss due to relaxation of strands between deck placement and final time, ksi.

Δf_{pSS} = Prestressing gain due to shrinkage of deck in composite section, ksi.

Time of load application is considered to be 1 day, time of erecting the PCPs is assumed to be 30 days, and time of CIP deck construction is taken as 40 days after casting of slab beams. Final time is taken as 10 years (3650 days).

A.5.2.3.1 Prestress Losses Due to Shrinkage

The prestress loss due to shrinkage of girder concrete between time of transfer and deck placement is determined as:

$$\Delta f_{pSR} = \varepsilon_{bid} E_p K_{id} \tag{A.50}$$

Where:

ε_{bid} = Concrete shrinkage strain between transfer and deck placement, in./in.

K_{id} = Transformed section coefficient that accounts for time-dependent interaction between concrete and bonded steel in the section being considered for time period between transfer and deck placement.

$$K_{id} = \frac{1}{1+\left(\frac{E_p}{E_{ci}}\right)\left(\frac{A_{ps}}{A_g}\right)\left(1+\frac{A_g e_{pg}^2}{I_g}\right)\left(1+0.7\psi_b\left(t_f, t_i\right)\right)} \tag{A.51}$$

ψ_b = girder creep coefficient at final time due to loading introduced at transfer.

The calculation of prestress losses due to shear or creep depends on the shear strains and creep coefficients.

A.5.2.3.1.1 <u>Shrinkage Strain:</u>

Shrinkage is a volumetric change of concrete due to evaporation of excess water after hardening. Shrinkage causes tensile stresses, which may lead to cracking. There are several factors that increase the shrinkage amount, such as water-cement ratio, amount of moisture during curing, relative humidity, and member size. Shrinkage does not occur due to external stresses.

The shrinkage strain is calculated based on AASHTO LRFD Specifications (2012) Article 5.4.2.3 using the below formula.

$$\varepsilon_{sh} = k_s k_{hs} k_f k_{td} \left(0.48\right)\left(10^{-3}\right) \tag{A.52}$$

Where:

k_s = Factor for effect of the volume-to-surface ratio of the component.

$$k_s = 1.45 - 0.13\left(\frac{V}{S}\right) \geq 1.0 \tag{A.53}$$

V/S = Volume-to-surface ratio, in.

$$V = bdL \tag{A.54}$$

$$V = \left(\frac{60}{12}\right)\left(\frac{15}{12}\right)(48) = 300\,\text{ft}^3$$

$$S = 2\left[\left(\frac{60}{12}\right)(48) + \left(\frac{15}{12}\right)(48) + \left(\frac{60}{12}\right)\left(\frac{15}{12}\right)\right] = 612.5\,\text{ft}^2$$

$$k_s = 1.45 - 0.13\left(\frac{300}{612.5}\right) \times 12 = 0.686$$

k_{hs} = Humidity factor for shrinkage.

$$k_{hs} = 2.0 - 0.014H \tag{A.55}$$

H = Relative humidity, percent.

For College Station, the relative humidity is taken as 70 percent and $k_{hs} = 2.0 - 0.014(70) = 1.02$.

k_f = Factor for the effect of concrete strength.

$$k_f = \frac{5}{1 + f_{ci}^{'}} \tag{A.56}$$

$$k_f = \frac{5}{1+6} = 0.714$$

k_{td} = Time development factor.

Time development factor between end of curing and deck placement is:

$$k_{td} = \frac{t}{61 - 4f_{ci}^{'} + t} \tag{A.57}$$

$$k_{td} = \frac{35}{61 - 4(6) + 35} = 0.486$$

$f_{ci}^{'}$ = Concrete compressive strength at release, ksi.

t = Maturity of concrete (day), defined as age of concrete between time of loading for creep calculation, or time of curing for shrinkage calculations, and time being considered for analysis of creep or shrinkage effects, days.

Generally, prestressing factories apply the prestressing load after 24 hours, applying an accelerated curing. Based on the above introduced parameters and assumptions, shrinkage as a function of time is calculated.

Shrinkage strain at deck placement (40 days) is as follows.

$$\varepsilon_{sh} = (1.0)(1.02)(0.714)(0.486)(0.48)(10^{-3}) = 1.7(10^{-4})$$

A.5.2.3.1.2 *Creep Coefficient:*

When a girder is loaded, the girder deforms elastically. The girder continues deforming in time. The total deformation cannot be recoverable completely. This continued deformation is called creep. Creep deflection depends on many of the same factors that govern shrinkage. However, creep also depends on the age and magnitude of the load.

Both creep and shrinkage result from the removal of water from the calcium-silicate-hydrate (CSH) portion of the cement mix due to chemical reactions. This causes strain in the concrete, resulting in a volumetric change. The difference between these two is that creep is stress induced, while shrinkage is induced by ambient conditions. Because these phenomena are based on the same origin, they are interrelated. Since they occur simultaneously, it is impossible to test for them independently.

In order to estimate the amount of creep, the AASHTO LRFD Specifications (2012) method is employed. It uses a time-dependent function that is multiplied by factors that account for material and environmental effects. The creep coefficient is calculated using the below formula.

$$\psi_b(t, t_i) = 1.9 k_s k_{hc} k_f k_{td} t_i^{-0.118} \tag{A.58}$$

Where:

k_{hc} = Humidity factor for creep.

$$k_{hc} = 1.56 - 0.008H = 1.0 \tag{A.59}$$

Creep coefficient between deck placement and transfer:

$$k_{td} = \frac{39}{61 - 4(6) + 39} = 0.513 \tag{A.60}$$

$$\psi_b(t_d, t_i) = (1.9)(1.0)(0.714)(0.513)(1)^{-0.118} = 0.696$$

Creep coefficient between final time and transfer:

$$\psi_b(t_f, t_i) = (1.9)(1.0)(1.0)(0.714)(0.99)(1)^{-0.118} = 1.344$$

Next, the creep coefficient and shrinkage strains at the time of deck placement are calculated.

$$K_{id} = \frac{1}{1+\left(\frac{28500}{4696}\right)\left(\frac{8.568}{900}\right)\left(1+\frac{(900)(4)^2}{16875}\right)(1+0.7(1.344))} = 0.828$$

$$\Delta f_{pSR} = (1.7\times10^{-4})\times 28{,}500\times 0.828 = 4.01 \text{ ksi}$$

The prestress loss due to shrinkage of girder concrete after deck placement until the final time can be calculated as follows:

$$\Delta f_{pSD} = \varepsilon_{bdf} E_p K_{df} \quad \text{(A.61)}$$

Where:

ε_{bdf} = Concrete shrinkage strain between deck placement and final time = 3.462×10^{-4}.

K_{df} = Transformed section coefficient that accounts for time-dependent interaction between concrete and bonded steel in the section being considered for time period between deck placement and final time.

$$K_{df} = \frac{1}{1+\left(\frac{E_p}{E_{ci}}\right)\left(\frac{A_{ps}}{A_c}\right)\left(1+\frac{A_c e_{pc}^2}{I_c}\right)\left(1+0.7\psi_b\left(t_f,t_i\right)\right)} = 0.85 \quad \text{(A.62)}$$

A_c = Area of the composite section using the deck-to-girder modular ratio, in^2.

$$A_c = b_{eff}t + bd = 87.688\times 8 + 60\times 15 = 1601.5 \text{ in}^2 \quad \text{(A.63)}$$

e_{pc} = Eccentricity of the strands with respect to center of gravity of the composite section, in.

$$e_{pc} = y_b - (\text{d}/2 - \text{e}) = 12.537 - 3.5 = 9.037 \text{ in} \quad \text{(A.64)}$$

I_c = Moment of inertia of the composite section, in^4.

$$I_c = 72{,}753 \text{ in}^4$$

$$\Delta f_{pSD} = (3.462\times10^{-4})\times 28{,}500\times 0.85 = 8.387 \text{ ksi}$$

A.5.2.3.2 Prestress Losses Due to Creep

The AASHTO LRFD Specifications (2012) uses a time-dependent function that is multiplied by factors in order to represent material and environmental effects. This equation uses a similar approach as the shrinkage loss estimate; it is estimated in two phases. One is an

estimate of loss between time of transfer and deck placement, and the other is between deck placement and final time. The prestress loss due to creep of girder concrete between transfer and deck placement is determined as:

$$\Delta f_{pCR} = \frac{E_p}{E_{ci}} f_{cgp} \psi_b \left(t_d, t_i\right) K_{id} \tag{A.65}$$

Where:

$\psi_b(t_d, t_i)$ = Girder creep coefficient at the time of deck placement due to loading introduced at transfer.

$$\Delta f_{pCR} = \frac{28{,}500}{4696}(2.574)(0.6964)(0.828) = 9.0 \text{ ksi}$$

The prestress (loss is positive, gain is negative) due to creep of girder concrete between deck placement and final time is determined as:

$$\Delta f_{pCD} = \frac{E_p}{E_{ci}} f_{cgp}\left[\psi_b\left(t_f, t_i\right) - \psi_b\left(t_d, t_i\right)\right] K_{df} + \frac{E_p}{E_c} \Delta f_{cd} \psi_b\left(t_f, t_d\right) K_{df} \tag{A.66}$$

Where:

$\psi_b(\mathrm{t_f}, \mathrm{t_d}) = (1.9)(1.0)(1.0)(0.714)(0.989)(40)^{-0.118} = 0.869$

Δf_{cd} = Change in concrete stress at centroid of prestressing strands due to long-term losses between transfer and deck placement, combined with deck weight and superimposed loads, ksi.

$$\Delta f_{cd} = \left(\Delta f_p\right)_{id}\left(\frac{1}{A_g} + \frac{e_{pg}^2}{I_g}\right) + \frac{M_d e_{pg}}{I_g} \tag{A.67}$$

$\left(\Delta f_p\right)_{id}$ = Change in prestressing force between transfer and deck placement, kip.

$$\left(\Delta f_p\right)_{id} = NA_{ps}\left(\Delta f_{pSR} + \Delta f_{pCR} + \Delta f_{pR1}\right)_{id} \tag{A.68}$$

A_g = Gross area of slab beam section, in2.

e_{pg} = Eccentricity of strands with respect to centroid of the girder, in.

M_d = Moment due to deck weight and superimposed loads, kip-ft.

I_g = Moment of inertia of slab beam section, in^4.

Prestress loss is due to creep of girder between deck placement and final time and is calculated from Equation (A.66) as:

$$\Delta f_{pCD} = 14.46 \text{ ksi}$$

A.5.2.3.3 Prestress Losses Due to Relaxation of Prestressing Strands

The prestress loss due to relaxation of prestressing strands between transfer and deck placement can be calculated as:

$$\Delta f_{pR1} = \frac{f_{pt}}{K_L}\left(\frac{f_{pt}}{f_{py}} - 0.55\right) \quad \text{(A.69)}$$

Where:

f_{pt} = Stress in prestressing strands immediately after transfer, taken not less than 0.55fpy, ksi.

K_L = 30 for low-relaxation strands and 7 for other prestressing steel.

The relaxation loss may be assumed equal to 1.2 for low-relaxation strands. Research indicates that about one-half of the losses due to relaxation occur before deck placement; therefore, the losses after deck placement are equal to the prior losses.

$$\Delta f_{pR1} = \Delta f_{pR2} = 1.2 \text{ ksi}$$

A.5.2.3.4 Prestress Losses Due to Shrinkage of Deck Concrete

The prestress gain due to shrinkage of the composite section can be determined as:

$$\Delta f_{pSS} = \frac{E_p}{E_c}\Delta f_{cdf} K_{df}\left[1 + 0.7\psi_b\left(t_f, t_d\right)\right] \quad \text{(A.70)}$$

Where:

Δf_{cdf} = Change in concrete stress at centroid of prestressing strands due to shrinkage of deck concrete, ksi.

ε_{ddf} = Shrinkage strain of deck concrete between placement and final time.

ed = Eccentricity of deck with respect to the gross composite section, positive in typical construction where deck is above girder, in.

$$\Delta f_{cdf} = \frac{\varepsilon_{ddf} A_d E_{cd}}{\left[1 + 0.7\psi_d\left(t_f, t_d\right)\right]}\left(\frac{1}{A_c} - \frac{e_{pc} e_d}{I_c}\right) \quad \text{(A.71)}$$

$$\Delta f_{pSS} = 1.05 \text{ ksi}$$

Using Equation (A.49):

$$\Delta f_{pLT} = (4.01 + 9.0 + 1.2) + (8.387 + 14.46 + 1.2 - 1.05) = 37.2 \text{ ksi}$$

From Equation (A.41):

$$\Delta f_{pT} = 15.62 + 37.21 = 52.83 \text{ ksi}$$

$$f_{pe} = f_{pi} - \Delta f_{pT} = 202.5 - 52.83 = 149.67 \text{ ksi} \quad \text{(A.72)}$$

From Equation (A.40):

$$N = \frac{F_{req}}{A_{ps} f_{pe}} = \frac{1280}{0.153 \times 149.67} = 55.9 \approx 56$$

A.5.3 Stress Checks at Critical Sections

A.5.3.1 Stress at Midspan Immediately after Deck Placement

A.5.3.1.1 Tensile Stress at the Bottom Fiber of the Girder

Maximum tensile stress at the extreme bottom fiber of composite girder was calculated using Equation (A.73).

$$f_b = \frac{M_b + M_s}{S_b} \quad \text{(A.73)}$$

$$f_b = \frac{(549.1)(12)}{2250} = 2.93 \text{ ksi}$$

Total tension force at the extreme bottom fiber of the slab beam due to prestressing force and self-weight of slab beam plus deck must be smaller than the tensile stress limit.

$$-\frac{F}{A_b} - \frac{Fe}{S_b} + f_b < F_t \quad \text{(A.74)}$$

$$F = NA_{ps} f_{ped}$$

Where:

f_{ped} = Effective prestressing stress at the time of deck placement, ksi.

Prestress losses at the time of deck placement only include elastic shortening losses and part of the long-term losses. Long-term prestress losses between transfer and deck placement are:

$$\Delta f_{pLT} = \left(\Delta f_{pSR} + \Delta f_{pCR} + \Delta f_{pR1}\right)_{id} = 4.01 + 9 + 1.2 = 14.21$$

$$f_{ped} = f_{pi} - \Delta f_{pES} - (\Delta f_{pLT})_{\text{id}} = 202.5 - 15.62 - 14.21 = 172.67 \text{ ksi}$$

$$F = 56 \times 0.153 \times 172.67 = 1479.4 \text{ kips}$$

From Equation (A.74):

$$-\frac{1479.4}{900} - \frac{(1479.4)(4.0)}{2250} + 2.93 < F_t$$

$$-1.34 < F_t \equiv 0.5027 \text{ ksi}$$

A.5.3.1.2 Compressive Stress at the Top Fiber of the Girder

The maximum compressive stress at the extreme top fiber of the composite section was calculated from Equation (A.75).

$$f_t = \frac{M_b + M_s}{S_t} \tag{A.75}$$

$$f_t = \frac{(-549.1)(12)}{2250} = -2.93 \text{ ksi}$$

The compressive stress created by the prestressing force, the weight of the slab beam, and CIP deck concrete should be smaller than the allowable compressive stress limit. The compressive stress is considered as negative.

$$-\frac{F}{A_b} + \frac{Fe}{S_t} - f_t > F_c \tag{A.76}$$

$$-\frac{1479.4}{900} + \frac{(1479.4)(4.0)}{2250} - 2.93 > F_c$$

$$-1.94 > F_c \equiv -3.15 \text{ ksi}$$

A.5.3.2 Stress at the Ends of the Slab Beam Girder

The initial prestress applied to the strands is $f_{pt} = 202.5$ ksi , and the initial prestressing force per strand is $F_{pt} = f_{pt} A_{ps} = 202.5 \times 0.153 = 30.98$ kips . The elastic shortening loss occurs immediately after transfer, which means the initial stress for checking the end stresses should take the elastic shortening losses into account.

$$f_{pi} = f_{pt} - \Delta f_{pES} \tag{A.77}$$

Where:

f_{pi} = Initial prestressing stress immediately after transfer, ksi.

The total prestressing force at each section immediately after transfer along the length is calculated using the f_{pi} value per Equation (A.77). The initial prestressing stress immediately after transfer is a function of initial prestressing force immediately after transfer (due to f_{cgp} parameter in Δf_{pES} calculation). Therefore, the initial prestressing force immediately after transfer, F_{pi}, is assumed to be 90 percent of F_{pt}, and the calculation is iterated until desired accuracy is obtained for the F_{pi} value.

The other critical parameter is the transfer length for the prestressing force. Transfer length is the length over which prestressing force is transferred to the concrete by bonding in pretensioned members. This transfer does not occur immediately at the very end of the member. The full bonding between prestressing strands and the concrete develops within a specific distance from the end of the tendon. According to the TxDOT Bridge Design Manual (TxDOT 2013a), the prestress force may be assumed to vary linearly from zero at the end of the tendon to a full stress state at a distance of $60d_b = 60 \times 0.5 = 30$ in.

The elastic shortening calculation requires calculating the bending moment due to self-weight of the slab beam girder at the section of interest. Also, the stress state at the top and bottom surface of the prestressed slab beam is a function of the dead load moment and the prestressing force. The span length of an individual slab beam is considered to be the full length of the member based on the practices of the PGSuper Design Guide (PGSuper 2013) . The total length of the slab beam is $(46'-7'') + (1'-5'') = (48'-0'')$.

The initial stress at 30 in. from the end of the beam at the extreme top fiber of the beam is calculated as:

$$f_{ti} = -\frac{F_{pi}}{A_b} + \frac{F_{pi}e}{S_t} - \frac{M_b}{S_t} \tag{A.78}$$

$$M_b = \frac{wL_b}{2}x - \frac{wx^2}{2} \tag{A.79}$$

Where:

L_b = 48 ft, the total length of the slab beam.

M_b = Dead load moment due to self-weight of the slab beam (53.3 kip-ft at 30 in. from the end of the beam), kip-ft.

F_{pi} = Total initial prestressing force immediately after transfer, kips.

$$F_{pi} = A_{ps} N f_{pi} \tag{A.80}$$

Elastic shortening losses at the same section (30 in. away from the end) are calculated using the iterative process explained above and Equations (A.42) and (A.43).

$$(\Delta f_{pES})_{@30"} = 16.87 \text{ ksi}$$

$$f_{pi} = 202.5 - 18.75 = 183.75 \text{ ksi}$$

$$F_{pi} = 0.153 \times 56 \times 183.75 = 1574.4 \text{ kips}$$

$$f_{ti} = -\frac{1574.4}{900} + \frac{1574.4 \times 4}{2250} - \frac{53.3 \times 12}{2250} = 0.765 \text{ ksi}$$

The top stress immediately after transfer is higher than the increased tensile stress limit that is calculated as 0.588 ksi in Equation (A.13). This stress exceedance requires some of the tendons to be debonded. Whenever an increased tensile stress limit is used at a section with debonded strands, the AASHTO LRFD Specifications (2012) requires additional top mild steel for the tensile stresses that might develop.

A.5.4 Mild Reinforcement Calculation for Debonded End Regions

According to AASHTO LRFD Specifications (2012) Article 5.9.4.1.2, if an increased tensile limiting stress is used, the debonded ends must have mild steel located at the top of the beam to carry the extra tensile force. The following mild steel calculation procedure is laid out in AASHTO LRFD Specifications (2012).

The stresses at the top and bottom at the ends of the beam right after transfer can be found similarly to Section 3.8 of this report, as shown below.

$$f_{cit} = -\frac{F}{A_b} + \frac{Fe}{S_b} \tag{A.81}$$

$$f_{cit} = -\frac{1574.4}{900} + \frac{(1574.4)(4)}{2250} = 1.05 \text{ ksi}$$

$$f_{cib} = -\frac{F}{A_b} - \frac{Fe}{S_b} \tag{A.82}$$

$$f_{cib} = -\frac{1574.4}{900} - \frac{(1574.4)(4)}{2250} = -4.55 \text{ ksi}$$

Where:

f_{cit} = Initial tensile stress at the top fiber of the beam at 30 in. from the end, ksi.

f_{cib} = Initial compressive stress at the bottom of the beam at 30 in. from the end, ksi.

In order to calculate the average tensile force that is created in that section due to prestressing force, the depth of the neutral axis is calculated as:

$$x = \frac{hf_{cit}}{(f_{cit} - f_{cib})} \tag{A.83}$$

$$x = \frac{15(1.05)}{(4.55+1.05)} = 2.8 \text{ in.}$$

The required reinforcement is calculated as:

$$T = \frac{f_{cit}}{2} bx \tag{A.84}$$

$$T = \frac{1.05}{2}(60)(2.8) = 88.2 \text{ kips}$$

$$f_s = 0.5 f_y \le 30 ksi = 0.5(60) = 30 \text{ ksi} \tag{A.85}$$

$$A_s = \frac{T}{f_s} \tag{A.86}$$

$$A_s = \frac{88.2}{30} = 2.94 \text{ in}^2$$

Where:

T = Tension force that is calculated using average tensile stress block, kips.

f_s = Permitted tensile stress of the reinforcing steel, ksi.

A_s = Area of required mild reinforcing steel, in^2.

Assuming #6 bars, the number of bars and spacing are calculated as:

$$N_s = \frac{A_s}{A_{\#6}} = \frac{2.94}{0.442} = 6.65 \rightarrow 7 \text{ bars}$$

A minimum of seven #6 bars must be used at the end regions and should be extended along the whole length.

A.5.5 Debonding Requirements and Debonding Length Calculation

According to the TxDOT Bridge Design Manual (TxDOT 2013a), debonded strands must conform to AASHTO LRFD Specifications (2012) Article 5.11.43, except as noted below:

- No more than 75 percent of the total number of strands shall be debonded.
- No more than 75 percent of the number of strands in that row shall be debonded.
- The maximum debonding length must be the lesser of one-half the span length minus the maximum development length, 0.2 times the beam length, or 15 ft.
- Not more than 75 percent of the debonded strands, or 10 strands, whichever is greater, shall have the debonding terminated at any section, where section is defined as an increment (e.g., 3 ft, 6 ft, 9 ft).

According to AASHTO LRFD Specifications (2012):

- Maximum percentage of the debonded strands per row should not exceed 40 percent and maximum percentage of debonded strands per section should not exceed 25 percent of the total number of strands.
- No more than 40 percent of the debonded strands or four strands, whichever is greater, shall have debonding terminated at the same section.
- Debonded strands shall be symmetrically distributed about the centerline of the member. Exterior strands in each row shall be fully bonded. Debonded lengths of pairs of strands that are symmetrically positioned about the centerline of the member shall be equal.

A.5.5.1 Debonding Length

The AASHTO LRFD Specifications (2012) recommends that the length of debonding should be such that all limit states are satisfied with consideration of the total developed resistance at any section being investigated. TxDOT Bridge Design Manual (TxDOT 2013a) recommends that the maximum debonding length can be chosen as the lesser of 15 ft, 0.2 times the span length, or half the span length minus the maximum development length, as specified in AASHTO LRFD Specifications (2012) Articles 5.11.4.2 and 5.11.4.2.3.

- 15 ft
- $0.2L = 0.2(46.5833) = 9.317\ ft$

- $0.5L - l_d$

Where:

L = Span length, ft.

l_d = Development length, ft.

$$l_d \geq \kappa\left(f_{ps} - \frac{2}{3} f_{pe}\right) d_b \tag{A.87}$$

Where:

κ = 2.0 for pretensioned members where a portion of strands is not bonded and tension exists in the precompressed tensile zone.

f_{ps} = Average stress in the prestressing steel at the time for which the nominal resistance of the member is required, calculated with Equation (A.88), ksi.

f_{pe} = Effective stress in the prestressing steel after losses = 149.67 ksi.

d_b = Nominal strand diameter, 0.5 in.

$$f_{ps} = f_{pu}\left(1 - k\frac{c}{d_p}\right) \tag{A.88}$$

Where:

k = 0.28 for low-relaxation strands.

d_p = Depth of prestressing strands, $d_p = 15 - 3.5 = 11.5$ in.

$$c = \frac{A_{ps} f_{pu} + A_s f_s - A_s^{'} f_s^{'}}{0.85 f_c^{'} \beta_1 b + k A_{ps}\left(\frac{f_{pu}}{d_p}\right)} \tag{A.89}$$

$$c = \frac{(0.153)(56)(270)}{0.85(7.0)(0.7)(60) + 0.28(8.568)\left(\frac{270}{11.5}\right)} = 7.55 \text{ in.}$$

Using the c value calculated in Equation (A.89) gives:

$$f_{ps} = 270\left(1 - 0.28\frac{7.55}{11.5}\right) = 220.4 \text{ ksi}$$

Therefore, the minimum development length must be:

$$l_d \geq 2\left(220.37 - \frac{2}{3}149.67\right)0.5 = 120.6 \text{ in } (10.05 \text{ ft})$$

$$0.5L - l_d = 0.5(46.583) - 10.05 = 13.24 \text{ ft}$$

According to the above calculations for debonding length, the maximum debonding length should not exceed 9 ft 4 in. Table A.3 shows the initial stress calculation for critical sections at the ends of the slab beam immediately after transfer. The stress values at the top and bottom of the girder are kept within the allowable stress limits by debonding some of the strands at 3 ft increments. The calculation is done using a similar approach that is shown above in Section A.5.3.2.

In order to get the prestressing stresses at each section immediately after transfer, the elastic shortening losses are calculated at each section. The calculated loss values and initial prestressing stresses at each section are listed in Table A.4. Table A.3 shows that the maximum tensile stress occurs at 2.5 ft (transfer length) at the extreme top fiber of the beam. This stress can be kept within the allowable tensile stress limit by debonding six strands at that section. Also, the maximum compressive stress occurs at 4 ft away from the end. The compressive stress is kept within the allowable compressive stress limit by debonding four strands at that location. Therefore, only six strands are debonded up to 3 ft from the ends and four strands are debonded between 3 ft–6 ft from the ends.

A.5.6 Camber Estimate at Different Construction Stages

Prestressing is applied eccentrically in order to counteract the downward deflection due to gravity loads and service loads. The upward deflection of a flexural member due to eccentricity is called camber. The amount of camber depends on several factors, such as amount of prestressing force, span length, section properties, concrete modulus of elasticity, time, humidity, and concrete strength.

The amount of camber is a critical parameter in order to be able to adjust the haunch thickness throughout the span length at the time of PCP erection. However, prediction of deflections to a high degree of accuracy is not possible even in controlled conditions.

A.5.6.1 Camber Calculation at Different Stages

Total camber was calculated at different stages of construction until deck placement by solving Equation (A.90).

$$EIy'' = M$$

$$EIy' = Mx + c_1 \tag{A.90}$$

$$EIy = \frac{Mx^2}{2} + c_1 x + c_2$$

The boundary conditions for the simply supported beam are:

$$y(0) = 0$$
$$y(L) = 0$$

With the above boundary conditions, the solution of Equation (A.90) becomes:

$$y(x) = \frac{1}{EI}\left(\frac{Mx^2}{2} - \frac{ML}{2}x\right) \tag{A.91}$$

The moment in Equation (A.90) is taken as the moment caused by the prestressing force only in order to calculate the upward deflection due to prestress. The net camber is calculated by subtracting the dead load deflections at different construction stages.

The upward deflection at the midspan is:

$$\delta_c(t) = y\left(\frac{L}{2}\right) = \frac{F(t)e}{E(t)I}\left(\frac{L^2}{8}\right) \tag{A.92}$$

All the strands are assumed to be fully bonded. The effect of six strands being debonded over 3 ft is very small. The amount of upward deflection is a function of total prestressing force at that time and concrete modulus of elasticity at that time. The total prestressing force is calculated at each time step using the prestress loss formulas provided in Section A.5.2.3 as:

$$\begin{aligned} f_{pi} &= f_{pt} - \Delta f_{pES} - \Delta f_{pR1} \\ f_p(t) &= f_{pi} - \Delta f_{pSR}(t) - \Delta f_{pCR}(t) \\ F(t) &= A_{ps}\, f_p(t) \end{aligned} \tag{A.93}$$

Table A.3. Stress Check at Critical Sections Immediately after Transfer.

x (ft)	T_i (kips)	Bottom Row	Top Row	N	$N_{debonded}$	F_{pi} (kips)	e (in.)	M_g (kip-ft)	$f_{b.release}$ (ksi)	$f_{t.release}$ (ksi)
0.0	0.0	22	28	50	6	0.0	3.88	0.0	0.000	0.000
1.0	11.4	22	28	50	6	568.0	3.88	22.0	-1.493	0.231
2.0	22.8	22	28	50	6	1137.9	3.88	43.1	-2.997	0.468
2.5	28.5	22	28	50	6	1423.6	3.88	53.3	-3.752	0.588
3.0	28.5	22	28	50	6	1424.7	3.88	63.3	-3.702	0.536
4.0	28.4	24	28	52	4	1477.8	3.92	82.5	-3.779	0.495
5.0	28.5	24	28	52	4	1480.1	3.92	100.8	-3.688	0.399
6.0	28.5	24	28	52	4	1482.2	3.92	118.1	-3.601	0.307
7.0	28.3	28	28	56	0	1585.2	4.00	134.5	-3.862	0.339
8.0	28.3	28	28	56	0	1587.2	4.00	150.0	-3.785	0.258
9.0	28.4	28	28	56	0	1589.2	4.00	164.5	-3.713	0.182
10.0	28.4	28	28	56	0	1591.0	4.00	178.1	-3.646	0.111
23.3	28.6	28	28	56	0	1603.2	4.00	269.8	-3.193	-0.370

Table A.4. Elastic Shortening Loss Calculation at Critical Sections.

x (ft)	(F_{pi})assumed (kips)	f_{cgp}	Δf_{pES} (ksi)	f_{pi} (ksi)	Fpi (kips)
0.0	1417.3	2.84	17.23	185.27	1417.3
1.0	1419.9	2.78	16.89	185.61	1419.9
2.0	1422.4	2.73	16.57	185.93	1422.4
2.5	1423.6	2.70	16.41	186.09	1423.6
3.0	1424.7	2.68	16.26	186.24	1424.7
4.0	1477.8	2.76	16.75	185.75	1477.8
5.0	1480.1	2.71	16.47	186.03	1480.1
6.0	1482.2	2.67	16.20	186.30	1482.2
7.0	1585.2	2.88	17.49	185.01	1585.2
8.0	1587.2	2.84	17.25	185.25	1587.2
9.0	1589.2	2.80	17.02	185.48	1589.2
10.0	1591.0	2.77	16.81	185.69	1591.0
23.3	1603.2	2.53	15.38	187.12	1603.2

A.5.6.2 Concrete Compressive Strength as a Function of Time

Concrete strength varies over time; the variation is higher within the first month. Although 28-day concrete compressive strength is used as a reference parameter, it is important to know the change in concrete strength over time for an accurate estimate. Because the actual release and 28-day compressive strength of concrete is known, Equation (A.94) (Naaman 2004) can be used.

$$f_c'(t) = f_c'(28)\left(\frac{t}{b+ct}\right) \tag{A.94}$$

Where:

$f_c'(t)$ = Concrete compressive strength, ksi.

$f_c'(28)$ = 28-day concrete compressive strength, ksi.

t = Age of concrete, days.

b = Constant that changes the rate of increase.

c = Constant that changes the ultimate value.

The required coefficients are provided in Table A.5. taken from Naaman (2004). It is important to note that actual 28-day compressive strength may differ from the design 28-day strength. The fabricator generally uses a higher-strength mix in order to achieve the required release strength within 24 hours. As a result, the ultimate 28-day strength is often higher than the strength used to estimate the camber. However, for the design calculation, the specified 28-day concrete compressive strength is used.

Because the fabricator most likely will prefer accelerated curing, the accelerated cured constants are used for the estimation of time-dependent strength.

Table A.5. Concrete Compressive Strength Modeling Coefficients.

Curing Condition	Constant	Recommended (Naaman 2004)	Best Fit
Accelerated Cured	b	0.3	0.15
	c	0.98	1.06
Moist Cured	b	2.3	0.8
	c	0.99	0.99

A.5.6.3 Modulus of Elasticity of Concrete

The modulus of elasticity is estimated based on the concrete compressive strength. Although there are different methods in the literature, only the AASHTO LRFD Specifications (2012) method is introduced and used herein for camber calculation. The following elastic modulus equation is defined as a time-dependent parameter based on time-dependent compressive strength.

$$E_c(\mathrm{t}) = 33{,}000\gamma^{1.5}\sqrt{f_c^{'}(\mathrm{t})} \tag{A.95}$$

Where:

γ = Unit weight of concrete, kcf.

$f_c'(t)$ = Concrete compressive strength, ksi.

Unit weight of the concrete is taken as 0.15 kcf because normal weight concrete is used.

A.5.6.4 Deflection Due to Self-Weight of the Slab Beam Girder

The deflection due to self-weight of the slab beam at midspan is also calculated as a function of time.

$$\delta_b(\mathrm{t}) = \frac{5w_bL^4}{384E_c(\mathrm{t})I_g} \tag{A.96}$$

A.5.6.5 Deflection Due to PCPs

The PCPs are assumed to be erected at 14 days after casting of the slab beams. The deflection is subtracted from the total camber at 14 days.

$$\delta_p = \frac{5w_pL^4}{384E_cI_g} \tag{A.97}$$

$$\delta_p = \frac{5\left(\frac{0.267}{12}\right)(12\times48)^4}{384(5098)(16875)} = 0.37 \text{ in.}$$

A.5.6.6 Total Camber Considering Creep Effect

The total amount of camber at each time step is calculated using Equation (A.92). This equation only considers the time-dependent effects on total prestressing force and modulus of elasticity. The applied prestressing force causes creep over time, and creep is more prominent

during the early ages of concrete. This creep effect is taken into account as an average creep at each time step and is calculated as:

$$\delta_c(t) = \delta_c(t_i) - \sum_0^t \left(\delta_c(t_{n-1}) - \delta_c(t_n)\right) + \sum_0^t \left(\psi(t_n - t_i) - \psi(t_{n-1} - t_i)\right)\left(\delta_c(t_{n-1})\right) \quad \text{(A.98)}$$

$$\delta(t) = \delta_c(t) - \delta_b(t_i)\left(1 + \psi(t - t_i)\right) \quad \text{(A.99)}$$

Where:

δ_c = Camber at the time considering the time-dependent losses, in.

δ = Total camber, upward deflection being positive, in.

Figure A.7 shows the camber of a slab beam at each day until deck construction.

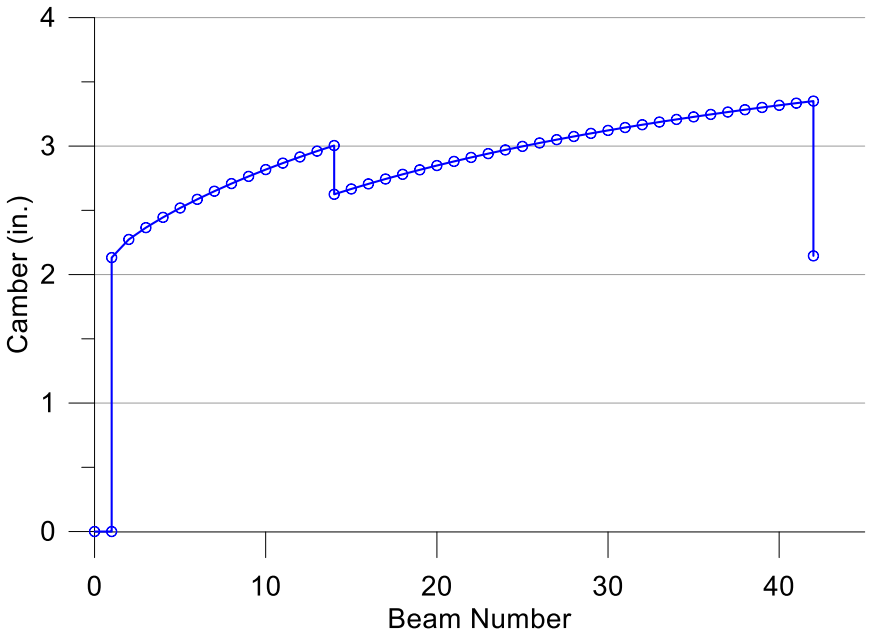

Figure A.7. Camber until CIP Deck Construction.

A.6 ULTIMATE STRENGTH CHECK

Prestressed concrete members are assumed to remain uncracked under service loads, and the allowable stress design philosophy is adopted from the AASHTO LRFD Specifications (2012). The specifications also require an ultimate strength check of prestressed members that are designed based on allowable stresses.

AASHTO LRFD Specifications 2012(2012) defines the Strength I limit state for ultimate conditions as:

$$Q = 1.25(DC) + 1.5(DW) + 1.75(LL + IM) \tag{A.100}$$

Where:

Q = Total factored load.

DC = Dead load of structural components and nonstructural attachments.

DW = Dead load of wearing surface and utilities.

LL = Vehicular live load.

Design requirements for flexural members is summarized in AASHTO LRFD Specifications (2012) Article 5.7.3. For rectangular sections under flexure about one axis, an approximate stress distribution is used. The formulation is summarized below. If f_{pe} is not less than $0.5\, f_{pu}$, the average stress in prestressing steel (f_{ps}) may be taken as:

$$f_{pe} = 149.7 \text{ ksi} > 0.5 f_{pu} = 135 \text{ ksi}$$

$$f_{ps} = f_{pu}\left(1 - k\frac{c}{d_p}\right) \tag{A.101}$$

Where:

f_{pe} = Effective prestressing stress at final time after all losses, ksi.

f_{ps} = Average stress in prestressing steel, ksi.

k = 0.28 for low-relaxation strands.

For rectangular section behavior:

$$c = \frac{A_{ps} f_{pu} + A_s f_s - A_s' f_s'}{0.85 f_c' \beta_1 b + k A_{ps}\left(\frac{f_{pu}}{d_p}\right)} \tag{A.102}$$

Where:

$f_c^{'}$ = Specified compressive strength of concrete, 5 ksi.

β_1 = Ratio of depth of the depth of the equivalent uniformly stressed compression block assumed in the strength limit state to the actual depth of the compression zone, 0.85 for 4 ksi compressive strength.

d_p = Distance from extreme compression fiber to the centroid of the prestressing tendons, in.

d_p = 15 + 8.5 – 3.5 = 20 in.

The minimum bedding strip thickness is 0.5 in. Therefore, with the high expected camber, it is assumed that the deck slab thickness is 8.5 in. at midspan.

$$c = \frac{56(0.153)(270)}{0.85(4)(0.85)(116)+0.28(56)(0.153)\frac{270}{20}} = 6.29 \text{ in.}$$

$$a = \beta_1 c = 0.85(6.29) = 5.35 \ \ in. < t_s$$

The depth of the effective compressive stress block is smaller than the thickness of the deck slab. Therefore, the neutral axis does not go into the slab beam girder. The calculated c value is correct, with no need for iteration. Using the calculated c value in Equation (A.101) gives:

$$f_{ps} = (270)\left(1-0.28\frac{6.29}{20}\right) = 246.2 \text{ ksi}$$

The nominal flexural resistance of the slab beam can be calculated as:

$$M_n = A_{ps} f_{ps}\left(d_p - \frac{a}{2}\right) \qquad \text{(A.103)}$$

$$M_n = (56)(0.153)(246.22)\left(20-\frac{5.35}{2}\right) = 3046 \text{ k-ft}$$

The maximum moment under service loads is calculated using the Strength I load combination provided in Equation (A.100).

$$M_u = 1.25(549.1)+1.5(112.5)+1.75(625) = 1949 \text{ k-ft}$$

$$\phi M_n > M_u \Rightarrow 0.9(3046) = 2741 > 1949 \text{ k-ft}$$

The factored nominal ultimate strength capacity of the section is greater than the factored ultimate moment under service loads. The ultimate strength requirement is satisfied.

A.7 SHEAR DESIGN OF THE SLAB BEAM GIRDER

The shear resistance of the slab beam girder is checked using the guidelines provided by AASHTO LRFD Specifications (2012) Article 5.8.2. The shear resistance of the slab beam at the shear critical location is checked, and the required reinforcement is calculated. Due to the high cross-sectional area of the slab beam girders, the shear resistance of the concrete itself satisfies the required shear strength most of the time.

A.7.1 Transverse Shear Design

In line with the general approach for AASHTO LRFD Specifications (2012) Article 5.8.2.4, the following equation must be satisfied at each section.

$$V_r = \phi V_n \geq V_u \tag{A.104}$$

Where:

V_r = Design shear resistance, kips.

V_n = Nominal shear resistance, kips.

V_u = Factored shear force, kips.

ϕ = Strength reduction factor for shear = 0.9 for normal weight concrete.

The nominal shear resistance at a given section is the sum of the concrete contribution, transverse reinforcement, and transverse component of the prestressing force.

$$V_n = V_c + V_s + V_p \tag{A.105}$$

Where:

V_c = Contribution of concrete to the shear strength, kips.

V_s = Contribution of steel to the transverse shear resistance, kips.

V_p = Component of prestressing force in the direction of applied shear, kips.

Nominal shear resistance, Vn , is constrained by the following upper limit:

$$V_n \leq 0.25 f_c' b_v d_v + V_p \tag{A.106}$$

Where:

f_c' = 28-day design compressive strength of concrete, ksi.

b_v = Effective web width = 60 in.

d_v = Effective shear depth = de – a/2 in.

d_e = Effective depth for bending = 19.5 in.

d_v = The larger of $0.9d_e$ or $0.72h$.

$$d_v = \begin{cases} 19.5 - \dfrac{5.35}{2} = 16.83 \text{ in.} \\ 0.9(19.5) = 17.55 \text{ in.} \\ 0.72(23) = 16.56 \text{ in.} \end{cases}$$

The critical section near the support is located as the greater of d_v or $0.5d_v \cot(\theta)$ from the support face. As a preliminary estimate, use θ =29° and $0.5(17.55)\cot(29) = 15.83$ in. Therefore, the critical section for shear should be taken as 17.55 in. from the face of the support, since d_v is greater than $0.5d_v \cot(\theta)$. Considering the 9 in. bearing pad length, the critical section is $17.55 + 4.5 = 22$ in. away from the center of the bearing pad.

The critical shear load occurs when the rear axle of the HS20 truck is located at 22 in. from the center of the bearing pad. The shear forces calculated for dead and live loads when the vehicle is at that location are presented in Figure A.8.

The ultimate factored design shear at 2 ft from the support is calculated using the Strength I load combination.

$$V_u = 1.25V_{DC} + 1.5V_{DW} + 1.75V_{LL} \qquad \text{(A.107)}$$

$$V_{LL} = g_v(1.33V_{\text{TR}} + V_{\text{L}}) = 0.86 \times (1.33 \times 54.48 + 13.63) = 74 \text{ kips}$$

$$V_u = 1.25(43.2) + 1.5(8.85) + 1.75(74) = 196.8 \text{ kips}$$

The ultimate factored moment reaction under service loads at the critical shear section is also calculated. The moment value at the critical shear section is used to calculate the longitudinal strains in the web. The unfactored moment results at 2 ft from the support when the vehicle's rear axle is at 2 ft are shown in Figure A.8(c).

$$M_L = g_M(1.33M_{TR} + M_{LL}) = 0.676 \times (1.33 \times 108.97 + 28.53) = 117.3 \text{ kip-ft}$$

$$M_u = 1.25(90.1) + 1.5(18.53) + 1.75(117.3) = 345.7 \text{ kip-ft}$$

The shear resistance provided by the component of the prestressing force in the direction of the applied shear can be calculated as:

$$V_p = F \sin \alpha \tag{A.108}$$

Where:

α = The angle of the prestressing force with respect to the longitudinal axis of the beam.

$$V_p = F \sin 0 = 0$$

The shear resistance provided by the concrete can be calculated as:

$$V_c = 0.0316 \beta \sqrt{f_c'} b_v d_v \tag{A.109}$$

The shear resistance provided by the shear reinforcement can be calculated using the below formula.

$$V_s = A_v f_y \frac{d_v}{s} \cot \theta \tag{A.110}$$

Where:

β = Factor indicating the ability of diagonally cracked concrete to transmit tension between cracks.

A_v = Area of transverse reinforcing steel (in2) within a distance s, in.

f_y = Yield strength of the transverse steel reinforcement, ksi.

θ = Angle of inclination of diagonal compressive struts.

In order to determine the nominal shear resistance (V_c , V_s), the β and θ parameters must be calculated. For prestressed members, β and θ are calculated using Equations (A.111) and (A.112)

$$\beta = \frac{4.8}{(1 + 750\varepsilon_s)} \frac{51}{(39 + s_{xe})} \tag{A.111}$$

$$\theta = 29 + 3500\varepsilon_s \tag{A.112}$$

Where:

ε_s = Longitudinal strain in the web (assumed positive for tension), in./in.

s_{xe} = Crack spacing parameter, in.

$$\varepsilon_s = \frac{\frac{|M_u|}{d_v} + 0.5N_u + |V_u - V_p| - A_{ps} f_{po}}{E_s A_s + E_p A_{ps}} \tag{A.113}$$

AASHTO LRFD Specifications (2012) Article 5.8.3.4 suggests that the parameter f_{po} can be taken as:

$$f_{po} = 0.7 f_{pu} = 189 \text{ ksi}$$

If the strain equation comes out to be negative, ε_s should be taken as zero or the value should be recalculated using Equation (A.114).

$$\varepsilon_s = \frac{\frac{|M_u|}{d_v} + 0.5N_u + |V_u - V_p| - A_{ps} f_{po}}{E_s A_s + E_p A_{ps} + E_c A_{ct}} \quad \text{(A.114)}$$

Where:

A_{ct} = Area of concrete on the flexural tension side of the member, in^2.

From Equation (A.113):

$$\varepsilon_s = \frac{\frac{345.7 \times 12}{19.35} + 0.5(0.0) + |196.8 - 0.0| - 56(0.153)(189)}{29000(0.0) + 28500(56)(0.153)} = -4.95 \times 10^{-3}$$

The net longitudinal strain (ε_s) value is negative. In this case, AASHTO LRFD Specifications (2012) states that ε_s may be taken as zero or recalculated using Equation (A.114). The value for ε_s is conservatively taken as zero for the transverse shear strength check.

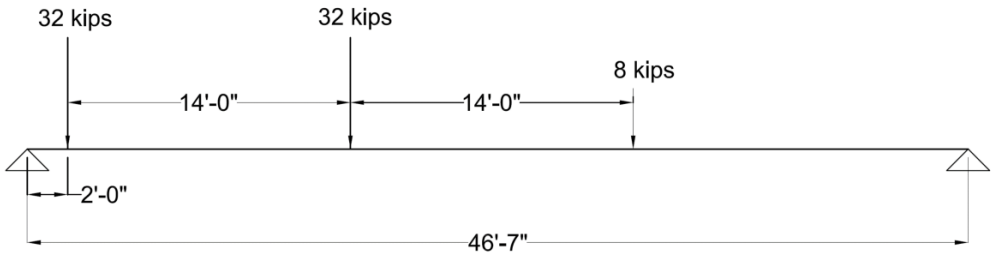

(a) HS20 Shear Critical Position

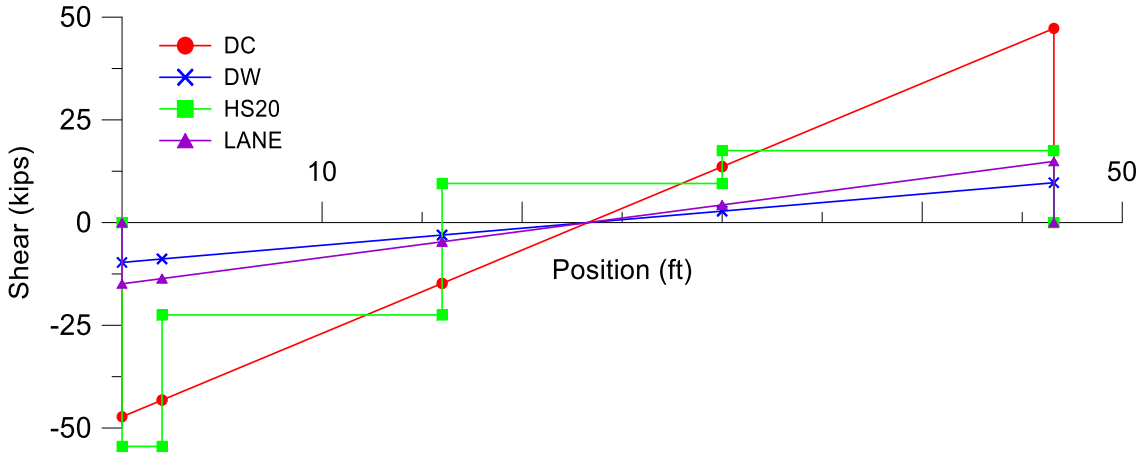

(b) Shear Forces

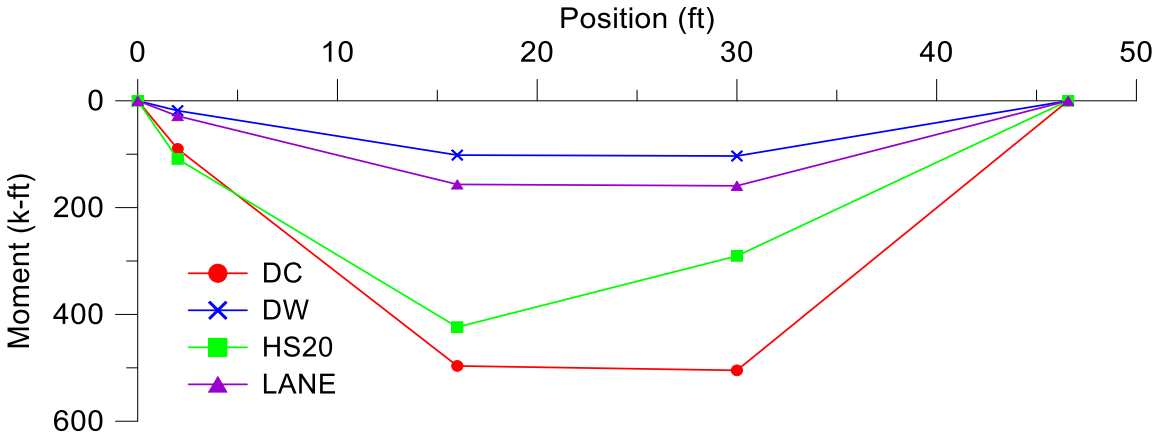

(c) Moment Reactions at Shear Critical Section

Figure A.8. Moment and Shear Reaction When Vehicle Is at Shear Critical Position.

The crack spacing parameter can be determined using the equation below.

$$s_{xe} = \frac{s_x 1.38}{a_g + 0.63} \tag{A.115}$$

Where:

s_x = The lesser of dv or the maximum distance between layers of longitudinal crack control reinforcement, in.

a_g = Maximum aggregate size, in.

The value of s_x may be taken equal to d_v for the design of slab beams because no longitudinal crack control reinforcement is provided.

$$s_{xe} = \frac{(17.55)1.38}{3/8 + 0.63} = 24.1 \text{ in.}$$

Because the longitudinal strain value and crack spacing parameter are calculated, the β and θ parameters can be determined using Equations (A.111) and (A.112).

$$\beta = \frac{4.8}{1 + 750(0)} \frac{51}{(39 + 24.1)} = 3.88$$

$$\theta = 29 + 3500(0) = 29^{\circ}$$

Using the calculated β value, the concrete contribution to the shear strength can be determined.

$$V_c = 0.0316(3.88)\sqrt{7}(60)(17.55) = 341.6 \text{ kips}$$

$$0.5\phi V_c = 0.5(0.9)(341.6) = 153.7 \text{ kips} < V_u$$

Half of the reduced nominal shear strength contribution of the concrete ($0.5V_c$) is lower than the ultimate factored shear Vu at the shear critical section. Therefore, transverse shear reinforcement is required. Transverse steel currently provided in the TxDOT Bridge Division Standard Drawings (TxDOT 2013b) standard slab beam details is 04 in2/ft. The contribution of shear reinforcement to transverse shear resistance can be calculated as follows.

$$V_s = 0.4(60)\frac{17.55}{12}\cot(29) = 63.3 \text{ kips}$$

The nominal shear resistance is the lesser of:

$$\phi V_n = 0.9(404.9) = 364.4 > V_u = 196.8 \text{ kips}$$

$$V_n = 0.25 f_c' b_v d_v + V_p = 2031.8 \text{ kips}$$

Therefore, the transverse steel currently provided in the TxDOT standard slab beam details is adequate based on the design calculations.

A.7.2 Interface Shear Design

The factored interface shear resistance should be greater than the factored interface shear force due to total load at service.

$$V_{ri} = \phi V_{ni} \tag{A.116}$$

In addition, the design should satisfy:

$$V_{ri} \geq V_{ui} \tag{A.117}$$

Where:

V_{ni} = Nominal interface shear resistance, kips.

V_{ui} = Factored interface shear force due to total load, kips.

For a unit length segment, the factored shear force may be calculated as:

$$V_{ui} = \frac{12 V_u}{d_v} \tag{A.118}$$

Where:

d_v = Distance between the centroid of the tension steel and the mid-thickness of the slab, in.

$$d_v = 19.5 - 4 = 15.5 \text{ in.}$$

The haunch thickness is assumed to be 2 in.

$$V_{ui} = \frac{12(196.8)}{15.5} = 152.4 \text{ kip/ft}$$

Nominal shear resistance of the interface plane can be taken as:

$$V_{ni} = cA_{cv} + \mu\left(A_{vf} f_y + P_c\right) \tag{A.119}$$

The nominal shear resistance can be taken as the lesser of:

$$V_{ni} \leq K_1 f_c' A_{cv} \tag{A.120}$$

$$V_{ni} \leq K_2 A_{cv} \tag{A.121}$$

Where:

A_{cv} = $b_{vi}L_{vi}$ = Area of concrete that is engaged in interface shear transfer, in^2.

A_{vf} = Area of interface shear reinforcement, in^2.

b_{vi} = Interface width considered to be engaged in shear transfer, in.

L_{vi} = Interface length considered to be engaged in shear transfer, in.

P_c = Permanent net compressive force acting normal to the shear plane, kips.

c = Cohesion factor, ksi.

μ = Friction factor.

K_1 = Fraction of concrete strength available to resist interface shear.

K_2 = Limiting interface shear resistance, ksi.

Parameters, c, μ, K_1, and K_2 are specified in AASHTO LRFD Specifications (2012) Article 5.8.4.3.

For a cast-in-place concrete slab on clean concrete girder surfaces, free of laitance but surface not intentionally roughened, $c = 0.075$ ksi, $\mu = 0.6$, $K_1 = 0.2$, $K_2 = 0.8$ ksi.

The bedding strip thickness should be taken into account when calculating the effective width of the interface shear surface. The thickness of the bedding strip is taken as 2 in.

$$b_v = b - 2w_b = 56 \text{ in.} \quad \text{(A.122)}$$

The effective concrete surface area for a unit length is:

$$A_{cv} = b_v(1.0) = 56 \text{ in}^2/\text{in.}$$

The total interface shear force due to cohesion between deck concrete and slab beam concrete and provided interface shear reinforcement is:

$$V_{ni} = 0.075(56)(12) + (0.6)(0.8)(60) = 79.2 \text{ kips/ ft}$$

$$\phi V_{ni} = 0.9(79.2) = 71.28 \text{ kips/ ft} < V_{ui}$$

The amount of interface shear reinforcement provided for the standard slab beam type cannot achieve the required interface shear strength. Interface shear reinforcement must be increased to 1.8 in^2/ft for the first quarter of the span. A detailed methodology for determining interface shear demand of segments using global force equilibrium is shown in Section 3.

APPENDIX B

RIVERSIDE BRIDGE CONSTRUCTION

B.1 CONSTRUCTION PROCESS

The Riverside Bridge was built as an on-grade bridge. The elevation of the finished deck is the same as the adjoining runway. In order to create a bridge span, the runway pavement in the immediate area was removed and the soil below was excavated to a certain depth. The clearance underneath the slab beams allowed a workable space, and the depth was kept at an optimum level in order to limit substructure costs. It was decided that a 6.5 ft deep excavated pit, which allowed a minimum 4.5 ft clearance below the slab beams, would provide sufficient space to install instrumentation. Figure B.1 shows the bridge superstructure details

B.1.1 Soil Testing of the Bridge Site

In order to begin designing the substructure components, it was necessary to have the engineering parameters of the supporting soil. Two bore holes were drilled at the north and south ends of the bridge where the load-bearing elements would be constructed. The holes were drilled to a 60 ft depth.

Figure B.2 shows a view of drilling operations. The subsurface arrangement of the strata and groundwater conditions was evaluated at these two bore holes. Groundwater was observed at a depth of approximately 25 ft. Soil strength was tested by means of the Texas cone penetration (TCP) test. This test was performed by counting the number of blows required for a 170 lb hammer free falling from a 24 in. height to drive a conical point for two consecutive sets of 6 in. The test results helped determine the skin friction and load-bearing capacity. In addition to strength tests, geotechnical laboratory tests were conducted on the recovered samples to determine the engineering properties of the strata.

The test results were used to determine the skin friction and load-bearing capacity. In addition to strength tests, geotechnical laboratory tests were conducted on the recovered specimens in order to determine engineering properties of the strata. Table B.1 lists the engineering properties of each soil stratum, including friction angle and plasticity index (PI). In general, the soil stratigraphy from the surface to 12 ft indicated gray, brown, and multicolored lean clay, followed by brown and light brown sand from 12 to 25 ft, and then brown, gray, and multicolored fat clay (high plasticity) to the termination of the bore hole at approximately 60 ft below the existing grade.

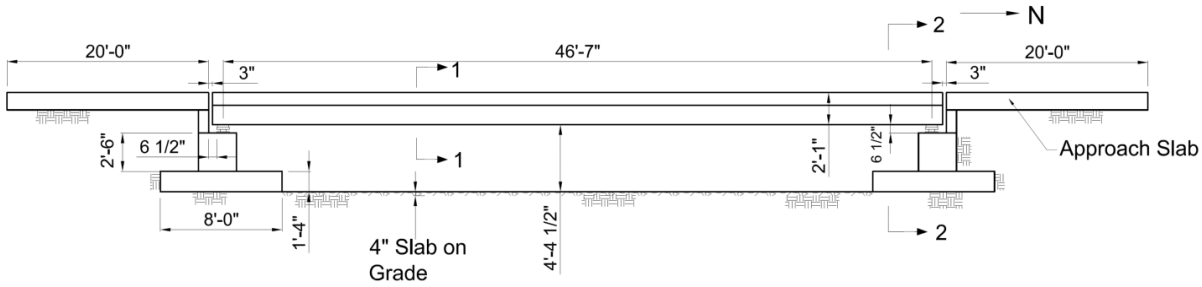

(a) Side Elevation View

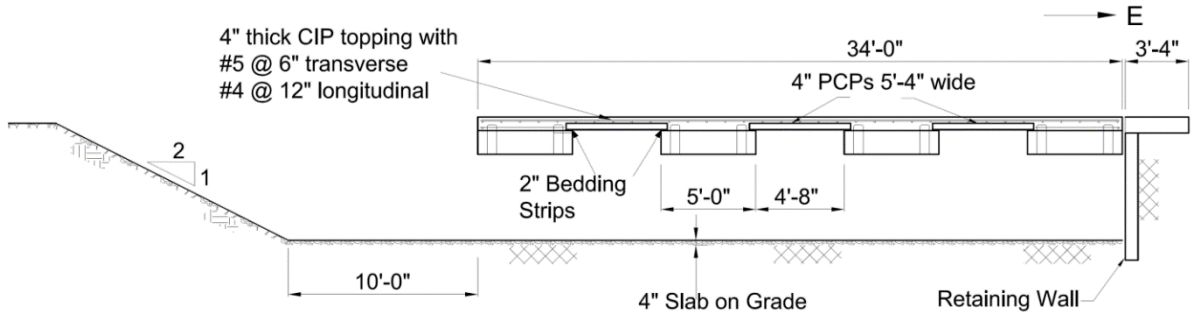

(b) Section 1-1: Cross-Section of Spread Slab Beam Deck

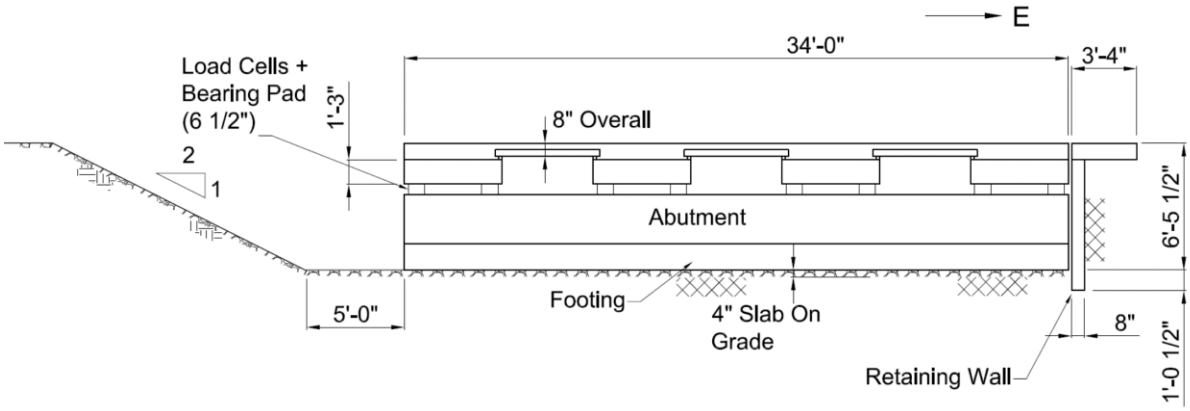

(c) Section 2-2: Cross-Section at Abutment

Figure B.1. The Riverside Bridge Superstructure.

As shown by the PI of the different soil strata, the soil at the construction site has a high shrink-swell potential. This type of clay is called fat clay and has high plasticity. The PI was taken into account when designing structural elements. For a deep foundation option (drilled piers supporting the bridge abutment), a depth versus skin friction capacity plot was provided for several different pier diameters. Figure B.3 shows the friction capacity of different diameter piers.

The deep foundation option was eliminated because of the high cost. A shallow foundation was designed for supporting the bridge abutment. The compressive strength of the soil for a shallow depth is provided in the log of the bore hole (Figure B.4).

Figure B.2. Soil Testing of the Bridge Site.

Table B.1. Engineering Properties of Each Soil Strata (Gessner 2012).

Depth (ft)	Strata	PI Range	Moisture Content Range (%)	Shear Strength (tsf); Friction Angle
0–12	Gray, Brown, and Multicolored Clay (CL)	6–33	4 to 8 Wet	0.4–1.5; N/A
12–24	Brown and Light Brown Sand (SP)	NP (Nonplastic)	2 to 6 Wet	N/A; 34.5o–41o
24–59	Brown, Gray, and Multicolored Clay (CH)	35–55	6 to 12 Wet	0.78–12.0; N/A

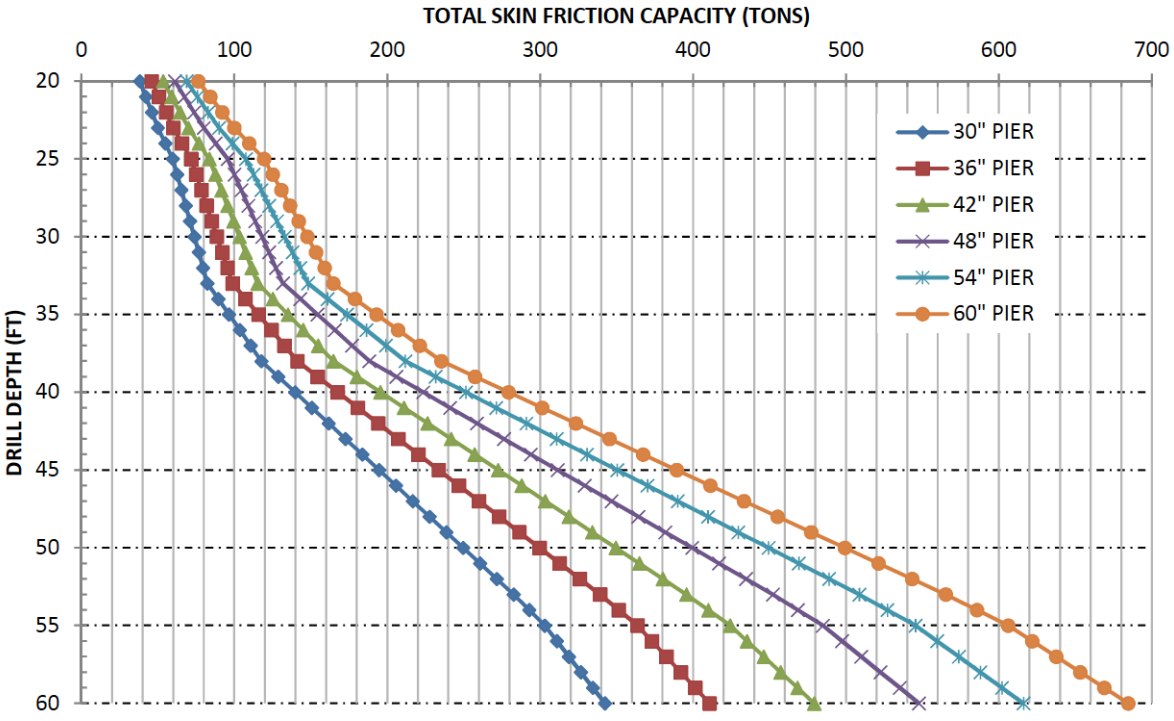

Figure B.3. Total Skin Friction Capacity of Pier (Gessner 2012).

LOG OF BORE HOLE

PROJECT: Bridge Footings
Runway 17L
College Station, Texas

BORING NO. #1
LOCATION: Bridge Abutments

PROJECT NO: 12-0251
CLIENT: Mr. James Frazier
DATE: June 12, 2012
DRILLER: Van and Sons

BORING TYPE: Core/Auger
GROUND ELEV: Cleared Pavement Area

SOIL TECHNICIAN: RT

Texas Cone Penetrometer Test
Shelby Tube Sample
Standard Penetration Test Sample
Augering (Disturbed) Sample
No Recovery
Initial Water Level
Water Level After

Depth (in feet)	Sample Type & Soil Symbol	Water Level	Penetrometer or Blow Count	Liquid Limit (%)	Plasticity Index	Moisture Content (%)	Dry Density Lbs./Cu. Ft.	Compressive Strength Tons/Sq. Ft.	% Passing #200 Sieve (%)	Bar Linear Shrinkage (%)	Description of Stratum
			1.0 2.0								Firm to Stiff Light Brown Clay (CL)
			3.0 4.5+ 6,6	41	26	19.1	110.5	2.44	82	16.3	Hard Gray Clay (CL)
5			4.5 1.5								Very Stiff to Firm Multicolored Clay (CL) -w/ Some Calcareous Nodules
			2.5 2.0 2,4	46	33	21.0	105.4	1.6	90	--	Stiff Multicolored Clay (CL) -w/ Some Calcareous Nodules
10											Stiff Multicolored Clayey Sand (SC) -w/ Some Calcareous Nodules
			25,26	--	NP	5.95	--	--	23	--	Very Dense Brown Sand (SP)
15			5/7/10								Medium Dense Brown Sand (SP)
20			16,24								
			6/8/12								Medium Dense Brown Sand (SP)
25			22,28								
			4/3/5	70	53	29.2	--	--	97	--	Stiff Multicolored Clay (CH)
30			7,10								

Figure B.4. Log of Bore Hole (Gessner 2012).

B.1.2 Design and Construction of Substructure Components

B.1.2.1 Reinforced Concrete Retaining Wall

The bridge cross-section in relation to the existing runway is shown in Figure B.5. Because the bridge span was built over an excavated pit at the edge of the runway, it created unstable soil conditions along the east edge of the bridge. Researchers had two options to overcome this problem: excavate at a slope, which would create a gap between the existing runway and the bridge deck, or install a retaining structure. Based on Texas A&M Riverside Campus regulations, researchers decided to build a retaining structure and have the top of the bridge deck flush with the rest of the existing runway.

Several different retaining structure options were evaluated and designed based on the soil test results. A steel sheet pile installation was investigated, but the option was relatively expensive due to the small size of the project relative to typical construction. Building a cantilever reinforced concrete retaining wall would have been as expensive as the sheet pile application and would have taken more time. Instead, a trenched retaining wall was built and anchored to the existing runway slab at the top and buried into soil at the bottom.

Figure B.5 shows the geometric and reinforcement details of the retaining wall. The retaining wall was designed based on the soil pressure and a possible surcharge that may result due to a vehicle driving near the wall. Soil parameters were used as provided by the soil test results. Based on an ultimate strength design, the same reinforcement was provided for positive and negative moments. One layer of #4 rebar mesh was provided at the mid-thickness of the 8 ft high and 8 in. thick retaining wall.

Figure B.6 shows the rebar preparation and installation procedure. Reinforcing bars were tied on the existing runway and lowered into the excavated trench with a forklift. The rebar mesh was aligned at the center of the excavated trench. The necessary clear cover between the mesh and soil was provided with 3 in. spacer wheels.

The retaining wall concrete was specified as Texas Department of Transportation (TxDOT) Class C having 3600 psi compressive strength. The slump was specified as 5.0–5.5 in. to have a relatively higher workability in the narrow trench. Fresh properties of concrete were tested, and specimens were fabricated to determine the mechanical properties of the concrete.

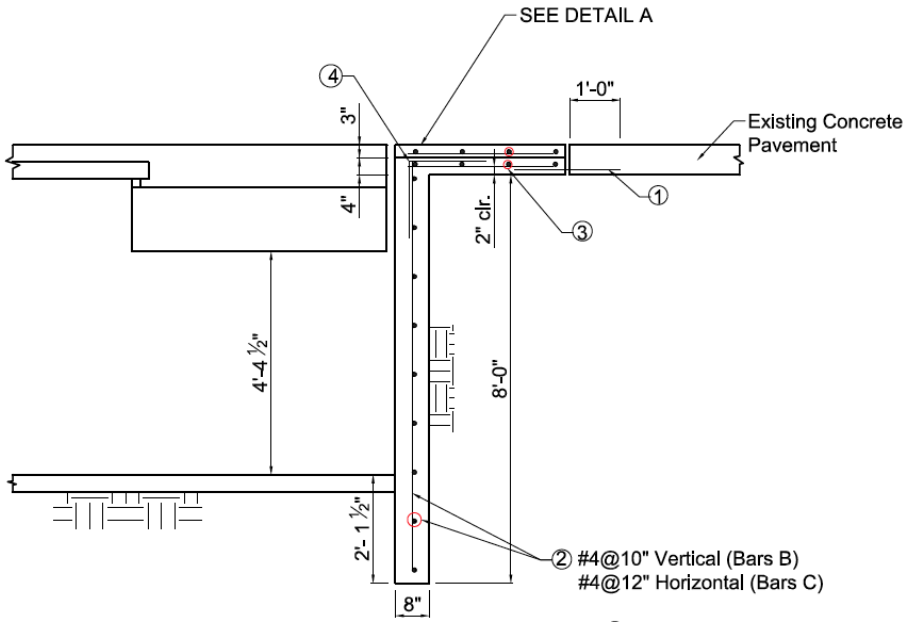

Figure B.5. Retaining Structure in Relation with the Existing Runway.

B.1.2.2 Reinforced Concrete Slab on Grade

Figure B.7 shows the excavation operation. A 75 ft long section along the retaining wall was excavated to about a 6.5 ft depth. The Texas A&M Transportation Institute (TTI) Riverside Campus crew performed the excavation using a trackhoe and hauled off soil as it was excavated.

Figure B.8 presents the elevations of the slab on grade below the transverse centerline of the bridge. The exact elevation of the slab on grade was adjusted during the formwork construction. The slope of the slab was provided toward the center of the bridge in the north-south direction and toward the west (toward the future drainage pit).

Reinforcing bars were tied on the runway before the start of the excavation. The objective was to place the reinforcing bar mesh immediately after excavation and to cast the slab on grade as soon as possible. Rain would have the potential of filling up the excavated pit and creating a muddy working area, and pumping the water out would also be time consuming. In order to avoid all these complications, the slab-on-grade construction was planned ahead of time and finished in two weeks.

(a) Rebar Tying

(b) Rebar Mesh Installation

(c) Slump Test

(d) Cylinder Specimens

(e) Retaining Wall Concrete Pour

Figure B.6. Retaining Wall Construction.

(a) Main Excavation of the Bridge Foundation

(b) Excavation for Slab on Grade below Footings

Figure B.7. Excavation of the Bridge Site.

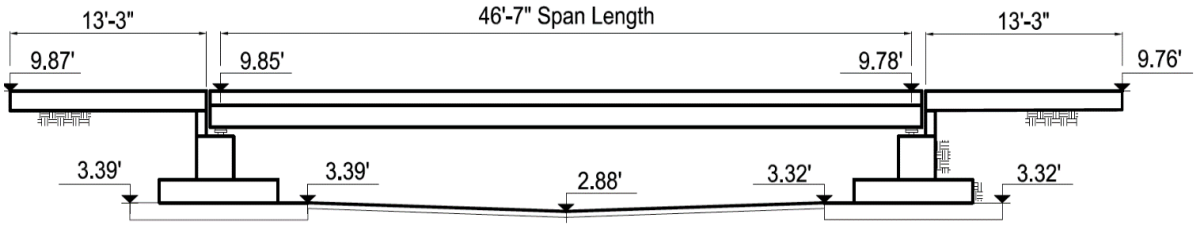

Figure B.8. Elevations of Structural Components.

Figure B.9 shows construction of the slab-on-grade under footings. These slabs were placed first to aid in the overall construction of the substructure elements. All the rebar meshes used for the slab on grade were #3 bars spaced at 12 in. centers. The on-grade slabs were poured in two steps. First, the 12 ft wide, 12 in. deep slabs below the north and south footings were poured. These slabs had two layers of #3 mesh. Based on the American Association of State Highway and Transportation Officials (AASHTO) Load and Resistance Factor Design (LRFD) Specifications (2012) requirements, reinforced concrete components that are in contact with soil should have 3 in. of clear cover. Therefore, 3 in. high chairs were used to provide necessary bottom clear cover. In addition, 6 in. high standees were used to keep the spacing between the two layers of steel constant. The formwork was supported by 2 in. by 4 in. (nominal dimensions) stakes nailed every 4 ft. The top of the formwork elevation was adjusted according to target elevations, which provided the required slope for each component.

The reinforcement layout and construction of the middle slab-on-grade are shown in Figure B.10. The slab on grade for the middle region was 4 in. thick and was cast in four sections separated by transverse construction joints. The continuity of the reinforcing bars was satisfied by feeding reinforcing bars through the drilled holes in the construction joint formwork. To provide a barrier between the slab and the expansive clay soil, a 10 mil plastic sheet was laid. The previously tied #3 reinforcement mesh was placed on 2 in. slab bolsters.

Figure B.9. Reinforcing Bar Mesh for the Slab-on-Grade.

(a) Formwork and Reinforcement

(b) Slab-on-Grade Pour

(c) View of Slab-on-Grade after Broom Finish

Figure B.10. Construction of Middle Section of Slab-on-Grade.

B.1.2.3 Footing and Abutment Construction

Several options were evaluated for the pier construction. First, drilled shafts were designed based on the TxDOT Bridge Design Manual (TxDOT 2013a) guidelines as load-carrying elements supporting the abutments. The deep foundation design was abandoned because of the high cost due to a relatively small number of piers as compared to standard projects. The spread footing solution was determined to be the most economical solution for this short-span bridge. The spread footing was designed by taking into account the highly plastic soil conditions of the site, which had high swell-shrink potential. Specifically, a conservative flexural design for the footing was used, including an increased footing depth for added stiffness.

The footing was designed according to the TxDOT Geotechnical Manual (TxDOT 2012) and the AASHTO LRFD Specifications (2012). A critical step for designing the footing was determining the strata and reasonable strength values to be assigned to each stratum so that the soil bearing capacity could be calculated at the base of the footing. The soil test data were reviewed, and the engineering parameters were taken from the geotechnical soil report.

For a structural load-bearing member to be safe in terms of geotechnical design considerations, it needs to satisfy certain safety requirements, including stability in terms of overturning moment, sliding, and bearing capacity. To investigate the most critical effect, the truck load was considered as a uniform distributed pressure for the calculation of active pressure forces, whereas for the resisting moment and shear force calculations, only the dead load of the structural components was considered. This approach led to a conservative design.

Because of the shallow depth of the abutment, overturning moment was not an issue. In addition, the large contact area of the 34 ft long footing provided adequate resistance against sliding. The geometry of the footing was controlled by the bearing pressure. Based on the bearing capacity of the soil (2246 psf), an 8 ft wide spread footing was found to be satisfactory according to allowable stress design.

Figure B.11 shows the reinforcement details and geometry of the footings and abutments. The reinforcement for the footing was designed based on the ultimate strength design and the AASHTO LRFD Specifications (2012). Although it was possible to achieve adequate strength with a 12 in. depth, the depth of the footing was increased to 14 in., and 20 percent more flexural reinforcement was provided for additional rigidity. The thickness of the slab on grade under each footing was also increased to 12 in. for additional bearing area and rigidity against the high plastic clay conditions of the bridge site. Reinforcing bars for footings and abutments were tied on the runway to save time during substructure construction work. A reinforcing bar cage for the footing and abutment is shown in Figure B.12.

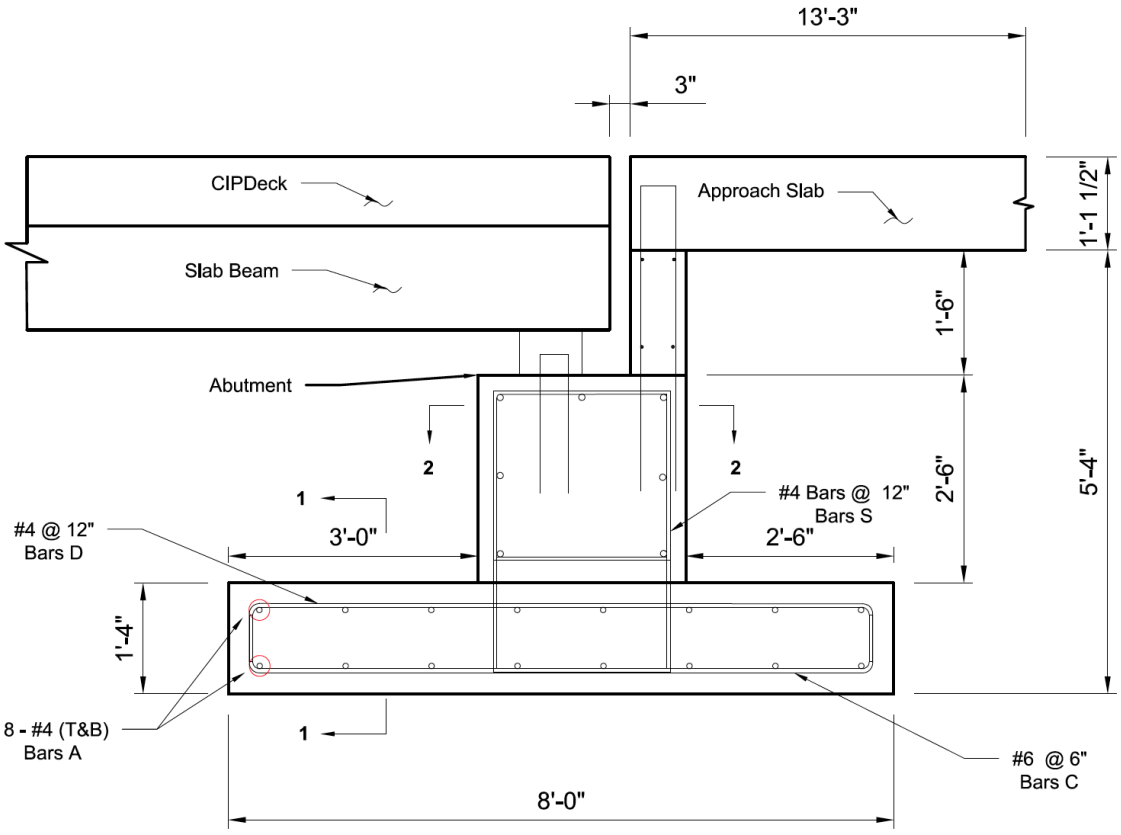

Figure B.11. Dimensions and Reinforcement of Footing and Abutment.

Figure B.12. Footing and Abutment Reinforcement Cage.

Because of the length of the longitudinal bars in the abutment, the rebar tying process was completed on the runway. The locations of both footings were measured precisely by using a total station, and the back face of the formwork was placed to have a reference point before placing the rebar cages. A TTI trackhoe was used to pick up the rebar cages and place them within the marked location at the north and south ends of the bridge. Figure B.13(a) shows the rebar placement operation.

After placement of the rebar, previously prepared formwork pieces were assembled for the footing construction. Concrete for all substructure components was specified as TxDOT Class C having 3600 psi compressive strength. The footing and abutment were cast in two different pours due to the geometry of the members. The pour for both footings took place during slight rain.

A silt fence was placed around the perimeter to hold back soil that washed down during each rainfall. Also, a sump pit was dug at the center on the west edge for pumping the water after rainy days. Eventually, a drainage manhole was constructed and connected to the main drainage channel.

All the rebar for the abutment was already tied and in place. The previously built abutment formwork was placed and assembled. The back faces of the formwork were supported by diagonal supports, and the front face was held using tie rods. Reinforcing bars for the back wall were tied because they needed to be connected to the abutment for interface shear resistance. Wing-wall reinforcement was also placed during this step. Figure B.13(c) shows the abutment and wing-wall formwork construction.

(a) Reinforcing Cage Placement

(b) Footing Concrete Pour

Figure B.13. Footing and Abutment Construction.

(a) Abutment and Wing-Wall Formwork Construction

(b) Abutment Concrete Pour

Figure B.13. Continued.

The abutment and half of the wing-wall concrete were poured together due to geometry and ease of construction. In order to provide a connection between the abutment and elevated pedestals located at the bearing pad locations, #5 rebar hooks were embedded into the fresh concrete. Concrete was poured and floated. Then an evaporation retardant agent was applied at the surface because of the hot weather. After the concrete was sufficiently hardened, cotton curing mats were placed and watered. A plastic sheet covered the curing mats. The curing process took place during the first four days after each pour.

B.1.2.4 Back-Wall, Elevated Pedestal, and Wing-Wall Construction

The back walls and the top half of the wing walls were cast together. This pour was the last pour of the substructure components before the slab beam girders were placed. The wing-wall thickness had already been changed from 12 to 8 in. during the design phase due to the load cell configuration to create more room at the back of the load cells.

The rebar for the back walls and wing walls was tied before the abutment pour to provide interface shear resistance. The only pieces that were constructed were the front faces of the back walls and elevated pedestals. Elevated pedestals were not part of the structure design and did not support the girders. They were placed as a replacement for the load cells in case the load cells were removed later.

Figure B.14 shows the abutment construction and backfilling operations. The formwork for all the substructure components was removed. The operation used 350 tons of Type A Grade 1 backfill material to backfill the abutments. A sheep-foot roller was used to compact the material. To achieve 100 percent compaction, the soil was watered until it was saturated and then was backfilled into the area in 4 to 6 in. thick layers. The compaction rate was tested twice for each bridge end.

B.1.2.5 Construction of the Drainage Line

The slab below the bridge is 6.5 ft deeper than the existing runway, and the bridge location is the low spot of the second runway. All runoff water comes toward the bridge site and fills up the excavated pit. The best option was to drain the water naturally without the use of a pumping system requiring long-term maintenance. The depth of the drop inlet close to the bridge site was 4 ft deeper than the floor level, so a trench was dug connecting the sump pit location to the main inlet collecting runoff. The slope of the trench was measured and adjusted using an automatic level to be approximately 1 percent.

Figure B.15 shows the drainage channel construction. To collect the water draining toward the center of the bridge floor, a manhole was constructed using a concrete pipe oriented vertically. A 6 in. diameter hole was drilled at the side of the pipe. A 100 ft long schedule 40 pipe was used for the drainage line. After the drainage pipe was connected to the manhole, the main inlet wall was drilled to provide access for a 6 in. diameter pipe. Figure B.15(c) shows the drainage trench and pipe before backfilling.

(a) Back-Wall, Pedestal, and Wing-Wall Pour

(b) View of the Substructure after Removal of the Forms

(c) Backfilling and Compaction Process

Figure B.14. Abutment Construction and Backfilling.

(a) Trench Excavation

(b) Manhole Placement

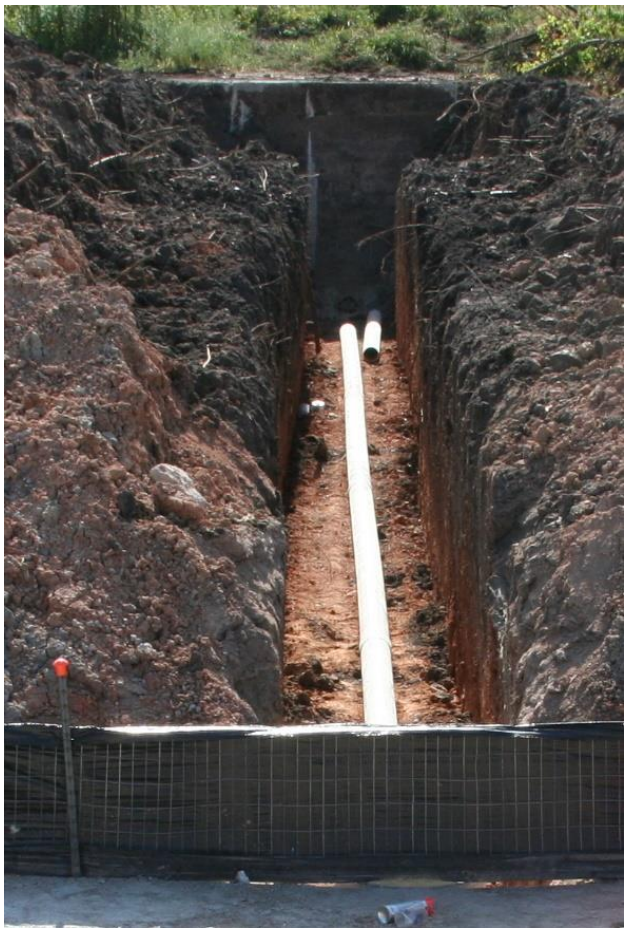

(c) Drainage Pipe Installation

Figure B.15. Construction of the Drainage System.

B.1.3 Construction of Bridge Superstructure

The bridge superstructure is composed of four slab beam girders spaced at 4 ft 8 in. apart, PCPs that span between girders as stay-in-place forms, and a CIP reinforced concrete deck that combines all the pieces and creates the monolithic bridge superstructure. Detailed dimensions and the geometry of these components are shown in Figure B.16.

The slab beam girders are standard TxDOT 5SB15 slab beams, and the PCPs are 4 in. thick, 8 ft long, and 5 ft 4 in. wide. The CIP deck thickness varies along the length due to the camber of the girders. The minimum deck thickness at the center of the bridge is 8 in. including the PCP thickness.

B.1.3.1 Precast Member Fabrication

The prestressed slab beam girders were designed based on the AASHTO LRFD Specifications (2012) and TxDOT Bridge Design Manual (TxDOT 2013a). The number of prestressing tendons and the amount of debonding required are shown in Figure B.16.

The mild steel reinforcing bars were placed based on the standard TxDOT drawing PSB-5SB15. The only detail that was changed was the length of the H-bars. The height of the H-bars was increased to 6 in. above the slab beam surface because the increased deck thickness allowed this dimension to be increased to provide proper development length into the CIP deck slab.

The prestressed slab beam and PCP construction was performed by Bexar Concrete Works in San Antonio, Texas. A detailed drawing for prestressing and mild reinforcement was provided to the precaster. Figure B.17 shows the slab beam construction process, with the reinforcing cage fabrication shown in Figure B.17(a). All 56 strands were stressed up to 31 kips per strand, and specified strands were debonded up to 6 ft from both ends of the girders. For debonding application, a plastic tube was placed around the strands, and then duct tape was used to cover the tube. The concrete was specified as self-consolidating concrete (SCC), having a compressive strength at release of 6 ksi and a compressive strength at service (28 days) of 7 ksi. To capture the different mechanical properties of the concrete, 96 cylinder samples and 12 modulus of rupture beam specimens were fabricated by the research team. Also, fresh concrete properties (slump flow, unit weight, and concrete temperature) were tested by the research team for each girder. Ambient temperature and humidity were also recorded

during the concrete pour. Detailed concrete properties and the mechanical property test results are provided in Section 2. Figure B.17(b) shows the cylinder molds that were prepared and oiled before the slab beam pour, along with a sample slump flow test.

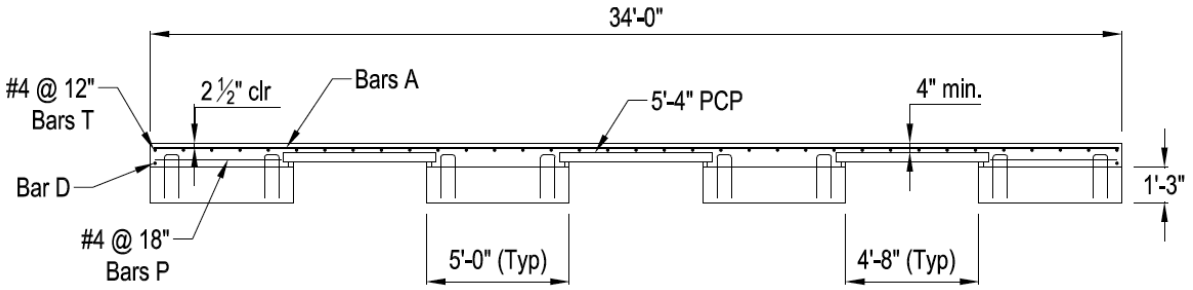

(a) Bridge Composite Cross-Section

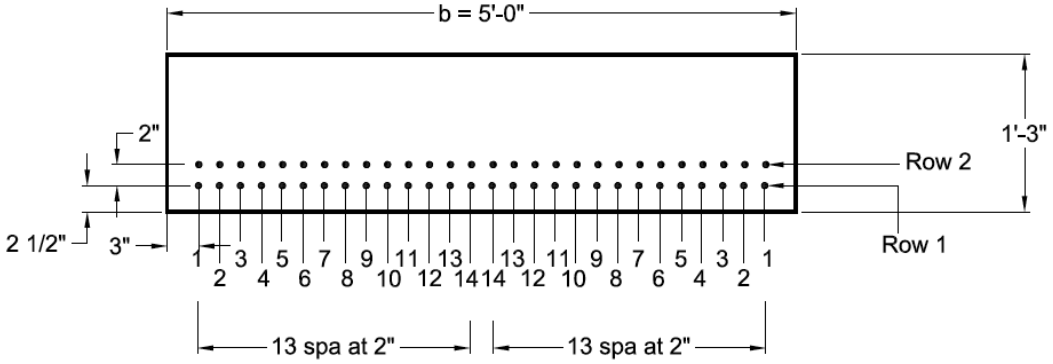

STRAND LOCATIONS
CROSS-SECTION

DEBONDING DATA		
Measurement from End	Strand No. (Row 1)	Number of Debonded Strands
0'-0" - 3'-0"	No.5,9,13	6
3'-0" - 6'-0"	No. 9,13	4

(b) Slab Beam Prestressing Detail

Figure B.16. Bridge Superstructure Cross-Section.

(a) Slab Beam Reinforcing Bar Placement

(b) Material Specimens and Slump Flow Tests

(c) Slab Beam Pour

Figure B.17. Slab Beam Construction.

Before closure of the formwork of the slab beams, the bottom of the formwork was cleaned and oiled. Steel forms were assembled along the sides of all four slab beams and supported from the top. The ends of the slab beams were separated by plywood caps. All four girders were poured together and then submerged in water.

Figure B.18 shows the reinforcement placement and concrete pour for the PCPs. Precast concrete panels were also cast at the same precast plant in San Antonio. Eighteen 8 ft long PCPs were cast to span the three openings between the 48 ft long slab beams. The width of the panels is 5 ft 4 in. As transverse reinforcement, 0.5 in. diameter prestressing strands, stressed at 16.1 kips, were placed at 6 in. spacing. As longitudinal reinforcement, deformed welded wire reinforcement was used as specified in the TxDOT Bridge Division Standard Drawings (TxDOT 2013b). The concrete for the PCPs was specified as TxDOT Class H with a release strength of 4 ksi and 28-day compressive strength of 5 ksi.

Figure B.18. Precast Concrete Panel Construction.

B.1.3.2 Erection of Precast Members

Before the erection of the slab beams, the load cell assembly was placed. Figure B.19 shows the load cell assembly. The load cell assembly consisted of a 1 in. thick bottom steel plate and a 1.5 in. thick top steel plate. There were two different load cell assemblies due to the two-bearing-pad and one-bearing-pad configurations. At the south end of the bridge, there were two bearing pads (9 in. x 9 in.) at the corners of the slab beam, and the steel plates are 10 in. x 10 in. At the north end of the bridge, the bearing pads (9 in. x 18 in.) were at the center of the bridge, and the steel plates are 10 in. x 20 in. The bottom plates were placed and attached to their exact locations using a high-strength fast-gain grout. Load cells were placed within circular indentations machined in the bottom steel plates. Then the top steel plates were placed on the buttons of the load cells.

The slab beams weighed around 45 kips each. Due to weight limitations on the highway, each slab beam was delivered by an 18-wheeler. A crane with a 100 ton capacity was rented and ready early in the morning. The bearing pads had already been placed on top of the steel plates, and the edges of the slab beams were marked on the abutment before the start of the crane operation. Four slab beams were successfully positioned at their locations. The spacing between the slab beams was 4 ft 8 in. per design. Figure B.20 shows the view of precast members during erection. After the erection of the slab beams, bedding strips were cut to the required depth. In order to have a flat deck surface, the depth of the bedding strip is critical. Before determining the bedding strip dimensions, the camber of the slab beams was measured to be 4.5 in., which was 1.5 in. higher than the expected value. The beams were expected to deform about 0.4 in. after the erection of PCPs and about 1.2 in. more after the CIP deck pour. The bedding strip depth was adjusted accordingly to compensate for the 3 in. camber difference. The bedding strip depth can be a minimum of 0.5 in. and a maximum of 4 in. according to the TxDOT Bridge Design Manual (TxDOT 2013a). Based on these dimensions, the bedding strip depth was taken to be 0.5 in. at the midspan and 3.5 in. at the end of the slab beams, changing linearly in between. The thickness of the bedding strips was 2 in., as specified by TxDOT Bridge Design Manual (TxDOT 2013a) standards. Dow® high-load 40 Styrofoam (extruded polystyrene foam), which conforms to the requirements in the TxDOT Bridge Design Manual (TxDOT 2013a), was used as bedding strip material. Bedding strip pieces were glued at the edges of the slab beams using the proper glue.

(a) South End Load Cell Assembly

(b) North End Load Cell Assembly

(c) Bridge Span Ready for Taking the Girders

Figure B.19. Load Cell Assembly.

(a) Slab Beam Erection Operation

(b) Bedding Strip Application

(c) Erection of Precast Concrete Panels

Figure B.20. Precast Member Placement.

Bedding strips were glued down two days before the erection of the precast panels. The glue was hardened at the time of PCP erection. Because of the relatively light weight of the PCPs, a smaller crane was used for the placement of the panels. Six PCPs were placed at each span between slab beams. According to the TxDOT Bridge Design Manual (TxDOT 2013a), the length of a PCP hanging over the bedding strip should be at least 1.5 in. For the Riverside Bridge, the length of PCP hanging over the bedding strip was designed as 2 in. During the erection of the panels, construction workers made sure that this distance was more than 1.5 in. at both ends for all panels.

B.1.3.3 Reinforced Concrete Deck Construction

The bridge deck reinforcing bars were placed based on TxDOT Bridge Division Standard Design Drawings (TxDOT 2013b), and #5 transverse reinforcing bars at 6 in. spacing and #4 longitudinal bars at 12 in. spacing were placed over the panels. One more layer of transverse reinforcement was provided at the top of the exterior girders only. Figure B.16(a) shows the reinforcing bar details and orientation. The deck design was checked based on ultimate strength design, and the strength of the PCPs was found to be adequate to carry the additional deck load and HS20 truckload.

The deck formwork plywood boards were assembled at the bridge site. The formwork was supported using wood wedges along the north, south, and east edges of the bridge. The formwork along the west edge was supported down to the ground level below the bridge. The deck formwork was not attached to the bridge girders because the bridge girders would deflect about 1 in. and the formwork should not move down with the edge girder. The finished deck formwork is shown in Figure B.21(a).

After building the formwork, reinforcing mesh was placed and tied together. According to TxDOT Bridge Division Standard Drawings (TxDOT 2013b), the clear cover at the top of the deck rebar should be 2 in. In order to keep the top covered, the rebar can be laid directly on top of the panels. Because of the high camber of the slab beams, the reinforcing mesh was laid on top of the panels at most places. Slab bolsters were provided only on the last panel at the ends of the slab beams. Reinforcing mesh construction is shown in Figure B.21(b).

(a) Deck Formwork Construction

(b) Deck Reinforcing Bar Construction

(c) Deck Concrete Pour

Figure B.21. Cast-in-Place Deck Construction.

For the deck pour, 40 cyds of TxDOT Class S concrete were ordered. The compressive strength of the concrete was specified as 4000 psi. The bridge deck slope was dictated by the elevation of the formwork, and the elevation of the northwest section of the bridge was similar to the rest of the runway. The deck concrete pour was subcontracted. The subcontractor adjusted the concrete slope by using string lines based on the formwork height.

The concrete surface was finished using a bull float. After it hardened to an appropriate degree, a medium-level broom finish was applied in the transverse direction. Figure B.22 shows the deck concrete surface finishing operation. The concrete was cured by covering it with wet blankets and a plastic sheet for four days. An evaporation retardant agent was not applied due to humid and cool weather conditions. A view of the curing practice is shown in Figure B.23.

Figure B.22. Deck Concrete Finishing.

Figure B.23. Curing of Deck Concrete.

B.1.3.4 Approach Slab Construction

Before the start of the approach slab construction, one more row of concrete pavement blocks was removed from the existing runway at both ends of the bridge due to damage during construction. With the removal of these pieces, the total length of the slab was 29 ft at each end of the bridge. The first 20 ft was designed as a 13 in. deep approach slab having two layers of reinforcing mesh, and the remaining 9 ft was designed as a 7 in. deep reinforced concrete slab having one layer of reinforcing mesh. Most of the approach slab region had already been backfilled and compacted. Recently excavated parts were also backfilled and compacted to create a stronger bearing surface under the slab.

The remaining top portion of the slab along the east edge of the deck was also poured with the approach slabs. The 3 ft 4 in. wide slab was 2 in. lower than the existing runway. This was done so that the top of the bridge deck could be smoothly transitioned to the existing runway.

A 1 in. thick bituminous expansion joint material was glued at both ends of the bridge as a separation between the bridge deck and approach slab. A 1 in. thick Styrofoam board was glued along the east edge of the bridge as an expansion joint. A 3 to 4 in. gap remained between the retaining wall and bridge deck along the east edge of the bridge. To close that gap, a 6 in. wide 0.25 in. thick steel sheet was attached to the top of the slab by wedge anchors. The rest of the small gaps, due to the roughness of the retaining wall surface, were sealed with expanding foam. Figure B.24 shows the expansion joint material and steel sheet formwork.

The west side of the approach slabs was closed using 2 in. x 12 in. nominal lumber. The reinforcing mesh was provided according to TxDOT Bridge Division Standard Drawings (TxDOT 2013b). The approach slab was 20 ft long. The bottom reinforcing mesh had #8 transverse bars at 6 in. spacing and #5 longitudinal bars at 12 in. spacing. The top mesh was #5 bars with 12 in. spaced mesh in both directions. The last 9 ft of the reinforced concrete slab had only #5 bars at 12 in. spacing. The top mesh of the approach slab was extended to the existing slab. Figure B.24(b) shows the reinforcing bar mesh construction for the approach slabs.

The concrete for the approach slab was specified as TxDOT Class S having 4000 psi compressive strength. This item was also subcontracted due to the large concrete finishing surface. The top of the deck elevation was about 1.5 in. higher than the existing runway. This difference caused a gradual slope away from the bridge at both ends of the bridge over a 29 ft length.

Figure B.24 shows the approach slab construction for both ends and the 3 ft 4 in. wide slab along the east edge that was poured at the same time. After the pour, the concrete was given a smooth surface concrete finish using a bull float. After the concrete hardened to a certain level, a medium-level broom finish was applied in the transverse direction, as was done for the bridge deck.

(a) Expansion Joint and Steel Sheet Form.

Figure B.24. Approach Slab Construction.

(b) Approach Slab Reinforcing Mesh

(c) Approach Slab Pour

(d) Approach Slab Broom Finish

Figure B.24. Continued.

B.2 MATERIAL PROPERTIES FOR RIVERSIDE BRIDGE

B.2.1 General

Several fundamental mechanical properties are essential to design structural members, including compressive strength, splitting tensile strength (STS), modulus of elasticity (MOE), and modulus of rupture (MOR). To obtain the concrete mechanical properties that could predict structural behavior, a large number of concrete samples including cylinders and beams for different structural components were fabricated and tested during the construction process of the Riverside Bridge. Slump tests were conducted before conventional concrete pours to verify workability, while slump flow was measured for SCC. In addition, for the purpose of controlling the quality of SCC for precast prestressed slab beams and PCPs, the ambient temperature, ambient humidity, concrete weight, and concrete temperature were measured.

B.2.2 Test Procedures

B.2.2.1 Mechanical Properties

B.2.2.1.1 Compressive Strength

Compressive strength is an important index for structural capacity design and is often used to predict other mechanical properties (MOE, MOR, and STS). Test samples were cast in accordance with American Society for Testing and Materials (ASTM) C31/31M, Standard Practice for Making and Curing Concrete Test Specimens in the Field (ASTM 2012a). Sample sizes were 4 in. x 8 in. cylinders. Cylinder molds for casting concrete test specimens conformed to the requirements of ASTM (2010c) C470/C470M, Specification for Molds for Forming Concrete Test Cylinders Vertically, and were placed on a level, rigid surface free of vibration and other disturbances. Concrete was placed in the mold in two layers of approximately equal volume, and 25 roddings and 10–15 light hand tappings were used for each layer. Specimens were not transported until at least eight hours after final set. For SCC, only 10–15 hand tappings for each layer were required in the process of making test cylinders.

In accordance with ASTM (2010a) C39/C39M, Standard Test Method for Compressive Strength of Cylindrical Concrete Specimens, the compressive strength of test specimens was determined at 24 hours, 3 days, 7 days, 28 days, and 90 days. The load was applied at a rate of

movement corresponding to a stress rate on the specimen of 35 ± 7 psi/s. A 500-kips capacity Materials Testing System (MTS) machine in the High Bay Structural and Materials Testing Laboratory at Texas A&M University was used to test all mechanical characteristics of the conventional concrete (CC) and SCC cylindrical specimens. The MTS testing machine is shown in Figure B.25.

B.2.2.1.2 Modulus of Elasticity

The MOE represents the stress-strain relationship in the elastic range and is used in the prediction of the deflection and camber of precast prestressed concrete members.

Test samples were cast in accordance with ASTM (2012a) C31/C31M, Standard Practice for Making and Curing Concrete Test Specimens in the Field. For the MOE test, the sample size was a 4 in. x 8 in. cylinder. The mold requirement, fabrication procedure, and curing regime were the same as those used in the compressive strength test.

In accordance with ASTM (2011) C469/C469M, Standard Test Method for Static Modulus of Elasticity and Poisson's Ratio of Concrete in Compression, two linear variable differential transducers (LVDTs) measured the strain of concrete in compression up to 40 percent of the compressive strength at the age of testing. The MOE test was conducted at 24 hours, 3 days, 7 days, 28 days, and 56 days. The compressometer with LVDTs used during testing is shown in Figure B.26.

The modulus of elasticity to the nearest 200 MPa (50,000 psi) was calculated according to Equation (B.1):

$$E = \left(S_2 - \mathrm{S}_1\right) / \left(\varepsilon_2 - 0.000050\right) \quad \text{(B.1)}$$

Where:

E = Chord modulus of elasticity, psi.

S_2 = Stress corresponding to 40 percent of ultimate load, psi.

S_1 = Stress corresponding to a longitudinal strain, ε_1, of millionths, psi.

ε_2 = Longitudinal strain produced by stress, S_2.

Figure B.25. MTS Testing Machine.

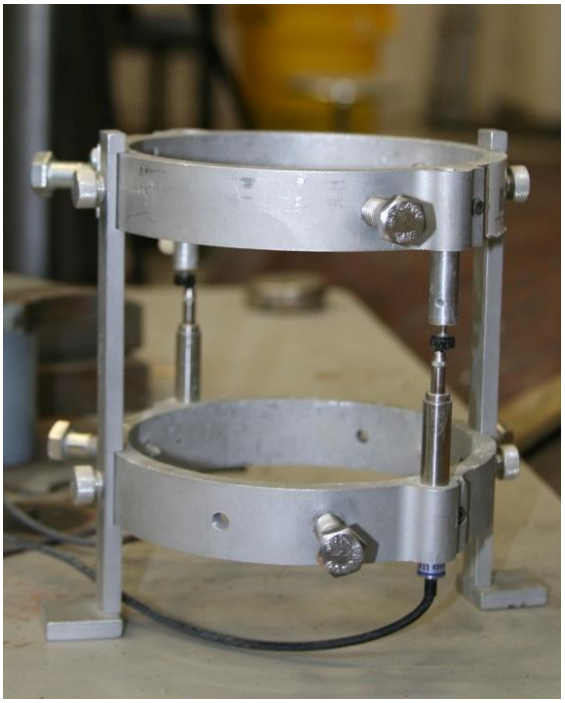

Figure B.26. Compressometer.

B.2.2.1.3 Modulus of Rupture

The MOR test is a measurement of flexural strength, and its value is also useful for the design and prediction of structural behavior (Trejo et al. 2008). Test samples were cast in accordance with ASTM (2012a) C31/31M, Standard Practice for Making and Curing Concrete Test Specimens in the Field. The standard beam was 6 in. x 6 in. in cross-section, and the beam length was 18 in. The concrete was placed in the mold in two layers of approximately equal volume, and each layer was consolidated as required. In placing the final layer, an amount of concrete was added to fill the mold after consolidation. The concrete was placed so that it was uniformly distributed within each layer. Specimens were not transported until at least eight hours after final set.

In accordance with ASTM (2010b) C78/C78M, Standard Test Method for Flexural Strength of Concrete (Using Simple Beam with Third-Point Loading), the load was applied continuously and without shock, at a constant rate within the range 100 to 200 psi/min tensile stress until failure of the specimen. The maximum applied load indicated by the testing machine at failure was recorded. The MOR test was conducted at 28 days. The apparatus for the MOR test is shown in Figure B.27.

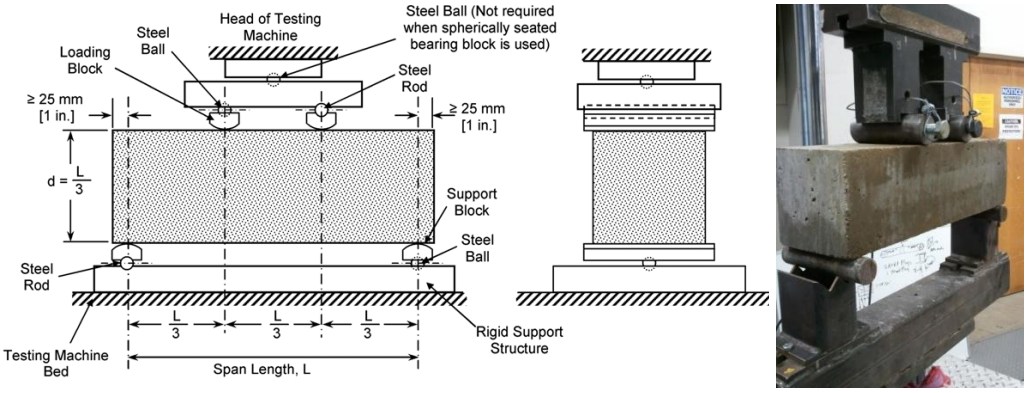

Figure B.27. Schematic and Photo of Apparatus for MOR Test (ASTM 2012a).

If the fracture initiates in the tension surface within the middle third of the span length, the modulus of rupture is calculated according to Equation (B.2):

$$R = \frac{PL}{bd^2} \tag{B.2}$$

Where:

R = Modulus of rupture, psi.

P = Maximum applied load indicated by the testing machine, lbf.

L = Span length, in.

b = Average width of specimen at fracture, in.

d = Average depth of specimen at fracture, in.

If the fracture occurs in the tension surface outside of the middle third of the span length by not more than 5 percent of the span length, the modulus of rupture is calculated according to Equation (B.3):

$$R = \frac{3Pa}{bd^2} \tag{B.3}$$

Where a is the average distance between the line of fracture and the nearest support measured on the tension surface of the beam measured in inches.

If the fracture occurs in the tension surface outside of the middle third of the span length by more than 5 percent of the span length, the results of the test are discarded.

B.2.2.1.4 Splitting Tensile Strength

The STS test is an indirect measurement of the tensile strength of concrete and is used to predict and limit the allowable stresses in critical regions in precast prestressed concrete members. Test samples were cast in accordance with ASTM (2012a) C31/31M. For the STS test, the sample size was a 4 x 8 in. cylinder. The mold requirements, fabrication procedure, and curing regime were the same as those in the compressive strength test.

In accordance with ASTM (2011) C496/C496M, Standard Test Method for Splitting Tensile Strength of Cylindrical Concrete Specimens, the load was applied continuously and without shock, at a constant rate within the range of 100 to 200 psi/min splitting tensile stress until failure of the specimen. The maximum applied load indicated by the testing machine at failure was recorded.

The splitting tensile strength of the specimen is calculated as follows:

$$T = 2P / \pi ld \tag{B.4}$$

Where:

T = Splitting tensile strength, psi.

P = Maximum applied load indicated by the testing machine, lbf.

l = Length, in.

d = Diameter, in.

B.2.2.2 Fresh Properties

B.2.2.2.1 Slump Test

The slump flow test should be conducted before placing the concrete to evaluate filling ability and stability. The slump test procedures for CC and SCC are different. In accordance with ASTM (2012b) C143, Standard Test Method for Slump of Hydraulic Cement Concrete, the slump test procedure of CC had the following steps:

1. Dampen the interior of the slump mold.
2. Place the mold on a flat, moist, nonabsorbent, and rigid surface.
3. Hold the mold firmly in place by standing on the two brackets on either side of the mold.

4. Using a scoop, fill the mold in three layers (of equal volume), moving the scoop around the perimeter of the mold opening to ensure an even distribution of the concrete.
5. Rod each layer 25 times throughout its depth.
6. Remove any concrete that has collected around the base of the mold during strike-off.
7. Immediately remove the mold by raising the mold in a steady, vertical direction. Lift the mold off the concrete a distance of 12 in. in 5 +/− 2 seconds.
8. Measure the slump immediately. This is the vertical distance between the top of the mold (upside down next to the specimen) and the displaced original center of the top surface of the specimen.

To evaluate the fresh properties of SCC, the slump was measured in accordance with ASTM (2009) C1611, Test Method for Slump Flow of Self-Consolidating Concrete. Slump flow is the measured maximum diameter of flow after lifting an inverted slump cone. The average diameter of the slump flow is the average value of two perpendicular measurements. The slump test measurements for CC and SCC are shown in Figure B.28 and Figure B.29, respectively.

Figure B.28. Slump Measurement (CC).

Figure B.29. Slump Measurement (SCC).

B.2.2.2.2 Density (Unit Weight)

Unit weight is measured in accordance with ASTM (2013) C138, Standard Test Method for Density (Unit Weight), Yield, and Air Content (Gravimetric) of Concrete. The unit weight test had the following steps:

- Determine the mass (pounds or kilograms) of the empty measure (bucket) to be used.
- Using a scoop, place the concrete in the measure in three layers of approximately equal volume, moving the scoop around the perimeter of the measure opening to ensure an even distribution of the concrete.
- Rod each layer 25 times throughout its depth; distribute the rodding uniformly over the cross-section of the measure, starting near the perimeter, and progress spirally toward the center.
- Tap the outside of the measure 10 to 15 times with the mallet to close voids left by the tamping rod.
- Completely clean the exterior of the measure and determine the mass (pounds or kilograms) of the measure filled with concrete.

B.2.2.2.3 Additional Fresh Properties

Ambient temperature, ambient humidity, and concrete temperature were also measured to evaluate external factors for the concrete.

B.2.3 Test Results

During the different stages of bridge construction, a large number of samples including cylinders and beams were made and then tested at the specified day in the High Bay Structural and Materials Testing Laboratory at Texas A&M University. The test results are summarized according to the sequence of the construction.

B.2.3.1 Retaining Wall

A 75 ft long retaining wall was built before the excavation to resist the soil pressure below the adjacent runway. TxDOT Class C concrete with compressive strength of 3.60 ksi at 28 days was required. Cylinder samples for compressive strength at 7 days and 28 days, MOE at 28 days, and STS at 28 days were taken in the field. The mechanical property test results are shown in

Table B.2. The slump test was also conducted before pouring the concrete; the slump value was 6.6 in., which is less than the target (7 in.) and was considered acceptable. The average compressive strength at 28 days was 6.28 ksi, which satisfied the design requirement.

Table B.2. Mechanical Property Test Results for Retaining Wall.

Sample No.	Compressive Strength					STS		MOE	
	f_c'/7d (ksi)	Avg. f_c'/7d (ksi)	f_c'/28d (ksi)	Avg. f_c'/28d (ksi)	Design f_c' (ksi)	T/28d (ksi)	Avg. T/28d (ksi)	E/28d (ksi)	Avg. E/28d (ksi)
1	4.04	4.11	6.34	6.28	3.6	0.710	0.693	5928.63	5980.34
2	4.13		6.32			0.711		6049.90	
3	4.16		6.18			0.659		5962.49	

B.2.3.2 Slab on Grade

A 58 ft 10 in. long, 34 ft wide, and 4 in. thick concrete slab on grade was provided at the base of the excavated pit. For this slab, TxDOT Class C concrete with 3600 psi compressive strength at 28 days and a 7 in. slump was specified. Three trucks of concrete were used in the construction process of the mud slab. For each truck, three cylinder samples for compressive strength at 28 days were taken in the field. The compressive strength test results are shown in Table B.3. The concrete compressive strength for the slab-on-grade satisfies the design requirement, and the compressive strength values increased as concrete age increased.

B.2.3.3 Footings

A 34 ft long, 8 ft wide, and 1 ft 4 in. high spread reinforced concrete footing was constructed at both ends of the bridge. For the spread footings, TxDOT Class C concrete with 3600 psi compressive strength at 28 days and 5 in. slump was required. Three trucks of concrete were used in the construction process for spread footings. For each truck, three cylinder samples for compressive strength at 28 days were taken. Three cylinder samples from Truck 1 for the MOE test at 28 days were also taken in the field. The compressive strength and MOE test results are shown in Table B.4. and Table B.5. , respectively.

Table B.4. shows that the concrete compressive strength for the spread footings satisfied the design requirement.

B.2.3.4 Abutments

Two 34 ft long abutments with 2.5 by 2.5 ft cross-sections were built at both sides. TxDOT Class C concrete with 3600 psi compressive strength at 28 days and 5 in. slump was required. Two trucks of concrete were used in the construction process for the spread footings. For each truck, three cylinder samples for compressive strength at 7 and 28 days were taken. The compressive strength test results are shown in Table B.6. The concrete compressive strength for the abutments satisfied the design requirement.

Table B.3. Compressive Strength at 28 Days for Slab-on-Grade.

Truck No.	Sample No.	f_c' (ksi)	Avg. f_c'(ksi)
1	1	4.65	4.63
	2	4.38	
	3	4.87	
2	1	4.67	4.84
	2	5.05	
	3	4.81	
3	1	4.79	5.00
	2	4.82	
	3	5.40	

Table B.4. Compressive Strength for Spread Footings.

Truck No.	Sample No.	f_c'/28d (ksi)	Avg. f_c'/28d (ksi)
1	1	6.02	5.96
	2	5.98	
	3	5.89	
2	1	6.26	6.39
	2	6.36	
	3	6.54	
3	1	5.88	5.81
	2	5.80	
	3	5.74	

Table B.5. MOE Values for Spread Footings.

Truck No.	Sample No.	E/28d (ksi)	Avg. E/28d (ksi)
1	1	6226	5842
	2	6017	
	3	5283	

Table B.6. Compressive Strength for Abutments.

Truck No.	Sample No.	f_c'/7d (ksi)	Avg. f_c'/7d (ksi)	f_c'/28d (ksi)	Avg. f_c'/28d (ksi)	Design f_c' (ksi)
1	1	4.46	4.43	5.94	5.92	3.6
	2	4.40		5.84		
	3	4.43		5.97		
2	1	4.31	4.36	5.70	5.61	
	2	4.36		5.49		
	3	4.41		5.65		

B.2.3.5 Slab Beams

After substructure construction work was finished, Bexar Concrete Works manufactured the slab beams by precaster in San Antonio, Texas. Four 48 ft long 5SB15 (15 by 5 ft) prestressed slab beams were needed for the bridge construction. High-strength TxDOT Class H concrete with f'ci = 6 ksi at release and f'c = 7 ksi at 28 days was required. In order to control the quality of the slab beam, a large number of specimens including cylinders and beams were taken in the field, and fresh properties tests were also conducted there. For different beams, cylinder samples were taken for compressive strength at 24 hours, 3 days, 7 days, 28 days, and 56 days; MOE at 7 and 28 days; and STS at 7 and 28 days. Beam samples for MOR tests were taken at 56 days. The cylinder casting procedures are shown in Figure B.30 and Figure B.31. The compressive strength values for each slab beam are shown in Table B.7.

Figure B.30. Test Specimen Casting.

Figure B.31. All Cylinder Samples.

Fresh properties including slump, unit weight test, ambient temperature, ambient humidity, and concrete temperature were measured in the field. The fresh properties of the concrete are shown in Table B.8. The relationship between concrete strength and concrete age is shown in Figure B.32. The splitting tensile strength values for each slab beam are shown in Table B.9. The relationship between splitting tensile strength and concrete age is shown in Figure B.33. The modulus values of elasticity values for each slab beam are shown in Table B.11. The MOR strength values for each slab beam are shown in Table B.10. The values in the table and relevant figures show that the compressive strength for the slab beams satisfied the strength requirement for the release strength and final design strength. As concrete age increased, the values of compressive strength and STS strength for the concrete increased.

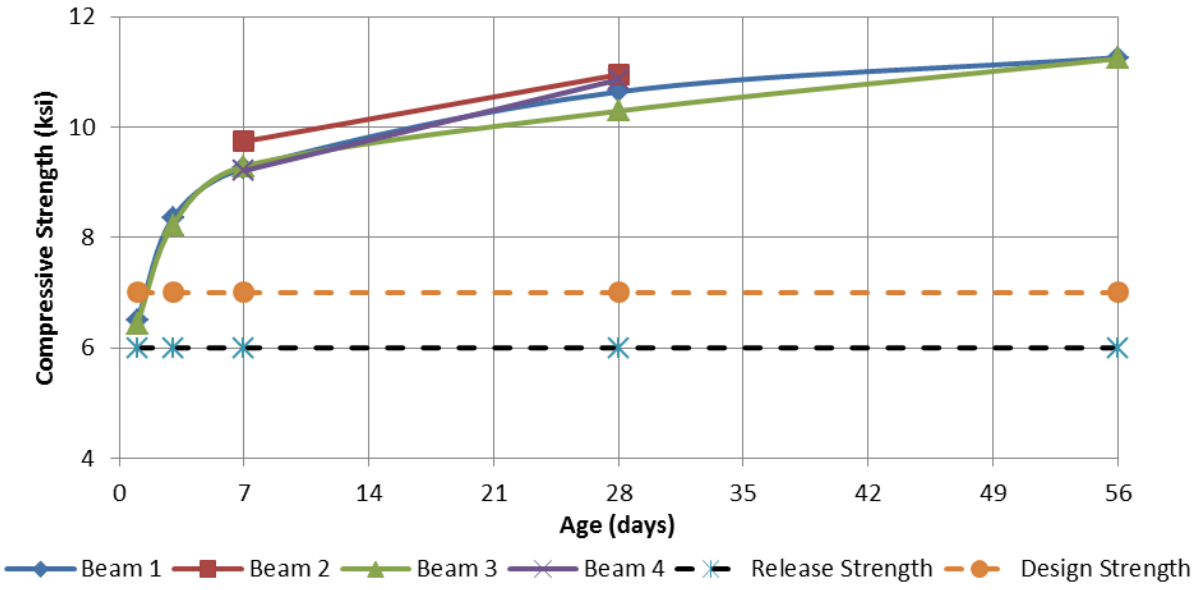

Figure B.32. Relationship between Compressive Strength and Concrete Age.

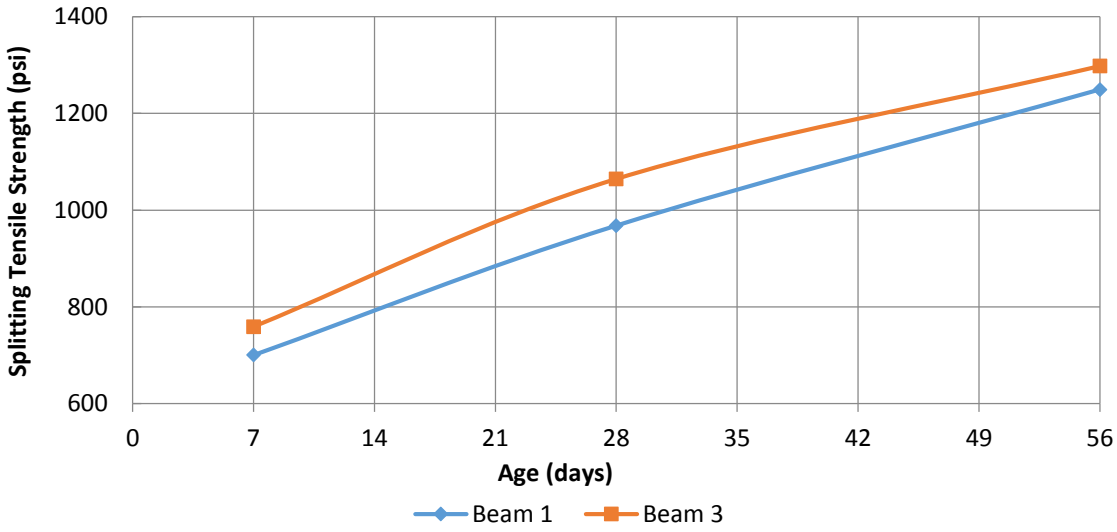

Figure B.33. Relationship between STS and Concrete Age.

Table B.7. Compressive Strength for Slab Beams.

Beam No.	Sample No.	f_c'/1d (ksi)	Avg. f_c'/1d (ksi)	f_c'/3d (ksi)	Avg. f_c'/3d (ksi)	f_c'/7d (ksi)	Avg. f_c'/7d (ksi)	f_c'/28d (ksi)	Avg. f_c'/28d (ksi)	f_c'/56d (ksi)	Avg. f_c'/56d (ksi)	Design f_c' (ksi)
1	1	6.49	6.50	8.27	8.35	9.10	9.25	10.63	10.64	11.25	11.26	3.6
	2	6.62		8.34		9.38		10.58		11.41		
	3	6.39		8.43		9.27		10.72		11.12		
2	1	–	–	–	–	9.89	9.74	10.96	10.95	–	–	
	2	–		–		9.55		11.57		–		
	3	–		–		9.78		10.31		–		
3	1	6.50	6.44	8.43	8.22	9.29	9.29	10.40	10.29	11.05	11.24	
	2	6.41		7.79		9.34		10.04		11.18		
	3	6.41		8.43		9.23		10.43		11.49		
4	1	–	–	–	–	9.05	9.21	11.04	10.86	–	–	
	2	–		–		9.58		10.95		–		
	3	–		–		8.99		10.60		–		

Table B.8. Fresh Properties of Concrete for Slab Beams.

Beam No.	Slump (in.)		Ambient Temperature (°F)	Ambient Humidity (%)	Unit Weight (kips/ft3)	Concrete Temperature (°F)
1	25	24	93.3	47.4	0.1462	88
2	24	23	94.6	45.0	0.1466	87
3	27	24	94.0	46.0	0.1468	87
4	28	25	92.3	48.6	0.1466	87

Table B.9. Splitting Tensile Strength for Slab Beams.

Beam No.	Sample No.	T/28d (ksi)	Avg. T/7d (ksi)	T/28d (ksi)	Avg. T/28d (ksi)	T/28d (ksi)	Avg. T/56d (ksi)
1	1	0.812	0.700	1.316	0.968	1.209	1.249
	2	0.873		0.951		1.342	
	3	0.617		0.637		1.197	
3	1	0.729	0.759	1.152	1.065	1.239	1.298
	2	0.776		0.787		1.294	
	3	0.772		1.256		1.361	

Table B.10. MOR Strength for Slab Beams.

Beam No.	Sample No.	R/56d (ksi)	Avg. R/56d (ksi)	Beam No.	Sample No.	R/56d (ksi)	Avg. R/56d (ksi)
1	1	0.666	0.648	3	1	0.708	0.660
	2	–			2	0.690	
	3	0.630			3	0.582	

Table B.11. Modulus of Elasticity for Slab Beams.

Beam No.	Sample No.	E/7d (ksi)	Avg. E/7d (ksi)	E/28d (ksi)	Avg. E /28d (ksi)	E/56d (ksi)	Avg. E /56d (ksi)
1	1	4656	4735	4980.36	4908	3349.32	4653
	2	4657		4951.85		5465.88	
	3	4891		4792.51		5143.19	
2	1	–	–	4318.34	4658	–	–
	2	–		4820.37		–	
	3	–		4833.90		–	
3	1	4607	4630	5036.29	4978	5393.22	5393
	2	4541		5005.38		5441.17	
	3	4740		4892.14		5343.97	
4	1	–	–	5214.23	5064	–	–
	2	–		4837.09		–	
	3	–		5140.89		–	

B.2.3.6 PCPs

Bexar Concrete Works also manufactured the PCPs by precaster in San Antonio, Texas. Eighteen total PCPs (8 ft long with a 4 in. depth and 5 ft 4 in. width) were needed for the bridge construction. TxDOT Class H concrete with f'ci = 4 ksi at release and f'c = 5 ksi at 28 days was required. Given that the manufacturer made the panels in a rush, only eight cylinder samples were taken and tested for mechanical properties including compressive strength, modulus of elasticity, and splitting tensile strength. The values of mechanical properties are shown in Table B.12. also shows that the compressive strength values for PCPs satisfied the design requirement.

Table B.12. Mechanical Property Test Results for PCPs.

Sample No.	Compressive Strength			STS		MOE	
	f_c'/7d (ksi)	Avg. f_c'/7d (ksi)	Design (ksi)	T/28d (ksi)	Avg. T/28d (ksi)	E/28d (ksi)	Avg. E/28d (ksi)
1	10.0	9.93	5	1.06	1.05	5086	5489
2	9.82			0.961		5891	
3	9.96			1.13		–	

B.2.3.7 Deck

The deck was cast in place after the slab beams and PCPs were positioned. TxDOT Class S concrete with 4000 psi compressive strength at 28 days was required. Fresh properties including slump, unit weight test, ambient temperature, ambient humidity, and concrete temperature were also measured in the field. The fresh properties of the concrete are shown in Table B.13. Cylinder samples for compressive strength at 28 days and MOE at 28 days, as well as beam samples for MOR at 28 days, were made in the field. The mechanical property test results are shown in Table B.14 and Table B.15. Table B.16. shows that the compressive strength for the deck satisfies the design strength requirement.

Table B.13. Fresh Properties of Concrete for Deck.

Truck No.	Slump (in.)	Ambient Temperature (°F)	Ambient Humidity (%)	Unit Weight (kips/ft3)	Concrete Temperature (°F)
1	5.6	77.4	88.8	0.1527	85
2	4.8	77.4	88.8	0.1545	90
3	5.5	77.4	88.8	0.1548	90
4	4.0	77.4	88.8	0.1531	91

Table B.14. Compressive Strength Values for Deck.

Truck No.	Sample No.	f_c'/28d (ksi)	Avg. f_c'/28d (ksi)
1	1	5.09	5.16
	2	5.35	
	3	5.03	
2	1	6.91	6.99
	2	7.09	
	3	6.98	
3	1	6.00	6.61
	2	6.97	
	3	6.87	
4	1	6.94	7.01
	2	7.05	
	3	7.05	

Table B.15. MOR Values for Deck.

Truck No.	Sample No.	R/28d (ksi)	Avg. R/28d (ksi)
2	1	0.865	0.851
	2	0.798	
	3	0.891	

Table B.16. MOE Values for Deck.

Truck No.	Sample No.	E/28d (ksi)	Avg. E/28d (ksi)
2	1	6312	6466
	2	6701	
	3	6385	
3	1	6736	6467
	2	6346	
	3	6320	

APPENDIX C

LDF TABLES FOR THE CONSIDERED BRIDGE GEOMETRIES

C.1 INTRODUCTION

Live load distribution factor (LDF) formulas were derived by analyzing 31 different spread slab beam bridge geometries using the finite element method (FEM). Key parameters (span L, spacing S, and girder depth d) were varied, and FEM shear and moment values were obtained for each girder, for both one-lane-loaded and multiple-lane-loaded cases. These shear and moment values were used to determine shear and moment LDF values for interior and exterior girders. LDF values were also calculated using the American Association of Sate Highway and Transportation Officials (AASHTO) Load and Resistance Factor Design (LRFD) Specifications (2012) spread box beam formulas, least square fitted relations, and proposed spread slab beam equations for all eight LDF cases. Detailed derivation of the least square fitted relations and proposed equations are provided in Section 7. The maximum moment and shear forces obtained by FEM analysis for all 31 bridge models are provided in Table C.1. The LDF values obtained using the three methods, for all eight equations, and their ratios to the LDFs obtained through FEM analysis are listed in Table C.2 through Table C.9. The median values and lognormal standard deviations of these ratios are also provided to show the accuracy and variation of these equations.

Table C.1. Maximum Moment and Shear Forces from FEM Analysis.

Bridge Parameters				One-Lane-Loaded				Multiple-Lanes-Loaded			
				Interior Beam		Exterior Beam		Interior Beam		Exterior Beam	
No.	*L* (ft)	*S* (ft)	*d* (in.)	Max. Moment (kip-ft)	Max. Shear (kips)	Max. Moment (kip-ft)	Max. Shear (kips)	Max. Moment (kip-ft)	Max. Shear (kips)	Max. Moment (kip-ft)	Max. Shear (kips)
1	29.58	9.67	15.0	181	39	138	21	297	53	281	46
2	33.58	9.67	15.0	198	41	160	23	333	56	319	49
3	37.58	9.67	15.0	214	42	181	23	369	58	357	51
4	39.58	9.67	15.0	223	43	193	23	389	59	378	52
5	41.58	9.67	15.0	232	43	206	23	409	60	399	53
6	44.58	9.67	15.0	250	44	227	24	447	61	439	54
7	45.58	9.67	15.0	255	44	233	23	459	62	451	54
8	44.58	7.00	15.0	210	33	206	23	371	41	371	37
9	44.58	7.67	15.0	221	38	212	24	389	47	388	42
10	44.58	8.33	15.0	230	41	218	24	410	54	408	48
11	44.58	9.00	15.0	240	42	223	24	429	58	424	52
12	44.58	9.67	15.0	250	44	227	24	447	61	439	54
13	44.58	10.33	15.0	260	45	229	22	466	64	454	55
14	44.58	11.00	15.0	271	46	230	21	523	67	472	57
15	44.58	8.75	15.0	226	42	214	24	415	56	395	50
16	44.58	9.25	15.0	234	43	218	24	433	59	411	52
17	44.58	9.75	15.0	244	44	223	23	452	61	426	54
18	44.58	10.25	15.0	253	45	225	22	471	63	440	55
19	39.58	9.67	12.0	215	41	189	22	379	57	370	51
20	39.58	9.67	13.5	219	42	191	23	384	58	374	51
21	39.58	9.67	15.0	223	43	193	23	389	59	378	52
22	39.58	9.67	16.5	228	44	195	23	394	60	382	53
23	39.58	9.67	18.0	233	44	196	23	399	61	386	53
24	39.58	9.67	19.5	238	45	197	24	404	61	390	54
25	39.58	9.67	21.0	242	46	199	24	410	62	394	54
26	39.58	7.33	12.0	187	35	183	24	321	41	319	37
27	40.58	6.50	12.0	166	29	167	22	280	37	280	33
28	35.58	10.00	12.0	207	41	175	24	355	57	343	51
29	49.58	7.25	15.0	226	37	222	23	392	43	392	39
30	36.58	9.00	12.0	192	39	175	24	385	52	322	48
31	49.58	7.00	15.0	209	33	210	23	453	40	454	36

Table C.2. LDF Results for One-Lane-Loaded Moment in Interior Beams.

Bridge Parameters				LDF Results and Ratios						
No.	*L* (ft)	*S* (ft)	*d* (in.)	FEM	AASHTO	AASHTO/ FEM	Fitted	Fitted/ FEM	Proposed	Proposed/ FEM
1	29.58	9.67	15.0	0.552	0.516	0.935	0.550	0.996	0.567	1.026
2	33.58	9.67	15.0	0.510	0.485	0.949	0.509	0.997	0.532	1.042
3	37.58	9.67	15.0	0.482	0.458	0.950	0.475	0.985	0.503	1.043
4	39.58	9.67	15.0	0.467	0.446	0.956	0.460	0.986	0.490	1.050
5	41.58	9.67	15.0	0.447	0.435	0.975	0.446	1.000	0.478	1.070
6	44.58	9.67	15.0	0.429	0.421	0.980	0.428	0.997	0.462	1.075
7	45.58	9.67	15.0	0.424	0.416	0.981	0.422	0.995	0.456	1.076
8	44.58	7.00	15.0	0.363	0.347	0.955	0.362	0.996	0.380	1.048
9	44.58	7.67	15.0	0.381	0.366	0.960	0.379	0.994	0.402	1.053
10	44.58	8.33	15.0	0.396	0.385	0.970	0.396	0.999	0.422	1.065
11	44.58	9.00	15.0	0.412	0.403	0.978	0.412	1.000	0.442	1.073
12	44.58	9.67	15.0	0.429	0.421	0.980	0.428	0.997	0.462	1.075
13	44.58	10.33	15.0	0.447	0.438	0.979	0.443	0.991	0.480	1.075
14	44.58	11.00	15.0	0.465	0.454	0.977	0.458	0.983	0.499	1.072
15	44.58	8.75	15.0	0.388	0.396	1.021	0.406	1.047	0.435	1.120
16	44.58	9.25	15.0	0.403	0.410	1.017	0.418	1.038	0.449	1.116
17	44.58	9.75	15.0	0.419	0.423	1.010	0.430	1.026	0.464	1.108
18	44.58	10.25	15.0	0.434	0.436	1.004	0.441	1.016	0.478	1.101
19	39.58	9.67	12.0	0.449	0.422	0.941	0.438	0.977	0.463	1.032
20	39.58	9.67	13.5	0.458	0.435	0.949	0.450	0.982	0.477	1.041
21	39.58	9.67	15.0	0.467	0.446	0.956	0.460	0.986	0.490	1.050
22	39.58	9.67	16.5	0.477	0.457	0.959	0.470	0.986	0.502	1.053
23	39.58	9.67	18.0	0.486	0.467	0.960	0.479	0.984	0.513	1.054
24	39.58	9.67	19.5	0.496	0.477	0.960	0.487	0.981	0.523	1.054
25	39.58	9.67	21.0	0.507	0.486	0.958	0.495	0.977	0.533	1.051
26	39.58	7.33	12.0	0.394	0.358	0.907	0.380	0.963	0.392	0.996
27	40.58	6.50	12.0	0.334	0.329	0.984	0.351	1.052	0.361	1.080
28	35.58	10.00	12.0	0.499	0.454	0.910	0.476	0.954	0.499	0.999
29	49.58	7.25	15.0	0.329	0.336	1.019	0.345	1.048	0.368	1.118
30	36.58	9.00	12.0	0.450	0.421	0.935	0.443	0.985	0.462	1.026
31	49.58	7.00	15.0	0.305	0.329	1.076	0.339	1.109	0.361	1.180
Median (50th Percentile)					–	0.9701	–	1.0004	–	1.0479
Lognormal Standard Deviation, β_D					–	0.0342	–	0.0295	–	0.0309

Table C.3. LDF Results for Multiple-Lane-Loaded Moment in Interior Beams.

Bridge Parameters				LDF Results and Ratios						
No.	*L* (ft)	*S* (ft)	*d* (in.)	FEM	AASHTO	AASHTO/ FEM	Fitted	Fitted/ FEM	Proposed	Proposed/ FEM
1	29.58	9.67	15.0	0.756	0.757	1.001	0.757	1.000	0.757	1.001
2	33.58	9.67	15.0	0.720	0.733	1.019	0.719	0.999	0.733	1.018
3	37.58	9.67	15.0	0.694	0.713	1.028	0.688	0.991	0.713	1.028
4	39.58	9.67	15.0	0.680	0.704	1.035	0.673	0.991	0.704	1.035
5	41.58	9.67	15.0	0.658	0.695	1.056	0.660	1.003	0.695	1.056
6	44.58	9.67	15.0	0.642	0.683	1.064	0.642	1.000	0.683	1.064
7	45.58	9.67	15.0	0.637	0.679	1.066	0.636	0.999	0.679	1.066
8	44.58	7.00	15.0	0.534	0.541	1.012	0.520	0.973	0.541	1.012
9	44.58	7.67	15.0	0.559	0.578	1.034	0.552	0.988	0.578	1.033
10	44.58	8.33	15.0	0.589	0.613	1.042	0.583	0.990	0.613	1.042
11	44.58	9.00	15.0	0.616	0.649	1.054	0.613	0.995	0.649	1.053
12	44.58	9.67	15.0	0.642	0.683	1.064	0.642	1.000	0.683	1.064
13	44.58	10.33	15.0	0.671	0.717	1.069	0.671	1.000	0.717	1.069
14	44.58	11.00	15.0	0.740	0.750	1.014	0.699	0.944	0.750	1.014
15	44.58	8.75	15.0	0.591	0.636	1.075	0.602	1.018	0.635	1.075
16	44.58	9.25	15.0	0.615	0.662	1.076	0.624	1.014	0.662	1.076
17	44.58	9.75	15.0	0.640	0.687	1.075	0.646	1.009	0.687	1.074
18	44.58	10.25	15.0	0.665	0.713	1.072	0.667	1.003	0.713	1.072
19	39.58	9.67	12.0	0.663	0.684	1.033	0.653	0.985	0.684	1.033
20	39.58	9.67	13.5	0.671	0.695	1.034	0.664	0.988	0.695	1.034
21	39.58	9.67	15.0	0.680	0.704	1.035	0.673	0.991	0.704	1.035
22	39.58	9.67	16.5	0.689	0.712	1.034	0.682	0.991	0.712	1.034
23	39.58	9.67	18.0	0.698	0.720	1.032	0.691	0.990	0.720	1.032
24	39.58	9.67	19.5	0.707	0.727	1.028	0.698	0.987	0.727	1.028
25	39.58	9.67	21.0	0.716	0.734	1.025	0.706	0.985	0.734	1.025
26	39.58	7.33	12.0	0.562	0.560	0.996	0.545	0.969	0.560	0.996
27	40.58	6.50	12.0	0.467	0.510	1.092	0.499	1.067	0.510	1.091
28	35.58	10.00	12.0	0.717	0.720	1.004	0.697	0.971	0.720	1.004
29	49.58	7.25	15.0	0.477	0.540	1.133	0.510	1.070	0.540	1.133
30	36.58	9.00	12.0	0.616	0.663	1.076	0.643	1.043	0.663	1.076
31	49.58	7.00	15.0	0.467	0.526	1.127	0.498	1.067	0.526	1.127
Median (50th Percentile)					–	1.0481	–	1.0004	–	1.0479
Lognormal Standard Deviation, β_D					–	0.0309	–	0.0271	–	0.0309

Table C.4. LDF Results for One-Lane-Loaded Moment in Exterior Beams.

Bridge Parameters				LDF Results and Ratios						
No.	*L* (ft)	*S* (ft)	*d* (in.)	FEM	AASHTO	AASHTO/ FEM	Fitted	Fitted/ FEM	Proposed	Proposed/ FEM
1	29.58	9.67	15.0	0.632	0.890	1.407	0.641	1.013	0.660	1.044
2	33.58	9.67	15.0	0.595	0.890	1.496	0.593	0.997	0.611	1.028
3	37.58	9.67	15.0	0.562	0.890	1.583	0.553	0.985	0.572	1.017
4	39.58	9.67	15.0	0.544	0.890	1.635	0.536	0.985	0.554	1.018
5	41.58	9.67	15.0	0.519	0.890	1.716	0.520	1.003	0.538	1.037
6	44.58	9.67	15.0	0.495	0.890	1.797	0.499	1.007	0.516	1.042
7	45.58	9.67	15.0	0.487	0.890	1.827	0.492	1.010	0.509	1.046
8	44.58	7.00	15.0	0.391	0.771	1.972	0.385	0.985	0.398	1.018
9	44.58	7.67	15.0	0.413	0.809	1.960	0.415	1.005	0.429	1.039
10	44.58	8.33	15.0	0.437	0.840	1.922	0.443	1.013	0.458	1.048
11	44.58	9.00	15.0	0.464	0.867	1.867	0.471	1.015	0.487	1.050
12	44.58	9.67	15.0	0.495	0.890	1.797	0.499	1.007	0.516	1.042
13	44.58	10.33	15.0	0.527	0.910	1.725	0.526	0.997	0.544	1.031
14	44.58	11.00	15.0	0.559	0.927	1.659	0.553	0.989	0.572	1.024
15	44.58	8.75	15.0	0.446	0.857	1.920	0.460	1.032	0.476	1.067
16	44.58	9.25	15.0	0.470	0.876	1.862	0.481	1.024	0.498	1.059
17	44.58	9.75	15.0	0.496	0.892	1.800	0.502	1.012	0.519	1.048
18	44.58	10.25	15.0	0.521	0.907	1.742	0.522	1.003	0.541	1.038
19	39.58	9.67	12.0	0.523	0.890	1.701	0.513	0.980	0.518	0.991
20	39.58	9.67	13.5	0.534	0.890	1.665	0.525	0.982	0.537	1.005
21	39.58	9.67	15.0	0.544	0.890	1.635	0.536	0.985	0.554	1.018
22	39.58	9.67	16.5	0.555	0.890	1.603	0.547	0.985	0.570	1.027
23	39.58	9.67	18.0	0.565	0.890	1.574	0.556	0.984	0.585	1.035
24	39.58	9.67	19.5	0.575	0.890	1.546	0.565	0.982	0.599	1.042
25	39.58	9.67	21.0	0.585	0.890	1.520	0.574	0.980	0.613	1.047
26	39.58	7.33	12.0	0.426	0.709	1.666	0.411	0.966	0.415	0.976
27	40.58	6.50	12.0	0.363	0.646	1.779	0.368	1.013	0.372	1.023
28	35.58	10.00	12.0	0.565	0.840	1.486	0.562	0.995	0.568	1.004
29	49.58	7.25	15.0	0.361	0.786	2.176	0.371	1.028	0.384	1.064
30	36.58	9.00	12.0	0.511	0.800	1.566	0.508	0.995	0.513	1.004
31	49.58	7.00	15.0	0.343	0.771	2.248	0.361	1.052	0.374	1.089
Median (50th Percentile)					–	1.7271	–	1.0002	–	1.0327
Lognormal Standard Deviation, β_D					–	0.1071	–	0.0182	–	0.0222

Table C.5. LDF Results for Multiple-Lane-Loaded Moment in Exterior Beams.

Bridge Parameters				LDF Results and Ratios						
No.	*L* (ft)	*S* (ft)	*d* (in.)	FEM	AASHTO	AASHTO/ FEM	Fitted	Fitted/ FEM	Proposed	Proposed/ FEM
1	29.58	9.67	15.0	0.663	0.801	1.207	0.663	0.999	0.673	1.014
2	33.58	9.67	15.0	0.651	0.776	1.191	0.644	0.989	0.656	1.007
3	37.58	9.67	15.0	0.638	0.754	1.182	0.629	0.985	0.641	1.005
4	39.58	9.67	15.0	0.630	0.744	1.182	0.621	0.986	0.635	1.007
5	41.58	9.67	15.0	0.620	0.735	1.186	0.615	0.992	0.629	1.014
6	44.58	9.67	15.0	0.608	0.723	1.188	0.605	0.995	0.620	1.019
7	45.58	9.67	15.0	0.603	0.719	1.191	0.602	0.998	0.617	1.023
8	44.58	7.00	15.0	0.515	0.572	1.111	0.501	0.972	0.511	0.992
9	44.58	7.67	15.0	0.531	0.611	1.150	0.528	0.994	0.539	1.015
10	44.58	8.33	15.0	0.553	0.649	1.173	0.555	1.002	0.567	1.025
11	44.58	9.00	15.0	0.579	0.686	1.186	0.580	1.003	0.594	1.026
12	44.58	9.67	15.0	0.608	0.723	1.189	0.605	0.996	0.620	1.020
13	44.58	10.33	15.0	0.640	0.758	1.186	0.629	0.984	0.645	1.008
14	44.58	11.00	15.0	0.672	0.794	1.182	0.653	0.973	0.670	0.997
15	44.58	8.75	15.0	0.550	0.672	1.223	0.571	1.038	0.584	1.062
16	44.58	9.25	15.0	0.575	0.700	1.217	0.590	1.025	0.604	1.049
17	44.58	9.75	15.0	0.602	0.727	1.208	0.608	1.011	0.623	1.035
18	44.58	10.25	15.0	0.628	0.754	1.200	0.627	0.997	0.642	1.022
19	39.58	9.67	12.0	0.620	0.724	1.167	0.611	0.985	0.621	1.001
20	39.58	9.67	13.5	0.626	0.735	1.174	0.617	0.986	0.628	1.004
21	39.58	9.67	15.0	0.630	0.744	1.182	0.621	0.986	0.635	1.007
22	39.58	9.67	16.5	0.635	0.753	1.187	0.626	0.986	0.641	1.010
23	39.58	9.67	18.0	0.639	0.762	1.192	0.630	0.986	0.646	1.012
24	39.58	9.67	19.5	0.643	0.769	1.197	0.634	0.986	0.652	1.014
25	39.58	9.67	21.0	0.647	0.776	1.201	0.637	0.985	0.656	1.015
26	39.58	7.33	12.0	0.512	0.593	1.158	0.519	1.015	0.526	1.027
27	40.58	6.50	12.0	0.448	0.540	1.205	0.481	1.074	0.487	1.087
28	35.58	10.00	12.0	0.630	0.762	1.209	0.638	1.013	0.647	1.027
29	49.58	7.25	15.0	0.469	0.571	1.218	0.499	1.065	0.511	1.089
30	36.58	9.00	12.0	0.576	0.701	1.216	0.596	1.035	0.604	1.048
31	49.58	7.00	15.0	0.447	0.557	1.245	0.489	1.093	0.500	1.118
Median (50th Percentile)					–	1.1901	–	1.0040	–	1.0254
Lognormal Standard Deviation, β_D					–	0.0205	–	0.0279	–	0.0269

Table C.6. LDF Results for One-Lane-Loaded Shear in Interior Beams.

Bridge Parameters				LDF Results and Ratios						
No.	*L* (ft)	*S* (ft)	*d* (in.)	FEM	AASHTO	AASHTO/ FEM	Fitted	Fitted/ FEM	Proposed	Proposed/ FEM
1	29.58	9.67	15.0	0.846	0.714	0.844	0.844	0.998	0.846	1.001
2	33.58	9.67	15.0	0.814	0.705	0.866	0.809	0.993	0.820	1.007
3	37.58	9.67	15.0	0.785	0.697	0.888	0.780	0.993	0.797	1.015
4	39.58	9.67	15.0	0.771	0.694	0.900	0.766	0.995	0.787	1.021
5	41.58	9.67	15.0	0.757	0.690	0.911	0.754	0.996	0.777	1.026
6	44.58	9.67	15.0	0.740	0.685	0.927	0.737	0.996	0.764	1.032
7	45.58	9.67	15.0	0.734	0.684	0.931	0.732	0.996	0.760	1.034
8	44.58	7.00	15.0	0.568	0.565	0.995	0.595	1.048	0.619	1.091
9	44.58	7.67	15.0	0.642	0.597	0.930	0.632	0.985	0.657	1.024
10	44.58	8.33	15.0	0.680	0.627	0.921	0.668	0.981	0.693	1.019
11	44.58	9.00	15.0	0.712	0.657	0.922	0.703	0.987	0.729	1.024
12	44.58	9.67	15.0	0.740	0.686	0.927	0.737	0.996	0.764	1.033
13	44.58	10.33	15.0	0.763	0.713	0.934	0.770	1.009	0.797	1.045
14	44.58	11.00	15.0	0.785	0.741	0.944	0.803	1.023	0.831	1.058
15	44.58	8.75	15.0	0.696	0.646	0.928	0.690	0.991	0.716	1.029
16	44.58	9.25	15.0	0.719	0.668	0.928	0.716	0.995	0.742	1.032
17	44.58	9.75	15.0	0.735	0.689	0.938	0.741	1.009	0.768	1.046
18	44.58	10.25	15.0	0.753	0.710	0.942	0.766	1.017	0.793	1.053
19	39.58	9.67	12.0	0.738	0.678	0.919	0.733	0.993	0.744	1.008
20	39.58	9.67	13.5	0.755	0.686	0.909	0.751	0.994	0.766	1.015
21	39.58	9.67	15.0	0.771	0.694	0.900	0.766	0.995	0.787	1.021
22	39.58	9.67	16.5	0.786	0.700	0.891	0.781	0.994	0.806	1.026
23	39.58	9.67	18.0	0.800	0.706	0.883	0.794	0.993	0.824	1.030
24	39.58	9.67	19.5	0.812	0.712	0.877	0.807	0.994	0.840	1.035
25	39.58	9.67	21.0	0.823	0.717	0.871	0.819	0.994	0.856	1.039
26	39.58	7.33	12.0	0.624	0.575	0.920	0.611	0.978	0.622	0.996
27	40.58	6.50	12.0	0.529	0.533	1.009	0.559	1.058	0.571	1.081
28	35.58	10.00	12.0	0.777	0.700	0.900	0.777	1.000	0.781	1.005
29	49.58	7.25	15.0	0.579	0.571	0.985	0.588	1.015	0.617	1.065
30	36.58	9.00	12.0	0.728	0.655	0.899	0.718	0.986	0.724	0.995
31	49.58	7.00	15.0	0.527	0.559	1.061	0.575	1.091	0.603	1.145
Median (50th Percentile)					–	0.9217	–	1.0028	–	1.0334
Lognormal Standard Deviation, β_D					–	0.0455	–	0.0226	–	0.0283

Table C.7. LDF Results for Multiple-Lane-Loaded Shear in Interior Beams.

Bridge Parameters				LDF Results and Ratios						
No.	*L* (ft)	*S* (ft)	*d* (in.)	FEM	AASHTO	AASHTO/ FEM	Fitted	Fitted/ FEM	Proposed	Proposed/ FEM
1	29.58	9.67	15.0	0.961	0.902	0.939	0.949	0.988	0.979	1.018
2	33.58	9.67	15.0	0.935	0.891	0.953	0.922	0.986	0.954	1.021
3	37.58	9.67	15.0	0.910	0.881	0.968	0.898	0.986	0.933	1.025
4	39.58	9.67	15.0	0.899	0.877	0.975	0.887	0.986	0.923	1.027
5	41.58	9.67	15.0	0.888	0.872	0.982	0.877	0.987	0.914	1.029
6	44.58	9.67	15.0	0.873	0.866	0.992	0.863	0.988	0.902	1.032
7	45.58	9.67	15.0	0.870	0.864	0.994	0.858	0.987	0.898	1.032
8	44.58	7.00	15.0	0.639	0.669	1.047	0.638	0.999	0.674	1.055
9	44.58	7.67	15.0	0.667	0.720	1.079	0.695	1.041	0.732	1.097
10	44.58	8.33	15.0	0.768	0.769	1.002	0.751	0.978	0.789	1.027
11	44.58	9.00	15.0	0.827	0.818	0.989	0.807	0.975	0.845	1.022
12	44.58	9.67	15.0	0.873	0.866	0.992	0.863	0.988	0.902	1.033
13	44.58	10.33	15.0	0.916	0.913	0.998	0.918	1.002	0.957	1.045
14	44.58	11.00	15.0	0.957	0.961	1.003	0.973	1.017	1.013	1.058
15	44.58	8.75	15.0	0.798	0.800	1.002	0.786	0.985	0.824	1.033
16	44.58	9.25	15.0	0.839	0.836	0.997	0.828	0.987	0.867	1.033
17	44.58	9.75	15.0	0.869	0.872	1.003	0.870	1.000	0.909	1.045
18	44.58	10.25	15.0	0.902	0.908	1.007	0.911	1.010	0.950	1.054
19	39.58	9.67	12.0	0.868	0.857	0.988	0.856	0.986	0.883	1.017
20	39.58	9.67	13.5	0.884	0.867	0.981	0.872	0.986	0.904	1.023
21	39.58	9.67	15.0	0.899	0.877	0.975	0.887	0.986	0.923	1.027
22	39.58	9.67	16.5	0.913	0.885	0.969	0.901	0.986	0.941	1.030
23	39.58	9.67	18.0	0.926	0.893	0.964	0.913	0.986	0.958	1.034
24	39.58	9.67	19.5	0.939	0.900	0.959	0.925	0.986	0.973	1.037
25	39.58	9.67	21.0	0.950	0.907	0.954	0.937	0.986	0.988	1.040
26	39.58	7.33	12.0	0.676	0.687	1.017	0.661	0.978	0.689	1.019
27	40.58	6.50	12.0	0.545	0.622	1.142	0.587	1.077	0.615	1.128
28	35.58	10.00	12.0	0.920	0.890	0.968	0.905	0.984	0.930	1.011
29	49.58	7.25	15.0	0.593	0.681	1.148	0.643	1.085	0.681	1.149
30	36.58	9.00	12.0	0.830	0.816	0.983	0.815	0.982	0.841	1.013
31	49.58	7.00	15.0	0.547	0.662	1.211	0.623	1.139	0.660	1.207
Median (50th Percentile)					–	1.0041	–	1.0006	–	1.0450
Lognormal Standard Deviation, β_D					–	0.0563	–	0.0342	–	0.0388

Table C.8. LDF Results for One-Lane-Loaded Shear in Exterior Beams.

Bridge Parameters				LDF Results and Ratios						
No.	*L* (ft)	*S* (ft)	*d* (in.)	FEM	AASHTO	AASHTO/ FEM	Fitted	Fitted/ FEM	Proposed	Proposed/ FEM
1	29.58	9.67	15.0	0.713	0.890	1.247	0.703	0.986	0.712	0.999
2	33.58	9.67	15.0	0.689	0.890	1.292	0.700	1.017	0.712	1.034
3	37.58	9.67	15.0	0.702	0.890	1.267	0.698	0.994	0.712	1.015
4	39.58	9.67	15.0	0.699	0.890	1.272	0.696	0.996	0.712	1.019
5	41.58	9.67	15.0	0.696	0.890	1.278	0.695	0.998	0.712	1.023
6	44.58	9.67	15.0	0.692	0.890	1.286	0.694	1.002	0.712	1.029
7	45.58	9.67	15.0	0.700	0.890	1.271	0.693	0.990	0.712	1.017
8	44.58	7.00	15.0	0.560	0.771	1.377	0.556	0.993	0.568	1.014
9	44.58	7.67	15.0	0.604	0.809	1.339	0.592	0.980	0.606	1.003
10	44.58	8.33	15.0	0.633	0.840	1.326	0.626	0.989	0.642	1.013
11	44.58	9.00	15.0	0.659	0.867	1.316	0.660	1.003	0.677	1.029
12	44.58	9.67	15.0	0.692	0.890	1.286	0.694	1.003	0.712	1.029
13	44.58	10.33	15.0	0.734	0.910	1.238	0.726	0.989	0.746	1.016
14	44.58	11.00	15.0	0.771	0.927	1.202	0.758	0.983	0.780	1.011
15	44.58	8.75	15.0	0.648	0.857	1.323	0.648	1.000	0.664	1.025
16	44.58	9.25	15.0	0.675	0.876	1.298	0.673	0.998	0.690	1.024
17	44.58	9.75	15.0	0.700	0.892	1.275	0.698	0.997	0.716	1.024
18	44.58	10.25	15.0	0.732	0.907	1.240	0.722	0.987	0.742	1.014
19	39.58	9.67	12.0	0.688	0.890	1.293	0.686	0.997	0.712	1.035
20	39.58	9.67	13.5	0.694	0.890	1.281	0.692	0.996	0.712	1.026
21	39.58	9.67	15.0	0.699	0.890	1.272	0.696	0.996	0.712	1.019
22	39.58	9.67	16.5	0.704	0.890	1.265	0.701	0.996	0.712	1.012
23	39.58	9.67	18.0	0.708	0.890	1.257	0.705	0.996	0.712	1.006
24	39.58	9.67	19.5	0.711	0.890	1.251	0.709	0.996	0.712	1.001
25	39.58	9.67	21.0	0.714	0.890	1.245	0.712	0.997	0.712	0.997
26	39.58	7.33	12.0	0.563	0.709	1.260	0.568	1.008	0.587	1.043
27	40.58	6.50	12.0	0.527	0.646	1.226	0.522	0.990	0.539	1.023
28	35.58	10.00	12.0	0.659	0.840	1.274	0.705	1.069	0.729	1.106
29	49.58	7.25	15.0	0.571	0.786	1.376	0.567	0.993	0.582	1.019
30	36.58	9.00	12.0	0.625	0.800	1.279	0.655	1.047	0.677	1.083
31	49.58	7.00	15.0	0.542	0.771	1.424	0.554	1.022	0.568	1.049
Median (50th Percentile)					–	1.2843	–	1.0001	–	1.0241
Lognormal Standard Deviation, β_D					–	0.0351	–	0.0173	–	0.0211

Table C.9. LDF Results for Multiple-Lane-Loaded Shear in Exterior Beams.

Bridge Parameters				LDF Results and Ratios						
No.	*L* (ft)	*S* (ft)	*d* (in.)	FEM	AASHTO	AASHTO/ FEM	Fitted	Fitted/ FEM	Proposed	Proposed/ FEM
1	29.58	9.67	15.0	0.627	0.948	1.512	0.622	0.992	0.667	1.064
2	33.58	9.67	15.0	0.631	0.936	1.482	0.627	0.993	0.667	1.056
3	37.58	9.67	15.0	0.635	0.925	1.457	0.632	0.994	0.667	1.050
4	39.58	9.67	15.0	0.637	0.920	1.445	0.634	0.995	0.667	1.047
5	41.58	9.67	15.0	0.639	0.916	1.434	0.636	0.996	0.667	1.044
6	44.58	9.67	15.0	0.640	0.910	1.420	0.639	0.997	0.667	1.041
7	45.58	9.67	15.0	0.649	0.908	1.399	0.640	0.986	0.667	1.028
8	44.58	7.00	15.0	0.549	0.703	1.279	0.530	0.966	0.549	1.000
9	44.58	7.67	15.0	0.569	0.756	1.329	0.559	0.983	0.580	1.020
10	44.58	8.33	15.0	0.591	0.807	1.366	0.586	0.992	0.610	1.031
11	44.58	9.00	15.0	0.611	0.859	1.405	0.613	1.003	0.639	1.045
12	44.58	9.67	15.0	0.640	0.910	1.420	0.639	0.997	0.667	1.041
13	44.58	10.33	15.0	0.679	0.959	1.413	0.664	0.978	0.694	1.022
14	44.58	11.00	15.0	0.715	1.009	1.411	0.688	0.962	0.720	1.008
15	44.58	8.75	15.0	0.598	0.840	1.405	0.603	1.009	0.628	1.051
16	44.58	9.25	15.0	0.620	0.878	1.416	0.623	1.004	0.649	1.047
17	44.58	9.75	15.0	0.644	0.916	1.422	0.642	0.997	0.670	1.041
18	44.58	10.25	15.0	0.673	0.953	1.417	0.661	0.982	0.691	1.027
19	39.58	9.67	12.0	0.641	0.900	1.405	0.638	0.996	0.667	1.040
20	39.58	9.67	13.5	0.639	0.911	1.425	0.636	0.995	0.667	1.043
21	39.58	9.67	15.0	0.637	0.920	1.445	0.634	0.995	0.667	1.047
22	39.58	9.67	16.5	0.635	0.929	1.464	0.632	0.995	0.667	1.050
23	39.58	9.67	18.0	0.633	0.937	1.481	0.630	0.995	0.667	1.053
24	39.58	9.67	19.5	0.631	0.945	1.497	0.628	0.996	0.667	1.056
25	39.58	9.67	21.0	0.629	0.952	1.512	0.627	0.996	0.667	1.059
26	39.58	7.33	12.0	0.527	0.722	1.369	0.544	1.033	0.565	1.072
27	40.58	6.50	12.0	0.496	0.654	1.317	0.509	1.025	0.525	1.059
28	35.58	10.00	12.0	0.604	0.935	1.548	0.646	1.070	0.680	1.126
29	49.58	7.25	15.0	0.542	0.715	1.320	0.545	1.006	0.561	1.036
30	36.58	9.00	12.0	0.572	0.857	1.497	0.609	1.065	0.639	1.116
31	49.58	7.00	15.0	0.523	0.695	1.330	0.534	1.022	0.549	1.051
Median (50th Percentile)					–	1.4194	–	1.0002	–	1.0472
Lognormal Standard Deviation, β_D					–	0.0443	–	0.0222	–	0.0232